CRANFIELD UNIVERSITY

Jonathan I Broadley

The Control of Trailing Edge Separation on Highly Swept Wings using Vortex Generators

1998

College of Aeronautics

Total Technology PhD

CRANFIELD UNIVERSITY

College of Aeronautics

Flow Control and Prediction Technology Group

Total Technology PhD

Academic Year 1997-8

Jonathan I Broadley

The Control of Trailing Edge Separation on Highly Swept Wings using Vortex Generators

Supervisor: Dr K. P. Garry

October 1998

Acknowledgements

The author wishes to thank the workshop staff and lab technicians at Cranfield University for manufacturing the experimental apparatus required for the wind tunnel tests and their assistance in solving many of the problems encountered in research projects; Dr Pat Ashill and Mr John Fulker of the DERA (Bedford) for their assistance with the experimental programme and aerodynamic expertise; Mr Andy Shires for his assistance with the CFD computations; the DERA (Bedford) 13' x 9' wind tunnel technicians; Mr Garth Ward of the Cranfield School of Management for his assistance with the non-technical aspect of the thesis and Dr Kevin Garry of the College of Aeronautics for his guidance, ideas and support throughout.

Summary

The results from a series of low speed wind tunnel tests on two half model highly swept wings (a symmetrical aerofoil section and a highly cambered aerofoil section) are presented in order to examine the trailing edge flow separation mechanism and its development with wing sweep between 30° and 60°. The tests involved surface oil flow visualisation, smoke flow visualisation, surface static pressure and force balance measurements at streamwise chord Reynolds numbers from 1.5 x 10^5 to 5.2 x 10^6 and Mach number from 0.09 to 0.17. These results are used to assess two viscous-inviscid interaction CFD methods (BVGK and VFP) and two boundary layer methods (TAPERBL and WAKELAG) used to predict the flow over the highly cambered wing.

A parametric study using cropped delta vane vortex generators in a co-rotating array was conducted on the 40° swept wing to investigate the effect of vane chordwise position, vane orientation, vane height relative to the boundary layer thickness and vane spacing on the prevention of the trailing edge separation. The performance of these flow control devices is assessed in terms of changes in; the wing surface flowfield, lift curve slope and the lift-dependant drag factor. In addition comparisons are made between the clean wing and flow control wing measured pressure distributions.

The results and analysis show that the performance of the vortex generators is improved when the height of the vortex generator is approximately equal to that of the local boundary layer thickness and when the vane angular deflection to the local upstream flow direction is between 14° and 21°. The performance is also seen to depend on the vanes position ahead of separation and on the adverse pressure gradient to be restored and may also depend on a vane spacing made non-dimensional on the wing normal chord rather than the vane height.

Similar performance improvements are observed with the wing swept to 50° using the positioning guidelines from this optimisation study. The performance of concave slats, canted cropped delta vanes, 'bent' wires and sub-boundary layer wires as vortex generating devices are seen to be not as effective as upright cropped delta vane vortex generators.

To assist in the interpretation of the parametric vortex generator study a low speed wind tunnel technique is developed using shear stress sensitive liquid crystals to investigate the downstream development of vortices from cropped delta vane vortex generators. The results show that:-

i) submerged vortices have less influence on the surface flow with downstream distance than vortices closer to the edge of the boundary layer, and
ii) the primary increase in skin friction arises in the flow adjacent to the upflow side of the vortex. This area increases with vortex size.

The results from this research programme are finally shown to be applicable in two market areas. The first is as a performance improvement on current highly swept winged military aircraft and the second is as flight controls on future aircraft from making the vortex generating devices active. The possible customers in these two areas are identified and marketing strategies developed for each case.

Contents

List of Tables

List of Figures

Notation

A	-	aspect ratio
A_T	-	wind tunnel working section cross section area
C_D	-	drag coefficient
C_{Do}	-	zero - lift drag coefficient
C_L	-	lift coefficient
C_p	-	pressure coefficient
C_q	-	rolling moment coefficient
C_m	-	pitching moment coefficient
C_n	-	yawing moment coefficient
C_f	-	skin friction coefficient
C_{fo}	-	skin friction coefficient for smooth wall
CFD	-	Computational Fluid Dynamics
D	-	drag force, vortex generator spacing
DERA	-	Defence Evaluation and Research Agency
F	-	force on load cell
K	-	lift dependent drag factor = $(C_D - C_{Do})\pi A/C_L^2$
K_o	-	lift dependent drag factor of wing without flow control devices
L	-	lift force
LC	-	liquid crystal
M	-	Mach number
MOD	-	Ministry of Defence
N	-	Newton
Nm	-	Newton metre
PC	-	Personal Computer
PM	-	pitching moment
PT	-	Preston tube
Re_c	-	Reynolds number based on streamwise chord
RM	-	rolling moment
S	-	wing planform area of half wing
TR	-	taper ratio
V	-	tunnel speed
V_{max}	-	maximum freestream speed
YM	-	yawing moment
b	-	wing semi-span
c	-	wing streamwise chord
c_o	-	wing normal chord
c_v	-	vortex generator root chord
d	-	wire diameter, depth of concave slats, Preston tube depth
h	-	vane height
h_w	-	2.5" x 2.5" transonic wind tunnel working section height
k	-	wind tunnel calibration constant
m	-	vortex generator tip chord
p	-	static pressure in isentropic flow equation
p_t	-	total pressure in isentropic flow equation

q	-	dynamic pressure
s	-	seconds
t	-	wing maximum thickness
x^*	-	Preston tube function
y^*	-	Preston tube function
x_m	-	moment reference position in x axis
y_m	-	moment reference position in y axis
x_v	-	vortex generator chordwise position
x	-	coordinate in freestream direction
y	-	coordinate in spanwise direction
z	-	coordinate normal to freestream and spanwise direction
α	-	wing angle of incidence
α_c	-	local freestream flow direction
α_v	-	vortex generator orientation relative to freestream (positive = toed out)
β	-	Prandtl-Glauert compressibility correction = $(1-M^2)^{1/2}$
β_c	-	difference in surface to local freestream flow direction (twist) from CFD
γ	-	ratio of specific heats (1.4 for air at standard conditions)
δ	-	boundary layer thickness
δ^*	-	boundary layer displacement thickness
ρ	-	density of air
τ_w	-	wall shear stress
Λ	-	wing sweep angle
ν	-	kinematic viscosity
η	-	spanwise position = y/b
ε	-	blockage correction = $\varepsilon_s + \varepsilon_w$
ε_s	-	solid blockage correction
ε_w	-	wake blockage correction
ω	-	model volume
ΔC_A	-	correction to force and moment coefficients
ΔC_p	-	correction to pressure coefficient
ΔK	-	lift dependent drag difference = $(K-K_o)/K_o$
ΔM	-	correction to Mach number
Δp	-	pressure difference
$\Delta\alpha$	-	correction to angle of incidence

1. Introduction

1.1 General outlook

For the foreseeable future, weapons will be delivered on to surface targets from airborne platforms. The next generation of combat aircraft to perform these tasks will need to combine stealth with agility and long range, requiring wing sweeps of 40° to 50° with highly swept trailing edges. From an aerodynamic standpoint these configurations represent a high risk since the flows are more complex than those on wings with low sweep angles (less than approximately 30°), being susceptible to scale or Reynolds number effects and prone to three-dimensional boundary layer separation on the upper surface at low speeds or high angles of incidence. The likelihood of this type of separation increases if trailing edge flaps are deployed or the wing camber is increased, since flow separation occurs in regions of adverse pressure gradient where the boundary layer has become sluggish. On a highly swept wing this is accompanied by large twist or crossflows in the boundary layer, leading to three-dimensional or 'ordinary' separations[1]. These separations increase drag significantly and degrade buffet characteristics of the aircraft. Since wing efficiency governs the combat performance of aircraft, any improvements in delaying the onset of separation will lead to significant reductions in aircraft drag and improved buffet performance.

At present the full scale or flight characteristics of these wing flows cannot be predicted confidently by either CFD methods or from wind tunnel tests since the nature of the flowfield, the separation mechanisms and the effects of changes in wing sweep and scale are not understood in sufficient detail. With an understanding of these wing flows and separation mechanisms, methods to control and prevent these separations can be sought which may be used to avoid costly and extensive reshaping of the wing.

There are several methods that have been used to modify the boundary layer upstream of the separation position on wings such that the boundary layer can overcome greater adverse pressure gradients. These methods include:-

i) introducing higher energy fluid elements into the boundary layer from blowing through a slot to produce a boundary layer with a fuller profile which is more robust than that upstream of the slot;

ii) removal of the decelerated fluid elements from the inner region of the boundary layer, before they cause separation, by boundary layer suction through a slot or a porous surface. This allows a new boundary layer with a velocity distribution capable of surviving the adverse pressure gradient to form downstream of the suction region; and

iii) re-energising the sluggish boundary layer air through mixing with the more energetic air of the freestream using a mixing device placed in the flow. This mixing is usually accomplished through the use of vortices, produced locally in the boundary layer, from conventional vane type vortex generators or from air jets.

1.2 Brief summary of the literature search results (Section 2)

Of these methods, conventional vane type vortex generators have been used on aircraft, with low wing sweep angles, to prevent shock induced separation, increase aileron and flap performance and to increase the buffet boundary. Flight and wind tunnel tests have identified several useful design parameters for the correct positioning and design (size and shape) of vortex generators for effective separation control on these wings. More recently, several different mixing devices, including some smaller sub-boundary layer mixing devices, have been studied.

On highly swept wings, fences have been used to prevent or reduce the natural crossflow out towards the wing tip. Pearcey[2] suggests that a co-rotating array of vortex generators arranged to generate vortices to oppose these crossflows would also be able to prevent separation. However, it has not been shown that these crossflows and the associated flow separation in the trailing edge region can be controlled using conventional vane type vortex generators or sub-boundary layer mixing devices. Similarly, if these devices are capable of controlling these complex three-dimensional separations and crossflows, their positioning may require some different guidelines than those already established for their application on unswept or wings of low sweep angle.

Improvements in experimental techniques and data analysis have enabled investigations of the downstream development and interactions of a single vortex and arrays of vortices to give a better understanding of how these mixing devices work and have allowed detailed flow models to be developed. However, the development of a single vortex or array of vortices in a three-dimensional boundary layer with an adverse pressure gradient is not well understood; neither is the effect that vortex generators have locally on the surface skin friction and how this changes with the boundary layer structure. A better understanding of these phenomena may ease finding an optimum arrangement for controlling the strong crossflows and preventing the associated flow separation on highly swept wings.

Before flow control devices can be positioned on highly swept wings the nature of both the flow and the separation must be understood. Previous work on swept wings has concentrated mainly on the overall aerodynamic properties, rather than the actual flow development, with fences being used to prevent the inherent spanwise crossflow towards the wing tip. An understanding of the nature of the flow and the type of separation mechanisms involved will enable validations to be made of current CFD methods used to calculate these flows and enable improvements to be made to them. At present the current CFD methods are either two-dimensional with the results translated to simulate a three-dimensional flow or three-dimensional where the complex nature of the flow separations are not modelled correctly.

1.3 Research aims

These deficiencies will only be resolved through research aimed at developing an understanding of complex wing flows through exploring experimentally the fundamental mechanisms of highly swept wing flows and methods of controlling and

preventing the associated flow separations. This thesis contains a programme of research investigating these highly swept wing flows, the nature of the associated flow separation and the use of vortex generators to control these separations. The research also forms part of a larger research project at DERA Bedford concerned with future combat aircraft wing flows funded by the Ministry of Defence, Figure 1-1.

1.4 Thesis overview

The thesis consists of wind tunnel and computational investigations into the low subsonic flow characteristics of highly swept wings (Λ = 30° to 60°) and the use of vortex generators to control the associated flow separations over the upper surface in the region of the trailing edge.

Experimental wind tunnel investigations are performed on two half model wings in two different wind tunnels (Cranfield University and DERA Bedford) to determine that the nature of the wing flows are quite general and independent of Reynolds number and wing section. The smoke flow visualisations in the Cranfield University test are used to determine the separation mechanism and to assist in the interpretation of the oil flow visualisation results from the larger swept wing wind tunnel investigation at DERA Bedford.

Viscous-inviscid interaction computational techniques are used to gain an understanding of the flow over the DERA swept wing before wind tunnel testing. The results from these computational methods are assessed against the experimental results and their limitations discussed.

The flow separations observed in the wind tunnel tests produce large suctions over the rear of the wing section resulting in large drag increments. The separations are also free to move on the smooth surface. This movement of the separation position may cause problems with buffeting at:-

1) transonic speeds when separation is caused by a shock wave which is free to move over the surface;
2) manoeuvre conditions when a flap is deflected;

which can result in a wing dropping action which can severely limit the performance of an aircraft and cause structural damage to the airframe. Pearcey[2] suggests that it should be possible to control these type of flow separations with a co-rotating array of vortex generators correctly positioned. However, vortex generators have not been used in this way before and so design rules for their performance are not available. A parametric study is therefore performed on the DERA wing, swept 40°, using conventional vane type vortex generators in co-rotating arrays to investigate the effect of:-

1) chordwise position;
2) vane size;
3) vane orientation; and
4) spacing (or number per unit length);

on separation control. This enables design guidelines for the positioning of effective configurations to be determined and compared to those previously known for use on unswept or wings of low sweep angle. These new design guidelines are verified on the DERA wing swept 50°.

The consideration of stealth aspects is also considered and vortex generating devices of lower radar cross section, including sub-boundary layer wires, are investigated on the DERA wing swept at 40°.

The interpretation of the flow control results is assisted from a wind tunnel investigation of the downstream development of vortices from various height vortex generators in a known boundary layer using a new shear stress sensitive liquid crystal technique. It is shown that vortices from shorter vortex generators have a reduced effectiveness with downstream distance than larger vortices from taller vortex generators and that the taller vortex generators produce a greater drag increment.

The thesis is therefore split into several sections. Section 2 contains a review of the available literature relevant to the topics discussed above:-

2.1 Swept wing flows and separation mechanisms;
2.2 Vortex generators; and
2.3 The measurement of skin friction.

Section 3 contains a description of the experimental facilities used and the wind tunnel models. Section 4 contains the test procedure and a summary of the computational methods used for predicting wing flows. Section 5 contains all of the results and analysis from the wind tunnel investigations and computational calculations. Section 6 contains a detailed discussion of these results. Section 7 contains a non-technical discussion to satisfy the Total Technology aspect of this thesis. This section utilises Project Management techniques to identify the different elements from the research project that will be combined together to produce the thesis and ensure that the project finishes on time. The application of the research results to existing aircraft and the development of the research for use on future aircraft is also discussed and potential customers are identified together with a possible marketing strategy for exploiting the research results. Section 8 contains the conclusions obtained from this research project and Section 9 highlights areas requiring further study.

2. Overview

This overview is divided into three sections to review the available literature relevant to the objectives of this thesis (Section 1). The three sections are:-

i) swept wing flows and separation mechanisms;
ii) vortex generators; and
iii) the measurement of skin friction.

2.1 Swept wing flows and separation mechanisms

2.1.1 The need for swept wings and the limitations of 2D theories (1940 - 1955)

Swept wings initially became of interest towards the end of the Second World War with the development of the jet engine for use in aircraft. With these new engines much higher speeds could be attained and, as the transonic region was approached and subsequently surpassed, the benefits of sweeping the wings, applying 'area rule' to the fuselage and developing super critical wing sections became apparent for sustained high speed flight. At this time though, the aerodynamics of swept wings were not well understood although, the effect of sweep on the boundary layer and separation were appreciated. Jones[3] describes the effect that wing sweep has on the pressure distribution and the subsequent crossflow this causes in the boundary layer leading to flow separation. This has come to be called 'three-dimensional separation'. Jones also shows that calculating the lift on highly swept wings from two-dimensional theory transformed into three dimensions is not an accurate method, since the nature of the flow on a highly swept wing is very different to that on an unswept wing or aerofoil for which the theory has been devised. The existing theories for calculating two-dimensional flows, such as Prandtl's laminar boundary layer theory, were also extended to three dimensions by Sears[4], but due to insufficient knowledge of turbulent boundary layers and their modelling the real flows could not be determined.

2.1.2 Wind tunnel studies (1950 - 1975)

To overcome these deficiencies and gain a better knowledge of factors affecting the aerodynamic performance of swept wings several studies were undertaken, predominantly at NACA[5-7] and RAE[8-11], during the 1950's. These studies focused on measuring pressure distributions and aerodynamic forces and moments, predominantly at low speed, on swept wings to assess the effect; aspect ratio, taper ratio, wing sweep (swept forward or backwards), aerofoil section, wing tip and, to a limited extent, Reynolds number and Mach number have on the overall aerodynamic characteristics of swept wings. The effect of flaps were also investigated in this manner at Cranfield University[12].

At the same time, but to a lesser extent, studies investigating the development of the boundary layer and the surface flow on swept wings were also undertaken. Black[13],

investigated the development of the surface flow with incidence, using paraffin and lamp black, on a thin tapered wing section with a leading edge sweep angle of 44° and found some interesting flow patterns caused by the sharp leading edge. Emslie et al[14], using a similar flow visualisation technique and tufts, investigated the flow over a 45° swept wing with a thickness ratio of 0.10c and of aspect ratio 4 at a wind speed of approximately 40 m/s and a Re_c of 0.52 x 10^6. They also measured the boundary layer through a 2 hole Conrad yawmeter. This study showed the flow to be very complicated with separation beginning in the trailing edge region near the tip and spreading inboard with incidence. Unfortunately, this flowfield was further complicated due to a leading edge vortex produced in the root region which interfered with the trailing edge separation as incidence increased, making the development of the flow in the trailing edge region difficult to interpret. However, the yawmeter results showed the boundary layer to be thicker towards the trailing edge and out towards the wing tip than that on an unswept wing due to the spanwise flow along the trailing edge. These results also showed the angle between the boundary layer flow and the freestream flow to increase with distance from the leading edge, with incidence and with closeness to the wing surface. Brebner[15], and Brebner and Wyatt[16], also investigated the boundary layer on wings of 45° and 55° sweep through the use of a yawmeter, wake surveys and flow visualisation at low wind speeds. Their results similarly showed the boundary layer to be thicker in the trailing edge region than that of an unswept wing due to the crossflow induced by the wing sweep.

Winter and Moss[17] investigated the effects of a transition strip on trailing edge separation on a half model wing body combination of 55° sweep over a wide range of Reynolds number, $2x10^6$ to $27x10^6$, at Mach numbers from 0.55 to 0.8. The results showed that changes in Reynolds number did not produce any marked change in the pressure distributions, but the lift depended on the boundary layer thickness at the trailing edge. A thinner boundary layer thickness at the trailing edge, obtained either by; increasing Reynolds number or by the presence of the laminar flow, gave an increase in lift. Trailing edge separation was also eliminated by increasing the Reynolds number.

2.1.3 Separation mechanisms

During this time period two-dimensional separation mechanisms were investigated further, particularly the cause and nature of leading edge stall and of laminar separation bubbles[18], and extended theoretically to give possible separation mechanisms for some three-dimensional flows. These two-dimensional separation mechanisms and their extension to some possible three-dimensional flow situations are discussed by Küchemann[19-21] and Maskell[22] and several possible separation scenarios are illustrated, Figure 2-1.

2.1.4 Design methods for swept wings and later wind tunnel studies

The results from these separate research programmes enabled design methods to be developed for swept wings and better theoretical methods to be developed for

determining flows over swept wings without separation but including the effects of crossflows, streamline divergence and compressibility. Bagley[23], Brebner and Cooke[24], Cooke and Hall[25] and Tani[26] all contain useful summaries of these design methods, two-dimensional separation mechanisms and the development of three-dimensional boundary layer theories.

Since the initial interest in understanding the aerodynamic characteristics of swept wings and the factors that affect their performance in the 1950's, these flows have not been investigated further. Isolated wind tunnel studies have been performed since such as those of Woodward and Lean[27] in the early 1970's investigating the lift and stalling characteristics of a 35° sweptback wing with a constant spanwise pressure distribution at a Mach number of 0.8 and Re_c between 0.51 and 1.02 x 10^6. The flow visualisation results though are similar to observations made in the 1950's by Emslie et al[14] with a leading edge stall and a vortex originating at the root and spreading out over the wing with increasing incidence.

However, the theory for calculating three-dimensional flows has continued to be developed and a useful summary is given by Hall[28]. More recently Smith[29-31] and Green[32] et al have developed integral methods for predicting three-dimensional compressible turbulent boundary layers and wakes which, with the arrival of powerful workstations, have been incorporated into CFD methods at the RAE.

These CFD methods[33] can predict compressible two-dimensional flows over aerofoils very accurately and methods are being developed to predict three-dimensional flows over wings and wing body combinations with greater confidence. However these methods, being viscous-inviscid interaction solvers, have difficulty in predicting flows over highly swept wings where the flow involves strong shear layers, large crossflows and twist through the boundary layer. Peake et al[34] summarises this, with examples of three-dimensional flow separations on aircraft and missiles, by concluding that 'greater effort needs expending in predicting three-dimensional flows since there is no method of predicting growth, separation and roll up of three-dimensional turbulent boundary layers.' These improvements will only be achieved though research aimed at developing an understanding of complex wing flows and wing body flows through exploring experimentally the fundamental mechanisms of these types of flow.

2.2 Vortex generators

2.2.1 The principle of boundary layer control using vortex generators

The principle of boundary layer control by vortex generators is to increase the mixing between the external stream and the boundary layer through a vortex trailing longitudinally over the surface. Fluid particles with high momentum in the stream direction are swept in helical paths towards the surface to mix with and replace the retarded air at the surface which is swept out and away from the surface. The mean streamwise momentum of the fluid particles in the boundary layer is thus increased. This process is continuous and therefore the natural retardation and growth of the boundary

layer, caused by surface friction and adverse pressure gradients, is inhibited enabling the boundary layer to encounter greater adverse pressure gradients or stronger shock waves without separating.

This method of controlling the boundary layer was realised in the late 1930's and early 1940's which Taylor[35] first exploited through using vane type vortex generators to control the airflow in wind tunnel diffusers. However it was soon realised that they may also be used for controlling flow phenomena such as wing buffet and shock induced separation on aircraft which were flying faster and experiencing new flight conditions. It was also realised by Pearcey[2] that a co-rotating array of vortex generators suitably positioned may be used to control the crossflows and associated flow separation on swept wings. This early research was mainly carried out by NACA and consisted of a large number of flight tests at high subsonic speeds and testing of half aerofoil models and wings in wind tunnels.

2.2.2 NACA flight and wind tunnel studies

Flight tests proved successful in delaying shock induced separation to higher Mach numbers and lift coefficients[36] and improving the performance of the flap[37] on a North American Mustang P-51D and also in alleviating the wing dropping action caused by shock induced separation[38] on a North American F-86A-5. Wing vortex generators were also flight tested with limited success on a Douglas D-558-1 aircraft[39].

The wind tunnel tests during this period focused on similar vortex generators to those used in the flight tests[40-42] as well as other novel ideas for controlling separation such as wedge shaped bodies[43,44]. These wind tunnel tests investigated the effect on separation control of many more variables than was possible in the flight tests such as Mach number, chordwise location, spanwise extent, spacing, angular deflection and array type.

2.2.3 Other flight and wind tunnel studies

Concurrent with the NACA work, ARL[45-47], ARC[48] and the Canadian NAE[49] were also conducting low speed wind tunnel tests investigating the many different design parameters for array types and for the vortex generator / mixing device in both zero and adverse pressure gradients. Schubauer and Spangenberg[50] investigated several different mixing devices such as ramps, wedges, ploughs, scoops, twist interchangers, fins, domes and sinks (Figure 2-2). Similarly, flight testing with vortex generators was also being performed by Avro (Avro A707A Vulcan[51]), English Electric (Canberra P.R.Mk7[52]), the Canadian NAE (T-33[49] and the CF-100[53]), Armstrong-Whitworth (Sea Hawk FGA Mk 4[54]) and Hawker Siddeley (P.1127[55]) to control shock induced separations, improve the buffet boundary and to improve manoeuvrability.

2.2.4 Design guidelines

These flight test results show that various vortex generator configurations improve the flow characteristics on several different aircraft and indicate that the performance of an array of vortex generators will depend on how they are applied relative to the undesirable flow phenomena. In addition, the wind tunnel and flight tests have produced some useful design guidelines:-

1) Conventional vane type vortex generators were shown to have a smaller drag penalty than the other mixing devices even though these other devices were able to effectively control separation.

2) A normal flat plate vortex generator was not inferior to an aerofoil section vortex generator

3) A tapered vane was just as effective as a rectangular vane.

4) The effectiveness of the types of array was dependent upon parameters such as the spacing of the vortex generators, angle of the vortex generator to the local flow direction, the distance ahead of separation and the height of the vortex generator relative to the local boundary layer thickness.

These results enabled NAE Canada to develop a theoretical analysis[53], which agrees qualitatively with experiment, on the principles and design of vortex generator configurations. This effectiveness parameter is related to the transfer of momentum across surfaces parallel to the wall induced by the trailing vortex and is a function of vane height, boundary layer height, vane lift coefficient, aspect ratio, spacing and array type but is independent of the boundary layer velocity profile. Pearcey[2] provides a useful summary of the effects these parameters have on the effectiveness of various vortex generator arrays and these are summarised in the following paragraphs.

2.2.5 Co-rotating arrays

A co-rotating array consists of a series of vanes set at the same angle to the flow direction, Figure 2-3a, which produces a very stable array of vortices which maintain a fixed height above the surface up to 100 generator heights downstream. The stability and steady height results from the vertical velocity component induced at a particular vortex by all the other vortices and their images beneath the surface being zero, Figure 2-3b. However a velocity induced by the images in the surface causes a lateral displacement of the vortices which decreases as the vortices decay downstream resulting in a curved path. At the ends of the array the vortices are displaced vertically due to the non-uniformity of the induced velocities in these regions (towards the surface at one end and away from it at the other end) and several vortices spiral around one another and reduce the effectiveness. The strength of the vortex does not vary rapidly with incidence for low aspect ratio vanes and so the array is relatively insensitive to changes in the surface flow

direction. However, the effectiveness of this type of array is dependent upon the spacing of the adjacent vortices, Figure 2-3c. At separations less than about three times the vane height the low energy air being swept out on one side of each vortex is swept back into the surface again by the adjacent one which reduces the effectiveness of the array.

These properties of a co-rotating array should be effective in preventing the crossflow out towards the wing tip on highly swept wings. By orientating the vortex generators in the array to be toed out relative to the local flow direction an array of co-rotating vortices will be produced with a lateral displacement towards the wing root to oppose the natural flow towards the wing tip.

2.2.6 Counter-rotating arrays

A counter-rotating array consists of a series of vanes set alternately at positive and negative angles to the flow direction, Figure 2-4a, to produce counter-rotating pairs of vortices of equal strength at the same height above the surface. The effectiveness of a counter-rotating array is dependent on the spacing of the vanes since for the vortices to delay separation the boundary layer between alternate pairs of vortices is thinned with the air of low momentum being swept out between the intermediate pairs of vortices, Figure 2-4b. However, as the vortices develop downstream the centres of the vortices move together in pairs due to the lateral induced velocity being in opposite directions for adjacent vortices, Figure 2-4c, and after grouping together, move away from the surface due to the resultant induced velocity where they eventually decay. Also if the divergent pairs are closer together than the convergent pairs the motion of the vortices is initially towards the surface before moving laterally away due to the image vortex, which is then the nearest vortex, towards its convergent neighbour as before, Figure 2-4d. This movement of pairs of vortices away from the surface limits their range of effectiveness to approximately 20 generator heights downstream and therefore the downstream distance before they move away from the wall needs to coincide with separation. The paths of these vortices can be calculated for the full array and the image vortices from a method developed by Jones[56]. The positioning of a counter-rotating array therefore requires much more care than that of a co-rotating array.

2.2.7 Biplane or alternate pair arrays

A biplane array consists of a series of vane pairs set alternately at positive and negative angles to the flow direction, Figure 2-5a, to produce alternate divergent and convergent counter-rotating vortex pairs. The divergent pairs of vortices induce a downward velocity upon each other and move closer towards the surface before moving laterally away from each other, due to the effect of the image vortices, whilst the convergent pairs of vortices induce an upward velocity upon each other and move away from the surface. The effectiveness of a biplane array is therefore dependent on the relative spacing and size of the vanes. The divergent pairs of vortices move under the convergent pairs of vortices, Figure 2-5b, which improves the mixing since the air of low momentum removed by the divergent vortices is transported further into the freestream by the

convergent vortices above. This causes an improvement in effectiveness compared to that of a conventional counter-rotating array; however the magnitude of these improvements is small compared to the increase in drag from the extra vortex generators.

2.2.8 Tandem arrays

A tandem array consists of more than one row of vortex generators. This arrangement can increase the chordwise range of effectiveness of a counter-rotating array but has no influence on the effectiveness of a co-rotating array which are, in any case, relatively persistent with streamwise distance. The second row of vortex generators requires careful placing so as not to interfere with the first row. Any improvement in effectiveness through using a tandem array is at the expense of a significant increase in drag.

2.2.9 Other mixing devices and vortex boundary layer interactions

Since this initial period of development attention has been focused more on interactions between boundary layers and vortices and the downstream development of single and arrays of vortices than on their use to control flow separations. However, wind tunnel tests since these initial investigations have confirmed vane type vortex generators to be superior to other mixing devices[57] and co-rotating arrays to be effective at controlling separation over a greater range of flow conditions than counter-rotating arrays[58]. Spangler and Wells[59] also showed the form drag of the vortex generators not to be significant and that the overall skin friction increased even though, locally, the skin friction was both reduced and increased in the presence of the vortex. They also showed that vortices generated well inside the boundary layer affect the skin friction and velocity profile far downstream of the point of origin and that the average effect on skin friction depends only on the number of elements per unit length and not on the spacing.

More recently, improvements in measurement techniques (smoke-laser techniques, X-wire probes to measure mean flow and turbulence quantities, two-component laser velocimeters, Laser Doppler Anemometry) have enabled more detailed investigations of boundary layer and vortex interactions. These studies have included investigation of the interaction between a single longitudinal vortex and a separated boundary layer at subsonic[60-62] and transonic[63,64] speeds and of the downstream development of pairs and arrays of vortices in two-dimensional boundary layers[65-69]. However, the results only verify in more detail the results obtained from the earlier studies in the 1950's. The most recent studies have been of the development of vortices in three-dimensional turbulent boundary layers[70] where the vortices are found to decay more rapidly than in two-dimensional turbulent boundary layers due to diffusion in the crossflow plane.

2.2.10 Sub-boundary layer vortex generators

Vortex generator research has also taken a well defined second route with the switch from conventional vane type vortex generators to sub-boundary layer vortex generators.

These sub-boundary layer vortex generators, compared to conventional vane type vortex generators, offer reductions in radar cross section which are of importance to modern military aircraft and also have a reduced drag penalty. Many different types of sub-boundary layer vortex generators have been used[71-73] from small vane type vortex generators to thin wires, cylindrical rods, sharp concave slats, ramped cones, Wheeler doublets and wishbones which have been as small as 30% of the boundary layer height, Figure 2-6. These sub-boundary layer vortex generators have been successful in reducing boundary layer separation on a flap in the landing configuration[74], controlling a small separation bubble[75] and in controlling leading edge separation on a highly swept and cambered wing[76,77]. These studies have also shown that sub-boundary layer vortex generators can equal the performance of conventional vane type vortex generators in controlling turbulent boundary layer separation with the performance being dependent on a similar set of parameters to those of the conventional vane type arrays.

2.2.11 Passive and active flow control methods

More recently studies have been performed using several passive and active methods to control separation[72,73,78-80] and comparisons have been made between the performance of air jets and sub-boundary layer vortex generators. However, the complexity of these new techniques and the difficulties involved in obtaining a reliable and practical operating system will ensure that conventional vane type and sub-boundary layer vortex generators, due to their simplicity, ease of manufacture and application will be used on aircraft for the foreseeable future. A useful summary has been produced by ESDU[81] for the positioning of vortex generators for effective separation control and makes a good starting point for any vortex generator flow control study.

2.3 The measurement of skin friction

In most applications of fluid mechanics a knowledge of the drag created by fluid flowing over a solid surface is essential for understanding the aerodynamic performance of the body. Considerable effort over many years has therefore been devoted to developing techniques for measuring skin friction. This is a difficult quantity to measure, since the measurements need to be very localised to measure the force induced on a small portion of the model surface.

2.3.1 Techniques available

There are several techniques available[82] for determining the shear stress such as direct measurements using skin friction balances, inferring the skin friction from measuring the boundary layer velocity distribution or through using Preston tubes or other small obstacles positioned in the flow to determine the dynamic pressure at a known point in the boundary layer to again infer the shear stress. Unfortunately these techniques are not practical for measuring the detailed distribution of skin friction on wind tunnel models since they can only measure the shear stress at one point. They also require a knowledge

of the local flow direction and boundary layer conditions to enable them to be aligned properly and the correct calibration to be used. To build up a picture of the shear stress distribution over a model is therefore a very time consuming process and for many of the techniques is impractical as the apparatus required would disturb the true nature of the flowfield being studied.

Heated films, sublimation methods and oil flow techniques are alternative methods which do not physically affect the wind tunnel model being studied. Heated films though are very delicate and expensive and only measure the shear stress at one point. Hence, as with the devices mentioned above, a large number would be required. Furthermore, heated films determine the skin friction from the rate of heat loss from its surface which is a difficult quantity to determine accurately. This is the case because heat is lost to the surrounding material as well as to the air flow passing over it and in a long wind tunnel test, particularly at high subsonic and supersonic speeds, the model and tunnel temperature changes which also affects the results.

Sublimation methods determine the skin friction from the time taken for a material to evaporate or sublime from the surface. However, this method has its limitations since evaporation can also occur depending on the subliming material chosen. The skin friction is determined from measuring the depth of the material before and after the test run and the length of time over which the test ran. This requires stopping the wind tunnel at each chosen condition to take a measurement which is a very time consuming process. Oil flows can be used in much the same way as the sublimation technique. In this case the deformation in the oil is determined from interferometry methods and then the skin friction is determined from lubrication theory[83]. Unfortunately, the oil requires renewing for each test condition and measurement which again is a very time consuming process. However, modern day techniques can utilise interferometry interference patterns caused by the deformed oil to determine the magnitude and direction of the skin friction[84].

2.3.2 Technique desired

It is therefore desirable to use a technique for measuring shear stress which:-

i) is not localised;
ii) will show the flowfield in the area of interest;
iii) is independent of temperature;
iv) is easy to apply;
v) has a response which is reversible so that many measurements with a single application can be made; and
vi) which will also leave the flowfield unaltered.

Shear stress sensitive liquid crystals provide a possible answer to this problem since they can be easily painted on to the area of interest, they have a quick response time, they are independent of temperature, their response is reversible and the particles themselves are fine enough to show all the features of the shear stress without altering the flow structure.

2.3.3 Liquid crystals

Liquid crystals[85] are materials that exist between the crystalline and the liquid states and exhibit optical properties characteristic of a crystalline solid and mechanical properties characteristic of a liquid state. Certain liquid crystals react to shear forces by changing colour while others react to temperature. They do this by selectively reflecting the white light incident upon them, giving rise to the reflection of almost monochromatic colours which are dependent upon the angles of illumination and viewing. The wavelength of the reflected light varies with shear force by changing colour towards the blue end of the spectrum as the shear force increases. For the best visualisation it is necessary to view against a matt black background to absorb the unreflected light. The crystals can only reflect wavelengths that are present in the illuminating source and therefore, to obtain a wide range of colours, the source should have a wide spectral distribution with intense colours being obtained from using a high intensity source.

The earliest use of liquid crystals for the study of boundary layers was by Klein[86] at NASA Ames in the late 1960's who determined the suitability of temperature sensitive liquid crystals for showing boundary layer flow patterns, such as transition and shock location, at a Mach number of 1.98 and Reynolds number of 3.83×10^6 / ft. This enabled the whole surface and temperature gradients to be visualised which helped in the design and choice of materials for supersonic aircraft. Klein, together with Margozzi, were the first to devise an experimental apparatus[87,88] for the quantitative calibration of the optical response of liquid crystal substances to shear, temperature, pressure and viewing angle. They also discovered that stable liquid crystal substances could be manufactured that had a low sensitivity to temperature and a good shear response. Since this work there has been a limited interest in developing the technique further. Shear stress sensitive liquid crystals have been used principally as a flow visualisation technique to show transition, separation and shock locations[89-92] from low subsonic speeds to hypersonic speeds. These studies have outlined some problems in the use of liquid crystals concerning the lighting and viewing angles and in applying the liquid crystals to attain a good adhesion to the model surface when the wind is applied.

2.3.4 The colourless liquid crystal state

Other techniques using shear stress sensitive liquid crystals have also been developed to detect transition. Bonnet[93] describes a method whereby after application to the test surface the liquid crystals are driven back to the colourless state through gentle heating. Once the shear stress is applied the time taken for the liquid crystals to turn red is used to determine the shear stress at that particular point. Mee et al[94] successfully employed this method for detecting transition on a flat plate but, unfortunately, the liquid crystal coating can only be used once.

2.3.5 The reversible liquid crystal state

The liquid crystals in the reversible state is the only useful method for continuous visualisation of the surface shear stress as shown by Reda[95,96] who has studied the flow on oscillating aerofoil sections using liquid crystals. The development of this work to visualise the development of flow in an injector-driven supersonic wind tunnel[97] showed the colour changes of the liquid crystals to change with viewing angle and with shear stress direction. This response to a change in the shear stress direction led to further tests[98] with shear stress sensitive liquid crystals on a flat plate upon which a jet was blown tangentially and normal to the surface to investigate the response of the liquid crystals to shear stress direction. The results from these investigations showed that any shear vector with a component directed away from the observer exhibited a colour change response dependent on the magnitude of the shear. However any shear vector with a component directed towards the observer exhibited no colour change response. This liquid crystal colour play response to changes in the relative surface shear stress magnitude and the viewing angle between the observer and the shear vector were quantified and a method devised for determining the magnitude and direction of shear stresses. The method involves visualising the shear stress field using liquid crystals and recording images on several video cameras at known viewing angles and combining the results from each camera to determine the magnitude and direction of the shear stress.

This method has been verified using an impinging jet on a flat plate and oil drop interferometry[99] and an application of the method has been used to investigate the flow direction and shear stress magnitudes at transition and shock locations on a wing[100] in a wind tunnel using two cameras (one looking upstream and one looking downstream). These results demonstrated that, by combining the two sets of results, a picture of the flowfield around transition and the shock could be produced. However, more cameras and viewing angles are required to obtain a detailed picture of the flowfield which may not be practical in some wind tunnels and on some shapes of models. Also a method for accounting for different viewing angles due to changes in model shape is required if the method is not to be limited to flat or near flat surfaces where viewing angles and lighting angles are known.

3. Experimental Details

3.1 Swept wing test in the Weybridge low speed wind tunnel at Cranfield University

3.1.1 The Weybridge wind tunnel

The Weybridge wind tunnel is a closed return, open working section wind tunnel, powered by a 40 hp electric motor and having a jet diameter of 1.067m. It is equipped with two static pressure rings in the nozzle and settling chamber for the measurement of dynamic pressure in the working section to enable the wind speed in the working section to be calculated (Appendix I) and adjusted to the required speed.

3.1.2 Model description

An existing wooden half model 45° swept wing of constant chord and without twist has been modified at the root such that the sweep angle of the wing can be set to 30°, 40°, 50° or 60° by fitment of the appropriate root insert (manufactured from UREOL 5450, a resin based material). The wing tip cannot be changed and is only streamwise with the wing swept at 45°. The aerofoil section (normal to the wing generator) is symmetrical with a 16% thickness to chord ratio and is similar to a NACA 65 series aerofoil (Figure 3-1). Table 3-1 gives the relative wing dimensions for each sweep angle used. Transition was fixed at 5% chord on both the upper and lower surfaces with a wire of 0.35 mm diameter. The wire diameter was determined from a method used at DERA Bedford (Appendix V).

3.1.3 The balance and model arrangement

The balance is a 5 component strain gauge balance which measures lift force, drag force, pitching moment, yawing moment and rolling moment in wind axes. The balance is attached to the Weybridge overhead-balance frame above the wind tunnel working section such that it points downwards towards the centre of the working section. A sharp edged splitter plate prevents interference from flow around the balance with that of the model and also acts as a reflection plane for the wing. A fairing shields the balance from the wind tunnel jet (Figure 3-2).

The splitter plate is a 2.5 mm thick aluminium plate of width 915 mm and length 1830 mm with a sharp leading edge. The model is positioned on the centreline of the splitter plate 620 mm from the leading edge and is attached to the rotatable shaft of the balance through a circular hole of approximately 80 mm diameter in the splitter plate. The splitter plate is adjusted using bracing wires with turnscrews and cylindrical support rods such that it lies horizontal with minimum clearances between the model and balance mounting bracket to the splitter plate.

The angle of attack of the model is set via a rotatable shaft in the balance such that the balance orientation does not alter with model incidence so lift and drag are measured directly. The model alignment for 0° incidence is set normal to the plane of the tunnel nozzle. However geometric alignment does not ensure alignment to the air flow.

3.1.4 Data acquisition

The balance measures forces and moments as changes in milli-voltages. The signals are filtered through 10 Hz low-pass filters before being amplified by a gain of 1000. The 5 data channels from the balance and one channel from the tunnel speed transducer are fed through a Strawberry Tree Mini-16 data acquisition card into a PC computer where the data is averaged over 5 seconds on a Quicklog data acquisition system and recorded to disk.

3.1.5 Data reduction

A PC computer with EXCEL software corrects the data for any wind-off offsets. The corrected data is then converted into forces and moments, using the balance calibration matrix (Appendix II), and wind tunnel speed, using the wind tunnel calibration (Appendix I). The pitching moment is then adjusted such that it is taken about the quarter chord position at mid-span and the directions of the forces and moments corrected to conform to the chosen system, Figure 3-3. These forces and moments are then made non-dimensional to coefficient form by dividing by the working section dynamic pressure and the appropriate reference area and moment arms. Wind tunnel blockage corrections are not applied to the data as this was intended simply as an exploratory investigation into the nature of the flow on a swept wing.

3.2 Swept wing and vortex generator test in the 13' x 9' low speed wind tunnel at DERA Bedford

3.2.1 The 13' x 9' low speed wind tunnel

The 13' x 9' low speed wind tunnel facility is a continuous closed circuit, closed working section atmospheric tunnel with a minimum airspeed of 15m/s and a maximum airspeed of 91m/s. The settling chamber is octagonal in cross-section with a maximum breadth of 14m giving a contraction ratio of 16:1. The working section measures 13ft (3.96m) wide and 9ft (2.74m) tall and has corner fillets tapering slightly over the length of the working section to ensure a negligible static pressure gradient along the working section. The tunnel working section centre is the point midway between the walls and roof and floor at the mid-streamwise station. Models are tested at or near to this centre.

The drive fan, of 9.35m diameter, is powered by a 1144kW ac synchronous motor with an 11kV ac feed. The speed control allows the tunnel operators to select the desired speed and uses a relationship between the pressure in the working section and the

pressure in the settling chamber similar to that used for setting the wind speed in the Weybridge wind tunnel (Appendix I).

3.2.2 Model description

The aerofoil section (normal to the wing generator), Figure 3-4, has a 14% thickness/chord ratio and was designed (using established CFD methods) specifically to give a pressure distribution representative of flows at high subsonic speeds or at manoeuvre conditions, Figure 3-5. The significant rear camber produces a severe adverse pressure gradient over the rear of the upper surface similar to that of a shock at higher subsonic speeds or a flap deflection. This gradient causes the flow to separate in the trailing edge region. In addition, to ensure that the flow remains attached at high incidence over the forward part of the aerofoil, the nose is drooped.

The wing, Figure 3-6, is cylindrical with a chord of 0.61m and a semi-span of 1.83m at 0° sweep. The wing is capable of being swept aft from 0° to 60° in 5° intervals and has interchangeable tip sections to give streamwise tips at 30°, 45° and 60°. Table 3-2 gives the relative wing dimensions for each sweep angle used. A splitter plate, mounted horizontally 0.15m above the tunnel floor, prevents the tunnel floor boundary layer from interfering with the wing root flow and also acts as a reflection plane for the wing. This splitter plate is not attached to the wing, the space between the wing and the splitter plate being sealed with soft foam rubber such that no loads are transferred to the balance.

The wing has pressure tappings at 5 spanwise stations, with 36 and 16 static pressure holes on the upper and lower surfaces, respectively, at each station. The lines of pressure tappings are inclined at 45° to the leading edge such that they are almost streamwise at sweep angles of interest. The static-pressure holes are concentrated near the leading and trailing edges where pressure gradients are highest (Appendix IV).

Transition is fixed on both the upper and lower surfaces at 5% chord using grade 70 carborundum particles embedded in a 5 mm band of Araldite adhesive. The particle size was determined from a method used at DERA Bedford (Appendix V).

3.2.3 The half model balance and model arrangement

The half model balance is a four component mechanical balance which measures normal force, axial force, pitching moment and root bending moment. Half model wings connect to the balance via a root block, directly onto the balance, Figure 3-7. The root block is mounted on two longitudinal slides on the live platform of the balance, with block adjustment of around 1.8m available using the slides. The balance mounts directly onto the underside of the turntable in the tunnel floor and model incidence is achieved by rotating the turntable. The balance and model rotate together in pitch and therefore forces on the balance are measured in the model datum axes, which is different to the arrangement in the Weybridge tunnel.

3.2.4 Pressure measurement

A total of 7 x 48 port scanivalves, each containing a 5 psi differential pressure transducer, are fitted inside the model to minimise the amount of pressure tubing required to measure the 260 pressure positions on the model. Only 42 of the 48 ports are available for measurements, the other 6 ports being required for the reference or calibration pressures (settling chamber pressure (ports 1, 46), working section pressure (ports 2, 47) and calibration pressure (ports 3, 48)). The transducers are driven and scanned together under computer control, with a manual option to allow visual inspection of the outputs, and the meters read via a dedicated digital link.

The settling chamber pressure is used as a wind speed indicator during the off-line data reduction. The working section pressure is fed to the reference port of the transducer to provide the datum against which the other pressures are measured. The calibration pressure is produced by a differential precision pressure controller and is referenced to the working section pressure so that it tracks it by 1 psi to provide a gain input. Thus a gain factor (reading / pressure) for each transducer is calculated at each data point during data reduction and any transducer or instrumentation drifts are neutralised.

3.2.5 Data acquisition and reduction

3.2.5.1 On-line

On-line data acquisition is computer controlled by a DEC PDP 11/44 machine. The 4 channels of balance data are processed on-line in the form of non-dimensional coefficients in balance axes, body axes and stability (wind) axes with no account made for balance interactions or corrections for tunnel constraint and blockage. This process involves five steps:-

a. Isolating the net aerodynamic readings by subtracting readings measured at zero wind velocity.

b. The net aerodynamic loads are obtained from the net aerodynamic readings using a linear calibration that assumes no interactions between the four components.

c. Loads are expressed as non-dimensional coefficients in the balance axes by dividing by the working section dynamic pressure and the appropriate model constants.

d. Transfer of coefficients from the balance axes to the model datum (body) axes by a simple transformation if the two sets of axes are not coincident.

e. Transfer of coefficients from the model datum (body) axes to the stability (wind) axes by a simple transformation.

Similarly pressure coefficients are produced based on a dynamic pressure uncorrected for tunnel blockage.

3.2.5.2 Off-line

Off-line data reduction is performed by a PRIME 4050 computer which re-computes the on-line data accounting for second order balance interactions to produce the final results. Corrections are then applied to these results to account for solid and wake blockage and also for the induced upwash on the wing due to interference caused by the tunnel walls (Appendix VI).

3.3 Vortex generator surface shear stress measurement in the 2.5" x 2.5" transonic wind tunnel at Cranfield University

3.3.1 The 2.5" x 2.5" transonic wind tunnel, Cranfield University

The 2.5" x 2.5" transonic wind tunnel, Figure 3-8 is an intermittent wind tunnel 'driven' by the suction of air at atmospheric pressure into two evacuated tanks. These tanks have a volume of $91m^3$ and are evacuated by a 50 kW electrically driven vacuum pump. A silica-gel bed at the beginning of the inlet duct dries the air and prevents condensation. The contraction in the wind tunnel has an area ratio of 144:1.

Plenum chambers, with a total volume equal to the test section volume, are located on the top and bottom walls which are made from electronic circuit-boards with 1 mm diameter normal holes and an open-area ratio of 12%. The side walls of the tunnel are solid, with one being made of glass so that the working section can be observed. At the end of the test section the jet expands into a rectangular chamber, 10 cm x 6.35 cm, which leads to a 10 cm diameter diffuser pipe, 0.9 m long. A variable second throat (gate valve) located at the end of the diffuser pipe is used to vary the Mach number.

The wind tunnel is equipped with two Druck 1.0 psi pressure transducers for pressure measurements. The first is connected to the stagnation pressure probe in the settling chamber and the second is used for measuring pressures in the working section. The outputs from both transducers are read via digital voltmeters after passing through electrical filters and amplifiers with a gain of 50.

To measure the absolute pressures recorded by these two pressure transducers the readings are first corrected for any offset voltage and the gain of the amplifiers before the appropriate transducer calibration factor is applied. The absolute pressure is then calculated knowing the atmospheric pressure.

Mach number is set using the isentropic flow equation

$$M = \sqrt{\frac{2}{\gamma - 1}\left[\left(\frac{p_t}{p}\right)^{\frac{\gamma-1}{\gamma}} - 1\right]}$$

and the stagnation pressure measured using a pitot probe in the settling chamber, and the static pressure measured via tappings placed in the nozzle liner and plenum chambers. Once the Mach number has been set, the stagnation pressure in the settling chamber is used as a reference for the Mach number measurement.

3.3.2 Shear stress sensitive liquid crystals

The liquid crystals are type TI511 manufactured by BDH Limited[101]. They have a low viscosity and are red at temperatures below 50° C. Above this temperature, the liquid crystals melt and their properties are lost. The liquid crystals dissolve in trichloroethane which can then be sprayed using an artists airbrush onto the test surface; however, the solvent may react with the black paint used on the surface (to minimise reflections) and also reduces the viscosity of the liquid crystals such that they flow once wind is applied rather than remaining fixed to the surface. A much more viscous coating can be applied through brushing on neat liquid crystal. The surface must also be clean as any contamination can alter the structure of the liquid crystals and hence their colour properties.

3.3.3 Liquid crystal colour analysis equipment

The equipment used to analyse the colour of the liquid crystals consists of a miniature Panasonic colour digital camera, an Oriel Fibre Optic Illuminator with a fibre optic cable and lens, a video recorder, an RGB (Red, Green, Blue respectively) decoder since the computer system requires RGB inputs from the camera, a colour monitor, a 486 MHz PC with a Colour Frame Grabber (CFG) board and software developed by DERA Bedford[102]. The arrangement is shown in Figure 3-9. The liquid crystal response is recorded on video and played back through the PC to the monitor where a snap shot is taken on the PC by the CFG board. An area on this frozen image can then be selected and the colours Red, Green and Blue of each pixel measured and the Hue, Intensity and Saturation calculated for each pixel using the software. Hue is a numerical representation of colour and its value is between 0 and 1. Intensity is a measure of the amount of light scattered by the liquid crystals and is the sum of the red, green and blue values from the camera. Saturation represents the amount of white light contained in the colour. The precise equations for observing hue, saturation and intensity from the red, green and blue values are:-

$$\text{Intensity} = \frac{(R + G + B)}{3}$$

$$\text{Saturation} = 1 - \frac{\min(R, G, B)}{\text{Intensity}}$$

$$\text{Hue} = 90 - \frac{\tan^{-1}\left(\frac{2R - G - B}{\sqrt{3}(G - B)}\right)}{360} + C$$

where

$$C=0;\ G \geq B \text{ and } C=180;\ G < B$$

The Hue is used to determine the shear stress since Intensity and Saturation vary with the thickness of the liquid crystal layer and not with shear stress.

4. Test Procedure and CFD Analysis Techniques

4.1 Cranfield swept wing study

To investigate the generality of the flows studied in more detail at DERA the nature of the flow on a swept wing and how this changes with wing sweep was carried out in the Weybridge low speed wind tunnel at Cranfield University using an existing symmetrical wing and balance arrangement (Section 3.1). Force and moment measurements were made with the wing swept at 30°, 40°, 50° and 60° for a wind speed of 30 m/s, corresponding to $Re_c \sim 5x10^5$ and M = 0.09, at incidences from -6° to 16°. Repeat measurements at 0°, 4° and 8° were made after returning the model to its original starting position and several sets of data were also taken at each wing sweep to check the repeatability of the balance (Appendix III).

The surface flow was visualised using Titanium dioxide dissolved in paraffin painted on the wing upper surface[103] for 4°, 8° and 12° incidence at each wing sweep. Black and white photographs of these surface flow patterns, illuminated under photographic lights, were taken when the oil had dried sufficiently.

At these same incidences, the air flow in the region of the trailing edge and separation was visualised using smoke in conjunction with a bright projector light shining along the wing span, Figure 4-1, at a low wind speed. The smoke was recorded on video tape via a black and white camera and a frame grabber on a PC was used to take an image from the video tape and produce a negative image of the flow over the wing.

4.2 Large scale DERA swept wing study

In order to investigate these swept wing flows and trailing edge separations in more detail and to investigate the possibility of controlling these separations through the use of vortex generators, a large swept wing wind tunnel model has been designed and manufactured at DERA Bedford for use in the 13' x 9' low speed wind tunnel (Section 3.2).

4.2.1 Basic wing flows

Force, moment and pressure measurements were made with the wing swept at 30°, 40° and 50° for incidences between -6° and 16° at wind speeds from 30 m/s to 80 m/s, giving a Re_c of 1.5 - 5.2 x 10^6 and Mach numbers from 0.088 to 0.235. Repeat measurements were made at 0°, 4° and 8° for each run after returning the model to its original starting incidence of -6° and some runs were repeated to check the repeatability of the balance, Appendix XIV.

The surface flow was visualised using fluorescent dye dissolved in kerosene (wind speeds below 50 m/s) or diesel (wind speeds above 50 m/s) painted on the wing upper surface at

4°, 8° and 12° incidence for each wing sweep at 60 m/s and at 8° incidence for each wing sweep at 40 m/s and 80 m/s. Photographs of the surface flow patterns, illuminated under ultraviolet lights, were taken when the oil had dried sufficiently.

4.2.2 Flow control study

4.2.2.1 Vortex generator design

The literature search (Section 2-2) showed that the performance of vane type vortex generators on unswept wings and wings with low sweep angles (less than 30°) depends on many variables such as the type of array, vane spacing, vane orientation, position relative to separation, vane height in relation to the local boundary layer thickness, spanwise extent of the array, vane shape and vane taper and aspect ratio.

The flow over the rear section of a swept wing at incidence curves to flow out towards the wing tip so vortex generators need to be positioned and oriented to oppose this motion and redirect the flow inwards. A co-rotating array of vortex generators toed out relative to the local flow direction was therefore chosen for the flow-control study since this produces an array of co-rotating vortices which causes a lateral displacement of the vortices towards the wing root and opposes the natural flow towards the wing tip (Section 2.2.5). This type of array should also be effective over a range of incidences. The vortices produced are relatively insensitive to changes in local flow direction (unlike a counter-rotating array) and the vortices remain stable over large distances. Therefore their position relative to separation should also be effective over a range of incidences.

The vane planform chosen was a flat cropped delta since the literature search showed that:-

1) normal flat plate vortex generators were not inferior to aerofoil section vortex generators;
2) a pointed vane may affect the stability of the vortex and therefore the taper ratio should be greater than zero;
3) if the aspect ratio was kept low the strength of the vortex would not vary rapidly with small changes in the local flow direction.

Vane heights were chosen after analysing the results from the boundary layer method WAKELAG[33] (Section 4.4.2) using the measured pressure distributions, Figure 4-2, such that in the region where the vortex generators were likely to be positioned (0.50c to 0.70c) the heights would be less than or similar to the local boundary layer thickness. With these design parameters given above six cropped delta vane vortex generator profiles were selected, Figure 4-3a. These were manufactured from 'shim' steel of 0.3 mm thickness and incorporated a 2 mm flange on the lower edge to enable them to be glued to the wing surface. The vanes were all a standard length of 16 mm and had a leading edge sweep angle of approximately 40°.

4.2.2.2 Vortex generator test parameters

Of the remaining design parameters relevant to co-rotating arrays, the vane position relative to separation, vane height in relation to the local boundary layer thickness and vane orientation were thought to be the most important parameters to study further and, to a lesser extent, the vane spacing. A parametric test program was therefore devised to investigate each of these parameters in turn on the wing swept at 40° at a wind speed of 60 m/s. Force and moment measurements were made on each configuration at incidences from -6° to 14° and surface oil flow visualisations, using the fluorescent dye technique, obtained for some of these configurations. Pressure measurements were also made of the most effective configurations. The individual vane configurations are detailed in Table 4-1.

4.2.2.3 Concave slats, canted cropped delta vanes and 'bent' wires

Three other types of vortex generator, which were thought to have a smaller radar cross section than the upright cropped delta vanes, were also investigated on the wing swept at 40° at a wind speed of 60 m/s. These were concave slats, canted cropped delta vanes and 'bent' wires. The concave slats were rectangular in side view but curved when viewed from the end, Figure 4-3b. The canted cropped delta vanes were produced from bending upright cropped delta vanes until the end profile made an angle of 45° to a flat surface, Figure 4-3c. The 'bent' wires were produced from a 20 mm length of 1.5 mm diameter wire bent upwards 6 mm from the leading edge, Figure 4-3d.

These vortex generators were positioned on the wing at 65% chord and toed out 25° to the freestream flow at a spacing of 8h. This arrangement corresponded to one of the more favourable positions obtained with the upright cropped delta vane vortex generators of the same height (Figure 5-42b) to enable direct comparisons to be made. Force and moment measurements were made on each configuration at incidences from -6° to 14° and surface oil flow visualisations, using the fluorescent dye technique, were obtained for the canted cropped delta vane and concave slat configurations at an incidence of 8°.

4.2.2.4 Wire sub-boundary layer vortex generators

The literature search showed that new types of small vortex generators are being used instead of the conventional vane type of vortex generator to successfully control separations in the vicinity of the leading edge[71-77]. Among these devices are thin wires which have been used to control leading edge separation on a highly swept and cambered wing[76,77]. Therefore the ability of these wires to control trailing edge separation was investigated on the wing swept at 40° at a wind speed of 60 m/s since the wires were simple to manufacture, Figure 4-3e, and attach to the wing. Several diameters of wire were investigated in various configurations, Table 4-2, using surface oil flow visualisation only to quickly and clearly show if any configurations had an effect on separation.

4.2.2.5 50° swept wing test

Five cropped delta vane vortex generator configurations were investigated on the wing swept at 50° at a wind speed of 60 m/s. These configurations, Table 4-3, consisted mainly of those that gave the most effective separation control on the 40° swept wing. Force and moment measurements were made on each configuration at incidences from -6° to 14° and surface oil flow visualisations, using the fluorescent dye technique, obtained for some of the configurations.

4.3 Vortex generator shear stress measurements

To both aid understanding of the DERA large swept wing flow-control results and to develop a new wind tunnel technique, the surface shear stress distribution of vortices produced from cropped delta vane vortex generators was investigated in the Cranfield University 2.5" x 2.5" Transonic wind tunnel (Section 3.3.1). A tunnel speed of 67 m/s was chosen since this produced a boundary layer, in conjunction with roughness strips, of a suitable thickness and profile (Appendix VII). Surface oil flows were used to visualise the flow along the working section wall and the shear stress distribution across the working section wall was obtained from Preston tube measurements and shear stress sensitive liquid crystals for the smooth wall and with vortex generators mounted on the working section wall. The vortex generators, Figure 4-4, were similar to those used in the DERA flow control study with heights of $\delta/3$, $2\delta/3$ and δ at their location in the wind tunnel which were orientated at an angle of 20° to the freestream flow direction.

4.3.1 Surface oil flow visualisation

The surface flow along the wind tunnel working section wall, after being painted black to minimise reflections, was visualised, using Titanium dioxide mixed with linseed oil, for the smooth wall and with each of the vortex generators in the working section. These surface flow patterns were illuminated with a photographic lamp and a black and white photograph taken with the wind on to avoid recording images containing deformations caused by gravity on the patterns produced after the wind ceased blowing.

4.3.2 Preston tube shear stress measurements

The surface shear stress was measured at three downstream positions ($3.125c_v$, $6.25c_v$ & $9.375c_v$) from the trailing edge of the vane for the three sizes of vortex generator and for the smooth wall using five Preston tubes, Figure 4-5. These positions were chosen to evenly cover the remaining section of the working section downstream of the vane in which the vortex could develop. The Preston tubes were positioned across the working section and aligned with the surface flow direction using the surface oil flow visualisation results. The pressure measurements from the Preston tubes were then converted to shear stresses using a standard calibration curve[82], Figure 4-6, and the skin friction coefficients calculated.

4.3.3 Shear stress sensitive liquid crystal measurements

The surface shear stress along the wind tunnel working section wall was visualised using shear stress sensitive liquid crystals (Section 3.3.2) applied to the working section wall with a fine paint brush after the surface had been sprayed with black paint to minimise reflections. The illumination and viewing angles were arranged such that they were both looking downstream at 65° and 75°, respectively, from the normal since this arrangement matches that of the calibration (Appendix VIII). However, it was observed during preliminary tests that when the vortex generator was present in the test section the liquid crystals behind the vane was blown away before the test conditions were reached (between 5 and 10 seconds, Appendix IX). It was also difficult to identify the changes in the liquid crystals when the vane was present to the smooth wall results due to the long interval of time required to reach the test conditions. Therefore a plug was designed, Figure 4-7, such that the tunnel wall remained smooth until the test conditions were reached. The vane was then introduced into the working section so any changes from the tunnel wall being smooth to having the vortex present could be observed since the liquid crystals have a reaction time of several milli-seconds. Using this method, images were recorded on video tape for the three sizes of vortex generator at the same downstream positions as those used for the Preston tube shear stress measurements. After each run the liquid crystals were re-applied with the fine paint brush to give a fresh result each time with no influence from the previous run. The hue profiles across the working section were then obtained immediately prior to the vane entering the working section, at the instant the vane entered the working section and at one second after the vane had entered the working section using the DERA software[102] (Section 3.3.3). These hue profiles were then averaged from several separate runs and converted into shear stresses using the calibration data (Appendix VIII) and the skin friction coefficients calculated.

4.4 CFD Analysis Techniques

4.4.1 Flow prediction

Four CFD methods (Section 4.4.2) were used to obtain information about the pressure distribution and boundary layer around the DERA aerofoil section and wing. Three of these methods, BVGK, TAPERBL and VFP, provided information prior to the wing being tested in the wind tunnel and the remaining boundary layer method, WAKELAG, provided information about the boundary layer from the measured pressure distributions for the design of vortex generators.

Calculations were performed using BVGK for the DERA aerofoil section at the experimental test conditions, $Re_c = 2.5x10^6$ and $M = 0.15$, for increasing values of lift coefficient up to that at which a numerically converged solution could not be obtained. These pressure distributions were then converted to represent those over infinite wings of 30°, 40° and 50° sweep and the boundary layers calculated using TAPERBL (Section 4.4.2).

Calculations were then performed using VFP for the DERA wing swept at 30°, 40° and 50° at the experimental tests conditions. However, numerically converged solutions could only be obtained at a wing sweep of 30°.

A brief description of these techniques is given below but a more detailed description can be found in Broadley[33].

4.4.2 CFD methods

BVGK[104] (a semi-inverse version of the Viscous, Garabedian and Korn method (VGK)[105]) uses a finite difference scheme, developed by Garabedian and Korn, for solving the potential flow equations for inviscid flow around two-dimensional aerofoils in subsonic and transonic flows and an inverse integration method to calculate the shear layers close to separation. The techniques used to calculate the boundary layer are those of Thwaites[106] for the laminar boundary layer and a lag-entrainment method[32] for the turbulent boundary layer. The code is very easy to use requiring the geometry of the aerofoil section and a data file containing the flow criteria to be met which, when run on a workstation, only takes a couple of minutes to obtain a numerically converged solution. The output file contains convergence history, the converged pressure distribution and boundary layer properties.

VFP[107-109] (Viscous Full Potential) is an extension of the viscous, Garabedian and Korn method for computing three-dimensional wing flows which can be applied to swept, cranked or tapered wings with or without a fuselage of circular cross-section. However, the viscous-inviscid interaction is directly coupled, rather than the semi-inverse coupling used in BVGK, and so numerically converged solutions are difficult to obtain when the flow is close to separating. The code requires the wing geometry and a data file containing the flow criteria to be met and a workstation to run efficiently. A numerically converged solution takes a couple of hours, however if the outboard stations are close to separation the solution can take significantly longer. The output files contain convergence history, the converged pressure distribution and boundary layer properties at each spanwise position used in the data file.

TAPERBL and WAKELAG are two computer programs for computing the turbulent boundary layer over aerofoils and wings from given streamwise pressure distributions which incorporate the same boundary layer modelling as that used in BVGK. However the calculation is performed only once since the pressure distribution is fixed.

TAPERBL calculates the boundary layer for swept infinite aerofoils and infinite tapered wings where the flow is essentially two-dimensional. The boundary layer is usually calculated from BVGK pressure distributions transformed to account for the sweep angle since the boundary layer obtained from BVGK is for an unswept aerofoil. These transformations for sweep angle are:-

$$M_{3D} = M_{2D}\sec\Lambda,\ C_{p3D} = C_{p2D}\cos^2\Lambda,\ C_{L3D} = C_{L2D}\cos^2\Lambda.$$

WAKELAG is an extension of TAPERBL to calculate the boundary layer from measured pressure distributions across the wing span for swept, tapered and cranked wings. A wing geometry file is required to use this code.

Both TAPERBL and WAKELAG are very easy to use and require very little processing power with the output file containing the boundary layer properties only taking a matter of seconds to compute.

5. Results and Data Analysis

5.1 Cranfield swept wing study

5.1.1 Aerodynamic forces and moments

The aerodynamic forces and moments measured on the Cranfield wing swept at 30°, 40°, 50° & 60° ($Re_c \sim 5x10^5$) are compared in Figure 5-1. These figures show, as expected,:-

1) the zero lift coefficient to be at zero incidence for each wing sweep since the wing aerofoil section is symmetrical.

2) the lift slope to decrease with increasing wing sweep. This is due mainly to the reduction in aspect ratio produced by increasing wing sweep. However the velocity components of the flow caused by the thickness of the wing are also reduced[110] as wing sweep is increased resulting in a reduced suction over the wing upper surface.

3) the drag coefficient to increase with wing sweep for a given lift coefficient above a lift coefficient of approximately 0.25. This is due to the reduction in aspect ratio, produced by increasing wing sweep, causing the induced drag to rise.

4) at zero lift coefficient the wing drag to be lower for a higher wing sweep due to a lower profile drag since the velocity components of the flow caused by the thickness of the wing are reduced[110] resulting in a reduced pressure distribution around the wing and therefore the component of drag from the pressure over the rearward facing part of the wing is reduced.

5) the magnitude of the pitching and rolling moments decrease with increasing wing sweep due to the associated reduction in lift. However at zero incidence when there is zero lift on the model the pitching and rolling moments are non-zero which is most likely caused by:-

    i) the wing section not being symmetrical over its entire span, due to manufacturing tolerances, resulting in an unbalanced lift distribution over the wing which has an overall zero lift force, or
    ii) non-uniform flow in the wind tunnel test section.

6) the magnitude of the yawing moment to decrease with increasing wing sweep at low incidences where the drag is less. However with increasing wing sweep the yawing moment becomes negative over an increasing part of the incidence range investigated which is also symmetrical about the zero incidence position. This indicates a

negative drag, or a thrust, which cannot possibly occur. This phenomena only became apparent after analysing the data after completing the wind tunnel test and it is thought to be caused by the 'wind off' offset changing as the model incidence is altered since the balance remains fixed in the wind axes. Had the phenomena been detected during the wind tunnel test a series of 'wind off' data could have been recorded at each incidence for each wing sweep angle to eliminate this anomaly.

The sudden change in the magnitude of the forces and moments at higher incidences for the greater wing sweeps, particularly at 50° and 60°, is thought to be caused by a vortex produced at the leading edge close to the root which can be seen in the surface oil flow visualisation pictures (Figure 5-5 ($\alpha = 12°$)).

5.1.2 Surface oil flow visualisation

The surface oil flow visualisation results, Figures 5-2 to 5-5 (the discontinuities arise from combining two separate photographs), show the development of the surface flow with incidence for each wing sweep. These oil flow patterns show that the chordwise separation position is not highly dependent on spanwise position except near the wing tip, for the wing swept 30° and 40°, and the wing root for all wing sweeps. In the wing root region the boundary layer on the wing is influenced by the boundary layer on the splitter plate which reduces the spanwise velocity component in this region and moves the separation position further downstream.

The separation position in the region of the wing tip depends on the orientation of the trailing edge of the tip relative to the leading edge of the tip, due to the fixed tip. For tip trailing edges outboard of the tip leading edge, Figures 5-2 & 5-3, the tip vortex is seen to merge with the trailing edge separation line. This is more noticeable with 30° sweep since the tip trailing edge is more outboard relative to the tip leading edge than with 40° sweep. For tip trailing edges inboard of the tip leading edge, Figures 5-4 & 5-5, the tip vortex does not remain attached to the trailing edge but separates early to proceed in the freestream direction. The separation line is also affected by this since in the region of the tip it does not curve towards the trailing edge, as seen with the 30° and 40° wing sweeps, but continues straight out towards an imaginable wing tip. It is presumed that when the flow along the separation line leaves the real wing tip it merges with the tip vortex flow as seen on the wing at sweep angles of 30° and 40°.

The oil flows also show the separation line to move upstream with increasing incidence as expected. By comparing the figures for different wing sweeps, it is observed (although not very clearly) that forward of the separation line the spanwise flow towards the wing tip increases with wing sweep. However, the resulting separation line appears to be in a similar position for each wing sweep. This increase in spanwise flow with wing sweep can be attributed to the change in transverse pressure gradient with wing sweep in the external stream which produces the secondary crossflow in the boundary layer[1]. The reduction in velocity in approaching the surface results in a decrease in the centrifugal

force which, outside the boundary layer, is in equilibrium with the transverse pressure gradient. Since the static pressure remains approximately constant through the boundary layer, the curvature of the streamlines in the boundary layer must be increased as the surface is approached and the velocity reduced to restore the centrifugal force to its required value. Behind this separation line the oil flows also indicate a region of reverse flow originating at the trailing edge.

At higher sweep angles and incidences a leading edge vortex can be identified (Figure 5-5 ($\alpha = 12°$)) which increases in strength with incidence and sweep angle. This vortex is seen to have an influence on the separation position out towards the wing tip where the separation line is deflected rearwards. This leading edge vortex does not merge with the separation line or the tip vortex.

5.1.3 Smoke visualisation

Images taken from the video film and a sketched interpretation of the flow pattern observed on the upper surface of the wing at all sweep angles once separation has occurred are shown in Figure 5-6. The smoke flow visualisation results show the flow over the wing surface to unsweep towards the rear of the wing section and flow spanwise towards the wing tip. An increase in curvature of the flow can also be observed in the smoke closer to the wing surface (Figure 5-6a). Behind the separation line the smoke has also detected a reverse flow region flowing towards the separation line from the trailing edge and out towards the wing tip (Figure 5-6b). This observed flow phenomena is illustrated in the accompanying sketched interpretation (Figure 5-6c).

The flow in the vicinity of the separation is sketched in Figure 5-7a which shows the separated flow forming a separated streamsurface along the separation line. This separated streamsurface extends into the wake and forms an enclosed region bounded by the streamline from the underside of the trailing edge. This enclosed region contains two separate circulations, to satisfy the boundary conditions, with the upper circulation producing the observed reverse flow phenomena from the trailing edge (Figure 5-7b). However, no indication could be seen from the video film of any variation in magnitude of the circulations and reverse flow with wing sweep angle. The merging of the tip vortex with the separation line was also not observed due to the wing tip not being in the illuminated region.

5.2 Large scale DERA swept wing study

5.2.1 General wing flows

5.2.1.1 Aerodynamic forces and moments

The aerodynamic forces and moments measured on the DERA wing swept at 30°, 40° and 50° ($Re_c \sim 3x10^6$) are compared in Figure 5-8. These figures show similar results to

those measured on the Cranfield wing where:-

1) the lift slope decreases with increasing wing sweep. This is due mainly to the reduction in aspect ratio produced by increasing wing sweep. However the velocity components of the flow caused by the thickness of the wing[110] and the streamwise camber are also reduced resulting in a reduced suction over the wing upper surface.

2) the drag coefficient to increase with wing sweep for a given lift coefficient above a lift coefficient of approximately 0.25. This is due to the reduction in aspect ratio, produced by increasing wing sweep, causing the induced drag to rise.

3) at zero lift coefficient the wing drag to be lower for a higher wing sweep due to a lower profile drag since the velocity components of the flow caused by the thickness of the wing and the streamwise camber line are reduced[110] resulting in a reduced pressure distribution around the wing and therefore the component of drag from the pressure over the rearward facing part of the wing is reduced.

4) the magnitude of the pitching and rolling moments decrease with increasing wing sweep due to the associated reduction in lift.

5.2.1.2 Surface oil flow visualisation

The surface oil flow visualisation results, Figures 5-9, 5-10 & 5-11, (the discontinuities arise from combining two separate photographs) show the development of the surface flow with incidence for each wing sweep at a wind velocity of 60 m/s. These oil flow patterns show similar characteristics to those from the Cranfield swept wing study, Figure 5-6c. Over the forward part of the wing the surface flow direction is streamwise for all the wing sweeps which then unsweeps over the rearward part of the wing to flow almost spanwise as incidence is increased to form a separation line. The spanwise flow over this rear section again increases with wing sweep and the separation becomes more three-dimensional in nature. However, for all the wing sweeps the final chordwise separation position is approximately at 70% chord and it is not highly dependent on spanwise position except near the tip where the flow is influenced by a tip vortex and near the wing root where the boundary layer on the wing is influenced by the boundary layer on the splitter plate; the spanwise velocity component in this region being reduced and moving the separation position further downstream. The similarity in these surface oil flow visualisation results with those from the Cranfield swept wing study suggest a similar flowfield and separation mechanism to that shown in Figure 5-7 for the Cranfield swept wing.

5.2.1.3 Pressure distributions

The variation in the pressure distributions with spanwise position at incidences of 0°, 4°, 8° and 12° for each wing sweep at a tunnel velocity of 60 m/s are shown in Figures 5-12, 5-13 & 5-14. These pressure distributions show that for each wing sweep the effect of the splitter plate on the wing flow is limited to a small region close to the wing root - splitter plate interception since the pressure distributions do not change significantly outboard of 30% span. It is also seen that the pressure distribution is of the required shape with a relatively uniform suction over the forward part of the wing followed by a severe adverse pressure gradient beginning at approximately 60% chord and extending aft to the trailing edge. The pressure distributions also show that large suction peaks in the leading edge region (which may cause unwanted flow characteristics such as leading edge separations and separation bubbles) have successfully been avoided up to incidences of approximately 8° as a result of designing the aerofoil section with a significant amount of leading edge droop. The pressure distributions also indicate that at incidence the majority of lift is produced over the forward part of the aerofoil section which illustrates why the pitching moment decreases with increasing incidence and eventually become positive (nose up).

The trailing edge pressure is observed to decrease with increasing incidence indicating that separation is likely. As incidence is increased further the pressure distribution towards the trailing edge levels off which shows the flow to have separated. The most upstream position of this flattened region has been used to determine the development of the separation line for each wing sweep with incidence, Figure 5-15, which compares favourably with the surface oil flow visualisation results of Figures 5-9, 5-10 & 5-11. These figures show separation to occur first at outboard positions which develop inboard and upstream as incidence increases to approximately 70% chord for each wing sweep. However, as wing sweep is increased the growth of the separation region inboard is inhibited and at the inboard pressure tapped location separation is non-existent for the 50° swept wing whereas the 30° swept wing has a separation point at approximately 75% chord. This is due to the increased adverse pressure gradient over the rear of the wing section produced by the thicker wing profile and associated increase in camber from reducing the wing sweep. The differences in these pressure distributions are illustrated in Figure 5-16 where the pressure distributions at 30% span for each wing sweep at incidences between 0° and 12° are compared. These pressure distribution comparisons also show the suction over the upper surface of the aerofoil section to decrease with increasing wing sweep which is why the lift coefficient and pitching and rolling moment coefficients increased with decreasing wing sweep.

5.2.1.4 Effect of Reynolds number

The effect of small changes in Reynolds number was investigated to show whether transition had been suitably fixed and that the flow in the vicinity of the leading edge did not form separation bubbles. The aerodynamic forces and moments, Figures 5-17, 5-18 & 5-19, show that for each wing sweep the flow on the model is well behaved and insensitive to small changes in Reynolds number. These results are further enhanced by

comparisons of the surface oil flow visualisations at Reynolds numbers less than (Figure 5-20) and greater than (Figure 5-21) those of Figures 5-9, 5-10 & 5-11. These figures show similar surface flows for each wing sweep over the range of Reynolds number investigated. Comparisons of the pressure distributions over the range of Reynolds number investigated for each wing sweep, Figure 5-22, also show no significant differences in the nature of the wing flow with separation occurring in similar positions.

5.2.2 Flow prediction comparisons

5.2.2.1 Pressure distributions

The suitably numerically converged calculated pressure distributions at the test conditions of 60 m/s for BVGK uncorrected for sweep and VFP at 30° sweep are shown in Figures 5-23 and 5-24 respectively. The solution is accepted as being numerically converged when changes in both the velocity potential (inviscid) and a boundary layer parameter (viscous) from the previous iteration are both less than a pre-determined convergence parameter. The BVGK results show the development of the pressure distribution for lift coefficients between 0.4 and 1.0 which follow a similar trend to those measured from the model itself. These pressure distributions do not show any flow separation in the trailing edge region but the trailing edge pressure is seen to decrease with lift coefficient indicating that the flow is approaching separation. Unfortunately numerically converged solutions were not achievable at higher lift coefficients where the flow has probably separated.

The VFP results also show similar trends to those measured from the model with the pressure distribution remaining similar at all spanwise positions except in the vicinity of the wing root and wing tip. It is also observed that VFP does not model the flow at the wing tip satisfactorily as the pressure distribution in the trailing edge region clearly illustrates. However inboard of the wing tip VFP is able to calculate the pressure distribution satisfactorily even with a significant amount of separation present.

The measured pressure distributions and the calculated pressure distributions of BVGK and VFP at a wing sweep of 30° are compared in Figure 5-25. An outboard position (approximately 60% span) has been chosen to make the comparison as the results show the pressure distributions not to vary significantly spanwise in these regions and the flow can be assumed to be two-dimensional to enable comparisons with BVGK to be made. The VFP result has also not modelled the splitter plate and so sensible comparisons in this region can not be made. The comparisons have been made with the BVGK results transformed (Section 4.4.2) to represent those at a wing sweep of 30° and the section lift coefficients calculated by integrating the pressure distributions over the aerofoil surface. The comparison shows that both BVGK and VFP are capable of predicting the pressure distributions and that the wing flow away from root and tip effects can be approximated to a two-dimensional flow. However BVGK does not model the flow in the vicinity of the leading edge as well as VFP and incorrectly models the flow in the trailing edge region which supports the idea that three-dimensional effects are important in this region. VFP is able to model the flow in the leading edge and matches that of the measured

result reasonable well, however the pressure recovery in the trailing edge region is over-estimated and the onset of separation through a decrease in trailing edge pressure is not correctly predicted. It does however show a reduction in trailing edge pressure with increasing incidence and indicates the flow separating through a levelling in the upper surface pressure distribution in the trailing edge region which eventually matches that of the measured pressure distribution.

The measured pressure distributions and the calculated pressure distributions of BVGK at wing sweeps of 40° and 50° are compared in Figures 5-26 & 5-27. Unfortunately satisfactory numerically converged solutions from VFP were not achievable. An outboard position (approximately 60% span) has again been chosen to enable sensible comparisons to be made with transformed BVGK results (Section 4.4.2), representing wing sweeps of 40° and 50°, and the section lift coefficients have similarly been calculated by integrating the pressure distributions over the aerofoil surface. The comparison shows that again the wing flow away from the root and tip regions can still be approximated to a two-dimensional flow but the flow in the vicinity of the leading and trailing edge regions will not be calculated accurately due to BVGK being a two-dimensional method only.

5.2.2.2 Boundary layer predictions

The calculated surface and local freestream flow paths over the model using the boundary layer code TAPERBL together with the BVGK pressure distribution results are shown in Figure 5-28 (a-c) for each wing sweep respectively. These results show the flow development to be similar for each wing sweep with the flow over the forward part of the wing being almost streamwise with very little curvature through the boundary layer as the surface is approached. However, the surface flow in the trailing edge region is seen to deviate considerably from that of the local freestream flow direction, with the surface flow unsweeping to flow towards the wing tip which occurs earlier as incidence increases. There are no significant differences in this trailing edge flow with changes in wing sweep. The results also show no signs of the flow separating. However, the measured pressure distributions used for comparison do not show the flow to separate either although the trailing edge pressure of these measured pressure distributions reduces indicating the onset of separation. If numerically converged BVGK pressure distributions were available for greater lift coefficients separation may have been indicated since the TAPERBL results for the twist in the boundary layer (Figure 5-28 (d-f)) show a maximum (or no result for 50° sweep at higher incidences) towards the trailing edge of the aerofoil. This maximum position progresses upstream over the aerofoil surface with incidence and can be used to indicate the onset of separation. In Figure 5-28 (d-f) this maximum position moves forward to approximately 96% chord at 2° incidence for wing sweeps of 30° and 40° and no results are possible above 92% chord at 2° incidence for the wing swept 50°.

The development of the separation line on the wing swept at 30° using the skin friction boundary layer data generated from the VFP calculations is shown in Figure 5-29 where it is compared to the separation line determined from the measured pressure

distributions. The VFP separation position is assumed to be where the skin friction is zero as VFP does not give the surface flow directions. The VFP separation line and its subsequent development with increasing incidence resembles that of the actual wing with separation beginning outboard and extending upstream and inwards as incidence increases. However, the separation position close to the wing root and wing tip does not resemble that of the actual wing as the splitter plate has not been modelled and close to the wing tip region VFP does not model the flow satisfactorily as was illustrated earlier in Figure 5-24. The comparison also shows that the separation line obtained from the measured pressure distribution agrees at an incidence of 4°. Unfortunately the VFP separation line develops more rapidly with incidence than the measured pressure separation line indicating that once the flow has started to separate VFP does not model this development accurately.

The calculated surface and local freestream flow paths over the model using WAKELAG and the measured pressure distribution results are shown in Figures 5-30 & 5-31 for wing sweeps of 40° and 50° only since these are the wing sweeps of most interest for investigating separation control. The results show the flow development to be similar for both wing sweeps with the flow over the forward part of the wing being almost streamwise with very little curvature through the boundary layer as the surface is approached. However, the surface flow in the trailing edge region is seen to deviate considerably from that of the local freestream flow direction, with the surface flow unsweeping to flow towards the wing tip which occurs earlier as incidence increases and with distance from the wing root similar to that shown in the surface oil flow visualisation photographs. Again there are no significant differences in this trailing edge flow with changes in wing sweep. The results also show no signs of the flow separating even though solutions were obtained from WAKELAG using measured pressure distributions with separated flow. The separation line shown in the figures has been determined from a sudden deviation in the boundary layer displacement thickness and also from the inflexion of the surface flow streamlines from the WAKELAG results (Appendix XIII). However, comparisons made of the surface flow directions from the surface oil flow visualisation results with those from WAKELAG do show that, forward of separation, WAKELAG is able to calculate the flow directions satisfactorily.

5.3 Flow control study

5.3.1 Cropped delta vane vortex generators

The selection of surface oil flow visualisation results, Figures 5-32, show the effect on separation prevention of several cropped delta vane vortex generator configurations. These results show that each configuration prevented separation to some degree, which is illustrated by the lack of spanwise flow out towards the wing tip and reverse flow in the trailing edge region. Instead, vortex paths are observed in the surface flow which are seen to extend to the trailing edge and eliminate the tendency of the flow to unsweep and flow spanwise towards the wing tip.

It can be seen in these surface oil flow visualisation results that the degree of separation prevention is sensitive to:-

1) the angle of the vortex generator to the local flow direction;
2) the height of the vortex generator;
3) the chordwise position of the vortex generator; and
4) the spacing between vortex generators.

It should also be noted that the oil flow visualisation technique is an intrusive method that can affect the real flow on the wing. The separations shown in the trailing edge region for some of the configurations may therefore be caused by the presence of the oil and so the flow patterns observed with vortex generators present should only be used as an indication of the performance of the configuration.

The prevention of flow separation is also observed in the pressure distributions with vortex generators present, Figure 5-33, which show for each spanwise station that separation is prevented over the range of incidences investigated. A comparison of the pressure distributions with vortex generators to that without vortex generators, Figure 5-34, shows that, except for local modifications in the vicinity of the vortex generators themselves, the pressure distribution is similar to that of the wing without vortex generators. However, with vortex generators present the flow is able to maintain a greater adverse pressure gradient over the rear of the section unlike the pressure distribution observed on the wing without vortex generators where the trailing edge pressure decreased and a flat region was formed on the wing upper surface where the flow had separated. The suction over the upper surface of the wing at a given incidence with vortex generators present is also seen to increase over that of the wing without vortex generators since the circulation around the wing is improved due to the suppression of separation and the ability of the flow to withstand greater adverse pressure gradients. This improved circulation around the wing section will improve the lift at a given incidence over that of the wing without vortex generators. The figure also shows that the pressure distributions from two very different vortex generator arrangements which are able to prevent separation are very similar over the range of incidences investigated except for local differences in the vicinity of the vortex generators themselves.

The associated balance results for these cropped delta vane vortex generator configurations are shown in Figures 5-35 to 5-41. The lift curves shown in these figures clearly show that each vortex generator configuration tested improves the lift of the wing by a similar amount at all incidences with the maximum increase in lift being approximately 10% at an incidence of 10°. At high incidence there is a degradation in performance of some of these configurations but the lift is still greater than that of the wing without vortex generators. The improvement in lift is due to the improved flow characteristics over the rear of the wing section caused by the vortices re-energising and re-directing the surface flow over the wing surface which enables the flow to successfully overcome the adverse pressure gradient in this region as shown in the surface oil flow visualisations and pressure distributions.

This improvement in lift over the rear of the wing also improves the pitching moment, as expected, and enables a steady nose down pitching moment to be maintained unlike that on the wing without vortex generators where trailing edge separation causes a forward shift in the centre of pressure leading to a nose up pitching moment. The pitching moment results also show the pitching moment to be almost insensitive to small changes in the vane orientation, height, chordwise position and spacing. However the pitching moment development is seen to alter with major changes in the arrangement of the vortex generators such as a large movement in chordwise position of the vanes with a change in height. This difference in development of the pitching moment is most likely caused by a movement in the centre of pressure produced by small changes in the pressure distribution from the vortex generator arrangement which only become significant when major changes are applied.

The improvement in lift also increases the magnitude of the rolling moment by a similar amount for each configuration over that of the wing without vortex generators.

The improvement in the flow over the wing with the addition of vortex generators is achieved at the expense of an increase in drag at low lift coefficients as illustrated in the drag polars of Figures 5-35 to 5-41. These figures show increases of up to 0.005 over the zero lift drag coefficient for the wing without vortex generators but at higher lift coefficients an improvement in drag can be seen for the majority of the configurations.

Although these balance results and the corresponding pressure distributions and surface oil flow visualisation results show each configuration of vortex generators to be able to improve the performance of the wing it is very difficult to assess the difference in performance between configurations. Therefore the following analysis of the vortex generators has been based on the lift dependent drag factor to determine the gain in wing lift at the expense of minimum drag where the zero lift drag penalty of the vortex generators themselves will not influence their efficiency at controlling separation. The results from this lift dependent drag factor analysis are shown, in Figure 5-42 (a-g), as percentage differences to the wing lift dependent drag factor with separation against lift coefficient such that a negative difference indicates a reduction in lift dependent drag factor. These results are shown for lift coefficients above 0.4 only since below this lift coefficient the percentage differences become very large and reduce the resolution of the figures.

These results clearly show some configurations to be better than others. The 0.0126c tall vanes are seen to be optimised at 65% chord, Figure 5-42a, with an angular deflection of 30°, Figure 5-42b, and produce a reduction in lift dependent drag factor of approximately 9% over the lift range shown. Changes in position or angular deflection from this condition cause considerable reductions in efficiency particularly at the lower lift coefficients and also changes in the height of the vane are seen to have a significant effect on the efficiency, Figure 5-42c. A slightly smaller vane 0.01c tall is observed to be more effective than the 0.0126c tall vane at low lift coefficients but further reductions or increases in the vane height cause significant reductions in efficiency over the lift range shown.

Smaller vanes are observed to be more efficient when they are positioned further forward, Figures 5-42 d & g, and appear to be less dependent on their angular deflection than those positioned further aft, Figure 5-42e. However the reductions in lift dependent drag factor only become apparent at higher lift coefficients with reductions of up to 6% which are not as great as taller vanes positioned further aft which also cover more of the lift range. The effect of the vane spacing is also seen to be of significance since 0.005c tall vanes at a spacing of 20h show an improvement in efficiency over arrays more widely spaced and a similar efficiency to an array of half the spacing, Figure 5-42f. These results are discussed in more detail in section 6.3.1.

5.3.2 Concave slats, canted cropped delta vanes and 'bent' wires.

The surface oil flow visualisation results, Figures 5-43 & 5-44, show the effect that 0.0126c tall concave slats and canted cropped delta vanes have on the surface flow when positioned at 65% chord with a spacing of 8h and an angular deflection of 25°. These figures show both arrangements to be able to prevent (to a limited extent) the flow from separating. However, when compared to those of the upright cropped delta vanes positioned in a similar arrangement, Figure 5-32, their performance is observed to be not as effective.

Each configuration shows an improvement in lift over that of the wing with separation, Figure 5-45, with the canted cropped delta vanes giving a similar improvement to that of the upright cropped delta vanes. These improvements in lift are again observed in the pitching moment and rolling moment. The drag polar shows the canted cropped delta vanes and the 'bent' wires to have a similar zero lift drag coefficient to that of the upright cropped delta vanes but the concave slats produce a significant increase in zero lift drag. However as incidence and lift is increased each of theses configurations produce significantly more drag than upright cropped delta vanes which is illustrated in Figure 5-46 showing the difference in lift dependent drag factor to that of the wing with separation. This figure shows that concave slats increase the drag factor by between 5% and 11% over the range of lift coefficients shown and the canted cropped delta vanes to cause a large increase in lift dependent drag factor at low lift coefficients which reduces as lift increases until at high lift coefficients a reduction is observed. However this reduction in lift dependent drag factor is still far less than for the upright cropped delta vanes. The 'bent' wires also cause a large increase in lift dependent drag factor at low lift coefficients which reduces as lift increases until at a lift coefficient of approximately 0.8 a small reduction is observed before a penalty of approximately 2% is encountered over the rest of the lift coefficient range.

5.3.3 Wire sub-boundary layer vortex generators

Surface oil flow visualisation results from a variety of wire sub-boundary layer vortex generator configurations showed that for all the wire diameters, chordwise positions, angular deflections and spacings investigated the effect on flow control was very localised and ineffective in preventing trailing edge separation.

5.3.4 50° swept wing

The surface oil flow visualisation results for the vortex generator configurations tried on the wing swept at 50° are shown in Figure 5-47. These surface flow results show that the vortex generator configurations which were effective on the wing swept at 40° are also effective in preventing separation on the wing swept at 50°. This effectiveness is also seen in the balance results shown in Figure 5-48. These results show a similar improvement in lift over that of the wing without vortex generators for each configuration tried, however, the maximum increase in lift is approximately 8% which is slightly less than the maximum increase in lift of 10% on the 40° swept wing. This improvement in lift performance is again illustrated by prolonging the nose down pitching moment and increasing the rolling moment compared to the wing with separation. The effect on the zero lift drag is not as significant as that of the 40° swept wing with all the configurations causing an increase of less than 0.002 in zero lift drag coefficient before reductions are attained at lift coefficients greater than 0.5. This is again illustrated as a percentage change in lift dependent drag factor to that of the wing with separation, Figure 5-49, which shows each configuration of vortex generators to produce a similar reduction in lift dependent drag up to a lift coefficient of approximately 0.7. Above this lift coefficient both the 0.0105c and 0.0021c tall vanes performance is seen to degrade whilst the 0.0042c tall vanes still retain a respectable reduction of between 6 & 7% in lift dependent drag factor. The effect of angular deflection is also seen to have little influence on the performance of the vortex generators at the more forward positions. A comparison with the results from the 40° swept wing shows that the efficiency of the taller vanes is of a similar magnitude whilst the efficiency of the shorter vanes at low lift coefficients has improved to match that of the taller vanes.

5.4 Vortex generator shear stress measurements

5.4.1 Surface oil flow visualisation

The surface oil flow visualisation results showing the wind tunnel wall flow characteristics for the smooth wall and with a vortex present are shown, with a sketch of the surface flow with a vortex present, in Figure 5-50. From these photographs the vortex path can clearly be seen from each vortex generator enabling the area of influence of the vortex on the tunnel surface to be measured and the flow directions determined for accurate alignment of Preston tubes for surface shear stress measurements. The figures also show that as the distance downstream from the vortex generator increases the influence of the smaller vortices on the surface flow reduces as the edges of the vortex are not as well defined and the angle between the flow under the vortex and the undisturbed surface flow decreases.

5.4.2 Surface shear stress sensitive liquid crystal measurements

A typical liquid crystal image with no shear applied and before and immediately after a vane has been introduced into the flow are shown in Figure 5-51. These figures clearly

show the difference in hue the liquid crystals emit with and without a shear applied and also show that it is very difficult to observe the change in hue of the liquid crystals with the naked eye when a vortex is present compared to when one is not present. However, the software developed by DERA[102] is able to detect these small hue changes and these are shown in Figures 5-52 to 5-54 after converting the hue to a shear stress via the liquid crystal calibration (Appendix VIII) and then converting this to a skin friction coefficient for each vane at the chosen downstream locations (Section 4.3). The approximate edges to the vortex shown in these figures have been obtained from the surface oil flow visualisation results for comparison.

These results show that the change in surface skin friction coefficient from the smooth wall to that with a vortex present is very small. However it is observed from these results that on the downflow side of the vortex the skin friction coefficient increases above that of the unaffected freestream and then steadily decreases through the vortex towards the upflow side where the skin friction coefficient is less than that of the unaffected freestream. These results also show that at the first downstream location ($3.125c_v$) the vortices from the $\delta/3$ and $2\delta/3$ tall vanes have a greater influence on the surface flow than the vortex from the δ tall vane and vice versa at the furthest downstream location ($9.375c_v$). This observation can also be seen in the surface oil flow visualisation results where at $9.375c_v$ downstream the angle the vortex makes with the boundary layer flow is much reduced for the shorter vanes. The $\delta/3$ tall vane makes an angle of 15° to the undisturbed boundary layer flow at $3.125c_v$ and 4° at $9.375c_v$ compared with the δ tall vane which makes an angle of 16° at $3.125c_v$ and 11° at $9.375c_v$.

The maximum change in surface shear stress for each vortex is of a similar magnitude with an increase of 0.0002 in skin friction coefficient on the downflow side of the vortex and a decrease of 0.0004 in skin friction coefficient on the upflow side of the vortex. The effect on the skin friction in the boundary layer adjacent to the vortex on the upflow side is also seen to increase in magnitude as the vortex develops downstream and is still present when the direct influence on the skin friction under the vortex itself is much reduced. However this will be discussed further in Section 6.4.1.

5.4.3 Preston tube shear stress measurements

The Preston tube shear stress measurements are shown as changes in surface skin friction coefficient from the smooth wall to that with a vortex present in the same figures (Figure 5-52 to 5-54) as those from the liquid crystal results for comparison. The shear stress measured by the Preston tubes has been transformed to be in the freestream direction since this is the direction that the shear stress was measured using the liquid crystals. This transformation multiplied the shear stress by the Cosine of the angle between the Preston tube orientation and that of the unaffected freestream. These results show a similar skin friction coefficient for the smooth wall of approximately 0.0023 to that obtained from the shear stress sensitive liquid crystal tests of approximately 0.0027. Similar changes in the skin friction coefficient from that of the freestream are observed through the location of the vortex at the first downstream location ($3.125c_v$). However at the other two downstream locations ($6.25c_v$ & $9.375c_v$) the changes in skin friction

coefficient measured by the Preston tubes, of the order of ±0.0008, are significantly greater than the changes measured by the liquid crystals of + 0.0002 and -0.0004. This is also discussed further in Section 6.4.1.

6. Technical Discussion

6.1 Wing flow comparisons

The aerodynamic force and moment results from the Cranfield swept wing (Figures 5-1) and the DERA swept wing (Figure 5-8) both showed the expected variations with incidence and wing sweep where:-

i) the lift slope decreased with increasing wing sweep,
ii) a lower profile drag at zero lift was exhibited with a larger wing sweep,
iii) the induced drag increased with incidence and wing sweep,
iv) pitching and rolling moments decreased with increasing wing sweep and increased with incidence.

The surface flow visualisation results (Figures 5-2 to 5-5 & 5-9 to 5-11) also showed both wings to exhibit similar flow characteristics where the surface streamlines were almost streamwise before unsweeping to flow spanwise towards the wing tip and separating from the wing surface. Separation started in the trailing edge region at an outboard position for both wings at each wing sweep and extended upstream to approximately 70% chord and towards the wing root with increasing incidence. However comparisons of the surface oil flow visualisation results showed an increase in spanwise flow towards the wing tip at higher wing sweeps for both wings indicating the nature of the flow separation to become more three-dimensional at greater wing sweep angles. In particular, at 30° wing sweep the DERA wing had a much reduced spanwise flow (Figure 5-9) at separation indicating a more two-dimensional type of separation. The change in the separation characteristics with wing sweep can be attributed to the severity of the adverse pressure gradient over the rear of the wings lessening with increasing wing sweep angle. The oncoming boundary layer could then unsweep fully in these reduced adverse pressure gradients and flow towards the wing tip.

The surface oil flow and smoke visualisation results from the Cranfield swept wing investigation indicated that this boundary layer separation along a line almost parallel to the trailing edge formed a separated streamsurface (Figure 5-7a). This separated streamsurface extended into the wake and formed an enclosed region bounded by the streamline from the underside of the trailing edge (Figure 5-7b). The enclosed region bounded by these two streamlines must then contain two separate circulations to satisfy the boundary conditions with the upper circulation producing the observed reverse flow phenomena from the trailing edge.

These results showed that the general flow characteristics and separation mechanism are applicable to very different wing sections over a large range of Reynolds number since the same flow characteristics were observed on a highly cambered aerofoil section at Reynolds numbers of the order of 4×10^6 and also on a symmetrical aerofoil section having a concave trailing edge at Reynolds numbers as low as 3.8×10^5.

6.2 CFD evaluation

The CFD methods[33] (Section 4.4.2) used to calculate the pressure distributions and boundary layer characteristics of the flow over the DERA wing all proved to be useful in giving an insight into the type of flows to be encountered on the wing from experiment. An assessment of each method is therefore given below.

6.2.1 Two-dimensional methods (BVGK and TAPERBL)

The pressure distributions calculated using the two-dimensional CFD method, BVGK (Figure 5-23), predicted the main features of the flow and, when matched on section lift coefficient (after transforming the two-dimensional pressure distribution to account for wing sweep angle), showed good agreement to those measured on the wing itself at spanwise positions away from the wing root and tip (Figures 5-25 to 5-27). The discrepancies between the measured and calculated pressure distributions are attributed to the approximation of two-dimensional flow when in reality the flow is three-dimensional. However, the calculated pressure distributions did not show the flow to separate but did show that the flow was approaching separation through a reduction in trailing edge pressure. Similarly, the boundary layer calculated at each wing sweep, using TAPERBL, did not show the flow to have separated but the experimental results also showed the flow not to have separated at these lift coefficients. TAPERBL was able to show that the surface flow would deviate considerably from that of the local freestream flow over the rear of the wing section and, as incidence increased, to unsweep more to flow out towards the wing tip (Figure 5-28 a-c). Upon inspection of the boundary layer twist results separation could be inferred by the position of the maximum in this value close to the trailing edge (Figures 5-28 d-f) and its progression forward with increasing incidence. However, the results from the available BVGK pressure distributions show this maximum to be very close to the trailing edge. Had BVGK been able to produce numerically converged solutions at higher incidences the development of separation upstream may have been shown by TAPERBL.

Although numerically converged solutions with separation were not achieved and the boundary layer was determined from a two-dimensional pressure distribution, the results provide a valuable insight into the type of flow to be expected on the wing itself. The increased unsweeping of the flow close to the surface and the greater deviation from the local freestream flow at higher incidences to flow spanwise towards the wing tip indicated that three-dimensional separation involving strong shear layers in the trailing edge region was to be expected for each wing sweep. Considering the fact that both BVGK and TAPERBL were relatively simple to use, were not time consuming and did not require powerful computers, they provided a reasonably accurate and useful insight in to what to expect on the wing itself.

6.2.2 Three-dimensional methods (VFP)

The pressure distributions calculated using the three-dimensional CFD method, VFP (Figure 5-24), predicted the main features of the flow and, when matched on section lift coefficient (Figure 5-25), showed good agreement to those measured on the wing itself at spanwise positions away from the wing root (since the splitter plate and its effect on the flow in the wing root region was not included in the calculations). Numerically converged solutions of the pressure distributions were also obtained with flow separation and the skin friction data from the calculated boundary layer was able to indicate that the surface flow would first separate just upstream of the trailing edge at a spanwise position close to the wing tip (Figure 5-29). This separated region would then extend upstream and towards the wing root with incidence up to approximately the 70% chord position. This agrees qualitatively with the separation development observed from experiment, since after the flow has separated the development of the separation line does not match that from experiment. VFP was also unable to predict the pressure distribution in the wing tip region satisfactorily which was thought to be due to incorrect modelling of the complex tip flows.

Although separation was predicted and its development with incidence resembled qualitatively that from experiment (Figure 5-29), numerically converged solutions were only obtained for the 30° swept wing. This was due to VFP, (a viscous-inviscid interaction method) being unable to provide results for flows involving strong shear layers, large crossflows and twist through the boundary layer encountered with these greater wing sweep angles. However the solutions obtained did not contain information on the surface flow streamlines and so the unsweeping of the flow towards the wing tip and the formation of a three-dimensional separation line could not be inferred. Similarly, the reverse flow from the trailing edge, once separation had occurred, could not be inferred since particle paths were not calculated and therefore the separation mechanism could not be determined. VFP was also very time consuming, taking several hours to obtain a numerically converged solution, and a trial and error approach in the choice of relaxation parameters and the number of spanwise points. The information produced from VFP, given the amount of time taken to produce a useful set of data, was therefore very limited and the method would benefit greatly from additions to enable three-dimensional flows to be calculated at greater wing sweep angles. The results would also be more useful if they contained information on the surface streamlines and particle paths to enlighten the user of the likely separation mechanism and the associated separated flow. However, with the increase in processing power available on modern workstations new methods incorporating the Euler and Navier Stokes equations are being developed. These methods are much more capable of calculating flows over highly swept wings than the viscous-inviscid interaction methods used above and so the development of these techniques to cope with more highly swept wings is unlikely.

6.2.3 Boundary layer calculations using WAKELAG

The boundary layer calculated for the 40° and 50° swept wings using WAKELAG and the measured pressure distributions showed that the surface flow would deviate

considerably from that of the local freestream flow over the rear of the wing section and, as incidence increased, to unsweep more to flow out towards the wing tip (Figure 5-30 & 5-31). However, separation was not predicted even though the pressure distributions used clearly showed the boundary layer to have separated (Figures 5-13 & 5-14). Separation was inferred from a sudden deviation in the boundary layer displacement thickness (Figure 4-2 and Appendix XIII) and also from inflexion of the surface flow streamlines (Figure 5-30 & 5-31). The development of this separation line with incidence was similar to that observed from experiment (Figures 5-9 to 5-11 and 5-15) with separation beginning in the trailing edge region at an outboard position which extended upstream to approximately 70% chord and towards the wing root with increasing incidence. Up to the point of separation the surface streamlines matched those observed from experiment and, considering that using WAKELAG was not time consuming and did not require a powerful computer, it provided a useful insight into what was happening in the boundary layer. These results show that in the absence of suitable surface oil flow visualisations the nature of the surface flow streamlines and separation line development can be obtained from WAKELAG.

In the absence of an adequate flow prediction method it was possible to position the vortex generators using the results from experiments on the basic wing. However, information was also required for determining the height of the vortex generators and their orientation to the flow. WAKELAG was able to provide this information and also proved to be extremely useful in the interpretation of the results.

6.3 Flow control study

6.3.1 Cropped delta vane vortex generators

The cropped delta vane vortex generator results showed that all the configurations investigated were able to oppose the spanwise flow towards the wing tip by being arranged in toed out co-rotating arrays and prevent trailing edge separation through the generation of a vortex which was able to energise the boundary layer over the rear of the wing section (Figure 5-32). The force and moment results (Figures 5-35 to 5-41) showed that the improvement in lift with separation control was similar for each configuration, with a maximum increase of approximately 10% at an incidence of 10°, over that of the wing with separation. This indicated that there was a limit on the benefit gained through preventing the flow from separating. The pressure distributions with separation control, for two very different vortex generator configurations (Figure 5-34), also showed that in preventing the flow from separating the same adverse pressure gradient was restored to the trailing edge and therefore the same suction over the rear of the section was restored resulting in the same increase in lift for each configuration (i.e. preventing separation results in restoring the same pressure distribution). Therefore to determine the gain in wing lift at the expense of minimum drag or efficiency for each configuration, the lift dependent drag factor was calculated. These lift dependent drag factor results clearly showed that the efficiency of the array in preventing separation could be improved with small alterations of the vortex generators' position and orientation. The following discussion therefore involves the factors that affected this efficiency.

Both the 0.0126c and 0.005c tall cropped delta vane vortex generators showed a maximum efficiency at 65% chord and 55% chord respectively (Figure 5-42a & d). The results from the CFD boundary layer method WAKELAG for boundary layer thickness (Appendix XIII) revealed that the vortex generators efficiency in controlling separation was improved if the height of the vortex generator was equal to or fractionally less than the local height of the boundary layer. The results from the various height cropped delta vane vortex generators positioned at 65% chord enhanced this deduction further (Figure 5-42c). An improvement in efficiency from that of the 0.0126c tall vane was observed at lower lift coefficients (thinner boundary layer) with the 0.01c tall vane while at higher lift coefficients (thicker boundary layer) the 0.0126c tall vane proved to be more efficient than the 0.01c tall vane. However, the 0.0151c tall vane whose height was much greater than the boundary layer thickness, only became efficient - although not as efficient as the 0.01c and 0.0126c tall vanes - at high lift coefficients when the boundary layer had thickened sufficiently such that the vortex produced from the vane was within the boundary layer rather than positioned above it. The vanes with heights significantly less than the boundary layer thickness showed no benefit in the lift dependent drag factor at all lift coefficients and also showed a reduced increase in lift over that of the wing with separation than the configurations with taller vanes. However, these shorter vanes were subject to a lower momentum flow and therefore the vortices produced were smaller and weaker than those produced nearer the edge of the boundary layer from the taller vanes. These smaller weaker vortices were unable to introduce as much higher momentum fluid from the freestream as the larger vortices nearer the top of the boundary layer. They also affected a smaller volume of the boundary layer such that a small volume of low momentum fluid was being removed from the surface which was not totally removed from the boundary layer and therefore their efficiency was reduced.

The results also showed that the vane height relative to the boundary layer thickness was not the only important parameter in obtaining the most efficient position of the vortex generators. Vane orientations of 25° and 30° (Figure 5-42b & e) produced the most efficient control of separation which corresponded to orientations between 14° and 21° to the local freestream flow direction obtained from the WAKELAG results (Figure 5-30 & Appendix XIII). However, the efficiency of the shorter vanes positioned further forward on the wing section were less sensitive to greater orientation angles than the taller vanes positioned further aft. A vane orientation of 20° which corresponds to an orientation less than 14° to the local freestream flow direction acted mainly as a flow deflector (Figure 5-32 comparing vane orientation) which produced a weakened vortex such that separation was not prevented as efficiently as those configurations set at greater orientations to the local flow direction. The reduced ability to control separation was also apparent from a reduced increase in lift over that of the wing with separation than those configurations set at greater orientations to the local flow direction (Figures 5-36 & 5-39).

The results also showed that a minimum spacing of 20h with the 0.005c tall vanes was sufficient to successfully prevent separation since a reduction in spacing to 10h produced no change in the efficiency of the array (Figure 5-42f). However, an increase in the spacing to 30h or 40h showed a reduction in efficiency and in the ability to control separation since the increase in lift over that of the wing with separation was less than the

configurations with closer spacings (Figure 5-40). The most efficient arrangement of 0.005c tall vanes therefore had a spacing ratio of 20 whereas a more efficient arrangement overall of 0.0126c tall vanes positioned at 65% chord and toed out 30°, had a spacing ratio of only 8. It may therefore be possible to achieve a similar or better efficiency with these taller vanes by increasing the spacing. However, the maximum efficiency of separation control may depend on a spacing parameter normalised on wing normal chord rather than on vane height. Comparisons of the surface oil flow visualisation results (Figure 5-32) show that the effect on the surface flow is similar for vortices produced from the 0.005c and 0.0126c tall vanes positioned at 0.55c and 0.65c respectively with spacings of $0.13c_o$.

Similar efficiencies were also achieved on the wing swept at 50° with the taller cropped delta vane vortex generators but the shorter cropped delta vane vortex generators efficiency improved to match that of the taller vanes (Figure 5-49). These efficiencies were all produced from vortex generator arrays matched to the local boundary layer thickness at various chordwise positions with a spacing of $0.13c_o$ which also suggests the use of a spacing parameter based on wing normal chord rather than on vane height. The improvement in performance of the shorter vanes can only be due to the boundary layer requiring a reduced amount of higher momentum fluid brought about by the mixing from the vortices to restore the adverse pressure gradient and not separate. It was shown in the comparisons of the pressure distributions for the different wing sweeps that the adverse pressure gradient over the rear of the wing section decreased with increasing wing sweep angle (Figure 5-16). This also explains the difference in efficiency on the wing swept at 40° where a vortex generator matched to the boundary layer thickness in a forward position on the wing surface was not as efficient at preventing separation as a taller vane in the same orientation at the same location. The shorter vortex generator produced a smaller vortex which did not introduce as much high momentum fluid into the boundary layer and remove as much lower momentum fluid from the boundary layer as the larger vortex did from the taller vane and therefore the efficiency of the smaller vortex at preventing separation was reduced in the adverse pressure gradient of increased magnitude.

The improvement in efficiency of the shorter vortex generators can also be seen in the lift to drag ratio figures (Appendix XV) for corresponding arrays of vortex generators at each wing sweep. For the 40° swept wing (Figure A-13) an improvement in lift to drag ratio is achieved above a lift coefficient of 0.4 with increasing vane height and proximity to separation whereas for the 50° swept wing (Figure A-14) a similar lift to drag ratio is achieved irrespective of the vane height and proximity to separation. It is also noticeable in these figures that at low lift coefficients the reduction in lift to drag ratio with vortex generators is much greater on the 40° swept wing than on the 50° swept wing, however the maximum increase in lift to drag ratio over that of the clean wing is still greater on the 40° swept wing (~7% improvement) than on the 50° swept wing (~5% improvement).

These results are similar to the guidelines given by ESDU[81] for positioning vortex generators, whereby the vane height should be approximately equal to that of the local boundary layer thickness and set to an angle to the local flow direction of approximately 16°. This present study has shown that for the best efficiency the vane height should be

fractionally less than the local boundary layer thickness. It is difficult to specify a single optimum angle that the vortex generator should be set at due to the changes in local flow direction with increasing incidence associated with swept wings but the angle suggested by ESDU[81] was included in the range of angles that gave the best efficiencies. The ESDU[81] guidelines also recommended positioning the vortex generators far upstream from the separation position, however the results showed that for the best efficiency the positioning of the vortex generators needed to be closer to separation as the magnitude of the adverse pressure gradient that the boundary layer had to negotiate increased. The best chordwise position for the vortex generators in this study with the wing swept 40° was only 0.05c upstream from the clean wing separation position. A vane spacing to height ratio of 8 was also suggested by ESDU[81]; however the present study indicated that a spacing ratio of 0.13 based on wing normal chord produced the largest improvement in efficiency when the vane was matched to the local boundary layer thickness.

6.3.2 Concave slats, canted cropped delta vanes and 'bent wires'

The results showed that these three devices did have an effect on the flow and were able to prevent separation. The balance results (Figure 5-45) showed an increase in lift over that of the wing with separation but the increase in lift from the concave slats and 'bent' wires was not as great as that of the upright cropped delta vane vortex generators. Similarly, the lift dependent drag factor results (Figure 5-46) showed all these devices not to be as efficient as normal upright cropped delta vane vortex generators with the canted cropped delta vane vortex generators being the only devices to obtain a significant reduction in lift dependent drag factor at high lift coefficients. This poor performance and efficiency is thought to arise from the design of the devices.

The concave slats and canted cropped delta vanes both acted as flow deflectors effectively (Figure 5-43 & 5-44) but the vortices produced are thought to be weaker than those from normal upright cropped delta vanes. The upright cropped delta vanes generate a vortex along the leeward side of the leading edge due to the pressure on the windward surface of the vane being much greater than the pressure on the leeward surface. Thus the flow in the vicinity of the leading edge tries to curl around the leading edge from the windward to the leeward surface and due to the leading edge being sharp causes the flow to separate along its length and form a vortex which is shed downstream.

The canted cropped delta vanes produce a vortex in the same manner except that the effect of tilting the vane reduces the pressure difference between the two surfaces and the resulting vortex shed downstream is weaker than that from an upright vane and therefore the efficiency was reduced. The concave slats produce a vortex in a similar manner to that of a wing where the pressure difference between the upper and lower surfaces causes the flow in the vicinity of the tip to curl around the tip from the windward side to the leeward side to form a vortex. These tip vortices are thought to be weaker than those produced from the leading edges of delta wings since they arise from the natural migration of the flow in the wing tip region towards the lower pressure side

whereas the vortex on a delta wing is a direct result from the change in pressure along the swept leading edge which is driven by the oncoming flow.

The 'bent' wires do not generate a vortex to remove the low momentum flow and replace it with a higher momentum flow from the freestream. Instead, the flow around the 'bent' wires, which can be considered as cylinders, separates and sheds a wake since the Reynolds number based on the wire diameter is approximately 7000 which is too great for the flow to remain attached or to form two distinct stable vortices. These wakes are shed downstream and, from their turbulent structure, were able to affect some mixing in the boundary layer such that separation was prevented at low incidences. However the random mixing from the turbulent wake appears to be not as efficient as the ordered mixing from a vortex.

6.3.3 Wire sub-boundary layer vortex generators

The results showed that none of the wire configurations investigated proved effective in controlling separation. This was not surprising since previous investigations using wires[76,77] have concentrated on leading edge flows on highly swept delta wings where they are positioned close to the leading edge in a thin boundary layer to redirect the vorticity of the flow. In this study the boundary layer on the wing, where the wires were positioned to prevent trailing edge separation, was much thicker with no significant vorticity to redirect (unlike that close to the leading edge on a delta wing) and since the wires probably only generate a limited amount of vorticity their relatively poor performance was perhaps to be expected.

6.4 Shear stress sensitive liquid crystal measurements

6.4.1 Vortex skin friction distributions

The shear stress sensitive liquid crystals were able to detect the effect of the vortex on the boundary layer skin friction since changes in hue with a vane present to that with no vane present were detected in the region where the surface oil flow visualisation results showed the vortex to affect the surface flow (Figures 5-52 to 5-54). These changes in hue showed an increase in shear stress on the downflow side of the vortex with a steady reduction in shear stress through the vortex towards the upflow side. This was expected since the action of the vortex reduces the thickness of the boundary layer on the downflow side and introduces higher momentum fluid particles from the upper boundary layer or freestream. This increases the momentum of the flow locally resulting in a greater velocity gradient through the boundary layer which increases the shear stress at the surface. On the upflow side of the vortex the existing boundary layer, as well as the lower momentum fluid from the boundary layer on the downflow side, combine to form a thicker boundary layer with a lower momentum flow. This decreases the velocity gradient of the boundary layer locally and reduces the shear stress at the surface. The action of the vortex on the upflow side also draws fluid in from the adjacent boundary layer which is thinned. The boundary layer in this region then has an increased velocity

gradient and increased local surface shear stress which was shown in the shear stress distribution measured from the liquid crystals as an increase in skin friction on the upflow side away from the vortex.

The results also showed that the interaction between the boundary layer and the vortex weakened more rapidly with a shorter vane, which was expected, since a shorter vane was subject to a lower momentum flow and therefore produced a weaker vortex. A similar observation to this was seen in the flow control study where vanes much shorter than the boundary layer thickness were less efficient than those with heights closer to the boundary layer thickness.

The change in shear stress under the vortex did not vary significantly with the size of the vortex but the increase in skin friction of the adjacent boundary layer on the upflow side of the vortex was seen to increase in magnitude and area with downstream distance as the vortex developed and with the size of the vane. This increase in skin friction was still present once the main interaction between the vortex and the boundary layer close to the surface had weakened considerably for the smallest vane. This increase in skin friction adjacent to the vortex on the upflow side appears to be the main cause of the drag increase associated with a vortex generator since under the vortex itself the skin friction is reduced on the upflow side and increased on the downflow side which has the effect of almost cancelling each other out. This observation also shows that a larger drag penalty will be produced from a taller vane, as shown in the flow control study drag polar results at zero lift (Figure 5-37), however this drag penalty may be offset by its sustained persistence downstream when used for flow control in the reduction of drag caused by flow separation. It may also be possible to improve the performance of an array of vortex generators by arranging the vanes to minimise this region of increased skin friction. However the overall performance of an array will also depend on the profile drag penalty of each extra device and on interference between the adjacent vortices if they are too close.

6.4.2 Accuracy and limitations of the technique

The measured skin friction coefficients from the liquid crystals for the smooth wind tunnel working section wall of 0.0025 to 0.0028 were of the same magnitude to that expected theoretically on a flat plate with a turbulent boundary layer in a zero pressure gradient of 0.0029 (Appendix XII). The measured values also agreed quantitatively with those obtained from the Preston tube measurements of 0.0022 to 0.0023 which were also able to show increases and decreases in the skin friction through the location of the vortex. However the liquid crystal method for determining the skin friction requires improvements since the magnitude of the errors in the calibration (Appendix VIII) are considerable.

The calibration errors arose from tiny imperfections in the machining of the disks on the calibration rig which slide over each other to apply a shear stress to the enclosed liquid crystal in the middle. These imperfections caused the thickness of the liquid crystal layer to vary around the disk which then caused the applied force on the layer to change since

the force transmitted depended upon the layer thickness. An overall average thicker layer causes a reduction in the shear stress transmitted and vice versa for a thinner layer. It was therefore unknown whether the measured shear stress was the true value for the recorded hue. This problem could not be resolved through setting the thickness at the same point on the disk or measuring the hue and shear stress at the same point on the disk since unknown systematic errors would be introduced (i.e. consistently measuring a smaller or greater average shear stress for the disk than the hue at the point of measurement).

One possible solution to this would be to take a snapshot of the liquid crystal at one instant encompassing the entire liquid crystal layer around the disk so that the average hue of the layer could be measured and calibrated against the instantaneous shear stress measurement. However this has its own problems since the calibration must be performed at the correct viewing and lighting angle and therefore several cameras and light sources would be required to take several snapshots at the same instant at several points around the disk.

Another solution would be to average the shear stress around the disk over a number of rotations and take hue measurements at several random points around the disk which could then be averaged to give a hue measurement for an average shear stress. This approach has been used in the calibration of the liquid crystal in this experimental investigation and the calibration curve is shown in Figure A-9 of Appendix VIII. The shear stress calculated from this calibration for a given hue has an error, obtained from the two worst fit lines, of 20% which is far from satisfactory. However, this large error in the absolute values of the skin friction will not be as significant when determining changes in skin friction between two flows which have used the same calibration - the magnitude of the changes does not depend on the absolute values of the skin friction used in the calculation.

Another source of error occurs from non-uniformities in the thickness of the liquid crystal coating applied to the wind tunnel surface. However considering that the liquid crystal was applied using a fine artists paint brush the repeatability of the results, shown in Figure A-11 of Appendix X, was to within ± 0.01 of the average hue value with or without a vortex present which corresponds to an error of ± 0.0003 in the skin friction coefficient. The thickness of the liquid crystal coating applied to the surface could not be measured but experience has shown that if the coating was too thick the liquid crystal flowed over itself once a shear was applied and exhibited no hue change whereas if the layer was too thin the intensity of the light reflected was insufficient to be detected and thus any change in hue with shear could not be detected.

The inability to measure the thickness of the liquid crystal coating or to create a coating of known uniform thickness also invalidated the accuracy of the liquid crystal calibration. However as discussed earlier the calibration rig had many imperfections in the surfaces of the disk to accurately know the thickness of the layer being calibrated. In calibrating the liquid crystals it was ensured that the liquid crystal between the two disks was unable to flow over each other so that all the liquid crystal between the plates was exposed to the shear stress. It was also observed during the calibration of the liquid crystals that if the

liquid crystal layer was too thin the disks were unable to slide smoothly over each other and the intensity of any hue changes due to shear were difficult to detect. In between these two extremes was where the calibration occurred and therefore ensuring that the liquid crystal applied to the wind tunnel surface was thin enough such that any hue changes were detectable and the liquid crystal could not flow but had to experience the shear stress applied from the wind tunnel flow it was assumed, considering the size of the errors in the calibration already mentioned, that the calibration was adequate.

After considering the errors discussed above for the liquid crystals and the error in repeatability of the Preston tube measurements (±0.0001 in the skin friction coefficient (Appendix XI) which will increase to ±0.0002 when differences are considered) the differences in the Preston tube skin friction coefficients with and without a vortex present agreed with the liquid crystal results close to the vortex generator. However, at greater downstream distances, where the developing vortex had more influence on the boundary layer, large differences were observed in the changes measured by the two methods. These differences may be due to a limitation in the use of Preston tubes[111] to measure skin friction in close proximity to a vortical flow where the velocity in the wall region may deviate considerably from the law of the wall and invalidate the calibration which was performed in a normal turbulent boundary layer. Therefore the pressure differences measured in and around the vortex may be interpreted into incorrect skin friction values.

6.4.3 Application of the technique to wind tunnel models

The liquid crystal technique has, even with all the uncertainties and errors associated with the thickness of the liquid crystal coatings and short comings of the calibration device, shown that useful quantitative results of the surface shear stress distribution can be obtained on a flat surface. The method has also shown that many cameras are not required to obtain shear stresses with vectors as used by Reda et al.[100] A knowledge of the surface flow streamlines obtained from surface oil flow visualisation combined with the shear stresses from the liquid crystals viewed from a single direction can give as much information about the observed flow. However for the liquid crystal technique to be used in wind tunnels to measure the skin friction distribution over a model several improvements will have to be made.

1) The liquid crystals used will need to be more viscous such that longer periods of testing can be performed before the liquid crystals need replenishing. However a more viscous liquid crystal may not have the same sensitivity as a less viscous type and some details of the flow may be missed. A balance between detail and the length of usable run time in between applications of the liquid crystals will need to be found.

2) The lighting and viewing angles and positions will also need careful thought since a peculiarity was observed in the shear stress results at the first downstream position when a vortex was present in the working section. This was detected by the liquid crystals as an

increase in the freestream skin friction to that of the smooth wall results. However, the increased hue measured, and therefore greater shear stress assigned, was the result of light reflecting off the vane itself since at this streamwise position the light was close to the vane and therefore the amount of light and the angle it made with the liquid crystals was altered and incorrect hue measurements were made. On a model that changes attitude the lighting and viewing angles could be synchronised with the model attitude so that they move together or extra calibrations could be made to cover the range of viewing and lighting angles encountered over the model attitude range. If, however, the model has a curved surface the technique will not be useful since there will be an infinite number of viewing and lighting angles to be considered and the more complex the model, the greater the likelihood is of unwanted reflections of the light source.

3) The thickness of the liquid crystal coating also poses a significant problem. Methods need to be developed to determine the depth of the liquid crystal coating and even if the depth can be determined at the start of the test the thickness of the coating is likely to change during the test as, inevitably, some liquid crystal will be blown away. The thickness of the coating also poses a problem in the calibration of the liquid crystal because two suitable uniform flat disc surfaces will be required in order to apply a steady shear stress to the liquid crystal at all points around the disks.

With an improvement in the viscosity of the liquid crystal coating and the development of an arrangement to synchronise the light source and camera with the attitude of the model, it should be possible to obtain quantitative skin friction measurements over a wing surface away from regions of high curvature (leading edge) by using this technique. This technique would then enable the areas causing the largest drag to be seen and the effect of any modifications made to the wing easily recognisable since the DERA[102] computer software proved to be extremely useful in detecting small hue changes enabling a shear stress to be assigned. It was also straight forward to use enabling almost any size area to be surveyed in whatever detail was necessary. In particular this technique would aid in the positioning of flow control devices since their effect on the drag of the wing, obtained from balance data, could then be better understood.

7. Non-Technical Discussion

7.1 General outlook

7.1.1 Performance improvements

When the vortex generators were correctly positioned and orientated on the wing upper surface an improvement in lift was observed with a decrease in drag at manoeuvre or high lift conditions, i.e. when performing a turn or at take-off. Therefore the vortex generators would improve the turning and take-off performance of a highly swept wing aircraft with highly swept trailing edges enabling larger payloads to be carried, shorter runways to be used or less powerful engines with the same payload as before. The performance of the ailerons could also be improved from positioning the vortex generators forward of the ailerons such that the ailerons are operating in a more energetic flow and effecting a greater control force for a given control input.

7.1.2 Possible aircraft applications

The vortex generators will primarily be of use on future military aircraft where the requirements for the next generation of combat aircraft will need to combine stealth with manoeuvrability and long range which necessitates wings with sweep angles between 40° and 50°. However future civil and transport aircraft will be required to have a higher cruising speed and be able to carry larger payloads than those of today. One method of achieving an increased cruising speed is to increase the wing sweep angle, however this also increases the take-off distance since a higher speed is necessary to generate the required lift force for take-off with more highly swept wings. Similarly if higher payloads are to be carried as well, the take-off distance will be increased further still. Therefore any method which can improve the high lift performance of the wing will be very beneficial in this market too as existing runways will still be able to be used by these larger and faster transport and civil aircraft.

7.1.3 Stealth requirements

The requirements for future stealthy military combat aircraft will necessitate the vortex generators to be manufactured from a radar absorbent material rather than from thin flat steel plate since the vortex generators will increase the radar cross section of the aircraft when viewed from certain positions. The vortex generators will also increase the drag of the aircraft at low lift coefficients when they are not necessary, such as during the cruise, and therefore a reduction in range, maximum speed and endurance will result. However it is thought that advances in technology will enable the vortex generators to be active such that they will lie flat with the wing surface until they are required when they will be activated by an electrical impulse to stand upright on the wing. This will then minimise the radar cross section of the aircraft during normal flight conditions with no penalty to drag and the subsequent reduction to range, maximum speed and endurance. This latter feature will also be important on civil and transport aircraft, which spend most of their

time under cruising conditions, if they are to benefit fully from the addition of vortex generators for flow control. Future development of this active control technique may also eliminate the need for a tail on the aircraft and reduce the radar cross section even more since by activating various vortex generators at various positions on either wing the lift and drag distributions about the aircraft may be altered to induce pitching, rolling and yawing moments which could be used to control and direct the aircraft.

7.1.4 Marketing the technology

There are therefore two marketable areas for this research. The first is to apply this technology to existing military aircraft to improve their manoeuvrability performance or 'dog fighting' capability and the second is to examine the possibilities of using active vortex generators to control a future aircraft. It is also thought that it may be possible to obtain a Patent for the results of this research and its applicabilion.

7.1.5 Section format

The following sections therefore discuss:-

1) the process of Patenting the technology,

2) the possible markets for the technology and how the technology should be marketed for:-

   i) application to existing aircraft, and

   ii) developed for active flight control,

3) setting up a business for manufacturing and applying the technology on existing aircraft and the development of the technology for active flight control,

4) a discussion on the feasibility of this marketing strategy with regard to the ownership of the technology, and

5) the use and assessment of the relevance of Project Management techniques in planning a PhD research project.

7.2 The process of patenting technology

7.2.1 What is a patent?

A patent is a document containing the full details, with drawings and diagrams, of the basic idea behind any product or process that is new and forms a sufficiently inventive advance over what was known before. These patents fulfil two roles:-

1) They provide legal protection for novel products and processes as far as the inventor is concerned, since the protection given by the patent is a monopoly to produce and / or sell the product or to operate the process within the country that the patent applies. This protection is given against all products or processes which fall within the definition of the invention in the patent and not only against copying of the inventors own product or process, and

2) They ensure that the knowledge of these products and processes is available to all, since the monopoly granted is considered to be part of a bargain with the state that in exchange for the monopoly the inventor will disclose for publication the full details of the invention. This bargain enables further work in the field of the invention to proceed without delay from the point reached by the inventor and ensures that when the monopoly ends (the maximum being 20 years) anyone wishing to make or use the invention will have the full information upon it.

Inventions do not need to be patented but may be kept secret, however, by keeping it a secret the inventor runs the risk of open competition and on a competitor stumbling upon the same idea and patenting it for themselves.

7.2.2 Is the technology patentable?

Patenting is a long, complicated and costly process, Figure 7-1, which involves many people such as patent agents, solicitors and barristers. Therefore, before applying for a patent it must be decided whether or not the discoveries are patentable. For them to be patentable they must not:-

1) have been disclosed publicly in any way anywhere in the world before the date of application for a patent,

2) be obvious to any normal technically informed person working in the relevant field,

since no one must be allowed to monopolise that which is already public knowledge or which might have been obtained from a public source. In the case of the current research there are two patentable discoveries. These are:-

1) the flow characteristics of wings with highly swept trailing edges at high lift and manoeuvre conditions can be improved through the use

of correctly positioned conventional vortex generators to increase lift and decrease drag, and

2) active conventional vortex generators on the wing surface which can each be independently activated may be used to control the aircraft in pitch, yaw and roll and thus eliminate the need for a tail-plane and fin.

7.2.3 The patent application

Having established the fact that the discoveries are patentable a patent application can be filed which normally takes a few weeks with the help of an agent. To limit the initial costs at this early stage the application is informal with the minimum requirement being an application form with a description of the discovery and a sketch and the payment of the specified fee to the Patent Office which issues a receipt carrying the filing date. The discovery can now be marked 'patent applied for' from this date of filing.

The content of these first papers must be correct since they will form the whole basis of the rights which may eventually be granted and therefore an inadequate first description may not be correctable later and valuable rights may be forfeited. It is therefore advisable to involve a professional advisor from the start, such as a patent agent. These agents belong to a very small group of specialists recognised by the Patent Office who act on behalf of others and, by virtue of their training and experience, have acquired an extremely wide and varied knowledge of technical subject matter which enables them to give correct and reliable advice.

7.2.4 Patenting developments of the technology

After the filing date no steps are taken for one year at the Patent Office. However, if the discovery is developed further during this period consideration must be given to filing these additional developments before they are published. However, adding new information to the original specification is not permitted and so a fresh application must be filed which may mean that by the time 12 months are up, there may be two or three applications on file. The information in these various applications may be combined into a further composite specification and filed as a further application (within the 12 months) which is allowed to be backdated to the very first filing date ('claiming priority'). This system can also work in reverse with a fresh application claiming priority from the previous application, within the first year, and thus extending the maximum life of the original patentable discovery by one year which may prove to be very useful if done successively over several years if the discovery proves to be valuable.

7.2.5 Novelty searches

It is also a good idea during this period to make a novelty search in order to determine whether the discovery is novel, since a thorough search will eventually be made by the Patent Office through the millions of patent specifications filed over more than a century in the patent offices of the major industrial countries, before granting a patent. The costs of continuing a patent application are substantial so a novelty search at this stage may save large costs later especially if the novelty search shows the discovery not to be new since the procedures can be terminated at this stage before substantial sums of money have been spent. The patent agent is also an ideal co-ordinator for these technical literature searches and can give advice on the outcome of the search results in relation to the patent rights involved. The patent agent will also have access to technical translators to assess foreign language documents.

7.2.6 Patenting in other countries

During this one year period an application can be made for a patent in other countries, since the filing and recognition of patents is international with a large amount of standardisation between patent procedures from different countries. The Paris Convention for the Protection of Intellectual Property of 1883 is the cornerstone of the modern patent system with almost one hundred signatory nations. This guarantees that each signatory will extend the rights it gives its own people to citizens of other signatory countries. The Convention provides for the right of priority with all of the applications being regarded as having been made on the same day as the first (Convention filing) which is of great importance. National filings still predominate, but the European and Patent Co-operation (World) Treaties have made supranational patents possible. The choice of national, regional (European) or World (PCT) patenting routes depends on many factors with the greatest of these being the relative cost of filing a patent and keeping it in force in each territory.

7.2.7 Patent application after one year

At the end of this first year after the filing date the formal definitions ('claims'), an abstract, a statement of who the inventors are, a formal request for the official search and preliminary examination must be filed at the Patent Office, and the official fee paid.

The 'formalised' application is passed to examiners who conduct the search and check that all formalities have been complied with. Any minor defects needing rectification will be pointed out and a search report issued. Once the Patent Office is satisfied the specification is passed for official publication, together with the results of the search, unless the application is withdrawn. This publication occurs approximately 18 months after the filing date and the contents of the application for the first time are made public. This publication date is also that from which any enforceable rights come into effect, however no actual legal action can be started until the patent is granted (it still may not be granted) but a claim may then exist for damages going back to the date of publication.

7.2.8 The full examination

The next step is the filing of a request (with fee) for a full examination if both the search result and the novelty search results show that the eventual grant of the patent is likely. Otherwise the application may be withdrawn saving the cost of the full examination and the corresponding work for the Patent Office. This request must be filed within six months of the publication date and the examination report can take anything up to 15 months to appear.

This report covers the novelty and inventiveness of the application, the clarity and consistency of the description and claims, and questions concerning compliance with other requirements of the Patent Act and sets a deadline by which any objections must be met (this is usually within four and a half years of the first filing date). Once the application has passed there is an administrative delay of a few months before the formal grant document is issued. This document includes a copy of a revised, printed specification and anyone who infringes the patent, as defined in the claim(s), can now be sued in the High Court.

7.2.9 The life and enforcement of a patent

The patent can last a maximum of 20 years from the application date but remains in force only so long as the annual renewal fees are paid to the Patent Office. If interest in keeping up the patent is lost and the renewal fee is not paid anyone else can use the information in the patent free of charge. However, having received a patent for the new product the patent rights may be commercialised in three ways;

i) outright sale,
ii) maintenance of a monopoly, and
iii) licence (exclusive, sole or non-exclusive).

7.3 Marketing the technology for application on existing aircraft

7.3.1 Identifying the potential aircraft

There are many different types of military aircraft operating around the world with various air forces and navies from many countries. These aircraft range from low speed training aircraft with unswept wings and large reconnaissance and transport aircraft with wings of low sweep to the fighter, interceptor, ground attack and bomber aircraft with delta, variable geometry and highly swept wings. From these, the aircraft which are most likely to benefit from the control of flow in the trailing edge region of the wing are the fighter, interceptor, ground attack and bomber aircraft which have highly swept wings but which do not have a delta or variable geometry wing since a delta wing has an unswept trailing edge or a trailing edge with a very small sweep angle and a variable geometry wing when manoeuvring or at take off will not have a very large wing sweep as it is designed to have the correct wing sweep position to suit the flying conditions, i.e.

it is able to cruise at a high supersonic speed in the swept configuration and manoeuvre and take off with a configuration that is unswept or of a lower sweep angle.

7.3.2 The potential customer countries and aircraft

The military aircraft that are operated today with highly swept wings with highly swept trailing edges tend to operate in countries of:-

Africa - Algeria, Angola, Egypt, Ethiopia, Libya, Somalia, Sudan, Tanzania, Zambia,

Asia - Afghanistan, Bangladesh, China, India, North Korea, Pakistan, Syria, Vietnam, Yemen,

Eastern Europe - Bulgaria, Byelorussia, Czech Republic, Hungary, Kazakhstan, Poland, Romania, Russia, Ukraine, Uzbekistan,

and

Cuba.

However the Italian Air Force operate the Aeritalia G91T and G91Y in the pilot training and light fighter, tactical support role and the French Navy and the Argentine Navy operate the Dassault Super Etendard in the strike fighter role.

The aircraft operated by the African, Asian and Eastern European countries and Cuba are all old Soviet designs from:-

Mikoyan-Gurevich - MiG-15, MiG-17 & MiG-19,

Sukhoi - Su-7,

and

Tupolev - Tu-16 & Tu-22,

or copies of these aircraft built by the Chinese as the:-

Nanchang Q-5/A-5 (based on MiG-19),

Shenyang J-5/F-5 (copy of MiG-17), J-6/F-6/JJ-6 (copy of MiG-19)

and

Xian H-6 (copy of Tu-16).

These old Soviet aircraft were all first designed in the late 1940's and early 1950's and are the first generation of military jet aircraft which, are therefore, all outclassed by the more modern aircraft of Western Europe, North America and Russia, in terms of manoeuvrability and avionics but are much cheaper to purchase and maintain. These areas would therefore be good markets for any simple devices which could improve the manoeuvrability of their aircraft since endurance and range are not a major priority in the

operational profiles of these types of aircraft but close in air to air combat where better manoeuvrability is necessary are part of their operational profiles.

7.3.3 North American stealth aircraft

The only other operational aircraft with the required highly swept wing trailing edges which may benefit from this research are the North American stealth aircraft, i.e. the Lockheed F-117A and the Northrop B-2. However, this is not a potential market for attaching these flow control devices to improve the aircrafts manoeuvrability since this would increase their radar signatures when viewed from various aspects and these two aircraft are not designed to participate in close in air to air combat where better manoeuvrability is necessary. Aircraft of this sort would benefit more from the active type of flow control over the trailing edges of highly swept wings which if developed sufficiently may eliminate the need for a tail and other control surfaces and reduce their radar signature significantly.

7.3.4 Methods of marketing the technology

There are three possible ways to market the technology to potential customers for use on existing aircraft. These are:-

7.3.4.1 Specific Excess Power calculations

The Specific Excess Power provides an estimate of the 'dog fighting' capability of an aircraft. These calculations could be performed on aircraft representative to those of the potential customers with and without the technology applied to provide an indication of what the likely benefits would be since, other things being equal, the aircraft with the superior performance is likely to win. Comparing plots of the Specific Excess Power versus Mach number or speed at different altitudes and under different 'g' loadings for the aircraft with and without the technology would show the areas of the flight envelope where the technology would have an advantage with similar comparisons made with other aircraft.

7.3.4.2 'Dog fight' simulations

'Dog fight' simulations could be performed on high powered computers or workstations where fighter pilots from customers interested in the technology could fly their aircraft with and without the technology in 'dog fights' against each other and the success rate compared to the success rate without the technology.

7.3.4.3 Flight tests

The technology could be applied to some of the customers aircraft and a series of flight trials performed to assess the operational performance of the technology in terms of 'dog fight' success results.

7.3.5 Market assessment

Of these three marketing methods the Specific Excess Power calculations and the analysis of the results would not be a very time consuming and expensive study since there are very few different types of aircraft to model and the software required to calculate the Specific Excess Power can be run on a PC or workstation with each configuration only taking a few minutes. The cost of these Specific Excess Power calculations would be in obtaining the software and a PC or workstation capable of performing the calculations. The calculations would only take a couple of days and so to keep costs low the software and PC or workstation could be hired or the facilities at a University or other institution rented. However, 'dog fight' simulations and flight tests are, by comparison, very expensive since the simulations would require several high powered workstations, depending on the number of pilots taking part, with the relevant simulation software and hardware, and the flight tests require the modification of an aircraft and a test program which would involve many people.

Therefore to gauge the level of interest before any large sums of money are invested the Specific Excess Power calculations would be performed and the results sent to the potential customers 'free of charge'. This letter would also outline the possibilities of the 'dog fight' simulations and flight testing to further show the potential benefits of employing this new technology to their existing aircraft.

7.3.6 Marketing 'dog fight' simulations

Thus, depending upon the level of interest, a decision would have to be taken as to hiring or purchasing the workstations for these 'dog fight' simulations. However, the software and hardware would still need to be purchased and a computer specialist employed to assist in the 'setting up' and the running of the simulations. The cost of these simulations would be set for the first customer to cover the costs of the hardware and software and accommodation costs for the technicians and consultants over the evaluation period since the pilots would be supplied by the interested customer. However the results from these simulations may interest other customers from which profits would be made or result in a flight test program.

7.3.7 Marketing flight tests

The first customer interested in a flight test program would receive the technology for free on the trials aircraft in exchange for access to and assessment of the flight test results. If these flight trials proved successful and the customer feels the technology is worth investing in, the technology would then be applied to their aircraft at a price to cover costs and materials only. The vortex generators would not cost much to manufacture being made from sheet steel with no need for any specialist tooling or processes and, initially for the flight trial period, they would only need to be glued to the wing surface with a very strong adhesive. The vortex generators could be riveted to the aircraft wings to effect a more permanent attachment to the aircraft if the customer was

satisfied with the flight trials, however this may require the expertise of an aircraft structural engineer and a new airworthiness certificate which could prove expensive and so this would have to be left to the customer to decide.

The vortex generators may not change the aircraft drag significantly because many of the aircraft have fences on the wings to prevent spanwise flow which may be eliminated with this new technology resulting in an increase in aircraft performance with little or no increase in drag. However, the removal of the fence may also require the services of an aircraft structural engineer and a new airworthiness certificate which again could prove expensive and so this would have to be left to the customer to decide.

7.3.8 Exploiting the technology

Once the first customer has bought the technology and shown its potential from improvements in performance, other countries with these types of aircraft would want the technology. There are several thousand of these types of aircraft in operation in the countries mentioned earlier and so there is a very large potential market where profits can now be realised. Depending upon the magnitude of this market, several people could be employed to manufacture and apply the vortex generators to the customers aircraft or a license could be granted to the customer for them to manufacture and apply the vortex generators to their aircraft. There should also be no need to be concerned about applying this technology to these aircraft, since they are far 'outclassed' by modern types in Western Europe, the USA and Russia and therefore there is no risk of their armed forces being better prepared than our own or other friendly nations.

7.4 The potential market for active flow control for flight control

7.4.1 Technological and financial considerations

The potential market for active flow control for flight control will be very limited due to the high technology involved in the type of aircraft it would be employed upon and on the maintenance involved, since highly specialised ground crew and equipment would be required. The pilots would also require special training. The cost of an aircraft having this type of flight control would cost several million pounds and there would be a considerable amount of expenditure in developing the manufacturing techniques and technology to be able to incorporate this type of flight control into an operational aircraft, i.e. computer software for flight control, wing manufacture employing the materials necessary to enable the flow control devices to be active, aircraft design and models built for wind tunnel testing and the cost of an extensive wind tunnel test program, prototypes for flight testing and the cost of an extensive flight test program, pilot training, ground crew training and specialised equipment for servicing.

However, with only partial development of this technology, the devices could be incorporated into conventional aircraft to assist the performance of the usual flight controls, i.e. rudder, elevators, ailerons and flaps. Also if damage occurs to any of these

flight controls the flight control software could be developed in such a way that the flow control devices supply sufficient flight control, in conjunction with the remaining flight controls, to safely fly and land the aircraft, as this technology would not rely on hydraulics, mechanical or electrical linkage to the pilots flight control inputs.

7.4.2 Potential customers

Unfortunately, due to the high operational, research, design and training costs, the purchasing cost per aircraft and the high technology demands of the aircraft the only countries that would be able to maintain and operate this technology would be the USA, Western European countries and maybe Russia. The Western European countries would, most likely, have to form a conglomerate to provide the necessary finance, technical skill and the facilities for such a project as has been so successfully done with the SEPECAT Jaguar and the Panavia Tornado and as is being done with the Eurofighter 2000. The USA, however, with their specialist knowledge gained from designing very high technology aircraft, such as the Lockheed SR-71, Lockheed F-117A and Northrop B-2, are the most likely customer to exploit this kind of technology first in an operational aircraft. However, the recent cut backs in defence funding in the USA and Western Europe and the reduction in armed forces in the USA, Western Europe and Russia suggests that funding for such projects may not be available.

7.4.3 Marketing strategy

To get a potential customer involved with vortex generators to be used as active flight controls the concept must first be shown to be feasible. This would involve a simple swept wing wind tunnel model placed in a low speed wind tunnel test facility, to keep costs down, and recording the forces and moments induced on the model from different combinations of vortex generators positioned on the wing. A two week test period should be sufficient to obtain a 'proof of concept' and to discover what 'is' and 'is not' possible. If the concept results are promising a research grant could be applied for and the technology developed further or the results could be presented to potential customers such as the Ministry of Defence in the UK, the Department of Defence in the USA and various other defence ministries in other European countries. However a point would be reached where the technology would have to be sold to a larger company or become part of a research program from a large company that is interested in this type of technology such as:-

British Aerospace or the Defence Evaluation and Research Agency in the UK,
Dassault, Mikoyan-Gurevich or Sukhoi in Europe, or
Boeing, Lockheed, McDonnell-Douglas, NASA, Northrop-Grumman or Rockwell in the USA.

The interest of a large company would eventually be required if the technology is to be used in a sophisticated future military aircraft since a small company will not have the

wide knowledge base and the finance to successfully develop all that is required to incorporate this new technology. Specialist knowledge of design, structures, materials, engines, avionics and weapon systems will be required. The new technology for active flight controls will also need to be developed which will be a major research project in itself.

7.5 Forming a business to manufacture and market the technology

7.5.1 Initial type of business

To perform this marketing strategy a business would need to be 'set-up'. Initially this could be as a sole trader or a partnership for the Specific Excess Power calculations as this is a relatively inexpensive and risk free venture to assess the potential market for the new technology. The finance required would be minimal, and could be found from private sources, since the calculations can be performed on a PC or a workstation requiring no special premises. The only costs would arise in obtaining the software and a PC or workstation for a short time period to perform the calculations and in mailing the results to the potential customers. The business could be set up as a private limited company but the additional costs involved (e.g. registering fee, a registered office, accountant, secretary, company stationery) for the added security afforded cannot be justified for this low risk market survey.

7.5.2 Changing to a private limited company

However, if sufficient interest is shown in response to these calculations for 'dog fight' simulations and flight tests it would make better business sense to form a private limited company rather than operate as a sole trader or in a partnership. This is because the risks are very much greater than before and sole traders or partnerships are liable for all the debts whereas in a limited company the members or shareholders have no liability to contribute to debts of the company beyond any amount unpaid on any shares issued to them. Private limited companies also have advantages for borrowing money in order to expand or to trade efficiently and profitably. This would be useful as if the market shows potential a significant amount of finance would be required for purchasing or leasing the equipment necessary for the 'dog fight' simulations and for manufacturing the vortex generators for applying on aircraft.

7.5.3 Choice of premises

However, no special premises would be required for the 'dog fight' simulations and flight trials as these would be performed on the customers premises. If large scale manufacture of the vortex generators and the application to aircraft is achieved premises may have to be sought depending on the amount of orders, but it may be more convenient to manufacture the vortex generators on site since the customers are all overseas or to have the vortex generators manufactured using the facilities of the customer or of a metal

working company. Since the customers are all overseas the location of the premises is not important and a large garage or small workshop should be sufficient for storing and manufacturing the vortex generators and for storing any other supplies such as the hardware for the flight simulations.

7.5.4 Expansion into active flight control

The success of the 'dog fight' simulations and the application of the vortex generators on existing aircraft would generate sufficient finance to proceed with the wind tunnel test program for the 'proof of concept' into flight control of an aircraft with active conventional vortex generators which could then be presented to potential customers. This would also not require a specialist building since a wind tunnel facility would be hired for the tests and the data analysed on a PC or workstation.

7.6 Who owns the technology?

Before investigating the market and forming a detailed business plan, of predicted costs, personnel and equipment required, to present to various sources of finance, such as banks, government grant departments, finance companies and private investors, it must be decided who owns the technology and the right to exploit it. The research project has been directed by DERA under an MOD contract into highly swept wing flows and so the MOD may feel that they own the rights of how the technology should be exploited and to whom the technology can be sold and they may already have a patent for the technology. However, the MOD may not have applied for a patent since they may not want other countries to know what types of technology they are interested in since this would give some indications as to what types of military aircraft may be developed in the future and prompt other countries into developing techniques to counteract the full effect of this new technology.

However, the technology developed during the PhD by the student will have to be published as a thesis and also in technical papers in Journals and Conference proceedings to satisfy the regulations of the University and therefore any of the potential customers will have free access to the technology from which they will be able to conduct their own modifications to improve the performance of their aircraft. It would therefore be in the interests of the MOD if they feel that they do have the rights to the way the technology is exploited to proceed with the marketing strategy and apply for a patent before the thesis and technical papers are published and made available to everyone. The PhD student could also apply for the patent and market the technology with the aid of the University if the MOD were not concerned about the technology being made available to other countries.

Whether or not the MOD feel they have the rights to exploit the technology the PhD student will still have gained an invaluable amount of knowledge which, from the perspective of the student, is much more valuable than any possible profits from making the technology available on the open market.

7.7 PhD plan using project management techniques

7.7.1 Work breakdown structure

Project management techniques have been used to identify the different elements from the research project which are to be used to produce the PhD thesis. This is shown as a work breakdown structure, Figure 7-2, where the first level in the structure illustrates where the components of the thesis will arise from and the second level the contributions from each of these areas. The final level shown illustrates some of these contributions in greater detail but it is impracticable to show anymore than this since the figure would become too cluttered. However, it clearly shows that the main contributions to the thesis will arise from wind tunnel programs and CFD calculations at DERA Bedford and two wind tunnel programs at Cranfield University's College of Aeronautics together with the associated literature search results. The contribution from the management aspect to satisfy the Total Technology requirements of the PhD is also illustrated.

7.7.2 Network path and time analysis

The work breakdown structure has been used as the basis to develop a network path for the main elements of the research project, Figure 7-3. This figure shows how all the separate elements of the research project will combine together to produce a PhD thesis and other reports required by the MOD and Cranfield University. This network path has then been used to perform a time analysis to identify any critical paths and available floats. This is shown in Figure 7-4 using the activity number allocated in the network path only and an estimate of the duration of each activity in weeks. The early start and finish and late start and finish are calculated, in weeks, for each activity and the float obtained. The time to complete the project using this type of analysis technique is much less than the time available for the project, 141 weeks (3 years less 5 weeks per year holiday), since several activities can be performed at the same time, and large floats are available. Unfortunately this is not the case since the project is to be performed by one person and therefore all the activities cannot be performed concurrently. However, the time analysis does show where more care shall be required in planning the project in more detail since those parts of the path with the smallest floats may cause problems which could delay the project significantly.

7.7.3 Gantt Chart

Using the results from the time analysis a Gantt chart, Figure 7-5, has been produced which includes other considerations such as deadlines for Milestone reports, wind tunnel availability, workshop manufacturing time for wind tunnel models and equipment and lecture courses. Care has also been taken to ensure that concurrent activities will be feasible, i.e. it is possible to perform two literature searches at the same time but not to attend a lecture course at Cranfield University and perform a wind tunnel test at DERA Bedford.

7.7.4 Assessment of project management techniques for a PhD project

The project management techniques proved to be very useful in initially planning the PhD project because when beginning a PhD three years seems a long period of time. However going through the procedure of drawing a work breakdown structure, developing a network path and performing a time analysis to eventually produce a Gantt chart showed that without careful planning three years will not be sufficient. The procedure also illustrated when deadlines had to be met and the work involved to meet these deadlines which may not have been realised if a plan had not been drawn. The relative importance of the elements was shown and it was possible to move the less critical elements to more relaxed periods in the Gantt chart which would not have been realised had the project not been planned correctly.

Although the project was initially planned using the project management techniques the nature of a research project may change significantly depending on research and test results. In this case the nature of the project has not changed significantly but developing some of the experimental techniques has taken longer than anticipated and the results from these new techniques has prompted further investigation which was not accounted for in the initial plan. Extra activities have also been imposed such as writing technical papers for Journals and attending and presenting the research results at Conferences. However without the use of the project management techniques at the beginning of the project the completion may have taken much longer and the direction of the PhD squandered.

8. Conclusions

The low speed experimental investigation, involving surface oil flow visualisation and the measurement of forces, moments, pressures and surface shear stress, has provided an understanding of the flowfields around two highly swept constant chord wings and enabled several computational methods and techniques for preventing the flow from separating to be assessed.

The wing flow investigation showed that the flowfield and the associated separation mechanism, although complicated, were similar on two very different wing planforms over a range of Reynolds number. Both flowfields were also seen to increase in the degree of three-dimensionality with increases in wing sweep angle.

The computational investigation, using CFD methods to calculate these flows (BVGK, TAPERBL, VFP and WAKELAG), produced pressure distributions and boundary layer information that agreed, qualitatively if not quantitatively, with those from the experimental investigation. However, the results, when taken on their own, did not enable an understanding of the observed wing flow but when used in conjunction with each other a more detailed picture was constructed. However, none of the methods were able to:-

1) show the reverse flow region behind the separation line,
2) accurately predict the surface streamlines in the separation region,

and

3) show the separation mechanism.

In particular, VFP would require further development to enable flows on wings swept more than 30° to be calculated and additions made to the boundary layer results to enable surface streamlines and particle paths to be determined.

The experimental investigation into controlling the flow showed that the complex three-dimensional flow separations over the upper surface of the wing could be prevented using a single co-rotating array of vortex generators arranged to oppose the spanwise flow towards the wing tip and produce a vortex to re-energise the boundary layer in the trailing edge region. This was achieved using upright and canted cropped delta vanes, concave slats and 'bent' wires where the efficiency of each configuration was determined from the reduction in lift dependent drag factor compared to that of the wing with separation. Wire sub-boundary layer vortex generators proved to be ineffective since these function by re-directing the vorticity of the flow (which in the region of the trailing edge is relatively weak) and not from generating vorticity through the action of mixing the oncoming flow.

The upright cropped delta vane vortex generators proved to be the most efficient type of vortex generator used, and the parametric study involving: the local orientation, chordwise location, height relative to the local boundary layer, and the spacing between the vortex generator in the array has shown that significant improvements in this

efficiency can be achieved with reductions in lift dependent drag of up to 10% and increases in lift to drag ratio of up to 7%. The observations are summarised below.

1) A vortex generator height fractionally less than or equal to the local boundary layer thickness gives highest efficiency compared with other vortex generator heights.

2) A vortex generator whose height is much less than the thickness of the boundary layer is not efficient.

3) Orientation of the vortex generators between 14° and 21° to the local flow direction gives best performance compared with other orientations.

4) The efficiency of a co-rotating array of vortex generators is determined by the magnitude of the adverse pressure gradient to be restored. A greater adverse pressure gradient requires larger vortices to be efficiently restored.

5) The distance ahead of separation for a co-rotating array of vortex generators to be efficient is determined by the magnitude of the adverse pressure gradient to be restored. A greater adverse pressure gradient requires the vortices to be closer to separation to improve efficiency.

6) A spacing ratio based on wing normal chord is more important in obtaining an efficient co-rotating array than maintaining a fixed spacing ratio based on the height of the vortex generator.

The understanding of these flow control results was aided by the results from the shear stress sensitive liquid crystal technique. These results showed that:-

1) the influence on the surface flow of a vortex produced from a vane submerged in the boundary layer weakened much more rapidly with downstream distance than a vortex produced from a taller vane,

2) the main component of drag was caused by an increase in skin friction in the boundary layer adjacent to the upflow side of the vortex and not from under the vortex itself,

and

3) the magnitude of the increase in skin friction and the affected area in the boundary layer adjacent to the upflow side of the vortex to increase with vane size.

The magnitude of the surface shear stress measured using this liquid crystal technique agreed with that from theory and measured values using Preston tubes. However, the technique at present is subject to large uncertainties in the magnitude of the measured

quantities and would benefit greatly from improvements to the calibration apparatus. Improvements are also required in the application of liquid crystals to obtain a uniform coating of known thickness which will require very little maintenance throughout a prolonged test period if useful surface shear stress measurements are to be gained from wind tunnel models. There are also problems associated with the lighting and viewing angles which will limit its use to flat surfaces or surfaces of very little curvature. However the technique could prove to be useful for interpreting wing flows using a single camera if surface flow directions are known from surface oil flow visualisations or for determining local effects on skin friction from small modifications to a surface in the flow.

9. Future Work

This research programme has shown the flows on highly swept wings to be very complicated in the region of the trailing edge once separation has occurred and an attempt has been made to understand this separation mechanism. Further insight would be gained from detailed measurements of the flowfield over the wing and in the wake using optical based flow monitoring techniques. This would give insight into the off-surface three-dimensional flowfield and enable the development of both the flowfield and separation mechanism (with wing sweep and incidence) to be determined accurately. It may also be possible to determine the strength of the circulations in the separation bubbles and any changes in the circulations with wing sweep or wing profile. Detailed boundary layer measurements would show if there are any secondary separations or re-attachments in the trailing edge region after separation has occurred since these could not be ascertained from the surface oil flow visualisation results or from the measured pressure distributions. The results from these optical based studies of the wake and flowfield around the wing and boundary layer measurements in the region of flow separation would enable validations of existing and future CFD methods.

The flow control study showed that upright cropped delta vane vortex generators were able to control separation and a set of guidelines was determined for positioning them for maximum efficiency. However, this set of guidelines is not complete as the number of vortices per unit length was not investigated fully to determine whether the efficiency depended on a minimum number of vortices per unit length for all sizes of vortex generator or just on the spacing of the vortex generators. Small improvements in the efficiency may also be gained through different vortex generator planforms or with cropped delta vane vortex generators of different aspect and taper ratios to those used in this thesis.

The new technique for measuring surface shear stress using liquid crystals showed that useful measurements could be obtained on flat surfaces. Unfortunately, the investigation showed that the magnitude of these measurements was subject to considerable errors that arose from limitations of the calibration apparatus and from not knowing the thickness of the liquid crystal coating applied to the surface. Therefore before the method can be utilised as a technique for measuring the skin friction upon wind tunnel models:-

1) a more satisfactory apparatus, manufactured to a higher standard, will be required for accurately determining a calibration of the liquid crystals;
2) a technique developed to enable a uniform coating of liquid crystals of known thickness to be applied repeatedly onto a surface, or a method developed such that the thickness can be determined - this may be possible from measuring the Intensity or Saturation of the liquid crystals.

References

1. Küchemann, D., 'The aerodynamic design of aircraft.' Pergamon Press, Oxford, pp 39-44, 1978.

2. Pearcey, H.H., 'Shock-induced separation and its prevention by design and boundary layer control.' In: 'Boundary Layer and Flow Control, its Principles and Applications', Vol. 2, Edited by G. V. Lachmann, Pergamon Press, Oxford, 1961.

3. Jones, R.T., 'Effects of sweep back on boundary layer and separation.' NACA R 884, 1947.

4. Sears, W.R., 'Boundary layers in three dimensional flows.' Applied Mechanics Review, July 1954.

5. Cahill, J.F. & Gottlieb, S.M., 'Low speed aerodynamic characteristics of a series of swept wings having NACA 65A006 airfoil sections.' NACA RM L9J20, March 1950.

6. Edwards, G.G., Tinling, B.E. & Ackerman, A.C., 'The longitudinal characteristics at Mach numbers up to 0.92 of a cambered and twisted wing having 40° of sweepback and an aspect ratio of 10.' NACA RM A52F18, September 1952.

7. Graham, R.R., 'Low speed characteristics of a 45° sweptback wing of aspect ratio 8 from pressure distributions and force tests at Reynolds numbers from 1,500,000 to 4,800,000.' NACA RM L51H13, October 1951.

8. Kirby, D.A., 'Low speed wind tunnel tests on a fully tapered wing with 81° leading edge sweep and a 6% thick RAE 101 section.' RAE TM Aero. 449, November1955.

9. Küchemann, D., Weber, J. & Brebner, G.G., 'Low speed tests on 45° sweptback wings. Part II: Balance and pressure measurements on wings of different aspect ratio.' RAE R Aero. 2419, May 1951.

10. Weber, J., 'Low speed measurements of the pressure distributions and overall forces on wings of small aspect ratio and 53° sweepback.' RAE TN Aero. 2017, 1949.

11. Weber, J. & Brebner, G.G., 'Low speed tests on 45° sweptback wings.' RAE R Aero. 2374, 1951; RAE R Aero. 2419, 1951. ARC R&M 2882, 1958.

12. Babister, A.W., 'Measurement of the pressure distribution on sweptback wings with trailing edge split flaps.' Cranfield College Of Aeronautics Report 43.

13. Black, J., 'A note on vortex patterns in the boundary layer of a sweptback wing.' Journal of the Royal Aeronautical Society, Vol. 56, pp 279 - 285, 1952.

14. Emslie, K., Hosking, L. & Marshall, W.S.D., 'Some experiments on the flow in the boundary layer of a 45° sweptback wing of aspect ratio 4.' Cranfield College Of Aeronautics Report 69, February 1953.

15. Brebner, G.G., 'Boundary layer measurements on wings of 45° sweep at low speed.' RAE TN Aero. 2298, 1954.

16. Brebner, G.G. & Wyatt, L.A., 'Boundary layer measurements at low speed on two wings of 45° and 55° sweep.' RAE TN Aero. 2702, 1960. ARC CP 554.

17. Winter, K.G. & Moss, J.B., 'Measurements of pressure distributions on a half model wing body combination of 55° sweep over a wide range of Reynolds number.' RAE TR 74149, 1974.

18. Crabtree, L.F., 'The formation of regions of separated flow on wing surfaces. Part I, Low speed tests on a two dimensional unswept wing with a 10% thick RAE 101 section. Part II, Laminar separation bubbles and the mechanism of the leading edge stall.' RAE R Aero. 2528, 1954 and 2578, 1957. ARC R&M 3122, 1957.

19. Küchemann, D., 'Types of flow on swept wings.' Journal of the Royal Aeronautical Society, Vol. 51, pp 683, 1953.

20. Küchemann, D., 'Flows with separations.' RAE TM Aero. 453, 1955, ARC 18222.

21. Küchemann, D., 'Boundary layers on swept wings. Their effects and their measurement.' AGARD AG/10/P9, 69, 1955.

22. Maskell, E.C., 'Flow separation in three dimensions.' RAE R Aero. 2565, 1955.

23. Bagley, J.A., 'Some aerodynamic principles for the design of swept wings.' RAE R Aero. 2650, 1961.

24. Cooke, J.C. & Brebner, G.G., 'The nature of separation and its prevention by geometric design in a wholly subsonic flow.' In: G.V. Lachmann, "Boundary layer and flow control", Vol. 1, pp 144, Pergamon 1961.

25. Cooke, J.C. & Hall, M.G., 'Boundary layers in three dimensions.' RAE R Aero. 2635, 1960.

26. Tani, I., 'Low speed flows involving bubble separations.' Progress in Aeronautical Science, Vol. 5, pp 70,1964.

27. Woodward, D.S. & Lean, D.E., 'The lift and stalling characteristics of a 35° sweptback wing designed to have identical chordwise pressure distributions at all spanwise stations when near maximum lift.' RAE TR 71050, 1971 (2 parts).

28. Hall, M.G., 'Scale effects in flows over swept wings.' RAE TR 71043, 1971. AGARD CP-83, 1971.

29. Smith, P.D., 'A calculation method for the turbulent boundary layer on an infinite yawed wing in compressible, adiabatic flow.' RAE TR 72193, December 1972.

30. Smith P.D., 'An integral prediction method for three dimensional compressible turbulent boundary layers.' ARC R & M No.3739, 1974.

31. Smith, P.D., 'The numerical computation of three dimensional boundary layers.' RAE TM Aero. 1945, April 1982.

32. Green, J.E., Weeks, D.J. & Brooman, J.W.F., 'Prediction of turbulent boundary layers and wakes in compressible flow by a lag-entrainment method.' ARC R & M 3791, January 1973.

33. Broadley, J.I., 'A brief description of theoretical method currently being applied to aerofoil and wing flows at the Defence Research Agency.' DRA/AS/HWA/WP95164/1, 1995.

34. Peake, D.J., Rainbird, W.J. & Atraghji, E.G., 'Three dimensional flow separations on aircraft and missiles.' AIAA Journal, Vol. 10, pp 567, 1972.

35. Taylor, H.D., 'Summary report on vortex generators.' United Aircraft Corp. R-05280-9, March 1950.

36. Lina, L.J. & Reed, W.H., 'A preliminary flight investigation of the effects of vortex generators on separation due to shock.' NACA RM L50J02, November 1950.

37. Morris, G.J. & Lina, L.J., 'A limited flight investigation of the effect of three vortex generator configurations on the effectiveness of a plain flap on an unswept wing.' NACA TN 3536, September 1955.

38. Mcfadden, N.M., Rathert, G.A. & Bray, R.S., 'The effectiveness of wing vortex generators in improving the maneuvering characteristics of a swept-wing airplane at transonic speeds.' NACA TN 3523, September 1955 and NACA RM A51J18, February 1952.

39. Beeler, D.E., Bellman, D.R. & Griffith, J.H., 'Flight determination of the effects of wing vortex generators on the aerodynamic characteristics of the Douglas D-558-1 airplane.' NACA/TIB/3336, August 1951.

40. Donaldson, C.D., 'Investigation of a simple device for preventing separation due to shock and boundary layer interaction.' NACA RM L50B02a, November 1950.

41. Weiberg, J.A. & McCullough, G.B., 'Wind tunnel investigation at low speed of a twisted and cambered wing sweptback 63° with vortex generators and fences.' NACA RM A52A17, March 1952.

42. Bursnall, W.J., 'Experimental investigation of the effects of vortex generators on the maximum lift of a 6% thick symmetric circular arc airfoil section.' NACA RM L52G24, October 1952.

43. McCullough, G.B., Nitzberg, G.E. & Kelly, J.A., 'Preliminary investigation of the delay of turbulent flow separation by means of wedge-shaped bodies.' NACA RM A50L12, March 1951.

44. Gambucci, B.J. & Wyss, J.A., 'Experimental investigation of the drag due to wedges along the trailing edge of a swept wing.' NACA/TIL/6030, June 1958.

45. Stevens, A.V. & Collins, G.A., 'Turbulent boundary layer control by ramps or wedges.' Australia, Aeronautical Research Laboratories Report A 85, April 1954.

46. Brown, A.P., 'An experimental investigation of the aerodynamic effects of forward facing wedges on the upper surface and leading edge of an aerofoil with emphasis at high angles of attack.' Aeronautical Research Laboratories - Aero. TM 356, August 1983.

47. Tanner, L.H., Pearcey, H.H. & Tracy, C.M., 'Vortex generators; their design and their effects on turbulent boundary layers.' Preliminary Report. Aeronautical Research Laboratories 16487, January 1954.

48. Curry, P.A.M., 'Some experiments on vortex generators.' ARC 16947, July 1954.

49. Newman, B.G., 'The use of normal vortex generators to delay the effects of shock induced separation in flight.' NAE Canada LR-152, December 1956.

50. Schubauer, G.B. & Spangenberg, W.G., 'Forced mixing in boundary layers.' Journal of Fluid Mechanics, Vol. 8, part 1, pp 10 - 32 , 1960.

51. Anon., 'Resume of flight experiments with vortex generators on AVRO 707A.' A. V. Roe & Co., Report Aero/707/164, March 1956.

52. Anon., 'Determination of the buffet boundaries of a Canberra P.R.Mk.7 aircraft and an investigation into the effects on these boundaries of fitting vortex generators to the mainplane.' English Electric FTN AF/192, October 1956.

53. Gould, D.G., 'The use of vortex generators to delay boundary layer separation - theoretical discussion supported by tests on a CF-100 aircraft.' Canada NAE LR-183, December 1956.

54. Anon., 'Sea Hawk F.G.A.Mk.4-W.V.825. Longitudinal manoeuvrability trials with air brakes extended and also with vortex generators fitted.' Armstrong - Whitworth Flight Test Section, Report F.T.S. 74, November 1955.

55. Strange, J.P., 'On wing fences, vortex generators and sawtooth fairings at transonic speeds (on the P.1127).' Hawker Siddeley Project Office Note 1138, April 1967.

56. Jones, J.P., 'The calculation of the paths of vortices from a system of vortex generators and a comparison with experiment.' ARC CP 361, March 1955.

57. Mcewan, A.D. & Joubert, P.N., 'A simple means of measuring vortex strength and the performance of triangular ramp - type vortex generators in a uniform velocity field.' Royal Aeronautical Society Journal, Vol. 66, pp 783 - 785, December 1962.

58. Gadetskiy, V.M., Fomin, V.M. & Serebriyskiy, Y.M., 'Investigation of the influence of vortex generators on turbulent boundary layer separation.' NASA TT F 16056, 1972.

59. Spangler, J.G. & Wells, C.S., 'Effects of spiral longitudinal vortices on turbulent boundary layer skin friction.' NASA CR-145, December 1964.

60. Mehta, R.D., 'An experimental study of a vortex / mixing layer interaction.' AIAA 84-1543, June 1984.

61. Mehta, R.D. & Lim, T. T., 'Flow visualisation study of a vortex / wing interaction.' NASA TM 86656, October 1984.

62. Mehta, R.D., 'Effect of a longitudinal vortex on a separated turbulent boundary layer.' AIAA 85-0530, 1985.

63. Mehta, R.D., 'Vortex / separated boundary layer interactions at transonic Mach numbers.' AIAA Journal, Vol. 26, No. 1, January 1988.

64. Mehta, R.D., 'Interaction between a longitudinal vortex and a shock-induced turbulent boundary layer separation.' AIAA 86-0346, 1986.

65. Pauley, W.R. & Eaton, J.K., 'Experimental study of the development of longitudinal vortex pairs embedded in a turbulent boundary layer.' AIAA Journal, Vol. 26, No. 7, pp 816-823, July 1988.

66. Wendt, B.J., Greber, I. & Hingst, W.R., 'The structure and development of streamwise vortex arrays embedded in a turbulent boundary layer.' AIAA 92-0551, January 1992.

67. Humphreys, W.W. & Reynolds, W.C., 'An experimental study of the effect of streamwise vortices on unsteady turbulent boundary layer separation.' AD-A205462; TF-42; AFOSR-89-0275TR, December 1988.

68. Shabaka, I.M.M.A., Mehta, R.D. & Bradshaw, P., 'Longitudinal vortices imbedded in turbulent boundary layers. Part 1. Single vortex.' Journal of Fluid Mechanics, Vol.155, pp 37-57.

69. Westphal, R.V., Eaton, W.R. & Pauley, W.R., 'Interaction between a vortex and a turbulent boundary layer in a streamwise pressure gradient.' In: 'Turbulent shear flows Vol. 5', Springer Verlag, Berlin, 1986.

70. Shizawa, T. & Eaton, J.K., 'Interaction of a longitudinal vortex with a 3D turbulent boundary layer.' AIAA Journal, Vol. 30, No. 5, May 1992.

71. Rao, D.M. & Kariya, T.T., 'Boundary layer submerged vortex generators for separation control - an exploratory study.' AIAA 88-3546-CP. In: 'AIAA 1st National Fluid Dynamics Congress Part 2, Cincinnati, Ohio', July 1988.

72. Lin, J.C., Howard, F.G., Bushnell, D.M. & Selby, G.V., 'Investigation of several passive and active methods for turbulent flow separation control.' AIAA 90-1598, June 1990.

73. McCormick, D.C., 'Shock-boundary layer interaction with low-profile vortex generators and passive cavity.' AIAA 92-0064, January 1992.

74. Lin, J.C., Robinson, S.K., McGhee, R.J. & Valarezo, W.D., 'Separation control on high lift airfoils via micro-vortex generators.' Journal of Aircraft, Vol. 31, No. 6, November - December 1994.

75. Kerho, M., Hutcherson, S., Blackwelder, R.F. & Liebeck, R.H., 'Vortex generators used to control laminar separation bubbles.' Journal of Aircraft, Vol. 30, No. 3, May - June 1993.

76. Ashill, P.R. & Riddle, G.L., 'Control of leading edge separation on a cambered delta wing.' DRA, November 1993.

77. Ashill, P.R., Riddle, G.L., & Stanley, M.S., 'Control of three - dimensional separation on highly swept wings.' ICAS 1994.

78. Compton, D.A. & Johnston, J.P., 'Streamwise vortex production by pitched and skewed jets in a turbulent boundary layer.' AIAA 91-0038, January 1991.

79. Johnston, J. & Nishi, M., 'Vortex generator jets: a means for passive and active control of boundary layer separation.' AIAA 89-0564, January 1989.

80. Selby, G., Lin, J. & Howard, F., 'Jet vortex generators for turbulent flow separation control.' In: 12th Turbulence Symposium, Rolla, MS, USA, September 1990.

81. ESDU, 'Transonic data memorandum - vortex generators for control of shock - induced separation.' 93024 Part 1: introduction and aerodynamics. December 1993. 93025 Part 2: guide to use of vane vortex generators. June 1994. 93026 Part 3: examples of applications of vortex generators to aircraft. December 1993.

82. Winter, K.G., 'An outline of the techniques available for the measurement of skin friction in turbulent boundary layers.' Progress in Aerospace Sciences, Vol. 18, No. 1, pp 1-57, 1977.

83. Monson, D.J., Matur, G.G., & Mentor, F.R., 'Boundary layer transition and global skin friction measurement with an oil fringe imaging technique.' SAE 93-2550, September 1993.

84. Seto, J. & Hornung, H.G., 'Two directional skin friction measurements utilising a compact internally mounted thin liquid film skin friction meter.' AIAA 93-0180, 1993.

85. Fergason, J.L., 'Liquid crystals.' Scientific American, Vol. 211, pp 76-85, August 1964.

86. Klein, E.J., 'Liquid crystals in aerodynamic testing.' Astronautics and Aeronautics, Vol. 6, pp 70-73, July 1968.

87. Klein, E.J. & Margozzi, A.P., 'Apparatus for the calibration of shear sensitive liquid crystals.' Review of Scientific Instruments, Vol. 41, No.2, pp 238-239, 1970.

88. Klein, E.J. & Margozzi, A.P., 'Exploratory investigation on the measurement of skin friction by means of liquid crystals.' NASA TM-X-1774, May 1969.

89. Gaudet, L. & Gell, T.G., 'Use of liquid crystals for qualitative and quantitative 2-D studies of transition and skin friction.' RAE TM Aero. 2159, June 1989.

90. Smith, S.C., 'The use of liquid crystals for surface flow visualisation.' AIAA 90-1382, June 1990.

91. Stanfield, J.H., 'The use of liquid crystals in the DRA 8ft x 8ft wind tunnel.' TM Aero./Prop. 11, August 1992.

92. Aeschliman, D.P. & Croll, R.H., 'Use of shear stress sensitive, temperature insensitive liquid crystals for boundary layer transition detection in hypersonic flows.' AIAA 93-3070, June 1993.

93. Bonnet, P., Jones, T.V. & McDonnell, D.G., 'Shear stress measurements in aerodynamic testing using cholesteric liquid crystals.' Liquid Crystals, Vol. 6, No. 3, pp 271-280, 1989.

94. Mee, D.J., Walton, T.W., Harrison, S.B. & Jones, T.V., 'A comparison of liquid crystal techniques for transition detection.' AIAA 91-0062, January 1991.

95. Reda, D.C., 'Liquid crystals for unsteady surface shear stress visualisation.' AIAA 88-3841CP, Proceedings 1st National Fluid Dynamics Congress, Cincinnati, Ohio, Part 2, pp 1069-1072, 1988.

96. Reda, D.C., 'Observations of dynamic stall phenomena on an oscillating airfoil with shear sensitive liquid crystal coatings.' AIAA Journal, Vol. 29, No. 2, pp 308-310, February 1991.

97. Reda, D.C., Muratore, J.J., Jr. & Heineck, J.T., 'Experimental investigations of the time and flow direction responses of shear stress sensitive liquid crystal coatings.' AIAA 93-0181, January 1993.

98. Reda, D.C. & Muratore, J.J., Jr, 'A new technique for the measurement of surface shear stress vectors using liquid crystal coatings.' AIAA 94-0729, January 1994.

99. Reda, D.C., Wilder, M.C., Farina, D.J., Zilliac, G., McCabe, R.K., Lehman, J.R., Hu, K.C., Whitney, D.J. & Deandorff, D.G., 'Areal measurements of surface shear stress vector distributions using liquid crystal coatings.' AIAA 96-0420, January 1996.

100. Reda, D.C., Wilder, M.C. & Crowder, J.P., 'Simultaneous, full surface visualisations of transition and separation using liquid crystal coatings.' AIAA 96-2182, June 1996.

101. Anon. 'Thermochromic liquid crystals.' BDH Limited Liquid crystals.

102. Toy, N., Savory, E. & Hoang, Q.H., 'Manual for the liquid crystal colour analysis system.' University of Surrey Report, February 1995.

103. Maltby, R.L. & Keating, R.F.A., 'The surface oil flow technique for use in low speed wind tunnels.' AGARDograph 70, part I.3, 1962.

104. Ashill, P.R., Wood, R.F. & Weeks, D.J., 'An improved, semi-inverse version of the viscous, Garabedian and Korn method (VGK).' RAE TR 87002, January 1987.

105. Collyer, M.R., 'An extension to the method of Garabedian and Korn for the calculation of transonic flow past an aerofoil to include the effects of a boundary layer and wake.' RAE TR 77104, July 1977.

106. Thwaites, B., 'Approximate calculation of the laminar boundary layer.' Aero. Qu., Vol. 1, pp245, 1949.

107. Firmin, M. C. P., 'Applications of RAE viscous flow methods near separation boundaries for three dimensional wings in transonic flow.'

108. Arthur, M. T., 'A method for calculating subsonic and transonic flows over wings or wing - fuselage combinations with an allowance for viscous effects.' RAE TM Aero. 1996, March 1984.

109. Forsey, C. R. & Carr, M. P., 'The calculation of transonic flow over three dimensional swept wings using the exact potential equation.' DGLR Symposium transonic configurations, Bad Harzburg. DGLR Paper 78-064, 1978.

110. Küchemann, D., 'The aerodynamic design of aircraft.' Pergamon Press, Oxford, pp 112-113, 1978.

111. Patel, V.C., 'Calibration of the Preston tube and limitations on its use in pressure gradients.' Journal of Fluid Mechanics, Vol. 23, pp 185 - 208, 1965.

112. Pope, A., 'Wind tunnel calibration techniques.' AGARDograph 54, April 1961.

113. Thompson, J.S., 'Present methods of applying blockage corrections in a closed rectangular high speed wind tunnel.' ARC Report Aero. 2225, 1948.

114. Rogers, E.W.E., 'Blockage effects in closed or open wind tunnels.' AGARDograph 109 "Subsonic wind tunnel wall corrections", October 1966.

115. Glauert, H., 'Wind tunnel interference on wings bodies and airscrews.' ARC R & M 1566, September 1933.

116. Acum, W.E.A., 'Corrections for symmetrical and tapered wings in rectangular wind tunnels.' ARC 13050, 1950.

117. Garner, H.C., 'Lift interference on three-dimensional wings.' AGARDograph 109 "Subsonic wind tunnel wall corrections", October 1966.

118. Schlichting, H., 'Boundary layer theory. 7th Edition.' Mcgraw-Hill series in Mechanical Engineering, pp 600-602 & 637, 1979.

Bibliography

Anon, 'Encyclopedia of World Military Aircraft.' World Air Power Journal, Aerospace Publishing Limited, London, 1996.

Anon, 'The Derwent Guide to Patents.' Derwent Publications Limited, London, 1995.

Anon, 'Introducing Patents - A Guide for Inventors.'

Abbot, I.H., von Doenhoff, A.E. & Stivers, L.S., 'Summary of airfoil data.' NACA/TIB/1201,1945.

Arnold, T. & Vaden, F. S., 'Invention Protection for Practicing Engineers.' Barnes and Noble, New York, 1971.

Bhamra, A. S., 'R40: Assessment of wind tunnel tests on wing 6.' BAE Warton, Ae/A/659, July 1981.

Bradshaw, P., Naaseri, M., 'Burst vortex / boundary layer interaction.' NASA R-182510, 1988.

Bragg, M.B. & Gregorek, G.M., 'Experimental study of airfoil performance with vortex generators.' Journal of Aircraft, Vol. 24, No. 5, May 1987.

Brett, H., 'The Patents Act 1977 - An Introductory Guide.' ESC Publishing Limited, Oxford, 1978.

Broadley, J.I., 'Effectiveness of vortex generator position and orientation on highly swept wings.' AIAA 97-2319, June 1997.

Brown, S.N. & Stewartson, K., 'Trailing edge stall.' Journal of Fluid Mechanics, Vol. 42, pp 561, 1971.

Calarese, W., Crisler, W. P., Gustafson, G. L., 'Afterbody drag reduction by vortex generators.' AIAA 85-0354, January 1985.

Capsey, S. R., 'Patents - An Introduction for Engineers and Scientists.' Newnes - Butterworths, London, 1973.

Chang, P. K., 'Computation of the turbulent boundary layer downstream of vortex venerator, Final Report.' Naval Ship Research and Development Center, Bethesda, MD. AD-A191544, DTRC-87/054, DTRC/AERO-1302, December 1987.

Edwards, J. B. W., 'Free flight tests of vortex generator configurations at transonic speeds.' RAE TN Aero. 2862, December 1962.

Eichelbrenner, E.A., 'Three dimensional boundary layers.' Annual Review of Fluid Mechanics, Vol. 5, pp 339, 1973.

Goldstein, B., 'How to form a private company - Starting up and running a private company.' Jordan & Sons Limited, Bristol, 1985.

Griffin, D. & Russell, D., 'Experimental study of a method for predicting the effects of vortex generators.' AIAA 94-2378, 1994.

Haines, A.B., 'Factors affecting the choice of a three dimensional swept wing design for high subsonic speeds.' AGARD CP-35, 1968.

Hargreaves, R., 'Starting a business - A practical handbook. 2nd Edition.' Heinemann, London, 1987.

Hayes, W.D., 'The three dimensional boundary layer.' NAVORD R 1313, 1951.

Hearn, P., 'The Business of Industrial Licensing.' Gower, Farnborough, 1981.

Holder, D. W. & Pearcey, H. H., 'Simple methods for the prediction of wing buffeting resulting from bubble type separation.' NPL Aero. Report 1024, June 1962.

Holmes, A. E., Hickey, P. K. & Hilton, D. A., 'The application of sub-boundary layer vortex generators to reduce canopy "Mach rumble" interior noise on the Gulfstream III.' AIAA 87-0084, January 1987.

Humphreys, W. W. & Reynolds, W. C., 'The effect of streamwise vortices on a turbulent boundary layer exposed to an unsteady adverse pressure gradient.' International Symposium on Nonsteady Fluid Dynamics - Presented at the 1990 Spring Meeting of the Fluids Engineering Division, Toronto, Ontario, Canada. June 4 - 7 1990.

Konold, W. G., Tittel, B., Frei, D. F. & Stallord, D. S., 'What Every Engineer Should Know About Patents. 2nd Edition.' Marcel Dekker Inc., New York and Basel, 1989.

Küchemann, D., 'Types of flow on swept wings (with special reference to free boundaries and vortex sheets).' RAE TN Aero. 2234, March 1953.

Küchemann D., 'The aerodynamic design of aircraft.' Pergamon Press, pp 39-43, 1978.

Lee, J. D., 'Boundary layers on airfoils in transonic flow and the control of shock - induced separation.' AD-731830; AROD-7113-1-E; DAHCO4-67-C-0051, August 1971.

Lock, R.C. & Rogers, E.W.E., 'Aerodynamic design of swept wings and bodies for transonic speeds.' Progress in Aeronautical Sciences, Vol. 3, pp 253, 1962.

Mogano, M., 'How to start and run your own business. 5th Edition.' Graham & Trotman Limited, London, 1985.

Morris, M. J., 'Starting a successful small business.' Kogan Page, London, 1985.
Osborne, J. & Pearcey, H.H., 'A type of stall with leading edge transonic flow and rear separation.' AGARD CP-83, 1971.

Pearcey, H. H., 'Some effects of shock induced separation of turbulent boundary layers in transonic flow past aerofoils.' ARC R&M 3108, 1959.

Poll, D. I. A., 'On the generation and subsequent development of spiral vortex flow over a swept back wing.' AGARD CP-342.

Rao, D. M., Kariya, T. T., 'Boundary layer submerged vortex generators for separation control - an exploratory study.' AIAA 88-3546-CP In: 'AIAA 1st National Fluid Dynamics Congress 1988, Part 2' Cincinatti, Ohio.

Rao, D. M. & Mehrotra, S. C., 'Flat-plate drag measurements with vortex generators in turbulent boundary layer.' NASA CR-172125, June 1983.

Ringleb, F. O., 'Flow control by standing vortices and the cusp effect.' Princeton University, Aero. Eng. Report 317, July 1955.

Scott, P. J., 'Wing research model R40 - wing 6 - Tests in the 1.2m HSWT to investigate the effects on the wing stalling behaviour of several arrays of vortex generator.' BAE Warton Div AXR 80, March 1981.

Shaw, L., 'The Practical Guide for People with a New Idea.' Butler & Associates Limited, Birmingham, 1982.

Storms, B. L., Jang, C. S., 'Lift enhancement of an airfoil using a gurney flap and vortex generator.' Journal of Aircraft, Vol. 31, No. 3, May - June 1994.

Viets, H., Piatt, M. & Ball, M., 'Unsteady wing boundary layer energization.' AIAA 79-1631, 1979.

White, T. A. B., Jacob, R. & Davies, J. D., 'Patents, Trade Marks, Copyright and Industrial Designs. 2nd Edition.' Concise College Texts, Sweet and Maxwell Limited, London, 1978.

Williams, J. F., 'A Managers Guide to Patents, Trade Marks & Copyright.' Kogan Page, London, 1986.

Λ	c (m)	b (m)	A	S (m^2)	x_m (m)
30°	0.184	0.592	6.4	0.1088	-0.134
40°	0.208	0.508	4.9	0.1054	-0.171
50°	0.248	0.408	3.3	0.1010	-0.193
60°	0.318	0.296	1.9	0.0941	-0.192

Pitching moment reference position is taken at the quarter chord position at mid - span and is measured from the balance centre line (rearwards is negative).

Table 3-1: Cranfield model dimensions and moment reference positions.

Λ	c (m)	Wing Tip	b (m)	A	S (m^2)	x_m (m)	y_m (m)
30°	0.7044	30°	1.9718	5.6	1.3889	-0.302	-1.607
40°	0.7963	45°	1.9111	4.9	1.4918	-0.517	-1.577
50°	0.9490	45°	1.6427	3.5	1.5203	-0.655	-1.443

x moment reference position measured from balance centre line (rearwards is negative) and y moment reference position measured from balance moment reference position (positive for starboard wing).
The moment reference position is taken at the quarter chord position at mid - span.
Wing span measured from tunnel floor and wing area is total wing area above tunnel floor.

Table 3-2: DERA model dimensions and moment reference positions.

h/c	x_v/c	D/h	α_v (°)
0.0126	0.70	8	25
0.0126	0.65	8	25
0.0126	0.60	8	25
0.0126	0.55	8	25
0.0126	0.65	8	30
0.0126	0.65	8	35
0.0126	0.65	8	20
0.0100	0.65	10	25
0.0075	0.65	13.33	25
0.0050	0.65	20	25
0.0151	0.65	6.66	25
0.0050	0.55	20	25
0.0050	0.50	20	25
0.0050	0.60	20	25
0.0050	0.55	20	30
0.0050	0.55	20	35
0.0050	0.55	20	20
0.0050	0.55	10	30
0.0050	0.55	30	30
0.0050	0.55	40	30
0.0025	0.50	40	30

Table 4-1: 40° swept wing cropped delta vane vortex generator configurations.

Configuration	d/c	x_v/c	D/d	α_v (°)
4 sets of 3 wires	0.0019	0.75	53.33	0
4 sets of 3 wires	0.0019	0.75	53.33	10
4 sets of 3 wires	0.0019	0.75	53.33	20
4 sets of 3 wires	0.0019	0.75	53.33	30
4 sets of 3 wires	0.0019	0.65	53.33	10
4 sets of 3 wires	0.0019	0.65	53.33	0
4 sets of 3 wires	0.0019	0.65	53.33	-10
4 sets of 3 wires	0.0019	0.65	53.33	-20
17 wires	0.0019	0.60	13.33	-15
8 wires	0.0019	0.65	26.66	-15
5 wires	0.0019	0.10	26.66	-20
3 sets of 4 wires	0.0050	0.65	20	-25
3 sets of 4 wires	0.0050	0.60	20	-20
3 sets of 4 wires	0.0050	0.55	20	-15
22 wires	0.0050	0.65	20	20

Table 4-2: 40° swept wing wire sub-boundary layer vortex generator configurations.

h/c	x_v/c	D/h	α_v (°)
0.0021	0.50	40	30
0.0042	0.55	20	30
0.0042	0.55	20	40
0.0105	0.65	8	25
0.0105	0.65	8	30

Table 4-3: 50° swept wing cropped delta vane vortex generator configurations.

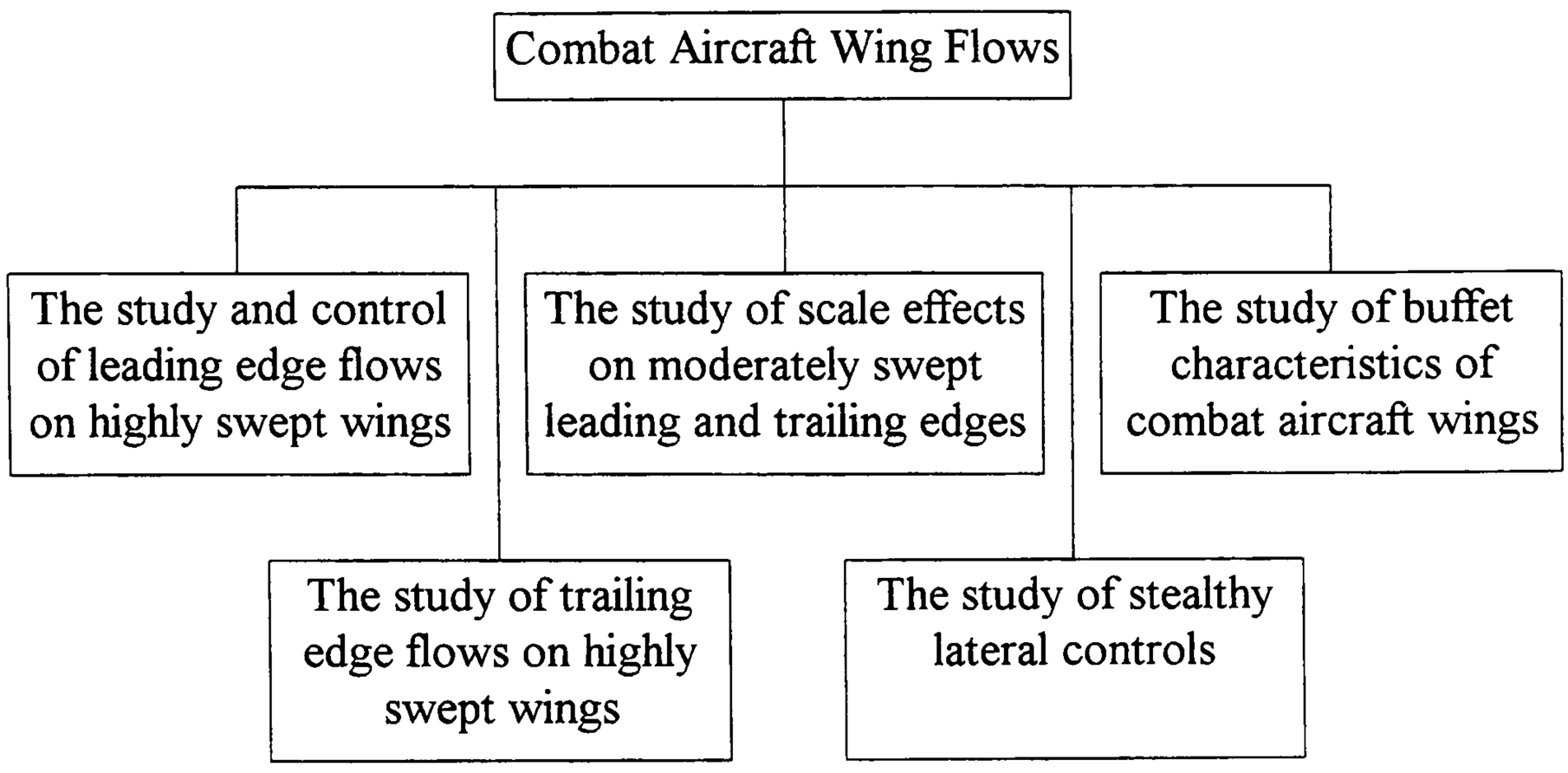

Figure 1-1: Combat aircraft wing flow project at DERA Bedford.

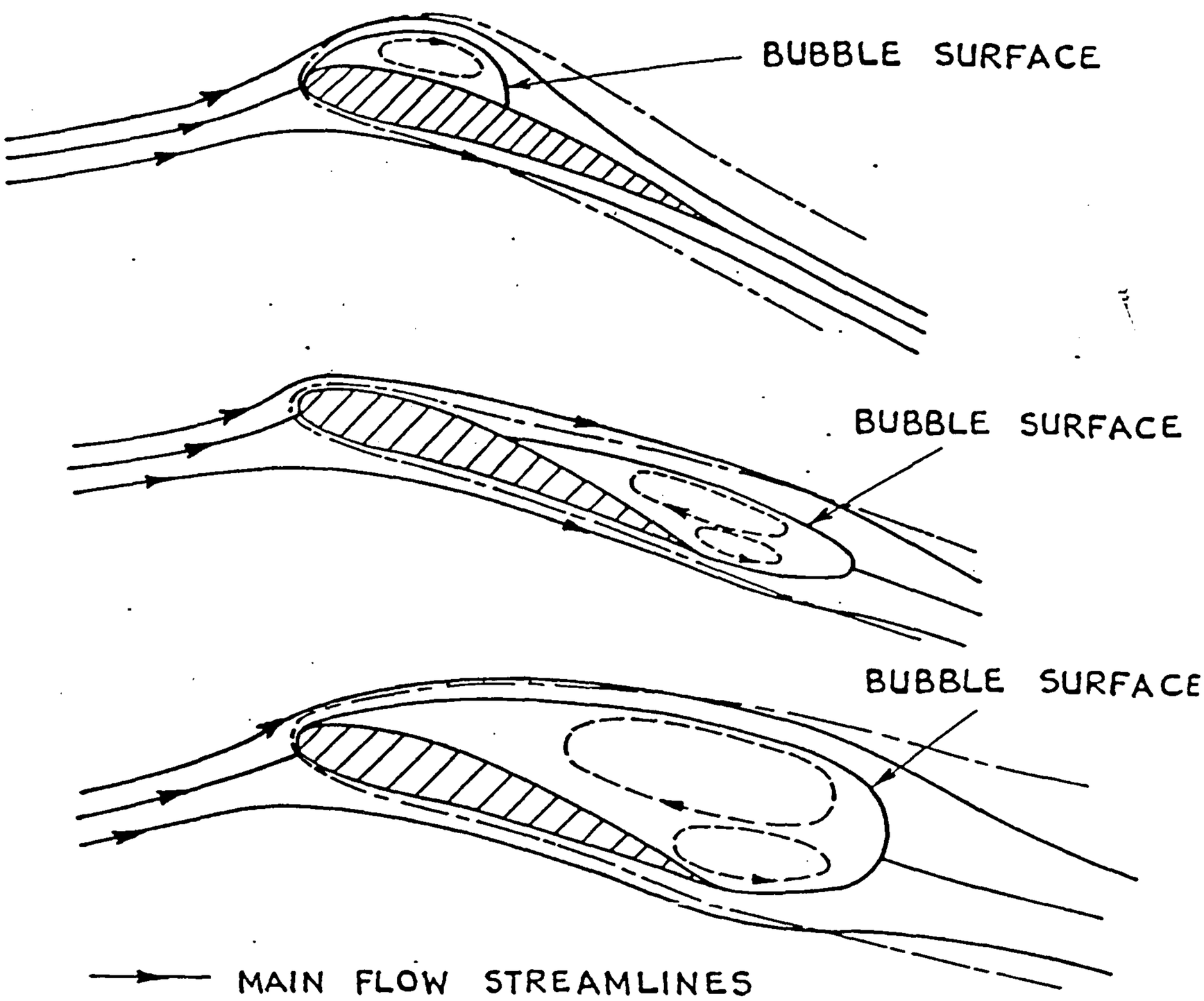

2D separation bubbles

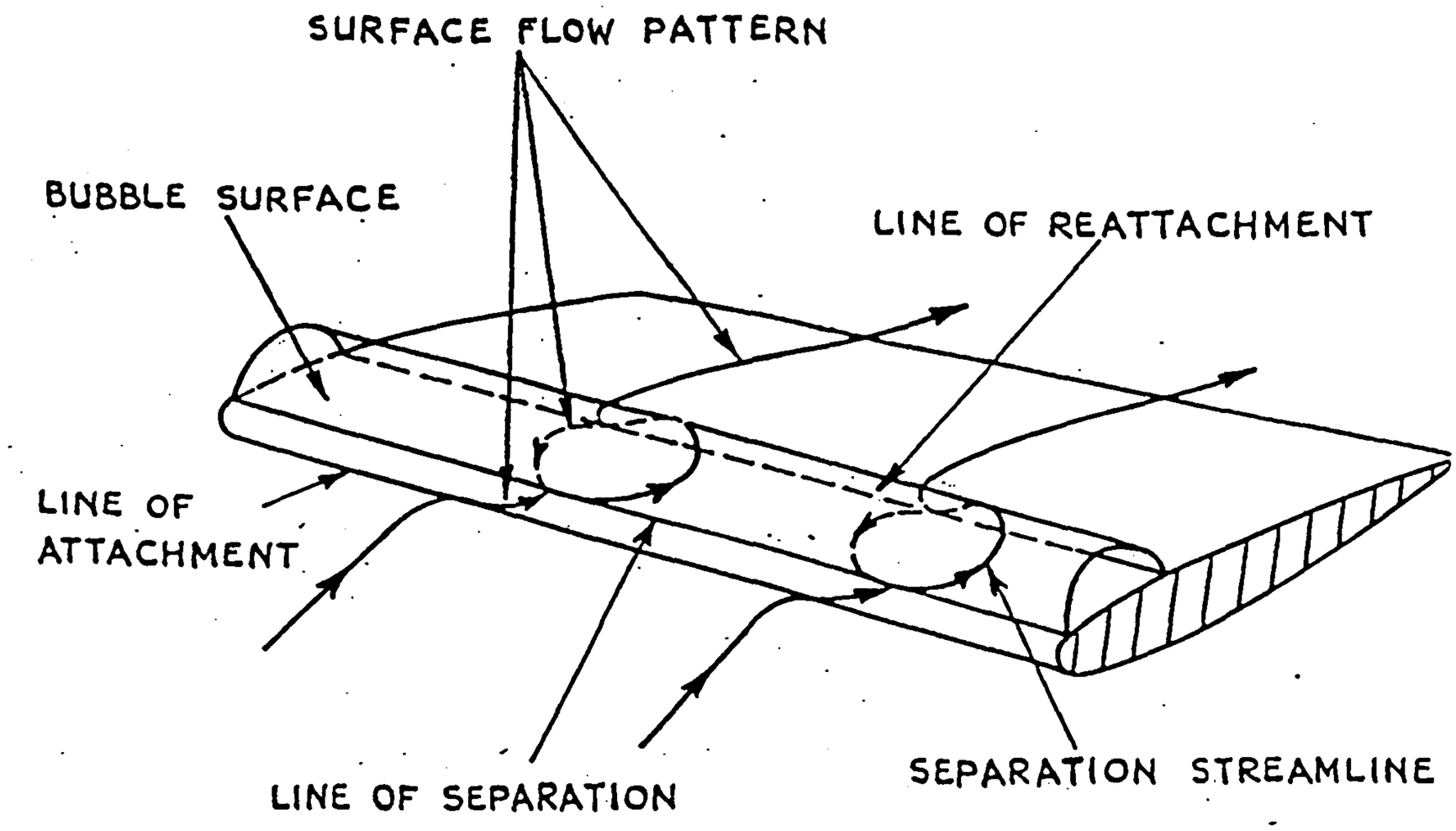

3D leading edge separation bubble on a wing

Figure 2-1: Examples of flow separation (from Maskell[22]).

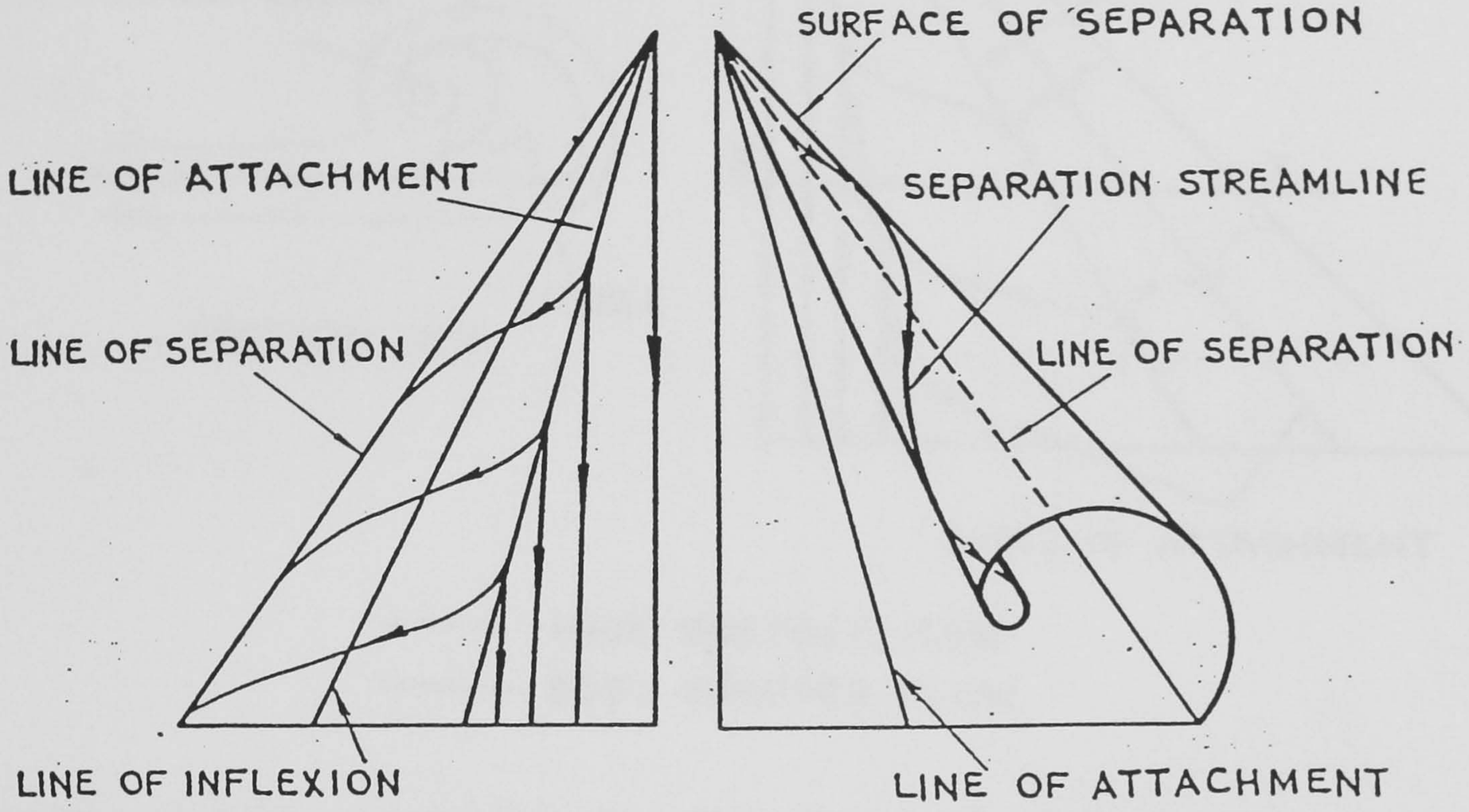

Separation on highly swept leading edges (Flow direction from top of page)

Figure 2-1 cont.: Examples of flow separation (from Maskell[22]).

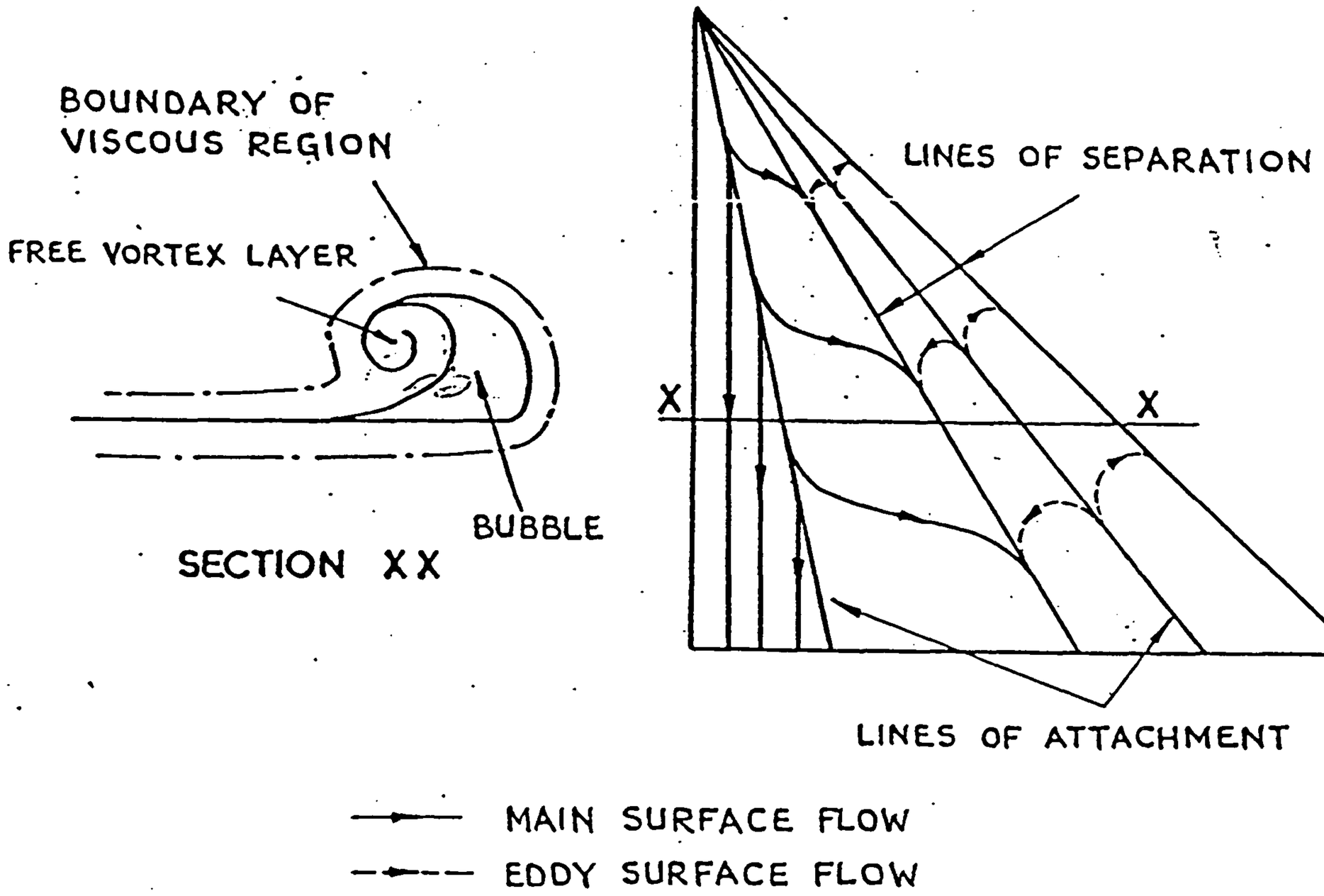

Separation on highly swept leading edges (Flow direction from top of page)

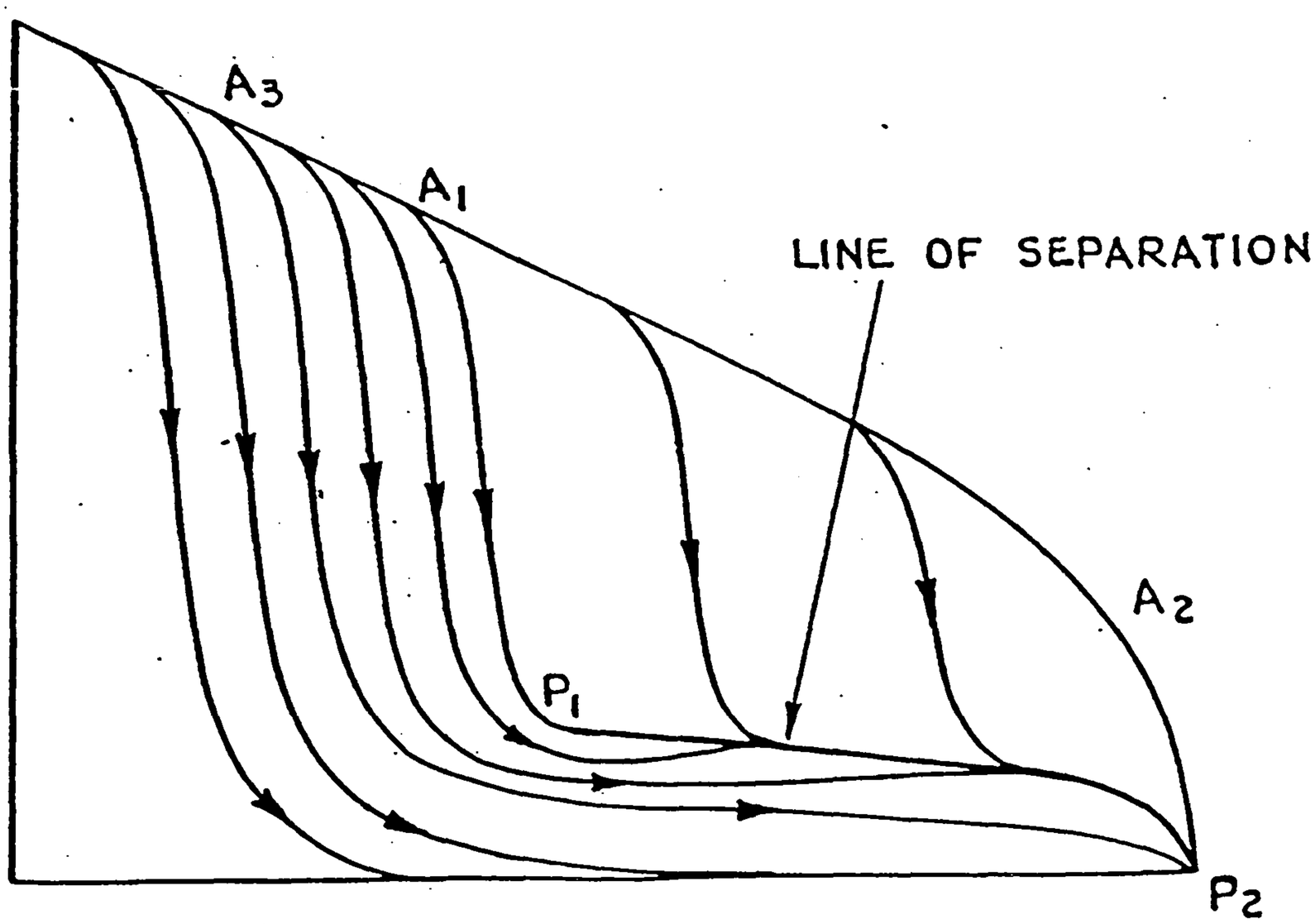

Surface flow pattern for a type of rear separation on a swept wing (Flow direction from top of page)

Figure 2-1 cont.: Examples of flow separation (from Maskell[22]).

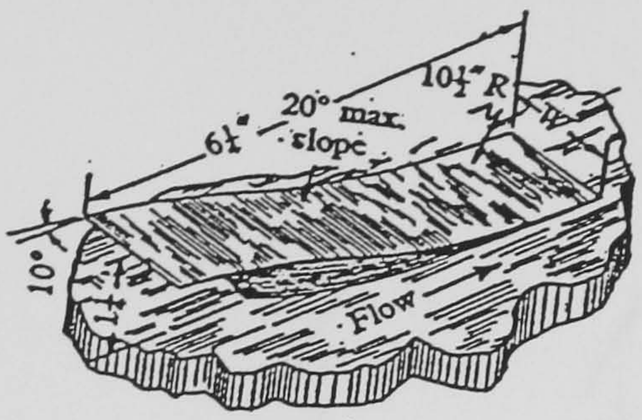

Simple plough

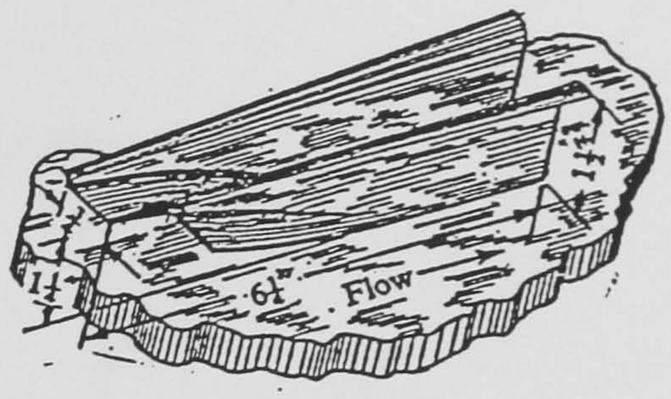

Shielded plough

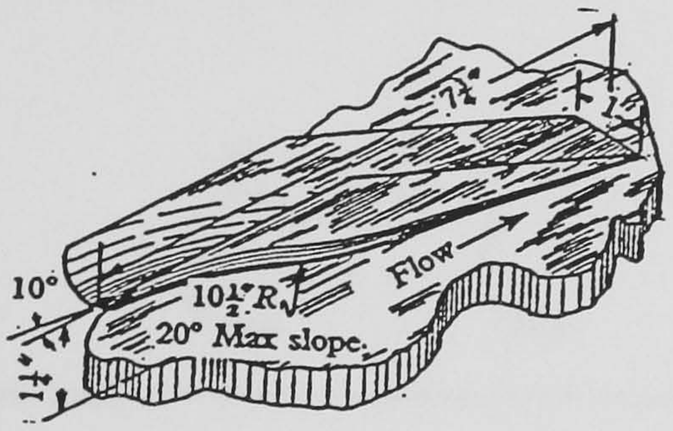

Scoop

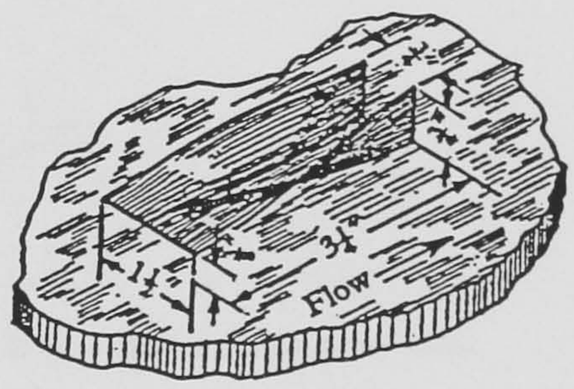

Twist interchanger

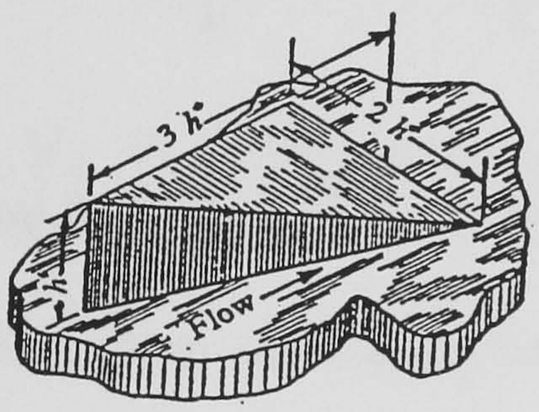

Triangular plough

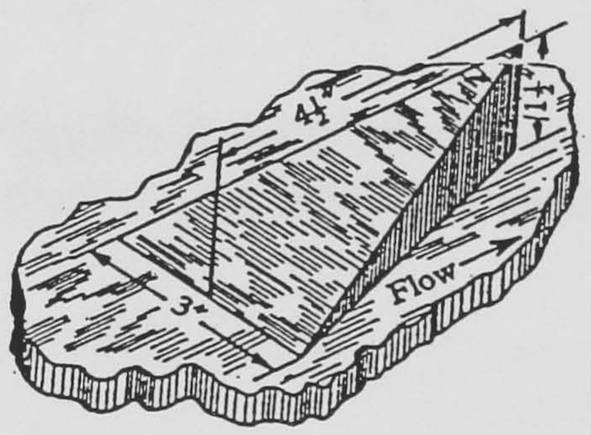

Ramp

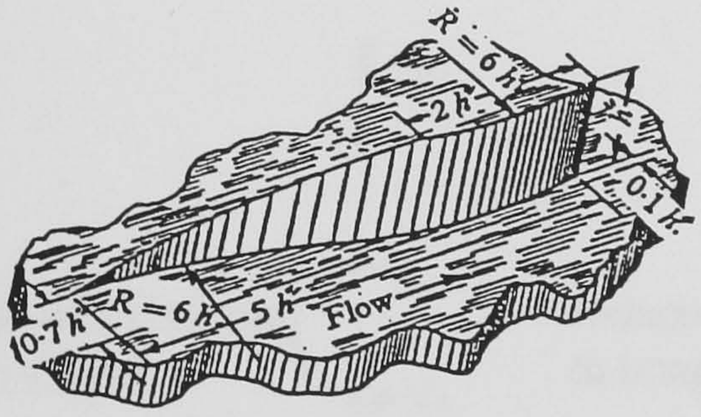

Tapered fin

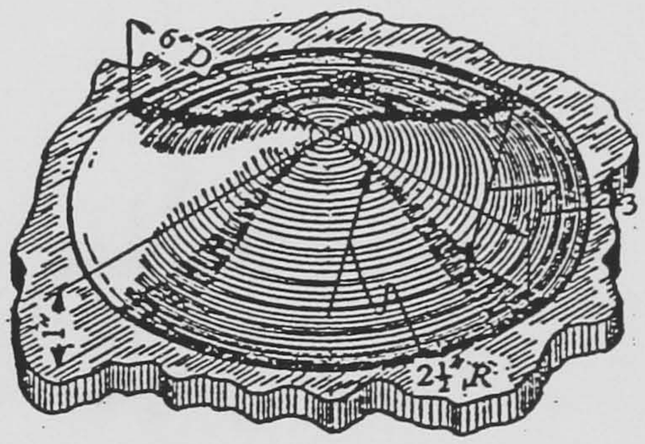

Dome

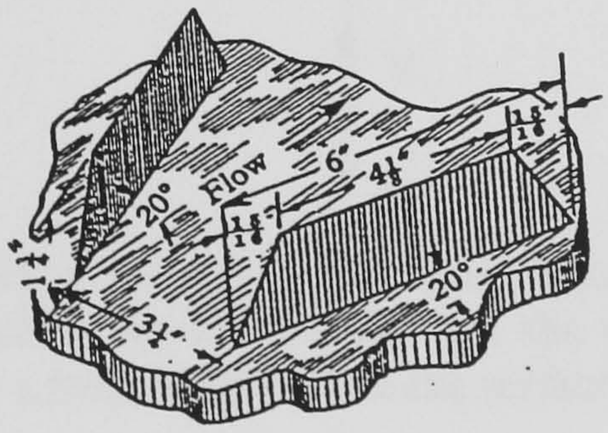

Vortex generator

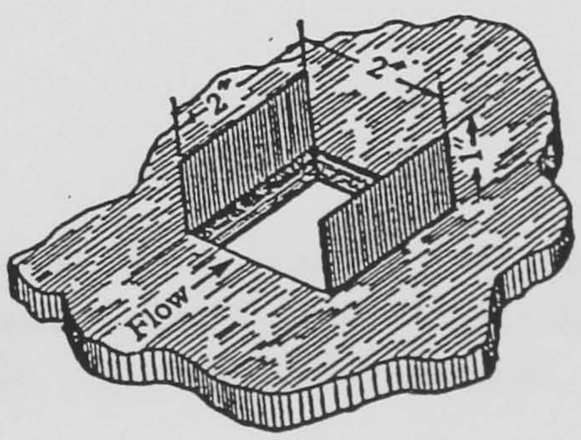

Shielded sink

Figure 2-2: Various flow mixing devices (from Schubauer and Spangenberg[50]).

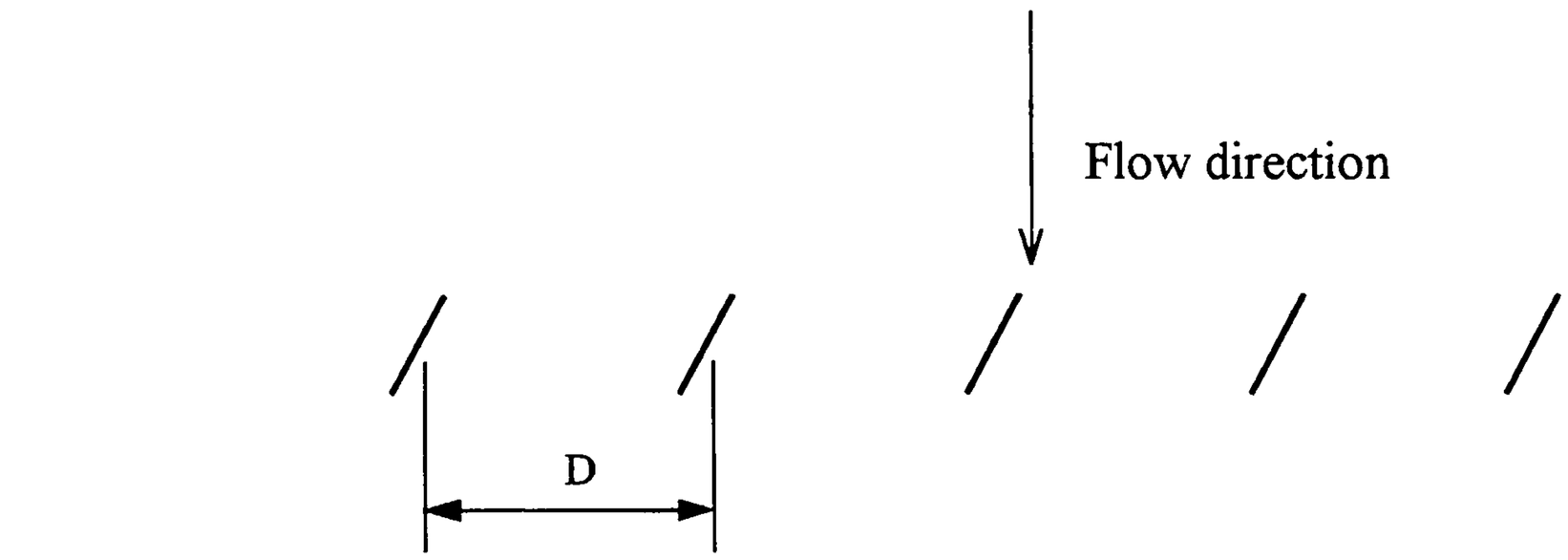

V_0, V_1, V_2, V_3 & V_4 are vortices produced from an equally spaced infinite co-rotating array and I_0, I_1, I_2, I_3 & I_4 are the images from these vortices in the surface respectively.

a. Infinite row of co-rotating vortices with images

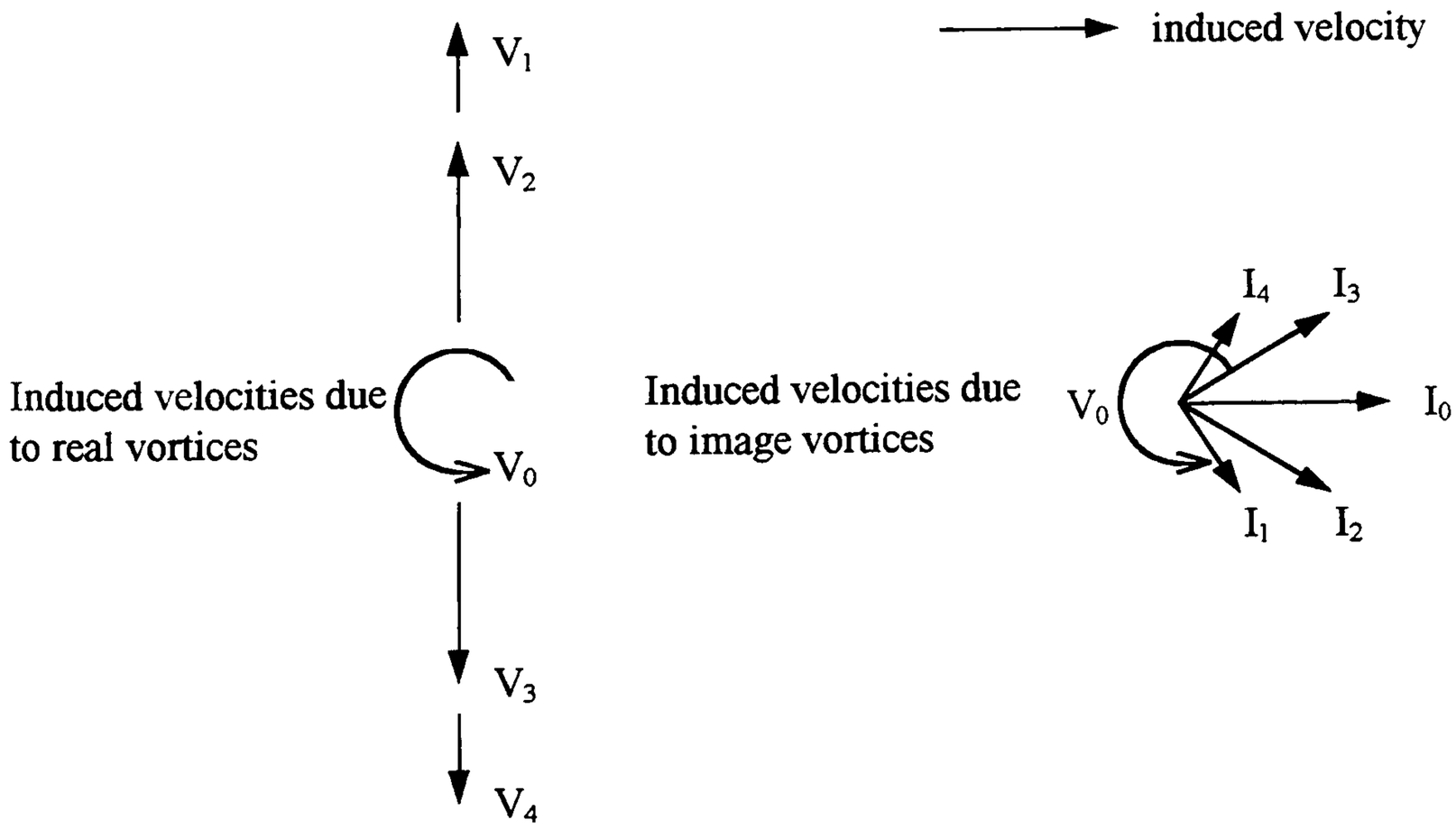

The adjacent vortices in the array induce velocities upon each other. These velocities are equal and opposite from the real vortices but the image vortices induce a lateral velocity. The vortices therefore maintain a fixed height above the surface which is displaced laterally with downstream distance.

b. Induced velocities

Figure 2-3: Co-rotating arrays.

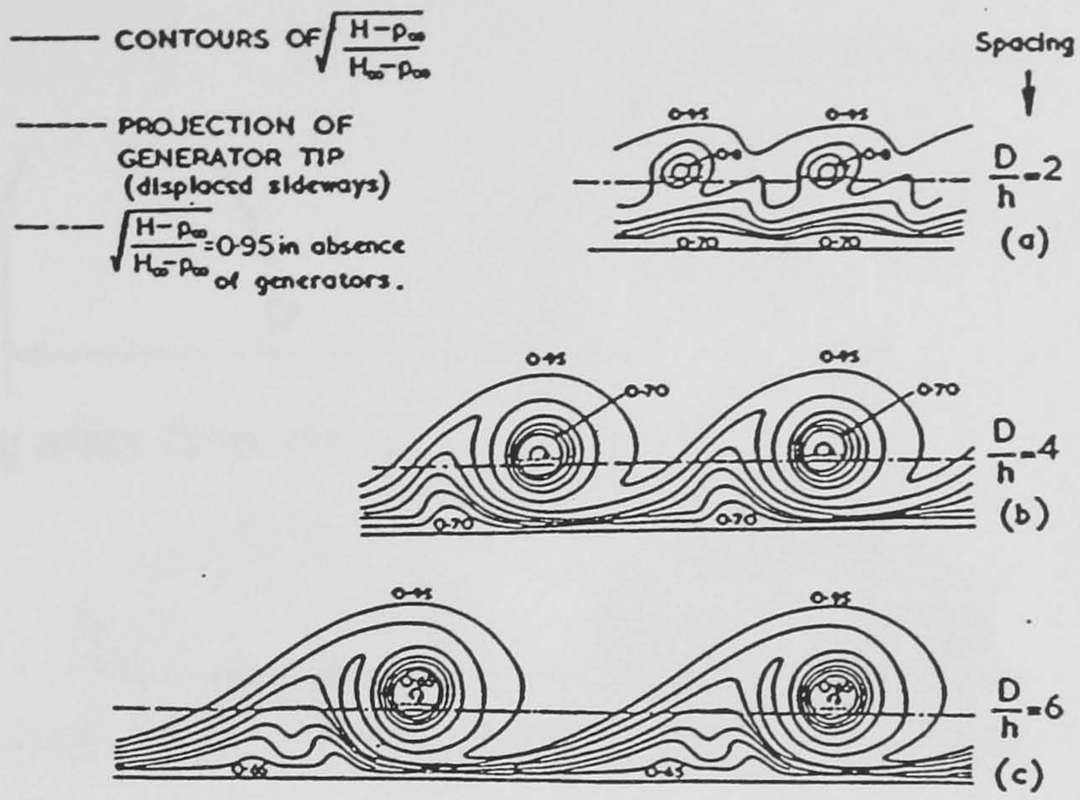

h - vortex generator height
P_∞ - freestream static pressure
H - local pitot pressure
H_∞ - value of pitot pressure outside boundary layer

c. Contour plots of pitot pressure from co-rotating arrays at different spacings (from Pearcey[2])

Figure 2-3 cont.: Co-rotating arrays.

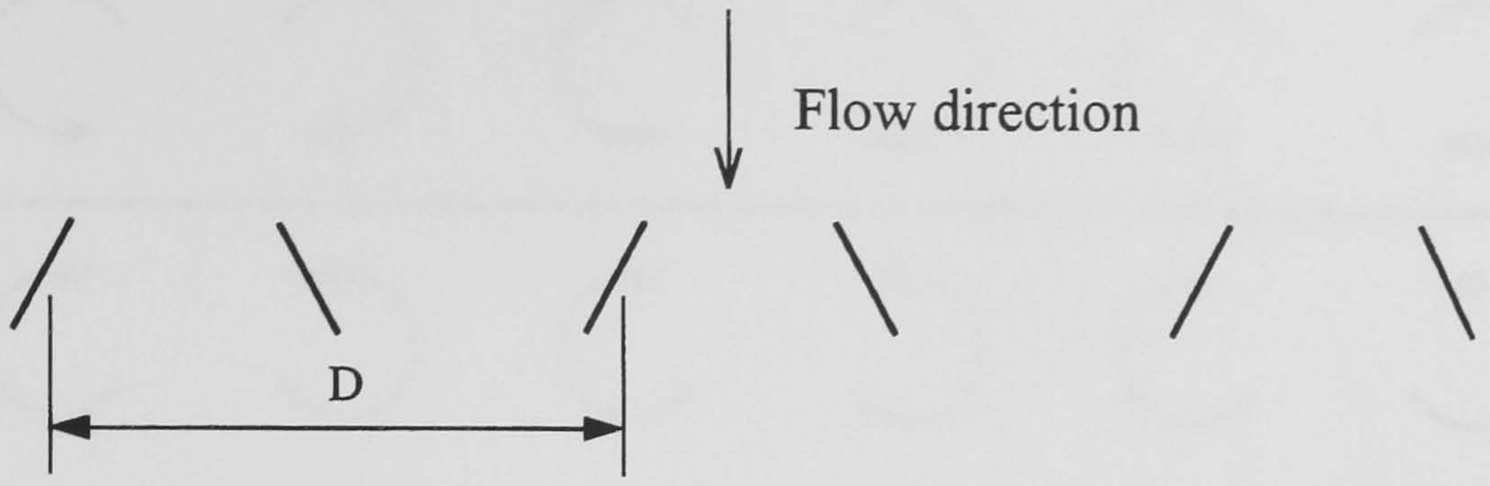

a. Counter rotating array (top view)

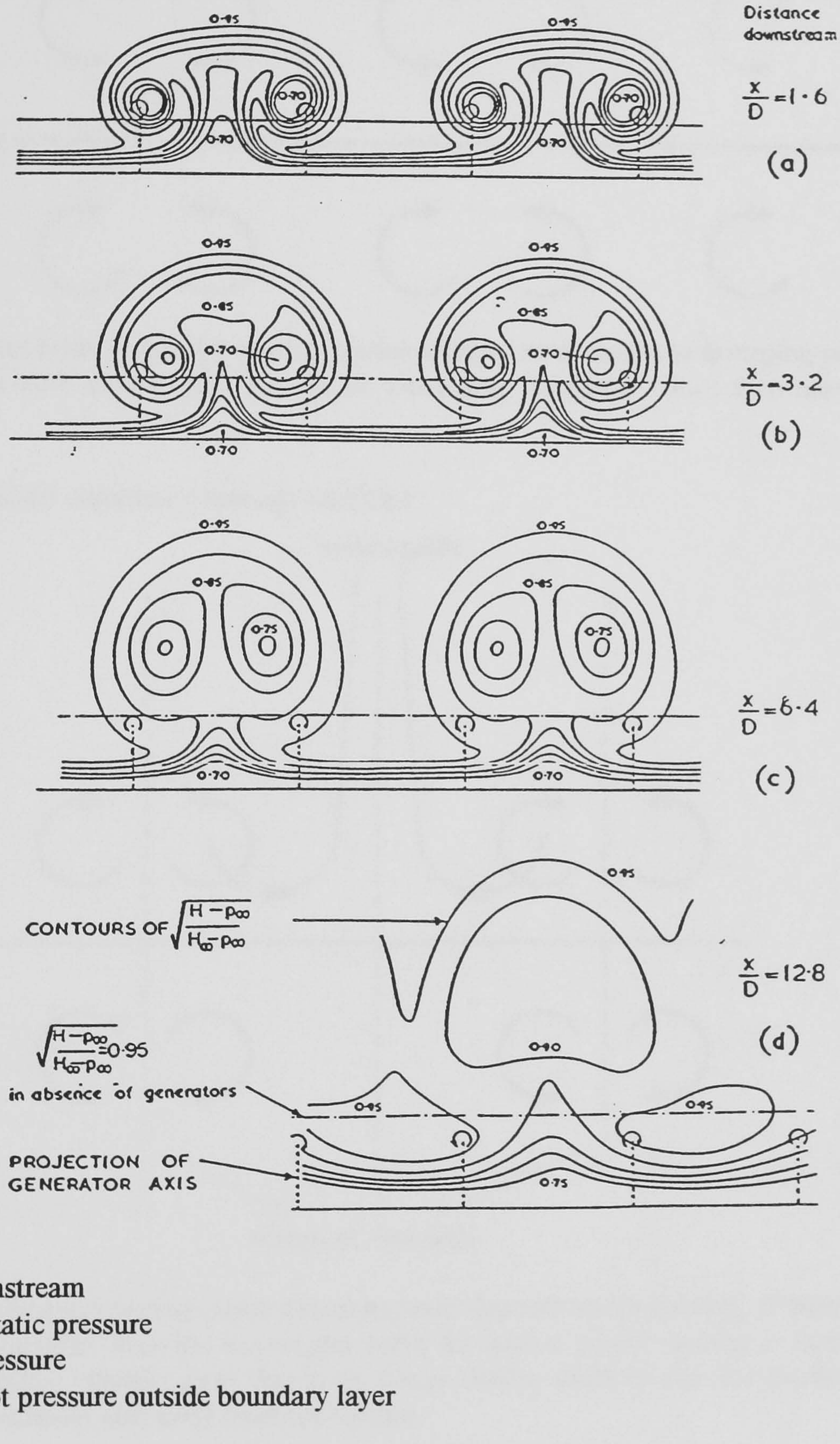

b. Contour plots of pitot pressure downstream from a counter-rotating array (from Pearcey[2])

Figure 2-4: Counter-rotating arrays.

x - distance downstream
P_∞ - freestream static pressure
H - local pitot pressure
H_∞ - value of pitot pressure outside boundary layer

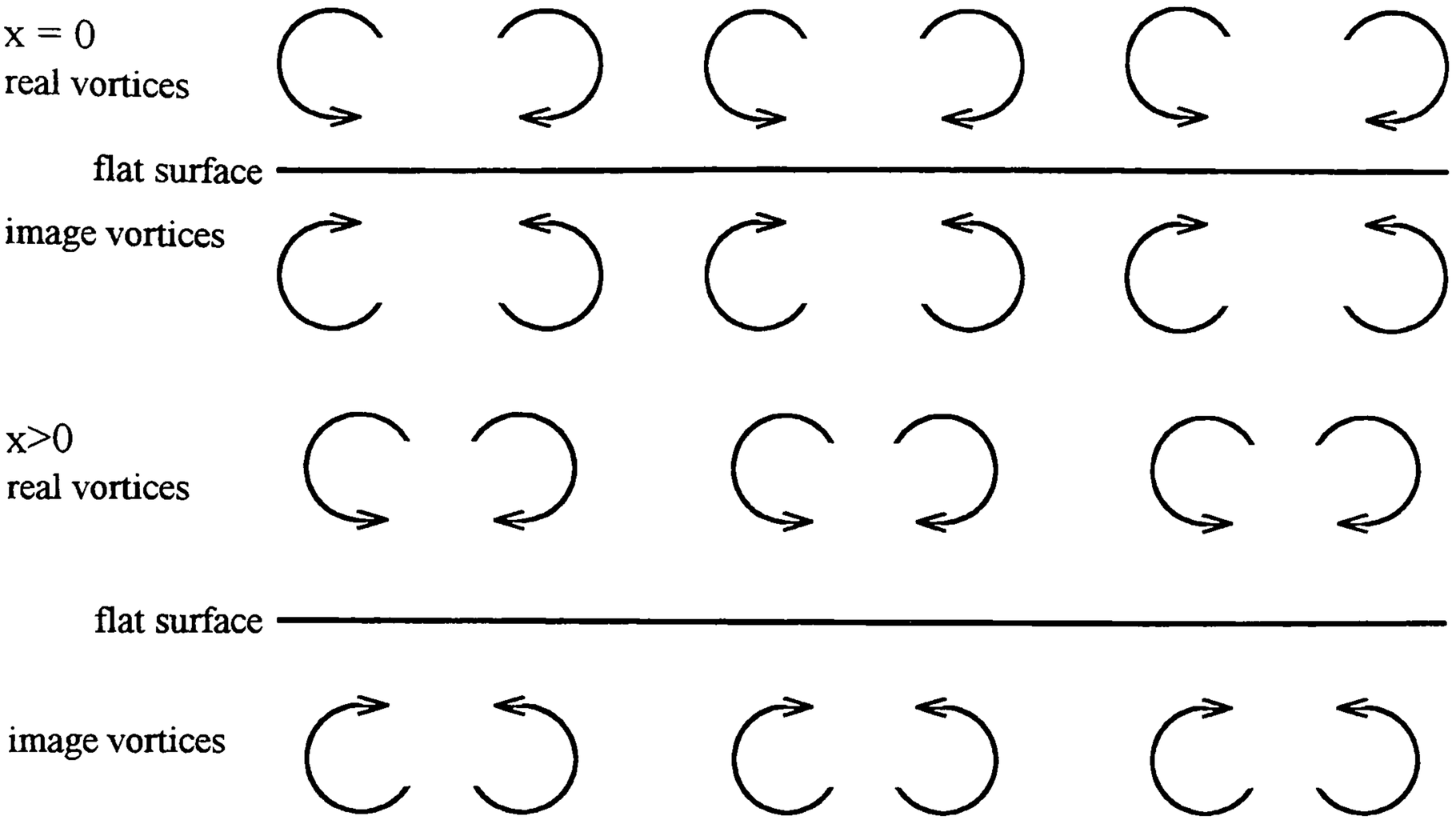

The image vortices from an equally spaced counter-rotating array cause the diverging pairs of vortices to move away from each other to pair up with its converging neighbour which then move away from the surface.

c. Equally spaced counter-rotating vortices

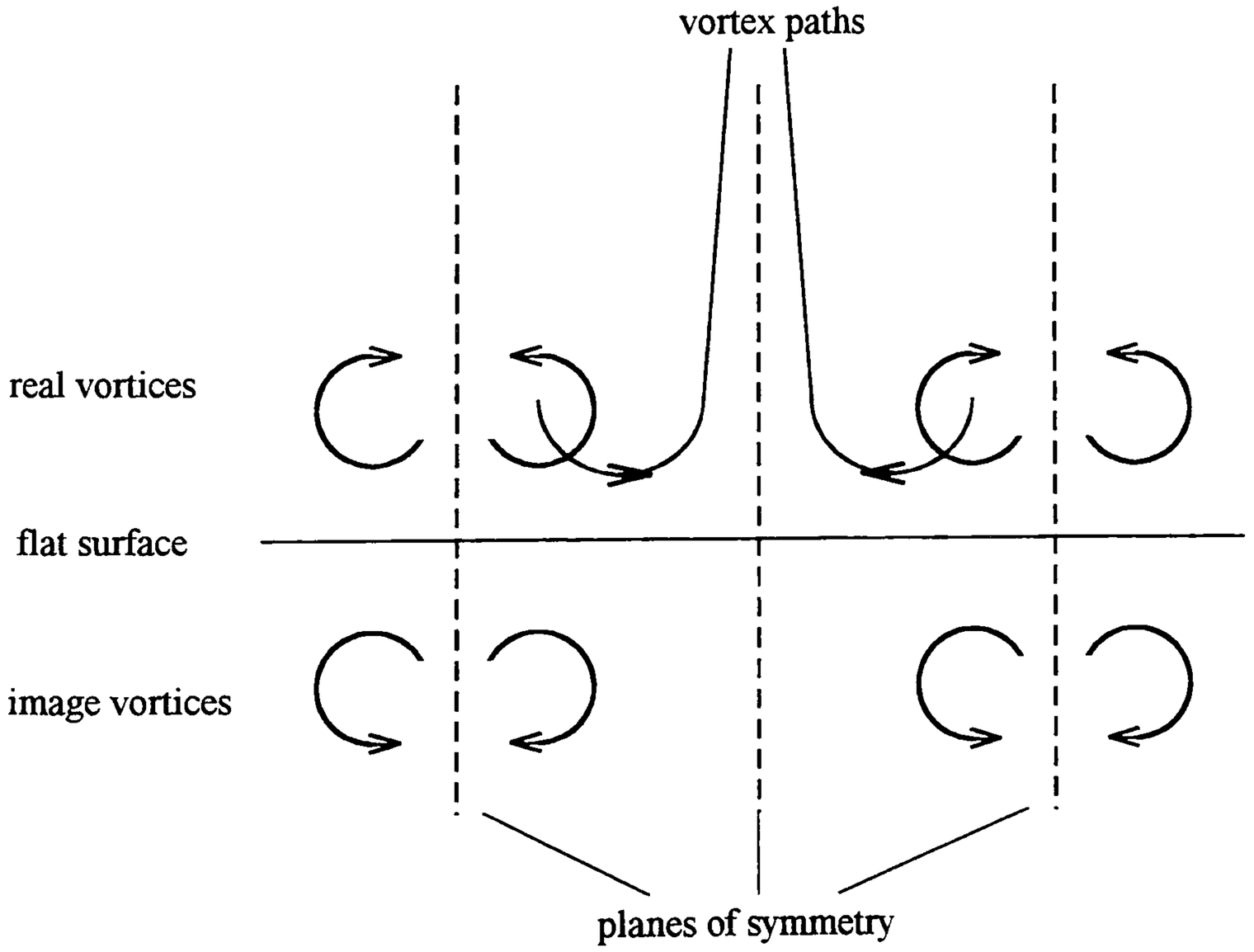

The vortex paths from an uneven counter-rotating array depends on the spacing. If initially the divergent pairs are closer together than the convergent pairs the motion of the vortices is initially towards the surface before moving laterally away due to the image vortex, which is then the nearest vortex, towards its convergent neighbour and away from the surface.

d. Vortex paths from uneven spaced counter-rotating vortices

Figure 2-4 cont.: Counter-rotating arrays.

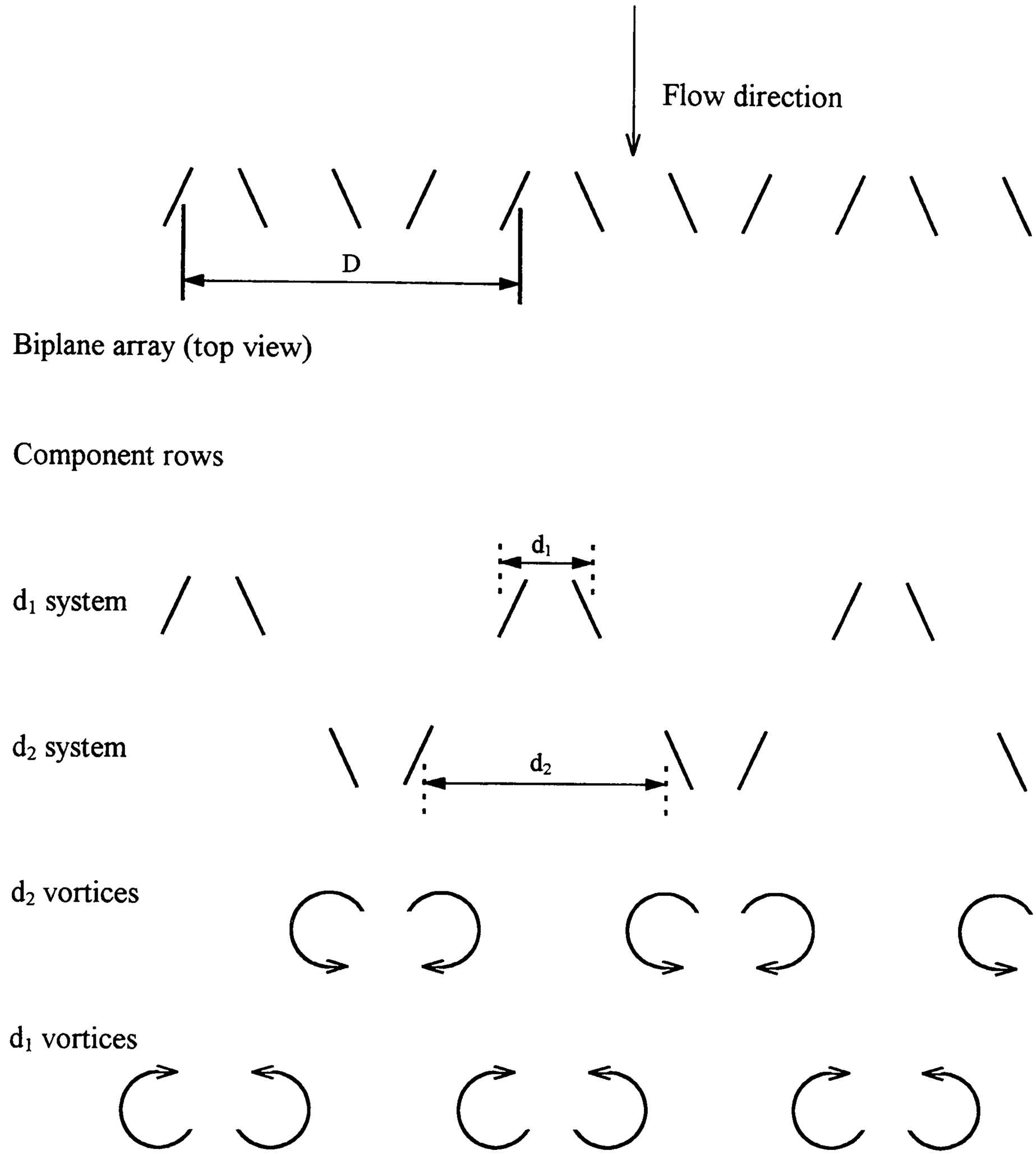

A biplane or alternate pair array consists of a series of vane pairs set alternately at positive and negative angles to the flow direction to produce alternate divergent (d_1 system) and convergent (d_2 system) counter-rotating vortex pairs. The divergent pairs of vortices (d_1) induce a downward velocity upon each other and move closer towards the surface before moving laterally away from each other due to the effect of the image vortices whilst the convergent pairs of vortices (d_2) induce an upward velocity upon each other and move away from the surface.

a. Biplane array showing the component rows

Figure 2-5: Biplane arrays.

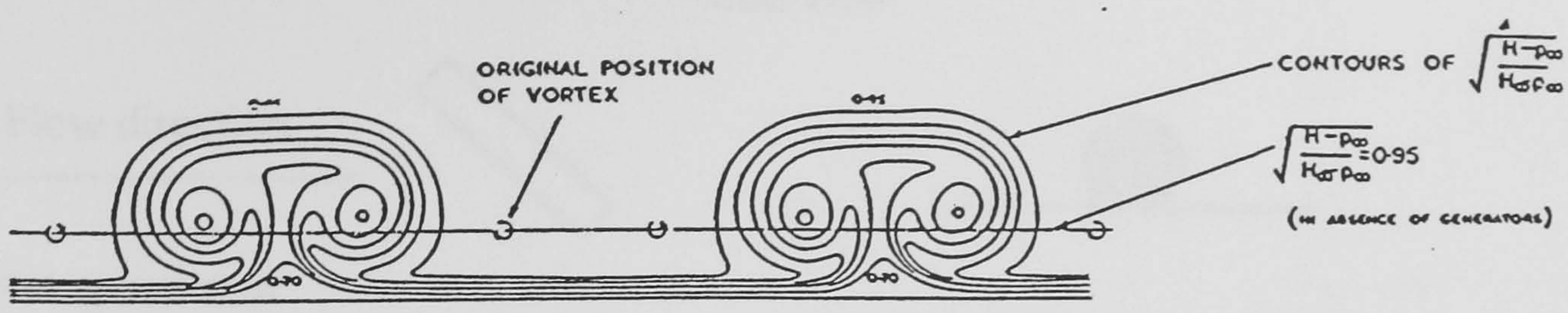

(a) COUNTER-ROTATING: $^{D}/_{d}=4$, $^{D}/_{h}=10$; at $^{x}/_{D}=3.2$

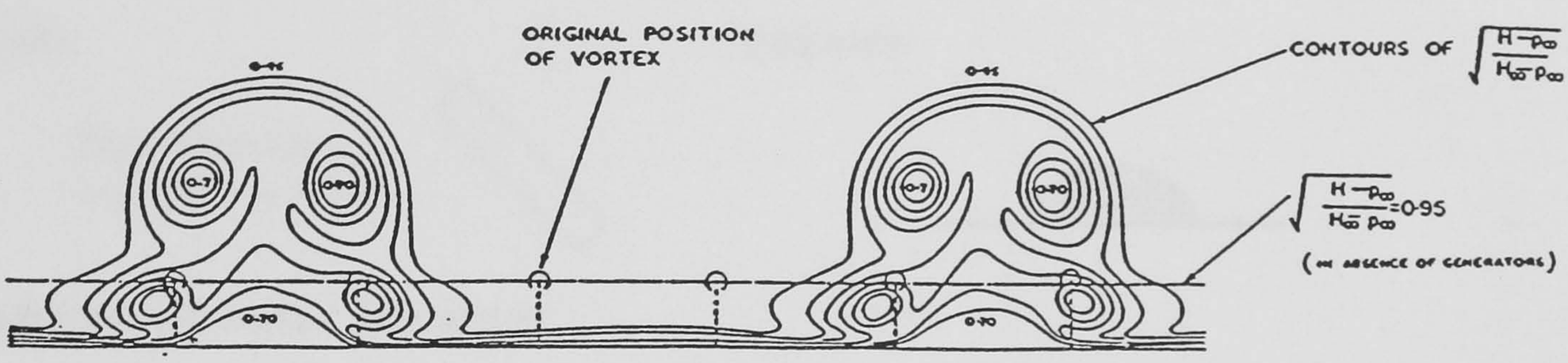

(b) BIPLANE: $^{D}/_{d_1}=4$, $^{D}/_{d_2}=^{4}/_{3}$, $^{D}/_{h}=10$; at $^{x}/_{D}=1.6$

P_∞ - freestream static pressure
H - local pitot pressure
H_∞ - value of pitot pressure outside boundary layer

The divergent pairs of vortices in the biplane array move under the convergent pairs of vortices which improves the mixing since the air of low momentum removed by the divergent vortices is transported further into the freestream by the convergent vortices above. This causes an improvement in effectiveness to that of a conventional counter-rotating array.

b. Contours of pitot pressure comparing a counter-rotating arrangement to a bi-plane arrangement (from Pearcey[2]).

Figure 2-5 cont.: Biplane arrays.

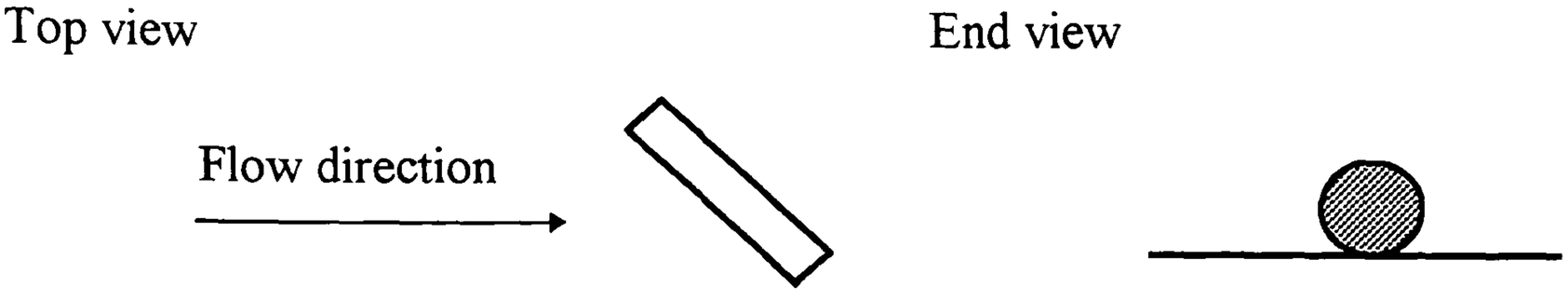

Wire vortex generator

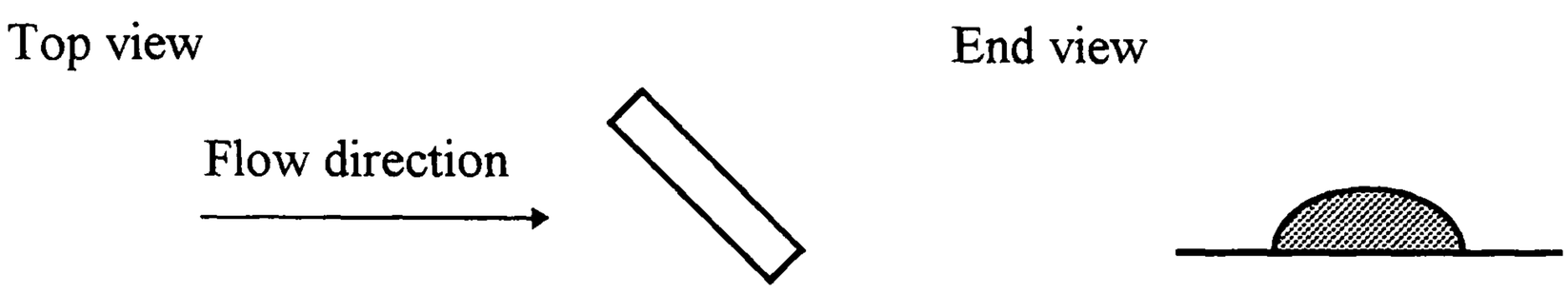

Cylindrical rod vortex generator

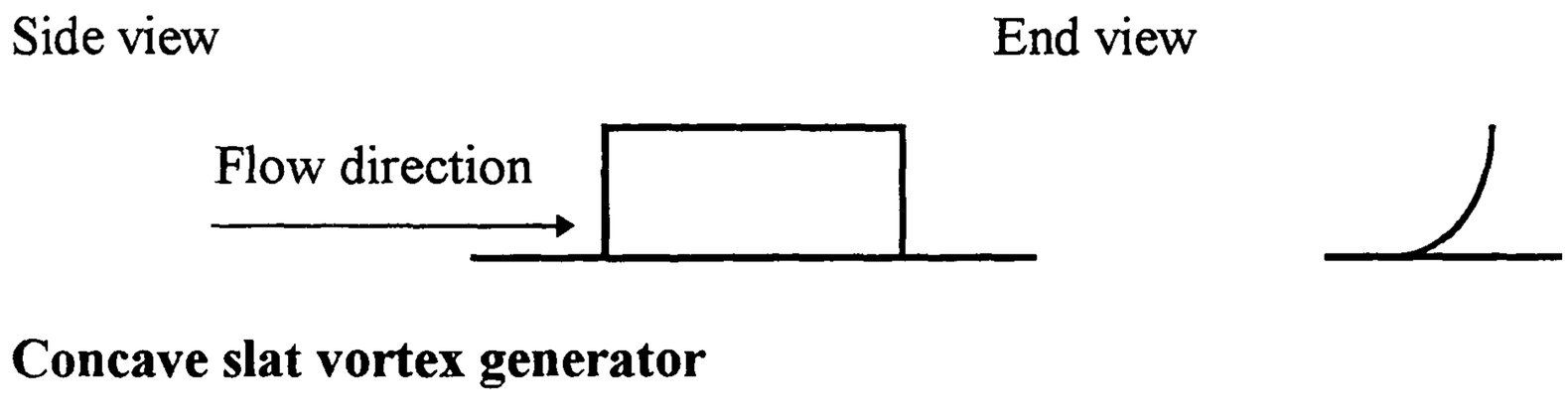

Concave slat vortex generator

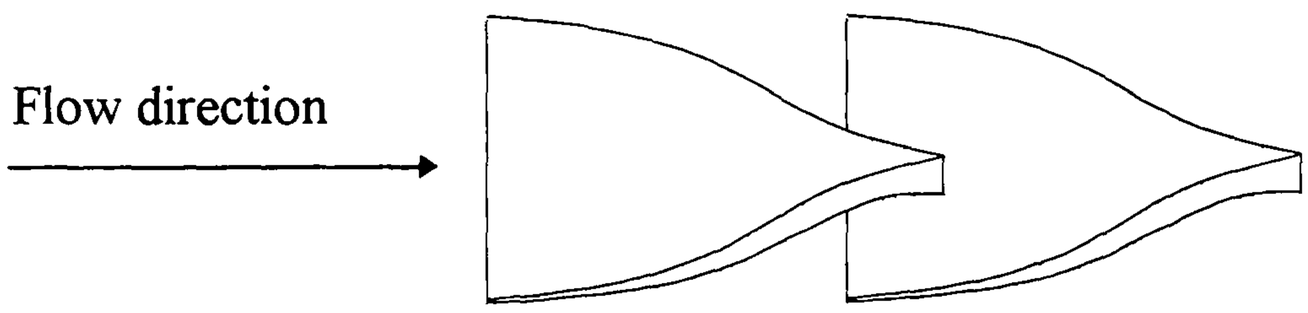

Wheeler doublet vortex generator

Wishbone

Figure 2-6: Sub-boundary layer mixing devices.

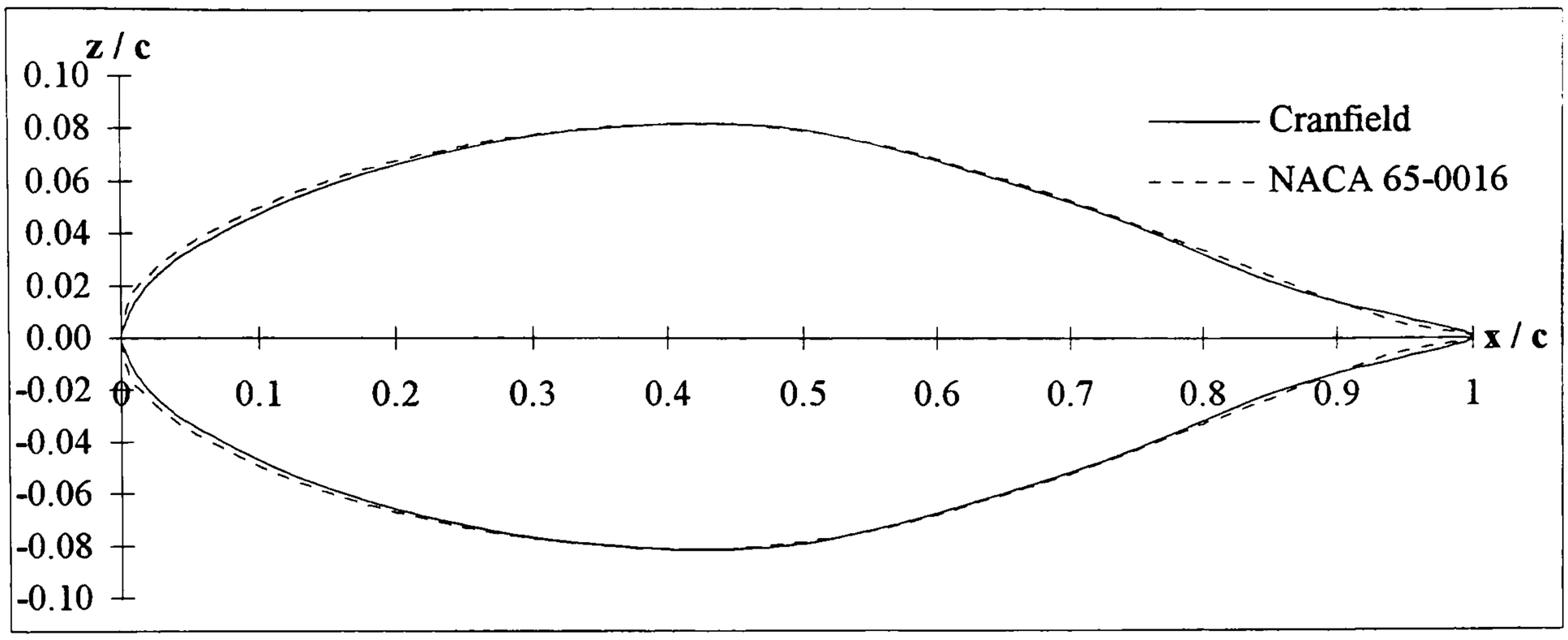

Figure 3-1: The Cranfield aerofoil section in comparison to a NACA 65-0016.

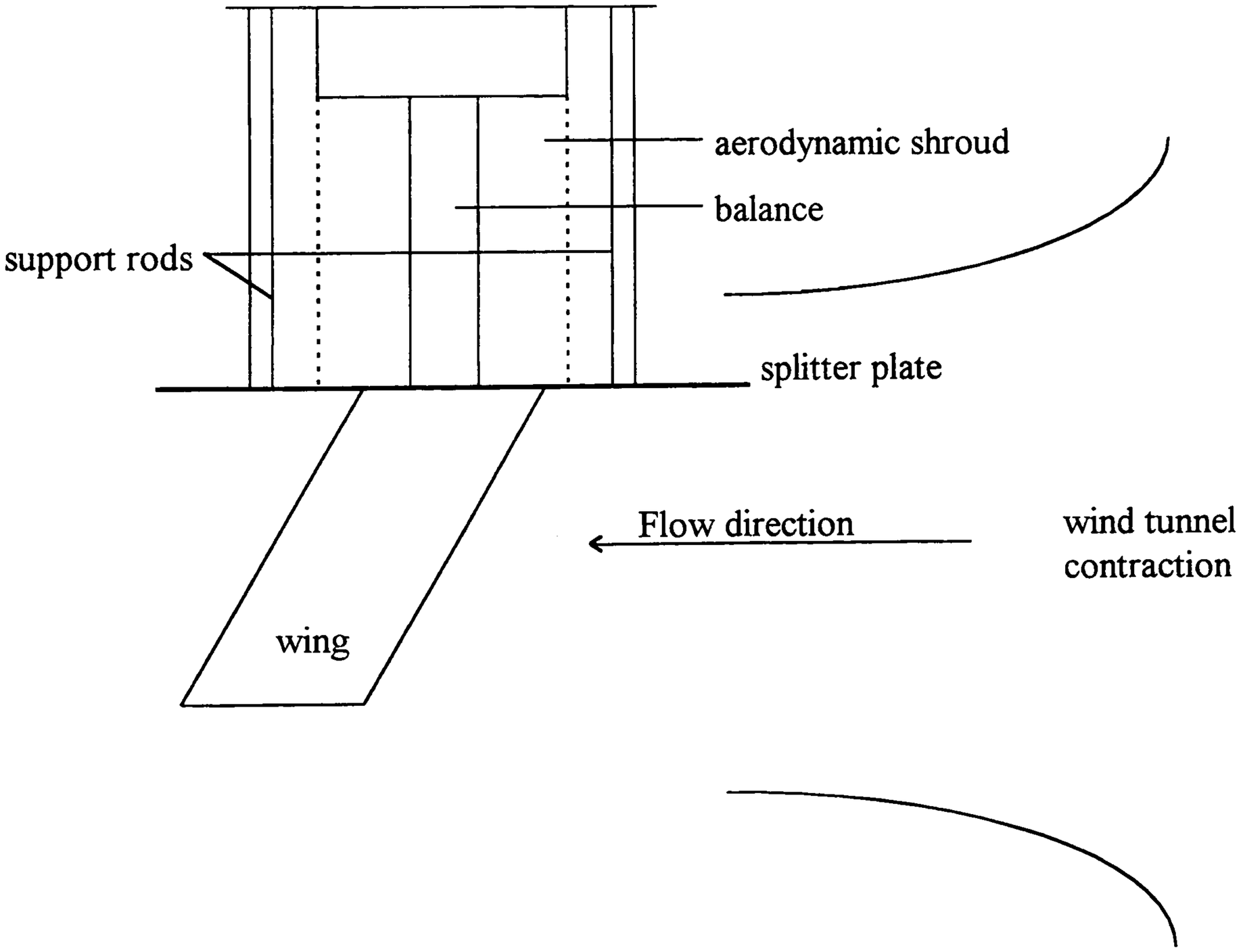

Figure 3-2: Schematic of Cranfield balance and model arrangement.

End view from wing root

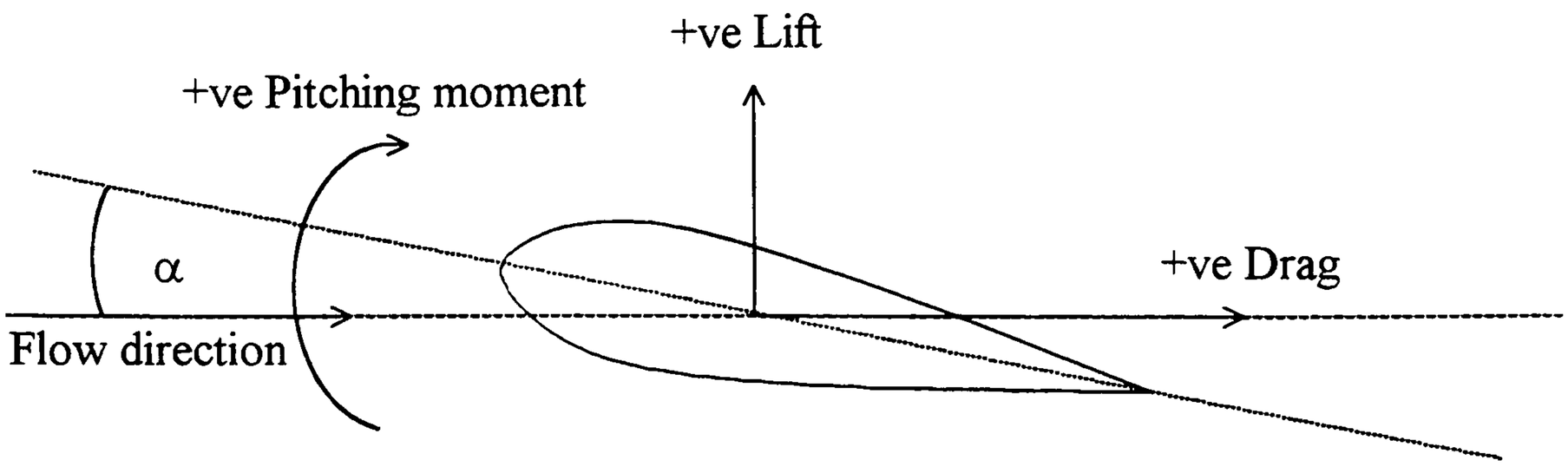

Aerofoil section

Front view looking downwind

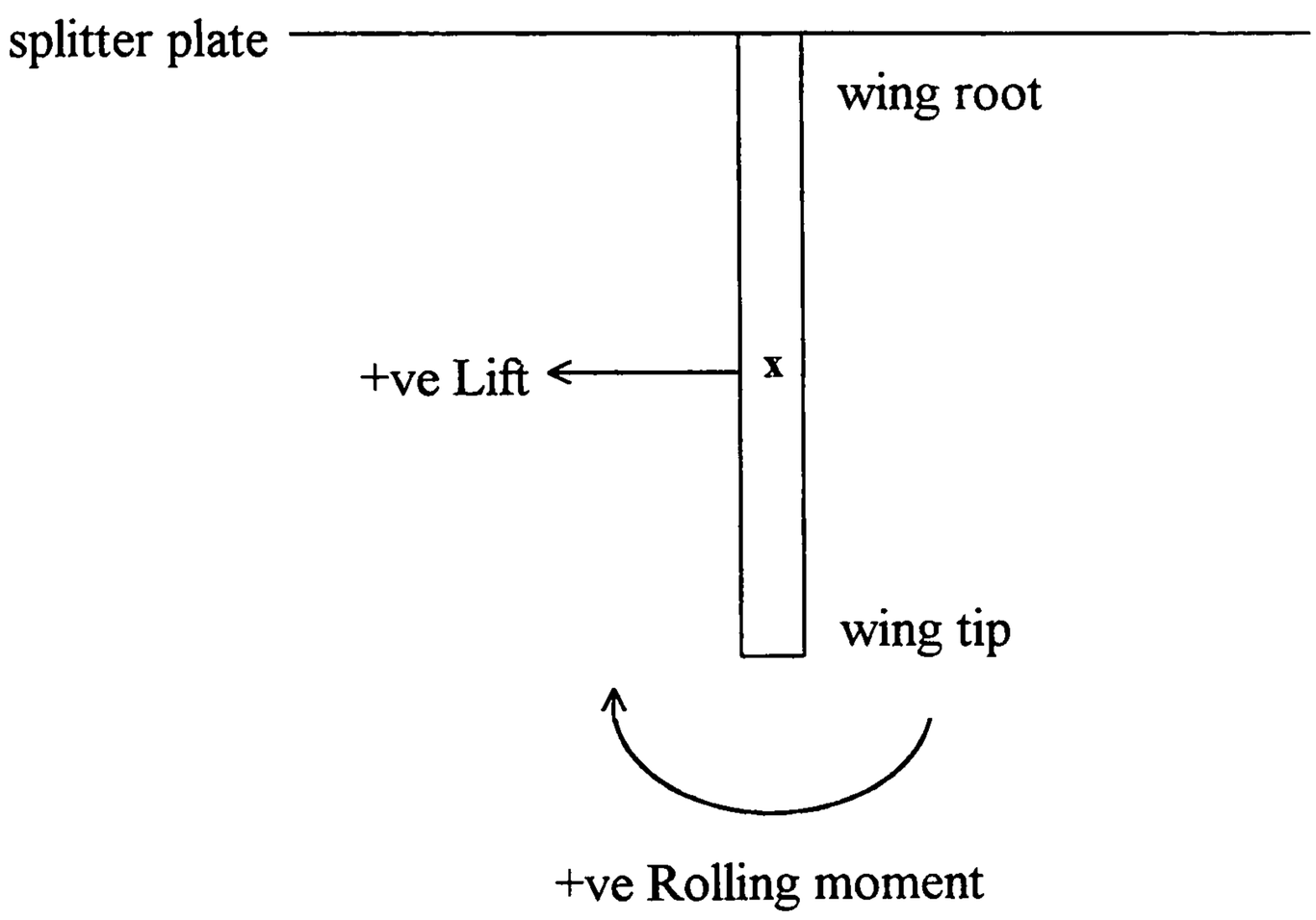

Side view

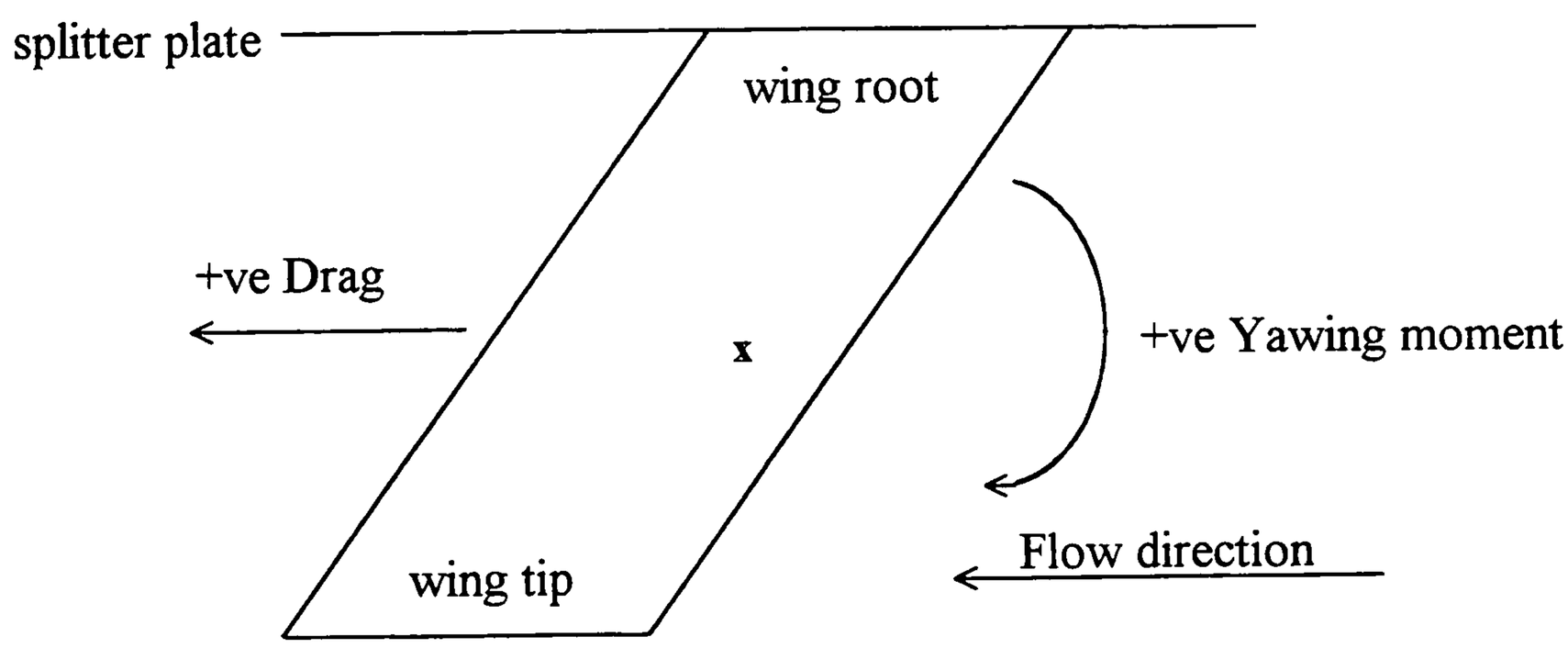

X marks moment reference position on model taken at the quarter chord and mid span position

Figure 3-3: Force and moment sign convention.

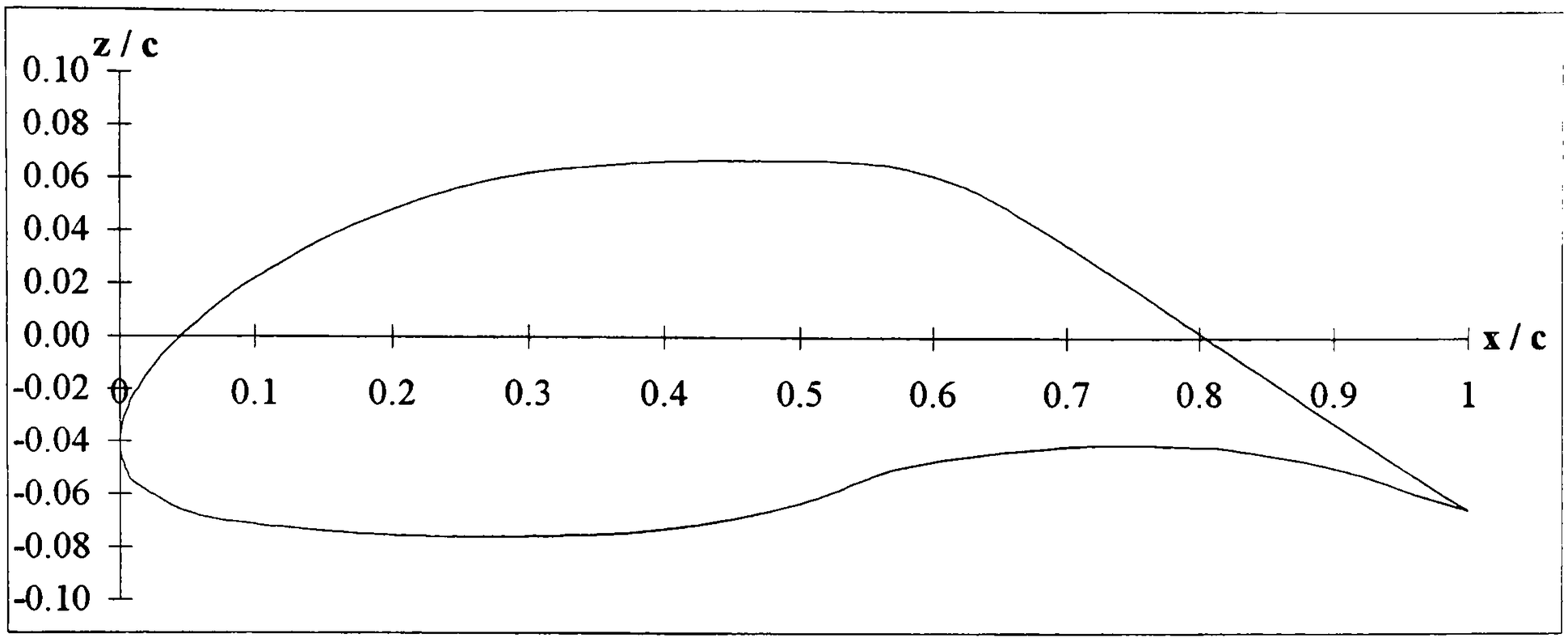

Figure 3-4: DERA aerofoil section.

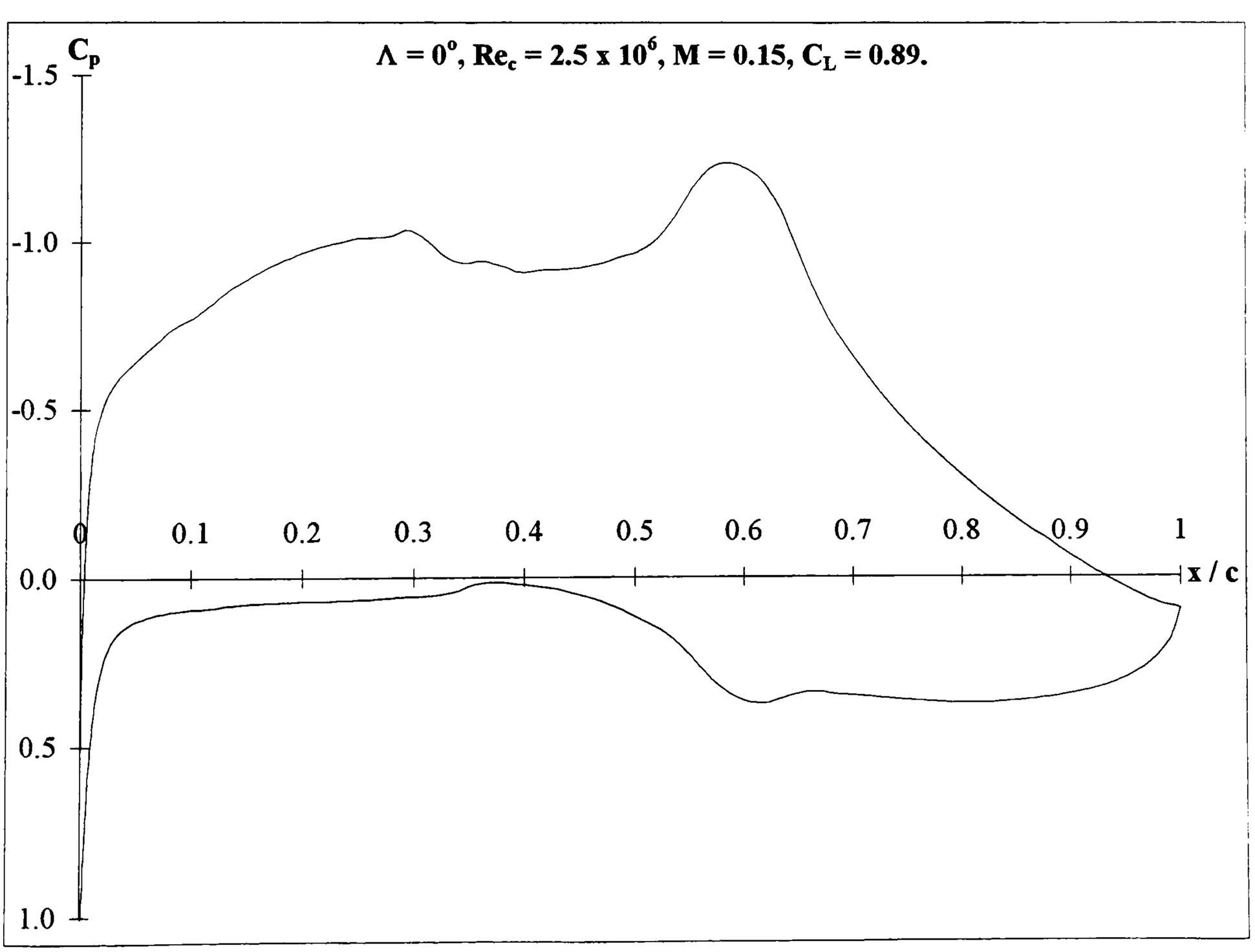

Figure 3-5: Typical pressure distribution on the DERA aerofoil section from BVGK.

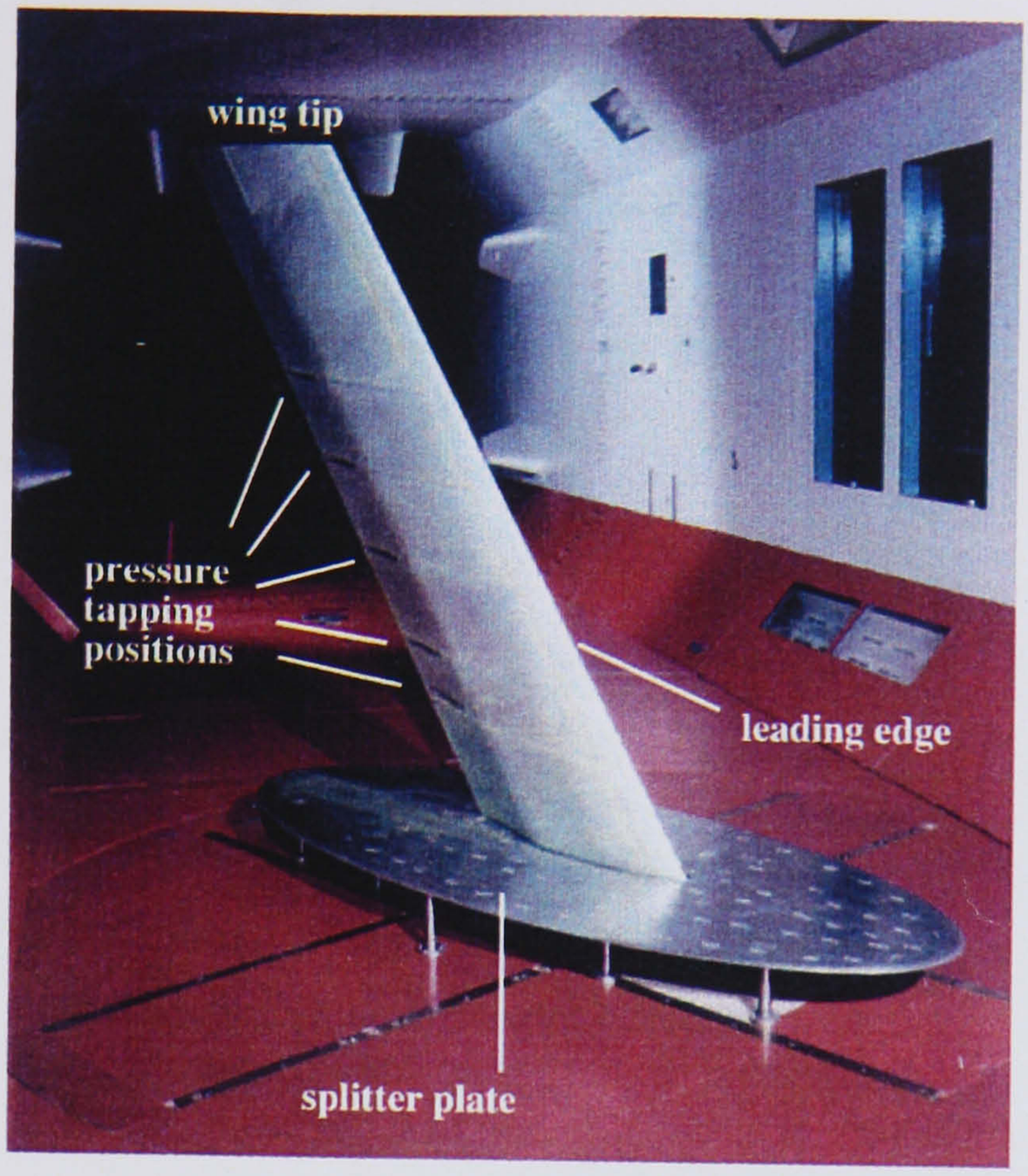

Figure 3-6: DERA wing in 13' x 9' wind tunnel.

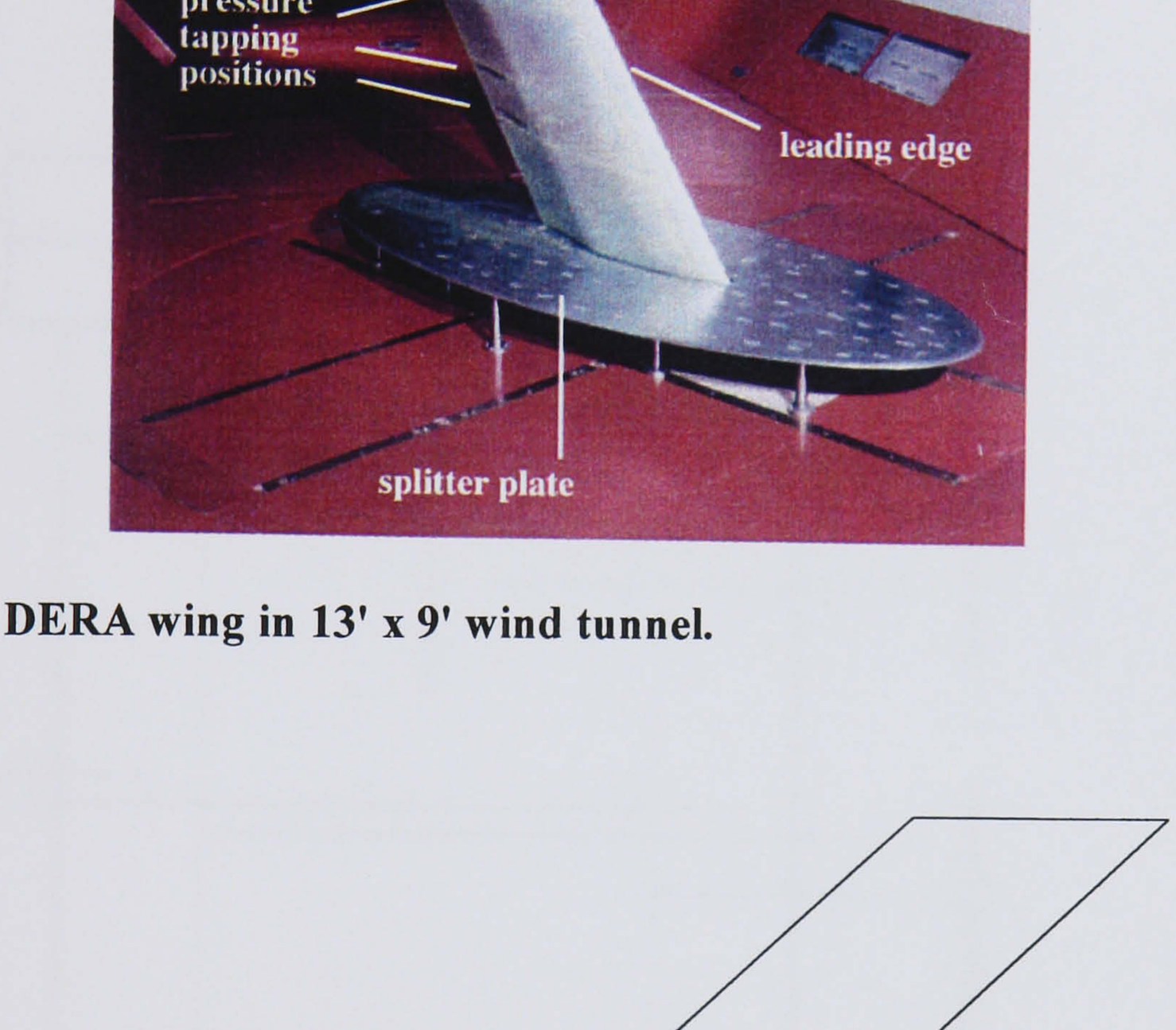

Figure 3-7: DERA wing arrangement (with dimensions) on half model balance.

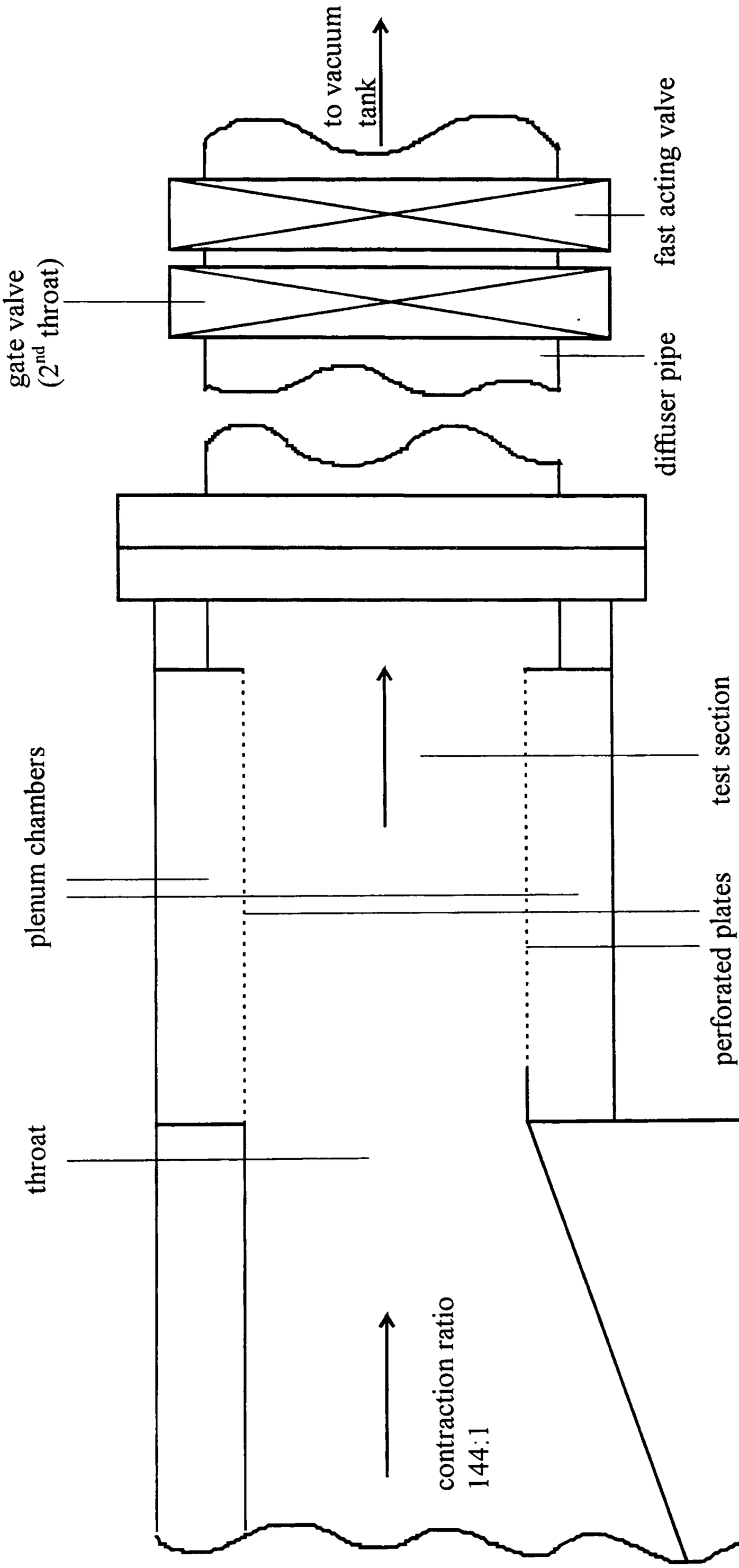

Figure 3-8: Schematic of the 2.5" x 2.5" transonic wind tunnel (not to scale).

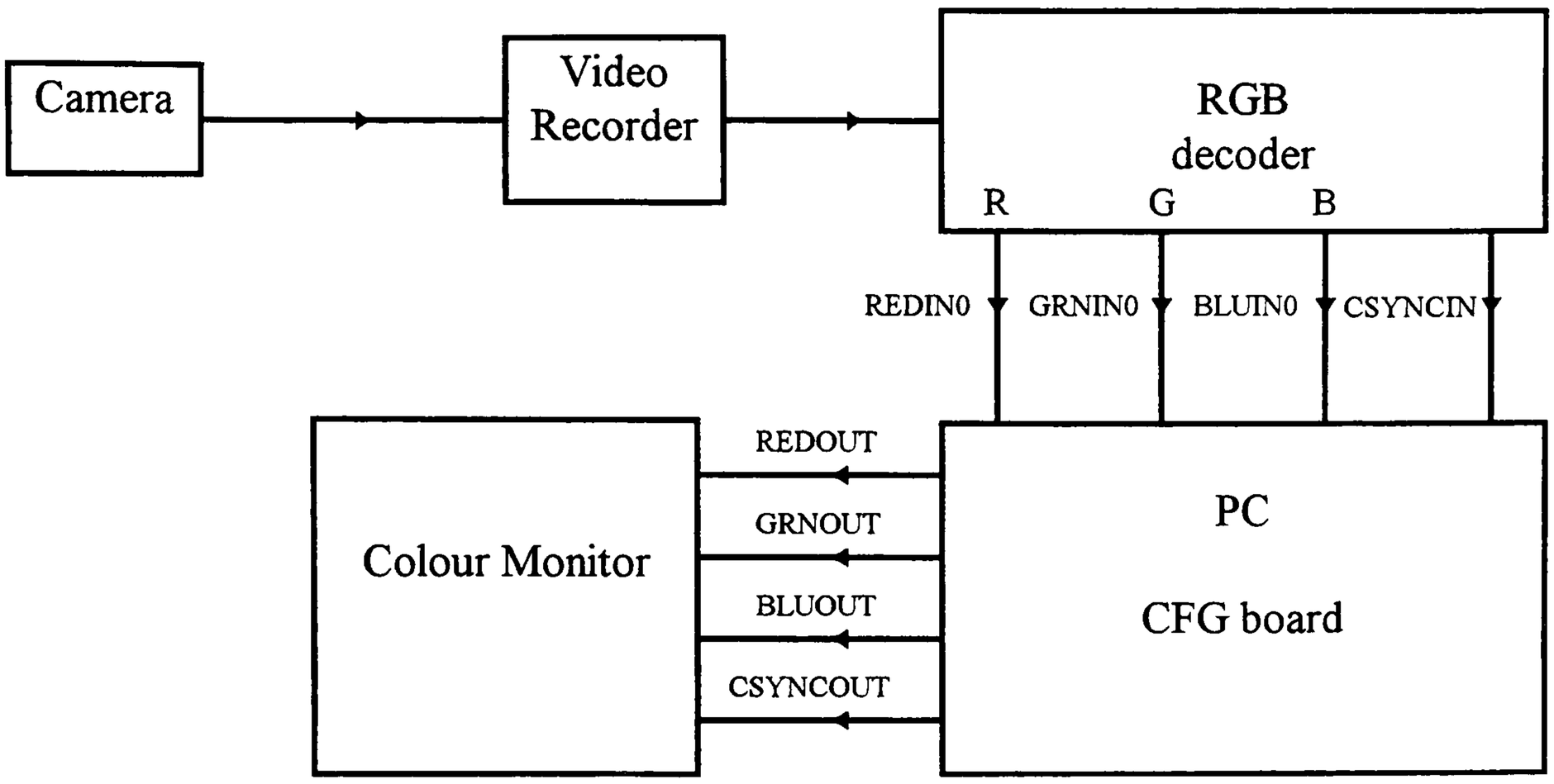

Figure 3-9: Liquid crystal colour analysis equipment.

Side view

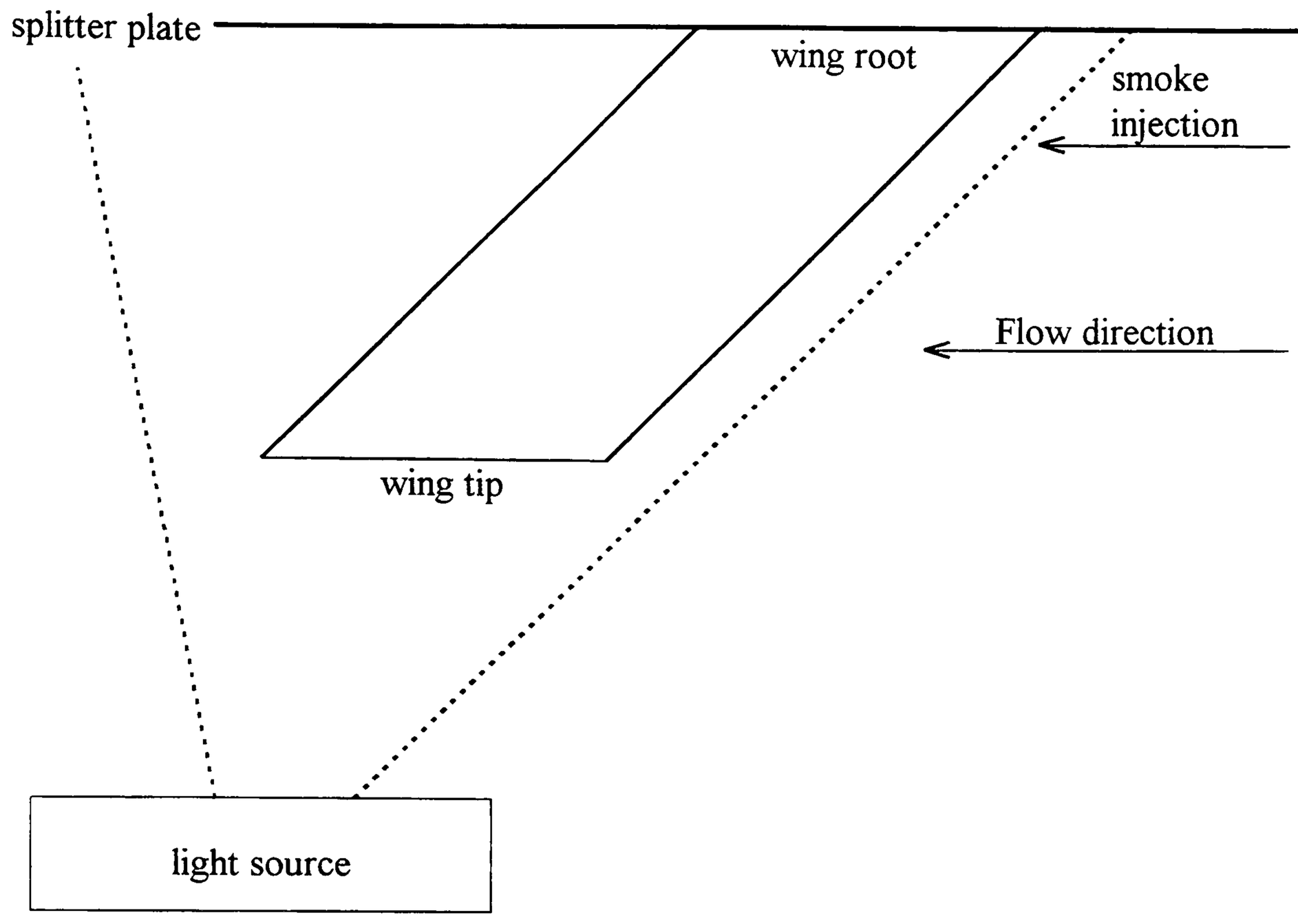

Front view looking downwind

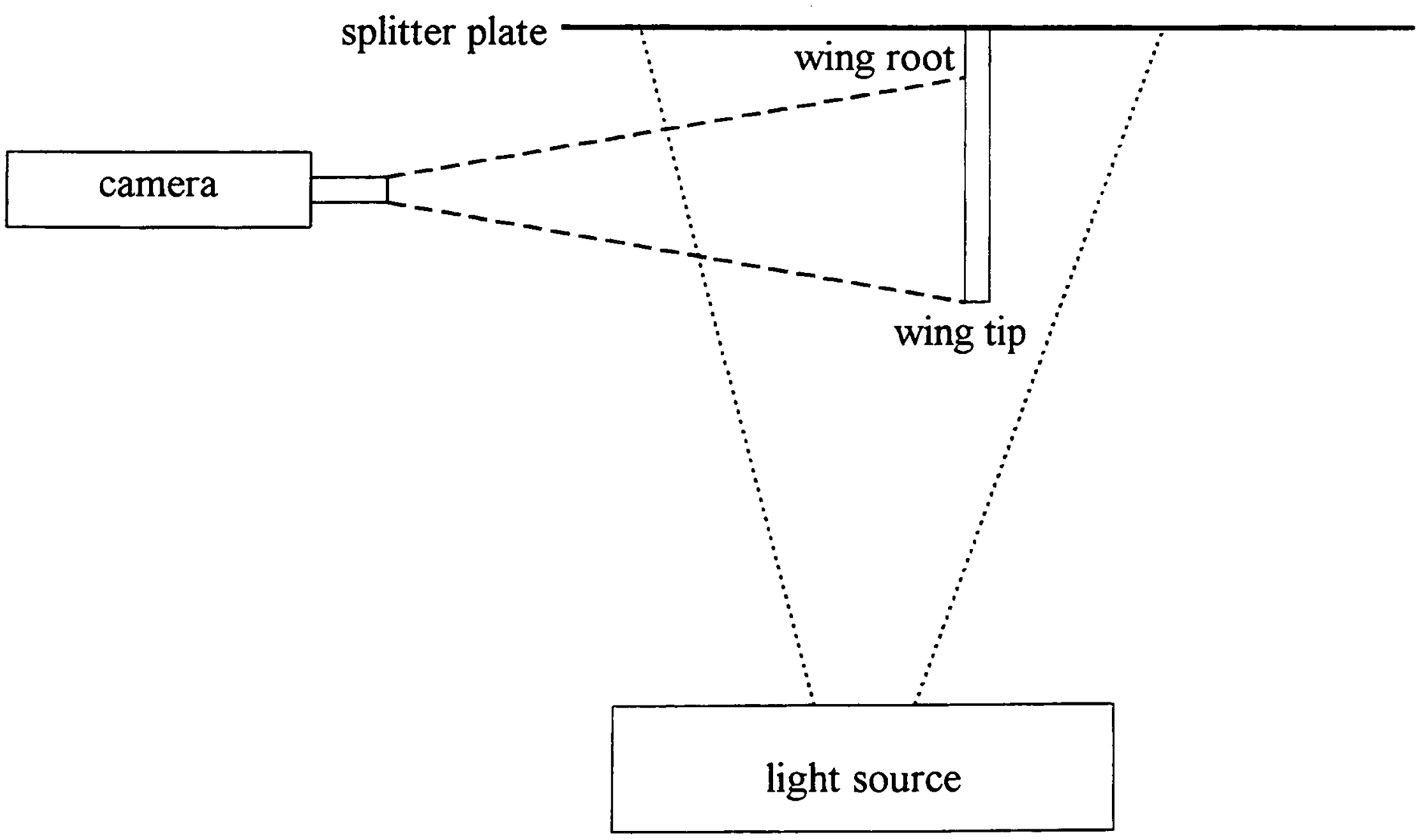

Figure 4-1: Smoke flow visualisation arrangement.

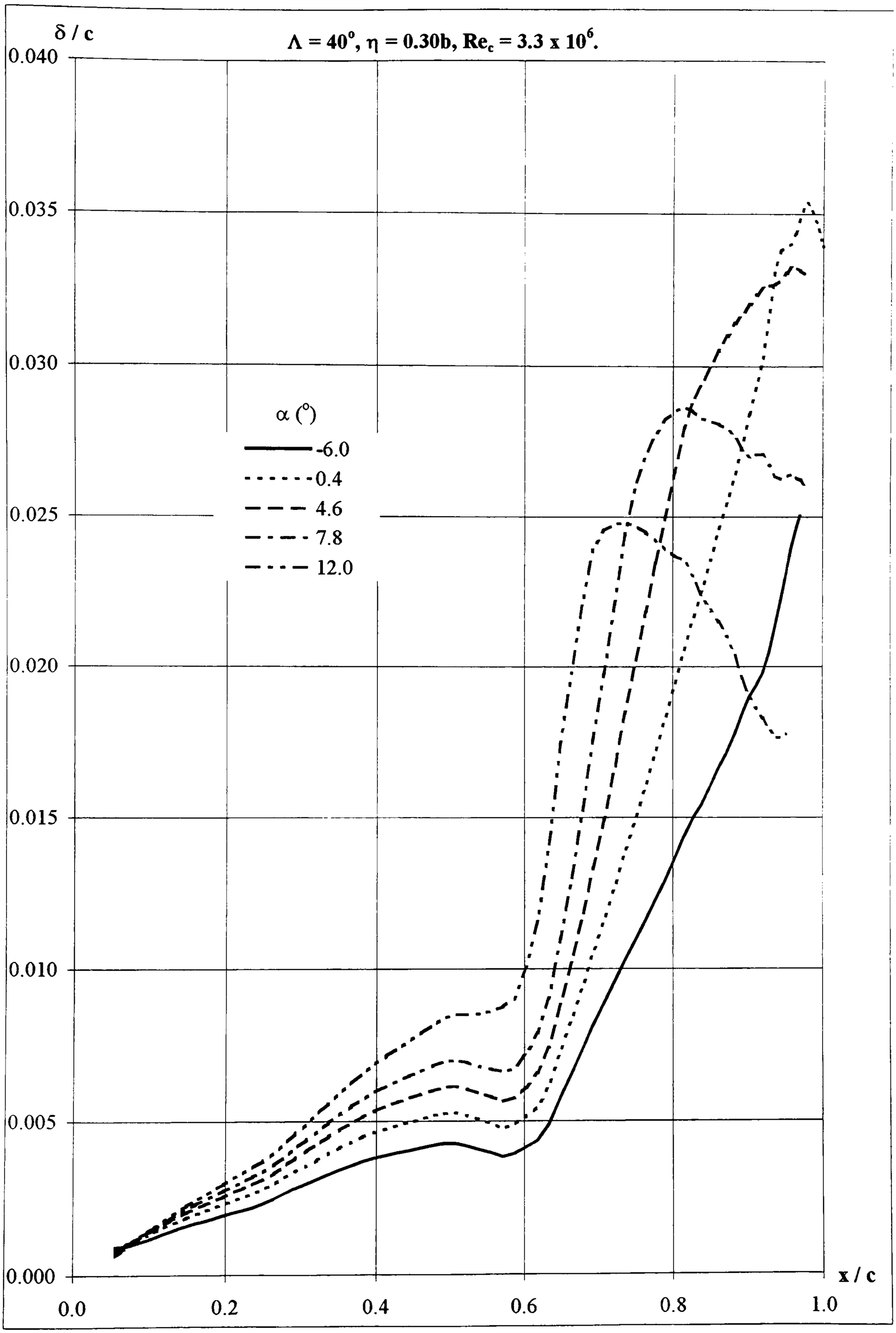

Figure 4-2: Calculated boundary layer thickness on the DERA wing using WAKELAG.

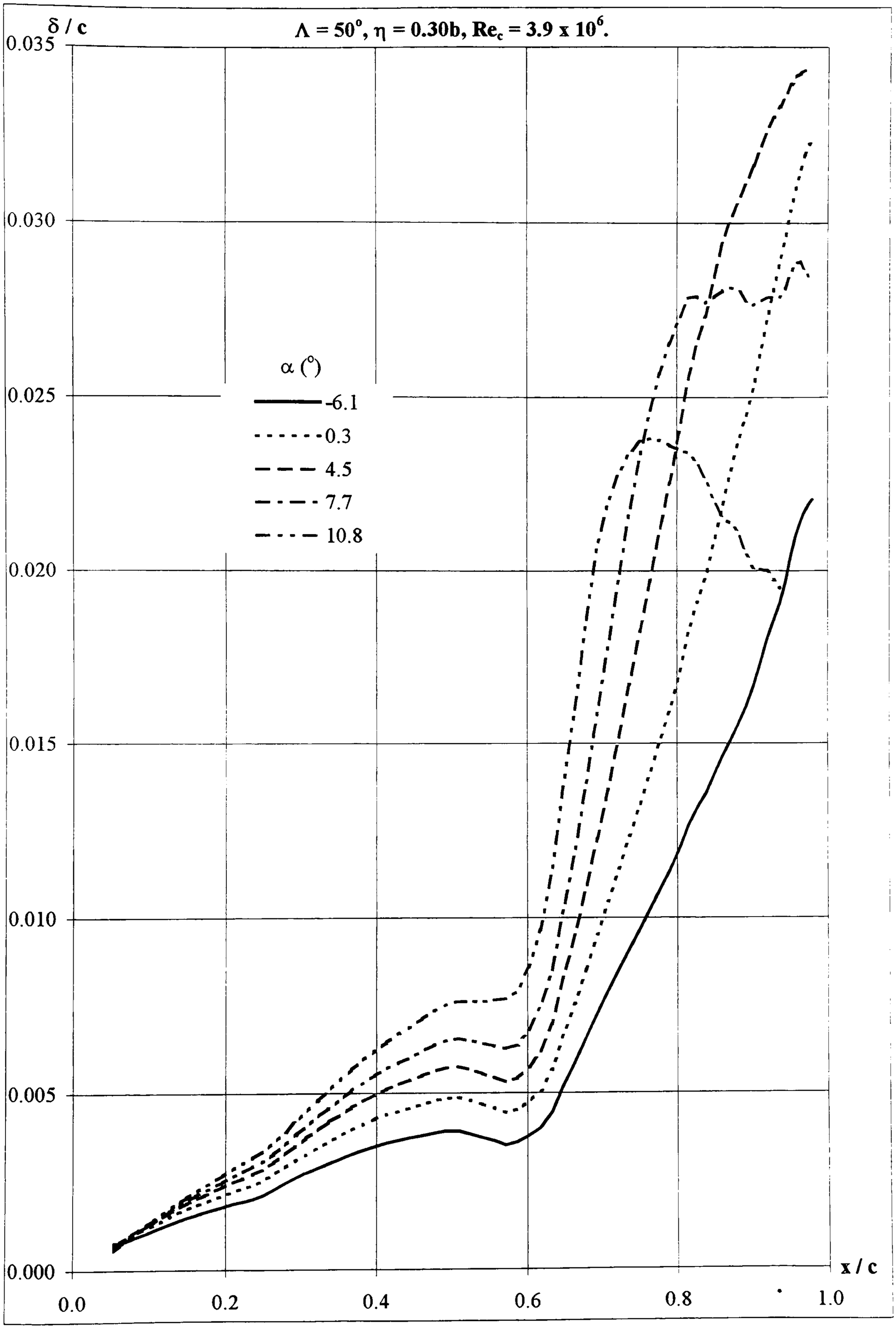

Figure 4-2 cont.: Calculated boundary layer thickness on the DERA wing using WAKELAG.

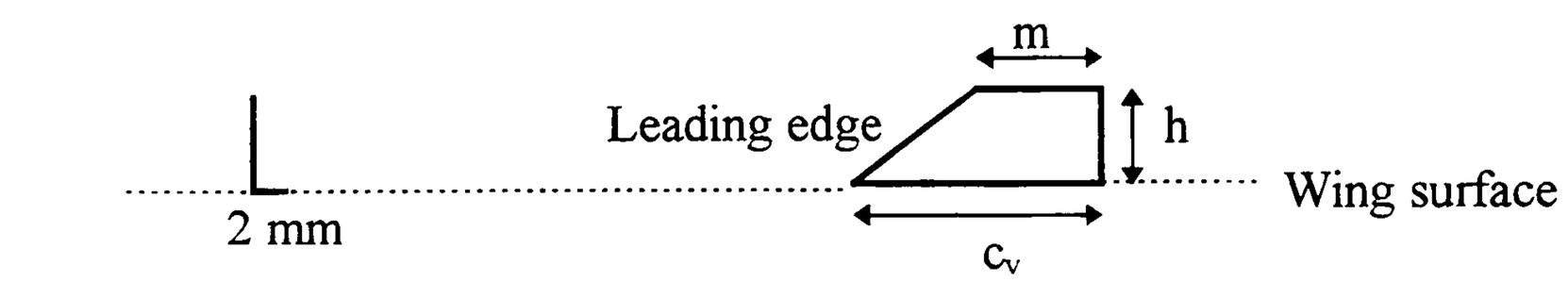

h (mm)	c_v (mm)	m (mm)	TR	A
12	16	2	0.125	2.67
10	16	4	0.250	2.00
8	16	6	0.375	1.45
6	16	8	0.563	0.96
4	16	10	0.688	0.59
2	16	12	0.875	0.27

a) Cropped delta vanes

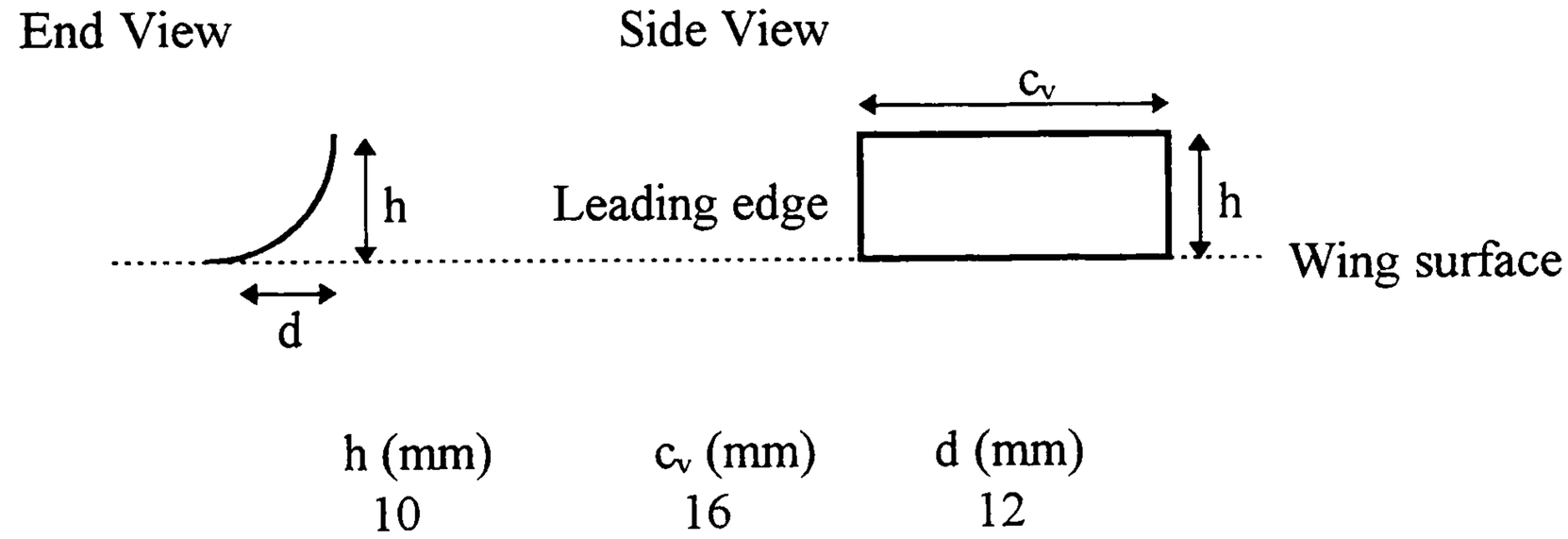

h (mm)	c_v (mm)	d (mm)
10	16	12

b) Concave slats

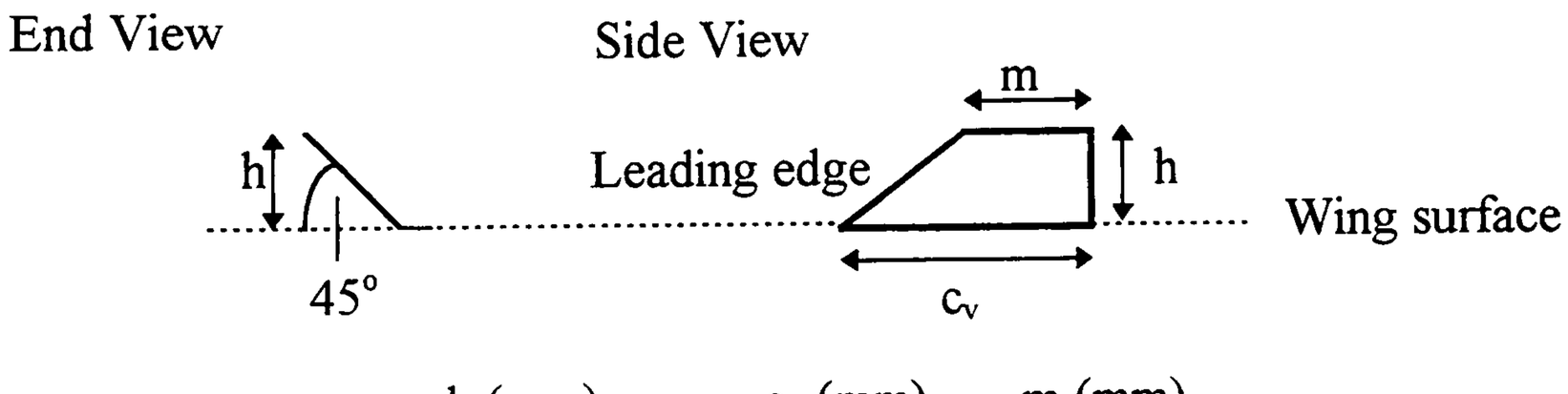

h (mm)	c_v (mm)	m (mm)
10	16	2

c) Canted cropped delta vanes

Figure 4-3: Vortex generator planviews and dimensions.

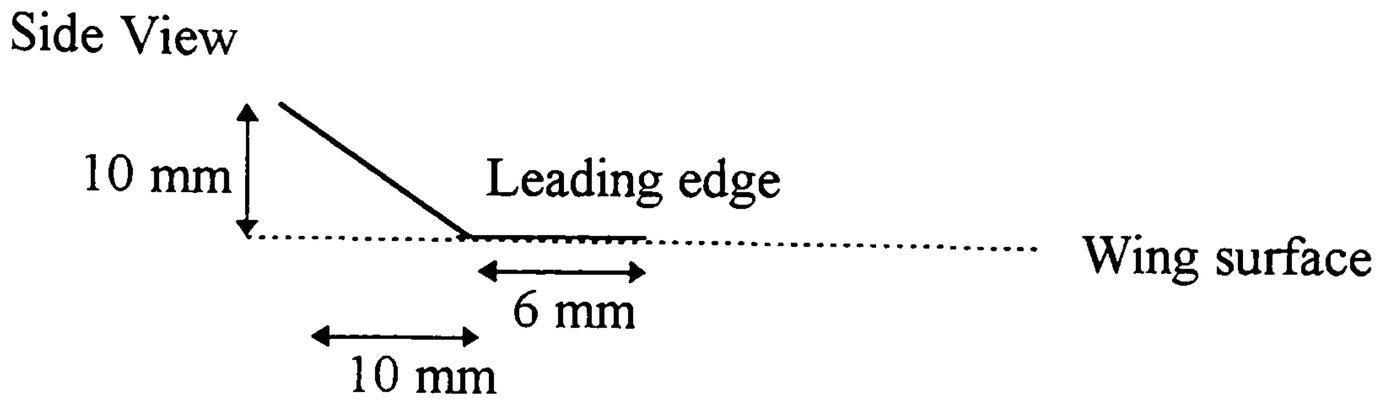

d) 'Bent' wires

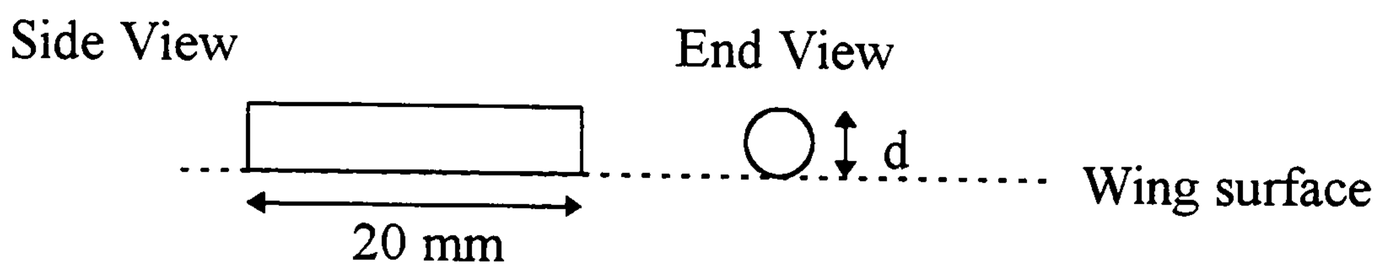

e) Wires

Figure 4-3 cont.: Vortex generator planviews and dimensions.

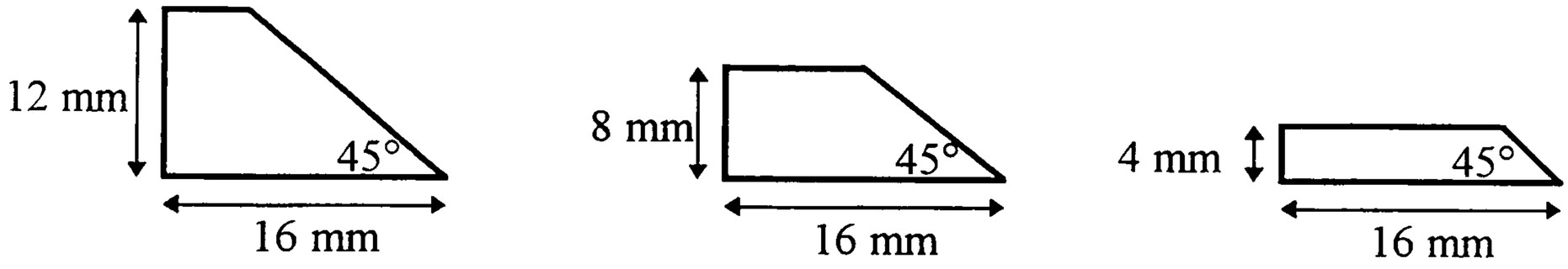

Figure 4-4: Cropped delta vortex generators used in surface shear stress investigation.

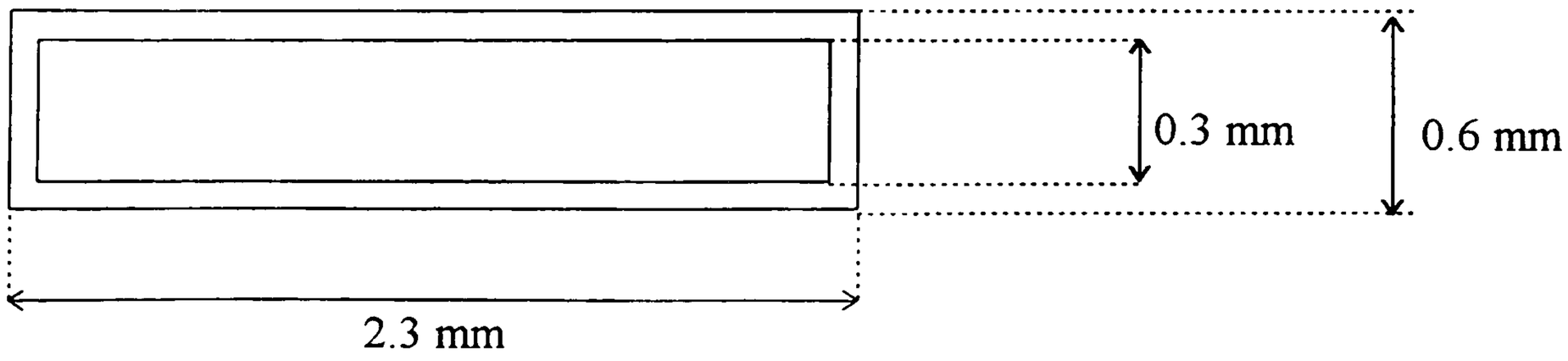

Figure 4-5: Preston tube dimensions.

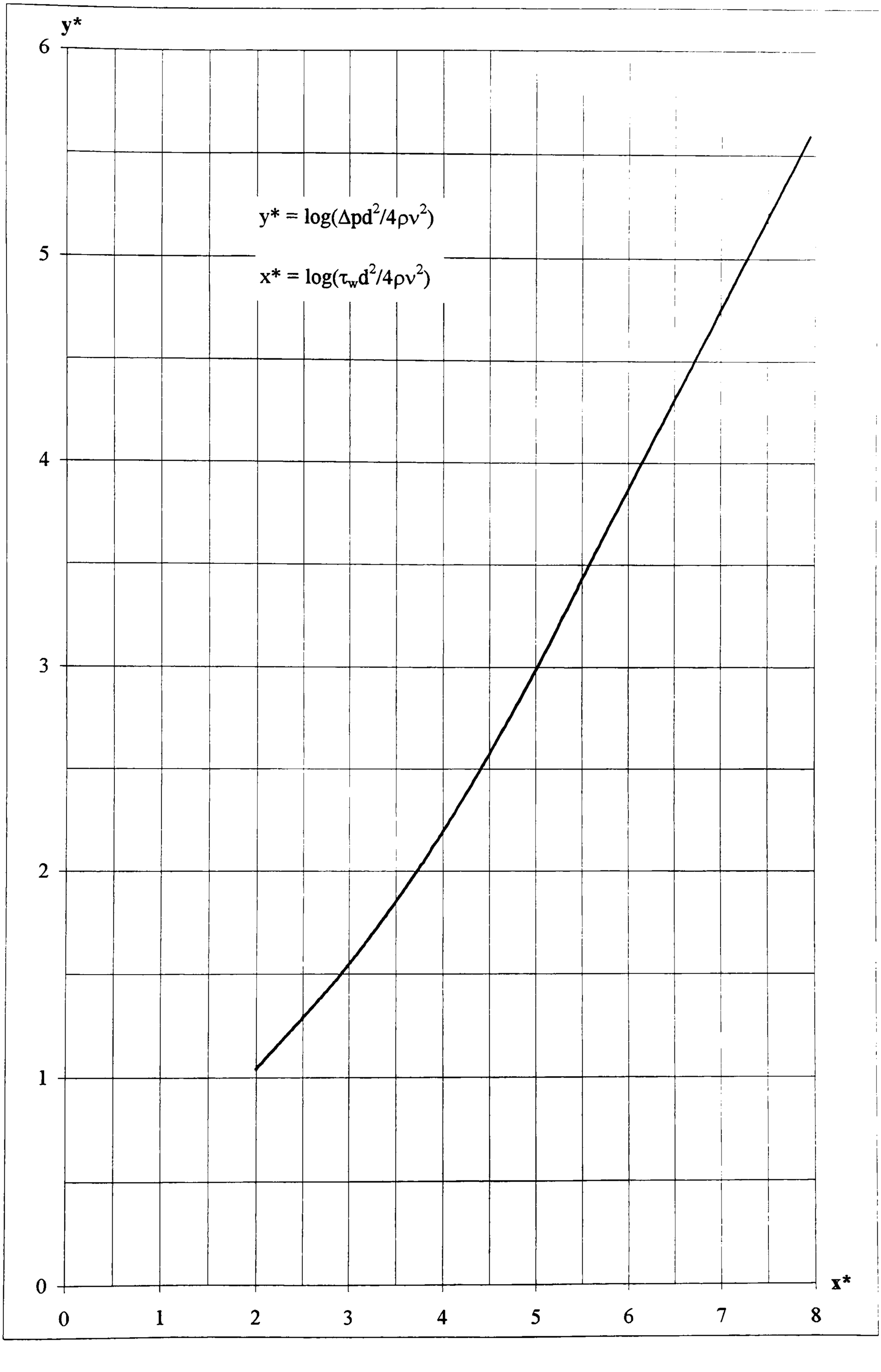

Figure 4-6: Head and Vasanta Ram Preston tube calibration curve[82].

End view

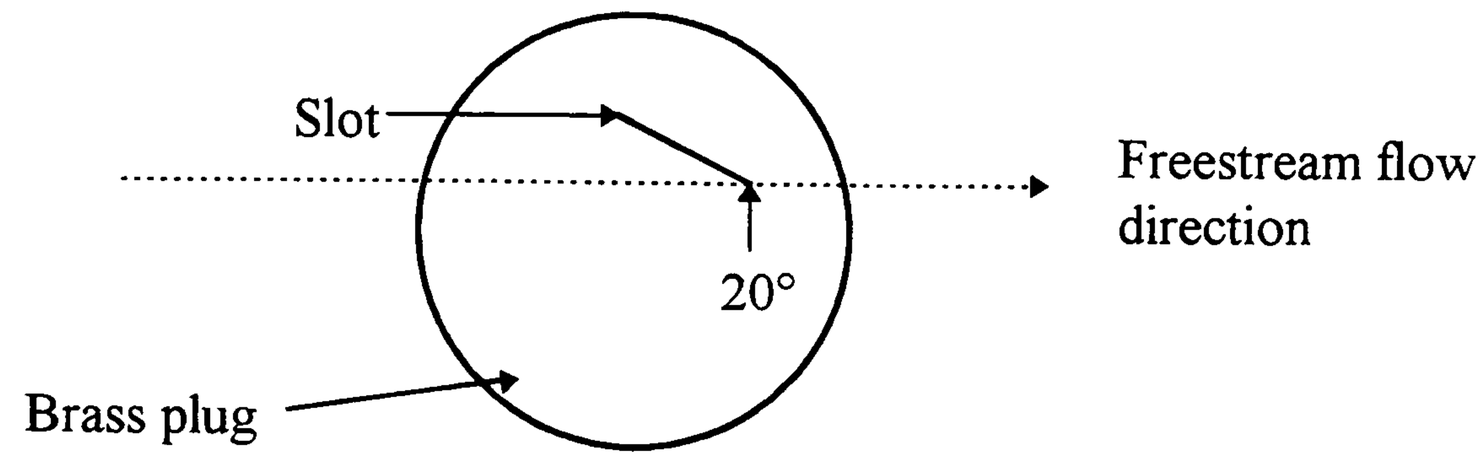

Side view (vane ready for insertion)

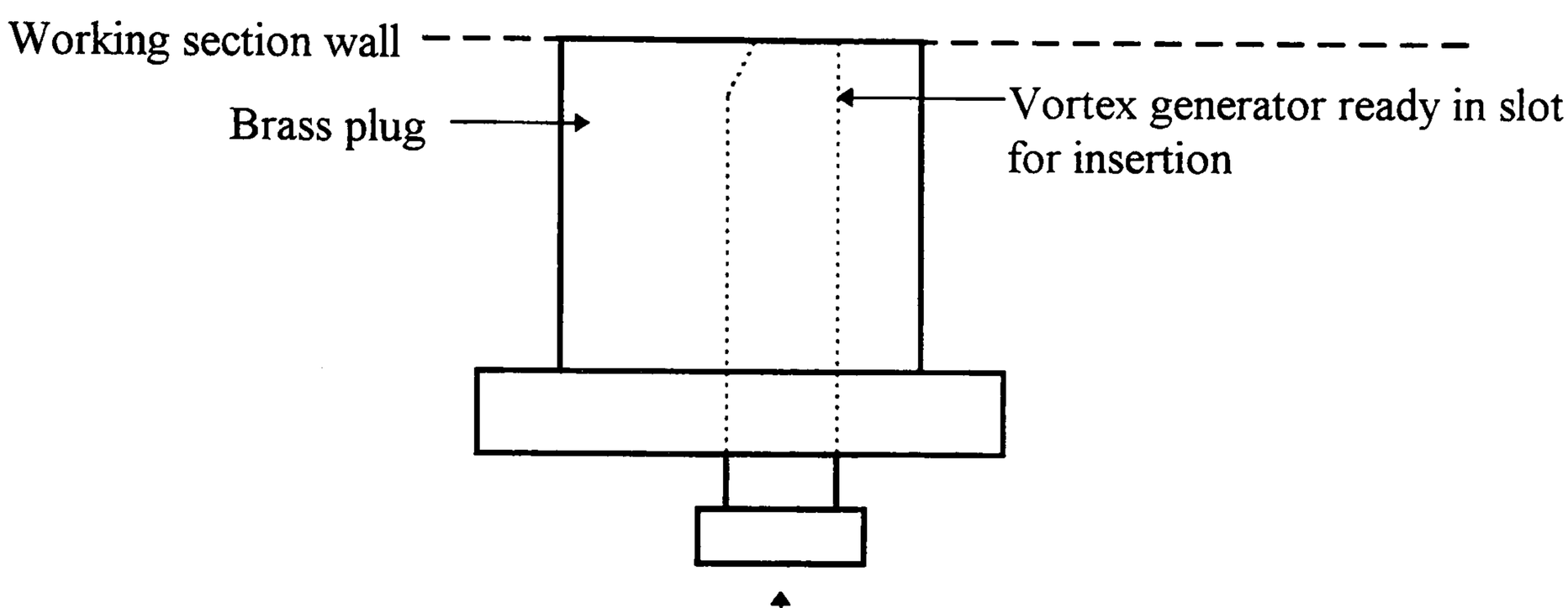

Side view (vane inserted)

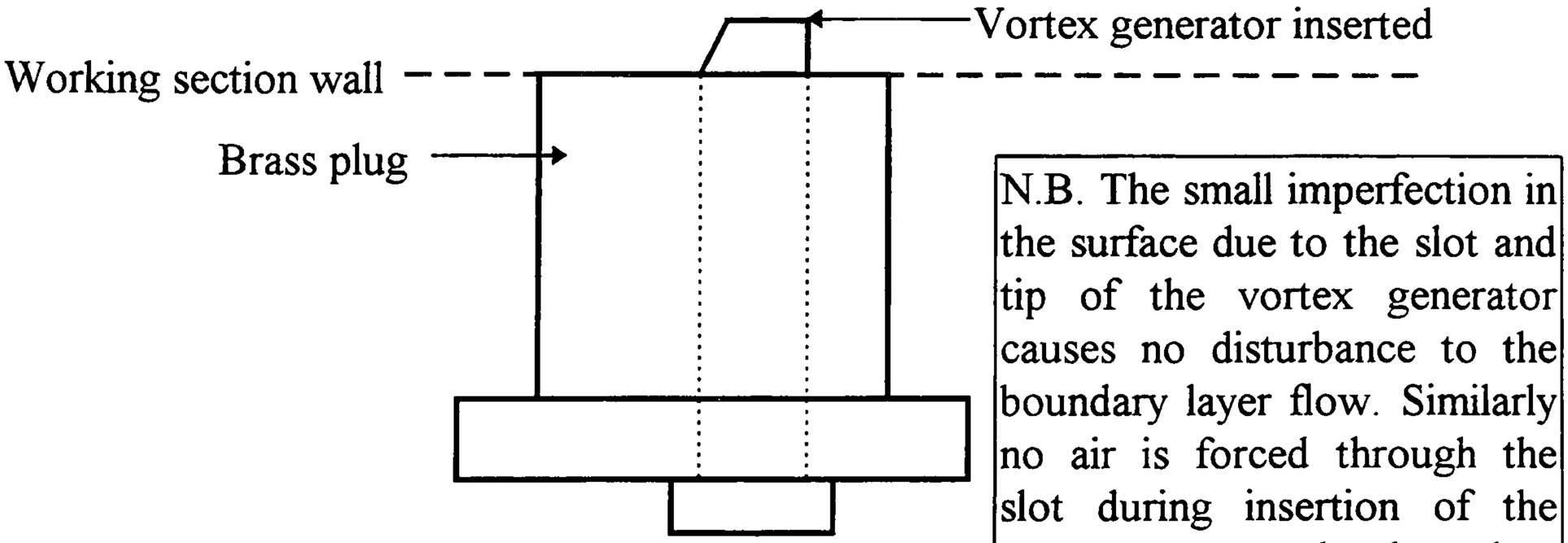

N.B. The small imperfection in the surface due to the slot and tip of the vortex generator causes no disturbance to the boundary layer flow. Similarly no air is forced through the slot during insertion of the vane to upset the boundary layer flow.

Figure 4-7: Vortex generator inserting plug.

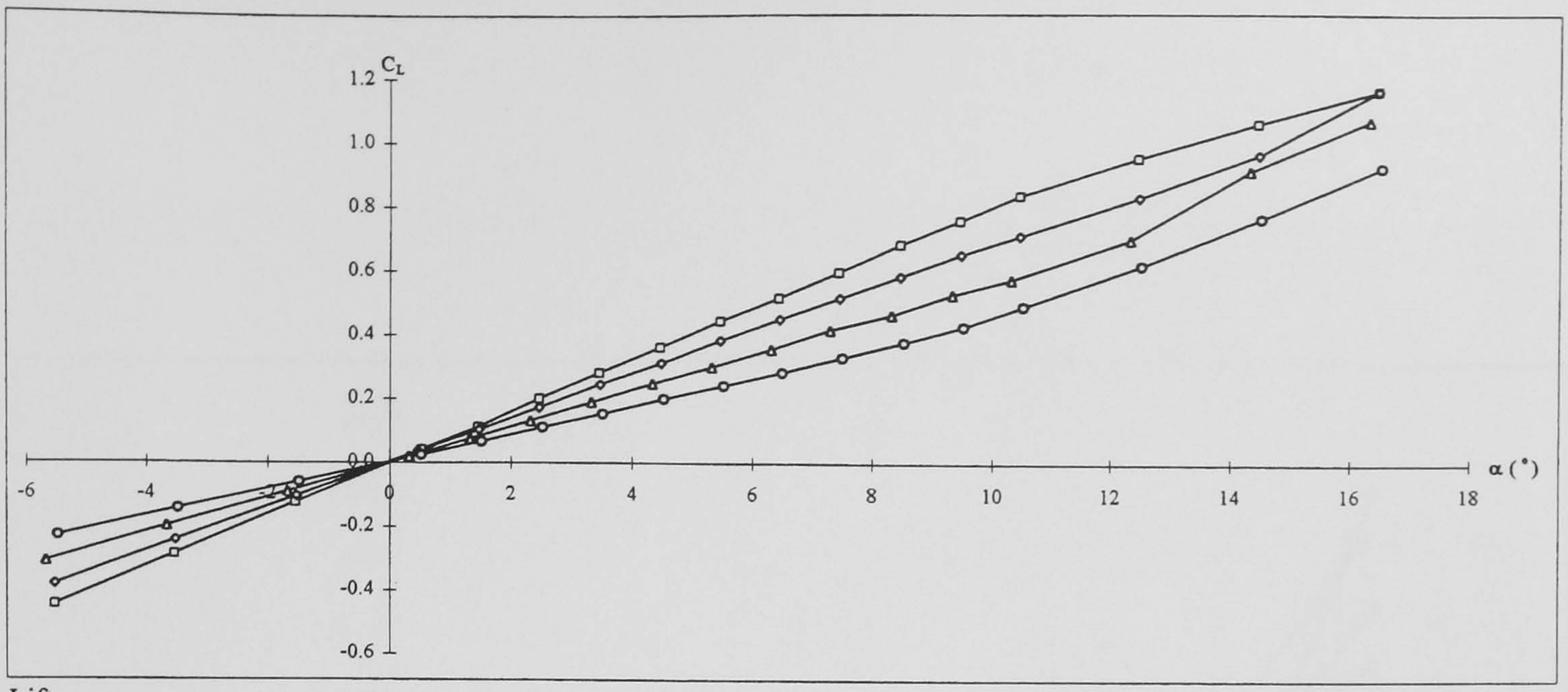

Lift

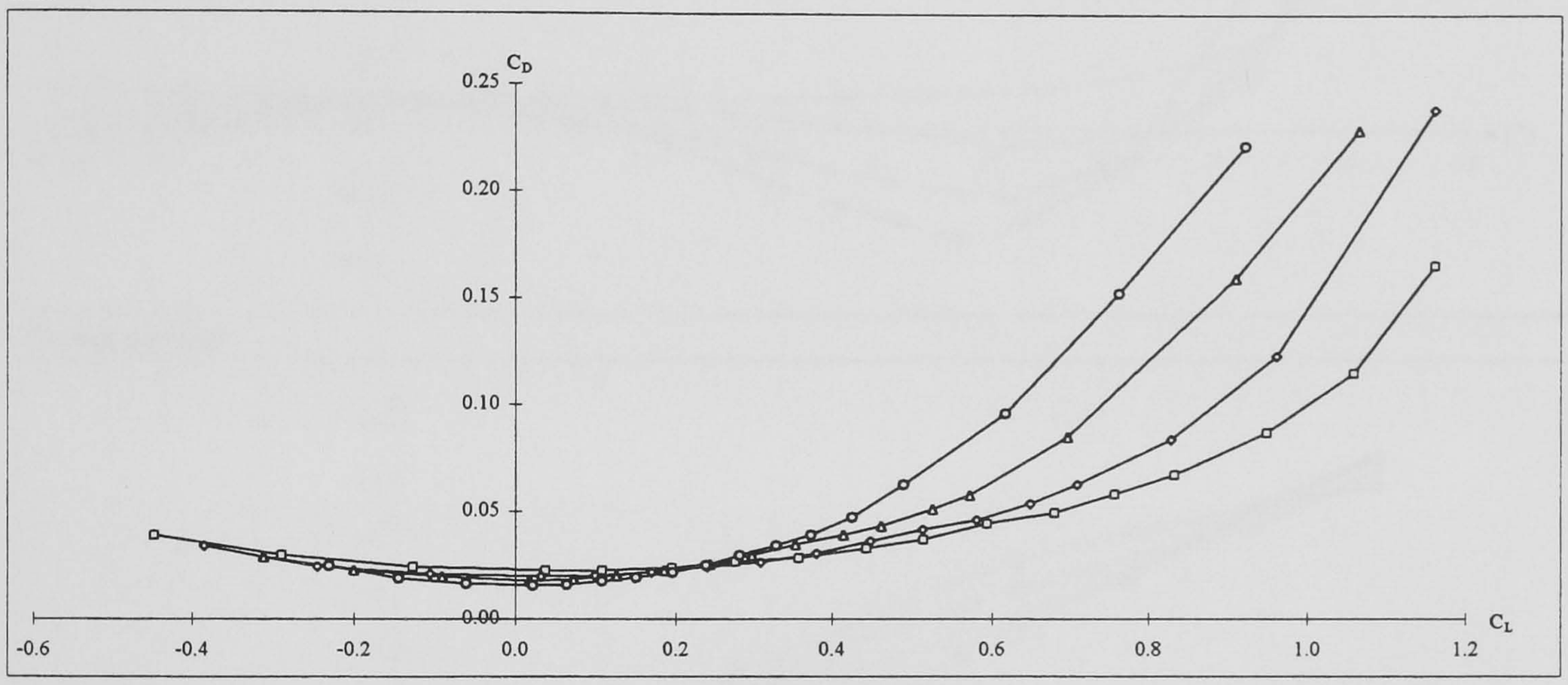

Drag polar

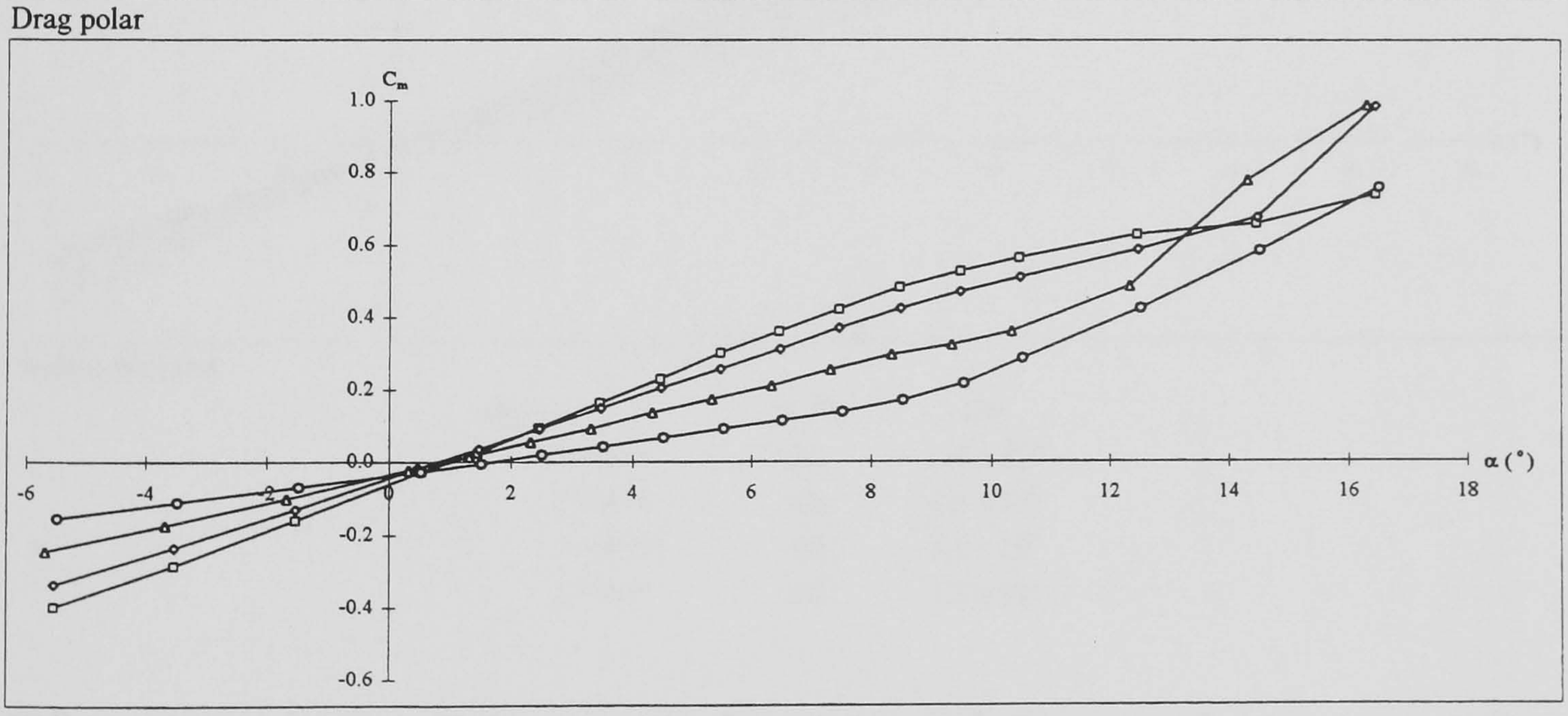

Pitching moment

Key	Λ (°)	Re_c
—□—	30	3.8×10^5
—◇—	40	4.3×10^5
—△—	50	5.1×10^5
—○—	60	6.5×10^5

Figure 5-1: Cranfield swept wing aerodynamic forces and moments results.

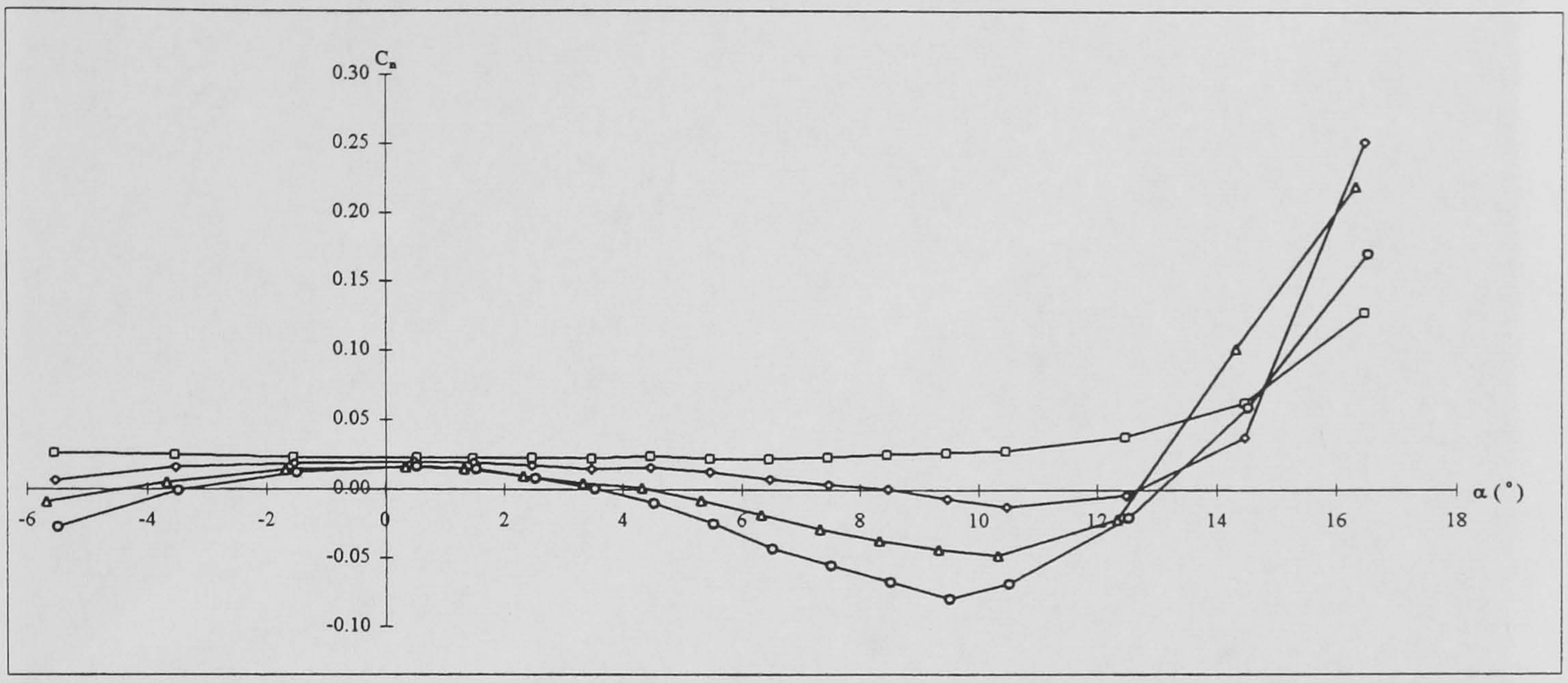

Yawing moment

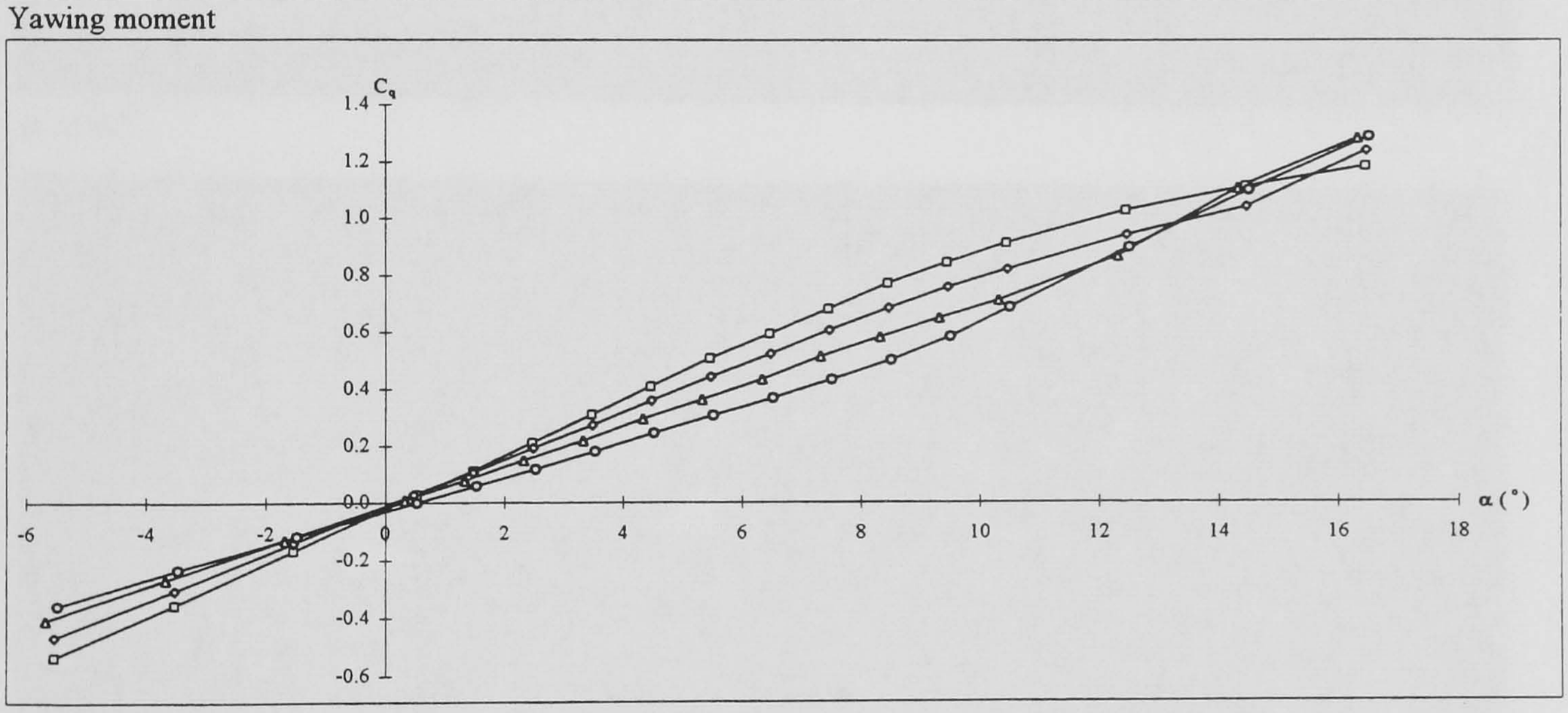

Rolling moment

Key	Λ (°)	Re_c
—□—	30	3.8×10^5
—◇—	40	4.3×10^5
—△—	50	5.1×10^5
—○—	60	6.5×10^5

Figure 5-1 cont.: Cranfield swept wing aerodynamic forces and moments results.

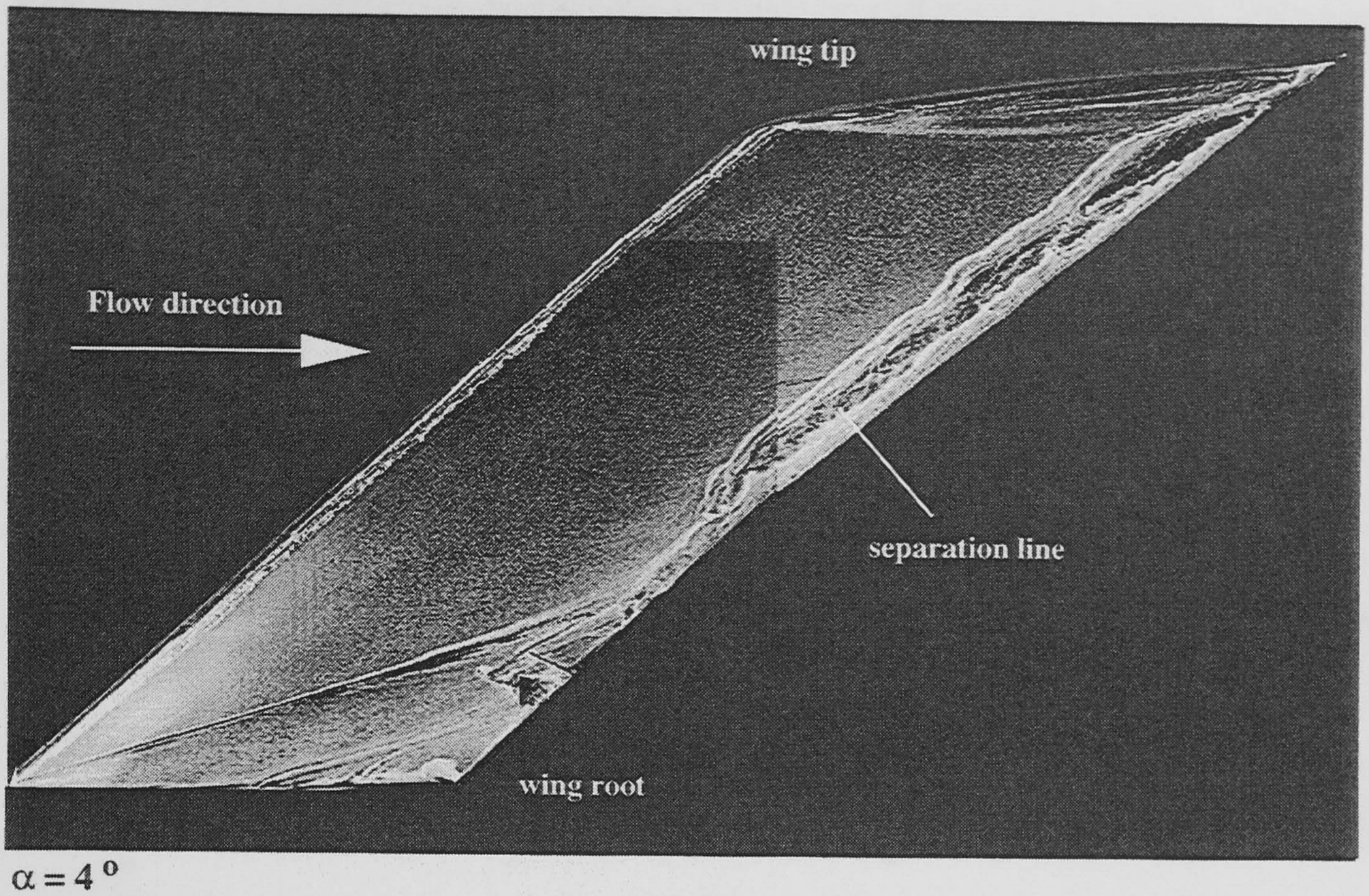

$\alpha = 4^{o}$

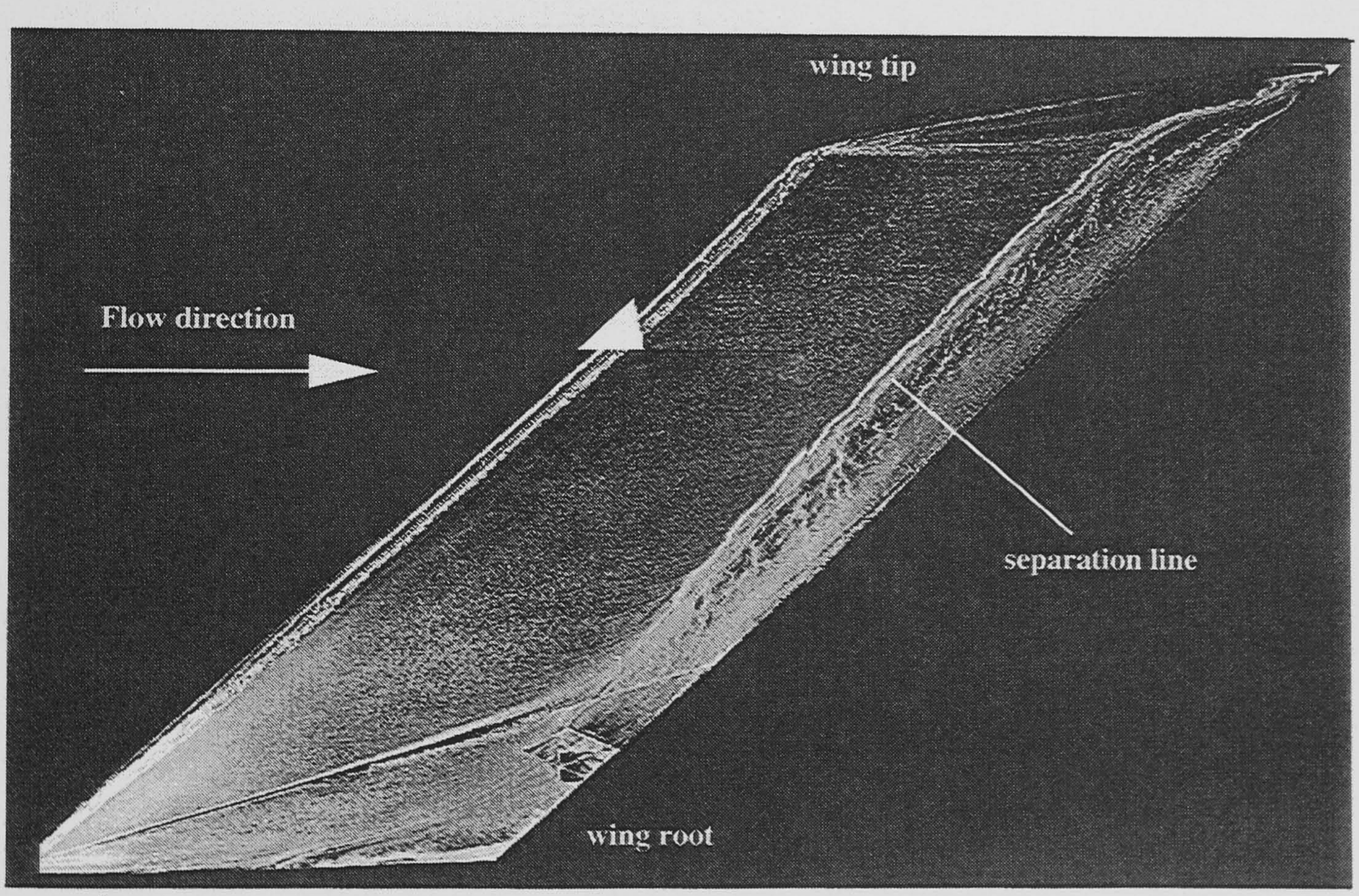

$\alpha = 8^{o}$

Figure 5-2: Surface oil flow visualisation results for the Cranfield swept wing. $\Lambda = 30°$, $Re_c = 3.8 \times 10^5$.

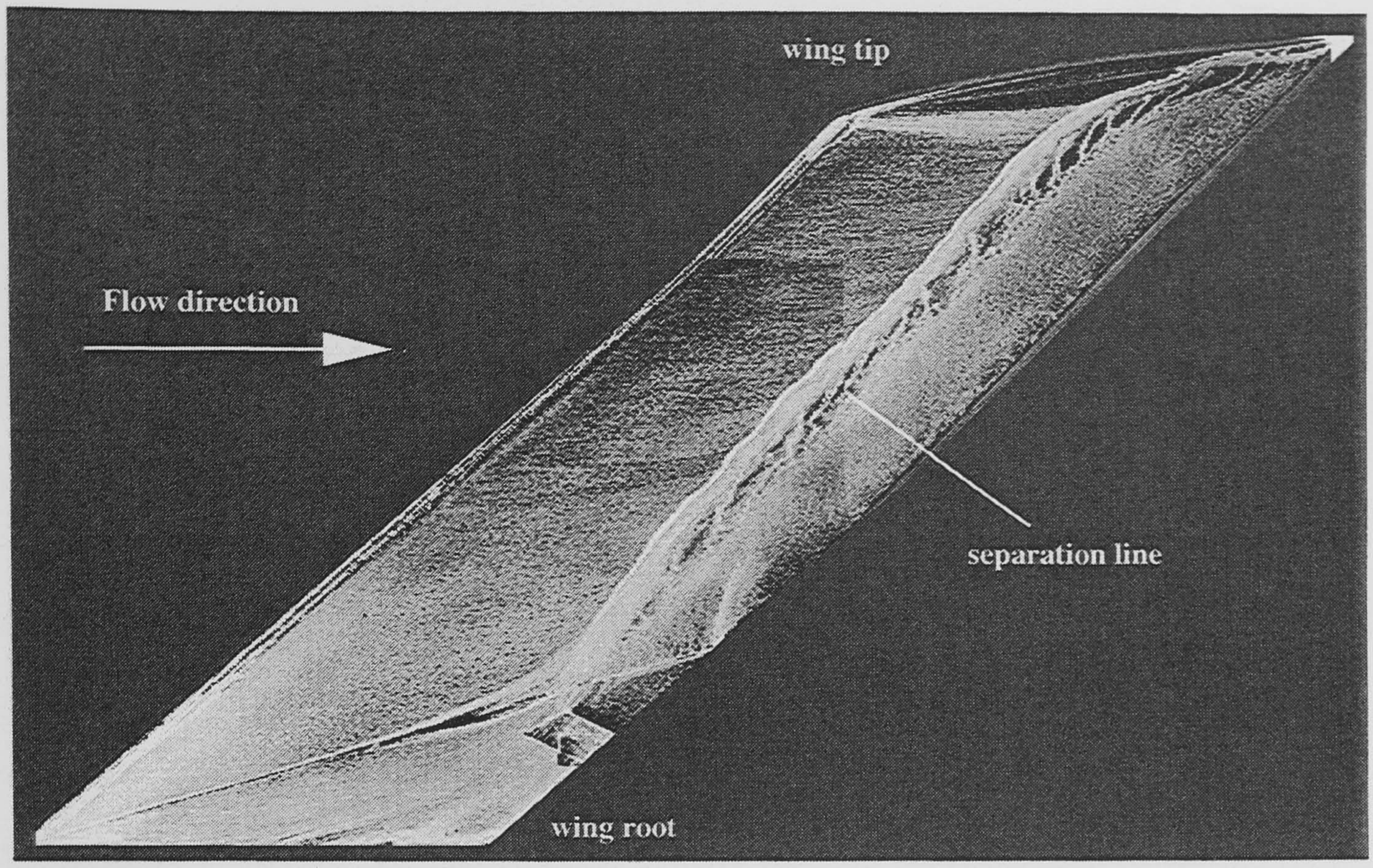

$\alpha = 12^{o}$

Figure 5-2 cont.: Surface oil flow visualisation results for the Cranfield swept wing. $\Lambda = 30°$, $Re_c = 3.8 \times 10^5$.

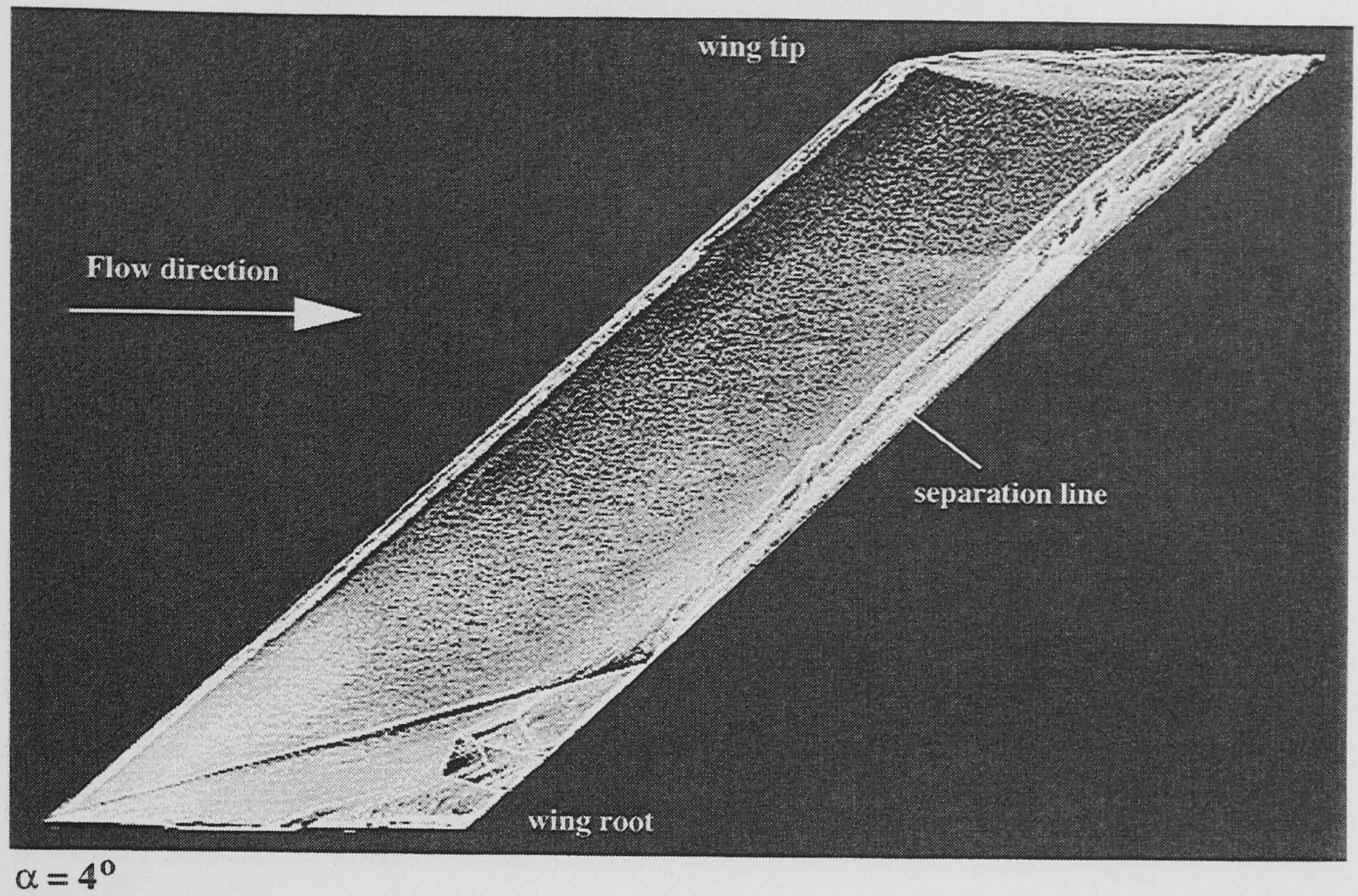

$\alpha = 4^o$

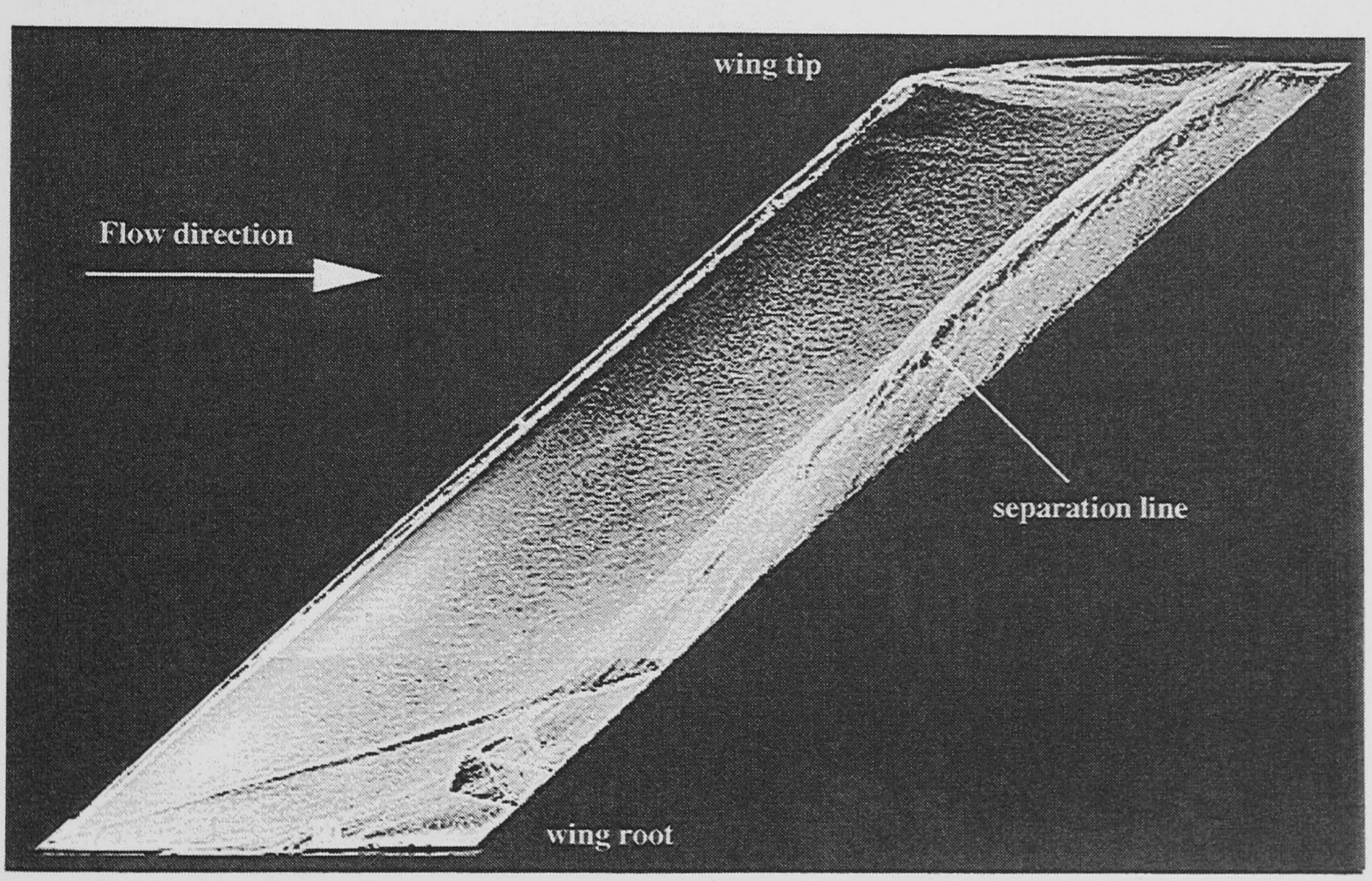

$\alpha = 8^o$

Figure 5-3: Surface oil flow visualisation results for the Cranfield swept wing. $\Lambda = 40°$, $Re_c = 4.3 \times 10^5$.

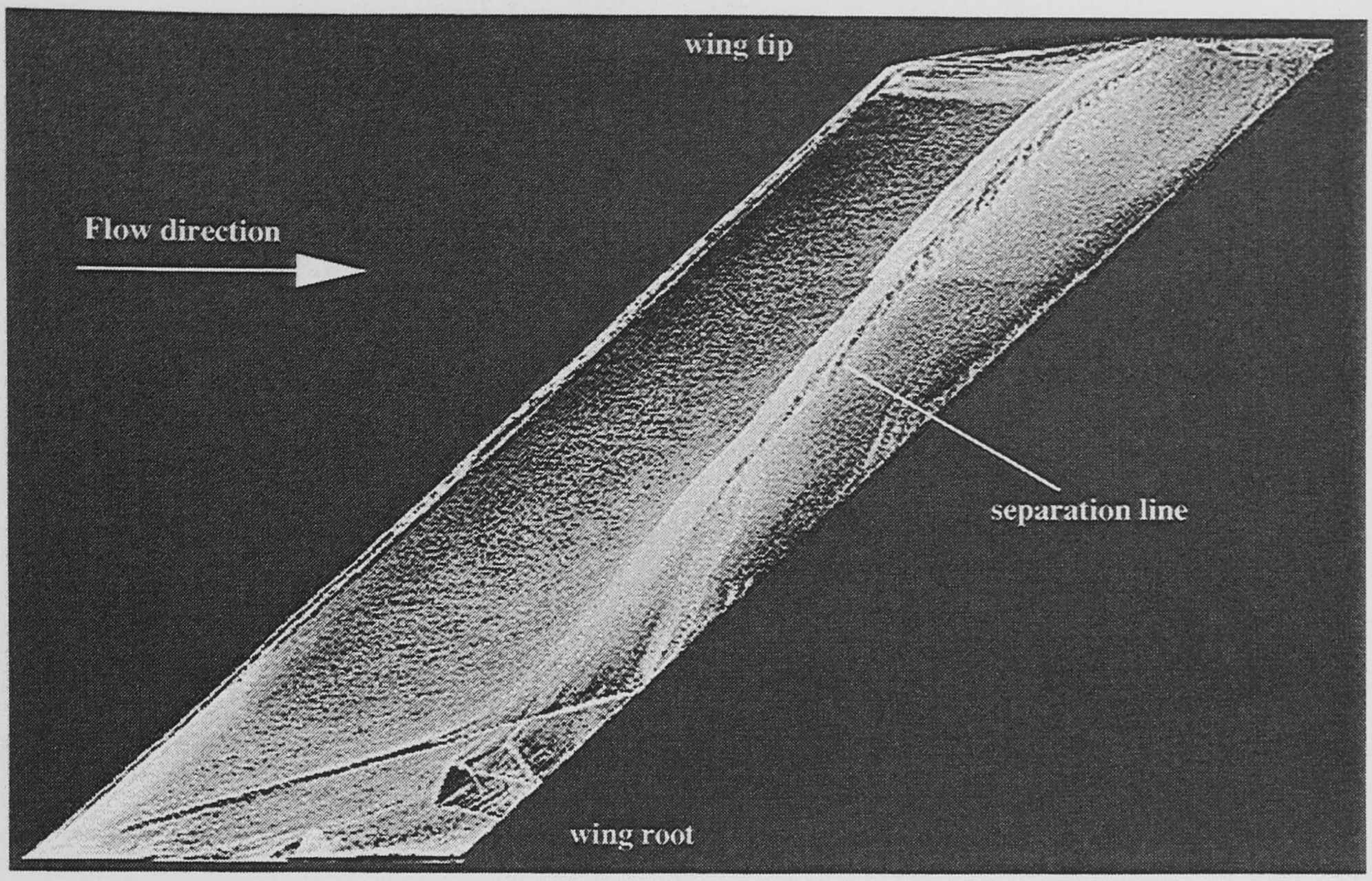

$\alpha = 12^{o}$

Figure 5-3 cont.: Surface oil flow visualisation results for the Cranfield swept wing. $\Lambda = 40°$, $Re_c = 4.3 \times 10^5$.

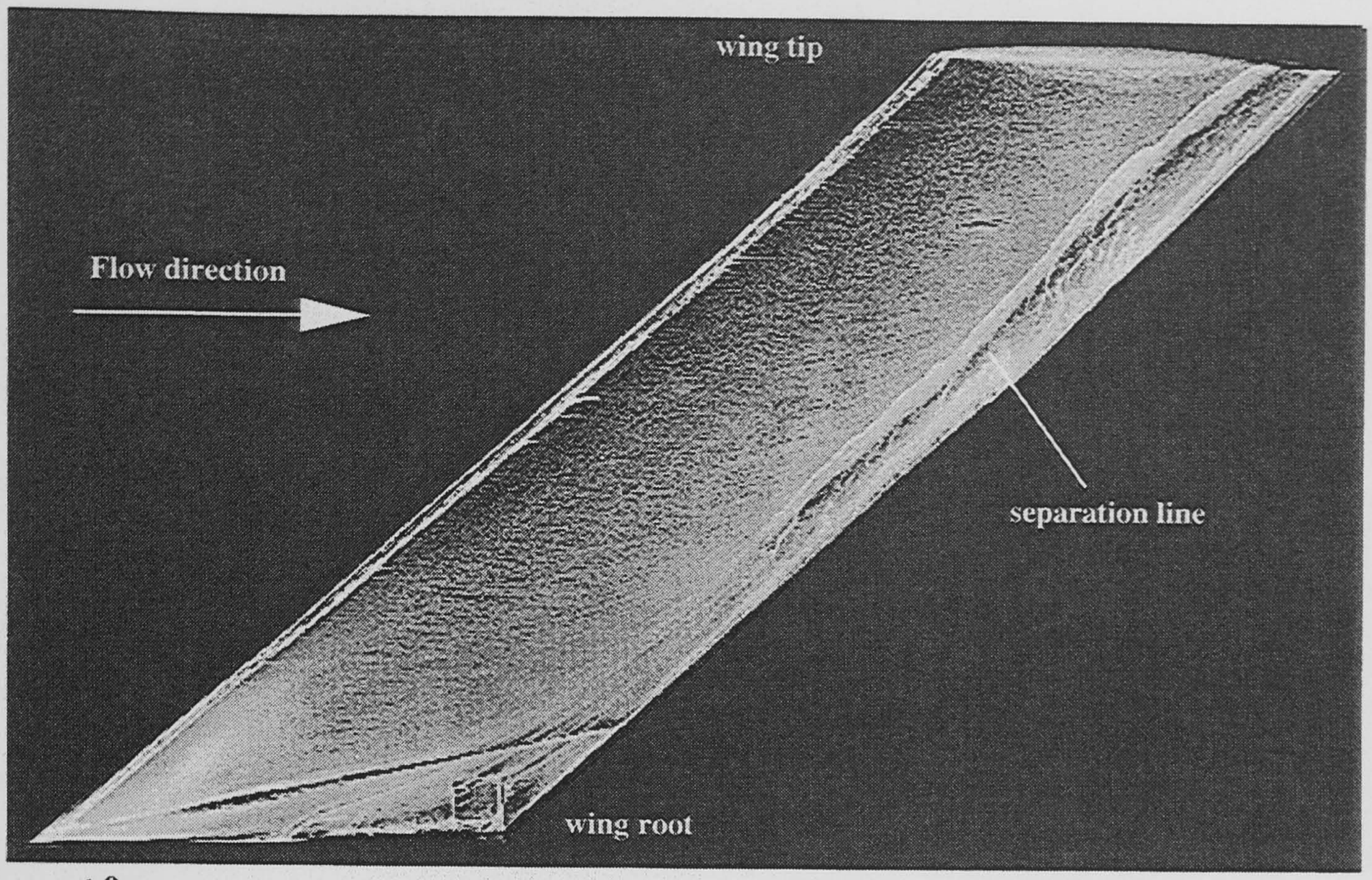

$\alpha = 4^{o}$

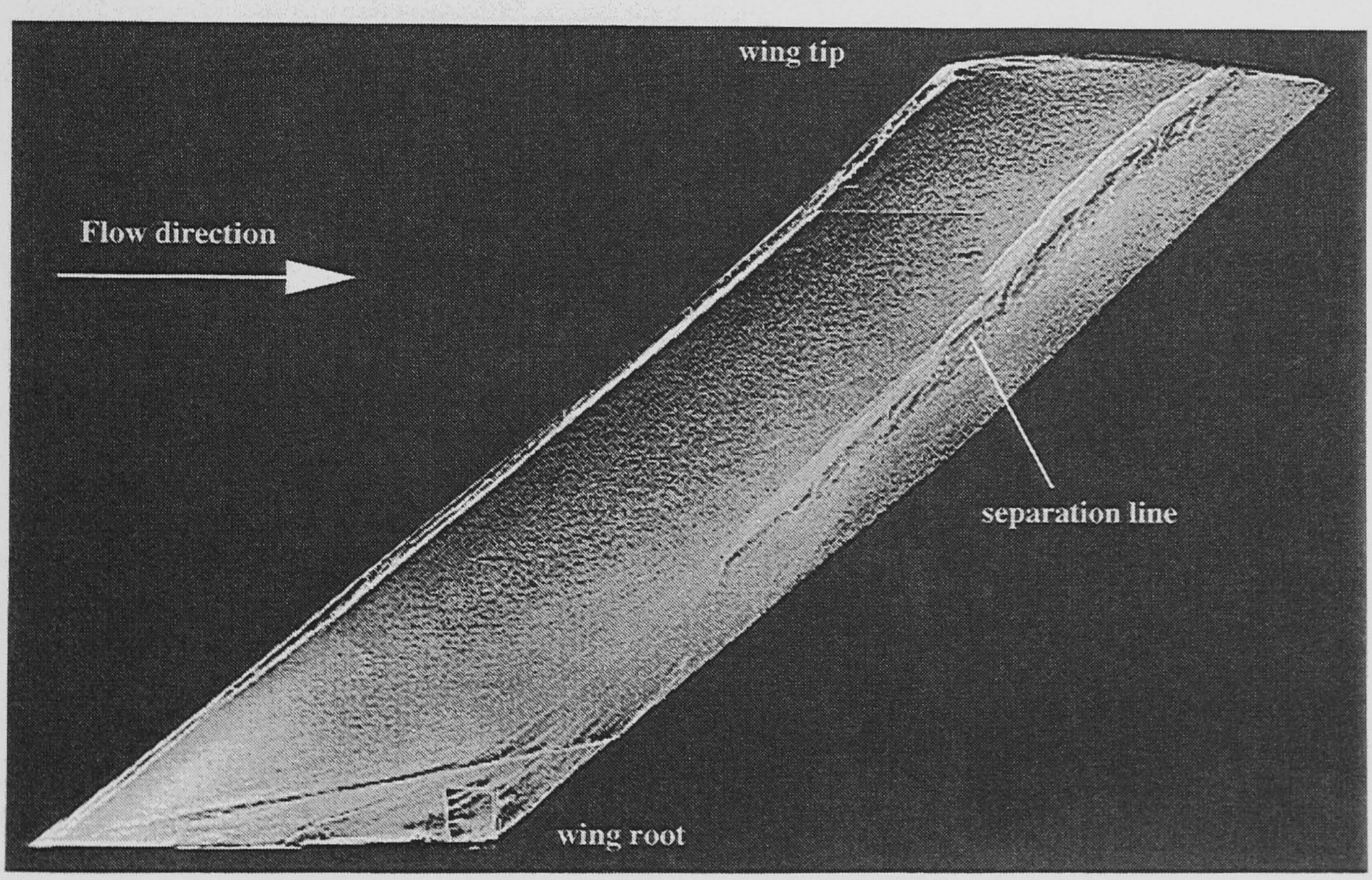

$\alpha = 8^{o}$

Figure 5-4: Surface oil flow visualisation results for the Cranfield swept wing. $\Lambda = 50°$, $Re_c = 5.1 \times 10^5$.

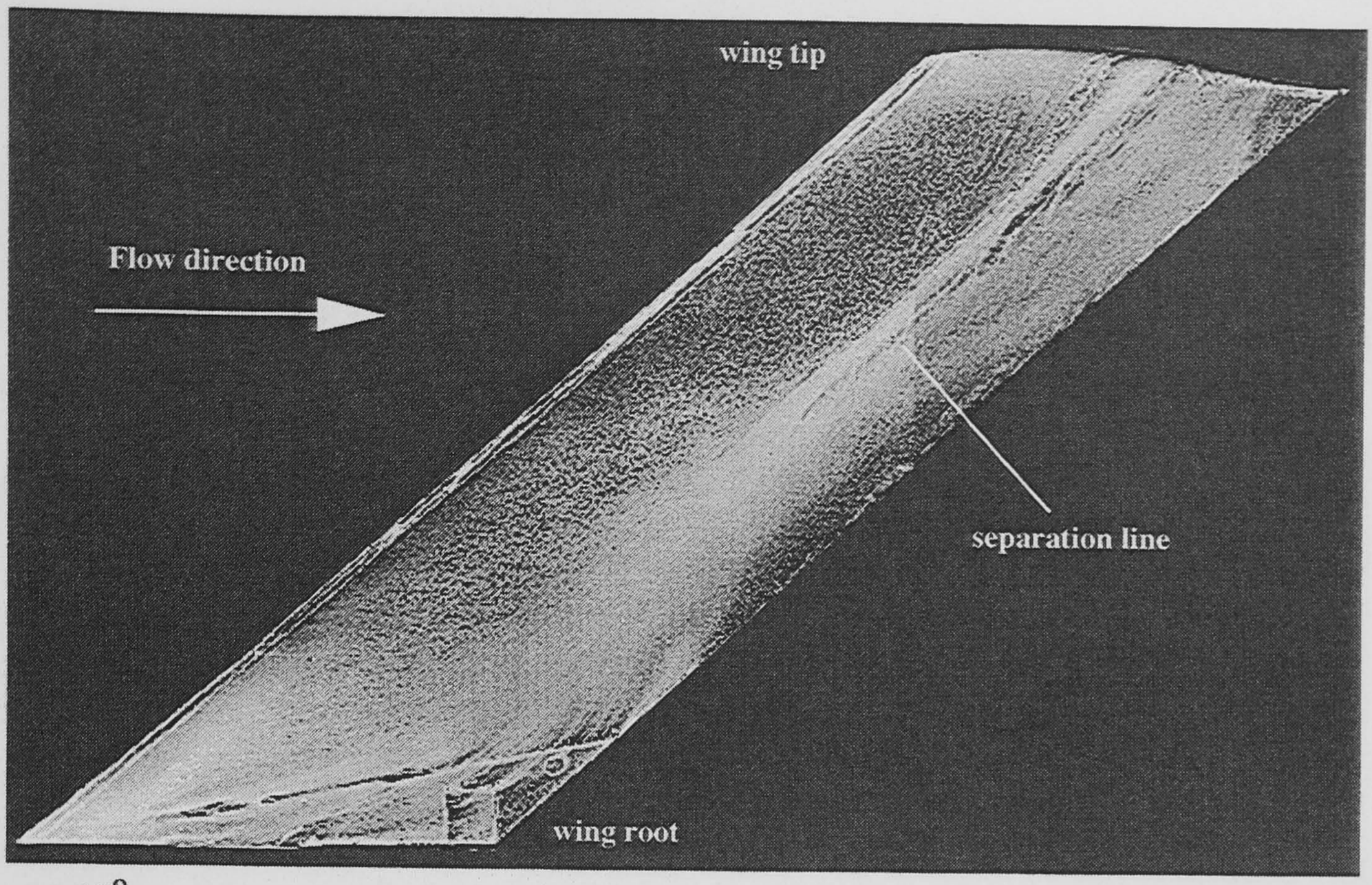

$\alpha = 12^{o}$

Figure 5-4 cont.: Surface oil flow visualisation results for the Cranfield swept wing. $\Lambda = 50°$, $Re_c = 5.1 \times 10^5$.

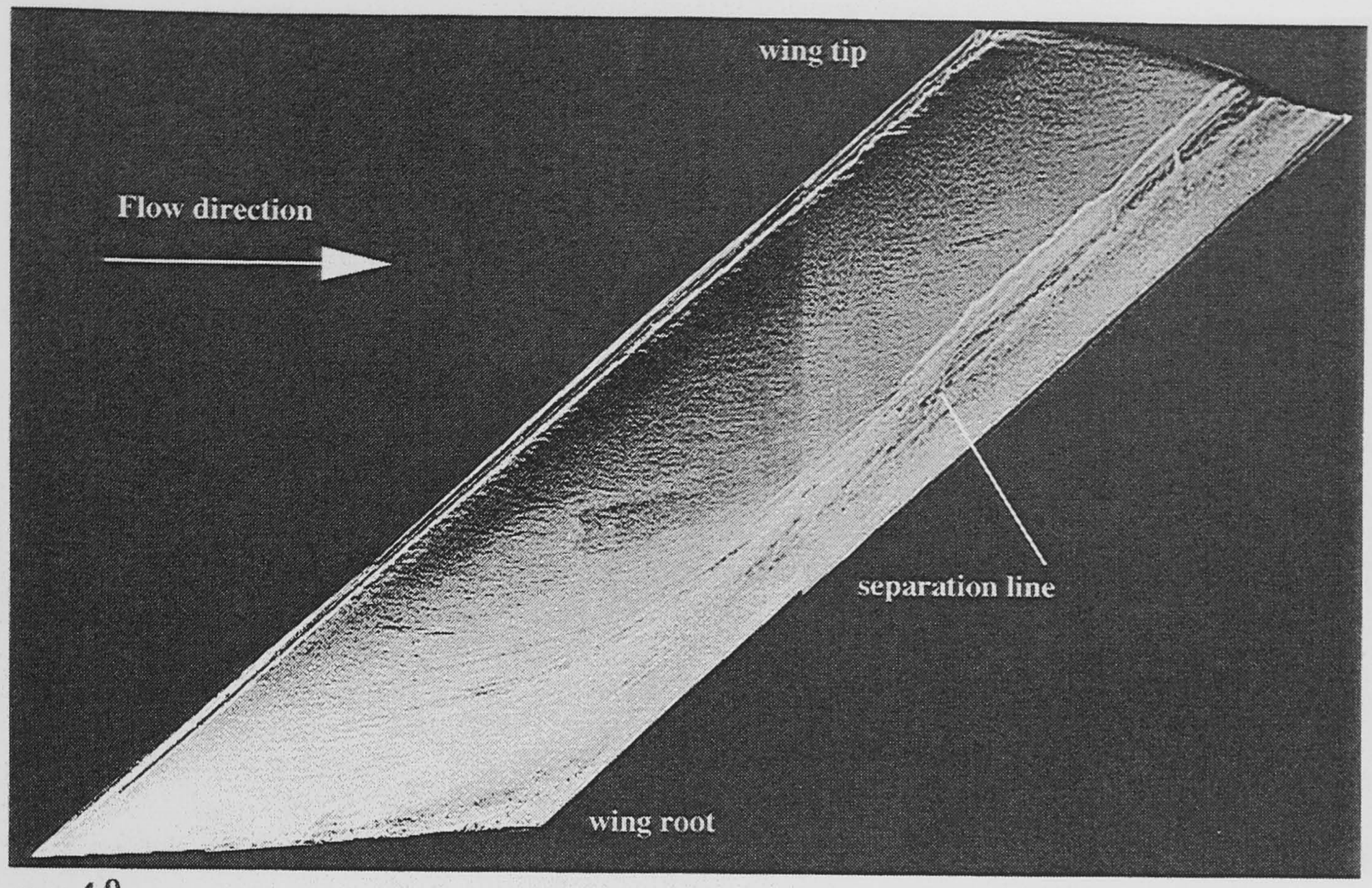

$\alpha = 4^{o}$

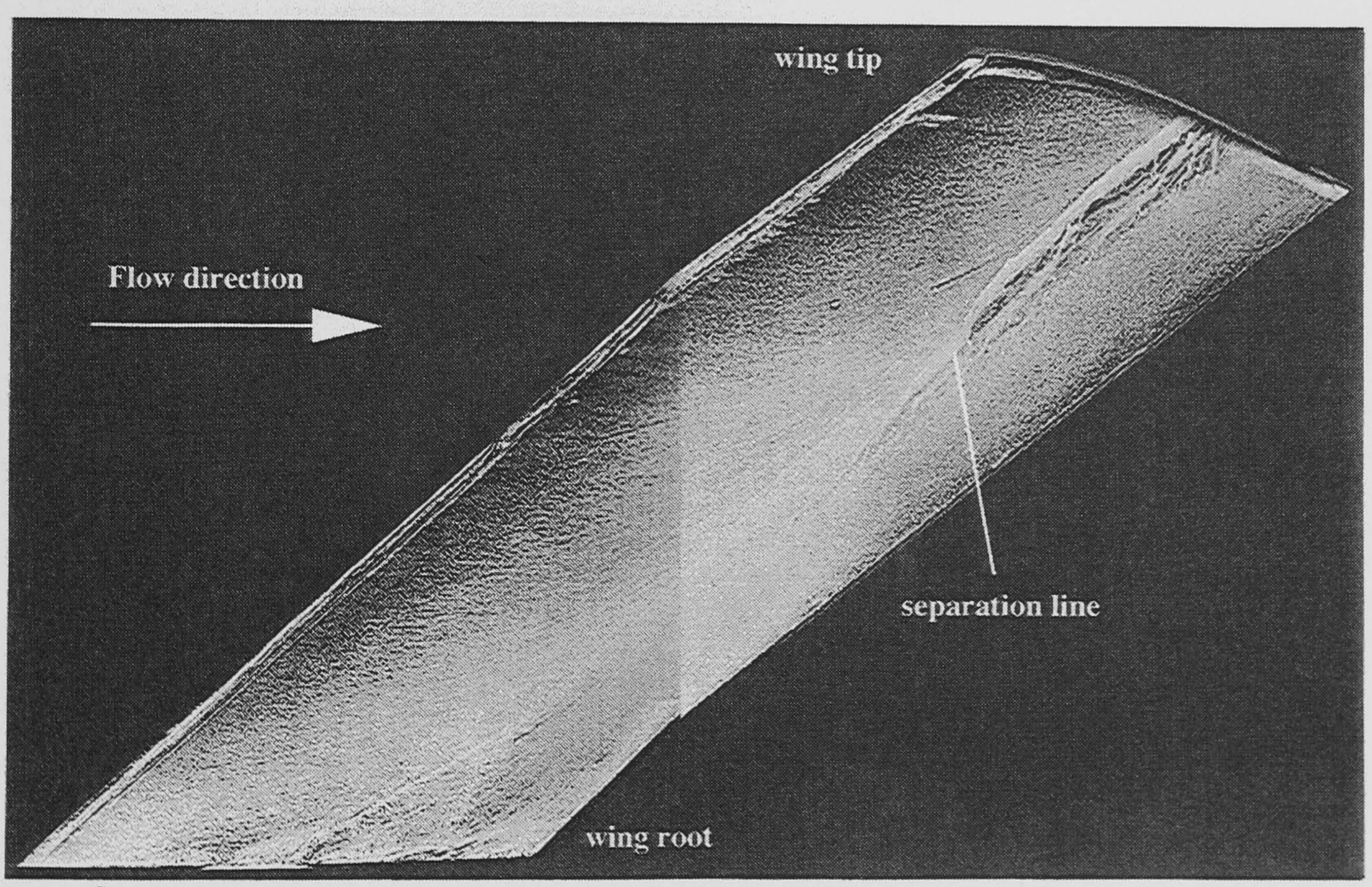

$\alpha = 8^{o}$

Figure 5-5: Surface oil flow visualisation results for the Cranfield swept wing. $\Lambda = 60°$, $Re_c = 6.5 \times 10^5$.

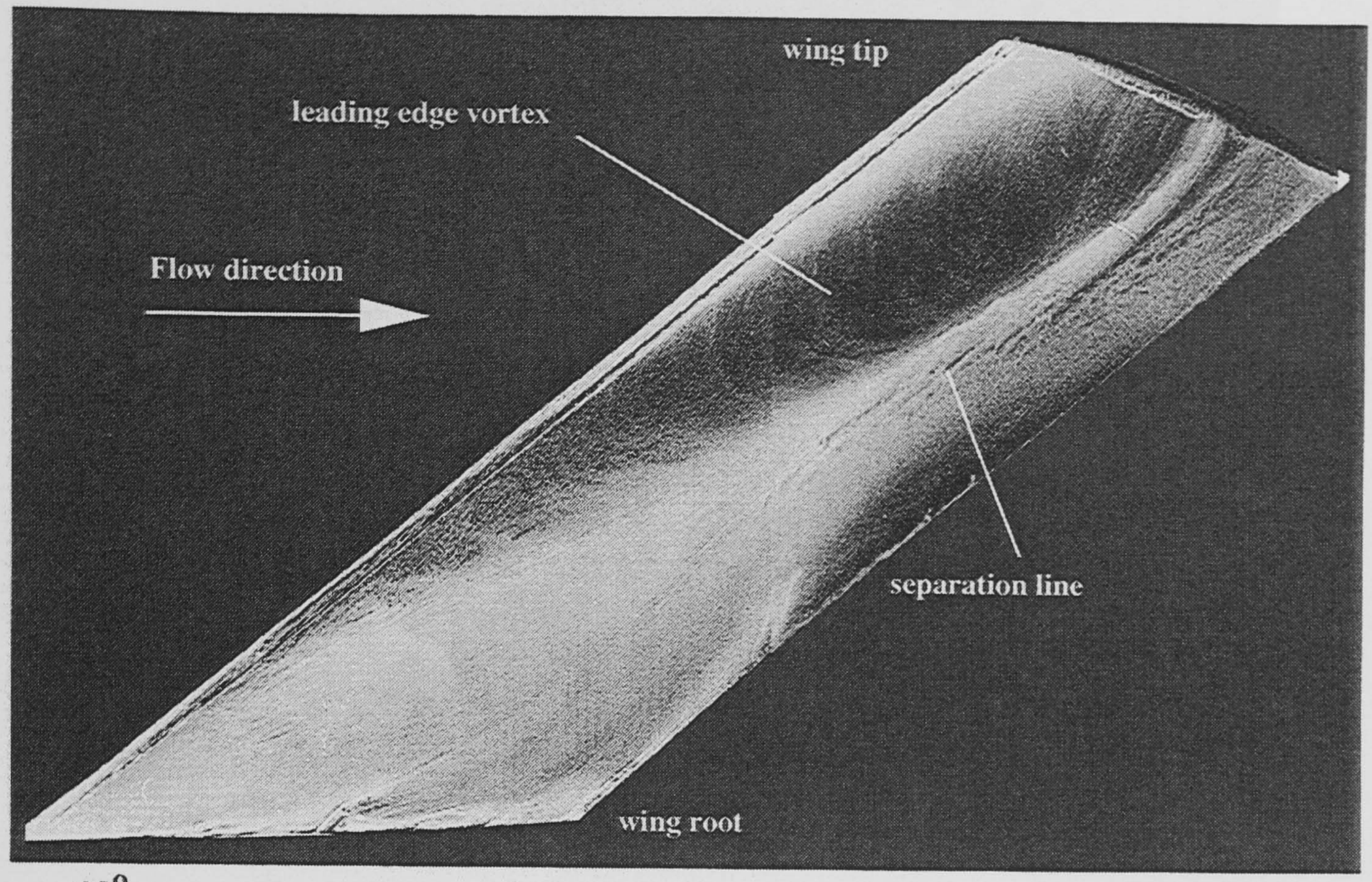

$\alpha = 12^o$

Figure 5-5 cont.: Surface oil flow visualisation results for the Cranfield swept wing. $\Lambda = 60°$, $Re_c = 6.5 \times 10^5$.

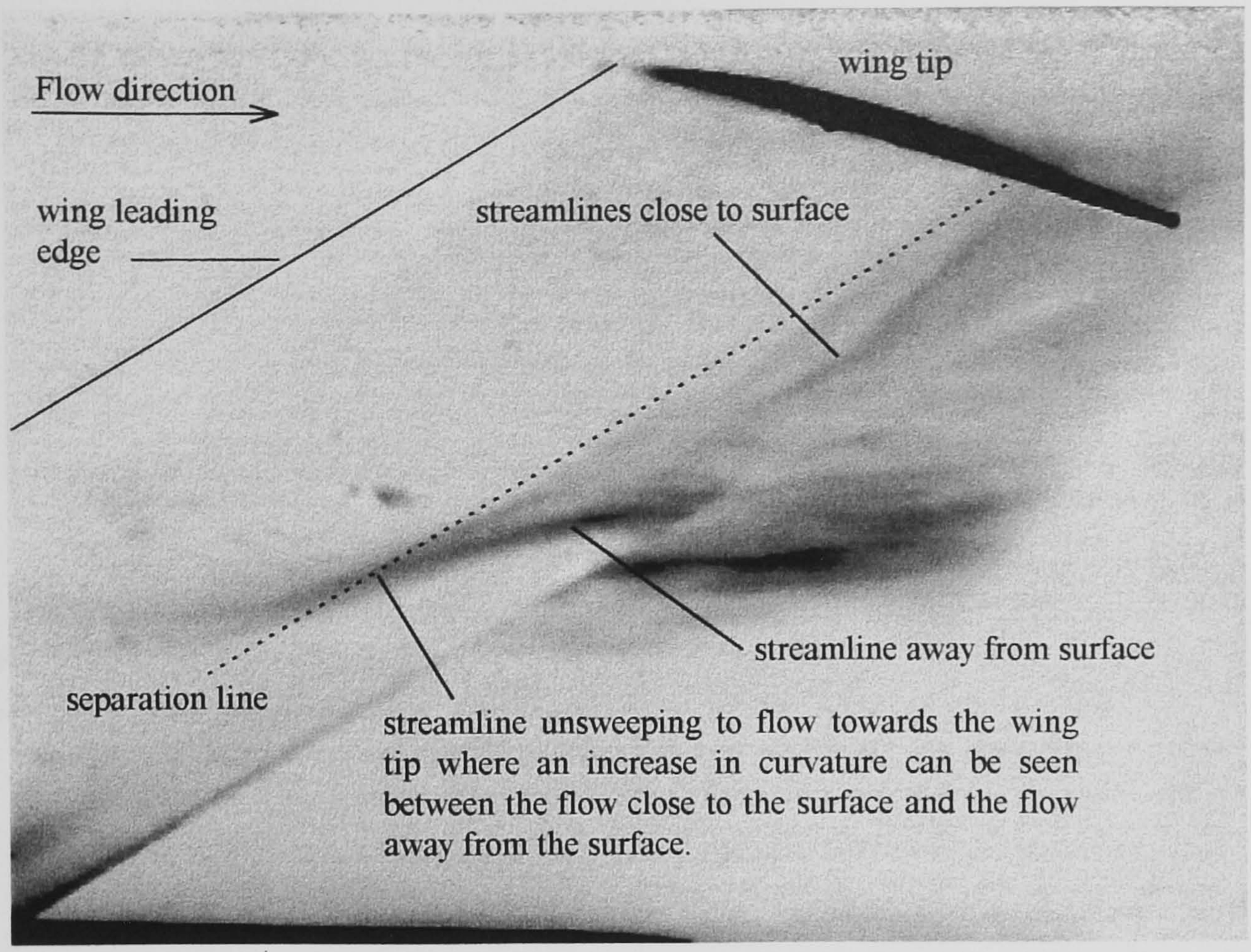

a) $\Lambda = 60°$ showing streamlines through the boundary layer as the surface is approached.

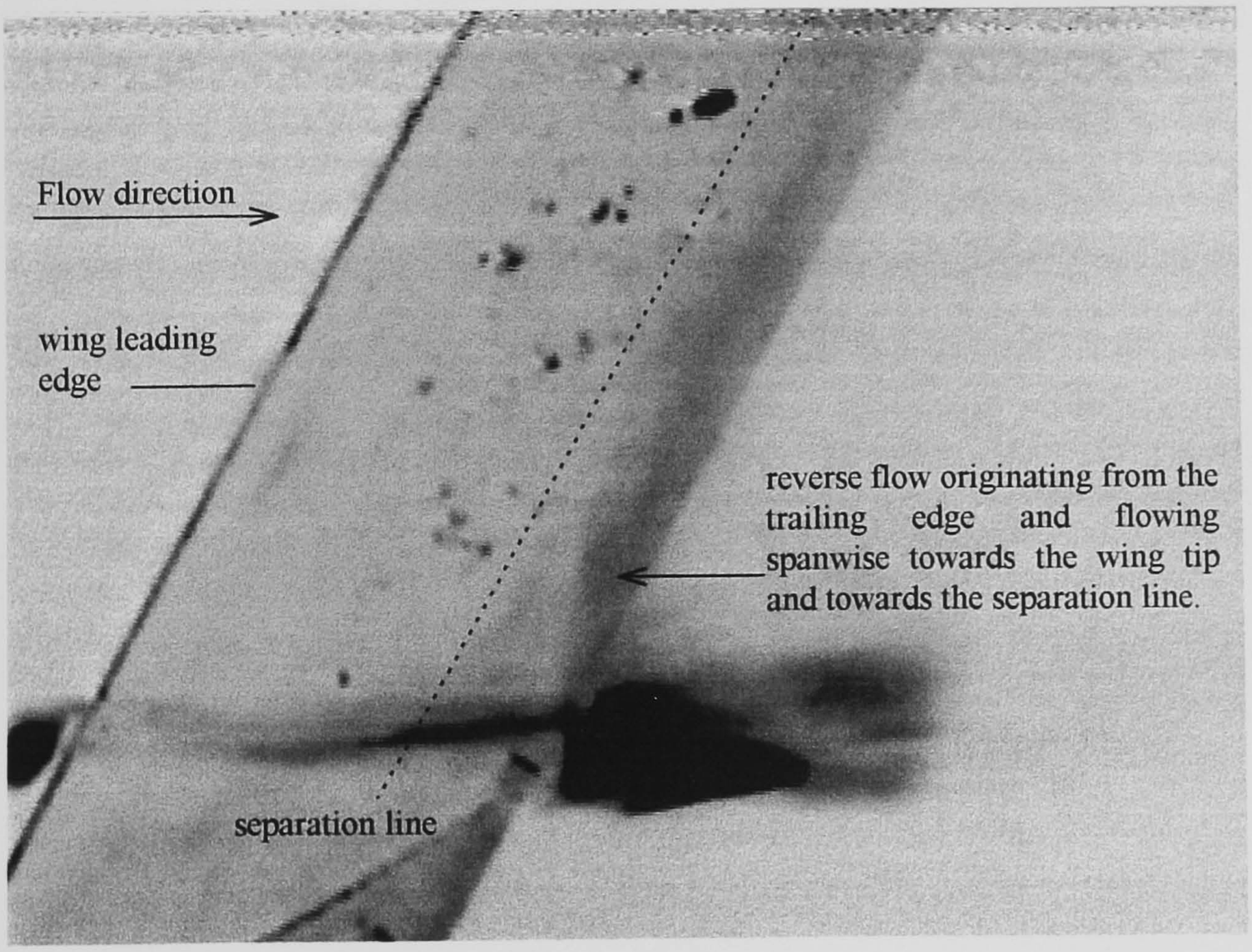

b) $\Lambda = 30°$ showing reverse flow from trailing edge.

Figure 5-6: Smoke visualisation images and a sketched interpretation of the surface flow once separation has occurred.

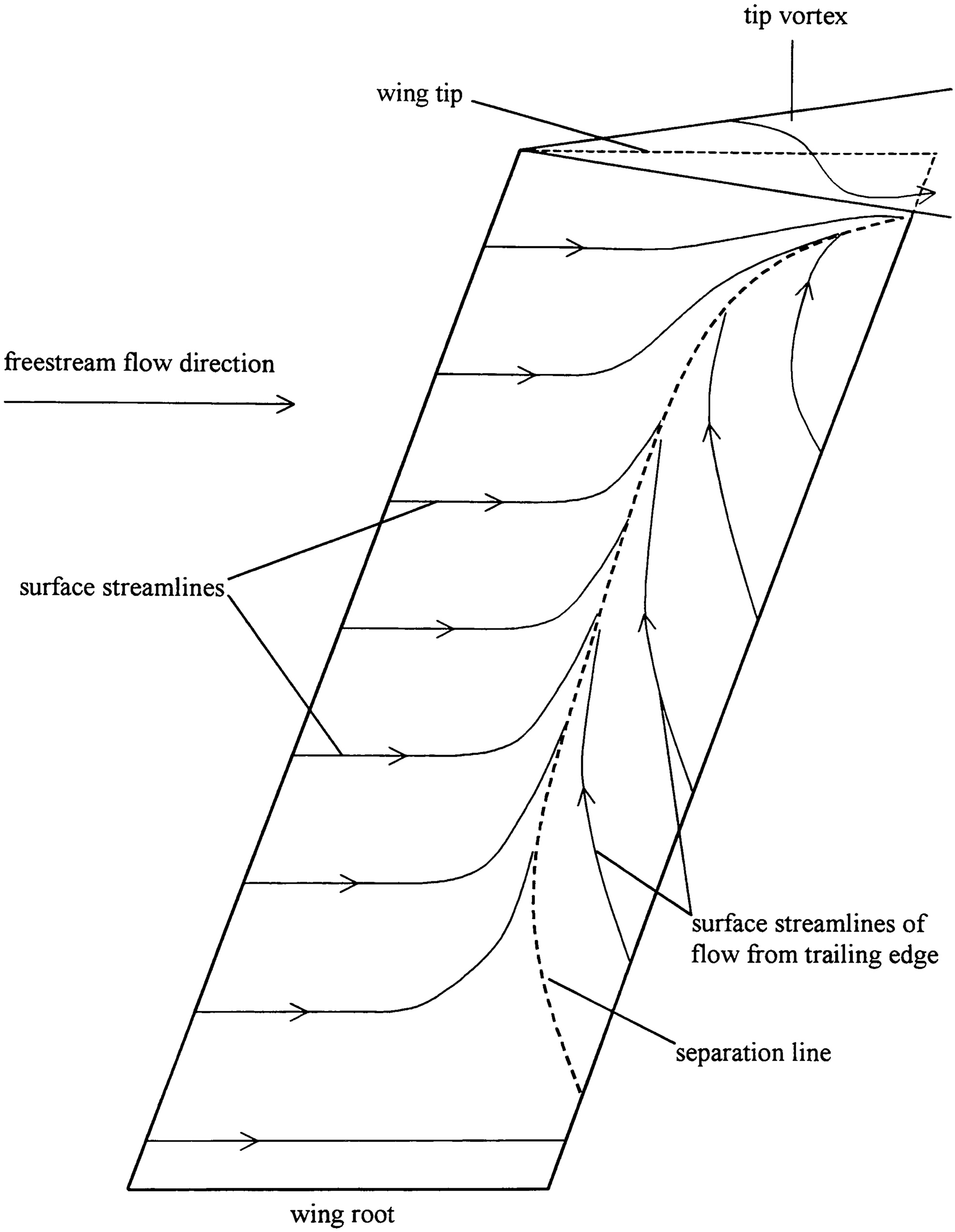

c) Sketched interpretation of the general flowfield

Figure 5-6 cont.: Smoke visualisation images and a sketched interpretation of the surface flow once separation has occurred.

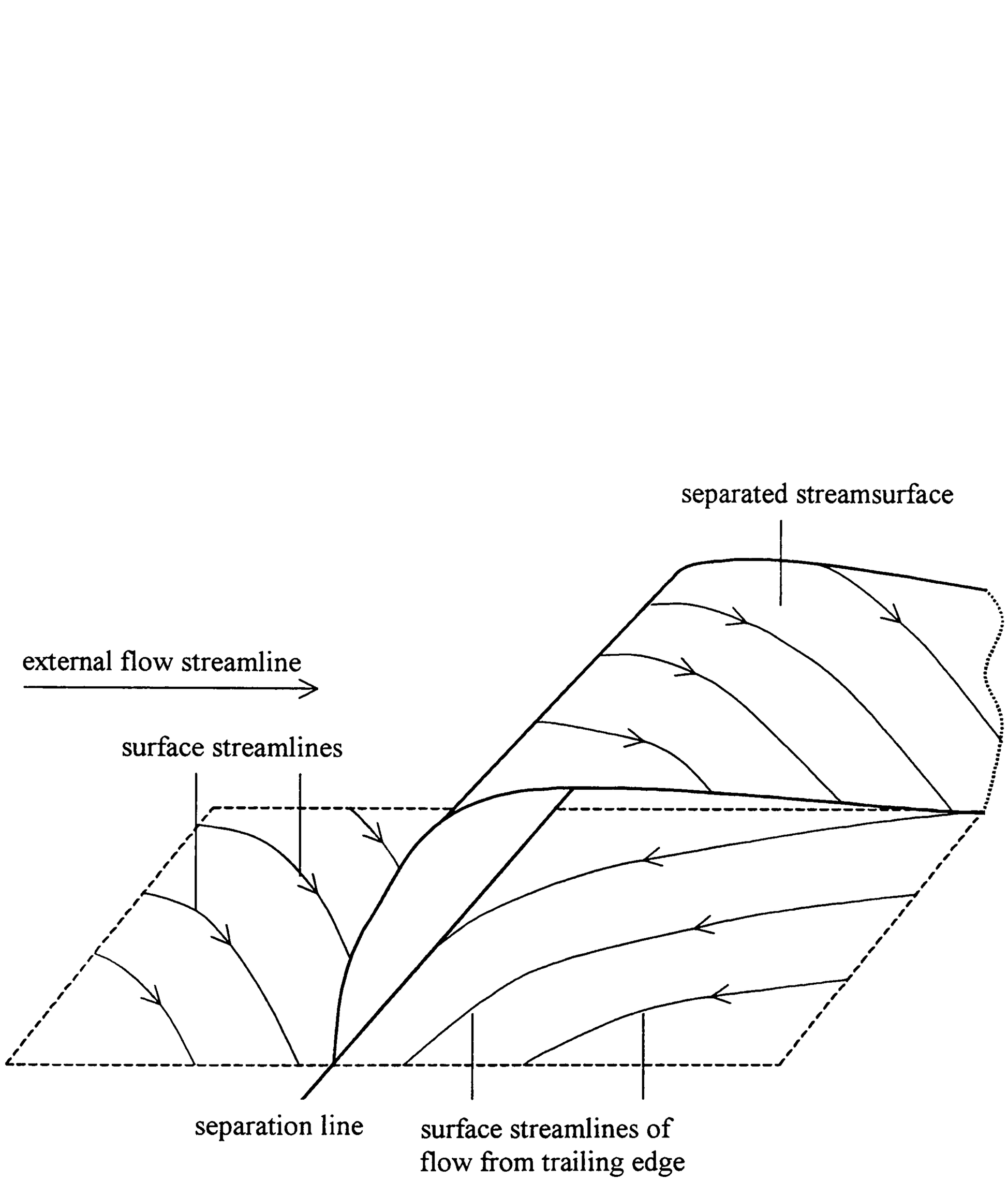

a) Surface flow streamlines in the separation region

Figure 5-7: Surface flow streamlines in the separation region and the external flowfield at incidence.

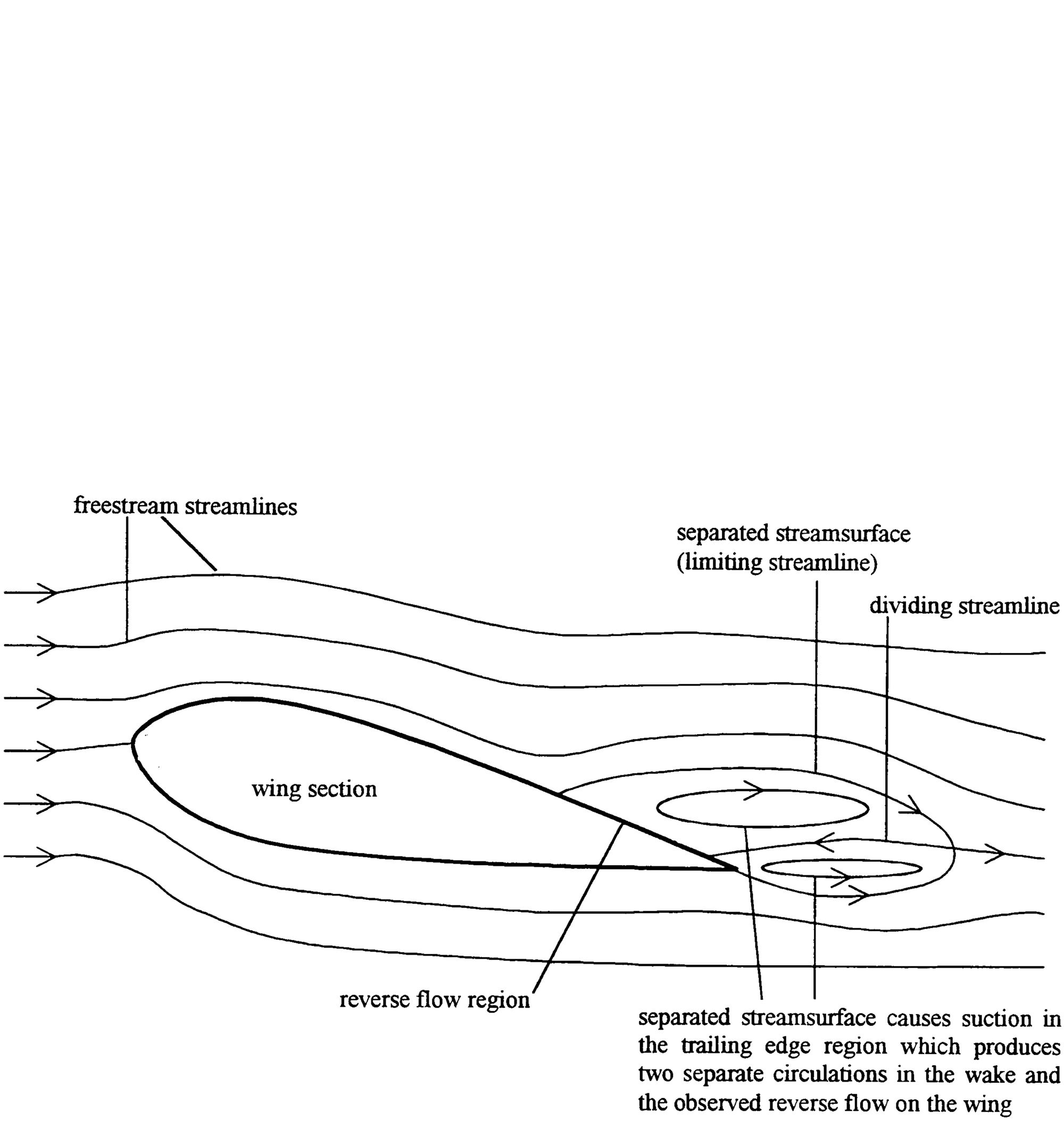

b) External flowfield at incidence.

Figure 5-7 cont.: Surface flow streamlines in the separation region and the external flowfield at incidence.

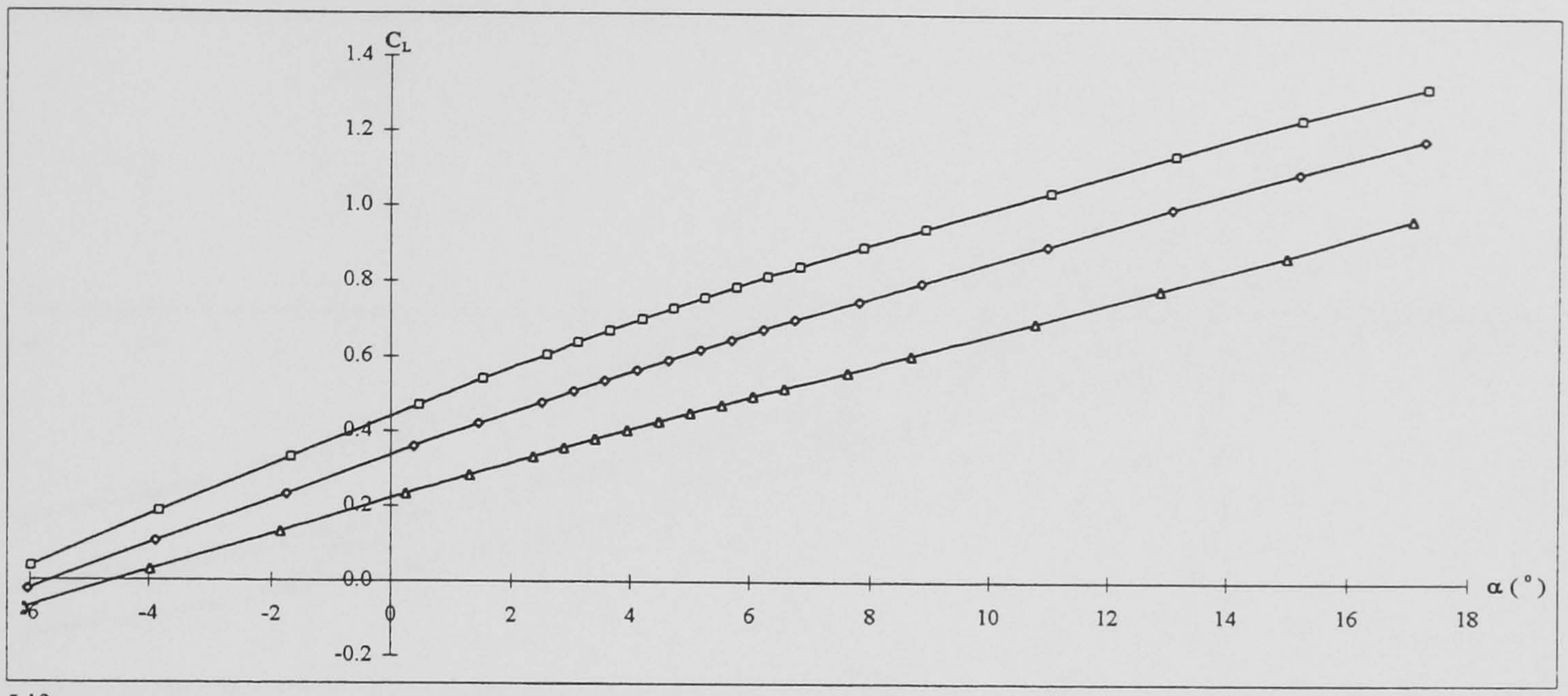

Lift

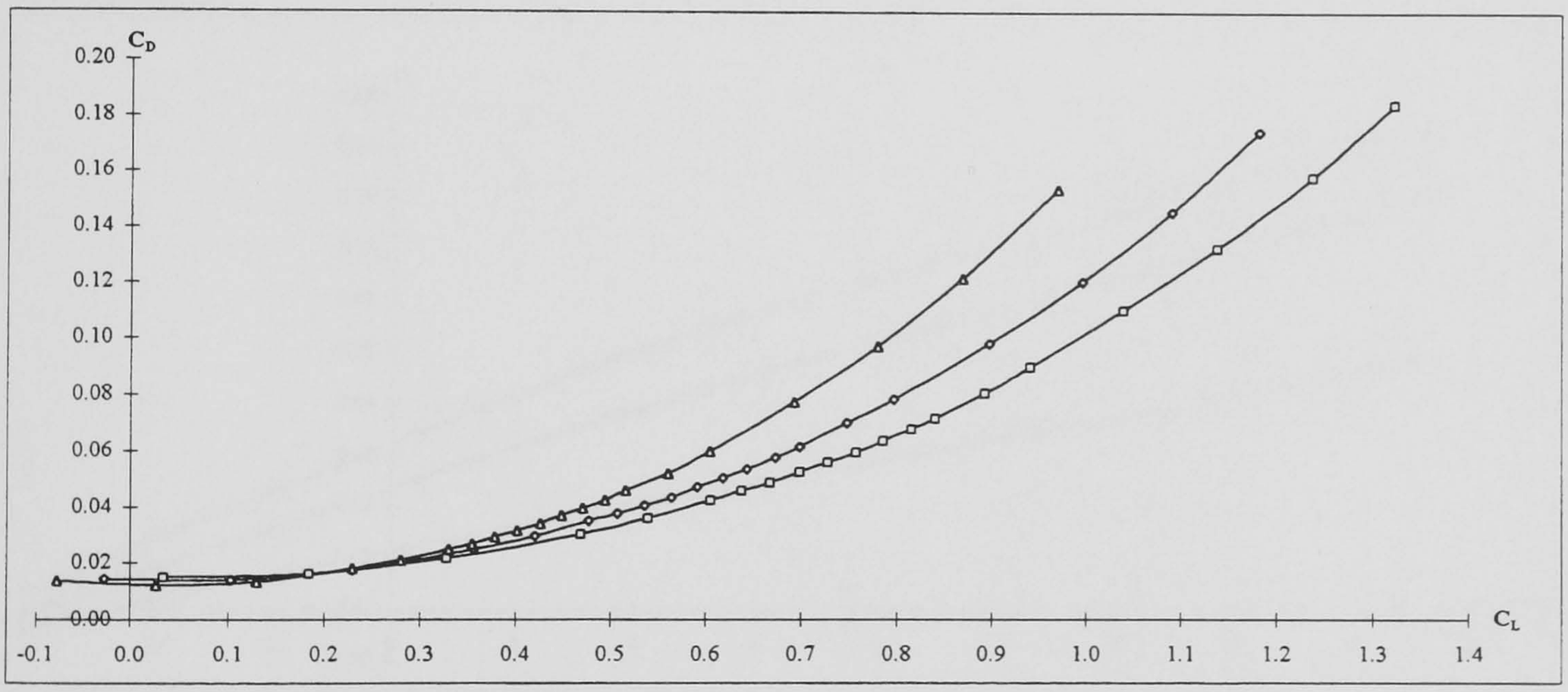

Drag polar

Key	Λ (°)	Re_c
—□—	30	2.9×10^6
—◇—	40	3.3×10^6
—△—	50	3.9×10^6

Figure 5-8: DERA swept wing aerodynamic forces and moments results.

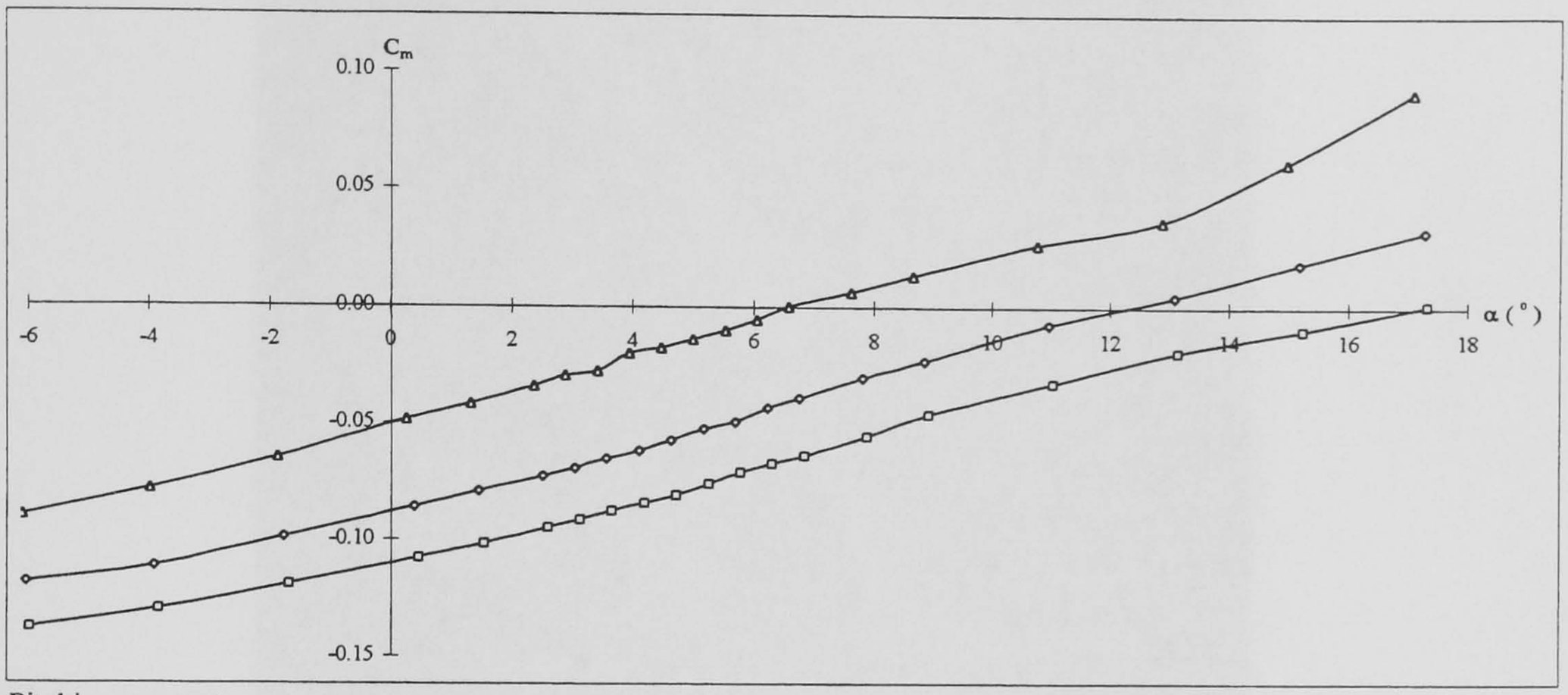

Pitching moment

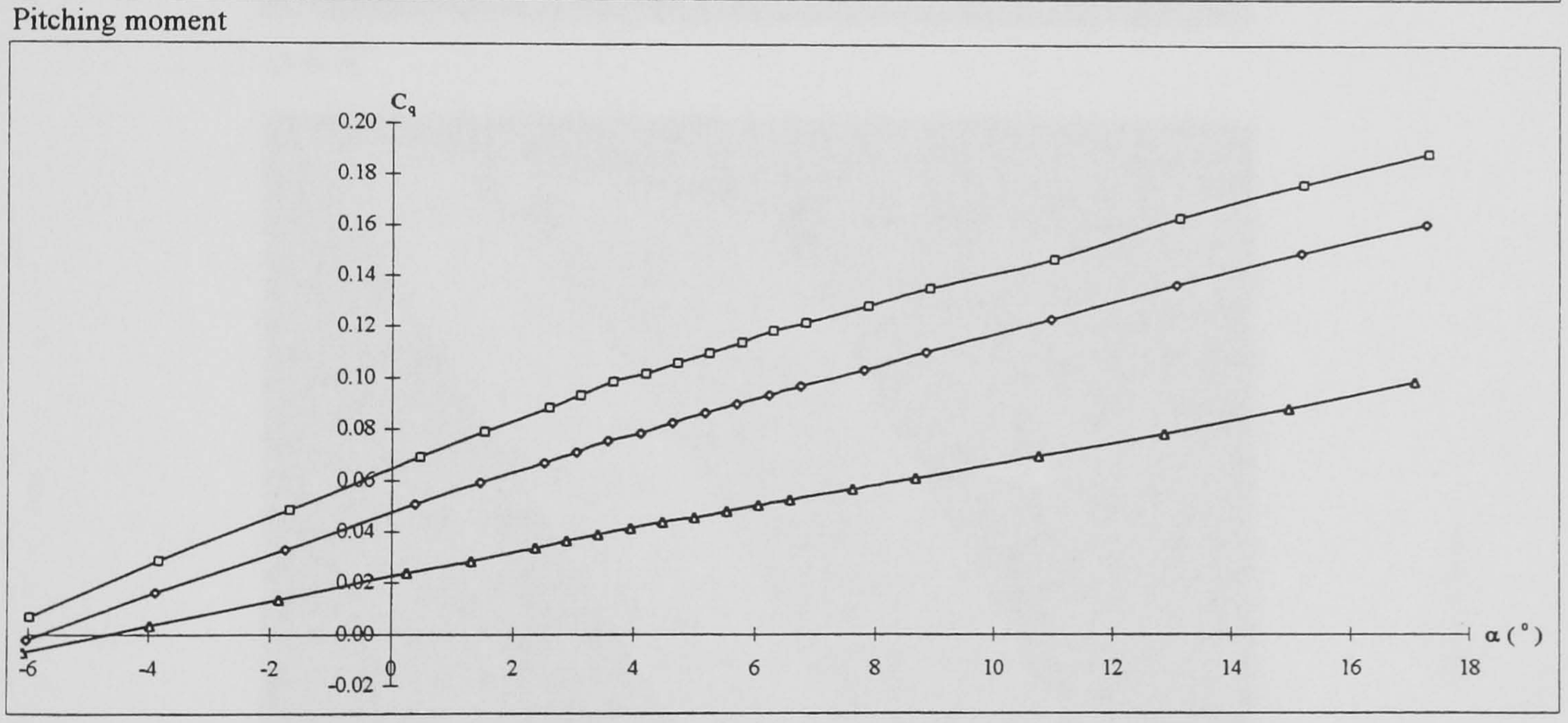

Rolling moment

Key	Λ (°)	Re_c
—□—	30	2.9×10^6
—◇—	40	3.3×10^6
—△—	50	3.9×10^6

Figure 5-8 cont.: DERA swept wing aerodynamic forces and moments results.

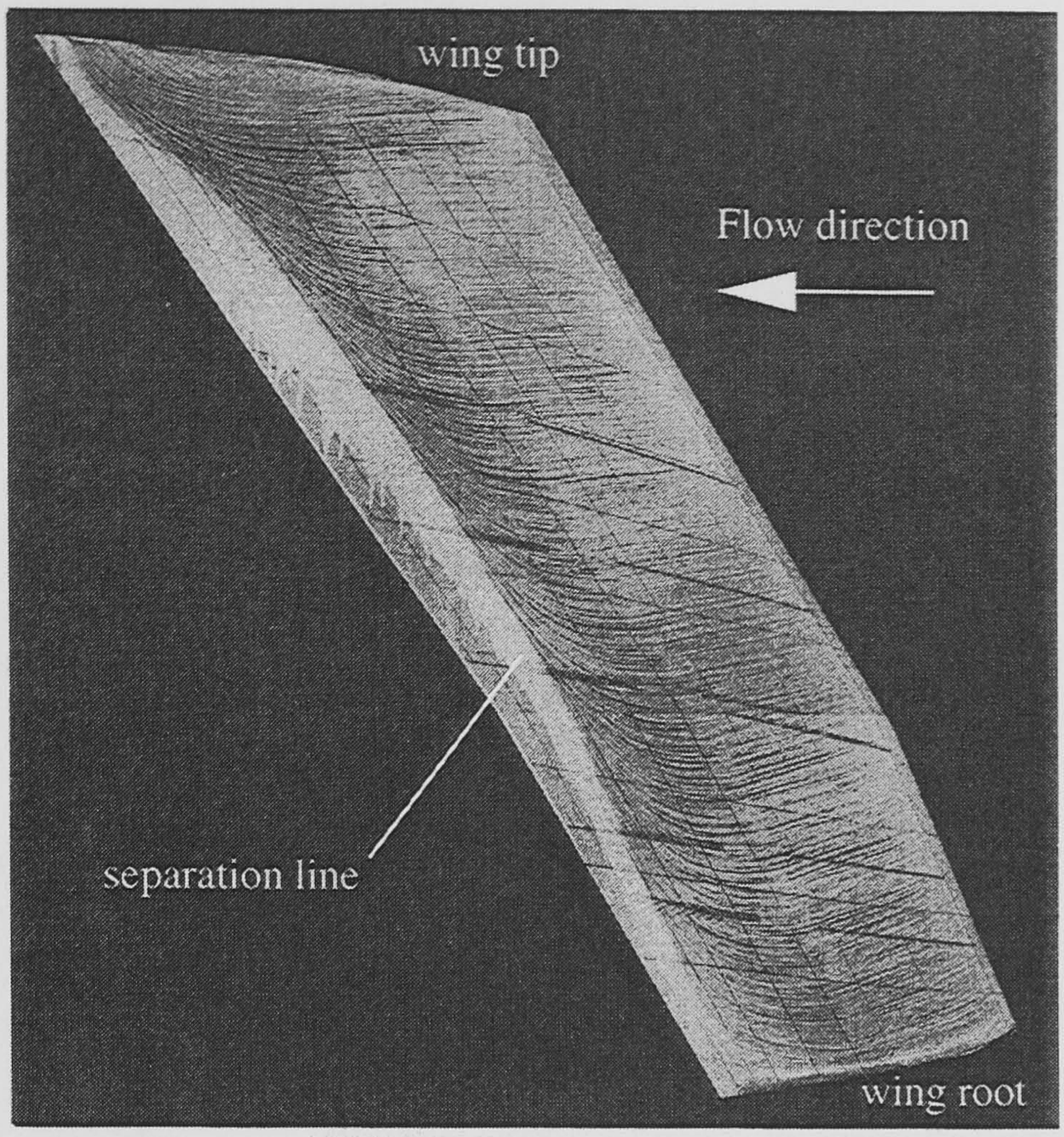

$\alpha = 4^{o}$

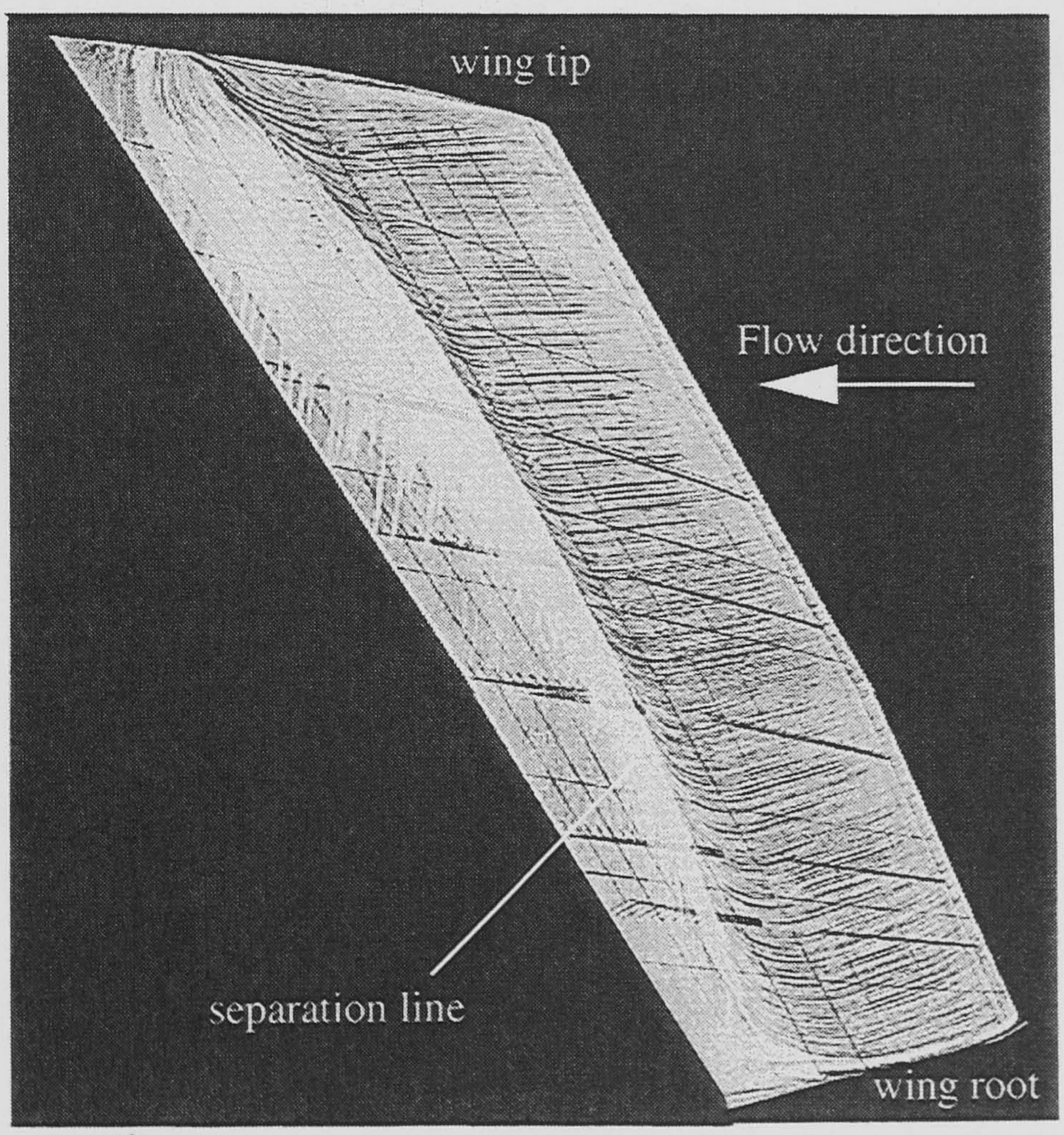

$\alpha = 8^{o}$

Figure 5-9: Surface oil flow visualisation results for the DERA swept wing. $\Lambda = 30°$, $Re_c = 2.9 \times 10^6$.

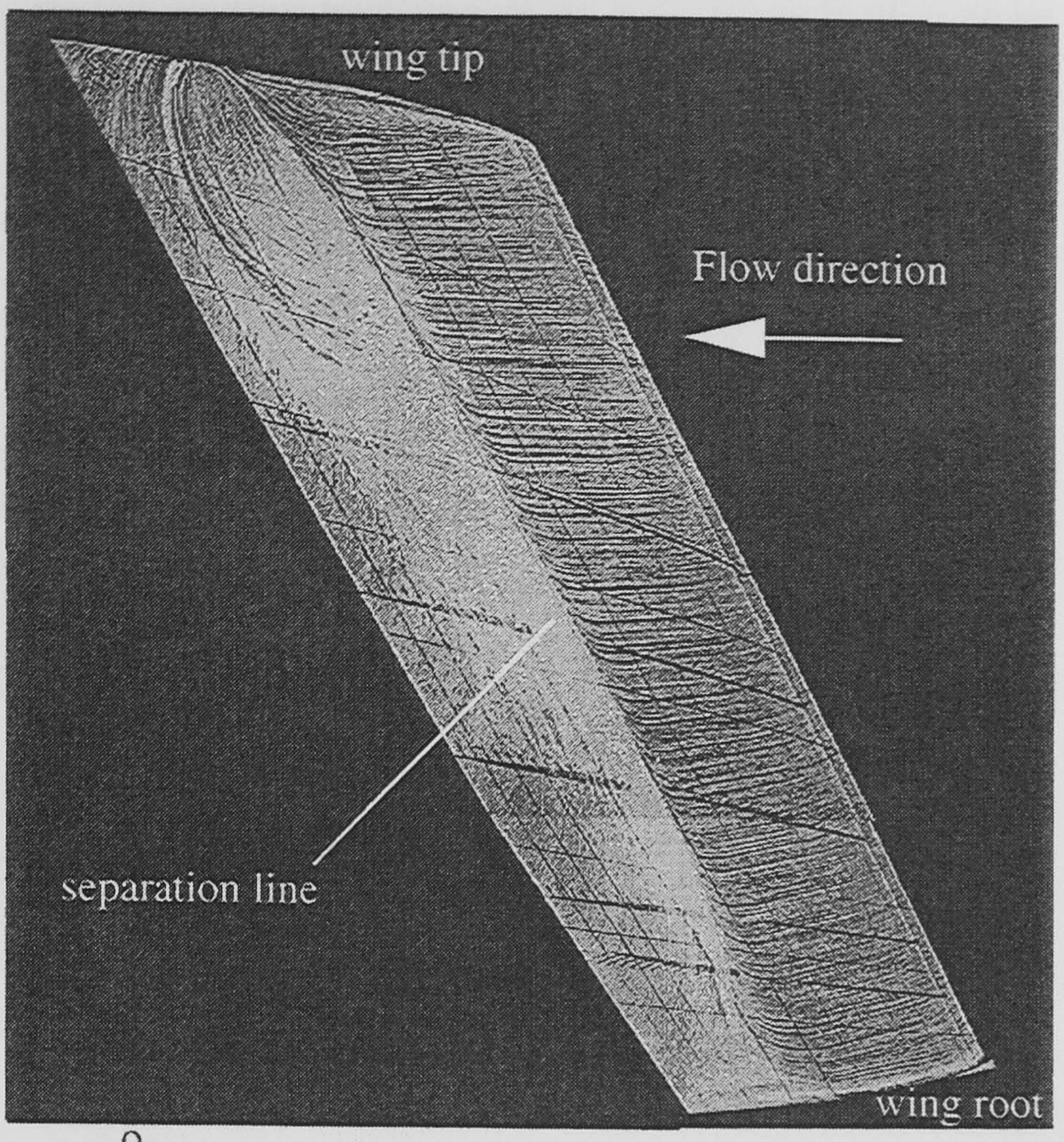

$\alpha = 12^{O}$

Figure 5-9 cont.: Surface oil flow visualisation results for the DERA swept wing. $\Lambda = 30°$, $Re_c = 2.9 \times 10^6$.

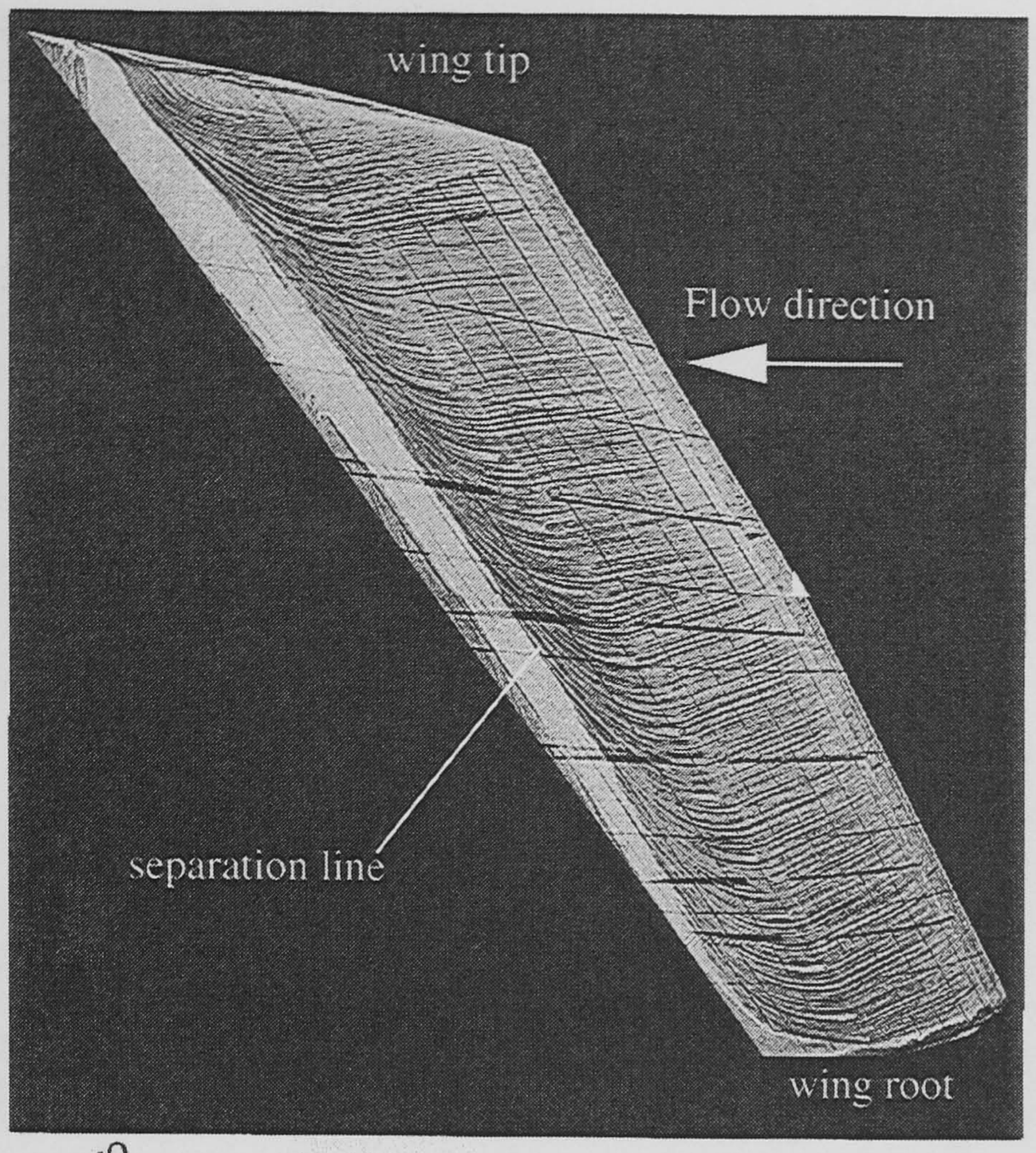

$\alpha = 4^{o}$

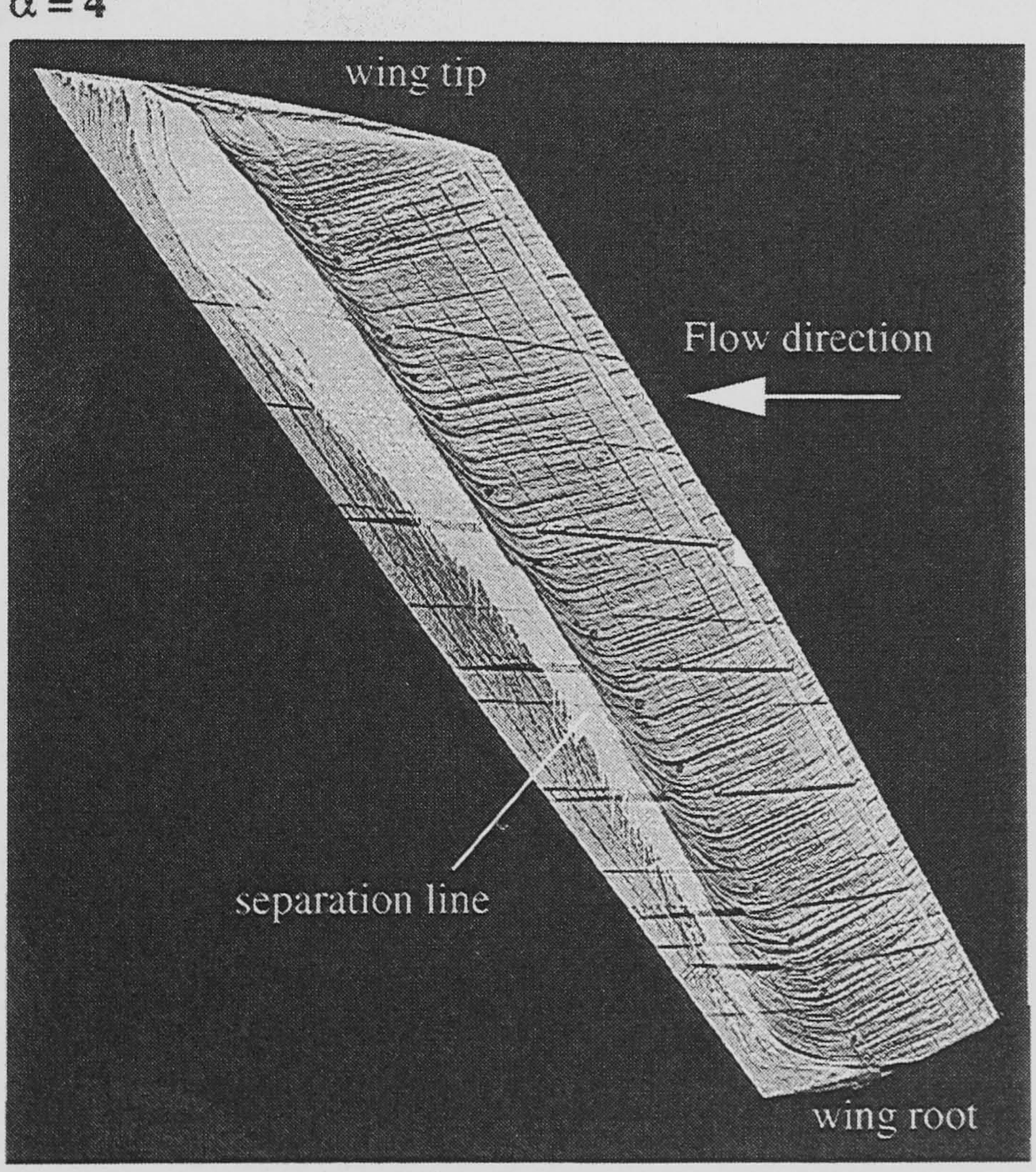

$\alpha = 8^{o}$

Figure 5-10: Surface oil flow visualisation results for the DERA swept wing. $\Lambda = 40°$, $Re_c = 3.3 \times 10^6$.

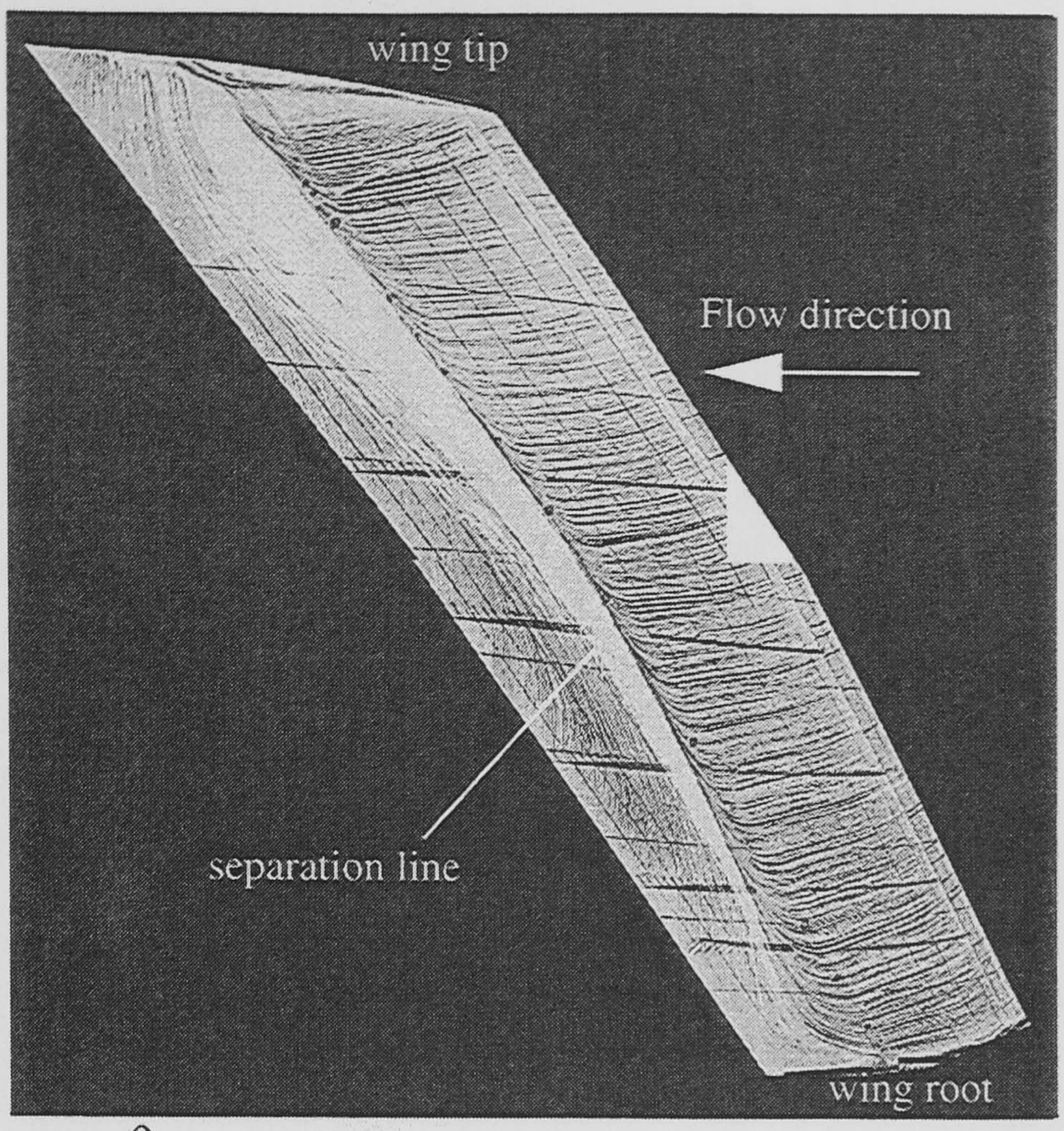

$\alpha = 12^{o}$

Figure 5-10 cont.: Surface oil flow visualisation results for the DERA swept wing. $\Lambda = 40°$, $Re_c = 3.3 \times 10^6$.

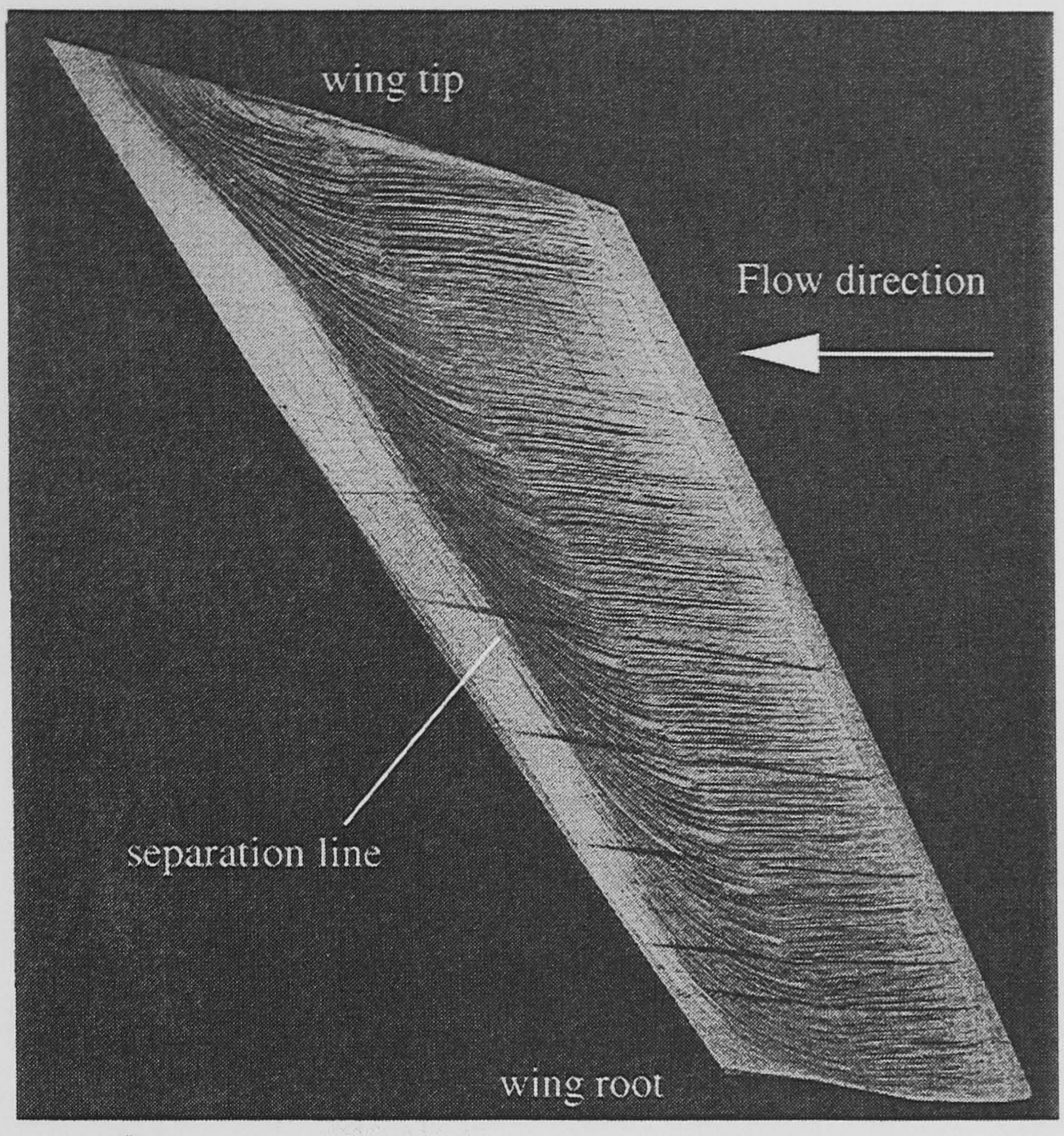

$\alpha = 4^{O}$

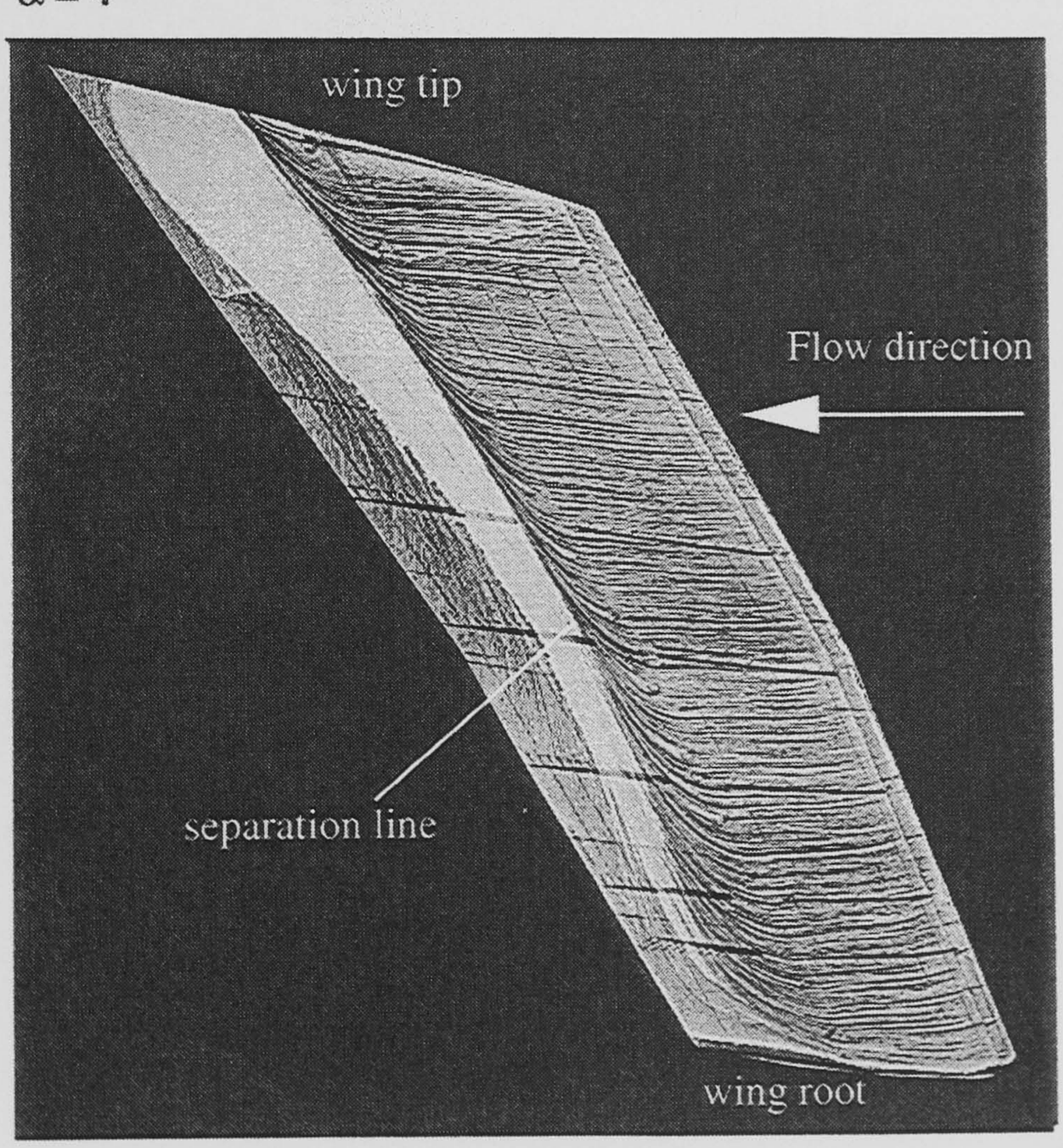

$\alpha = 8^{O}$

Figure 5-11: Surface oil flow visualisation results for the DERA swept wing. $\Lambda = 50°$, $Re_c = 3.9 \times 10^6$.

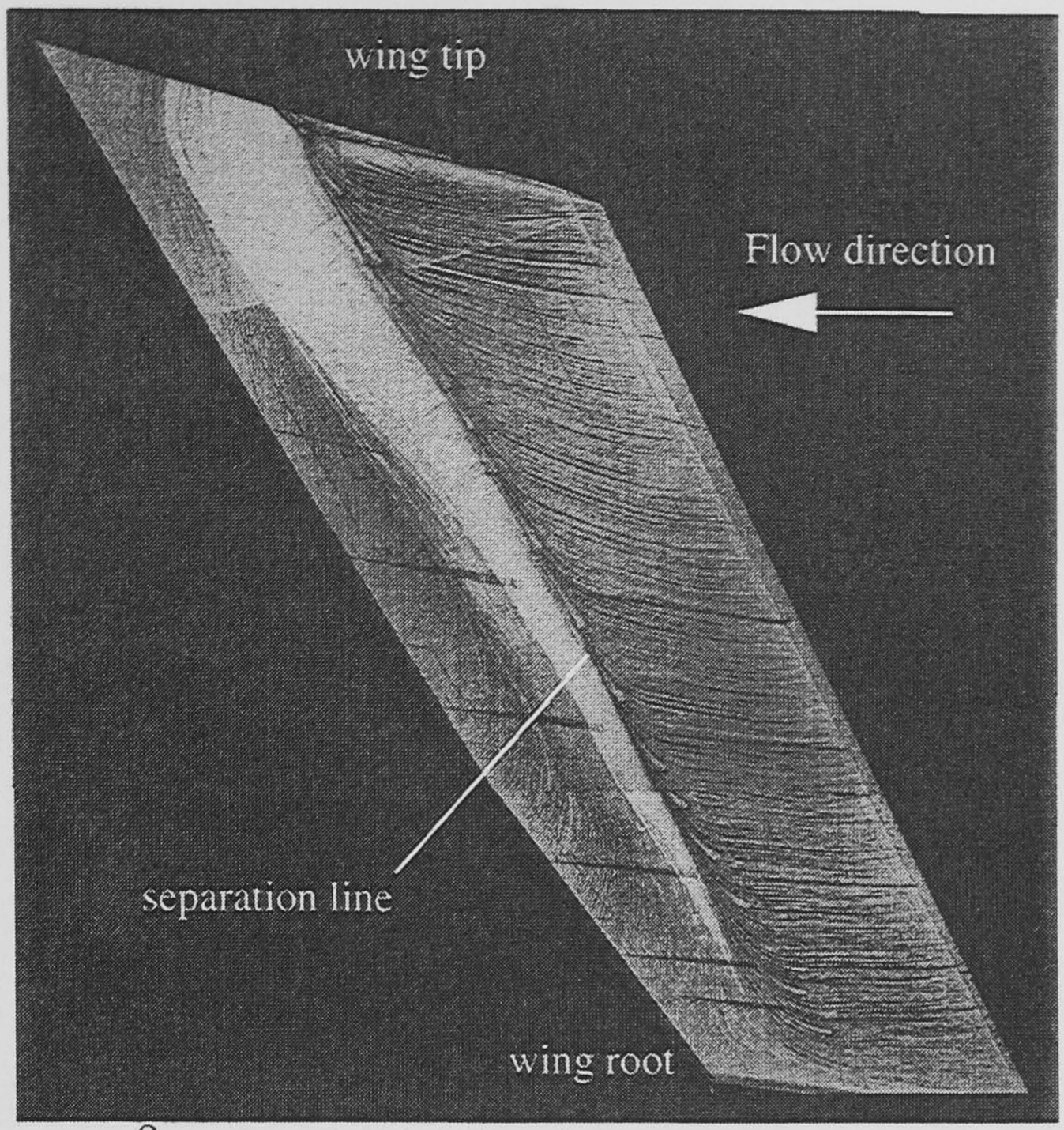

$\alpha = 12^{o}$

Figure 5-11 cont.: Surface oil flow visualisation results for the DERA swept wing. $\Lambda = 50°$, $Re_c = 3.9 \times 10^6$.

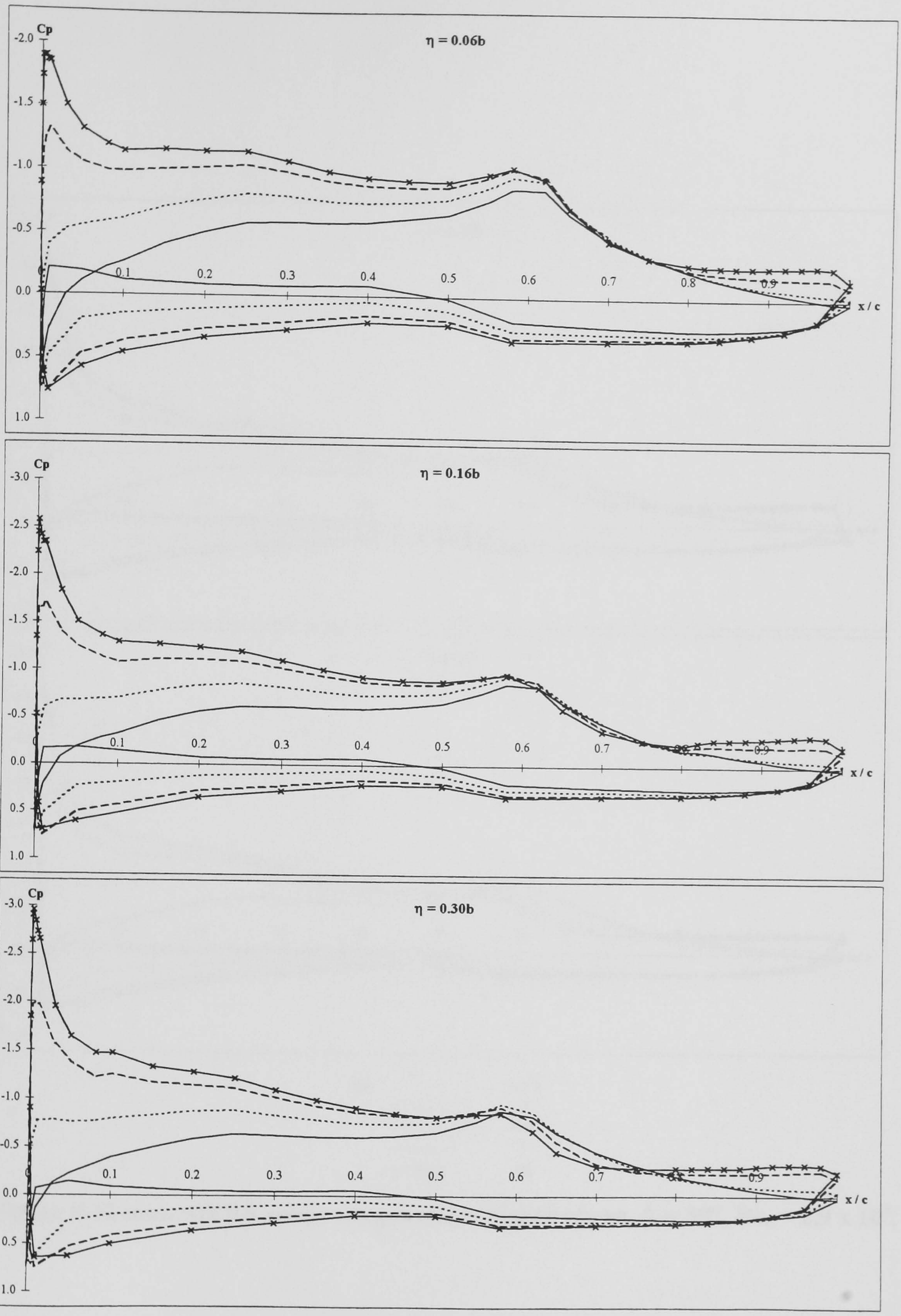

Figure 5-12: DERA swept wing pressure distributions. $\Lambda = 30°$, $Re_c = 2.9 \times 10^6$.

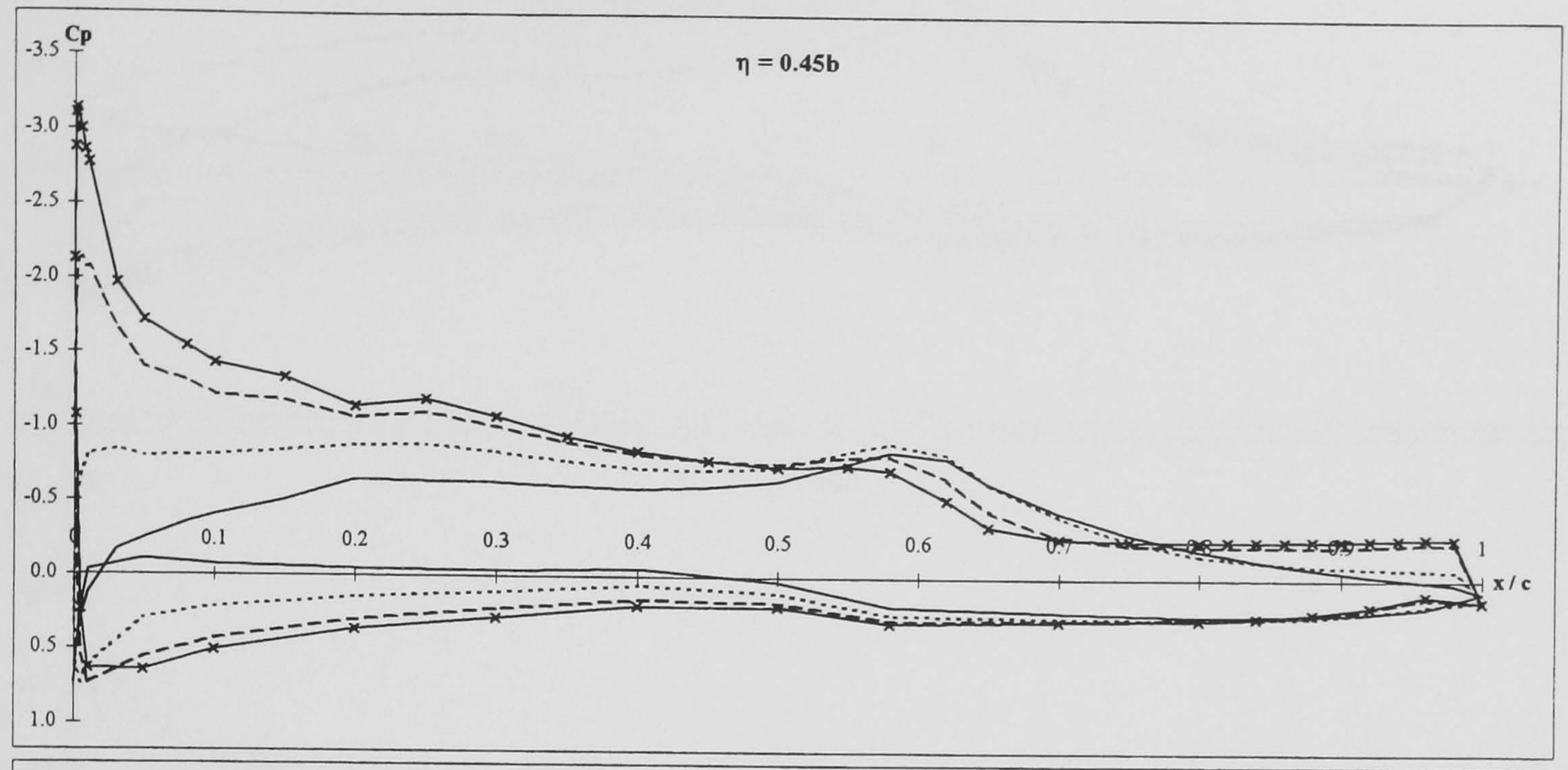

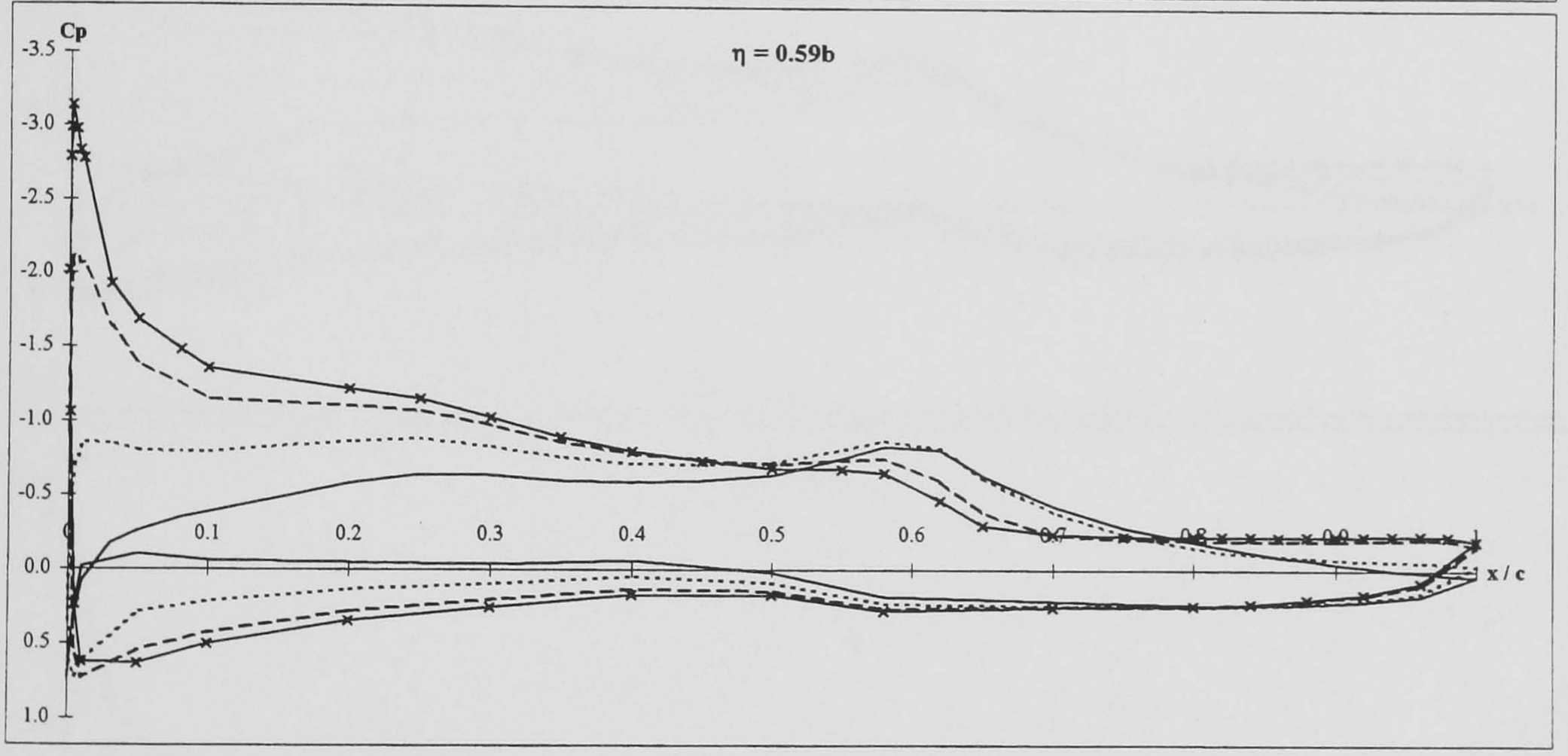

Key	α (°)
———	0
·····	4
- - - -	8
—×—	12

Figure 5-12 cont.: DERA swept wing pressure distributions. $\Lambda = 30°$, $Re_c = 2.9 \times 10^6$.

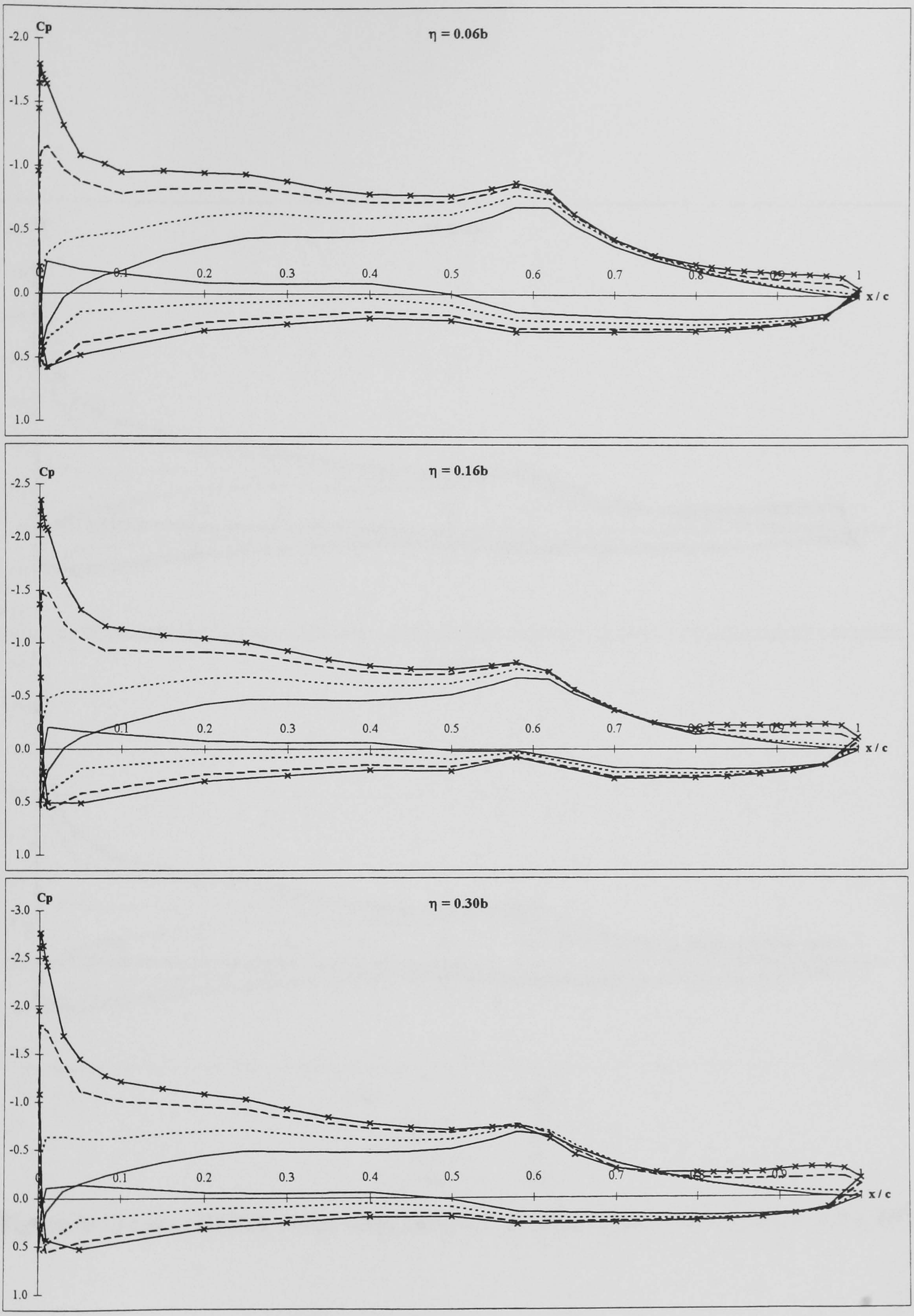

Figure 5-13: DERA swept wing pressure distributions. $\Lambda = 40°$, $Re_c = 3.3 \times 10^6$.

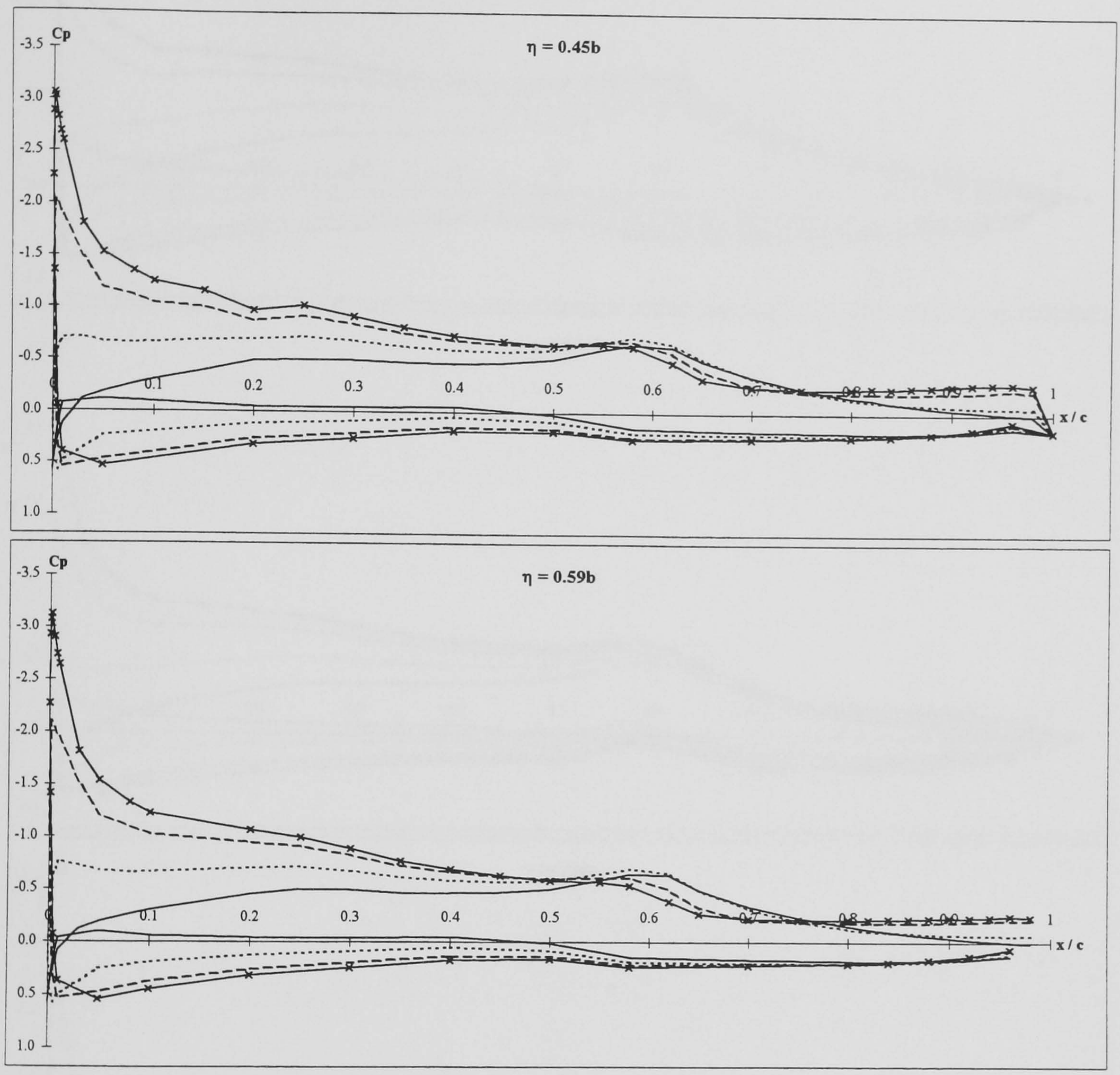

Figure 5-13 cont.: DERA swept wing pressure distributions. $\Lambda = 40°$, $Re_c = 3.3 \times 10^6$.

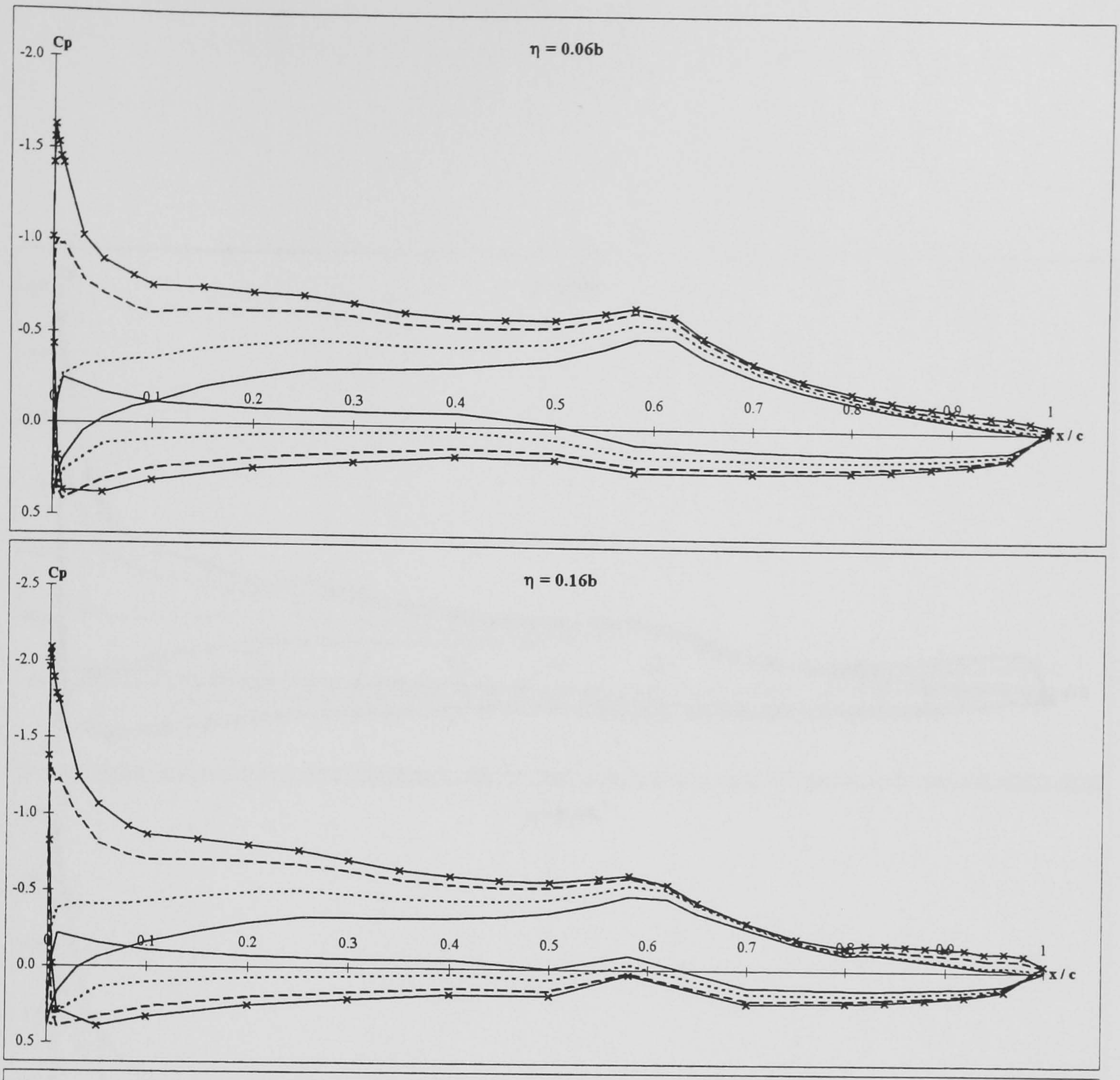

Figure 5-14: DERA swept wing pressure distributions. $\Lambda = 50°$, $Re_c = 3.9 \times 10^6$.

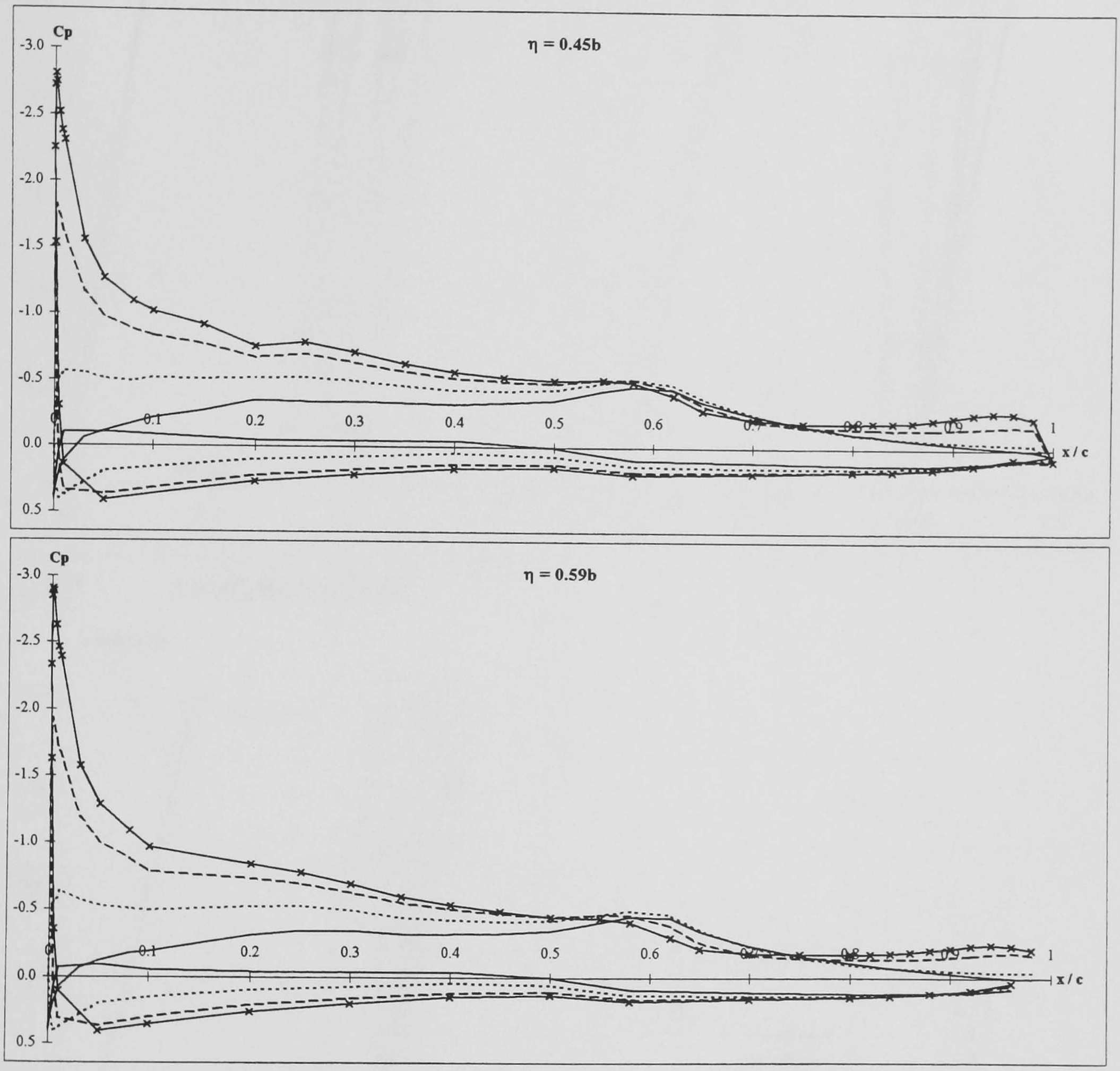

Figure 5-14 cont.: DERA swept wing pressure distributions. $\Lambda = 50°$, $Re_c = 3.9 \times 10^6$.

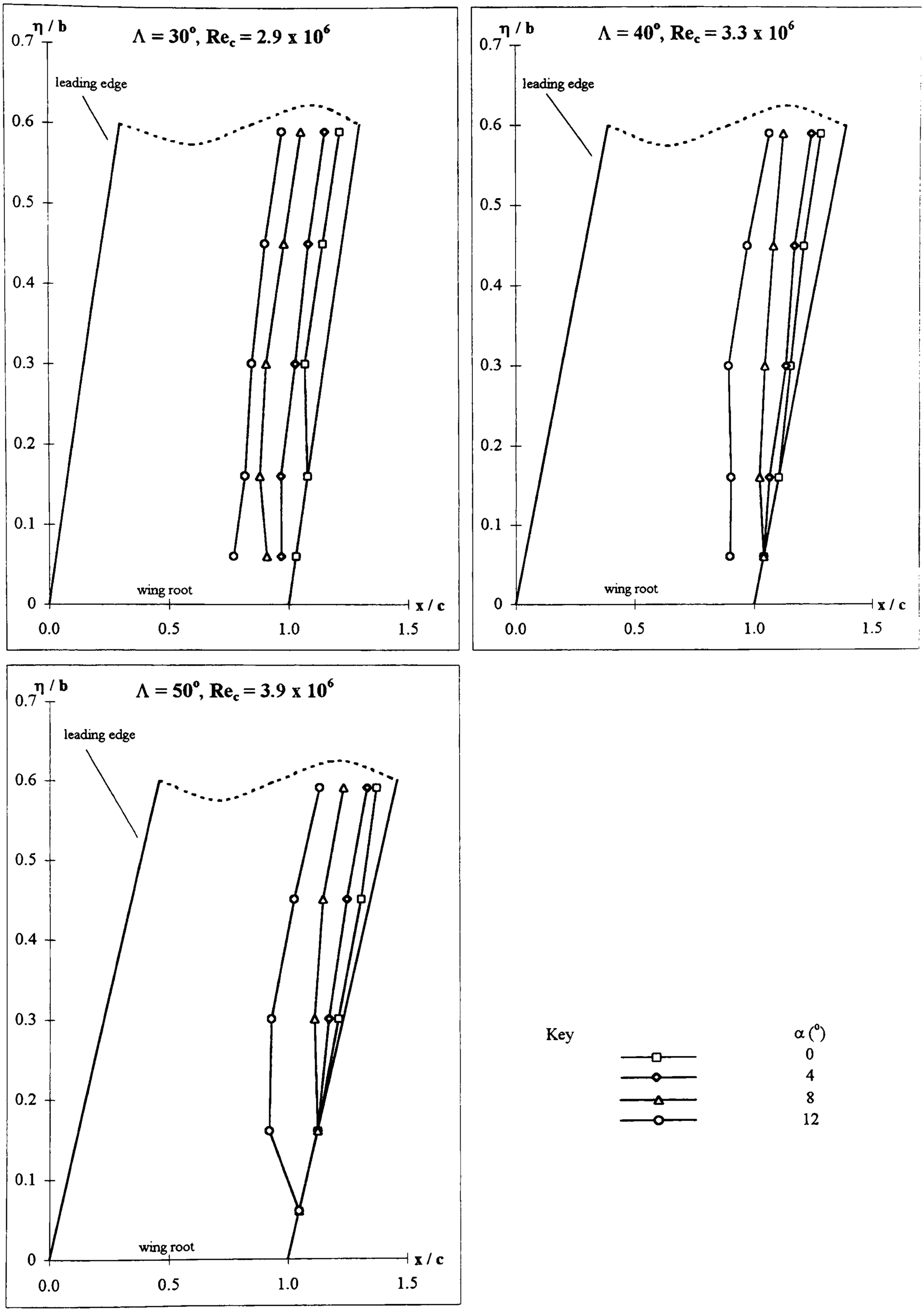

Figure 5-15: Separation line development on the DERA swept wing determined from the measured pressure distributions.

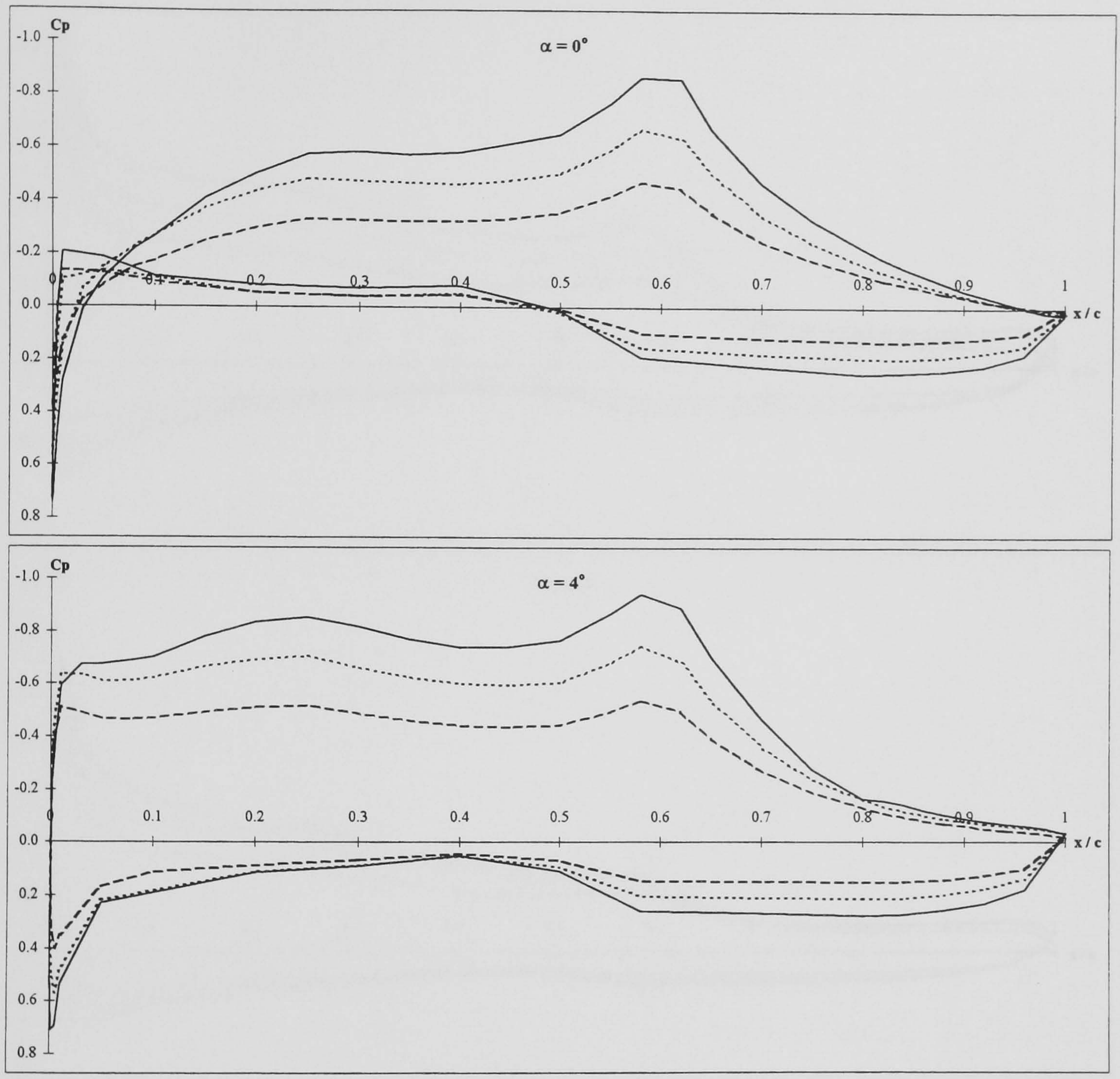

Key	Λ (°)	Re_c
———	30	2.9×10^6
.....	40	3.3×10^6
– – – – –	50	3.9×10^6

Figure 5-16: DERA swept wing pressure distribution comparisons. η = 0.30b, V = 60 m/s.

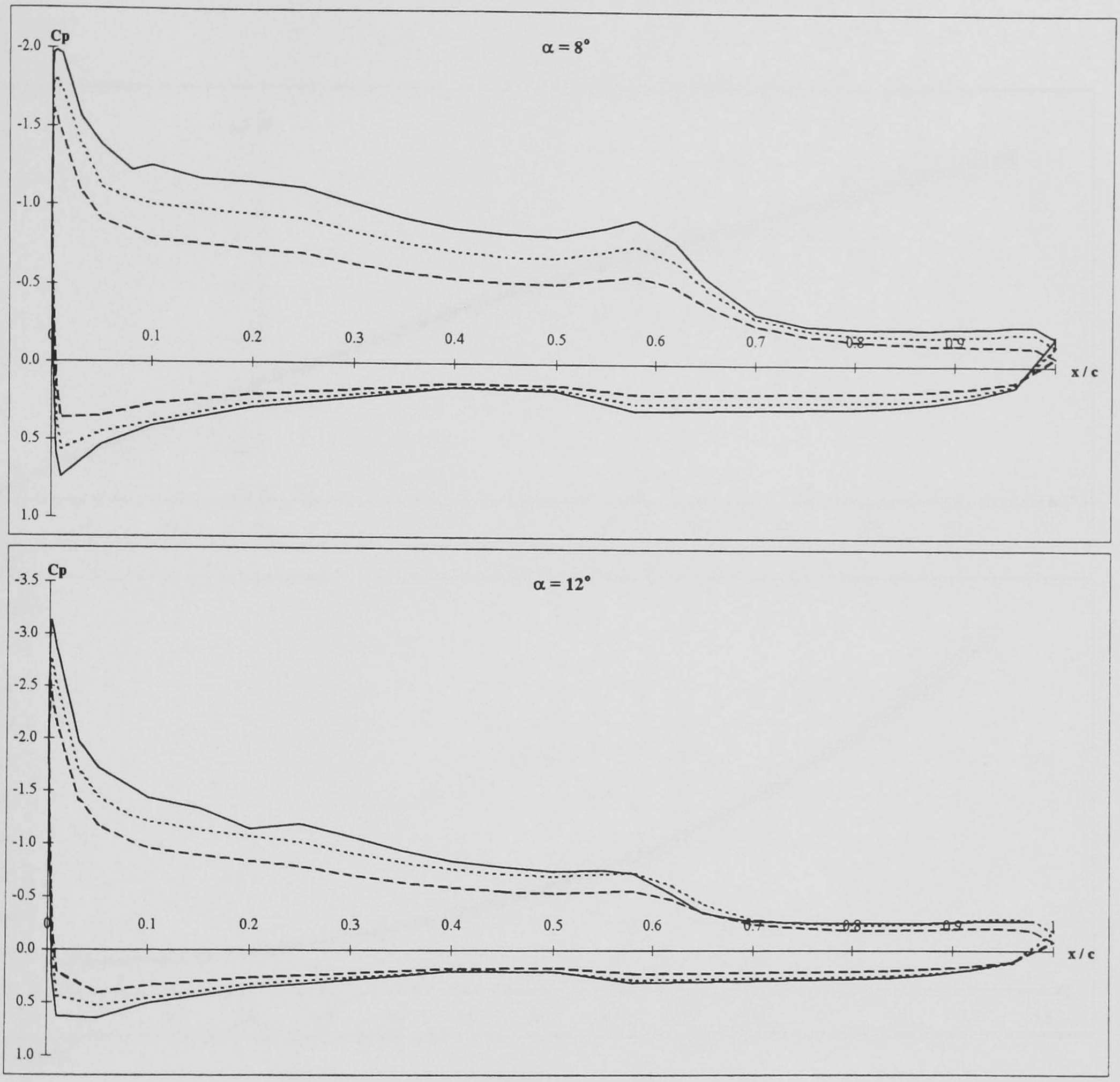

Key	Λ (°)	Re_c
———	30	2.9×10^6
.....	40	3.3×10^6
- - - - -	50	3.9×10^6

Figure 5-16 cont.: DERA swept wing pressure distribution comparisons. η = 0.30b, V = 60 m/s.

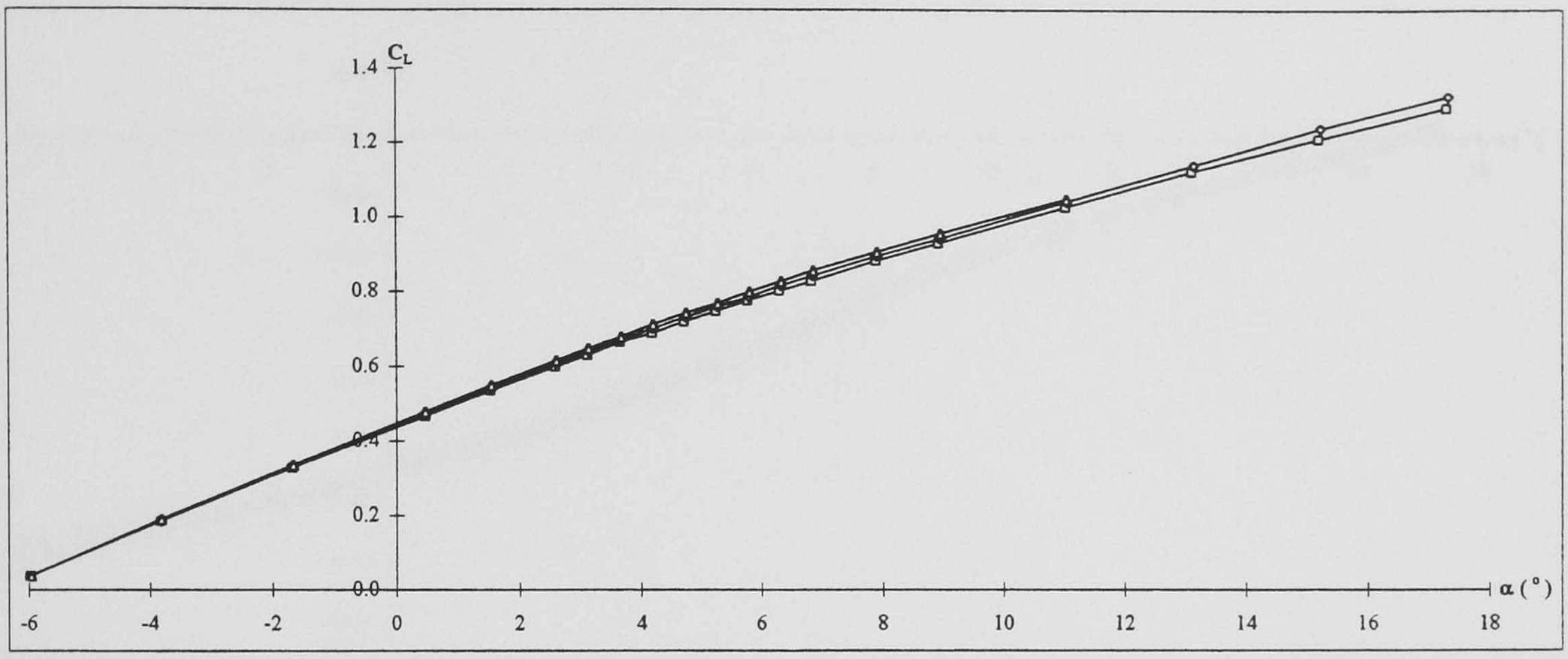

Lift

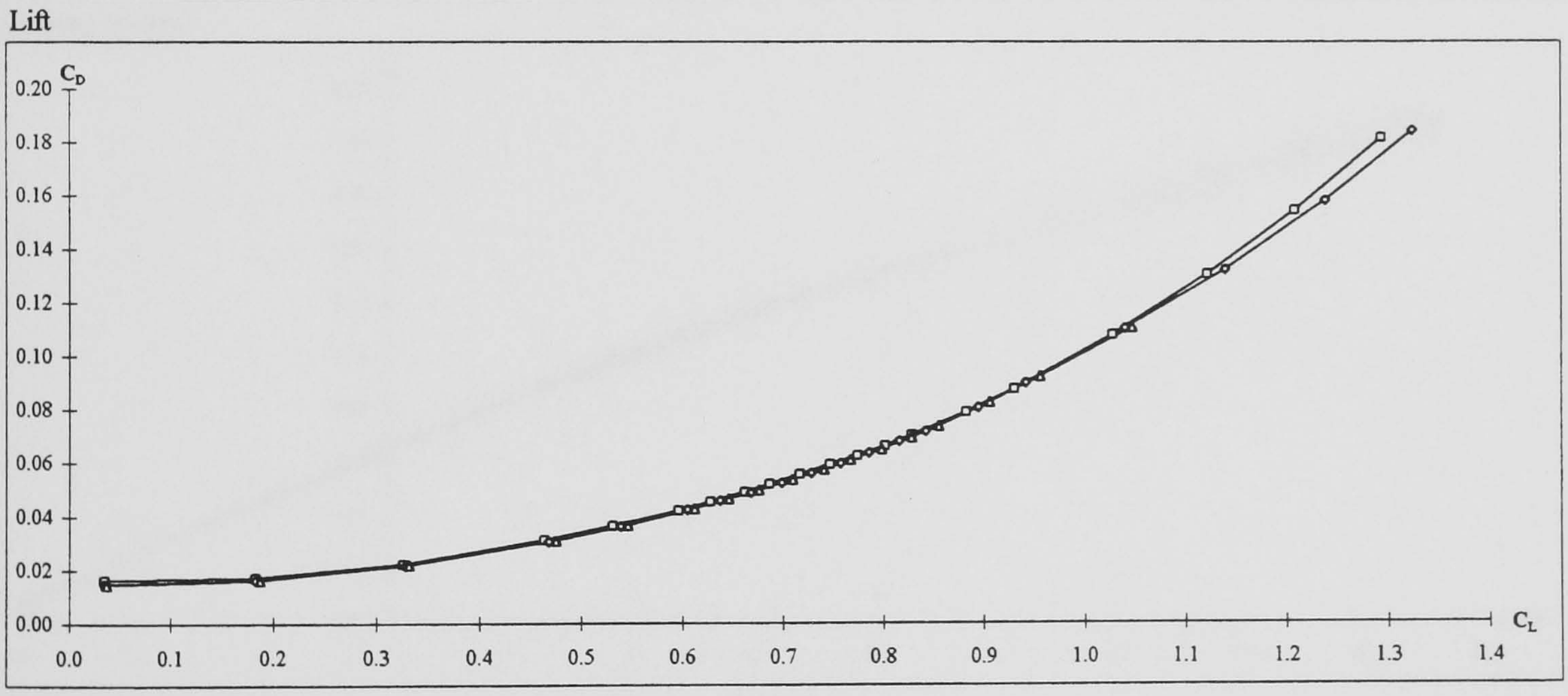

Drag polar

Key	V (m/s)	Re_c
—□—	40	1.9×10^6
—◇—	60	2.9×10^6
—△—	80	3.9×10^6

Figure 5-17: DERA swept wing aerodynamic forces and moments comparison with Reynolds number. $\Lambda = 30°$.

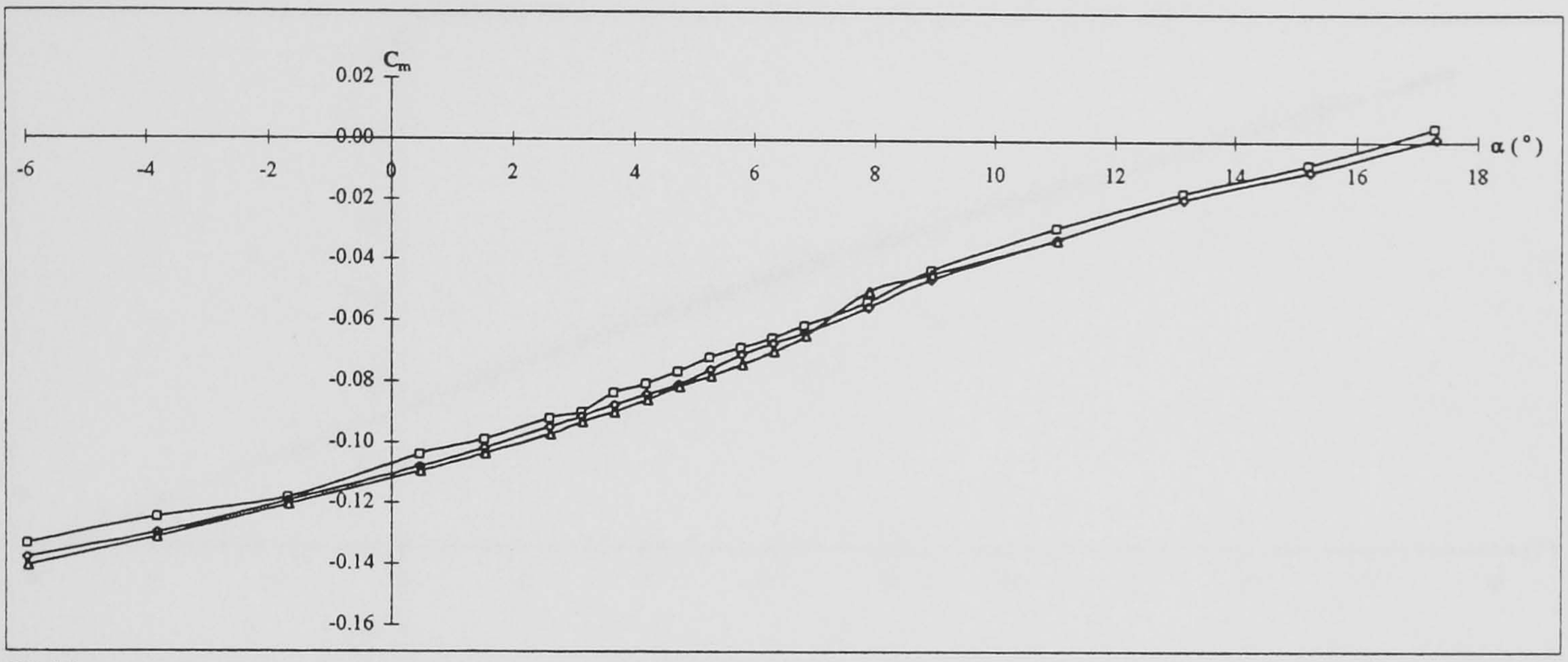

Pitching moment

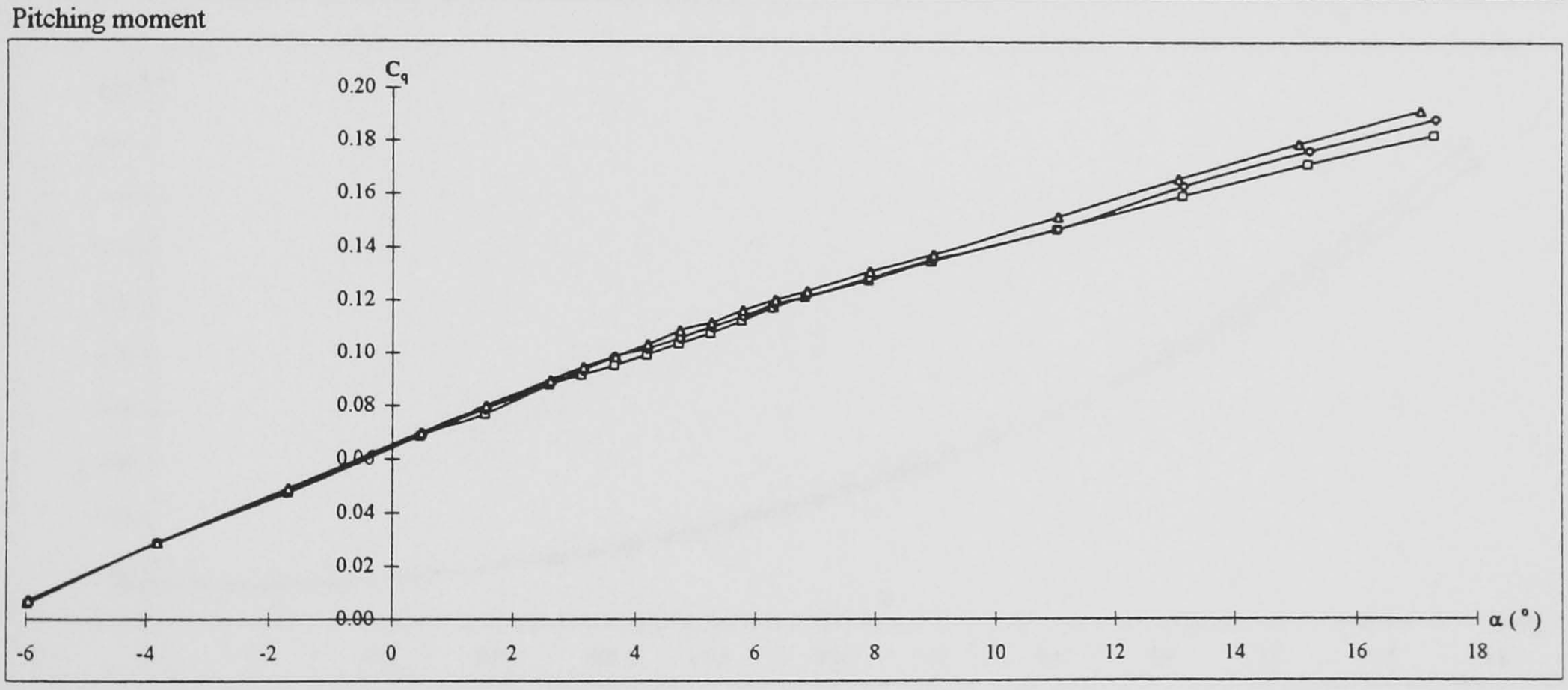

Rolling moment

Key	V (m/s)	Re_c
—□—	40	1.9×10^6
—◇—	60	2.9×10^6
—△—	80	3.9×10^6

Figure 5-17 cont.: DERA swept wing aerodynamic forces and moments comparison with Reynolds number. $\Lambda = 30°$.

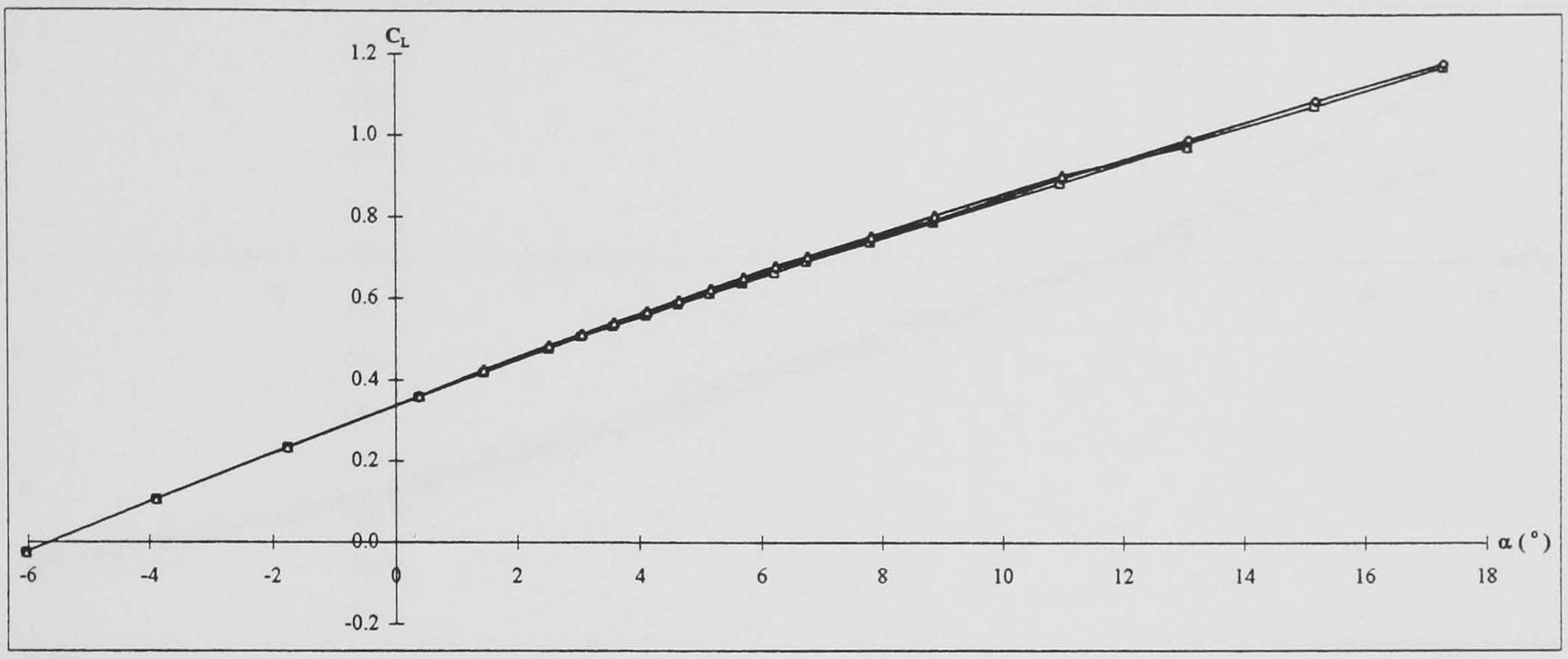

Lift

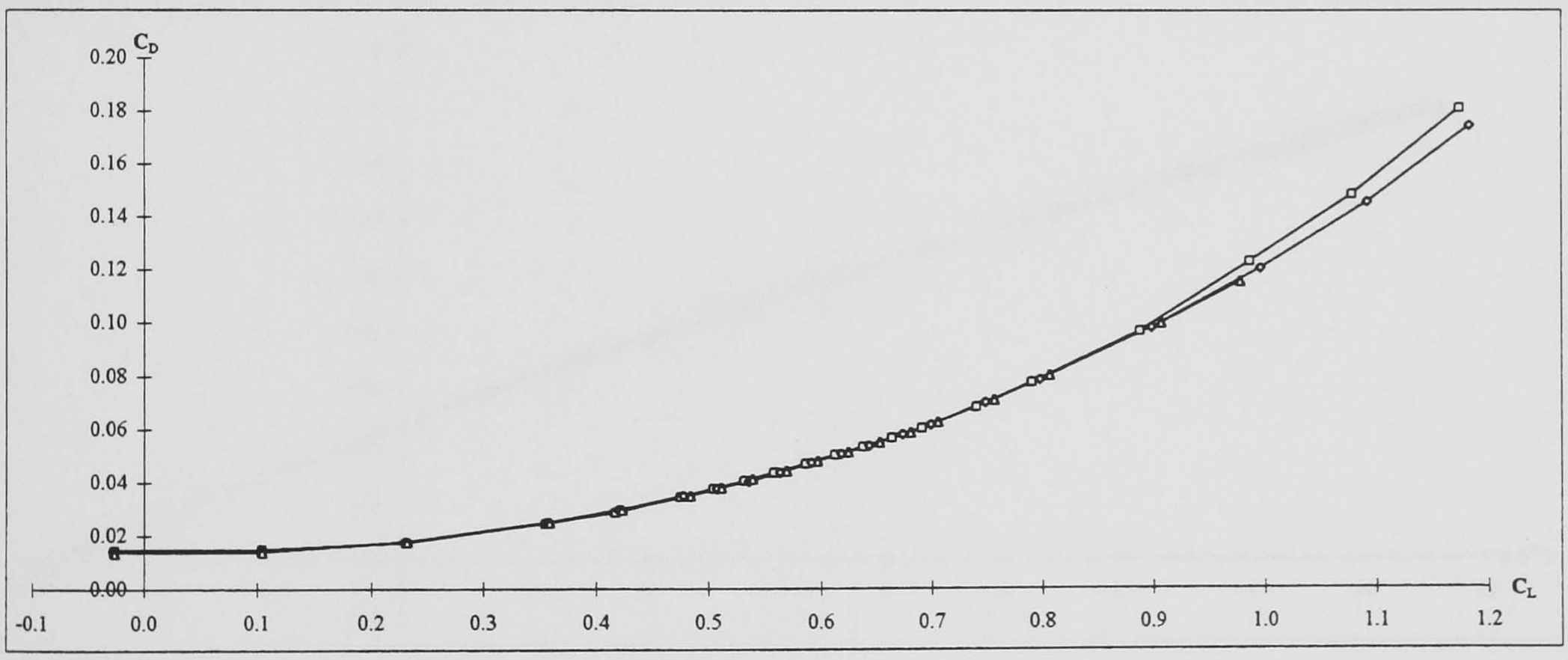

Drag polar

Key	V (m/s)	Re_c
—□—	40	2.2×10^6
—◇—	60	3.3×10^6
—△—	80	4.4×10^6

Figure 5-18: DERA swept wing aerodynamic forces and moments comparison with Reynolds number. $\Lambda = 40°$.

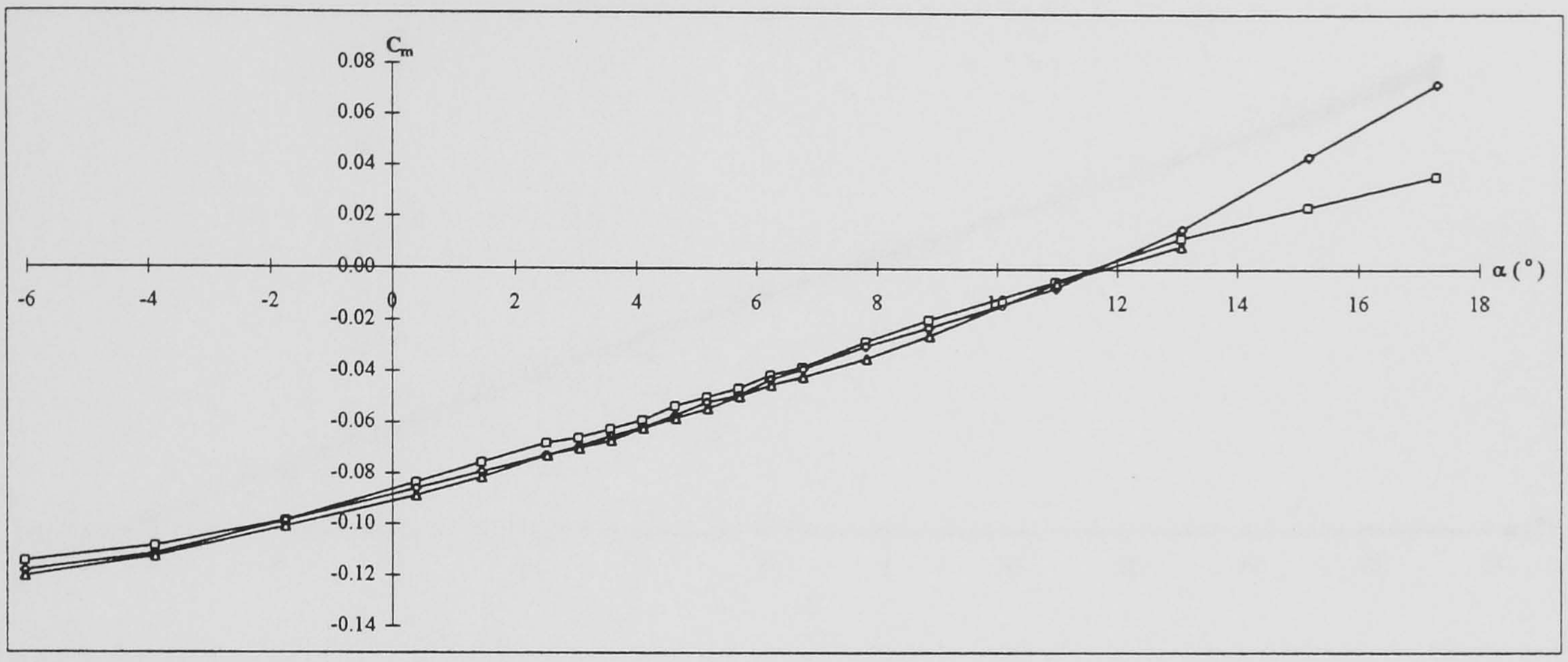

Pitching moment

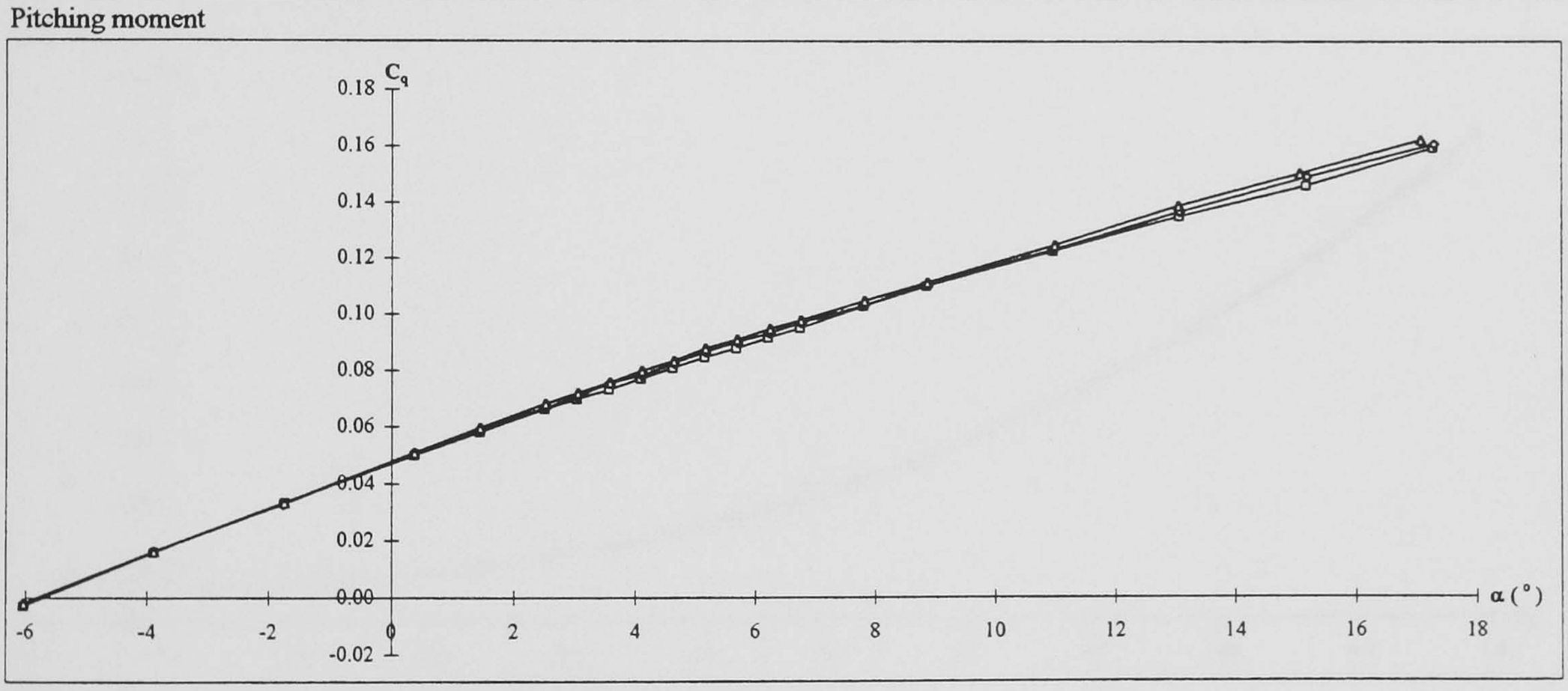

Rolling moment

Key	V (m/s)	Re_c
—□—	40	2.2×10^6
—◇—	60	3.3×10^6
—△—	80	4.4×10^6

Figure 5-18 cont.: DERA swept wing aerodynamic forces and moments comparison with Reynolds number. $\Lambda = 40°$.

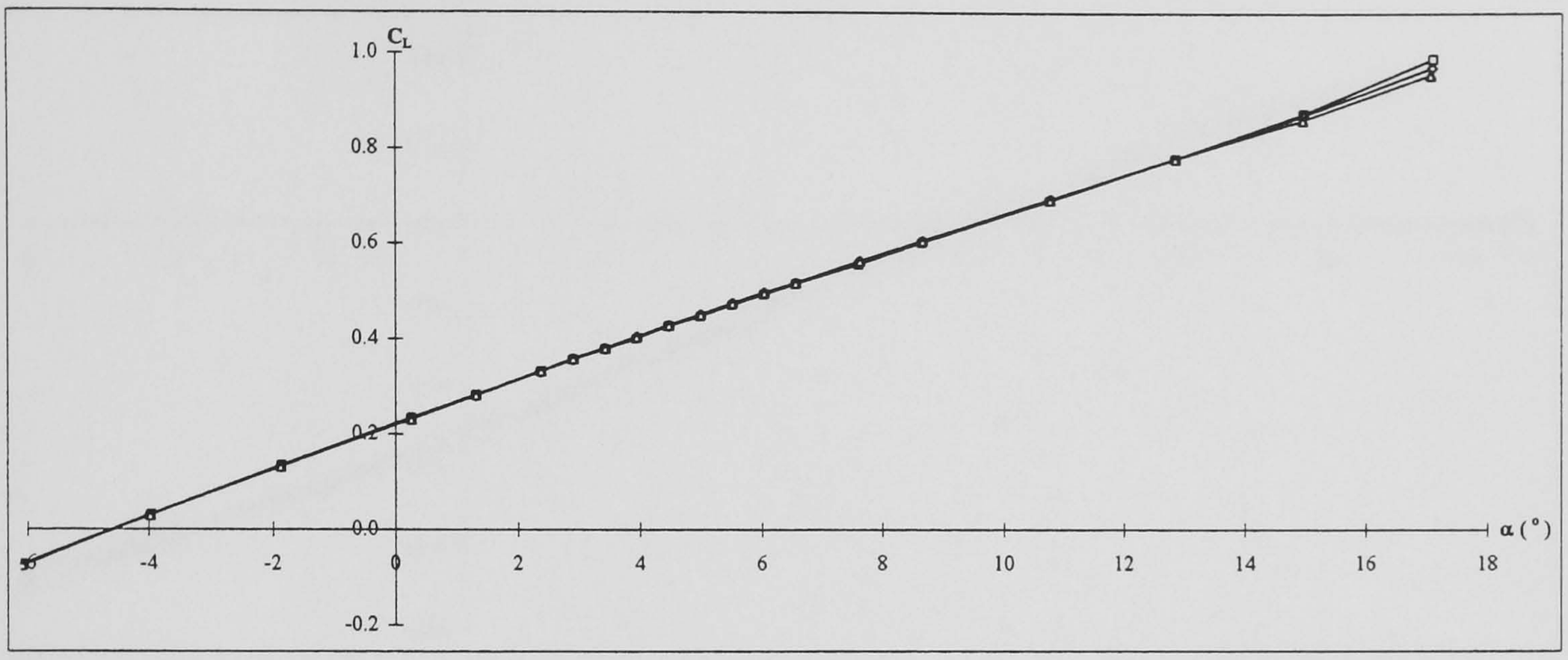

Lift

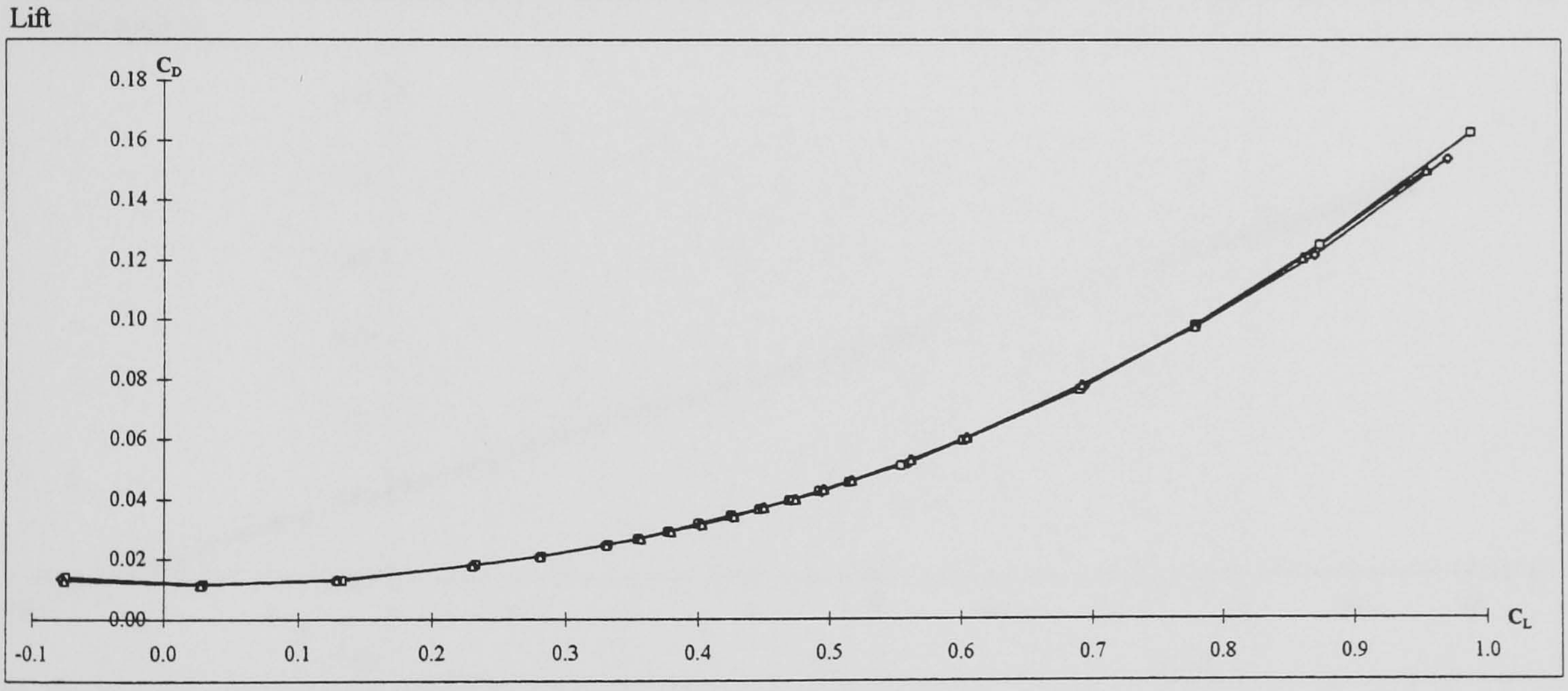

Drag polar

Key	V (m/s)	Re_c
—□—	40	2.6×10^6
—◇—	60	3.9×10^6
—△—	80	5.2×10^6

Figure 5-19: DERA swept wing aerodynamic forces and moments comparison with Reynolds number. $\Lambda = 50°$.

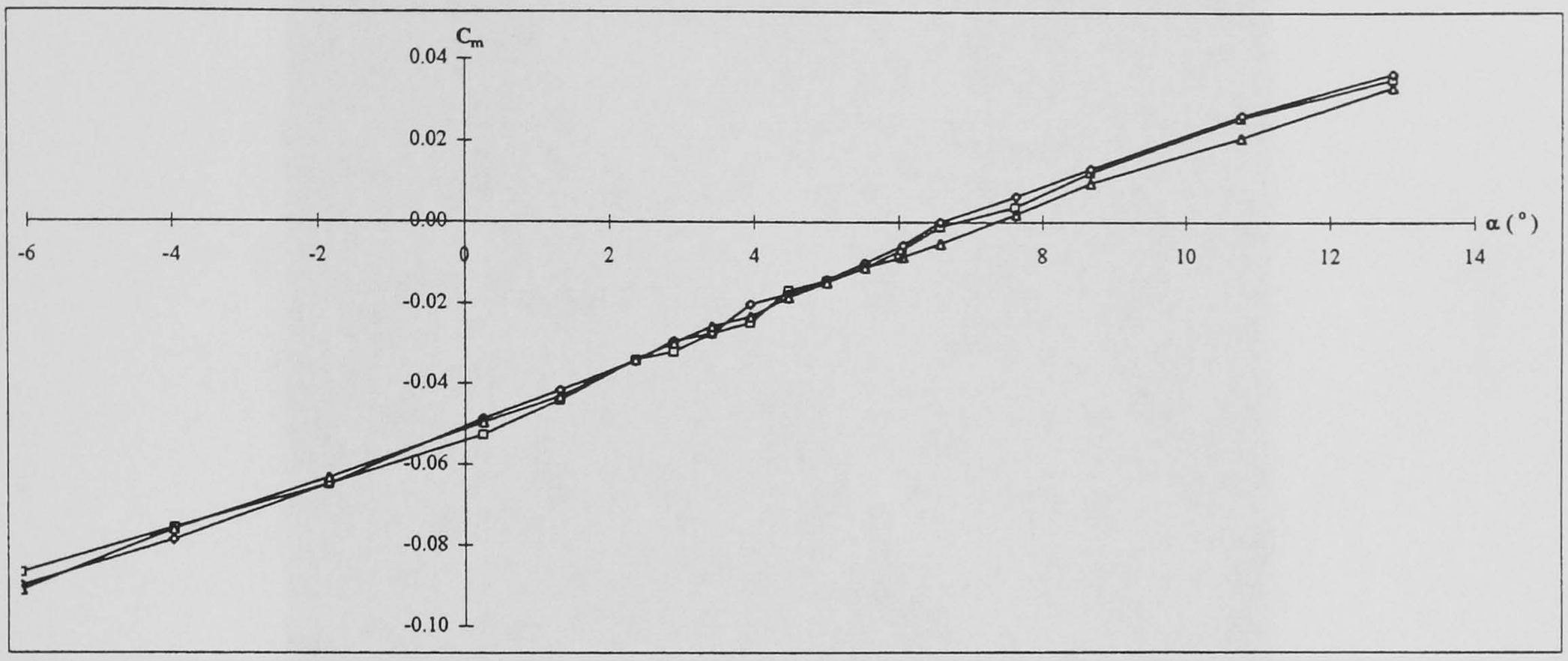

Pitching moment

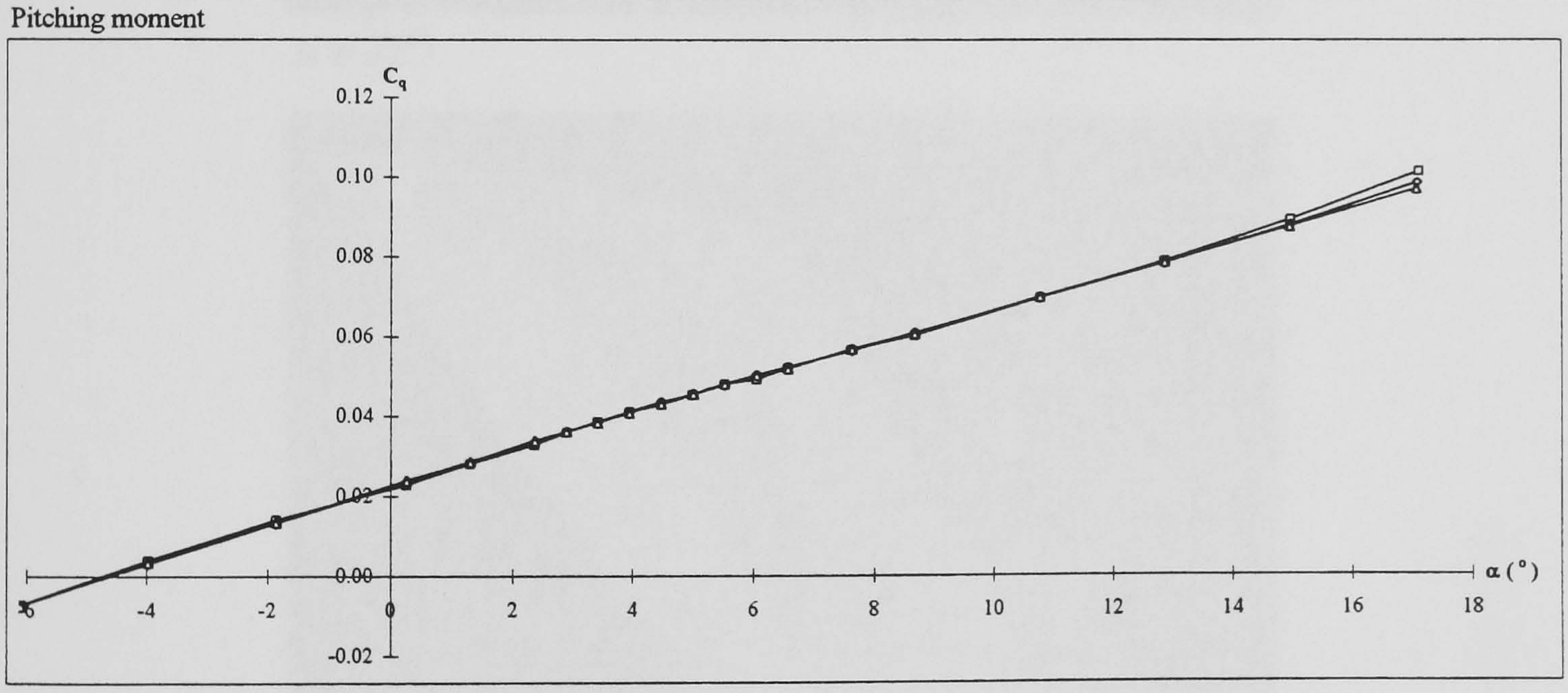

Rolling moment

Key	V (m/s)	Re_c
—□—	40	2.6×10^6
—◇—	60	3.9×10^6
—△—	80	5.2×10^6

Figure 5-19 cont.: DERA swept wing aerodynamic forces and moments comparison with Reynolds number. $\Lambda = 50°$.

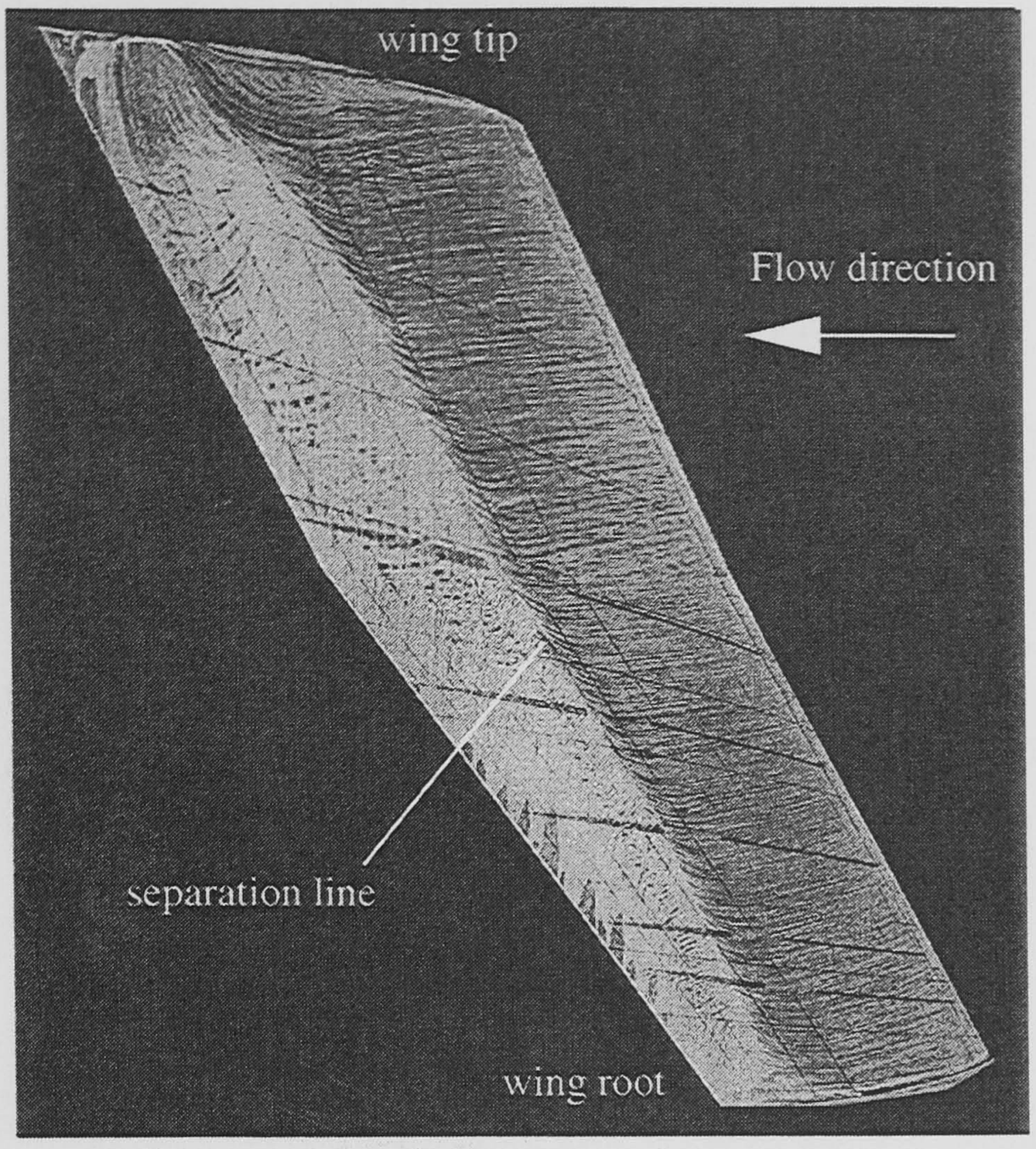

$\Lambda = 30^{\circ}$

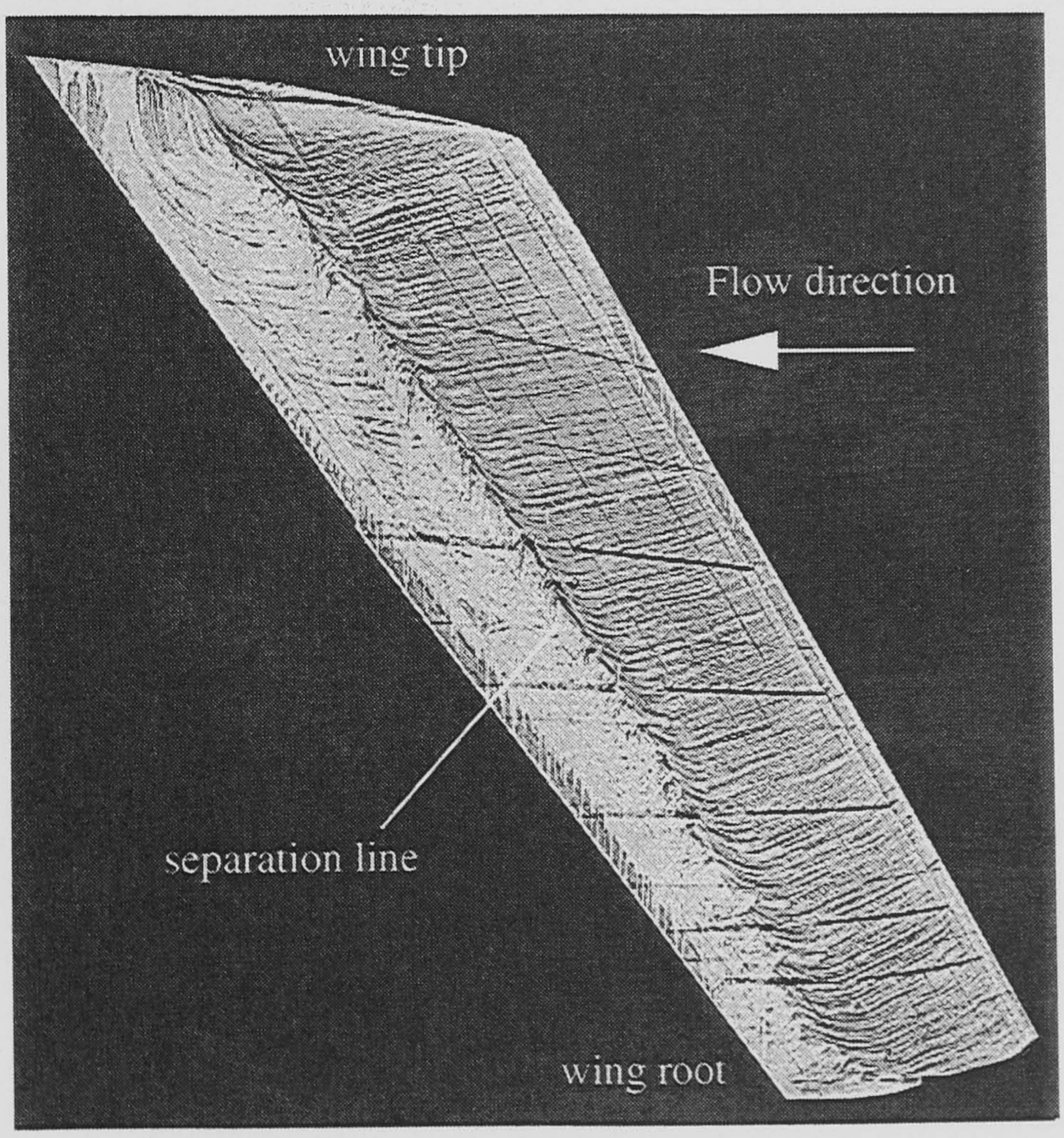

$\Lambda = 40^{\circ}$

Figure 5-20: Surface oil flow visualisation results for the DERA swept wing. $\alpha = 8°$, V = 40 m/s, $Re_c \sim 2.2 \times 10^6$.

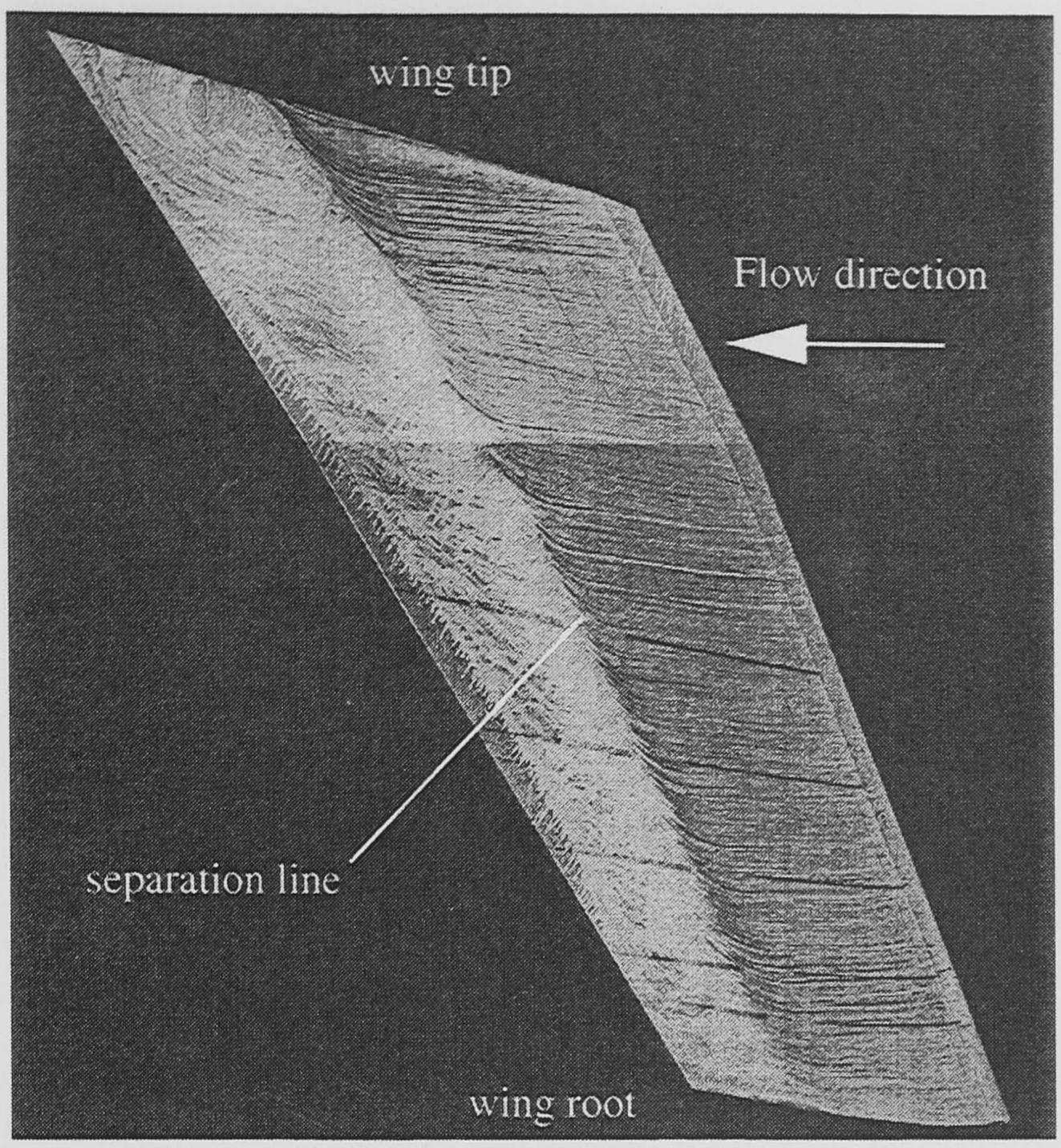

$\Lambda = 50^{\circ}$

Figure 5-20 cont.: Surface oil flow visualisation results for the DERA swept wing. $\alpha = 8°$, V = 40 m/s, $Re_c \sim 2.2 \times 10^6$.

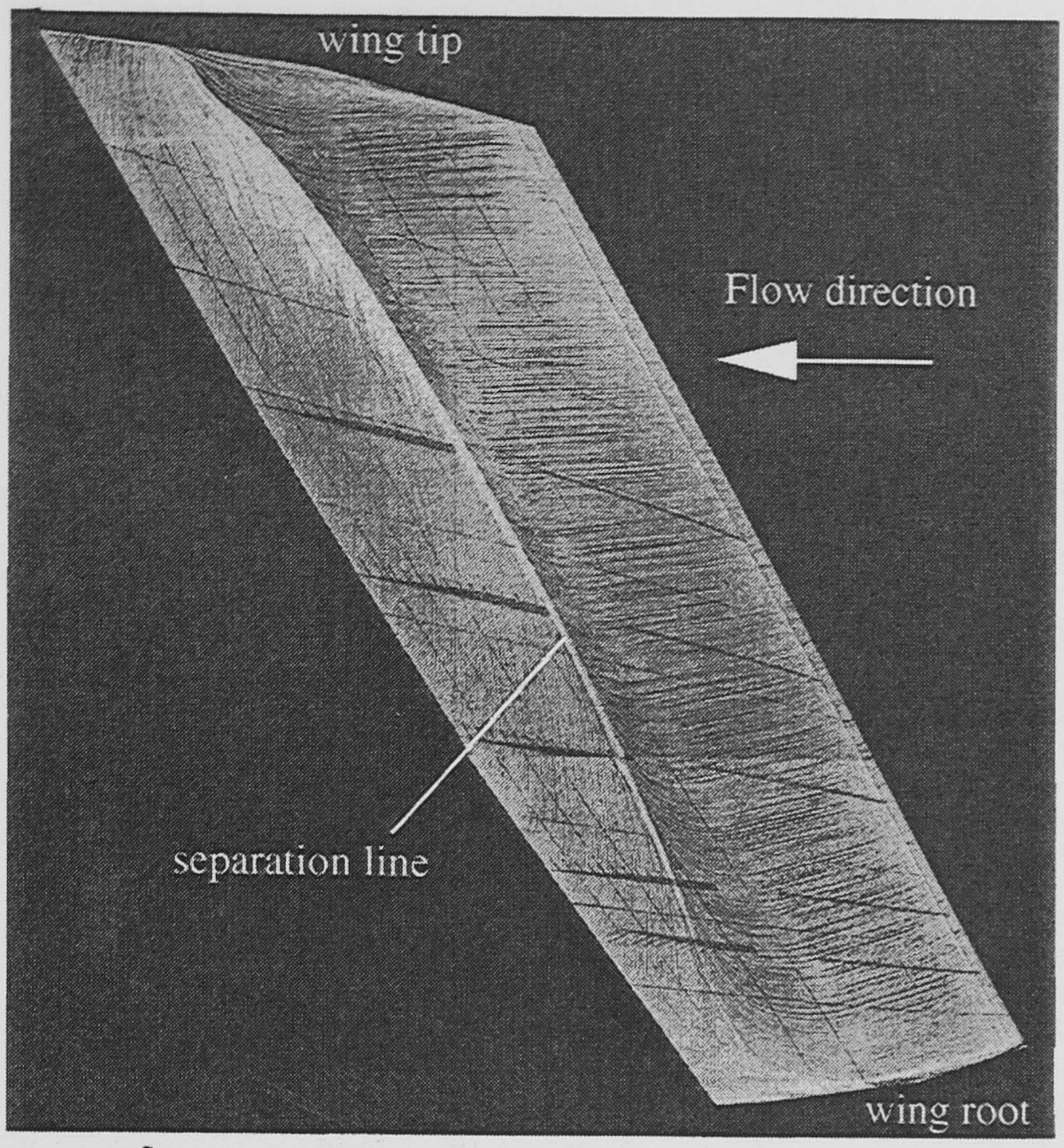

$\Lambda = 30^{\circ}$

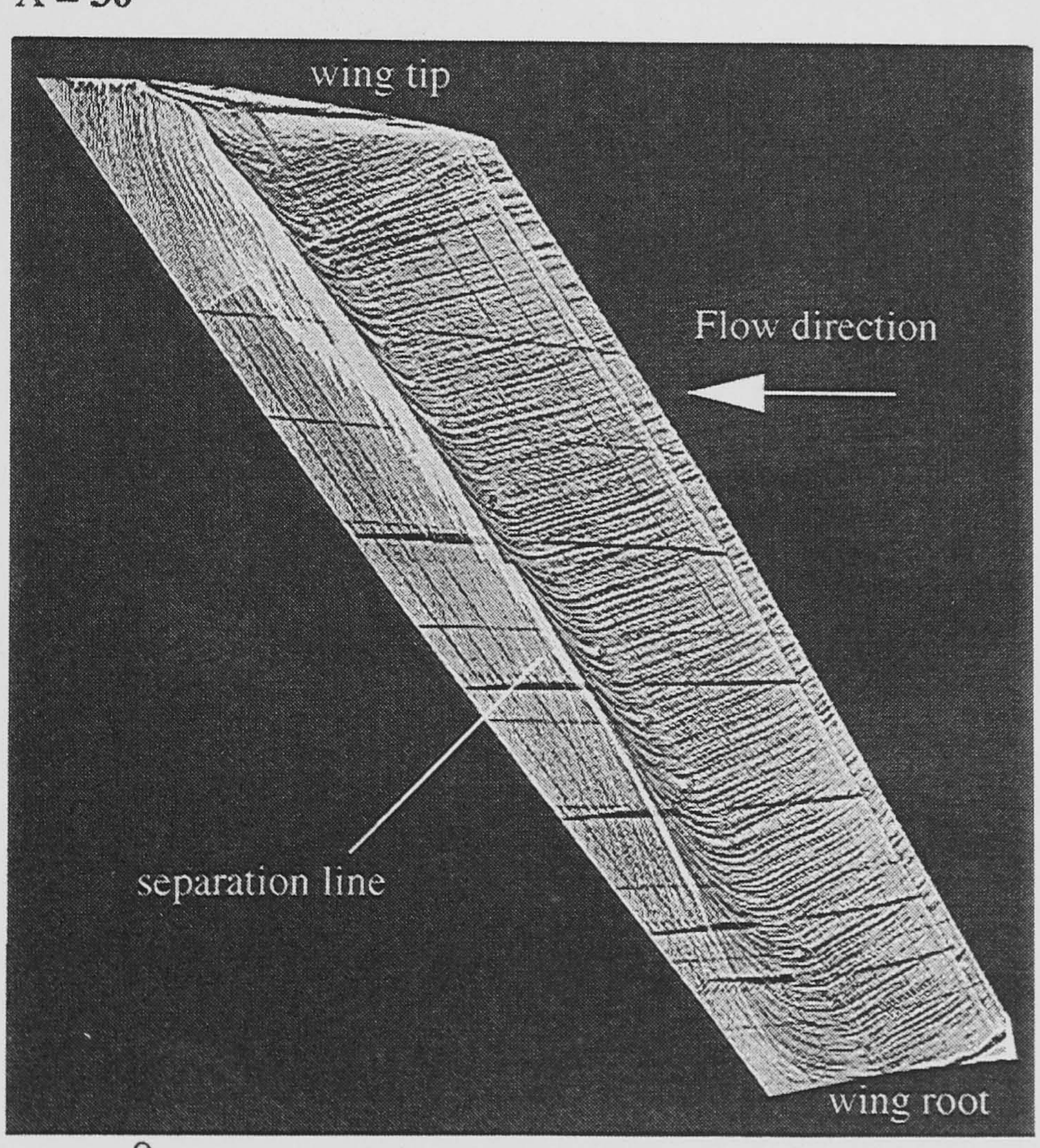

$\Lambda = 40^{\circ}$

Figure 5-21: Surface oil flow visualisation results for the DERA swept wing. $\alpha = 8°$, V = 80 m/s, $Re_c \sim 4.5 \times 10^6$.

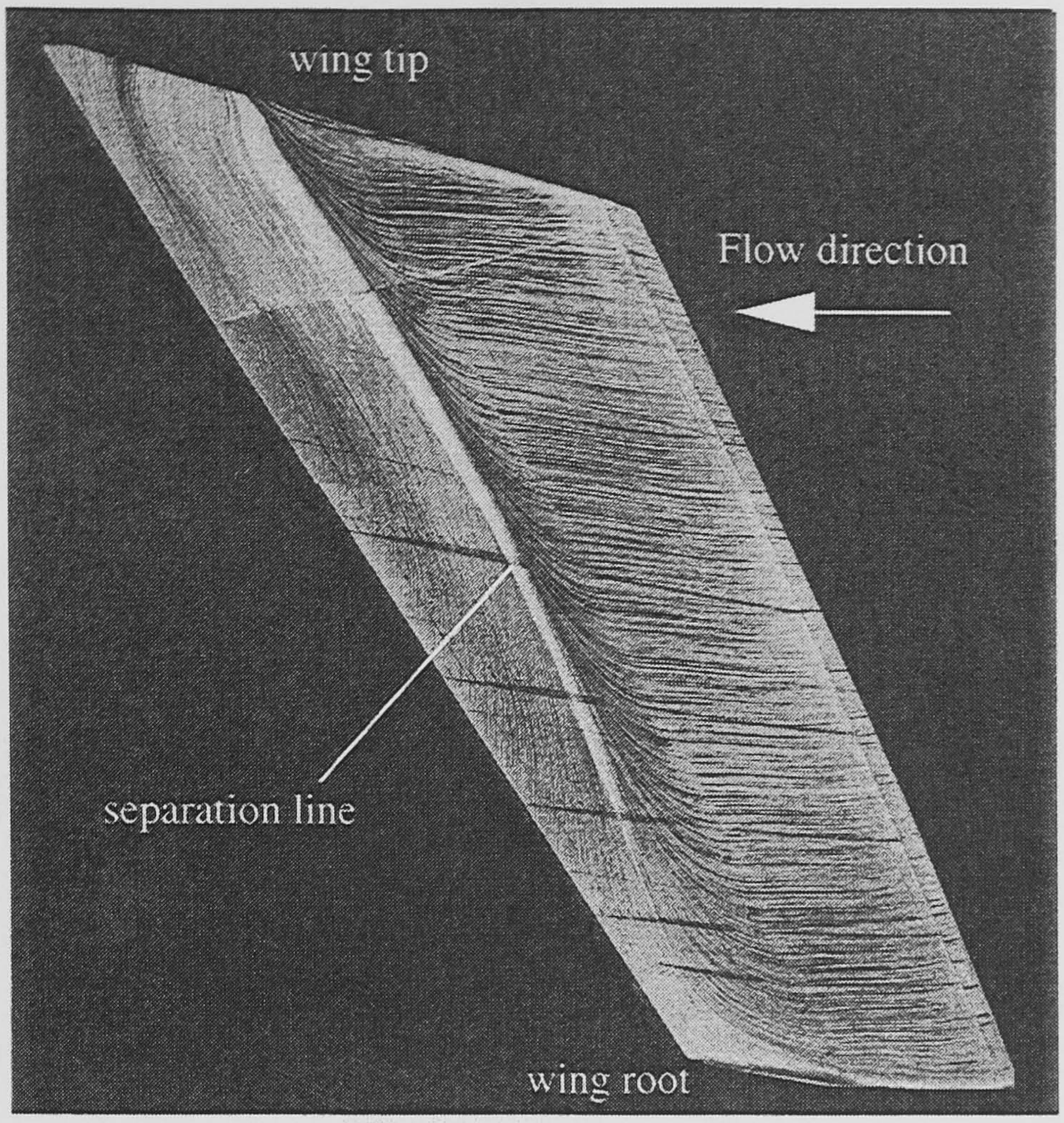

$\Lambda = 50^{\circ}$

Figure 5-21 cont.: Surface oil flow visualisation results for the DERA swept wing. $\alpha = 8°$, V = 80 m/s, $Re_c \sim 4.5 \times 10^6$.

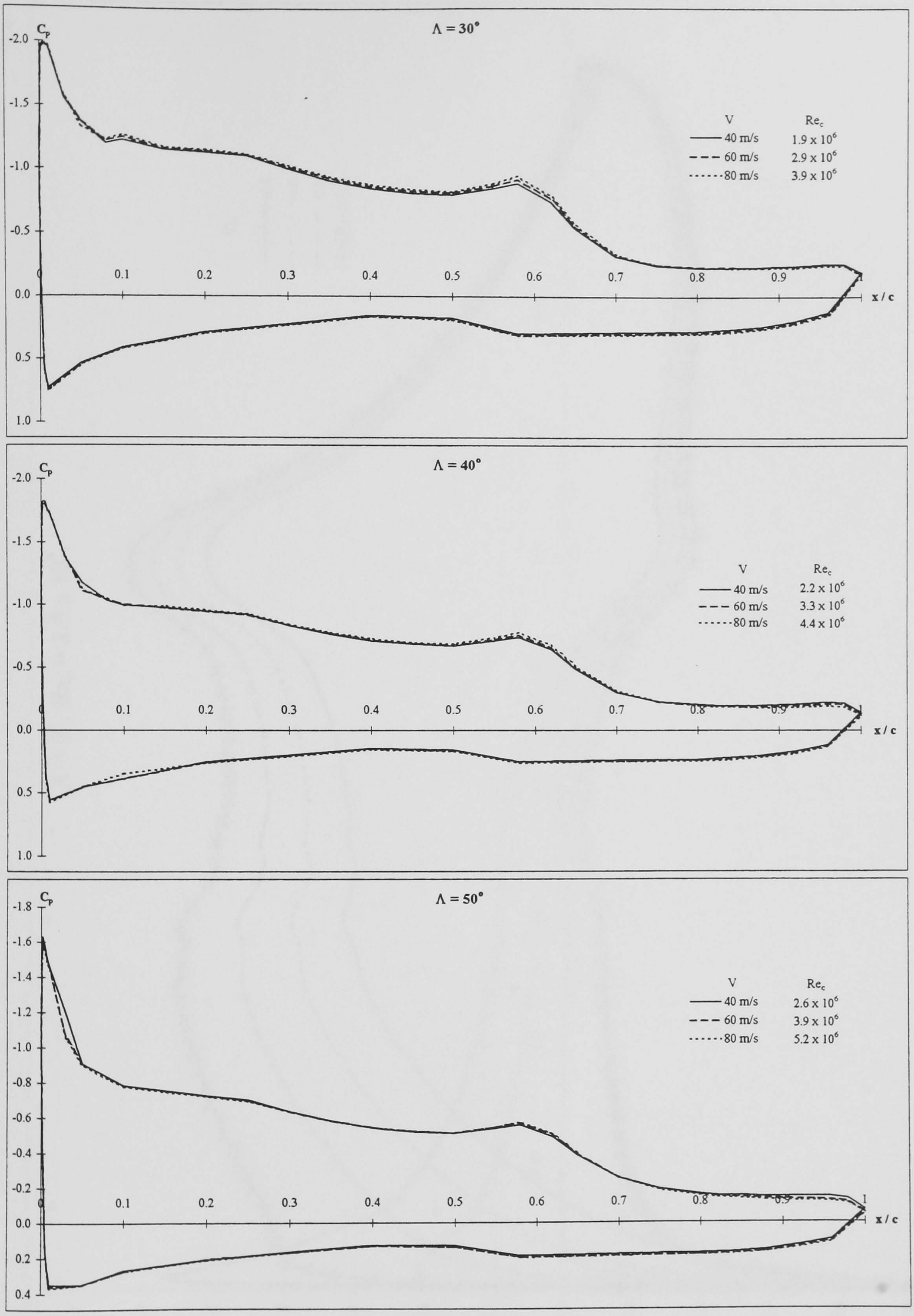

Figure 5-22: DERA swept wing pressure distribution comparison with Reynolds number. $\alpha = 8°$, $\eta = 0.30b$.

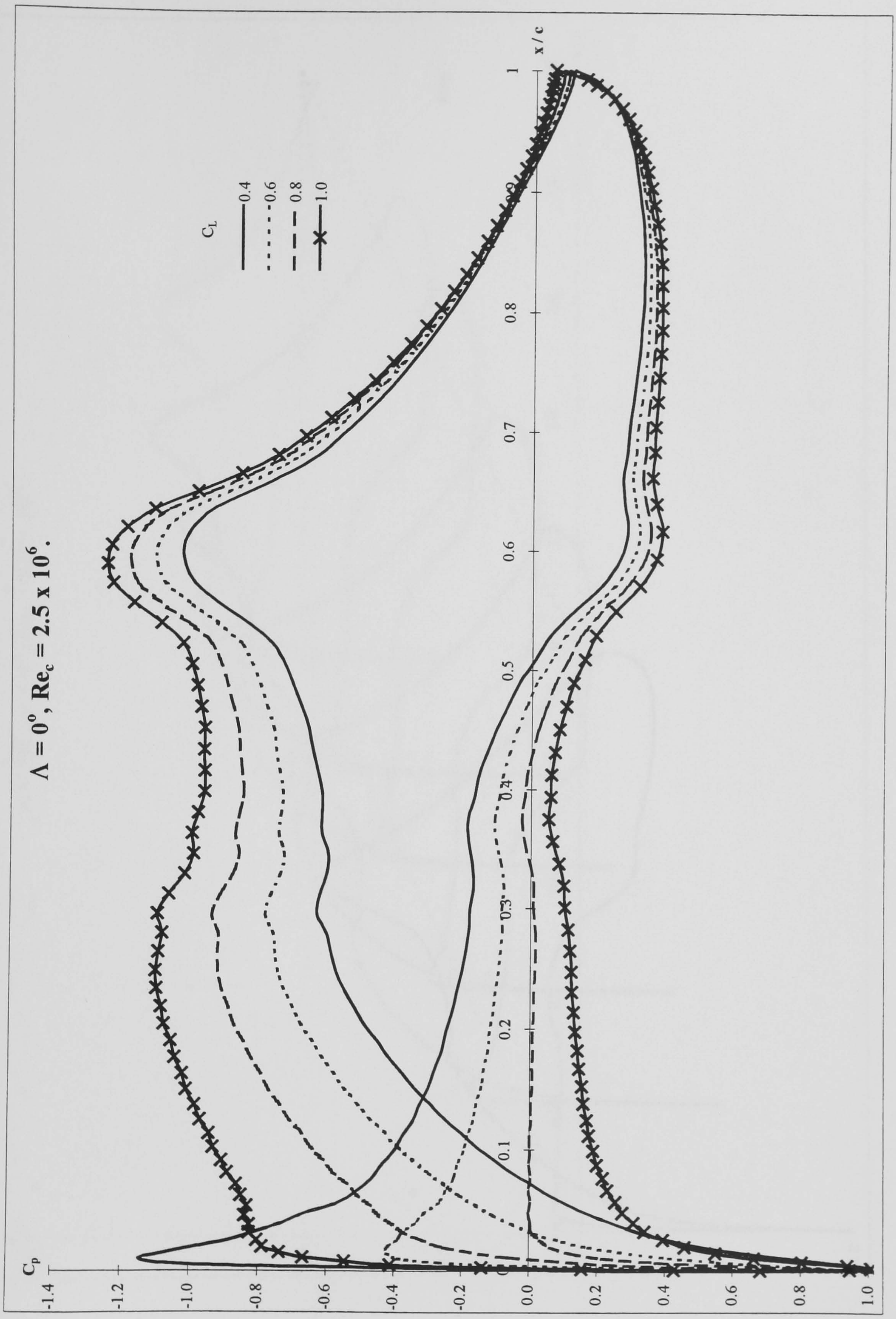

Figure 5-23: BVGK calculated pressure distributions for the DERA wing.

$\Lambda = 30^o$, $\alpha = 0^o$, $Re_c = 2.9 \times 10^6$.

Figure 5-24: VFP calculated pressure distribution for the DERA swept wing.

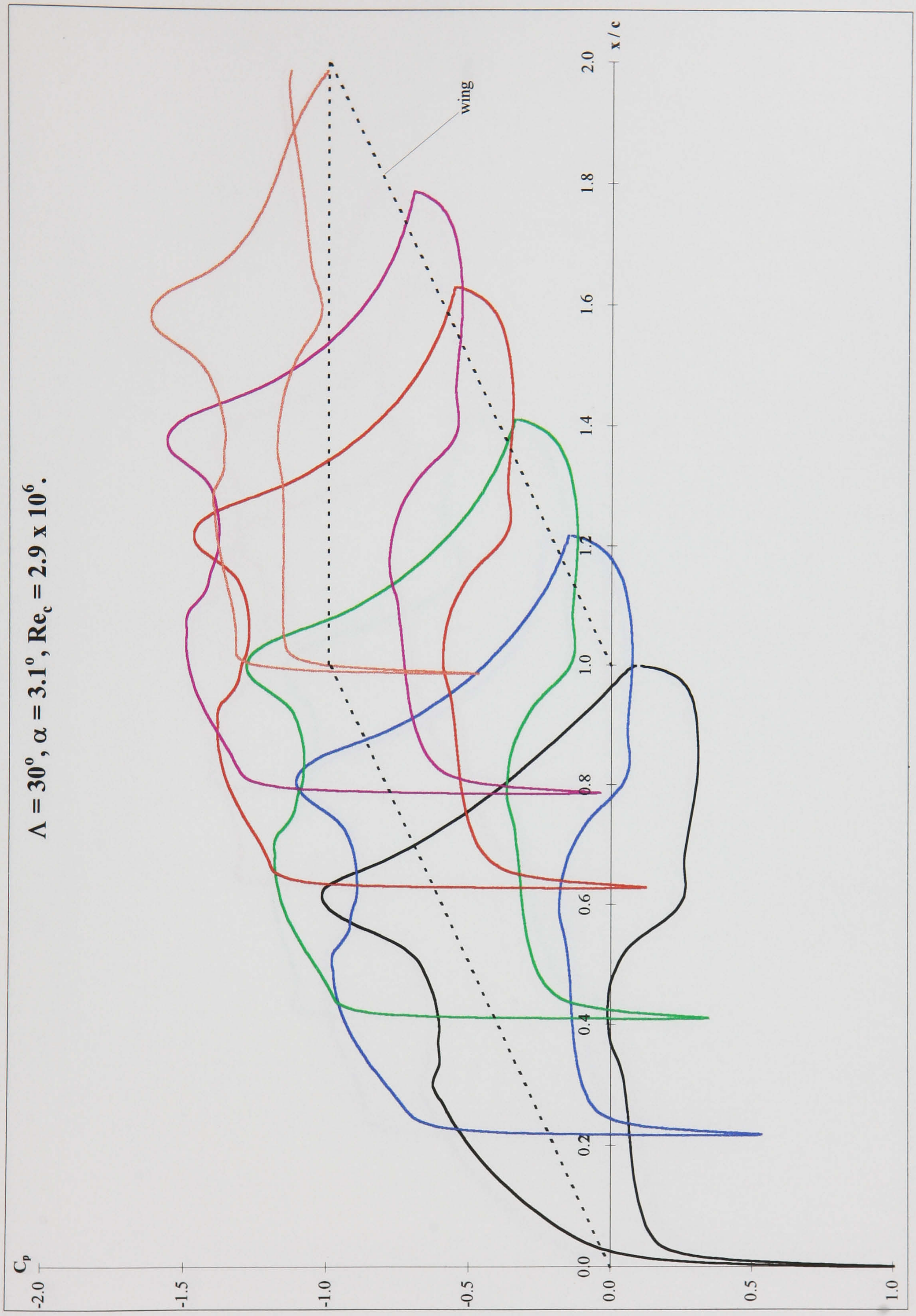

Figure 5-24 cont.: VFP calculated pressure distribution for the DERA swept wing.

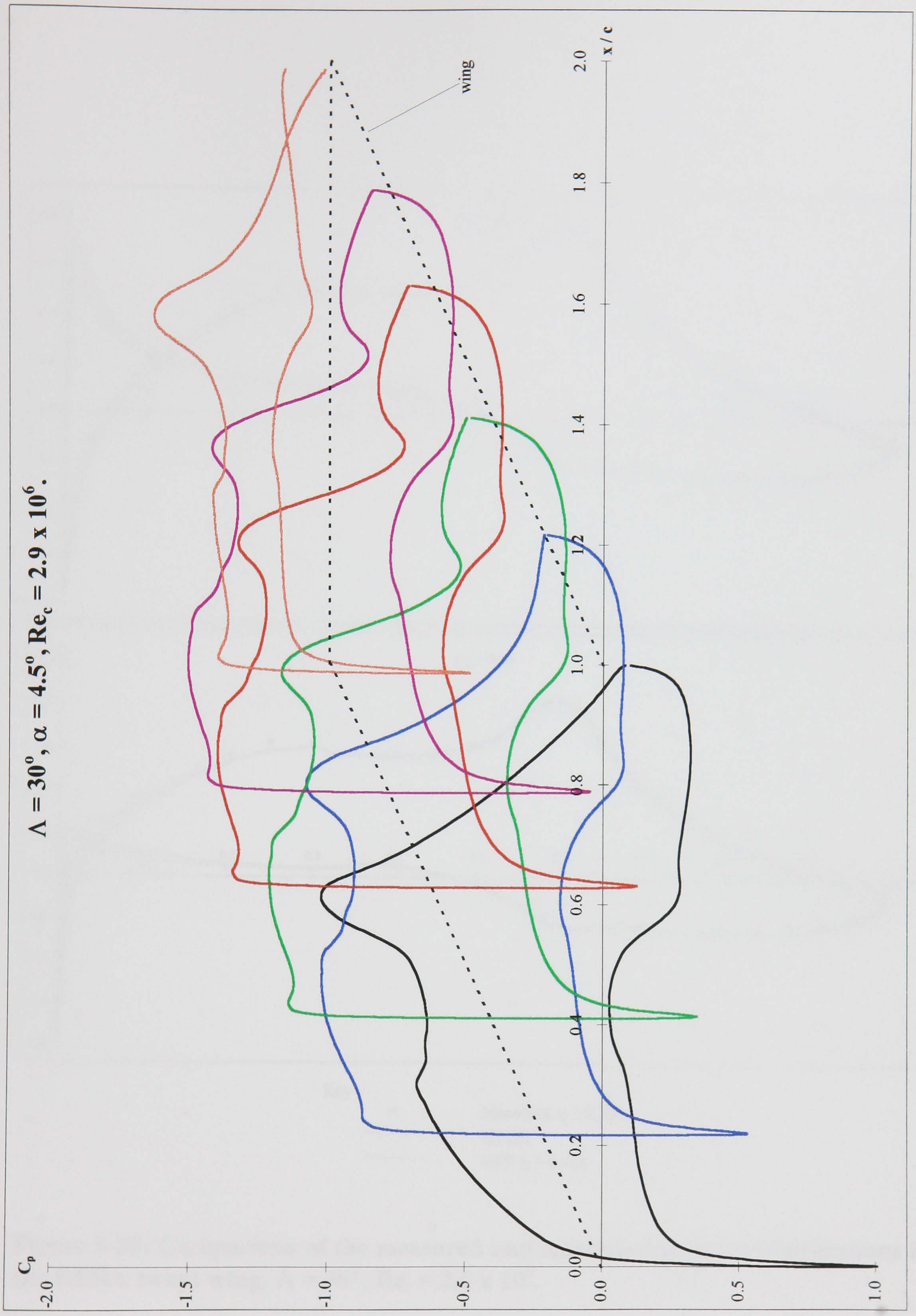

$\Lambda = 30^o$, $\alpha = 4.5^o$, $Re_c = 2.9 \times 10^6$.

Figure 5-24 cont.: VFP calculated pressure distribution for the DERA swept wing.

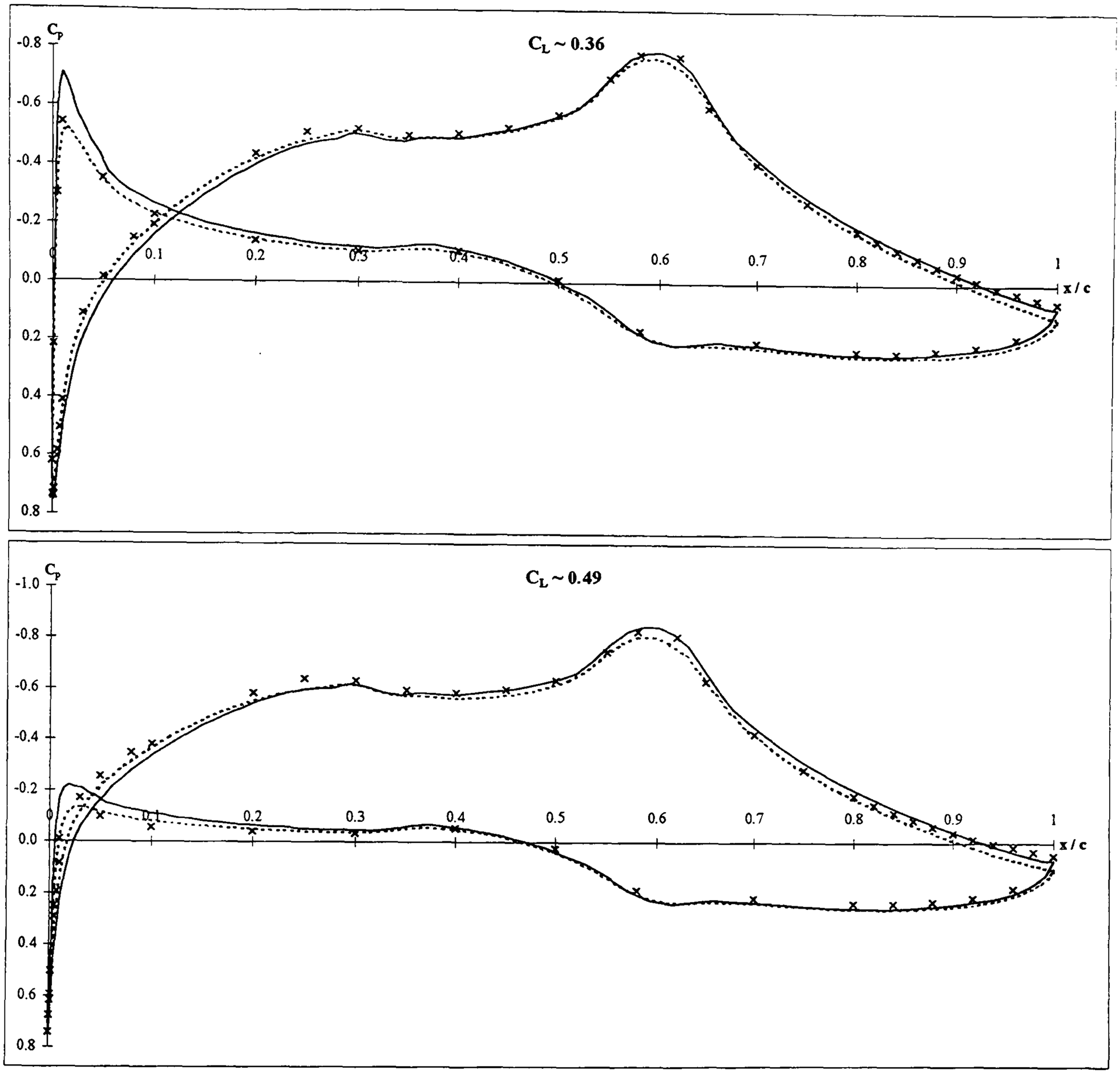

Figure 5-25: Comparison of the measured and calculated pressure distributions for the DERA swept wing. $\Lambda = 30°$, $Re_c = 2.9 \times 10^6$.

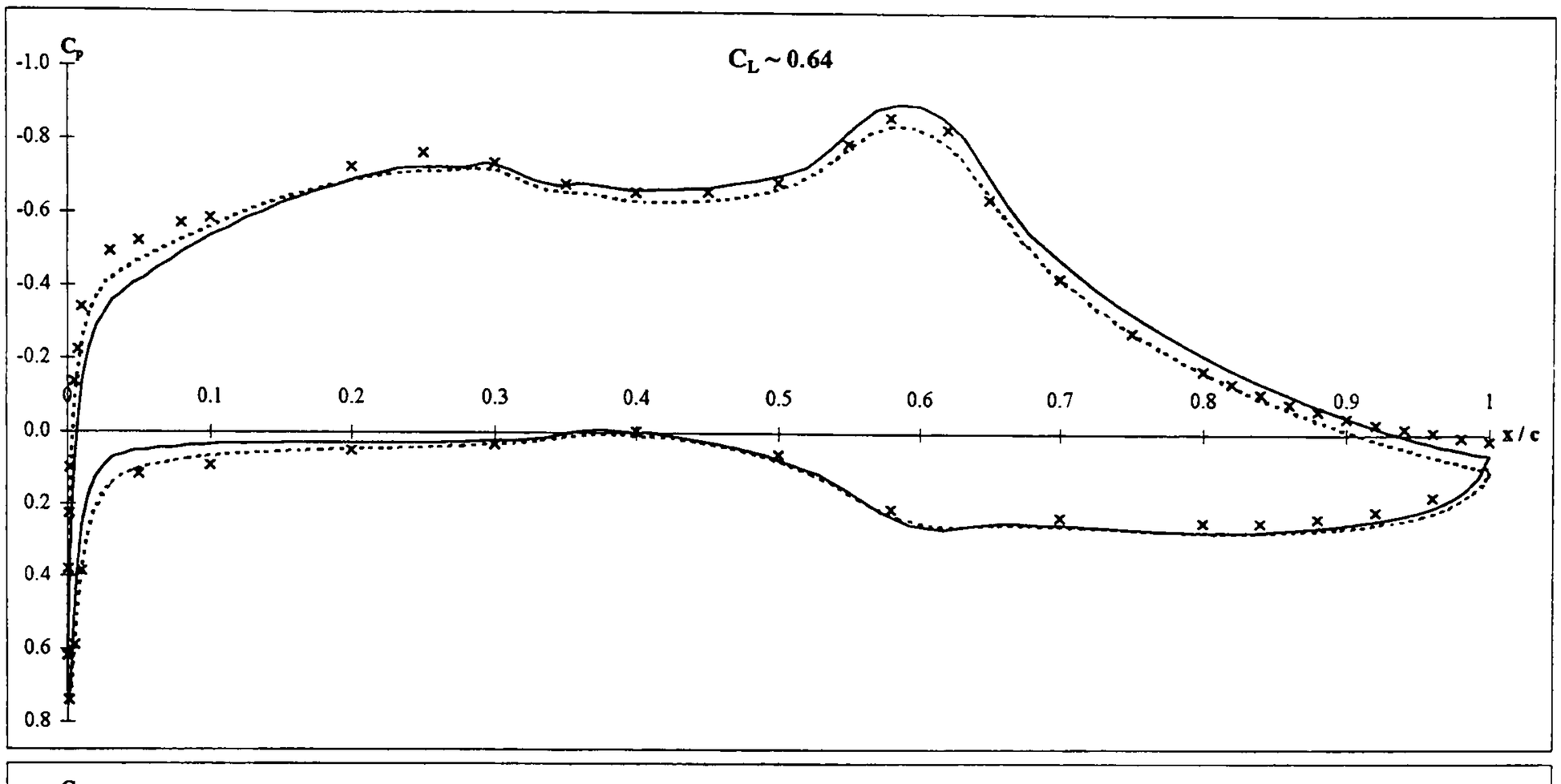

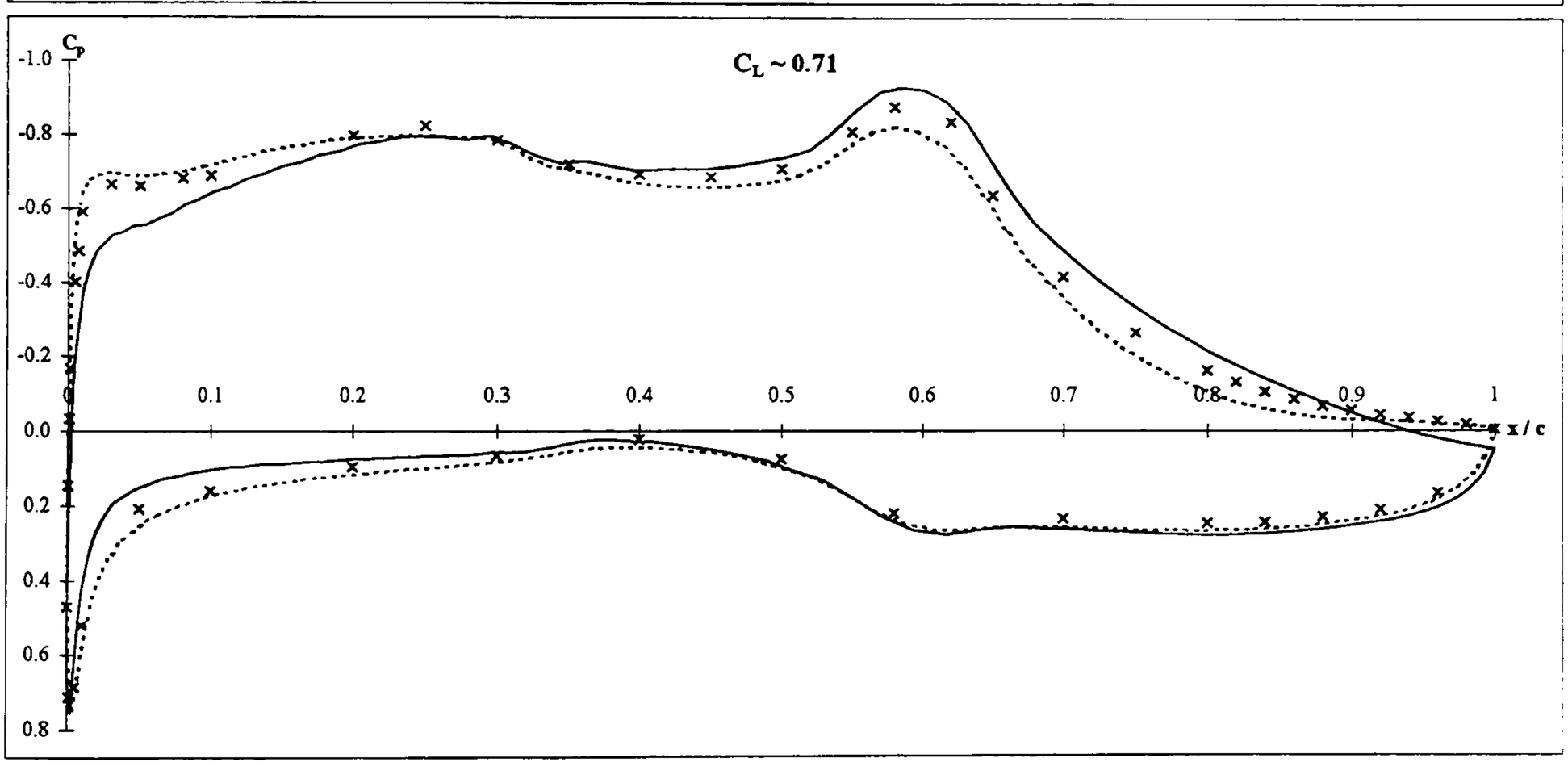

Key

×	Measured η = 0.59b
———	BVGK
·····	VFP η = 0.63b

Figure 5-25 cont.: Comparison of the measured and calculated pressure distributions for the DERA swept wing. $\Lambda = 30°$, $Re_c = 2.9 \times 10^6$.

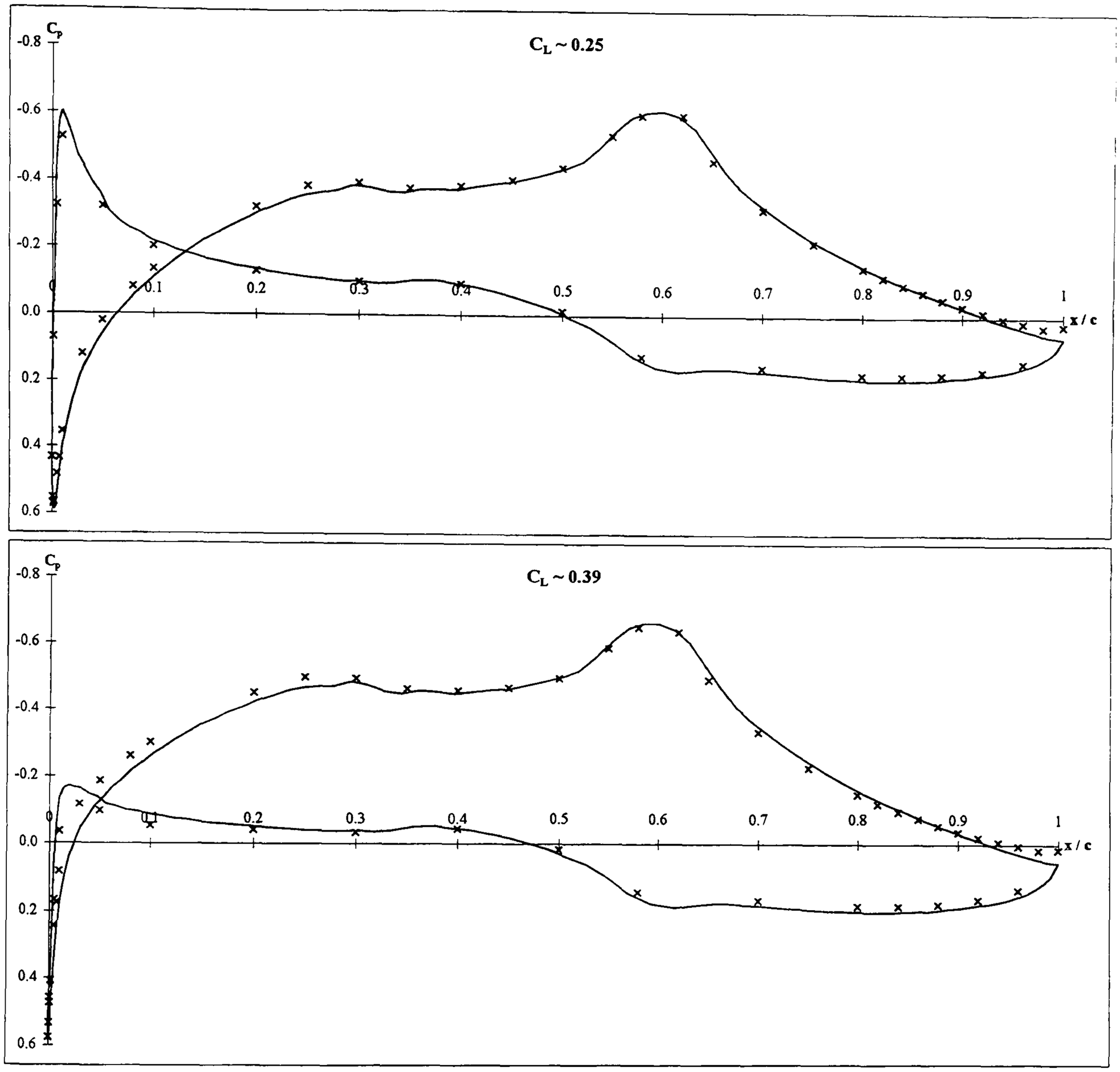

Figure 5-26: Comparison of the measured and calculated pressure distributions for the DERA swept wing. $\Lambda = 40°$, $Re_c = 3.3 \times 10^6$.

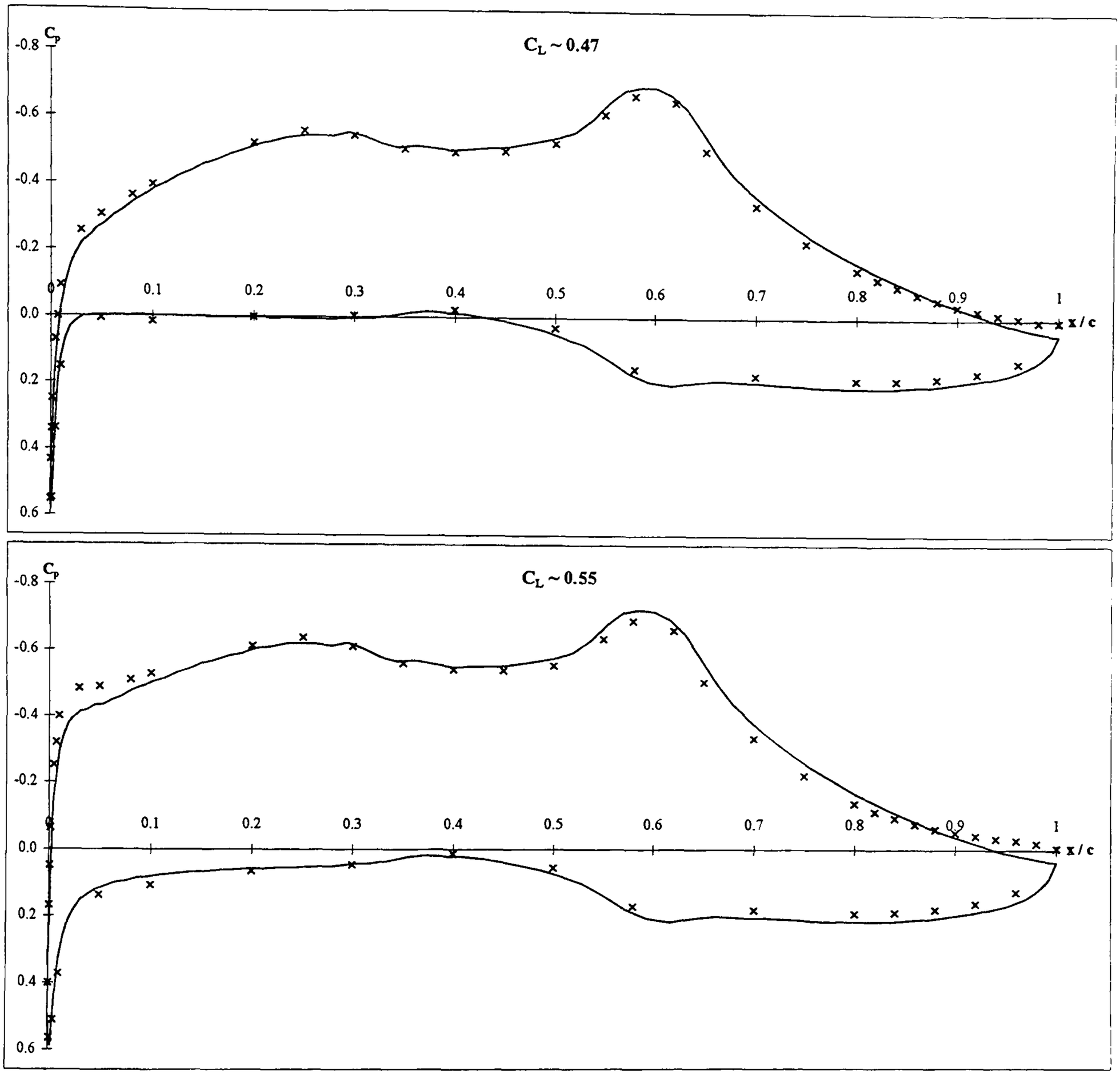

Figure 5-26 cont.: Comparison of the measured and calculated pressure distributions for the DERA swept wing. $\Lambda = 40°$, $Re_c = 3.3 \times 10^6$.

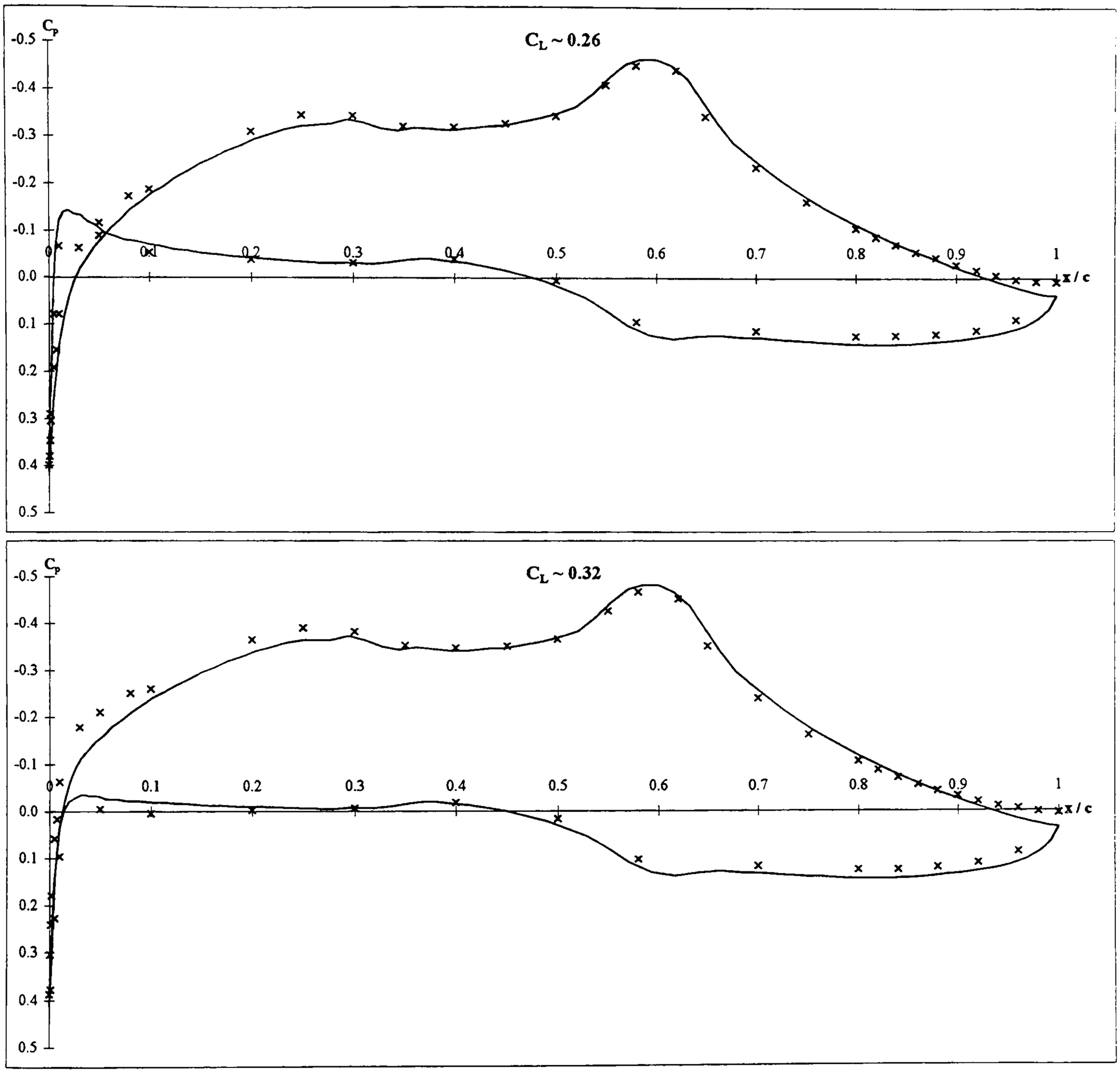

Figure 5-27: Comparison of the measured and calculated pressure distributions for the DERA swept wing. $\Lambda = 50°$, $Re_c = 3.9 \times 10^6$.

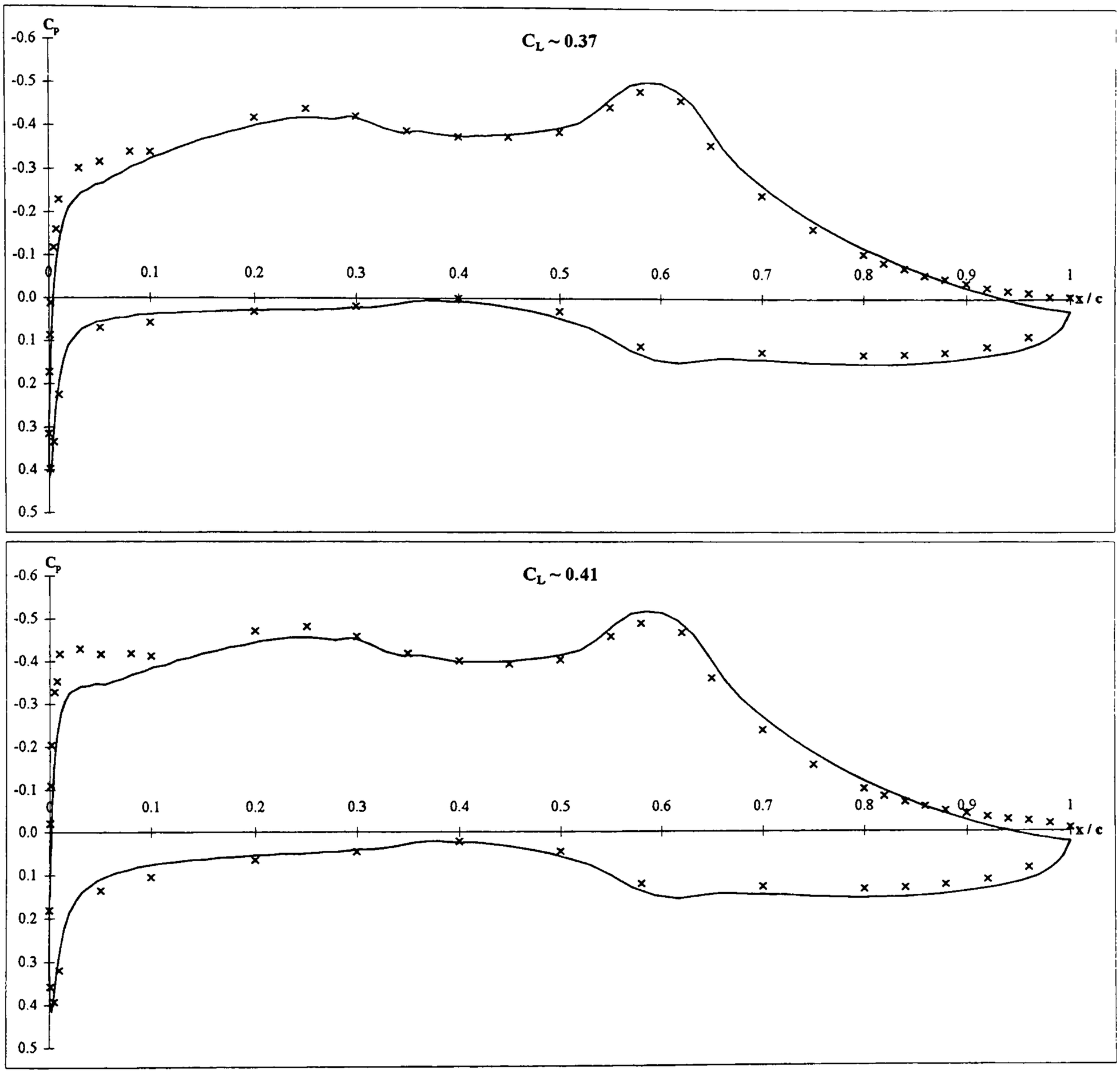

Figure 5-27 cont.: Comparison of the measured and calculated pressure distributions for the DERA swept wing. $\Lambda = 50°$, $Re_c = 3.9 \times 10^6$.

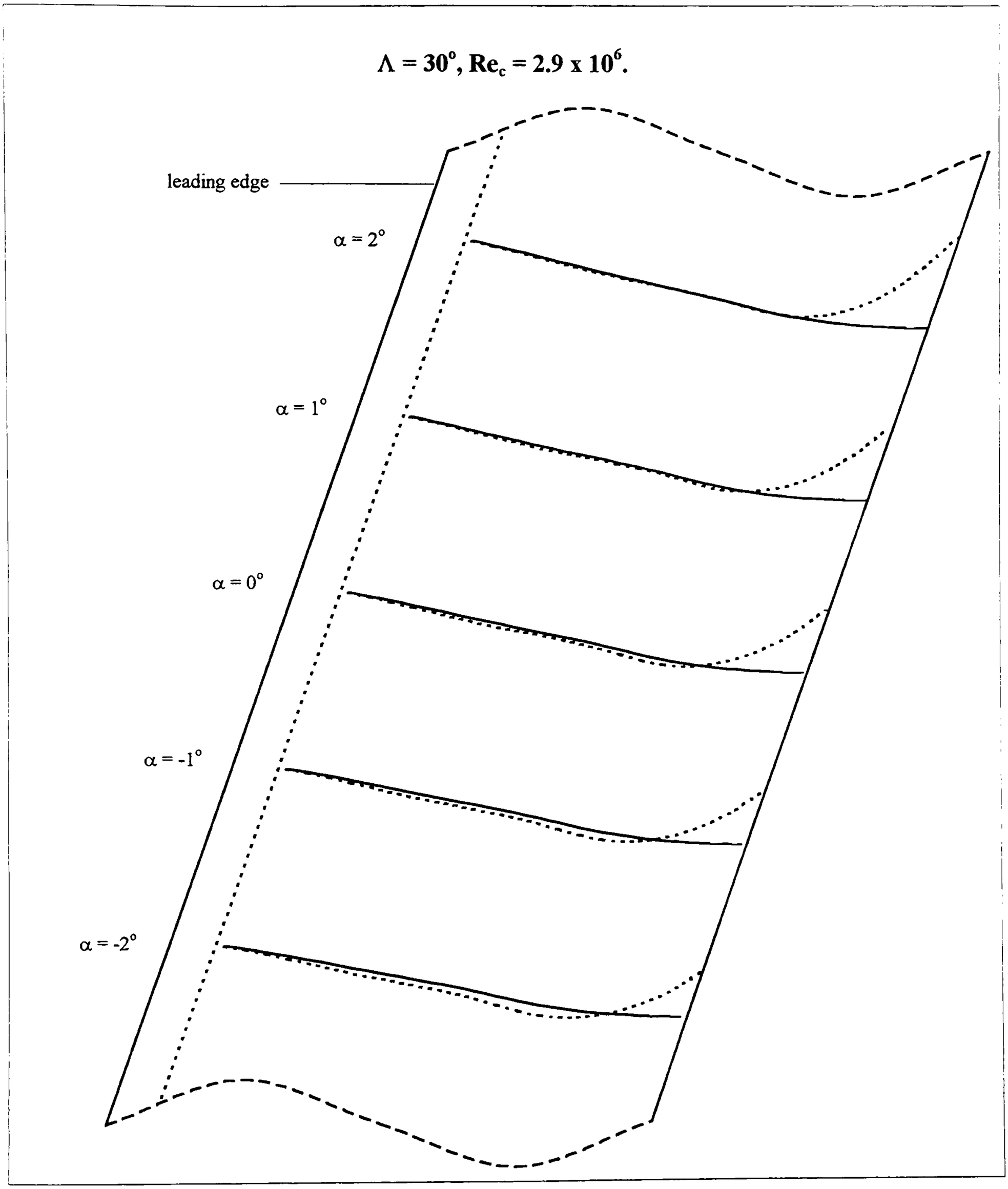

Figure 5-28a: Local freestream and surface flow streamlines on the DERA swept wing determined from TAPERBL using the BVGK pressure distributions.

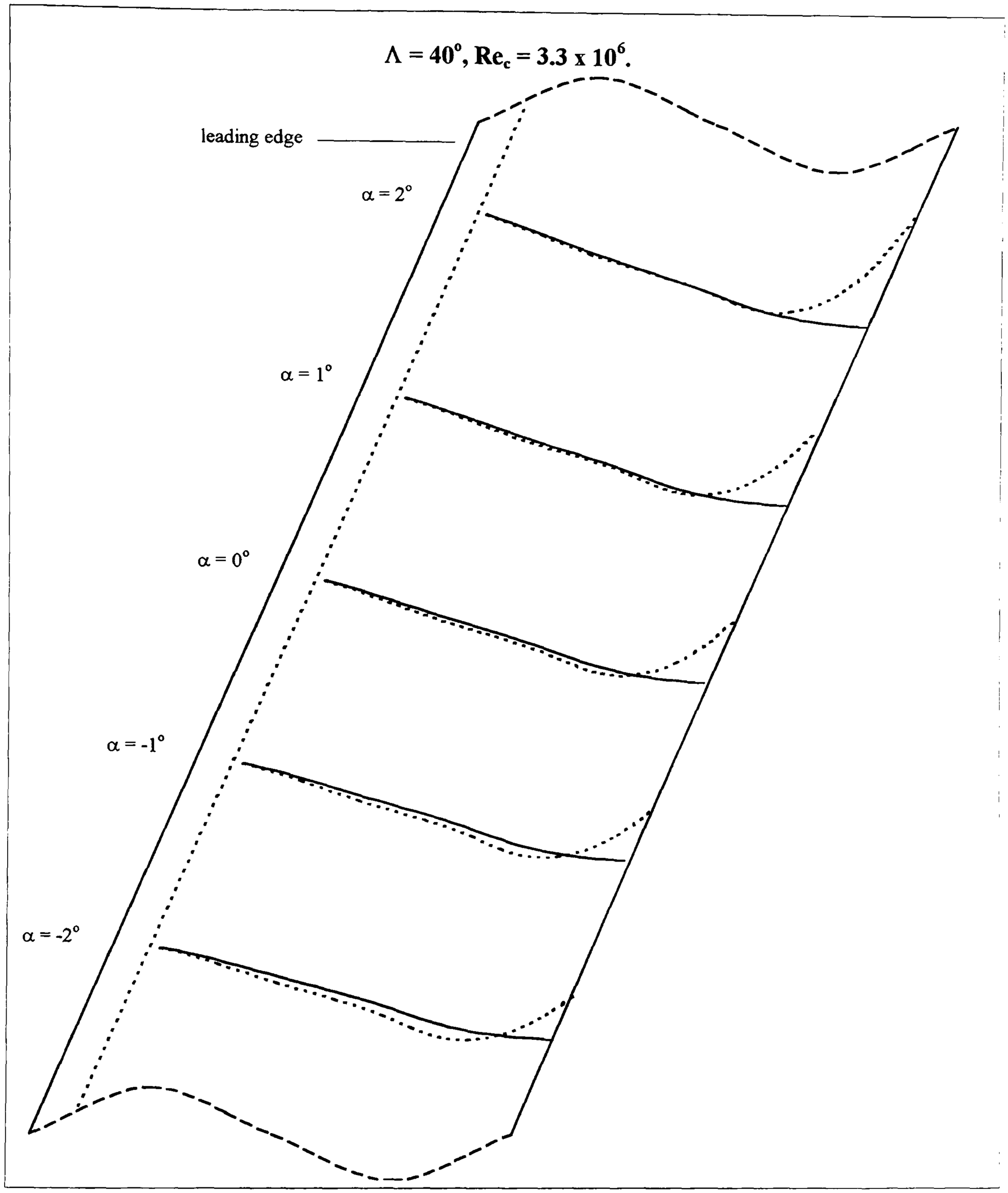

Figure 5-28b: Local freestream and surface flow streamlines on the DERA swept wing determined from TAPERBL using the BVGK pressure distributions.

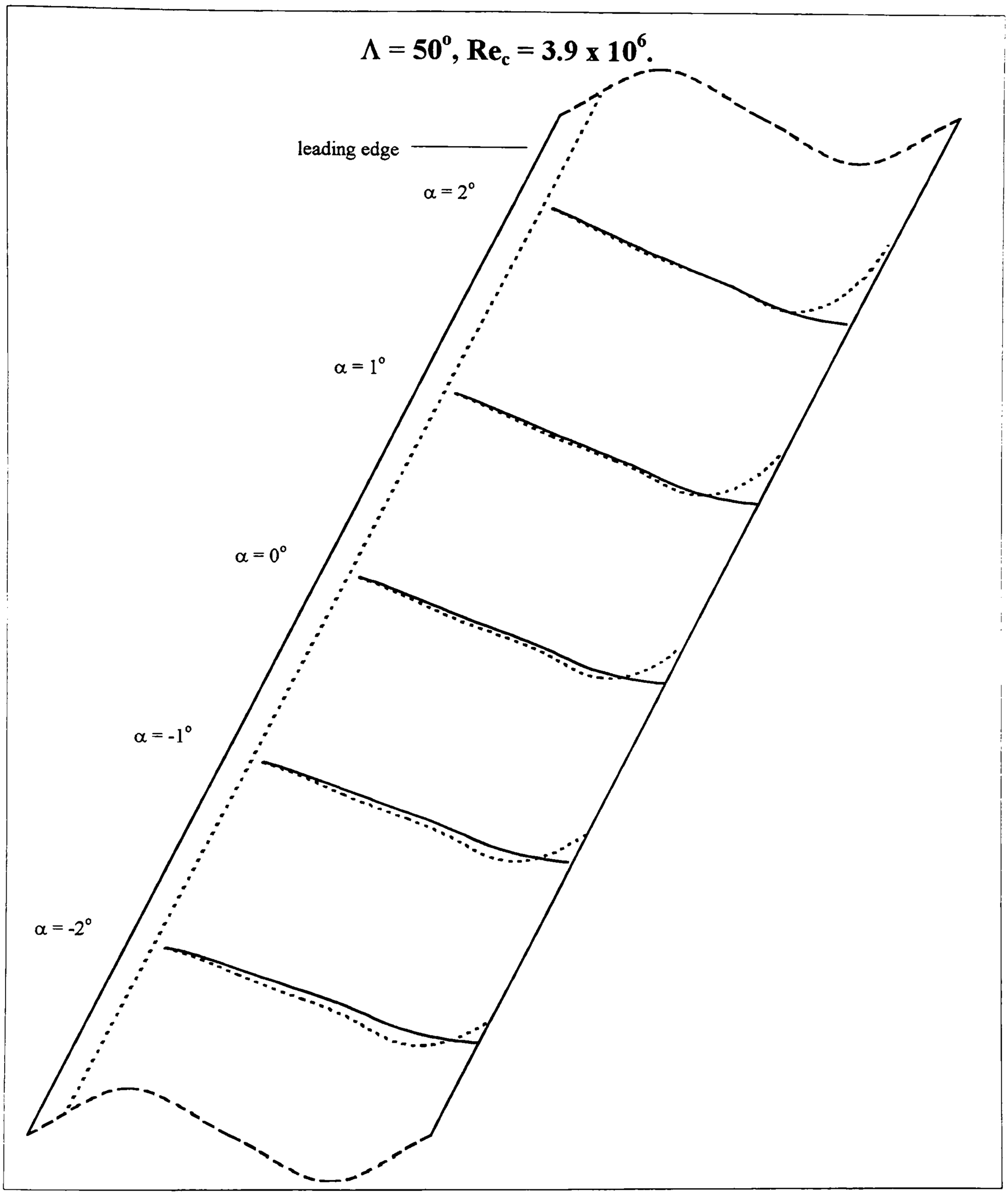

Figure 5-28c: Local freestream and surface flow streamlines on the DERA swept wing determined from TAPERBL using the BVGK pressure distributions.

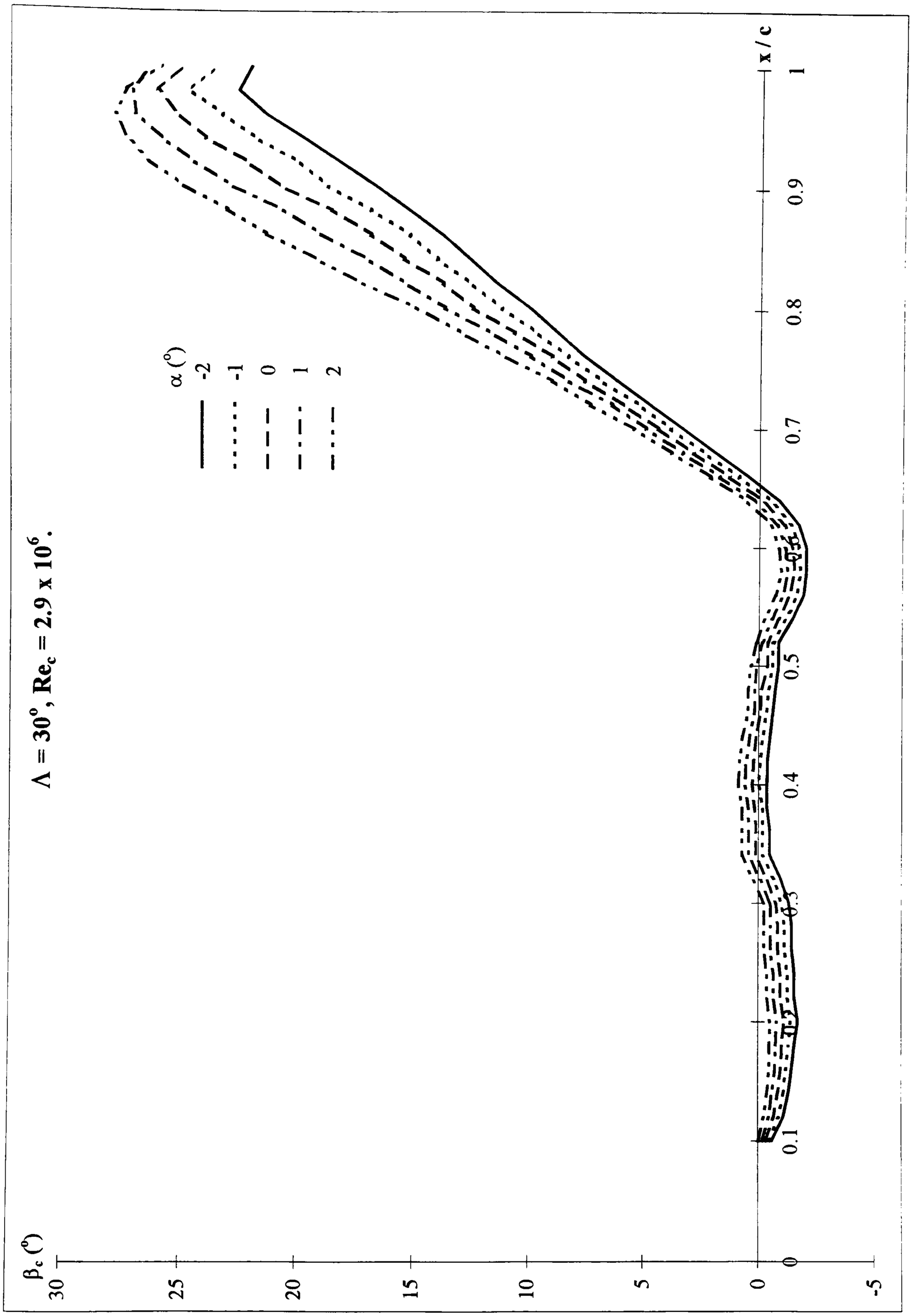

Figure 5-28d: Boundary layer twist development with chordwise position and incidence on the DERA swept wing determined from TAPERBL using the BVGK pressure distributions.

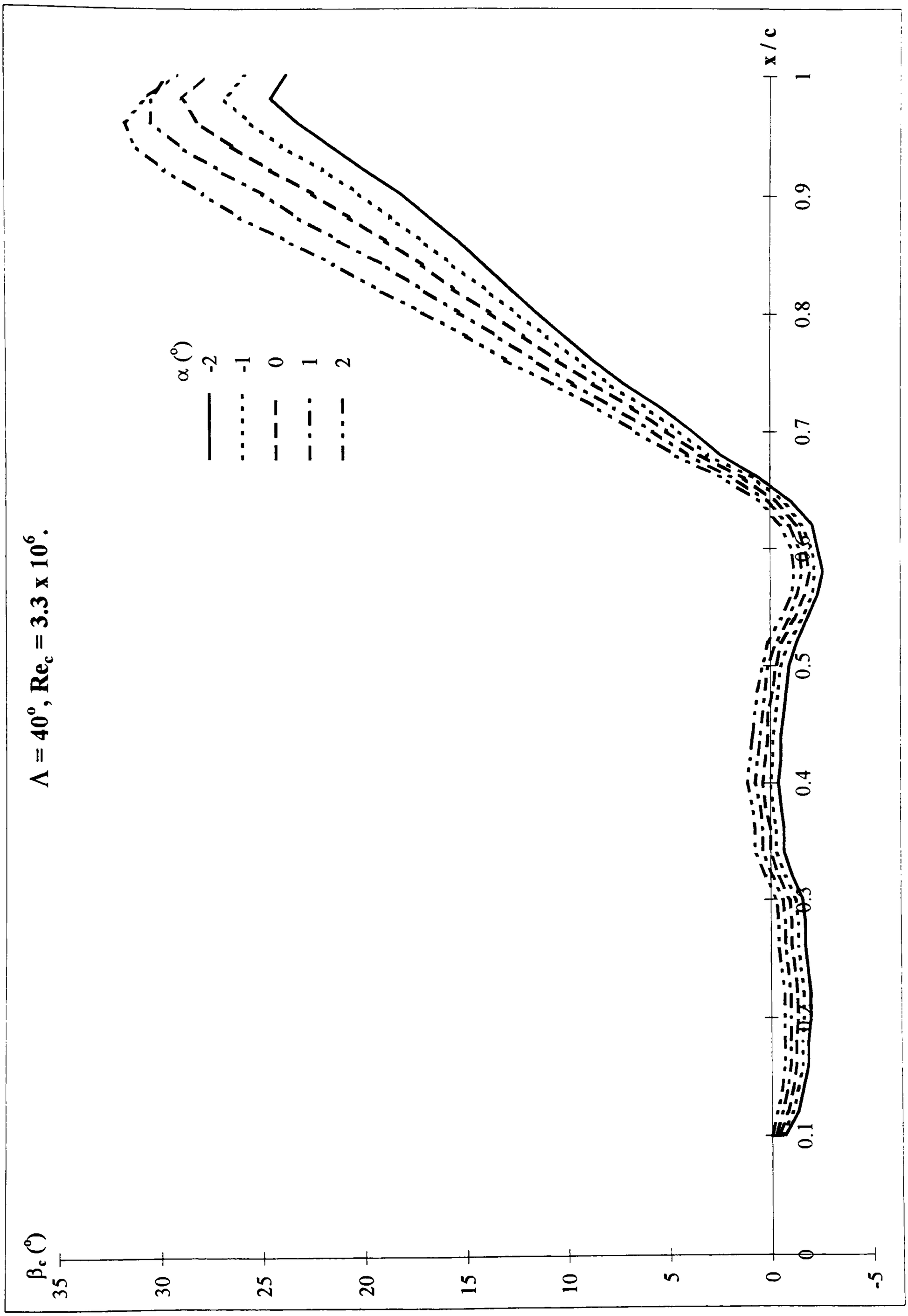

$\Lambda = 40^o$, $Re_c = 3.3 \times 10^6$.

Figure 5-28e: Boundary layer twist development with chordwise position and incidence on the DERA swept wing determined from TAPERBL using the BVGK pressure distributions.

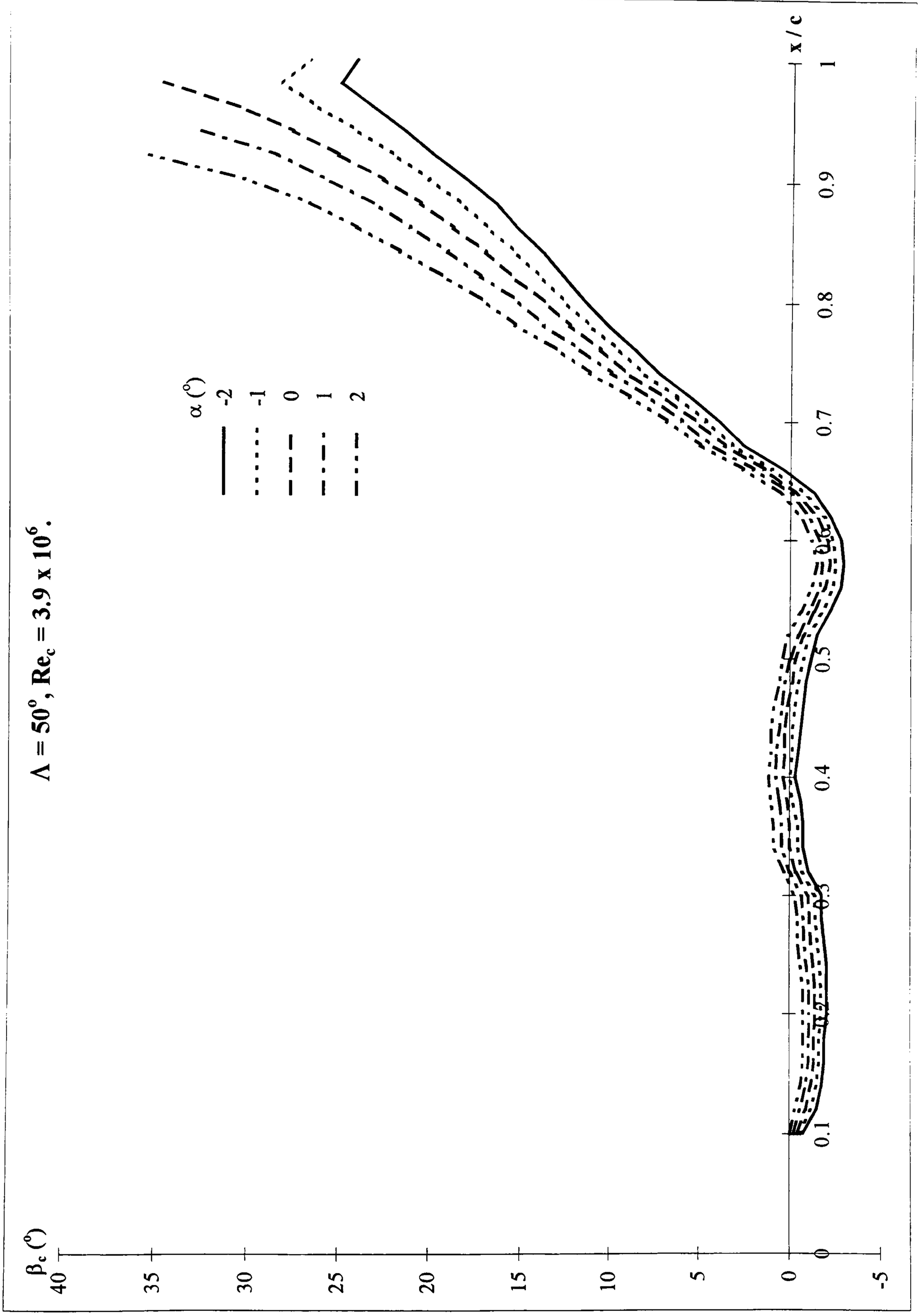

Figure 5-28f: Boundary layer twist development with chordwise position and incidence on the DERA swept wing determined from TAPERBL using the BVGK pressure distributions.

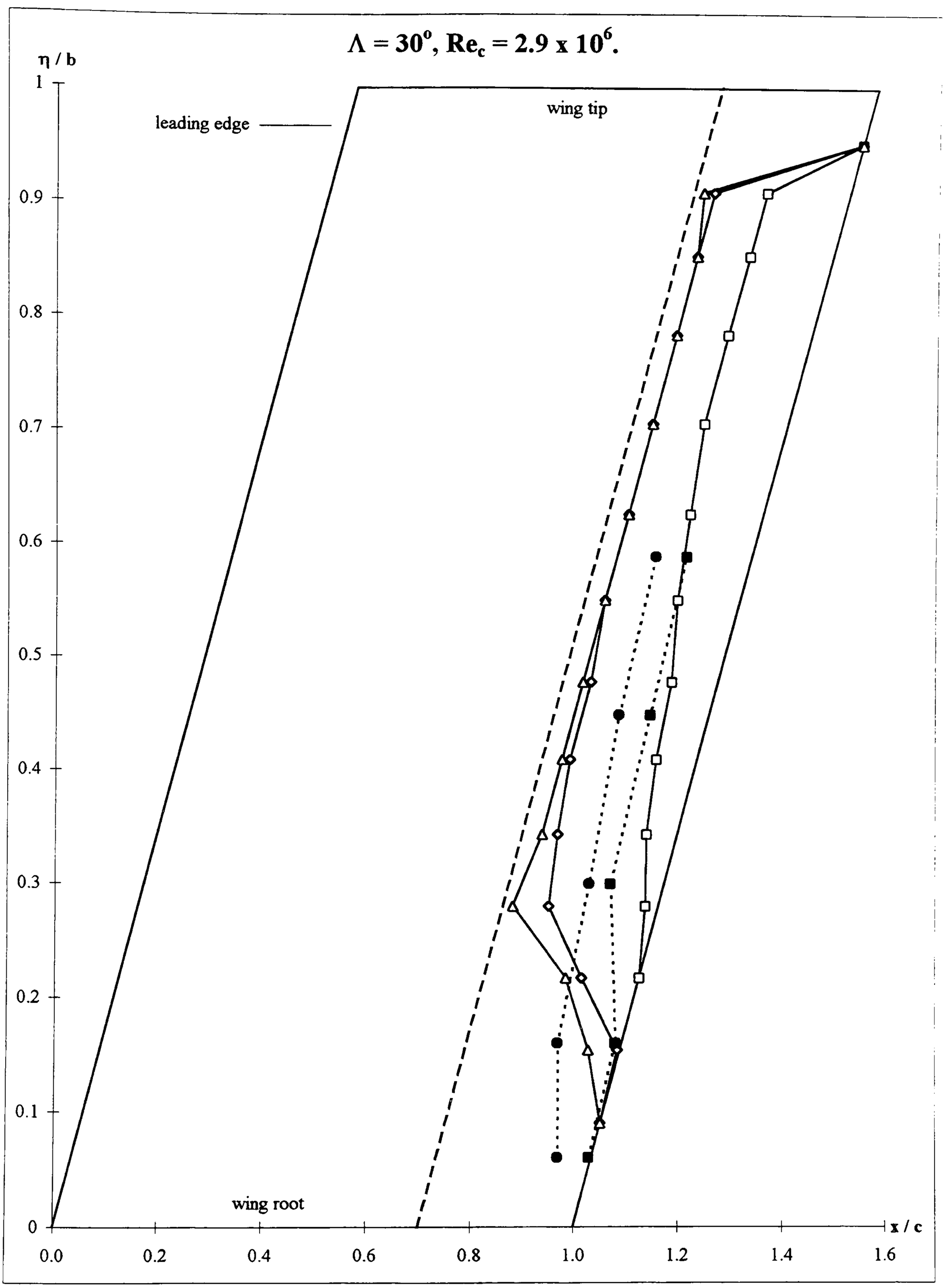

Figure 5-29: Separation line development on the DERA swept wing determined from VFP skin friction data and the measured pressure distributions.

$\Lambda = 40^o$, $\alpha = 0.4^o$, $Re_c = 3.3 \times 10^6$.

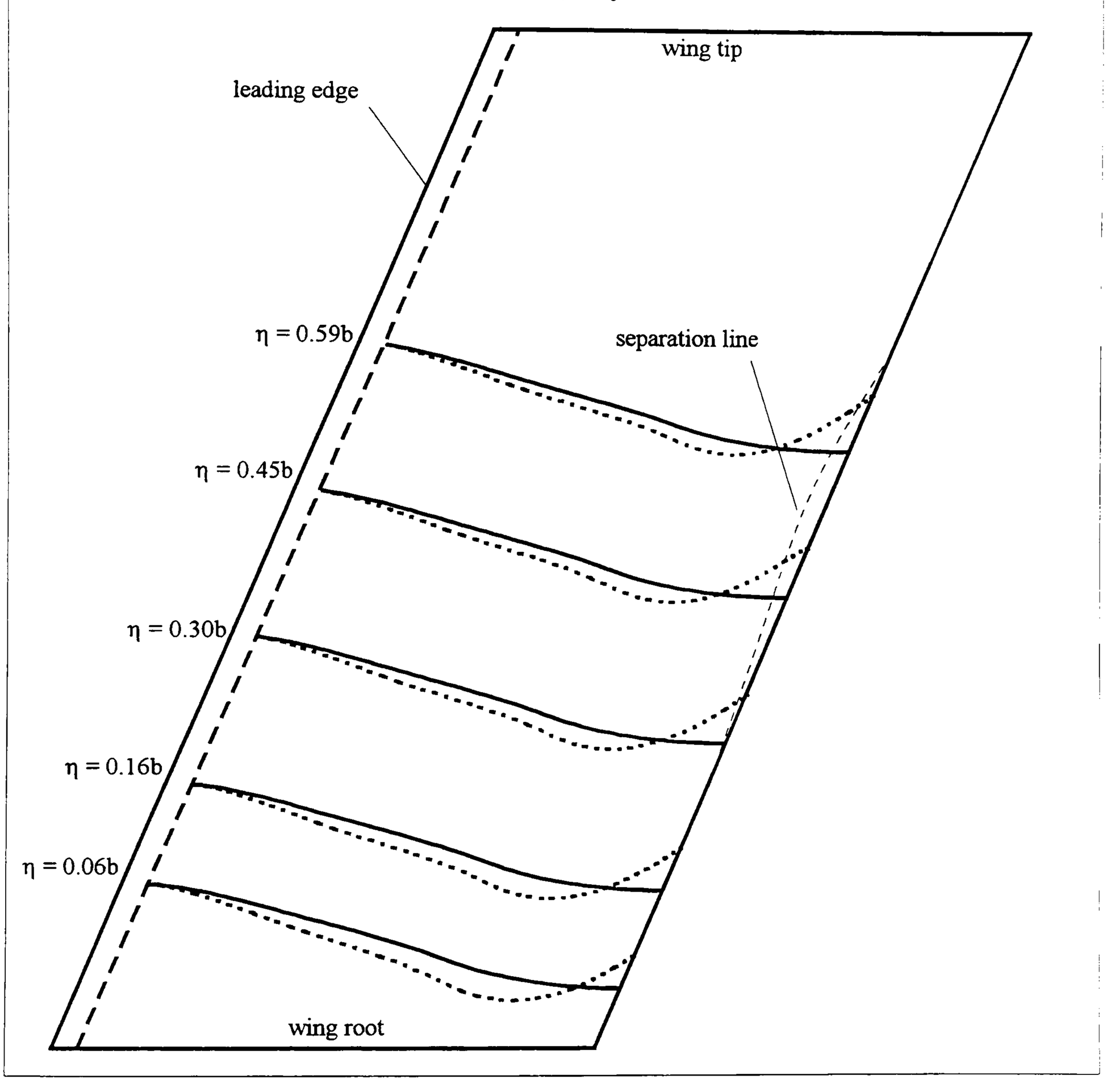

Key

local freestream flow

surface flow

Figure 5-30: Local freestream and surface flow streamlines on the DERA swept wing determined from WAKELAG using the measured pressure distributions.

$\Lambda = 40^o$, $\alpha = 4.6^o$, $Re_c = 3.3 \times 10^6$.

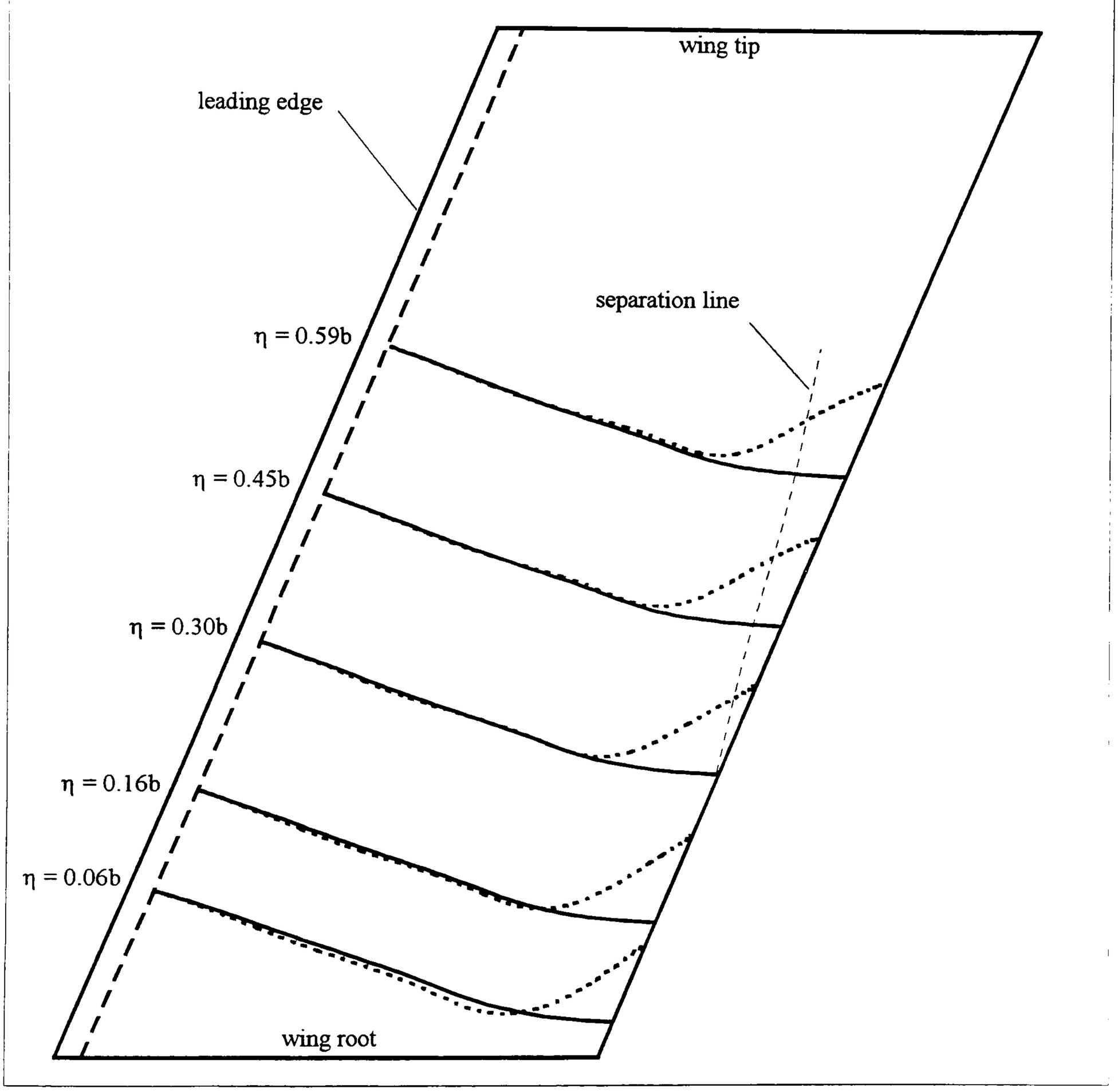

Figure 5-30 cont.: Local freestream and surface flow streamlines on the DERA swept wing determined from WAKELAG using the measured pressure distributions.

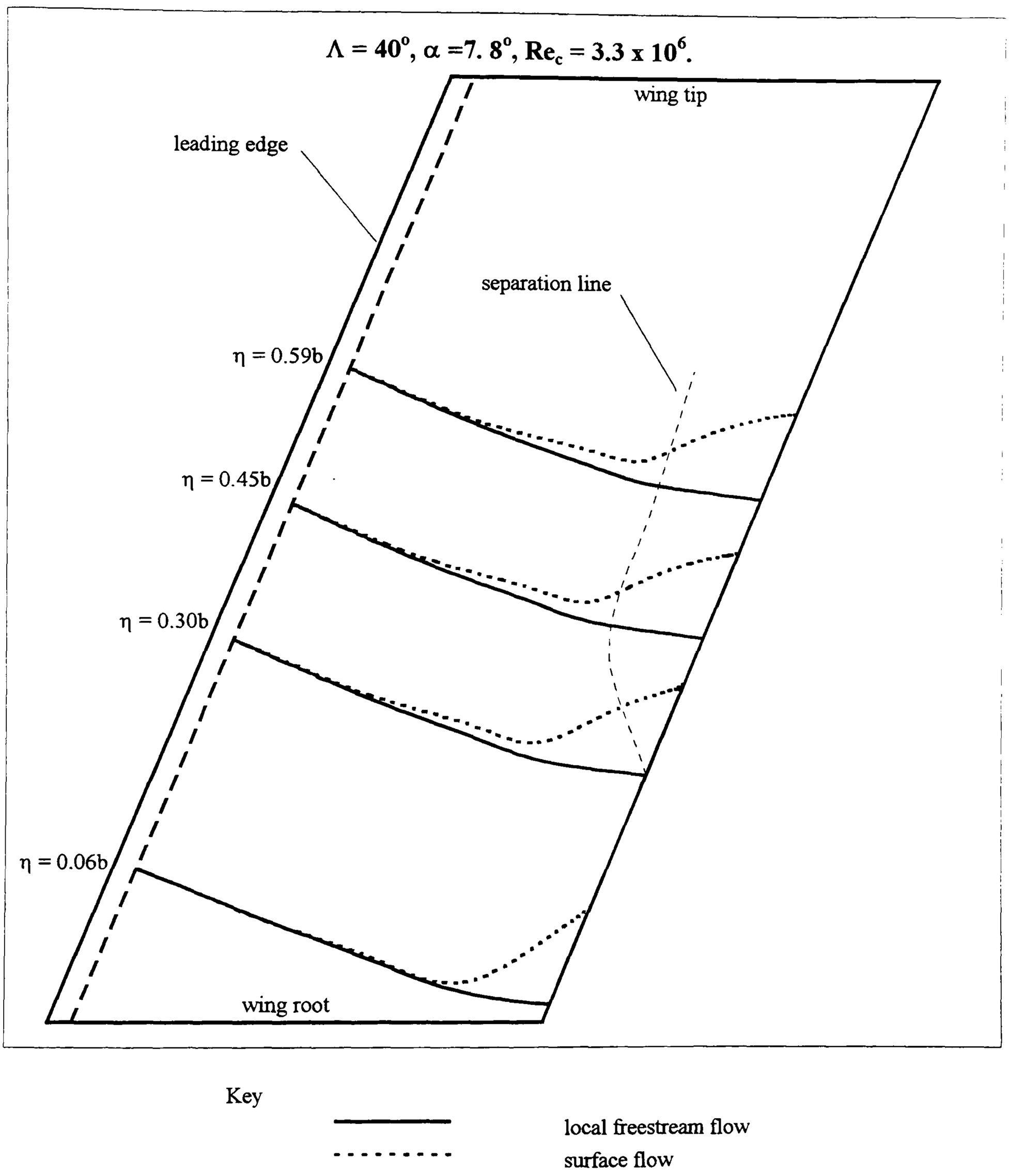

Figure 5-30 cont.: Local freestream and surface flow streamlines on the DERA swept wing determined from WAKELAG using the measured pressure distributions.

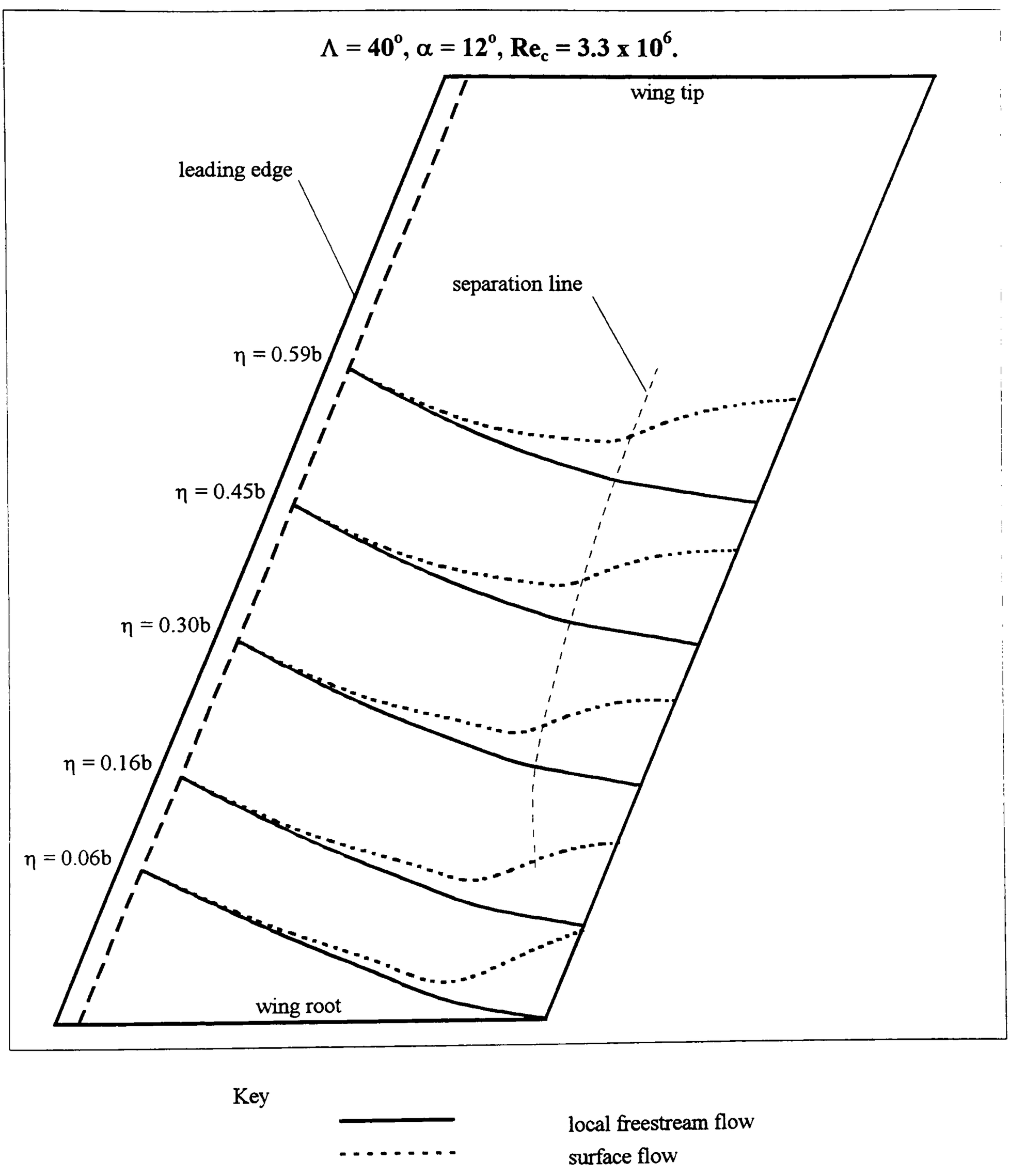

Figure 5-30 cont.: Local freestream and surface flow streamlines on the DERA swept wing determined from WAKELAG using the measured pressure distributions.

$\Lambda = 50^{o}$, $\alpha = 0.3^{o}$, $Re_c = 3.9 \times 10^{6}$.

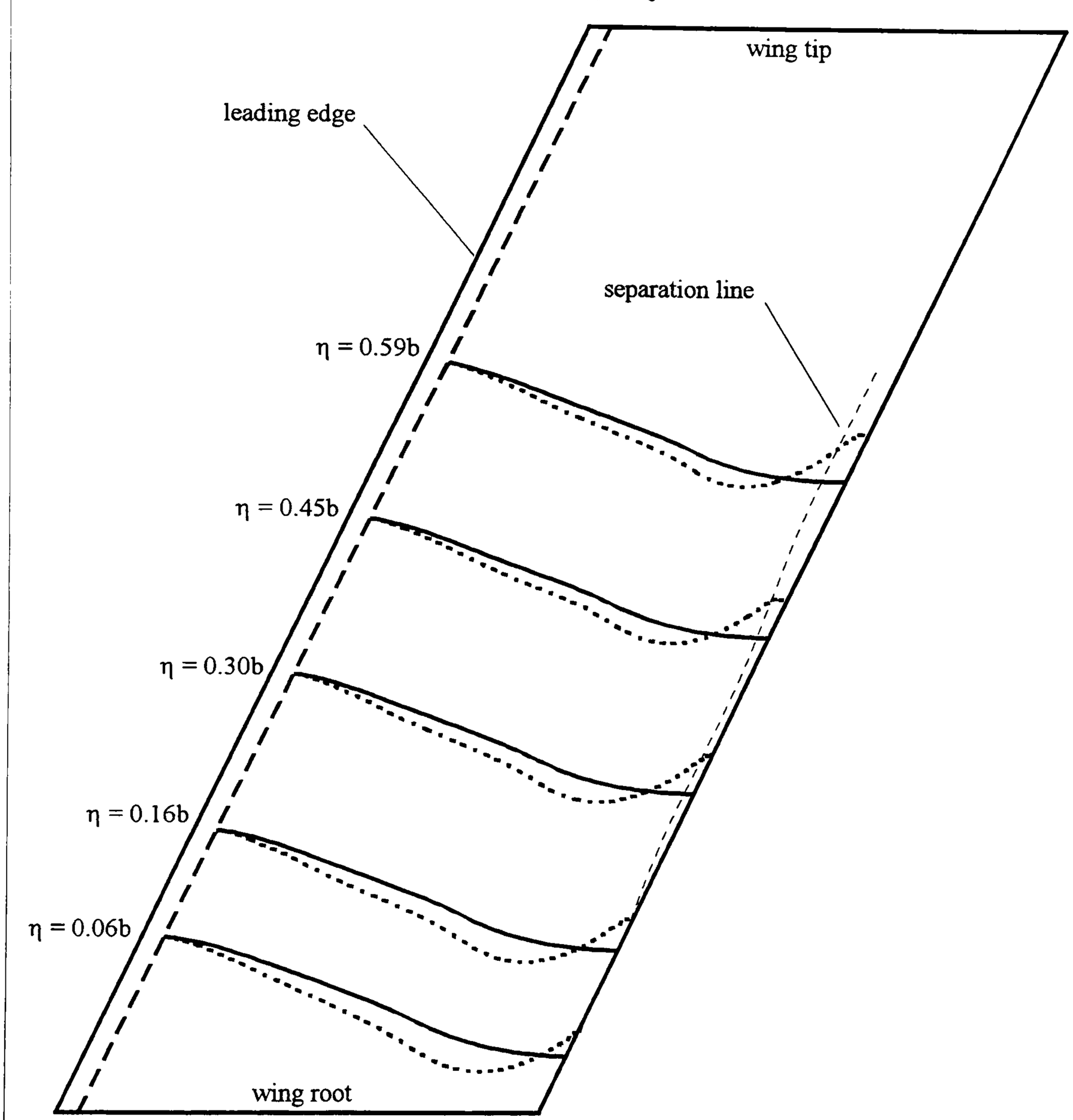

Figure 5-31: Local freestream and surface flow streamlines on the DERA swept wing determined from WAKELAG using the measured pressure distributions.

$\Lambda = 50^{o}$, $\alpha = 4.5^{o}$, $Re_c = 3.9 \times 10^{6}$.

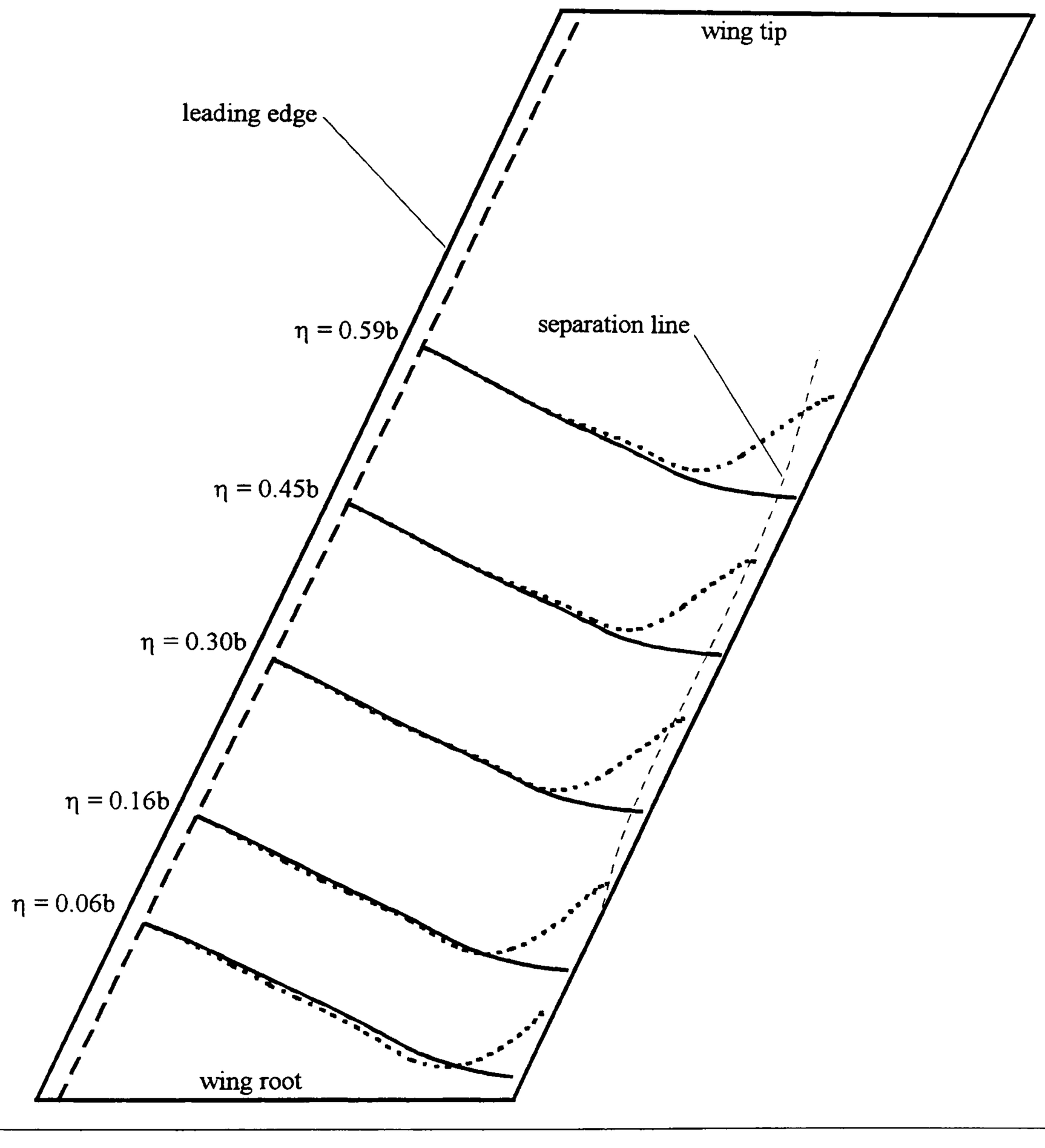

Figure 5-31 cont.: Local freestream and surface flow streamlines on the DERA swept wing determined from WAKELAG using the measured pressure distributions.

$\Lambda = 50^{o}$, $\alpha = 7.7^{o}$, $Re_c = 3.9 \times 10^{6}$.

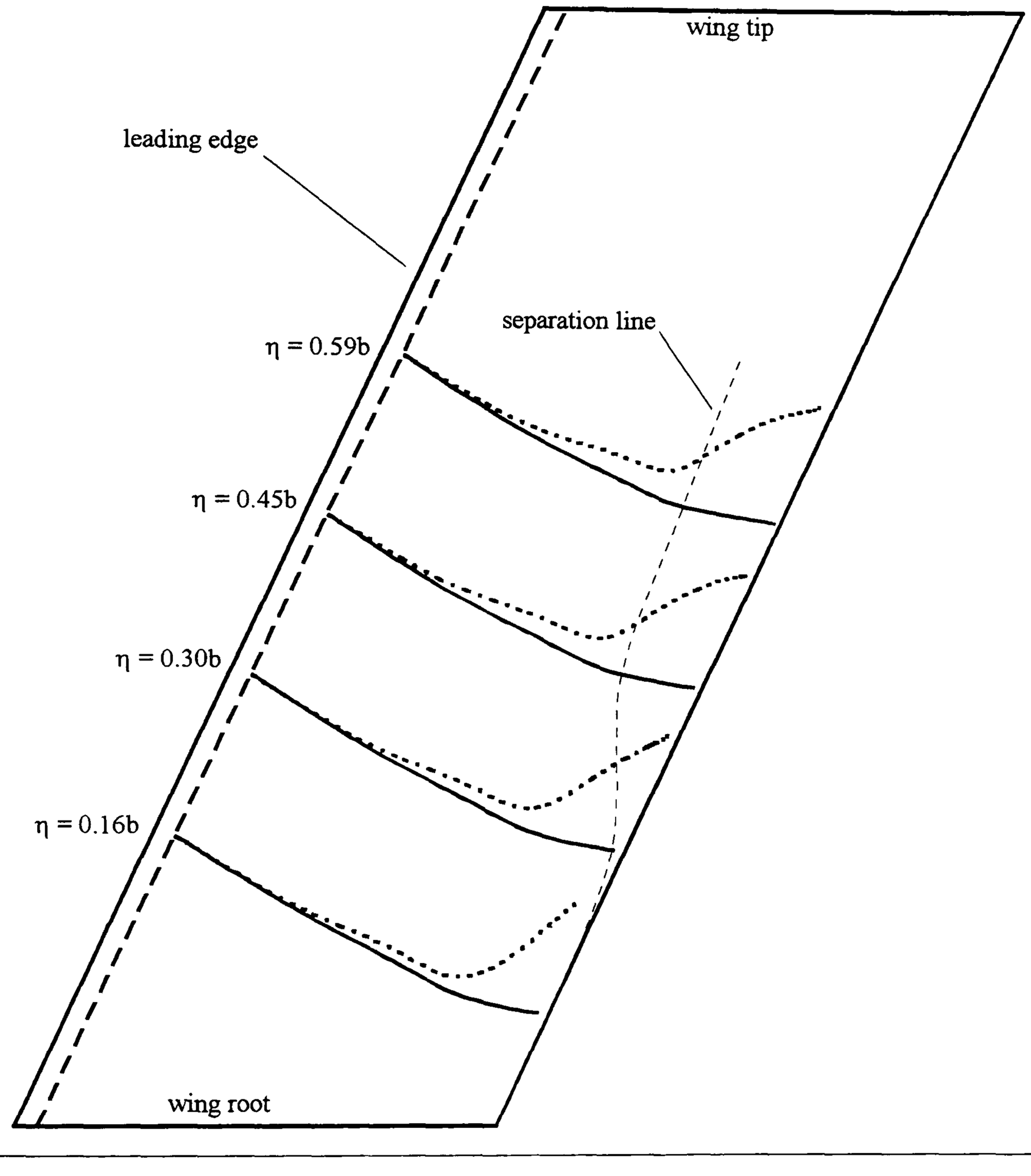

Figure 5-31 cont.: Local freestream and surface flow streamlines on the DERA swept wing determined from WAKELAG using the measured pressure distributions.

$\Lambda = 50^{o}$, $\alpha = 10.8^{o}$, $Re_c = 3.9 \times 10^{6}$.

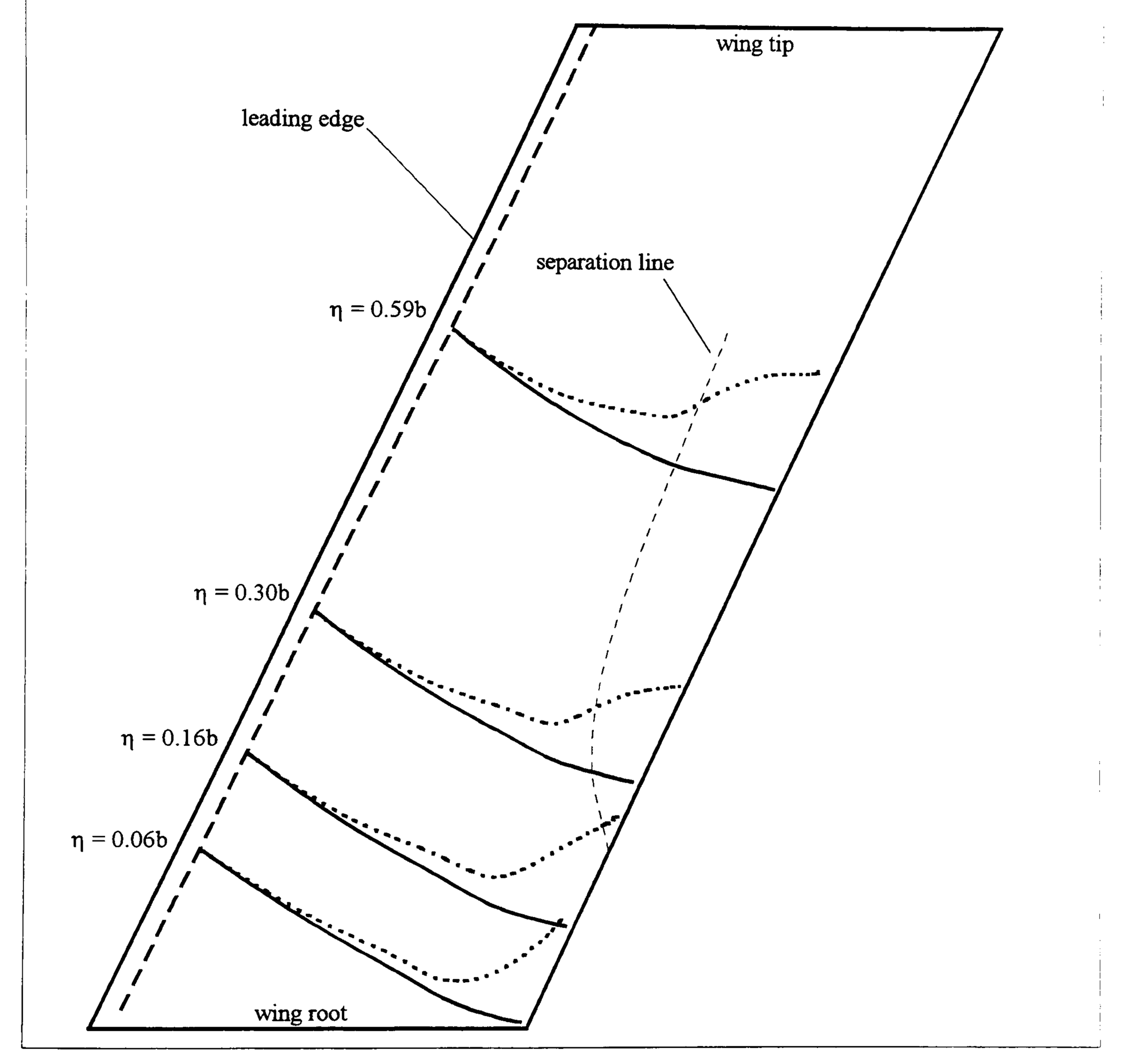

Figure 5-31 cont.: Local freestream and surface flow streamlines on the DERA swept wing determined from WAKELAG using the measured pressure distributions.

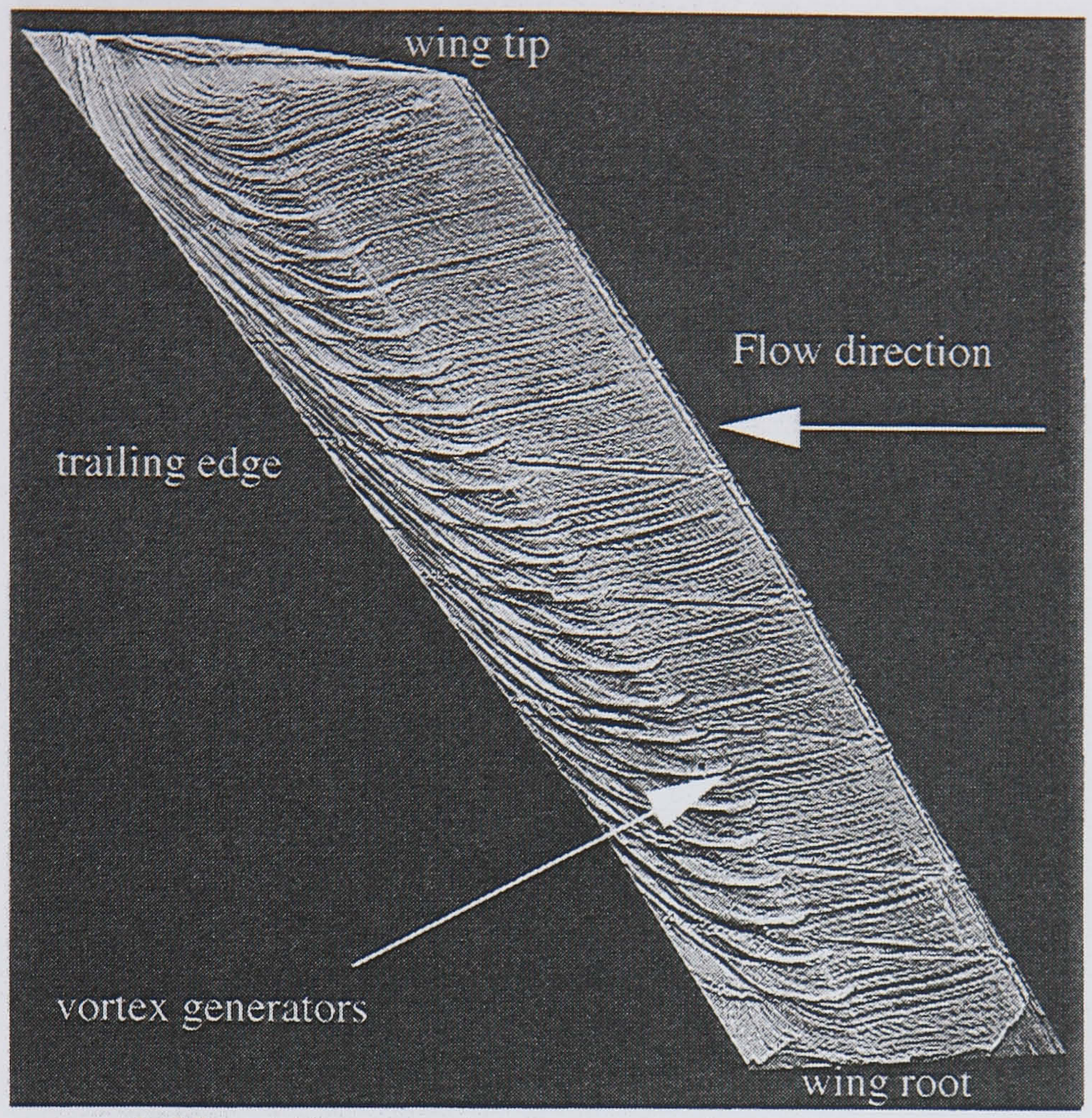

$x_v = 0.55c$

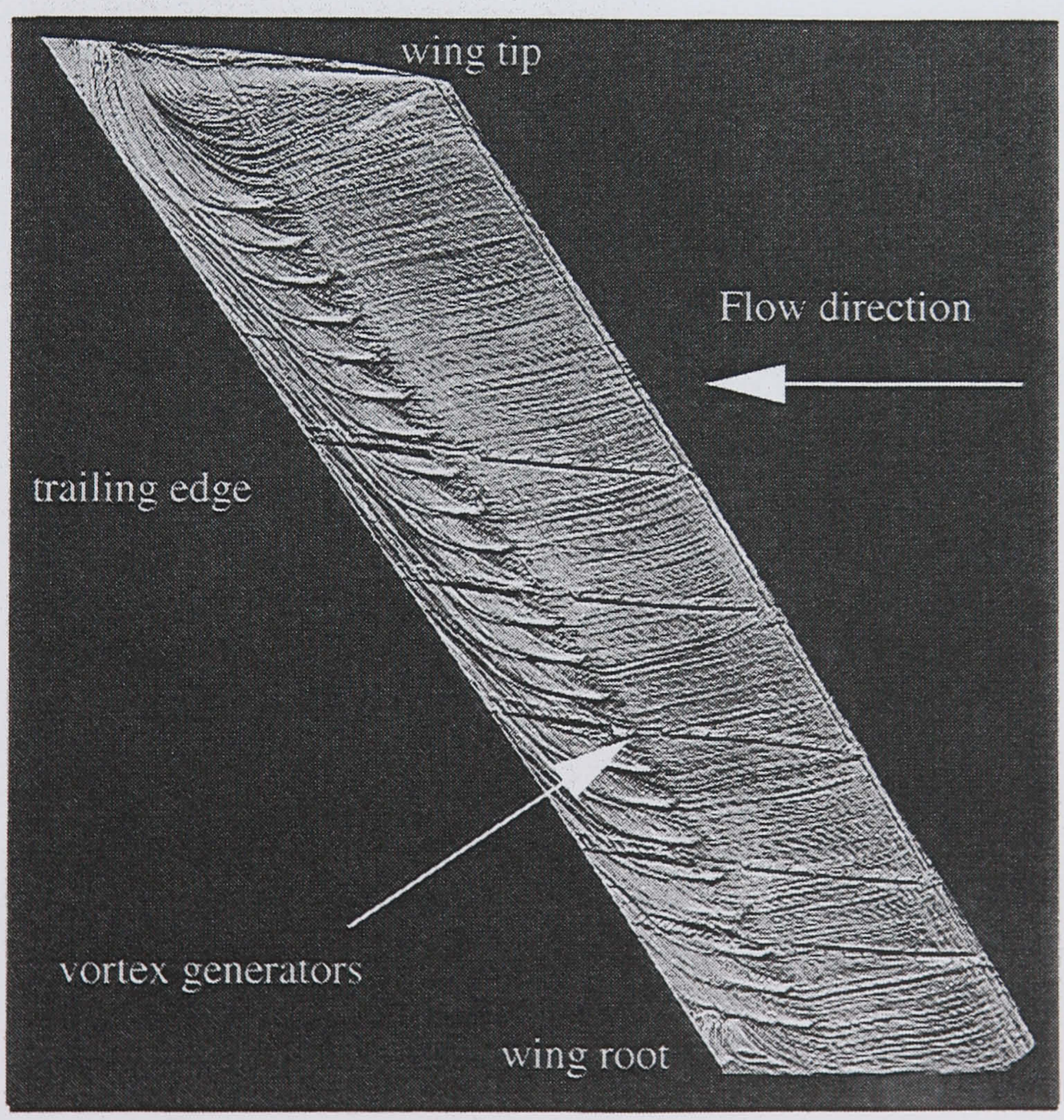

$x_v = 0.65c$

Figure 5-32: Surface oil flow visualisation results for the DERA swept wing with a co-rotating array of cropped delta vane vortex generators.
$\Lambda = 40°$, $\alpha = 10°$, $Re_c = 3.3 \times 10^6$, $h = 0.0050c$, $\alpha_v = 25°$, $D = 20h$.

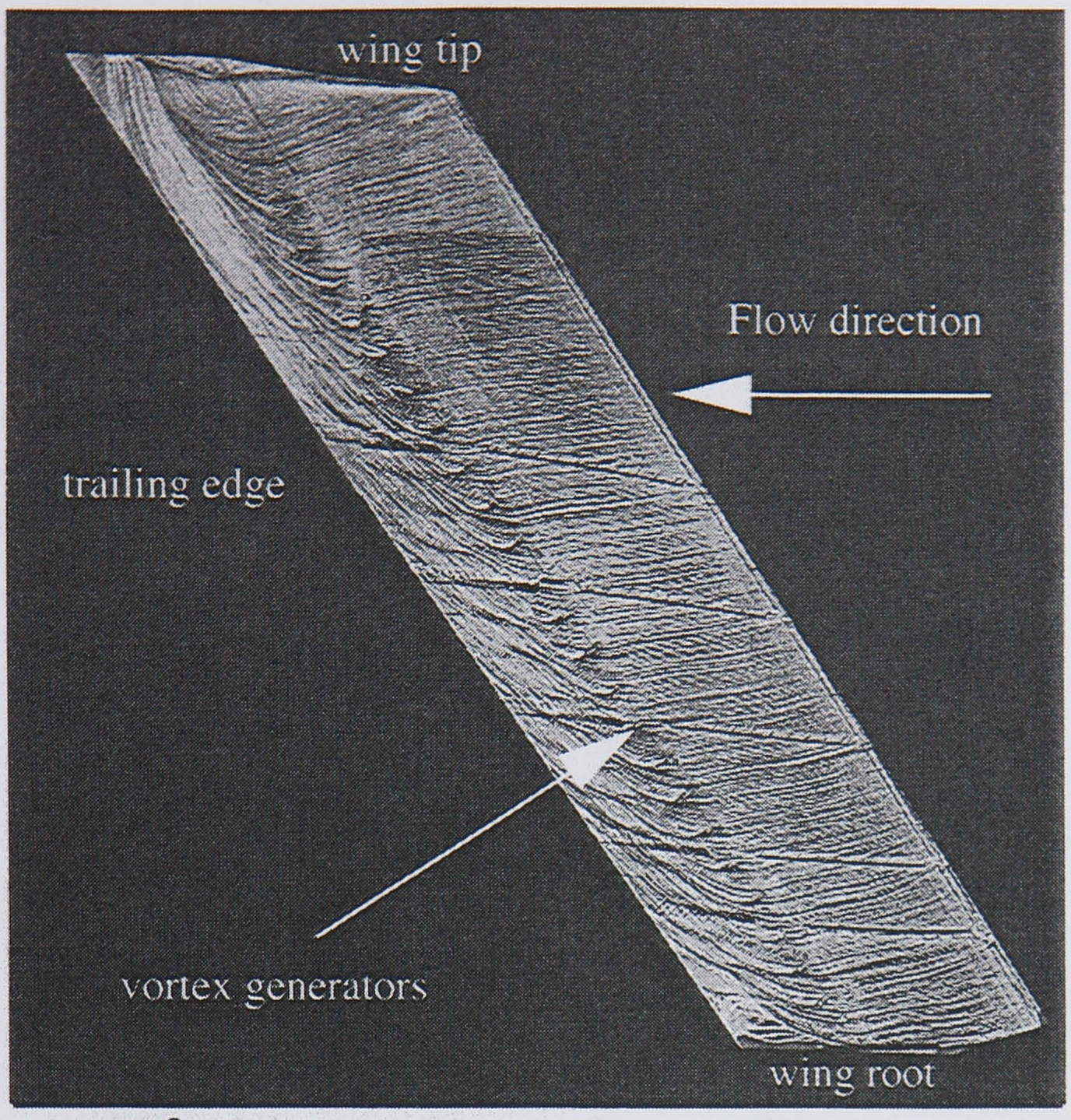

$\alpha_v = 20^o$

$\alpha_v = 30^o$

Figure 5-32 cont.: Surface oil flow visualisation results for the DERA swept wing with a co-rotating array of cropped delta vane vortex generators.
$\Lambda = 40°$, $\alpha = 10°$, $Re_c = 3.3 \times 10^6$, $h = 0.0126c$, $x_v = 0.65c$, $D = 8h$.

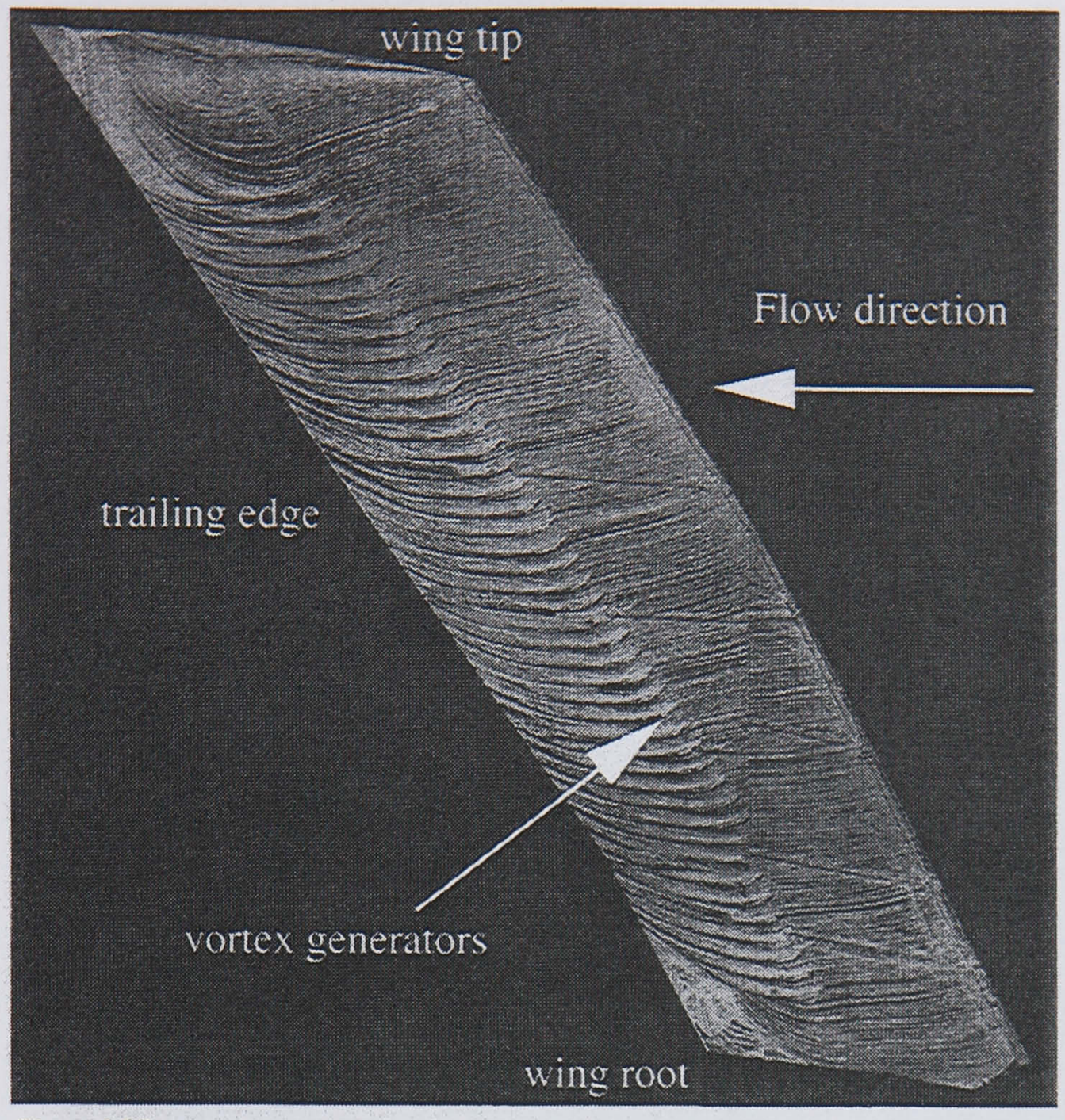

D = 10h

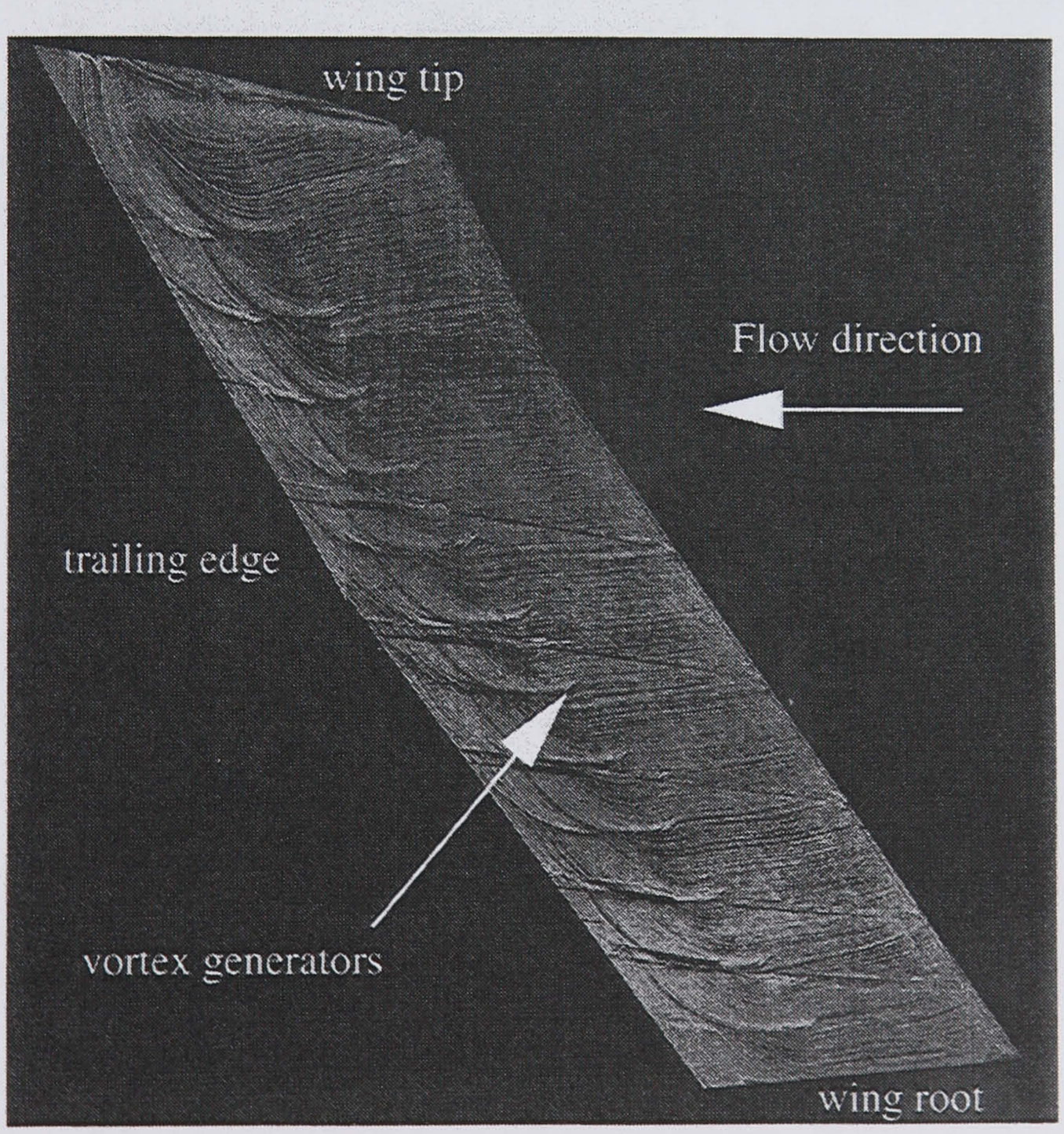

D = 40h

Figure 5-32 cont.: Surface oil flow visualisation results for the DERA swept wing with a co-rotating array of cropped delta vane vortex generators.
$\Lambda = 40°$, $\alpha = 10°$, $Re_c = 3.3 \times 10^6$, h = 0.0050c, $x_v = 0.55c$, $\alpha_v = 30°$.

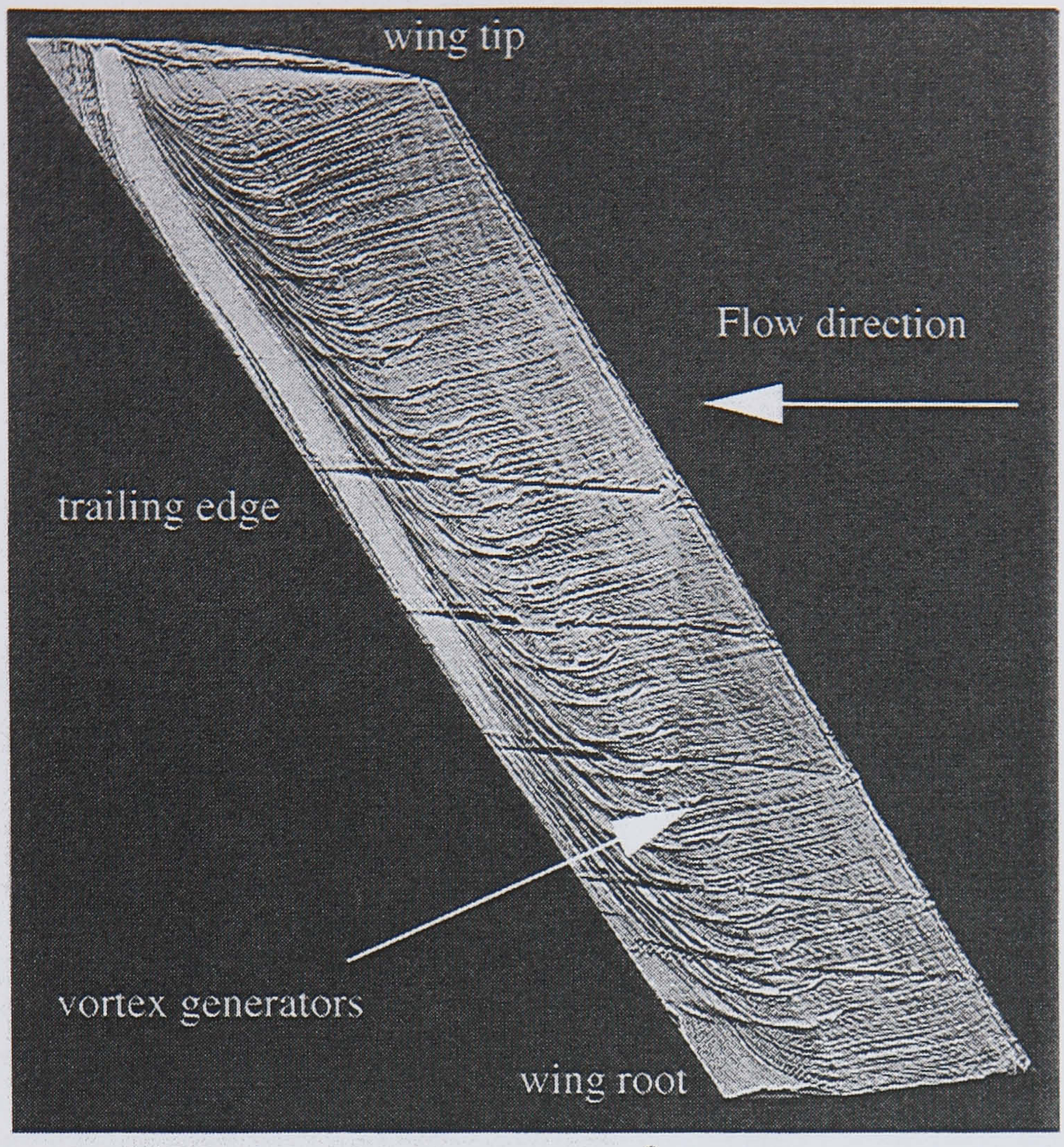

h = 0.0025c, x_v = 0.50c, $\alpha_v = 30^o$, D = 40h

Figure 5-32 cont.: Surface oil flow visualisation results for the DERA swept wing with a co-rotating array of cropped delta vane vortex generators.
$\Lambda = 40°$, $\alpha = 10°$, $Re_c = 3.3 \times 10^6$.

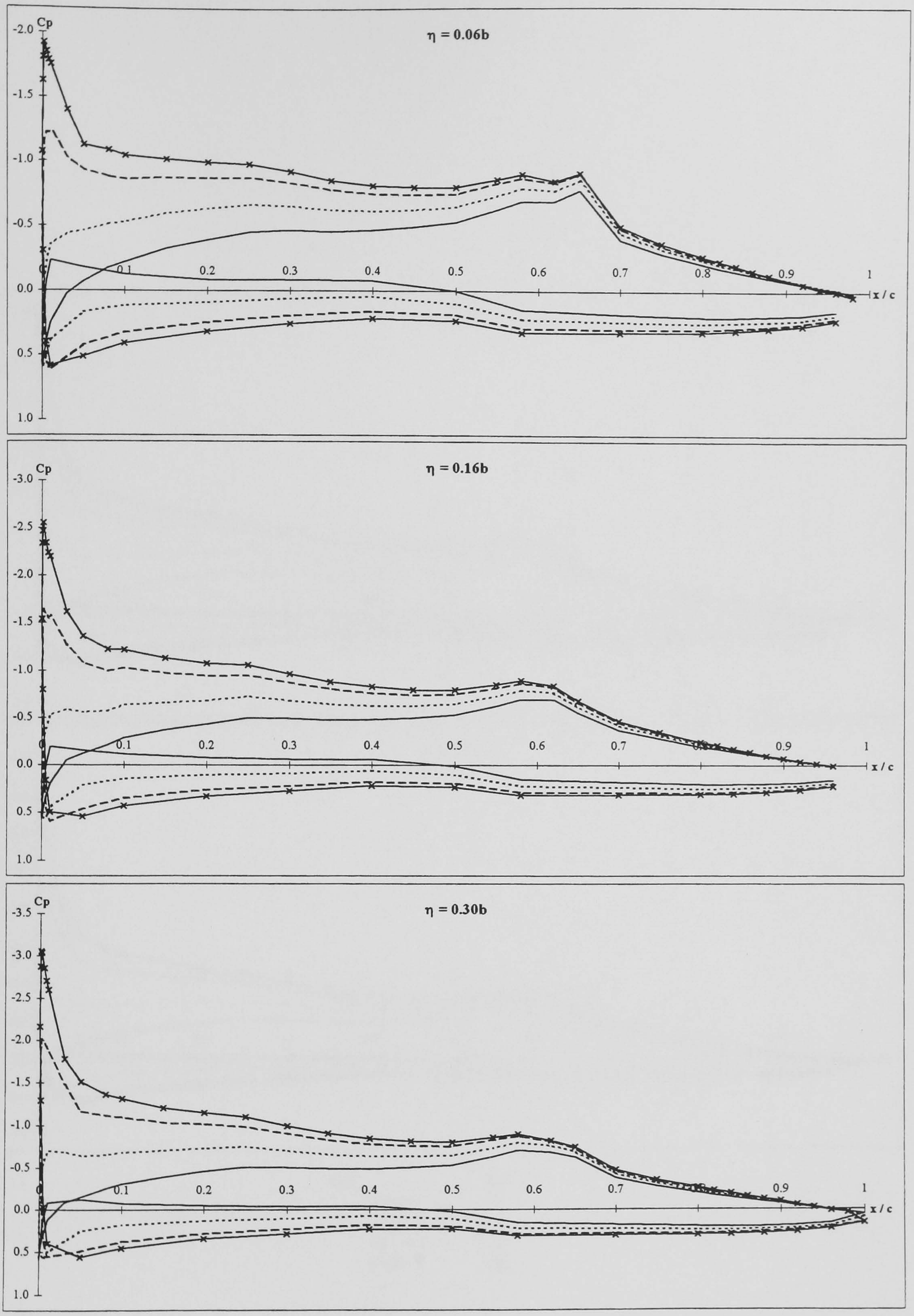

Figure 5-33: DERA swept wing pressure distributions with cropped delta vane vortex generators. $\Lambda = 40°$, $Re_c = 3.3 \times 10^6$, $h = 0.0126c$, $\alpha_v = 25°$, $x_v = 0.65c$, $D = 8h$.

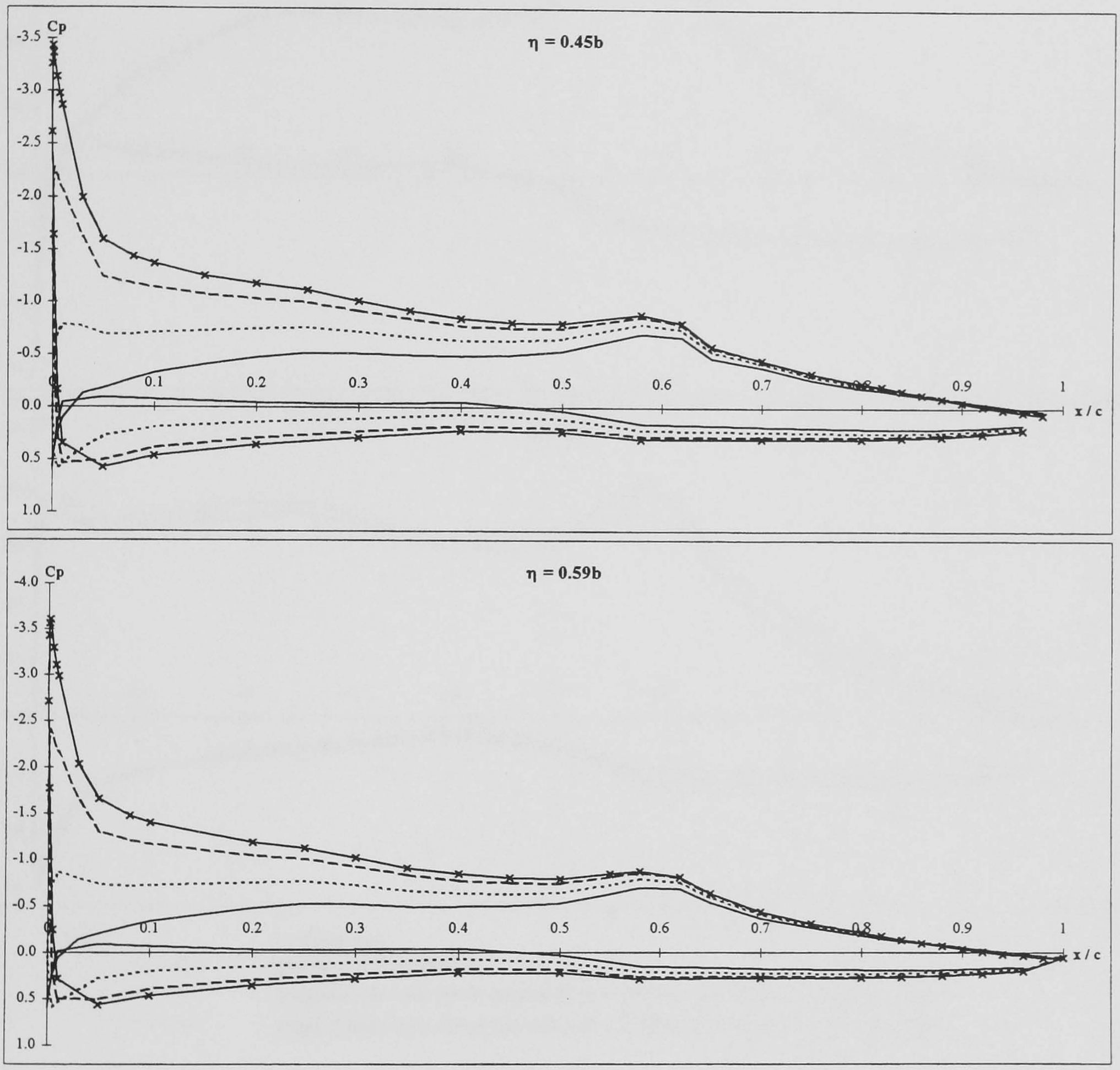

Key	α (°)
———	0
·····	4
- - - - -	8
—×—	12

Figure 5-33 cont.: DERA swept wing pressure distributions with cropped delta vane vortex generators. $\Lambda = 40°$, $Re_c = 3.3 \times 10^6$, $h = 0.0126c$, $\alpha_v = 25°$, $x_v = 0.65c$, $D = 8h$.

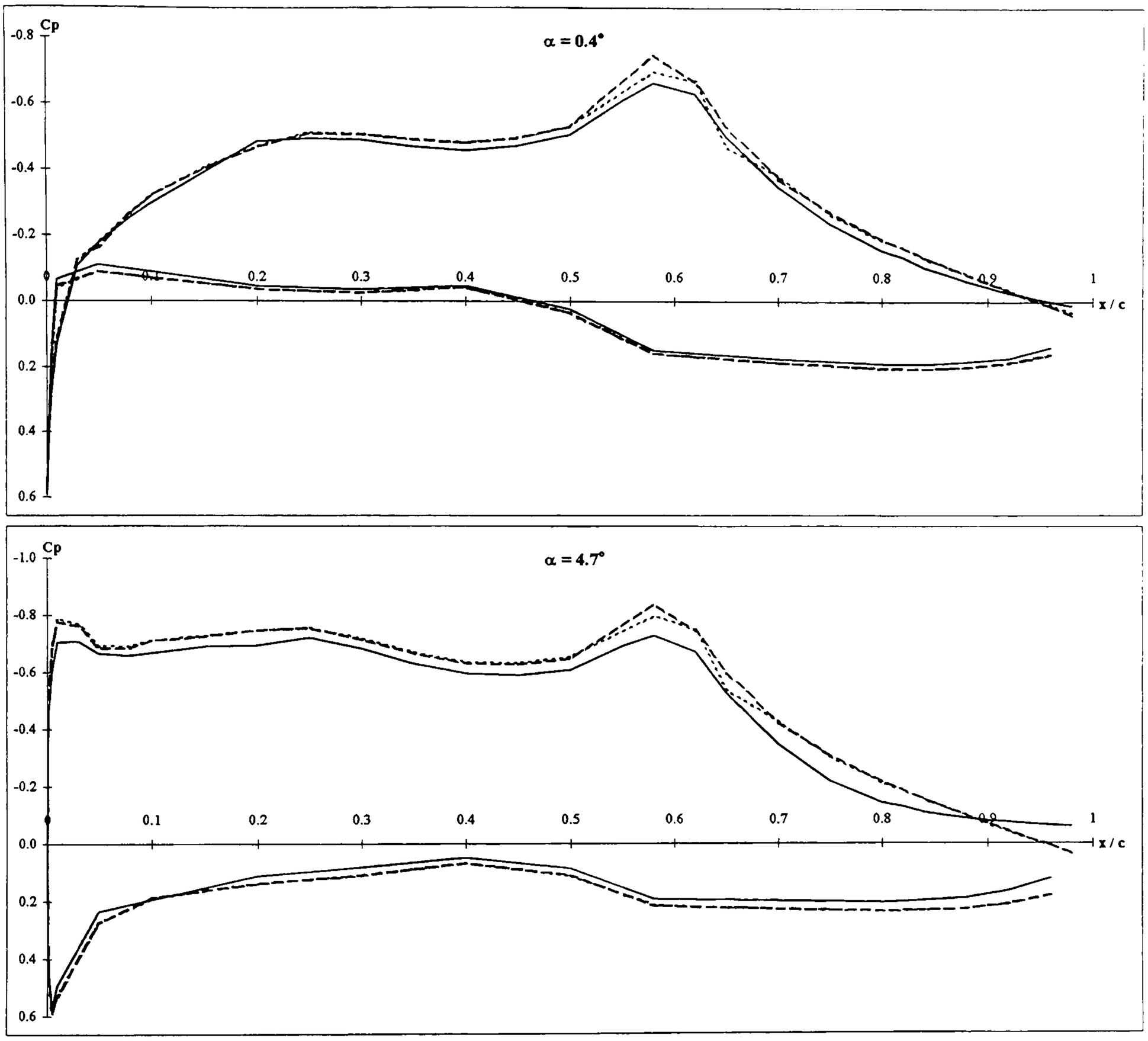

Key

configuration

——— without vortex generators

····· cropped delta vane vortex generators (h = 0.0126c, α_v = 25°, x_v = 0.65c, D = 8h)

– – – – cropped delta vane vortex generators (h = 0.0050c, α_v = 30°, x_v = 0.55c, D = 20h)

Figure 5-34: Pressure distribution comparisons on the DERA swept wing with and without cropped delta vane vortex generators. Λ = 40°, η = 0.45b, $Re_c = 3.3 \times 10^6$.

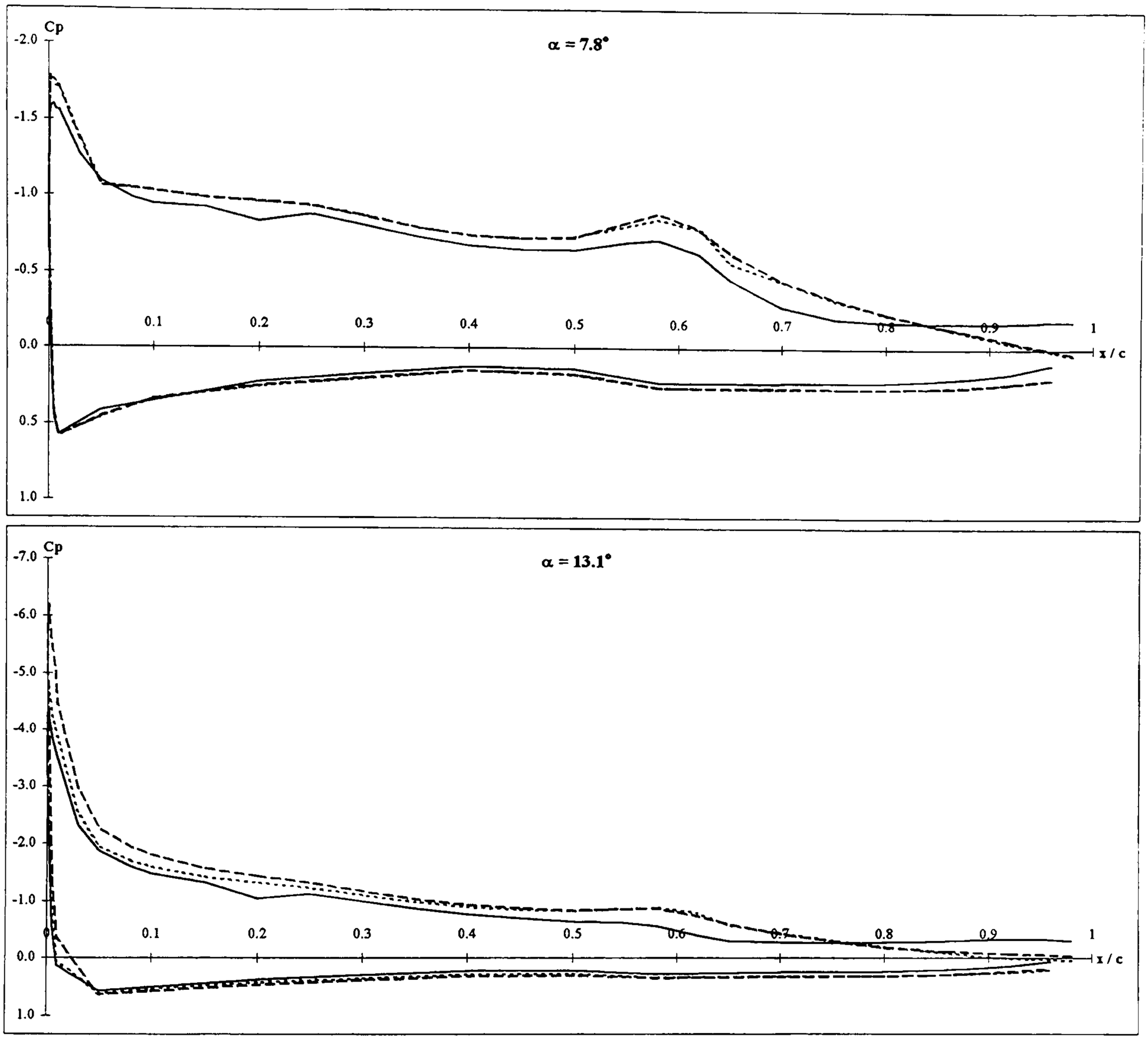

Key

	configuration
———	without vortex generators
·····	cropped delta vane vortex generators (h = 0.0126c, α_v = 25°, x_v = 0.65c, D = 8h)
– – – –	cropped delta vane vortex generators (h = 0.0050c, α_v = 30°, x_v = 0.55c, D = 20h)

Figure 5-34 cont.: Pressure distribution comparisons on the DERA swept wing with and without cropped delta vane vortex generators. $\Lambda = 40°$, $\eta = 0.45b$, $Re_c = 3.3 \times 10^6$.

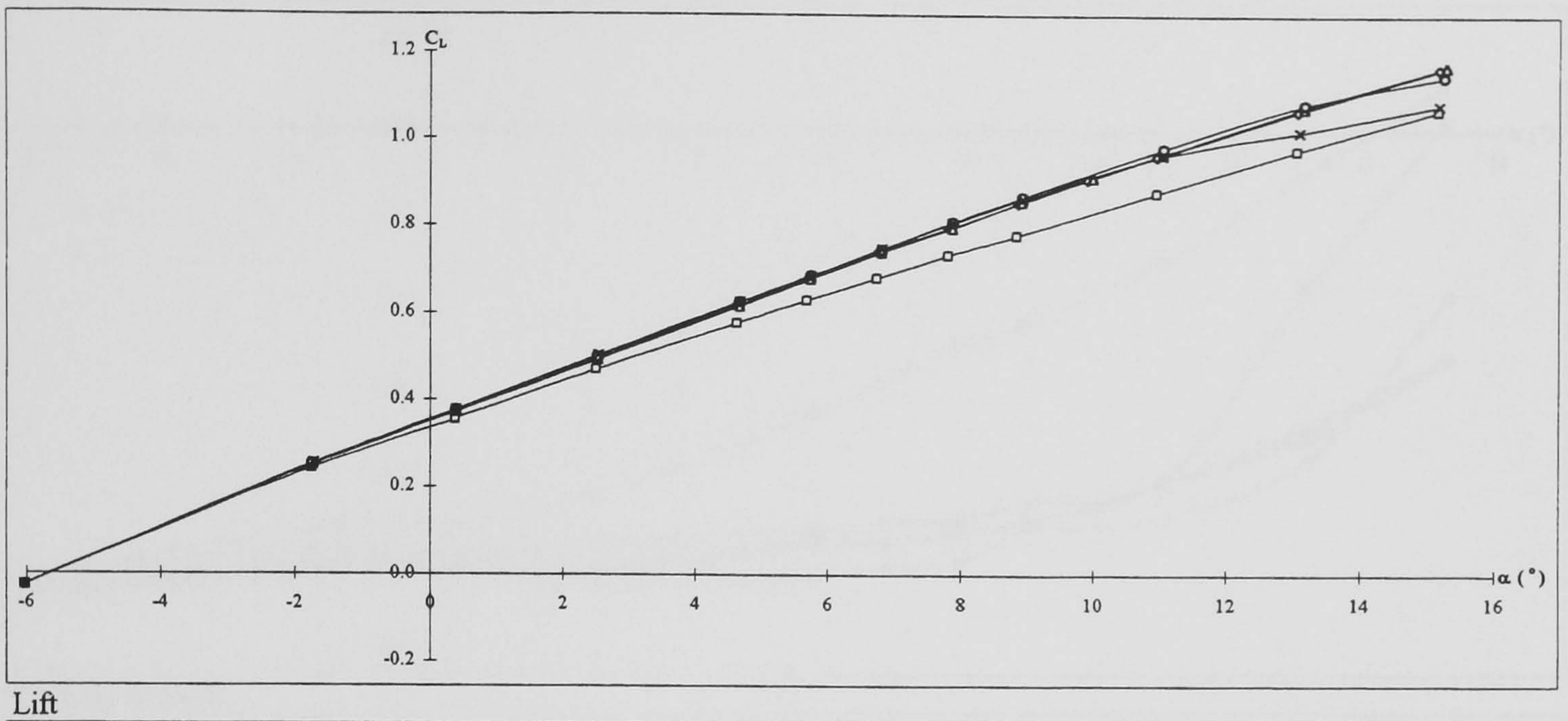

Lift

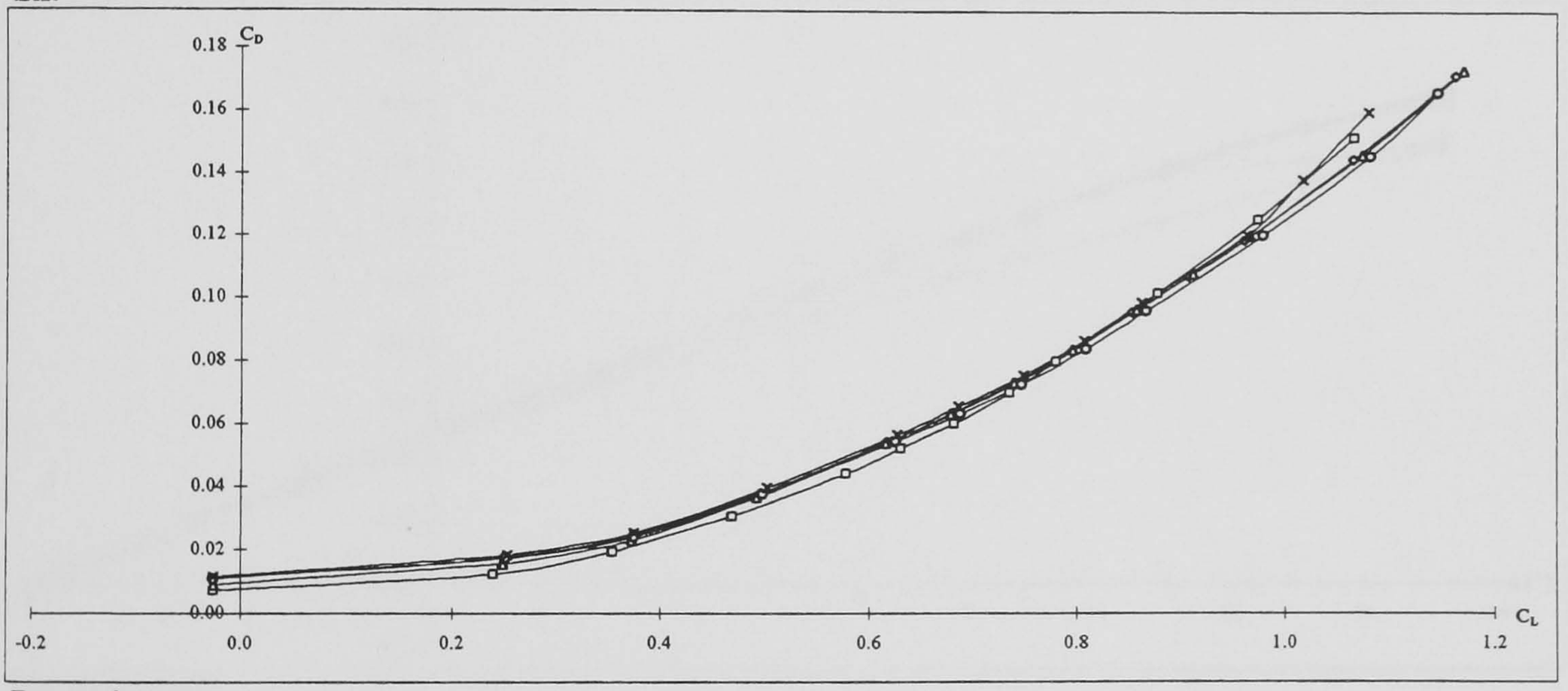

Drag polar

Key

0.55c
0.60c
0.65c
0.70c

Figure 5-35: DERA swept wing aerodynamic forces and moments with and without cropped delta vane vortex generators at various chordwise positions. $\Lambda = 40°$, $Re_c = 3.3 \times 10^6$, h = 0.0126c, $\alpha_v = 25°$, D = 8h.

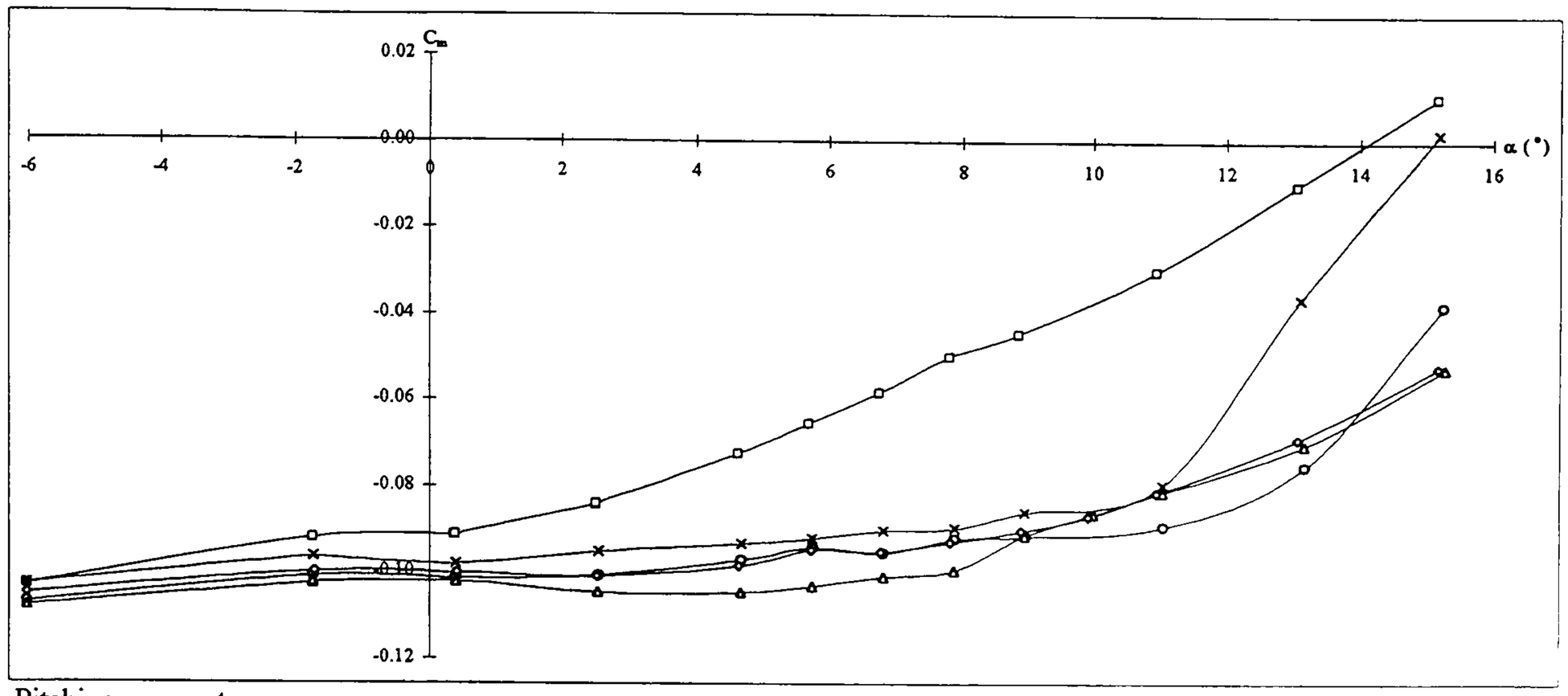

Pitching moment

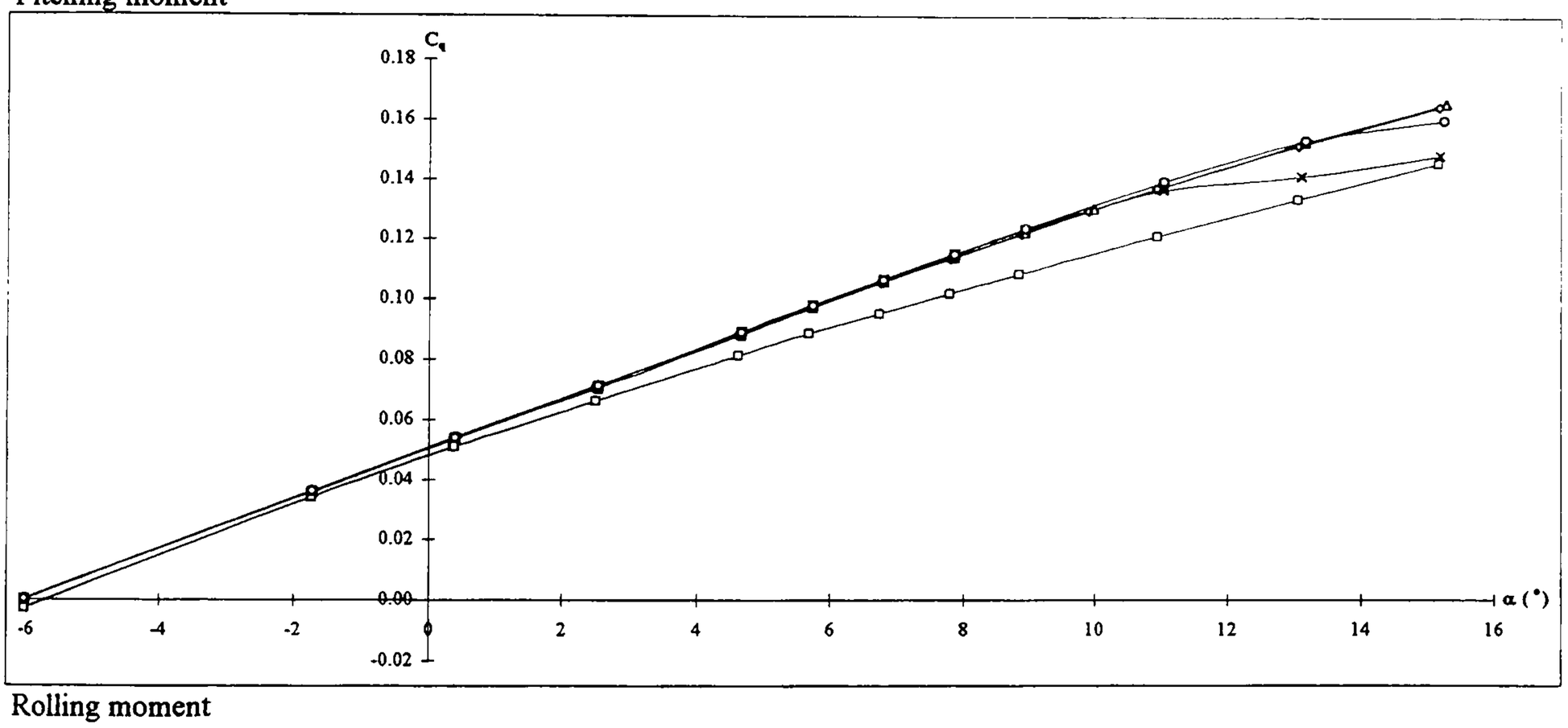

Rolling moment

Key	x_v
—□—	-
—◇—	0.55c
—△—	0.60c
—○—	0.65c
—×—	0.70c

Figure 5-35 cont.: DERA swept wing aerodynamic forces and moments with and without cropped delta vane vortex generators at various chordwise positions. $\Lambda = 40°$, $Re_c = 3.3 \times 10^6$, h = 0.0126c, $\alpha_v = 25°$, D = 8h.

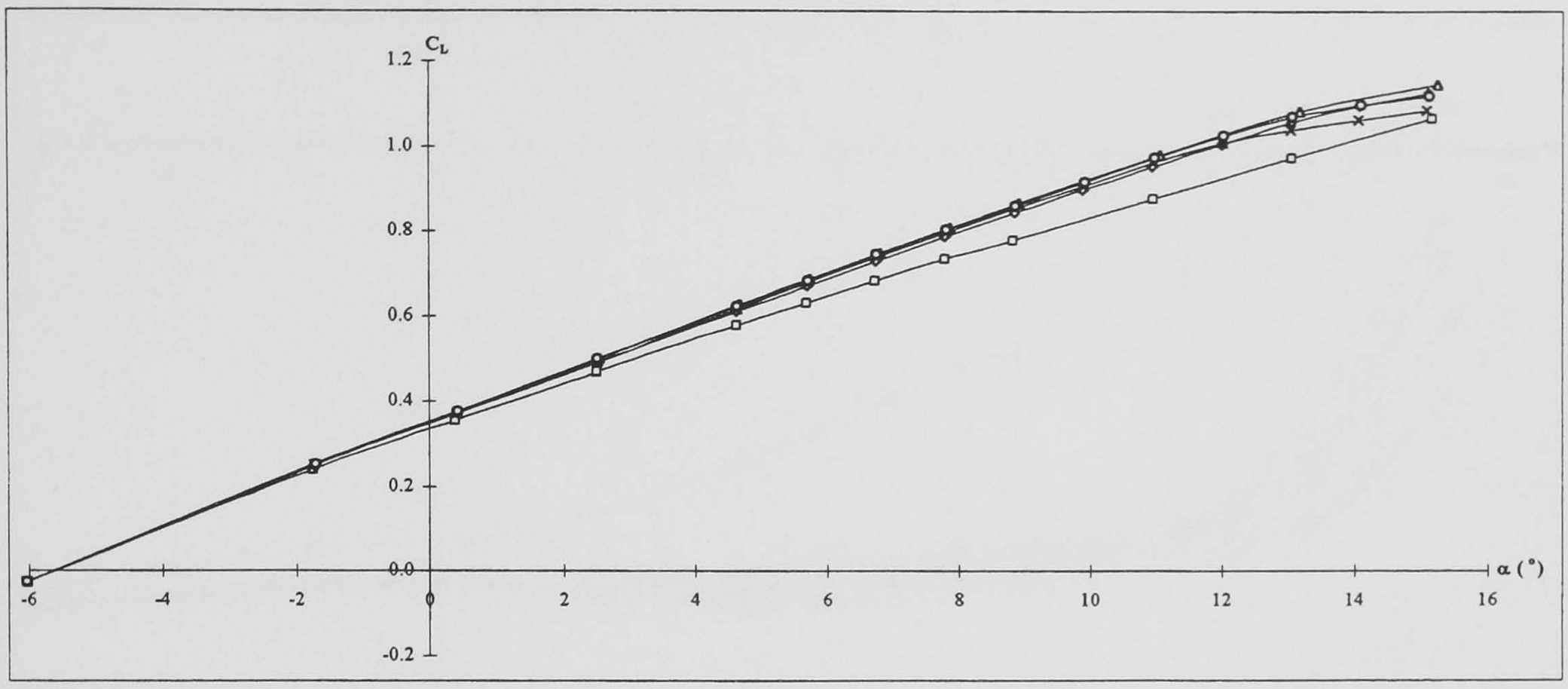

Lift

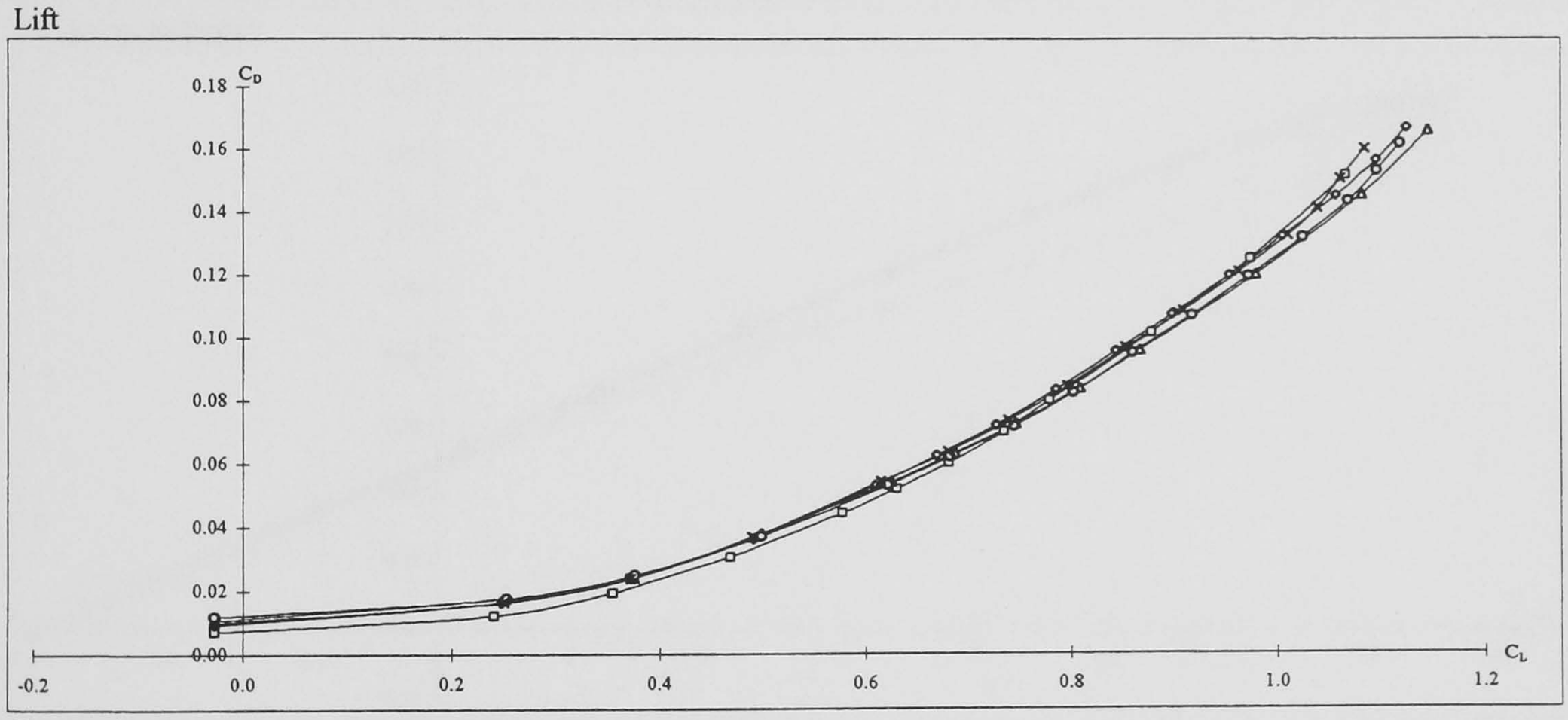

Drag polar

Key	α_v (°)
—□—	-
—◇—	20
—△—	25
—○—	30
—×—	35

Figure 5-36: DERA swept wing aerodynamic forces and moments with and without cropped delta vane vortex generators at various orientations to the flow. $\Lambda = 40°$, $Re_c = 3.3 \times 10^6$, $h = 0.0126c$, $x_v = 0.65c$, $D = 8h$.

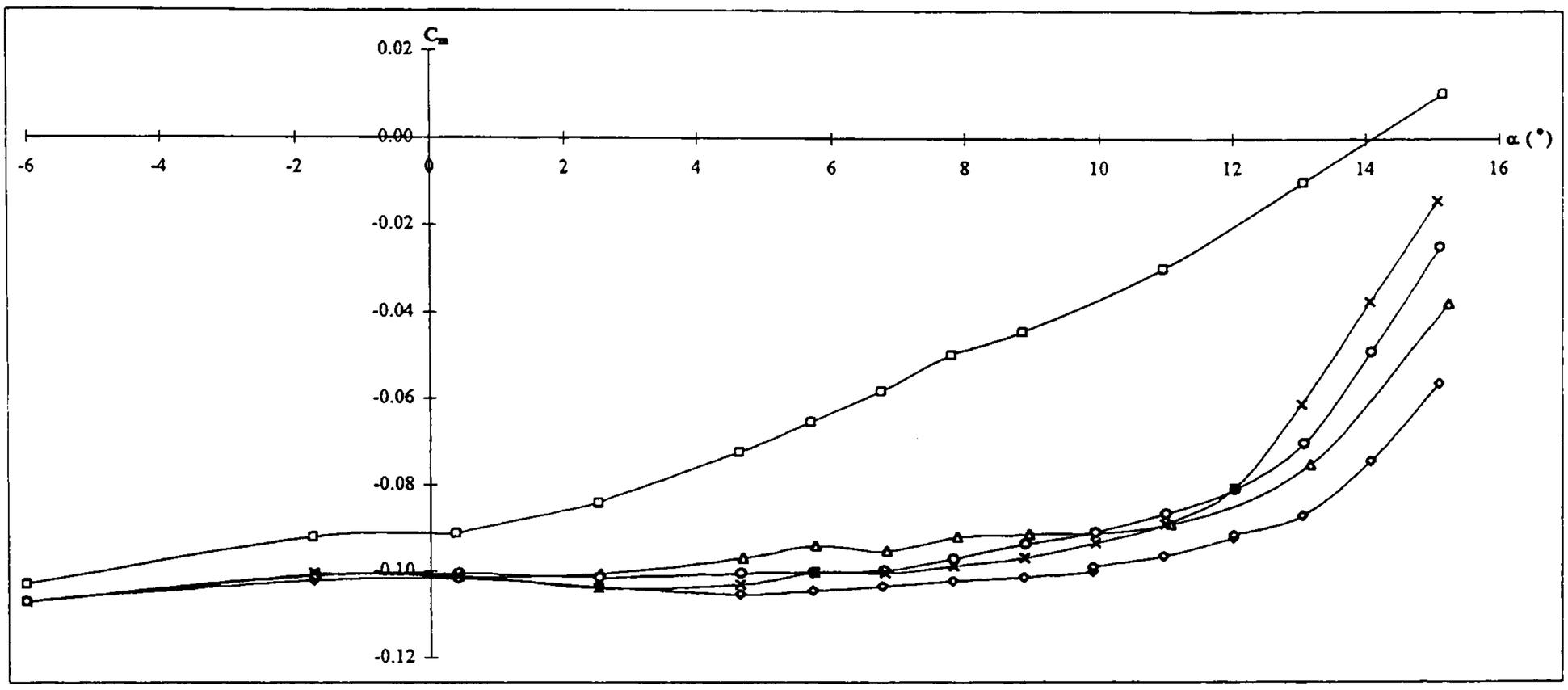

Pitching moment

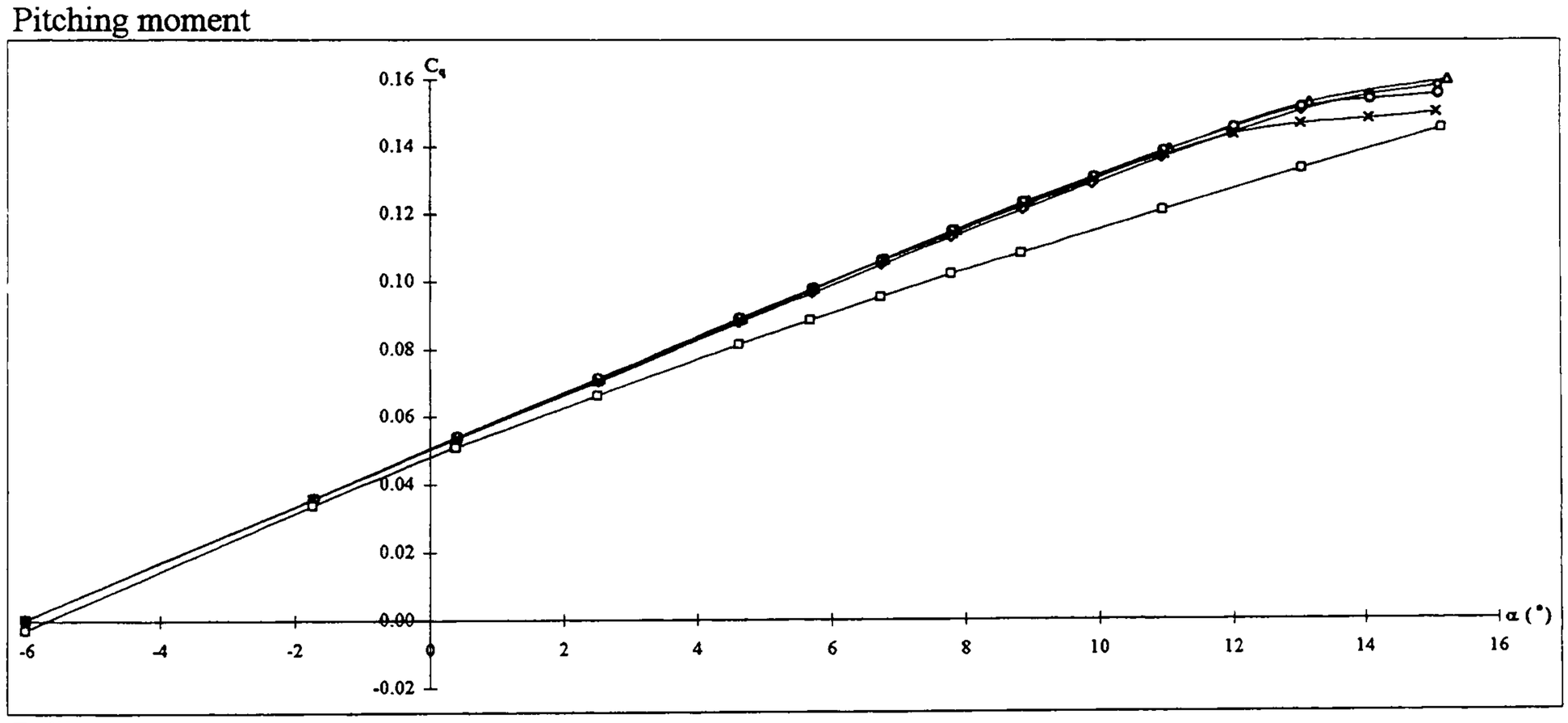

Rolling moment

Key	α_v (°)
—□—	-
—◇—	20
—△—	25
—○—	30
—×—	35

Figure 5-36 cont.: DERA swept wing aerodynamic forces and moments with and without cropped delta vane vortex generators at various orientations to the flow. $\Lambda = 40°$, $Re_c = 3.3 \times 10^6$, $h = 0.0126c$, $x_v = 0.65c$, $D = 8h$.

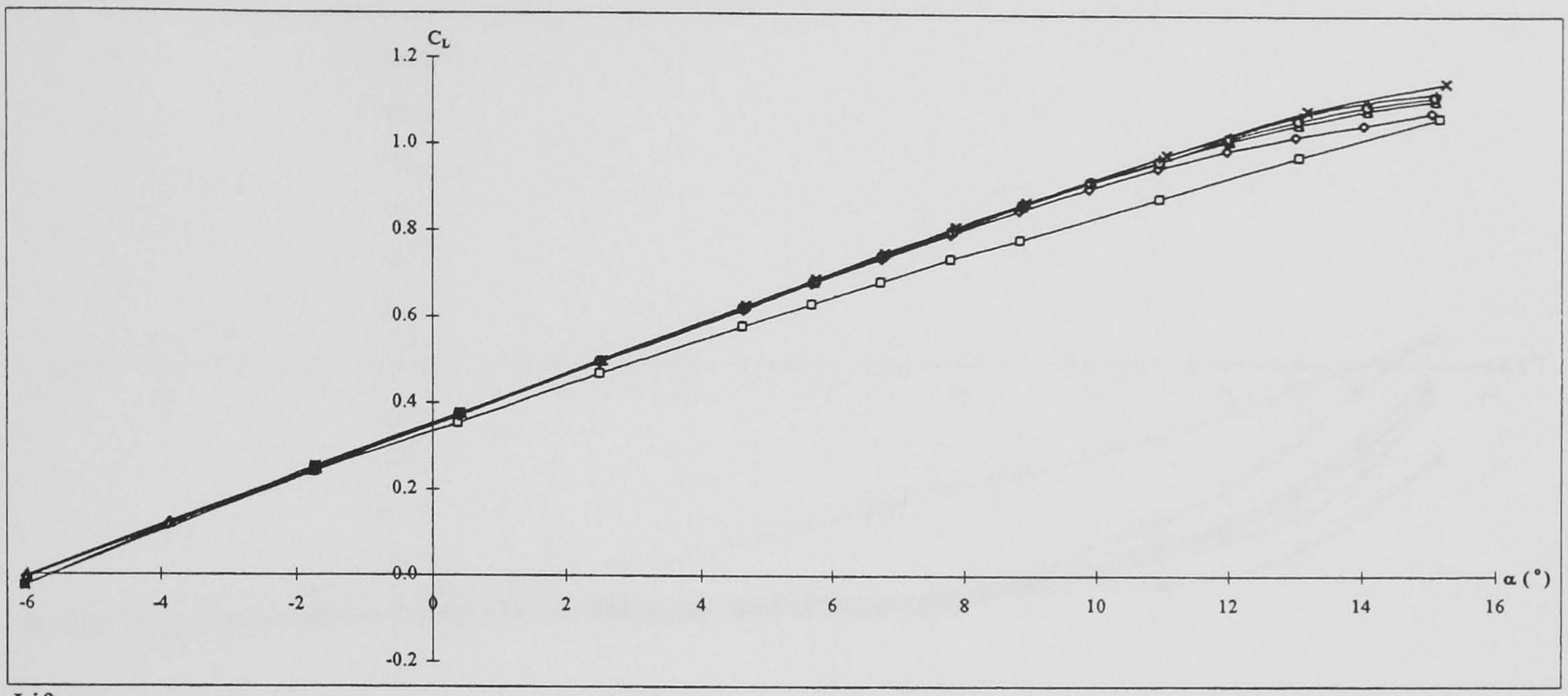

Lift

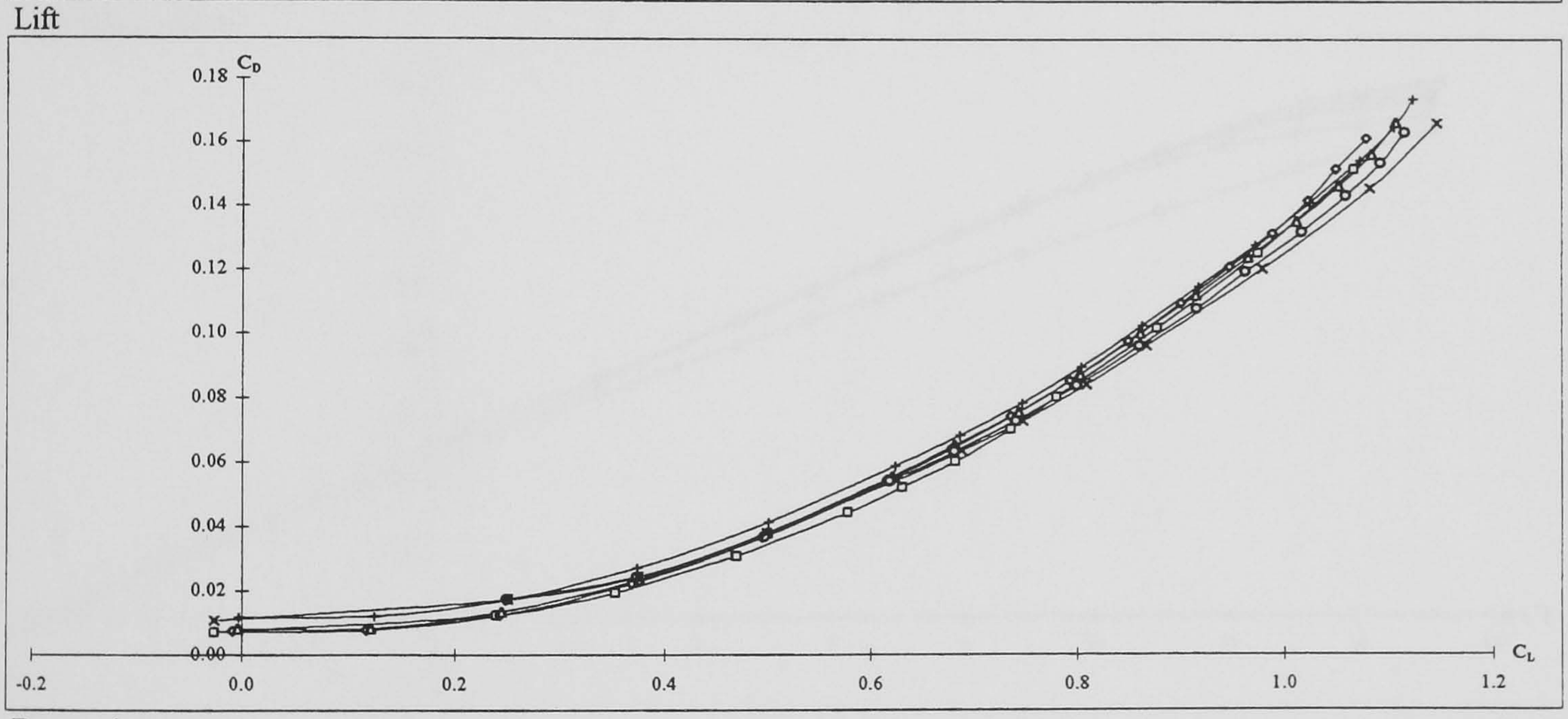

Drag polar

Key	h	D
—□—	-	-
—◇—	0.0050c	20h
—△—	0.0075c	13.3h
—○—	0.0100c	10h
—×—	0.0126c	8h
—+—	0.0151c	6.6h

Figure 5-37: DERA swept wing aerodynamic forces and moments with and without cropped delta vane vortex generators of various heights.
$\Lambda = 40°$, $Re_c = 3.3 \times 10^6$, $x_v = 0.65c$, $\alpha_v = 25°$.

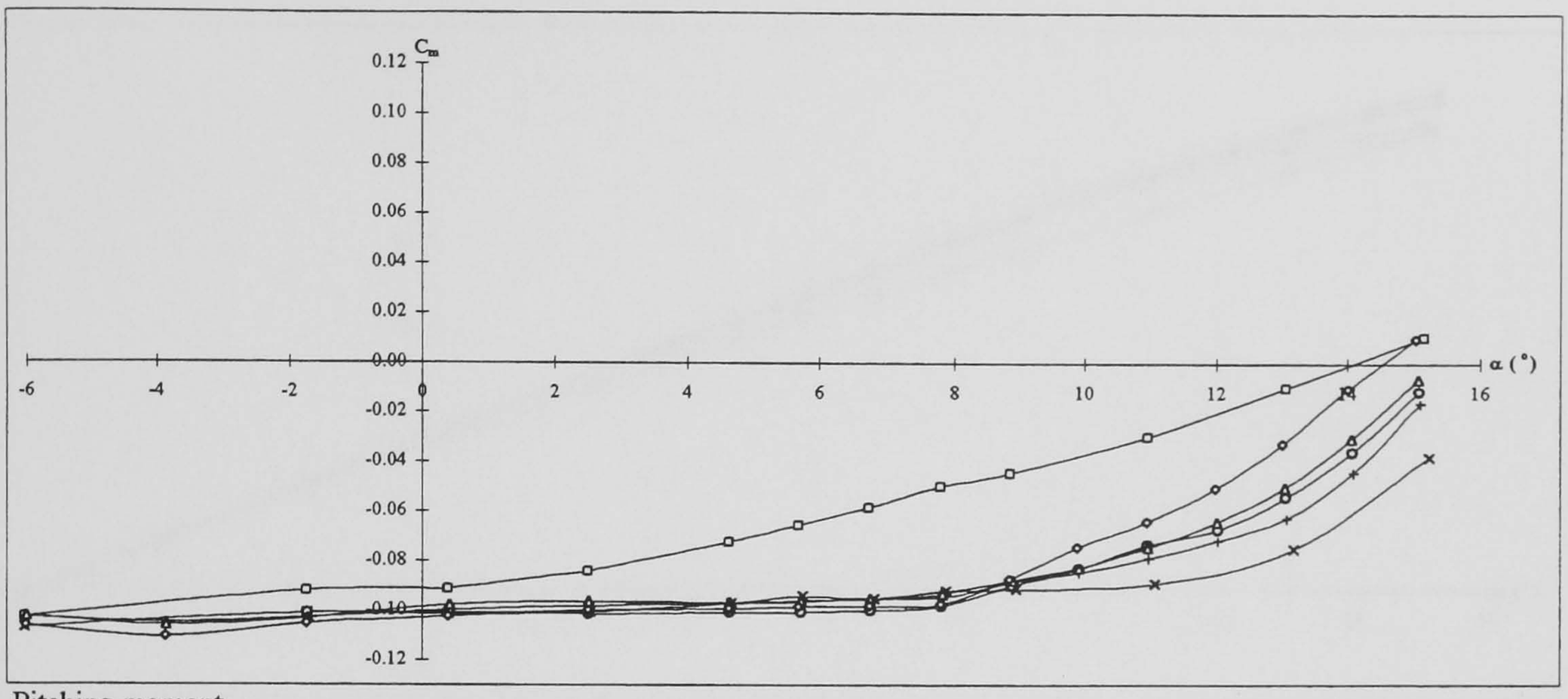

Pitching moment

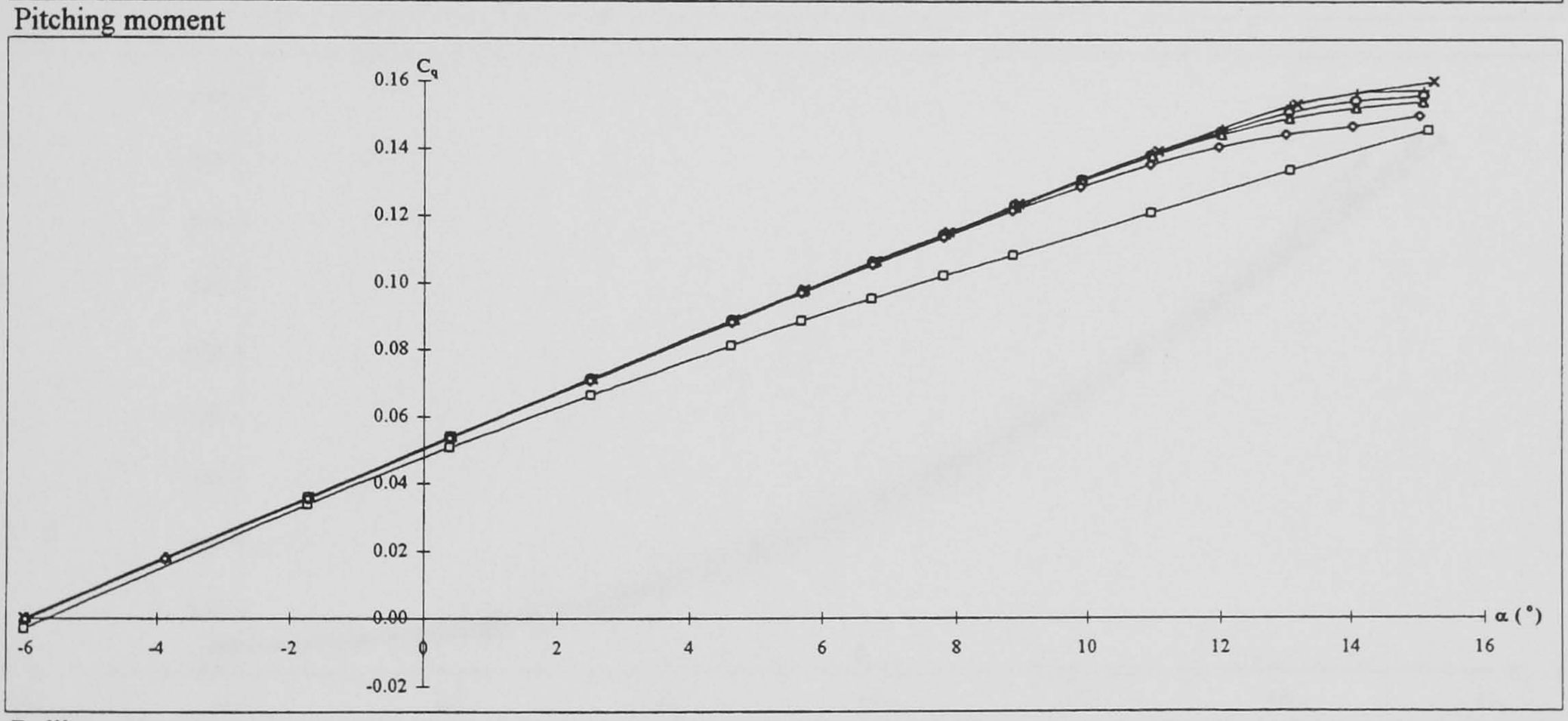

Rolling moment

Key	h	D
—□—	-	-
—◇—	0.0050c	20h
—△—	0.0075c	13.3h
—○—	0.0100c	10h
—×—	0.0126c	8h
—+—	0.0151c	6.6h

Figure 5-37 cont.: DERA swept wing aerodynamic forces and moments with and without cropped delta vane vortex generators of various heights.
$\Lambda = 40°$, $Re_c = 3.3 \times 10^6$, $x_v = 0.65c$, $\alpha_v = 25°$.

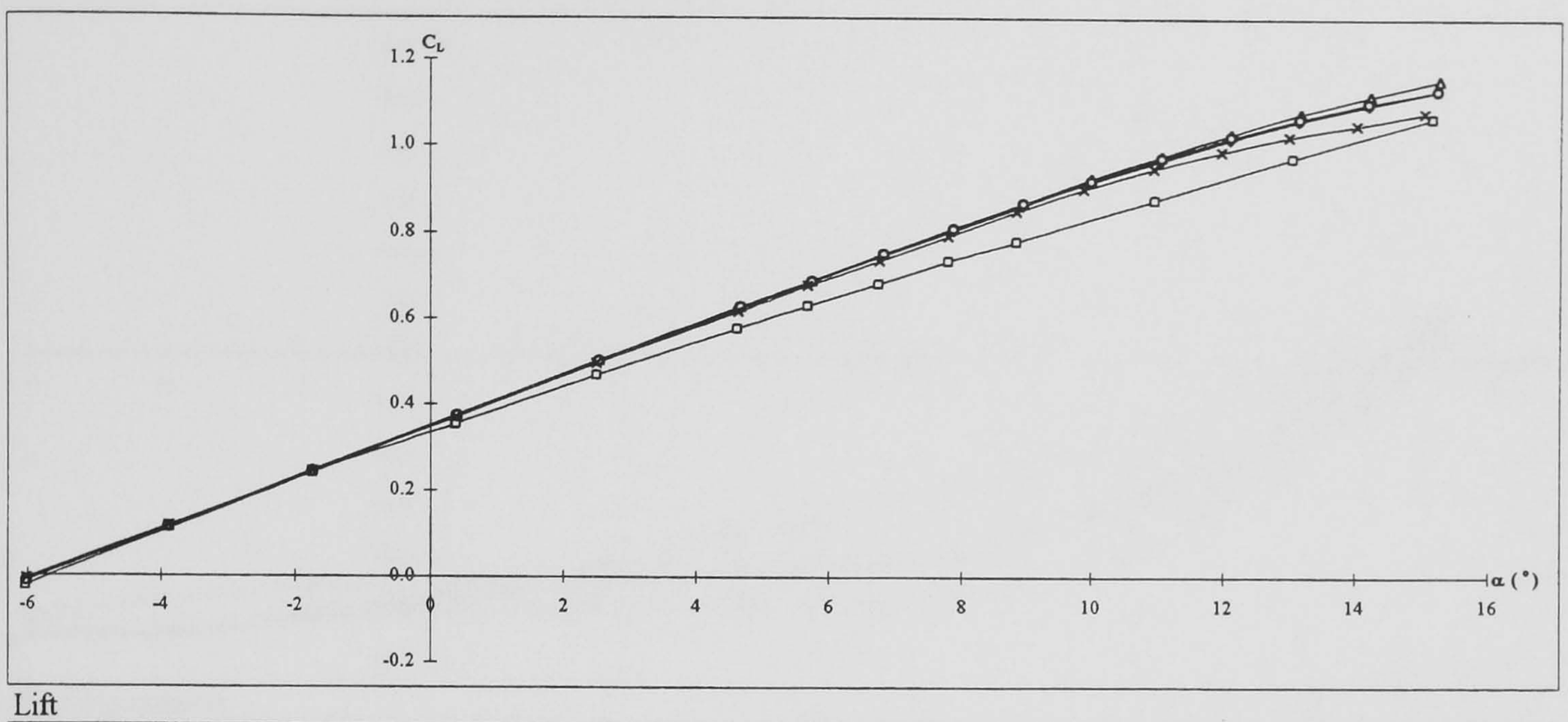

Lift

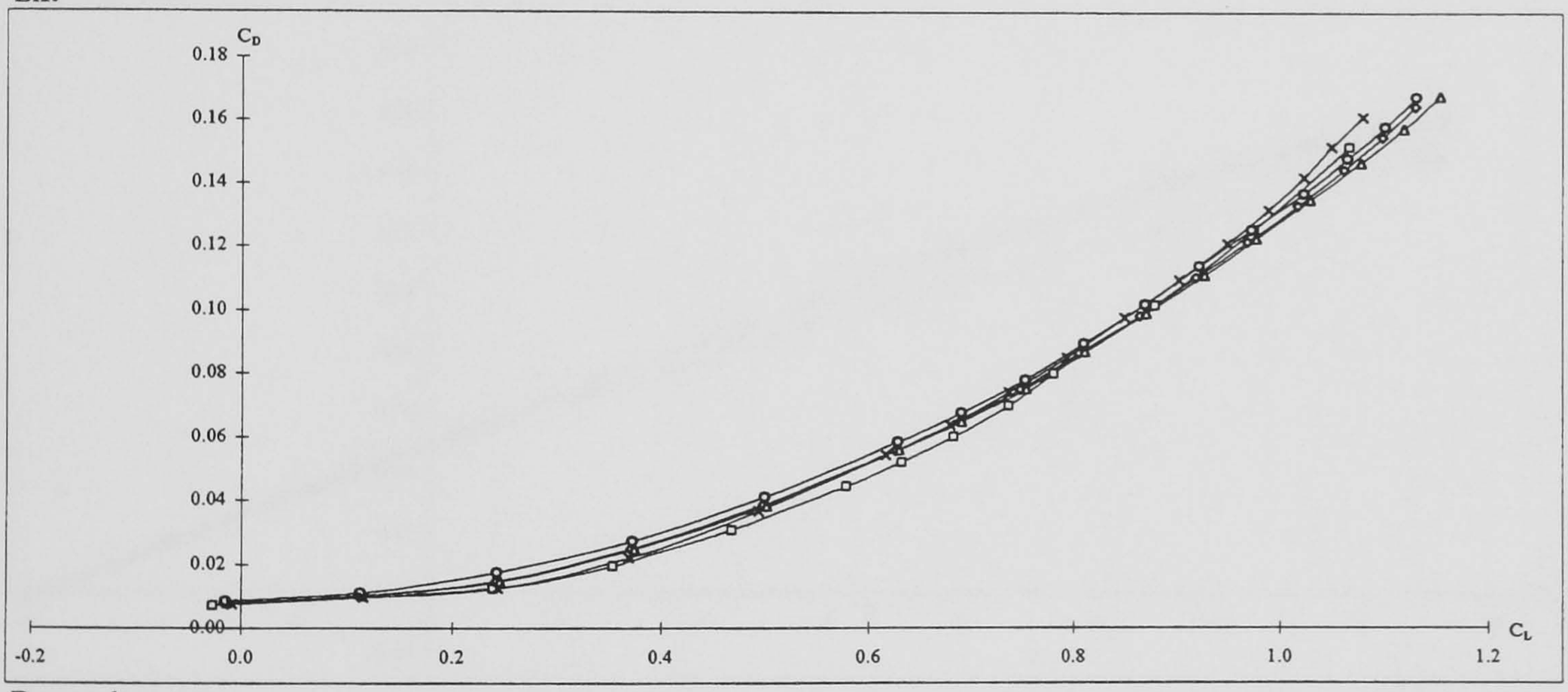

Drag polar

Key

	x_v
—□—	-
—◇—	0.50c
—△—	0.55c
—○—	0.60c
—×—	0.65c

Figure 5-38: DERA swept wing aerodynamic forces and moments with and without cropped delta vane vortex generators at various chordwise positions. $\Lambda = 40°$, $Re_c = 3.3 \times 10^6$, $h = 0.0050c$, $\alpha_v = 25°$, $D = 20h$.

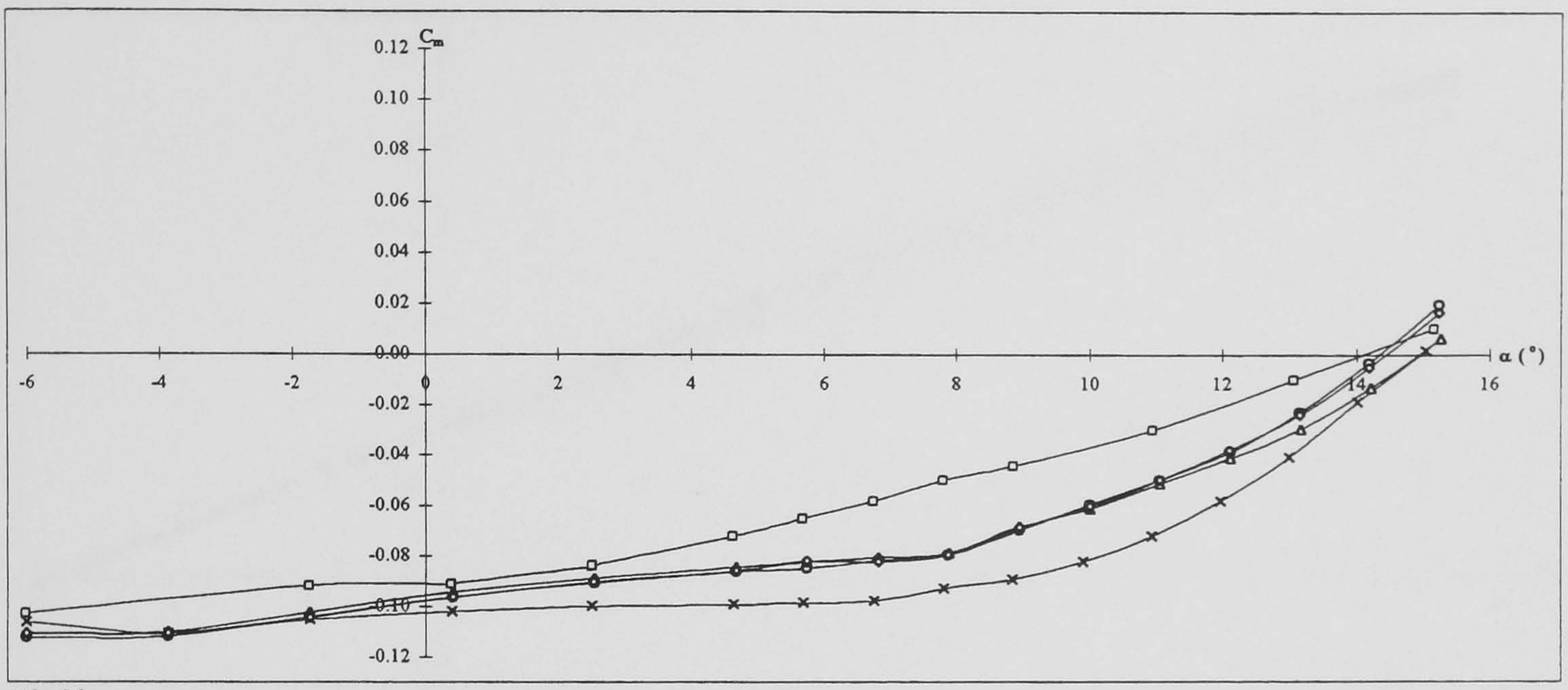

Pitching moment

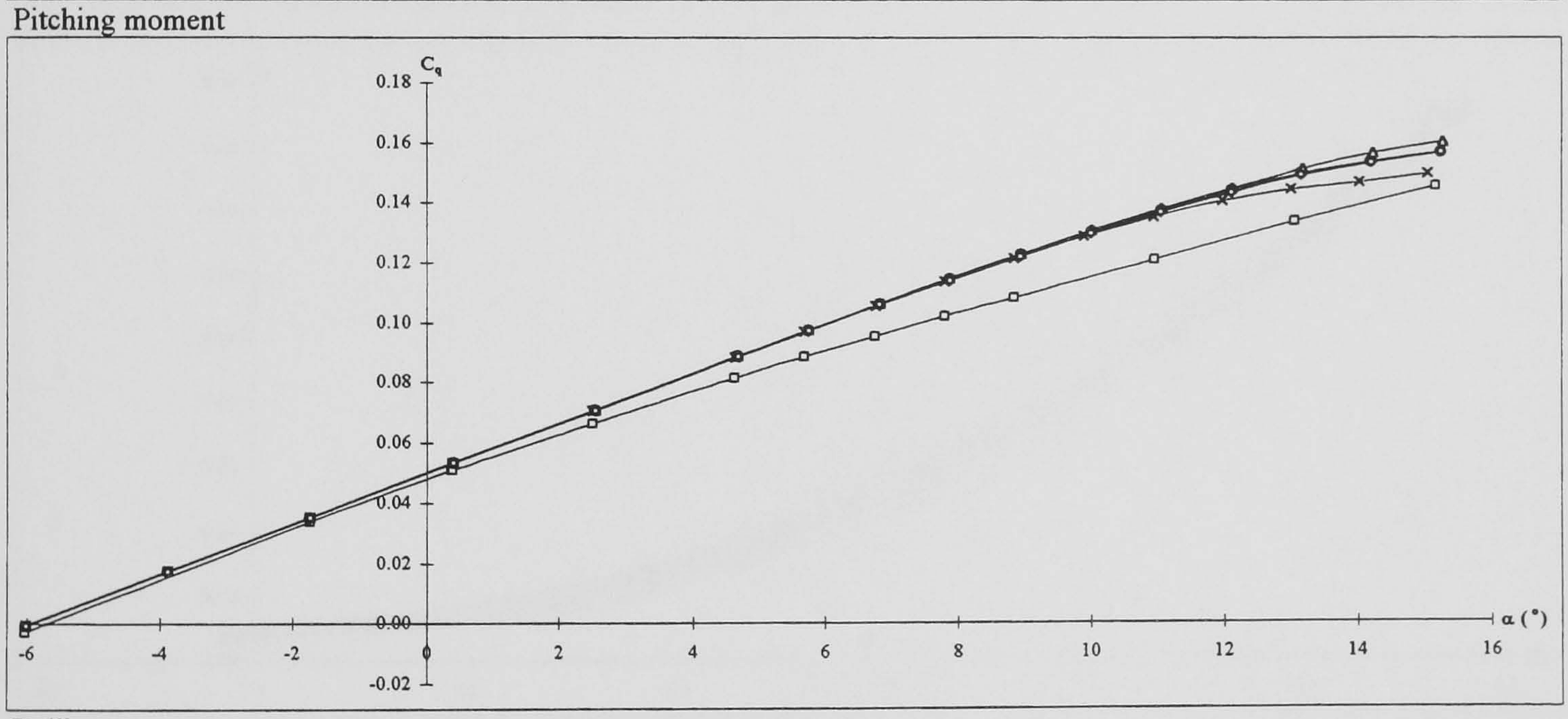

Rolling moment

Key	x_v
—□—	-
—◇—	0.50c
—△—	0.55c
—○—	0.60c
—×—	0.65c

Figure 5-38 cont.: DERA swept wing aerodynamic forces and moments with and without cropped delta vane vortex generators at various chordwise positions. $\Lambda = 40°$, $Re_c = 3.3 \times 10^6$, h = 0.0050c, $\alpha_v = 25°$, D = 20h.

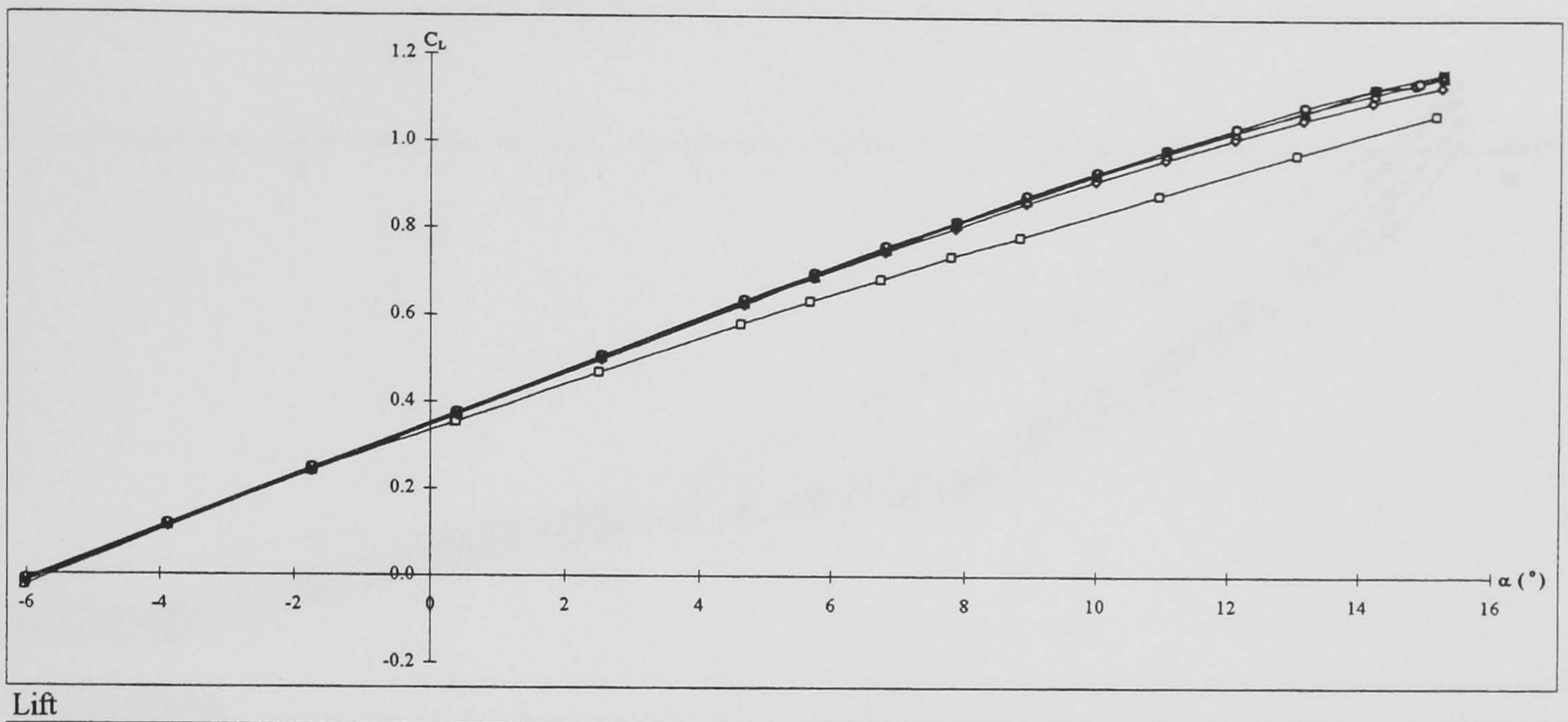

Lift

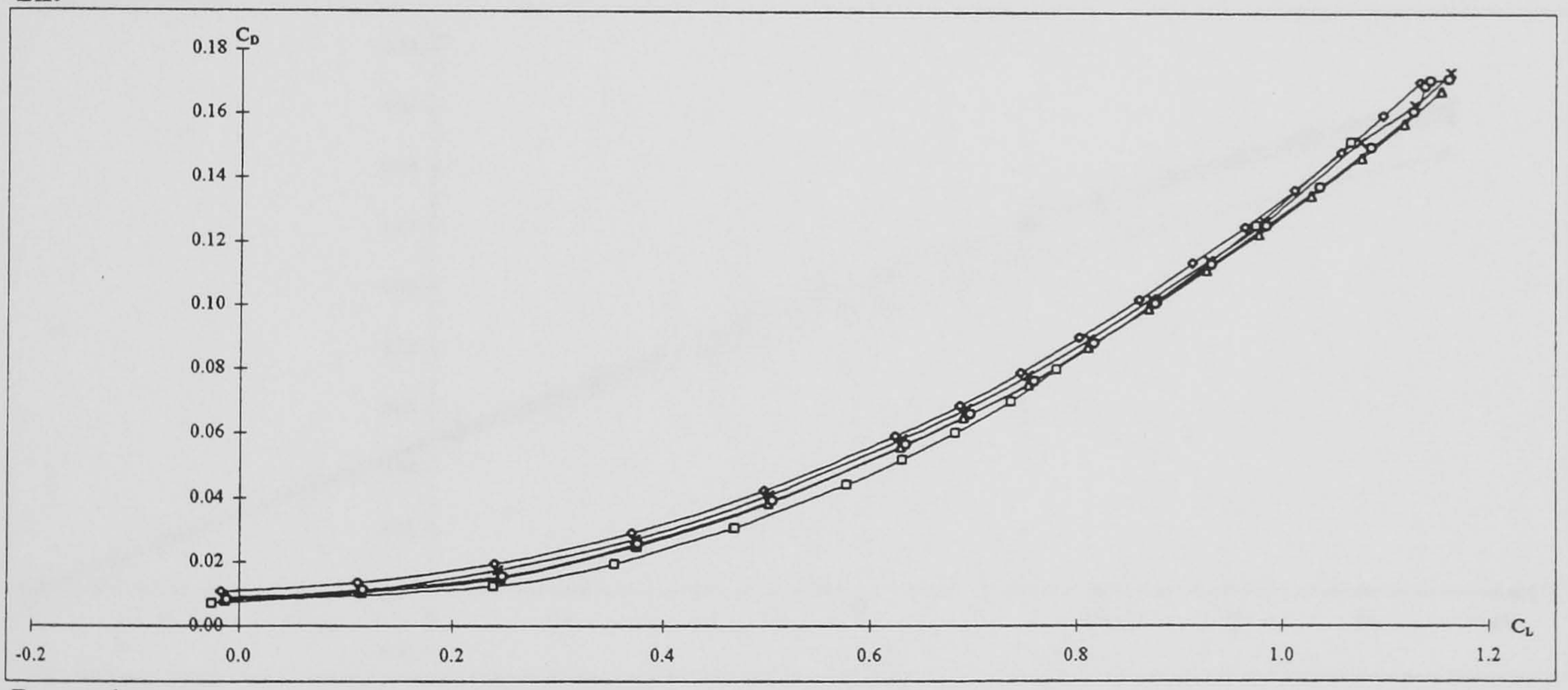

Drag polar

Key	α_v (°)
—□—	-
—◇—	20
—△—	25
—○—	30
—×—	35

Figure 5-39: DERA swept wing aerodynamic forces and moments with and without cropped delta vane vortex generators at various orientations to the flow. $\Lambda = 40°$, $Re_c = 3.3 \times 10^6$, $h = 0.0050c$, $x_v = 0.55c$, $D = 20h$.

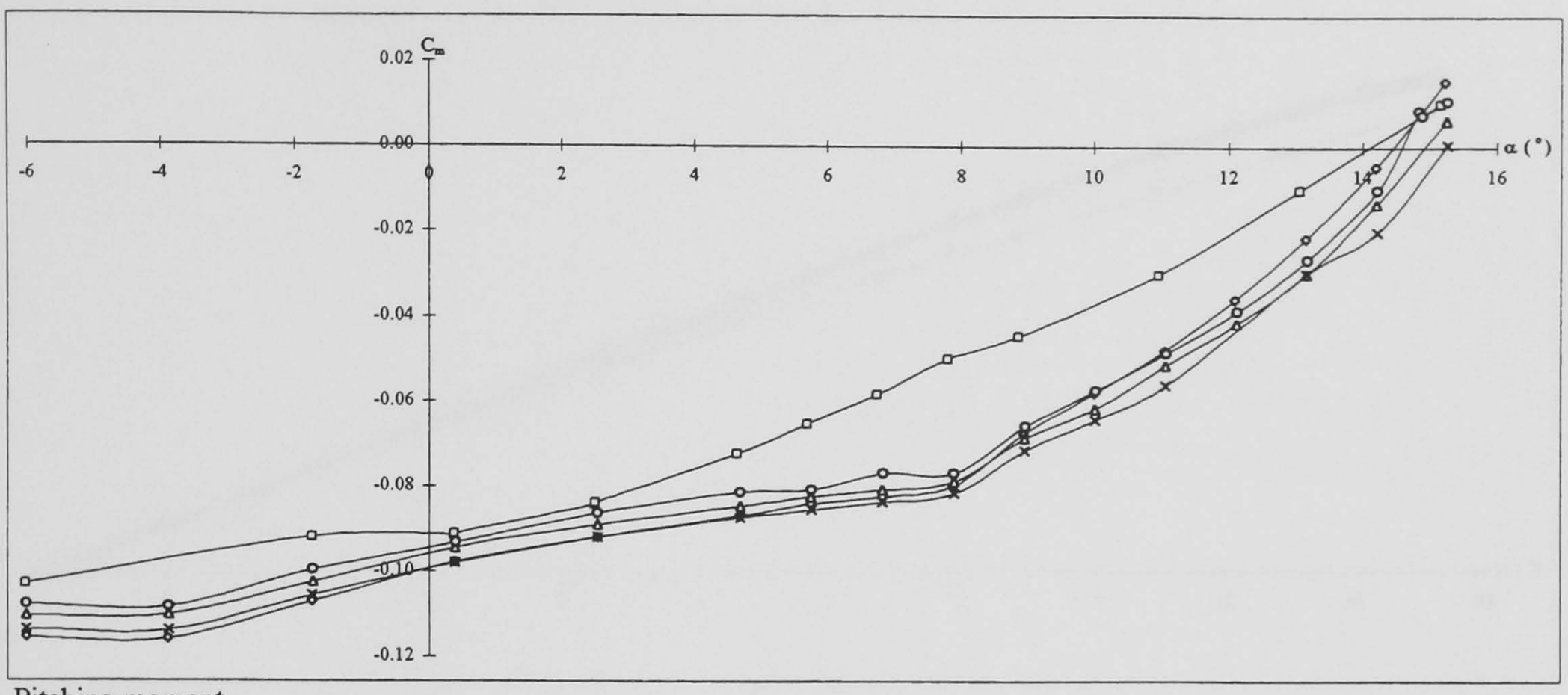

Pitching moment

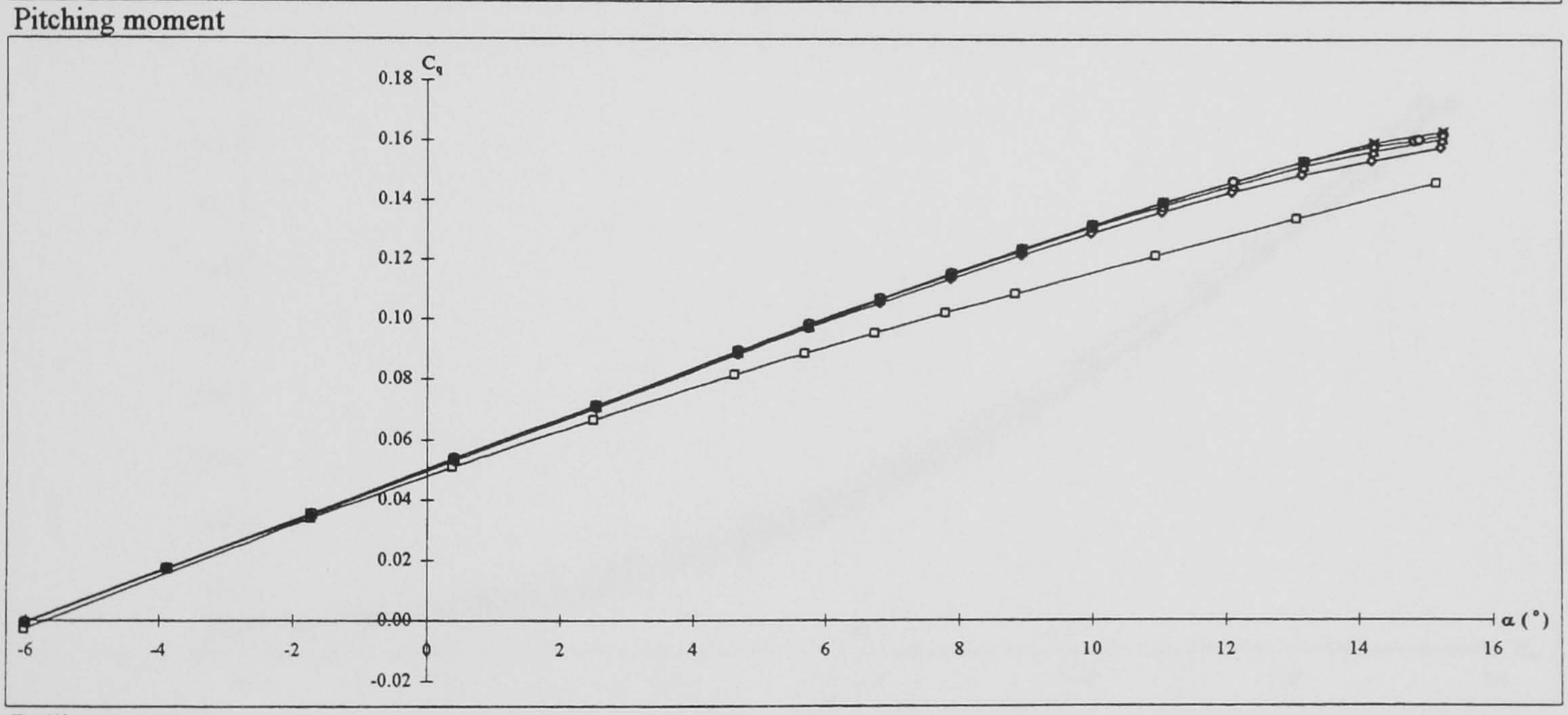

Rolling moment

Key	α_v (°)
—□—	-
—◇—	20
—△—	25
—○—	30
—×—	35

Figure 5-39 cont.: DERA swept wing aerodynamic forces and moments with and without cropped delta vane vortex generators at various orientations to the flow. $\Lambda = 40°$, $Re_c = 3.3 \times 10^6$, $h = 0.0050c$, $x_v = 0.55c$, $D = 20h$.

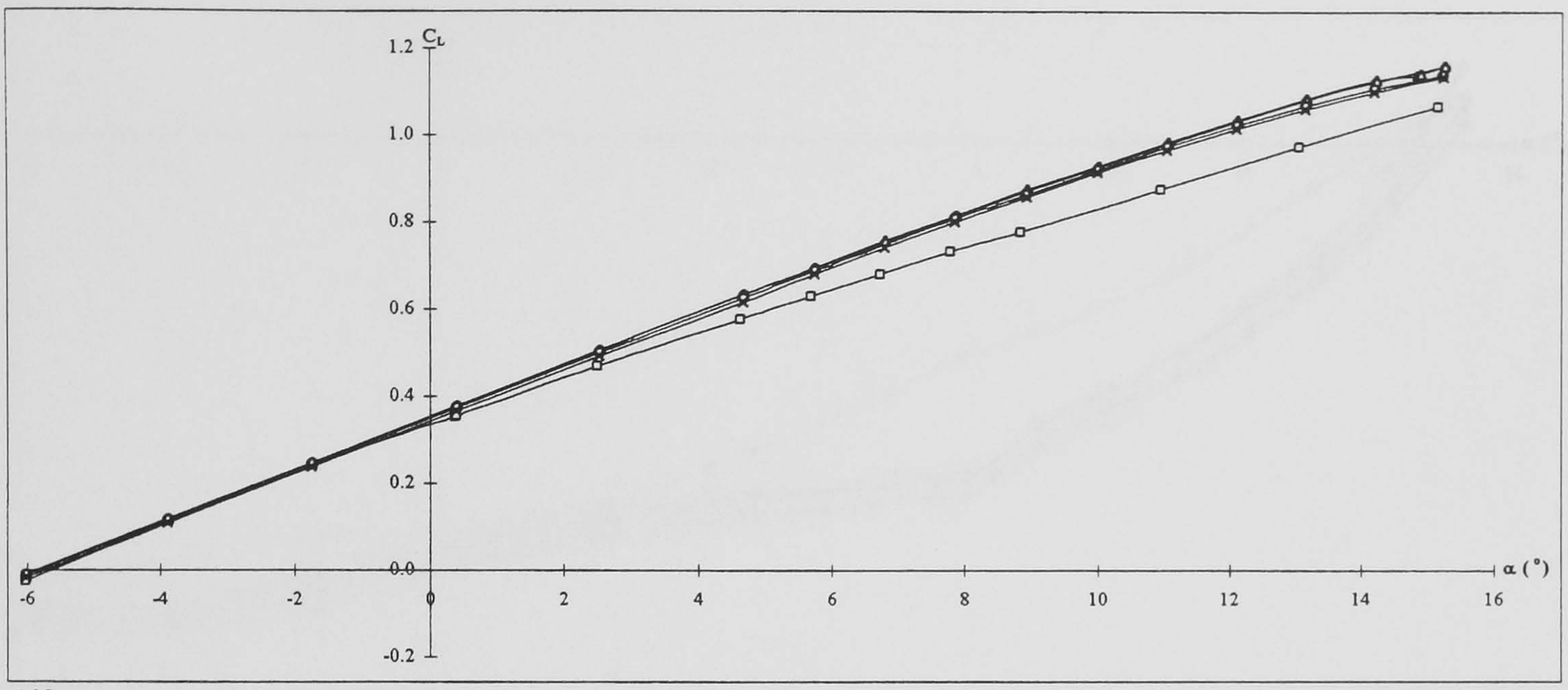

Lift

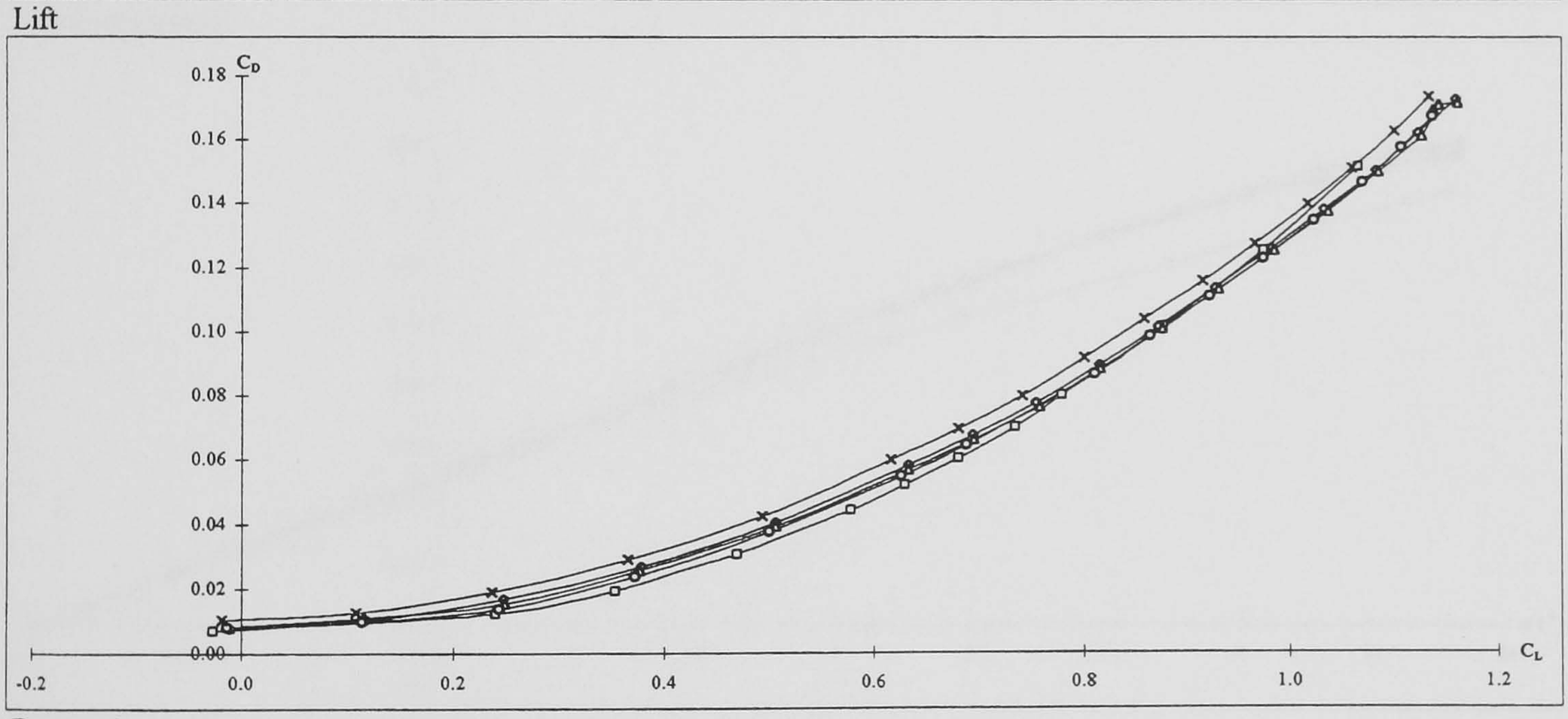

Drag polar

Key	D
—□—	-
—◇—	10h
—△—	20h
—○—	30h
—×—	40h

Figure 5-40: DERA swept wing aerodynamic forces and moments with and without cropped delta vane vortex generators at various spacings.
$\Lambda = 40°$, $Re_c = 3.3 \times 10^6$, $h = 0.0050c$, $x_v = 0.55c$, $\alpha_v = 30°$.

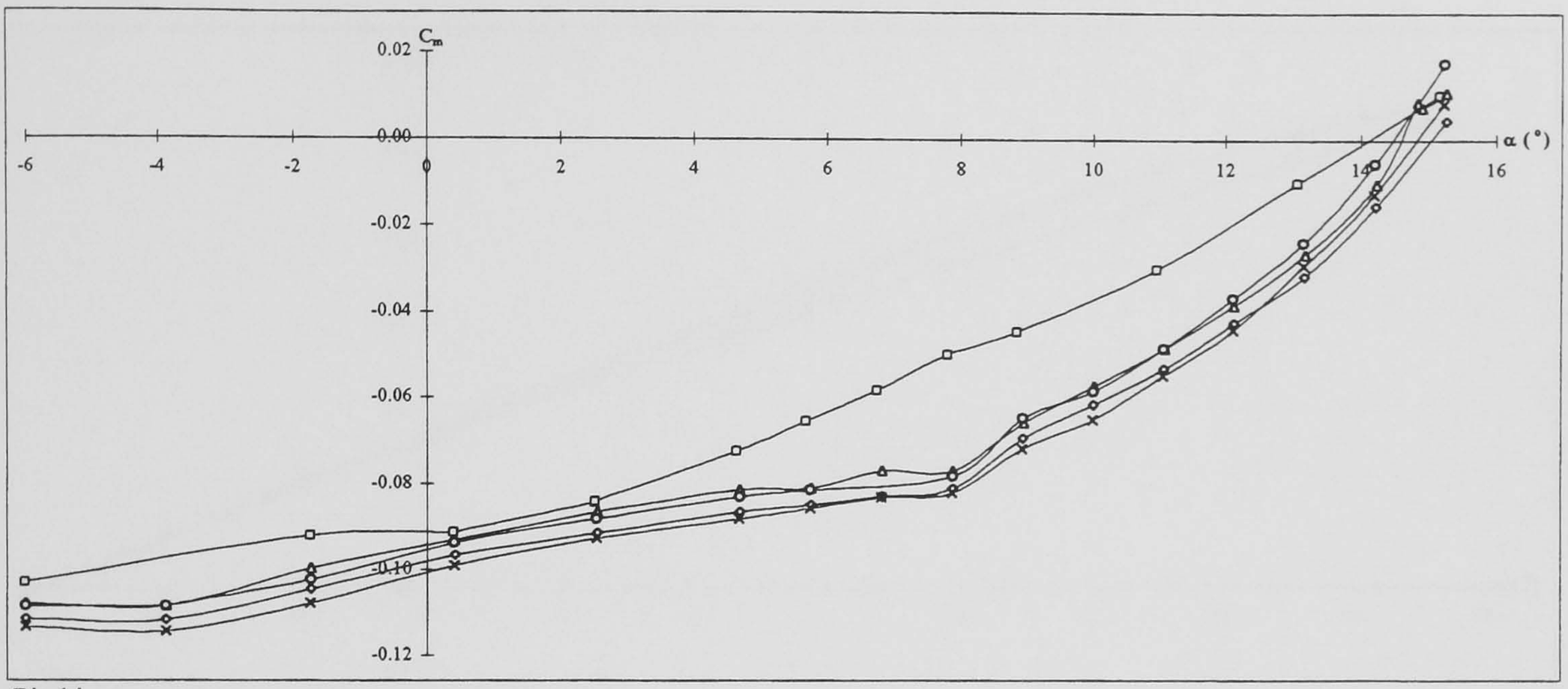

Pitching moment

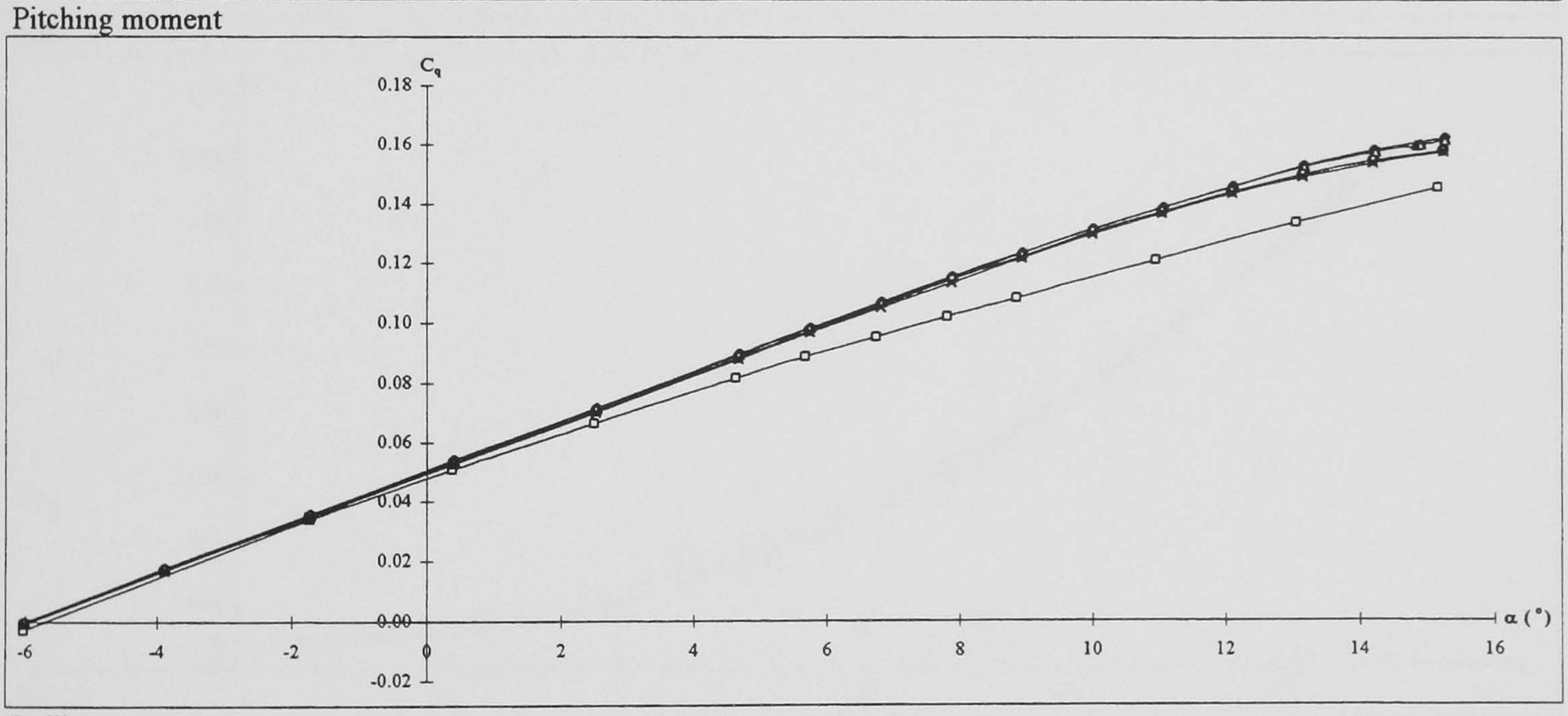

Rolling moment

Key	D
—□—	-
—◇—	10h
—△—	20h
—○—	30h
—×—	40h

Figure 5-40 cont.: DERA swept wing aerodynamic forces and moments with and without cropped delta vane vortex generators at various spacings.
$\Lambda = 40°$, $Re_c = 3.3 \times 10^6$, $h = 0.0050c$, $x_v = 0.55c$, $\alpha_v = 30°$.

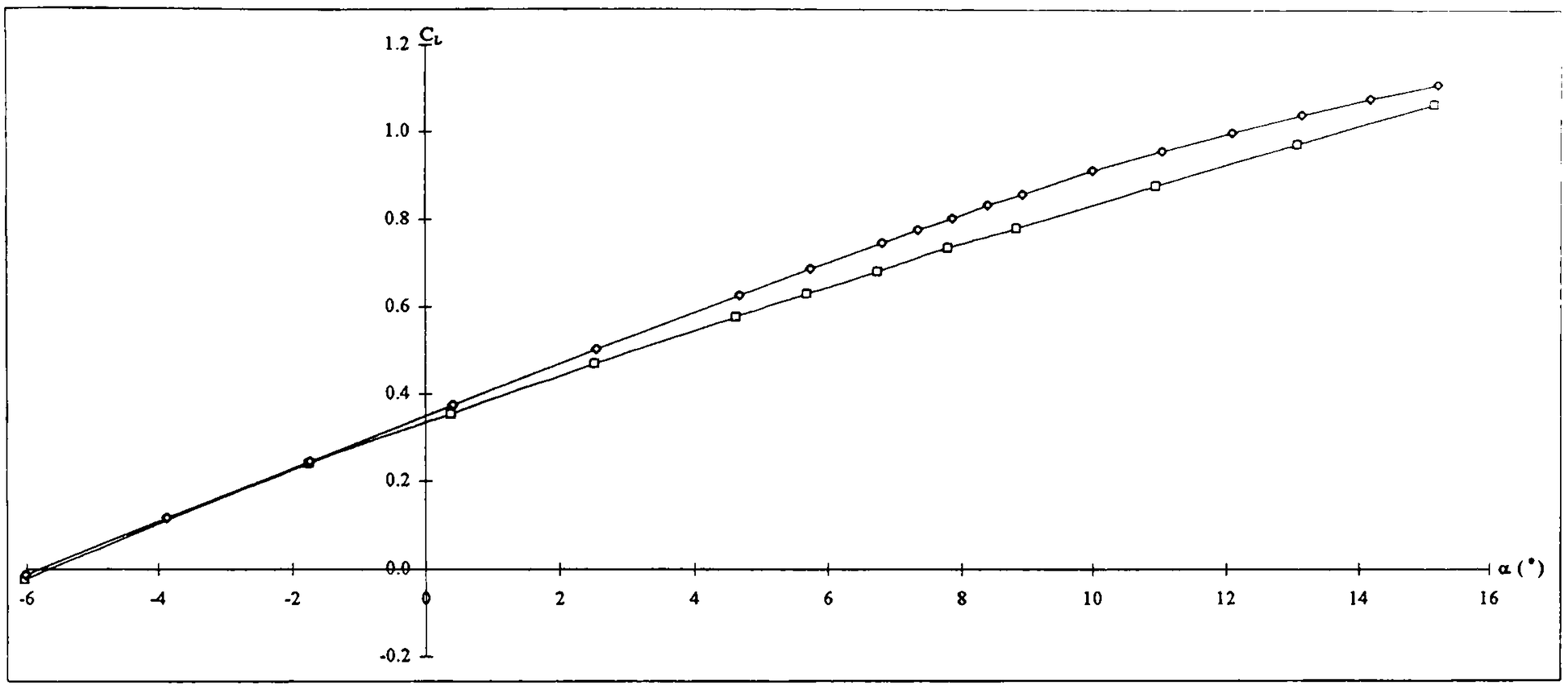

Lift

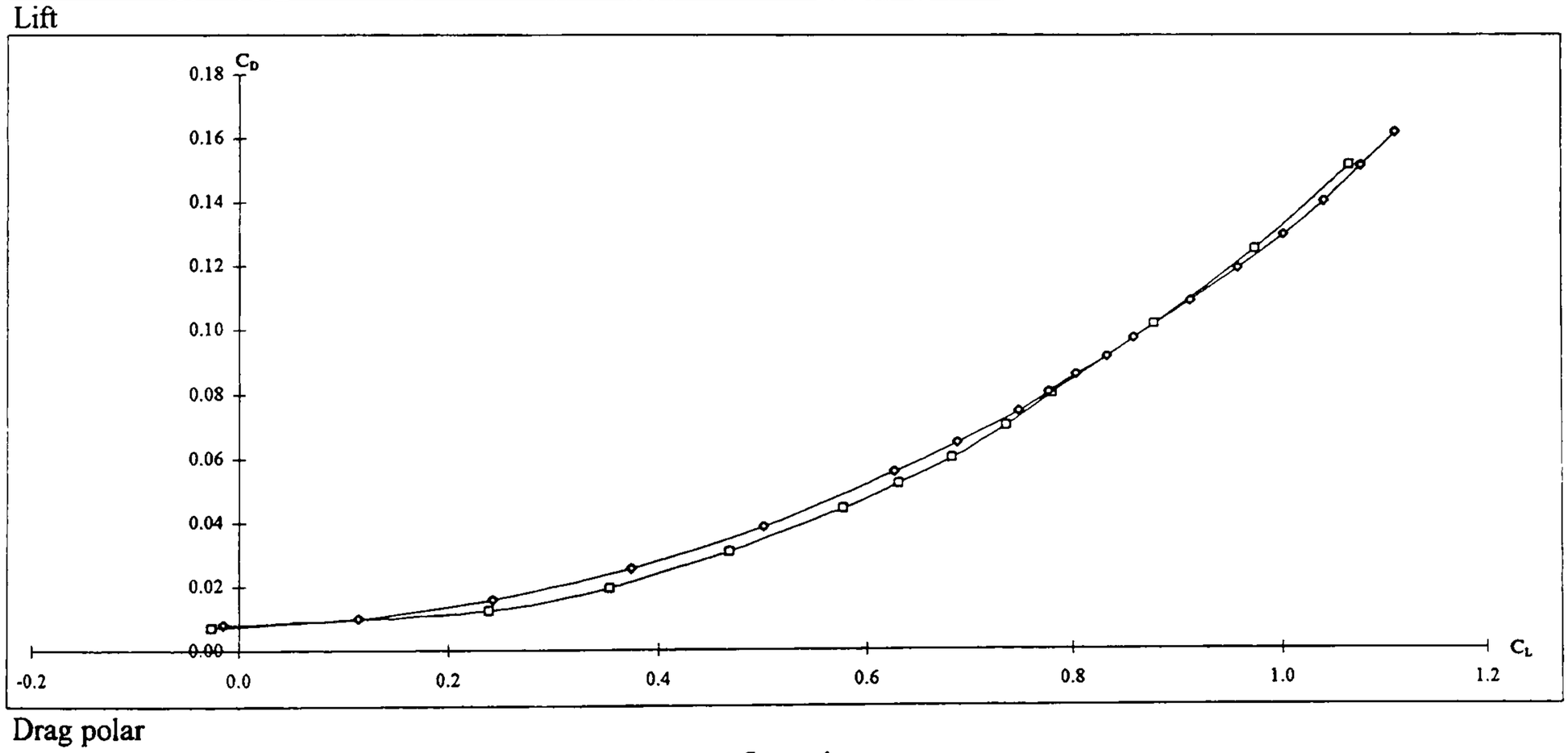

Drag polar

Key

configuration
without cropped delta vane vortex generators
with cropped delta vane vortex generators

Figure 5-41: DERA swept wing aerodynamic forces and moments with and without cropped delta vane vortex generators.
$\Lambda = 40°$, $Re_c = 3.3 \times 10^6$, $h = 0.0025c$, $x_v = 0.50c$, $\alpha_v = 30°$, $D = 40h$.

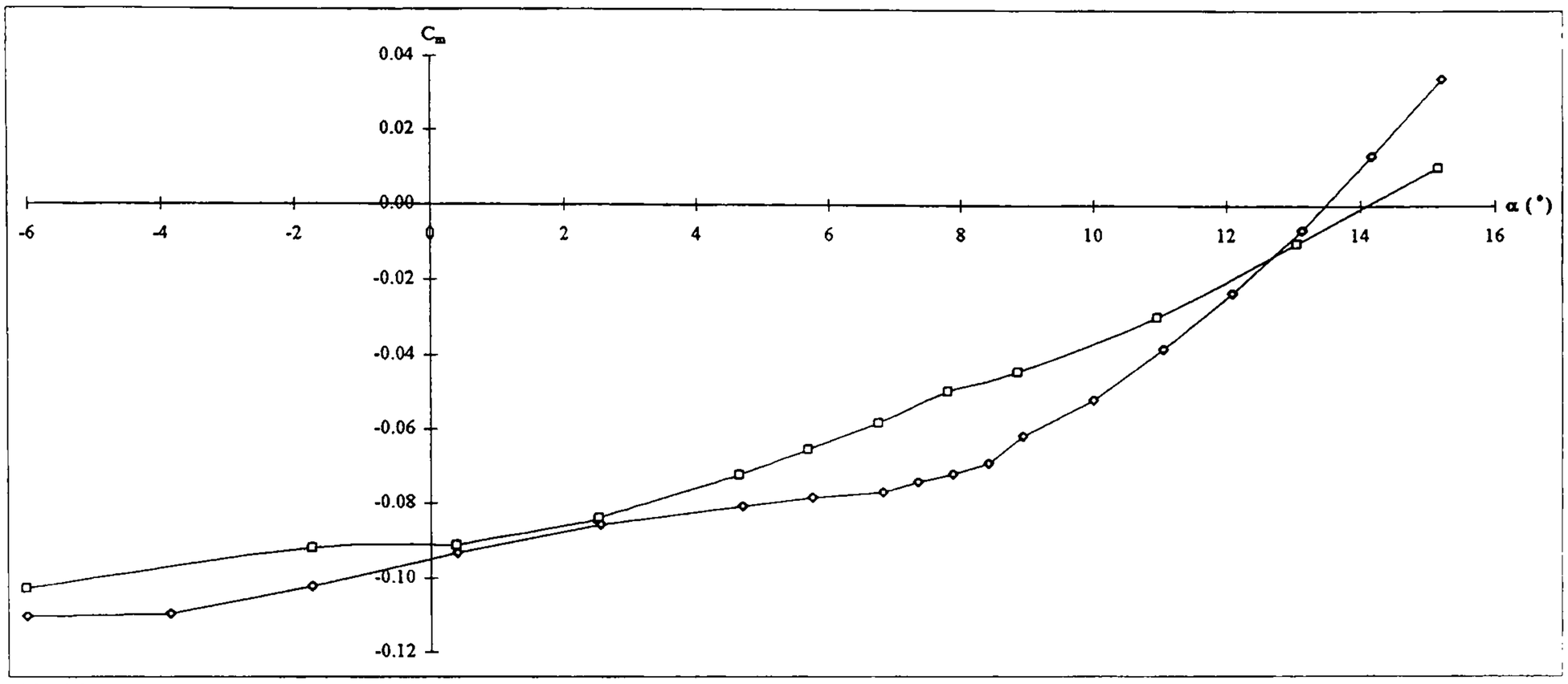

Pitching moment

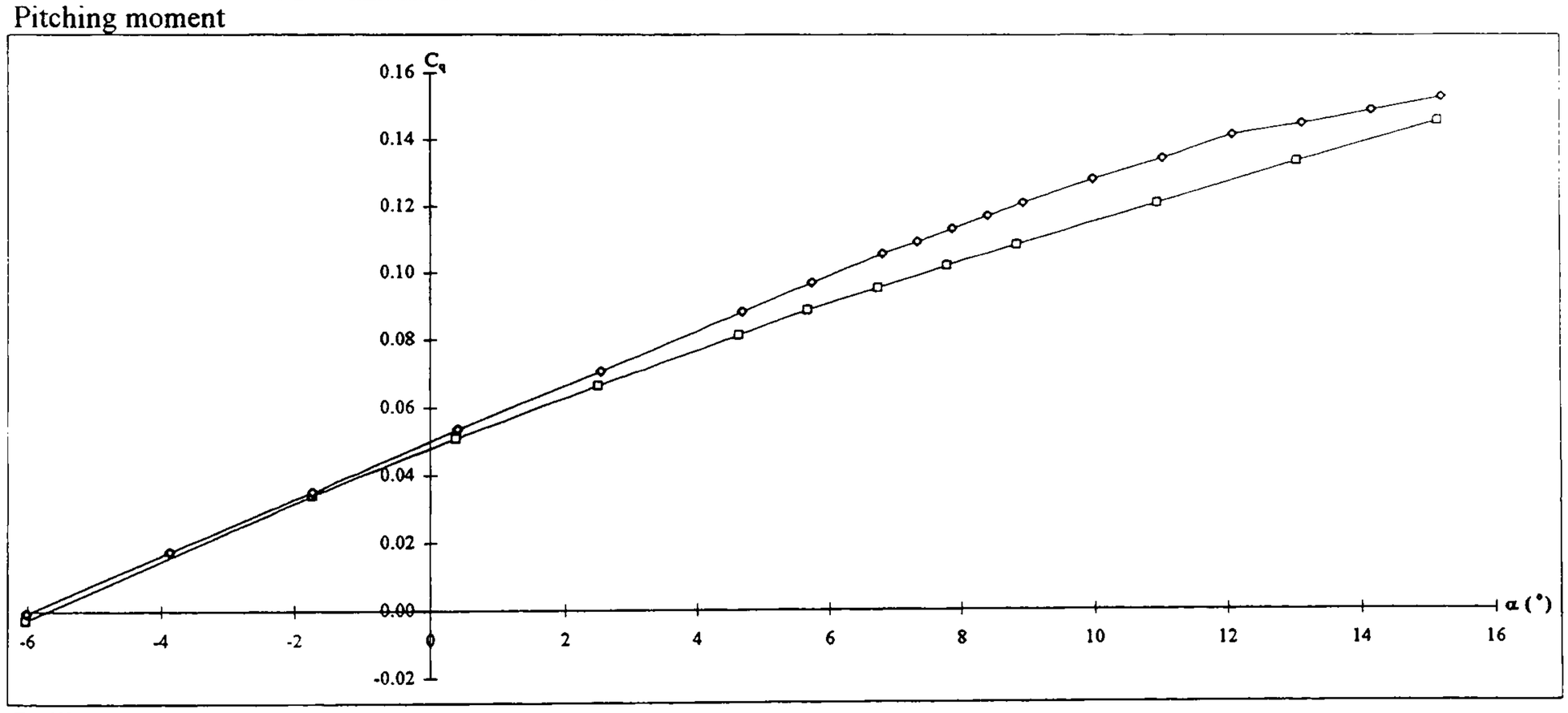

Rolling moment

Key

configuration

without cropped delta vane vortex generators

with cropped delta vane vortex generators

Figure 5-41 cont.: DERA swept wing aerodynamic forces and moments with and without cropped delta vane vortex generators.
$\Lambda = 40°$, $Re_c = 3.3 \times 10^6$, $h = 0.0025c$, $x_v = 0.50c$, $\alpha_v = 30°$, $D = 40h$.

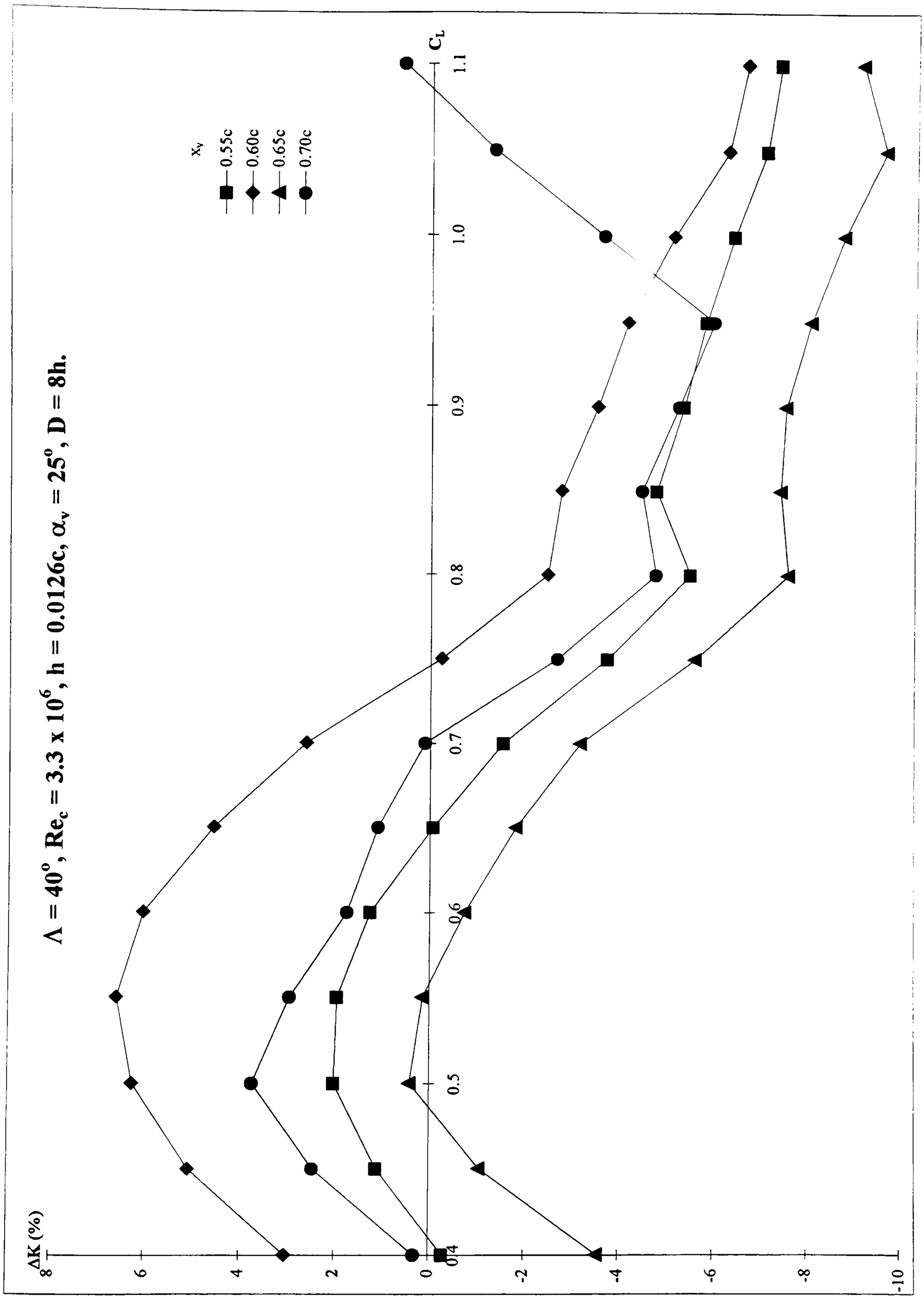

Figure 5-42a: Percentage change in lift dependent drag factor to that of the wing with separation versus lift coefficient for the DERA swept wing with cropped delta vane vortex generators at various chordwise positions.

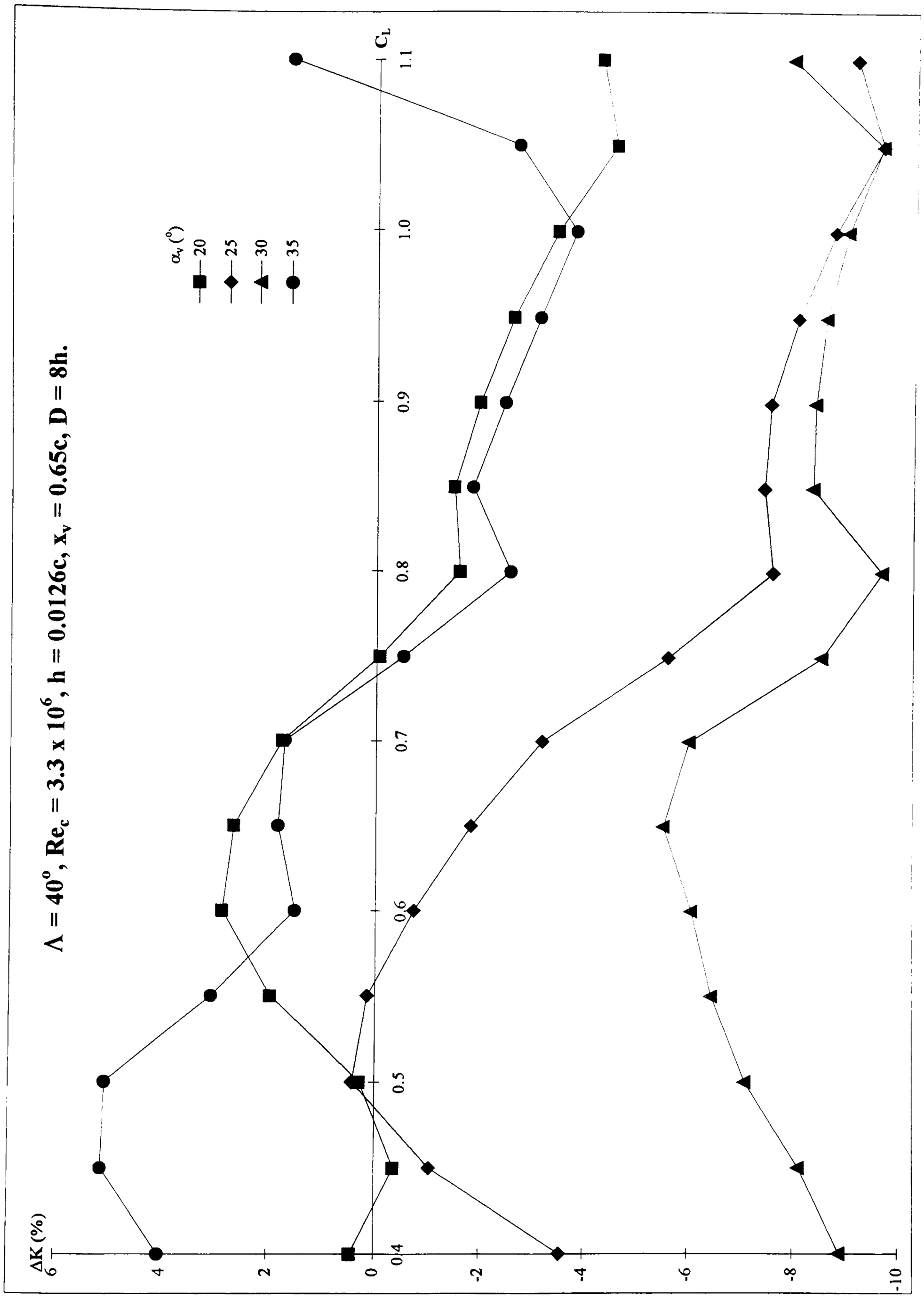

Figure 5-42b: Percentage change in lift dependent drag factor to that of the wing with separation versus lift coefficient for the DERA swept wing with cropped delta vane vortex generators at various orientations to the flow.

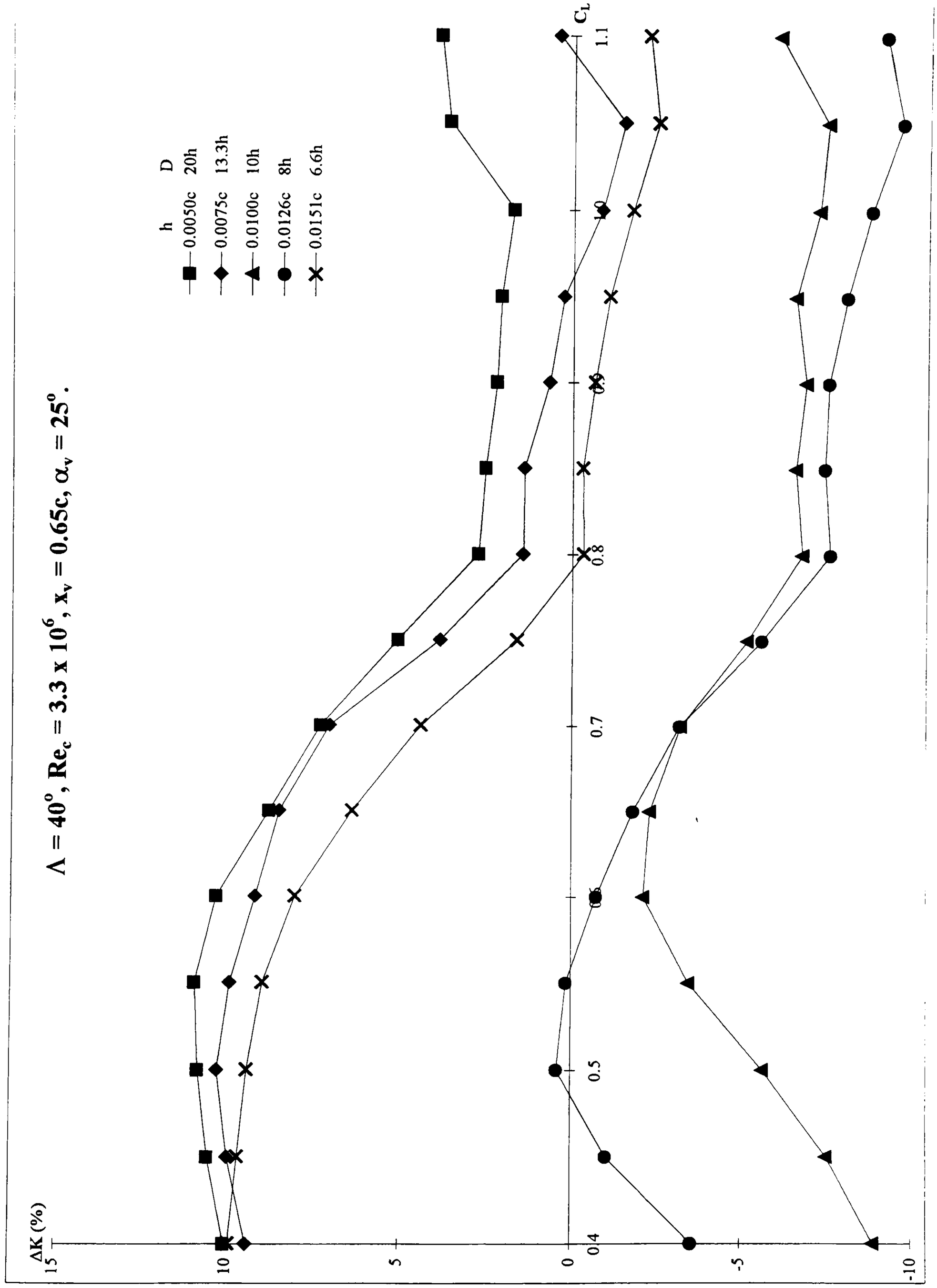

Figure 5-42c: Percentage change in lift dependent drag factor to that of the wing with separation versus lift coefficient for the DERA swept wing with cropped delta vane vortex generators of various heights.

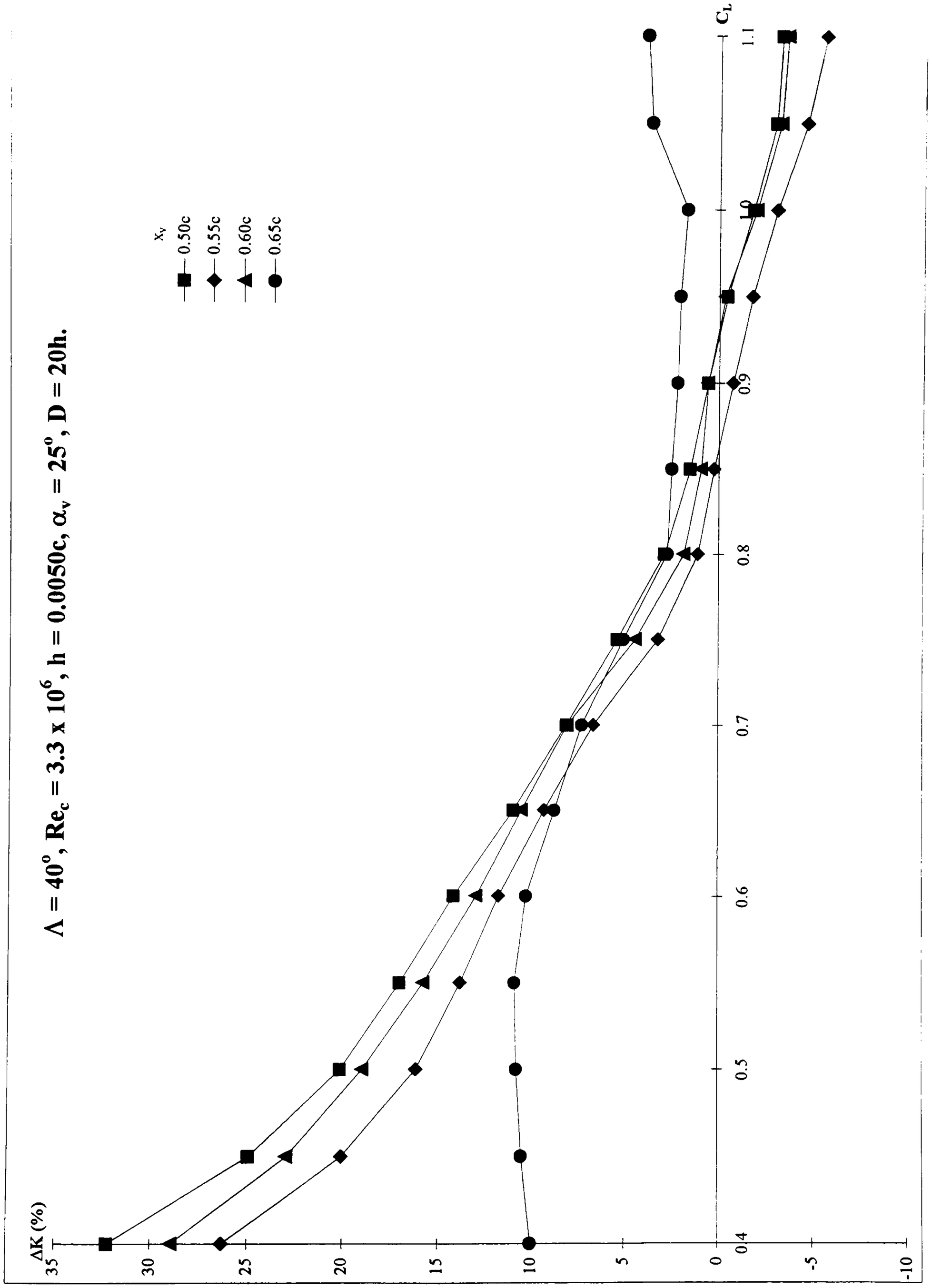

Figure 5-42d: Percentage change in lift dependent drag factor to that of the wing with separation versus lift coefficient for the DERA swept wing with cropped delta vane vortex generators at various chordwise positions.

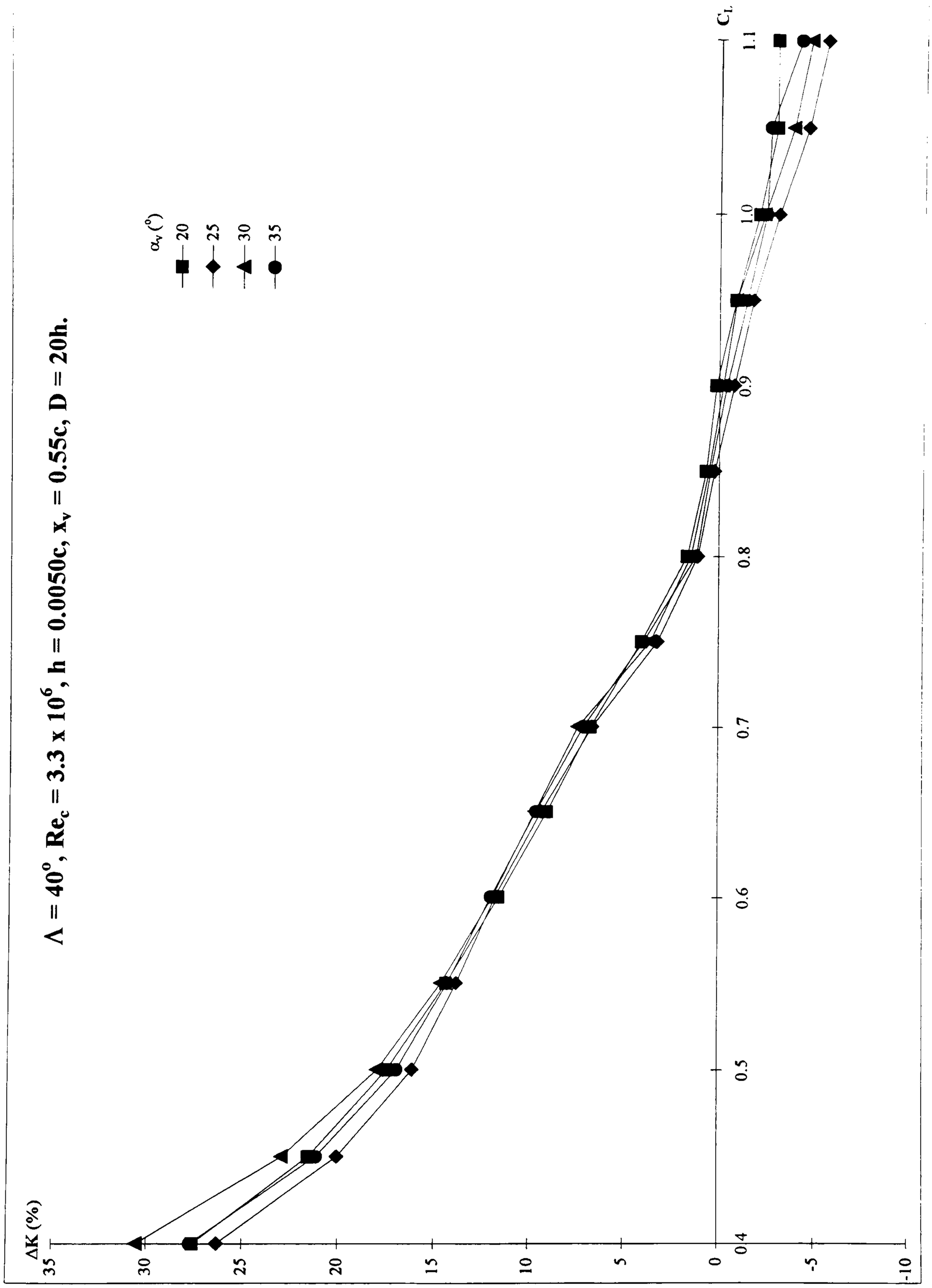

Figure 5-42e: Percentage change in lift dependent drag factor to that of the wing with separation versus lift coefficient for the DERA swept wing with cropped delta vane vortex generators at various orientations to the flow.

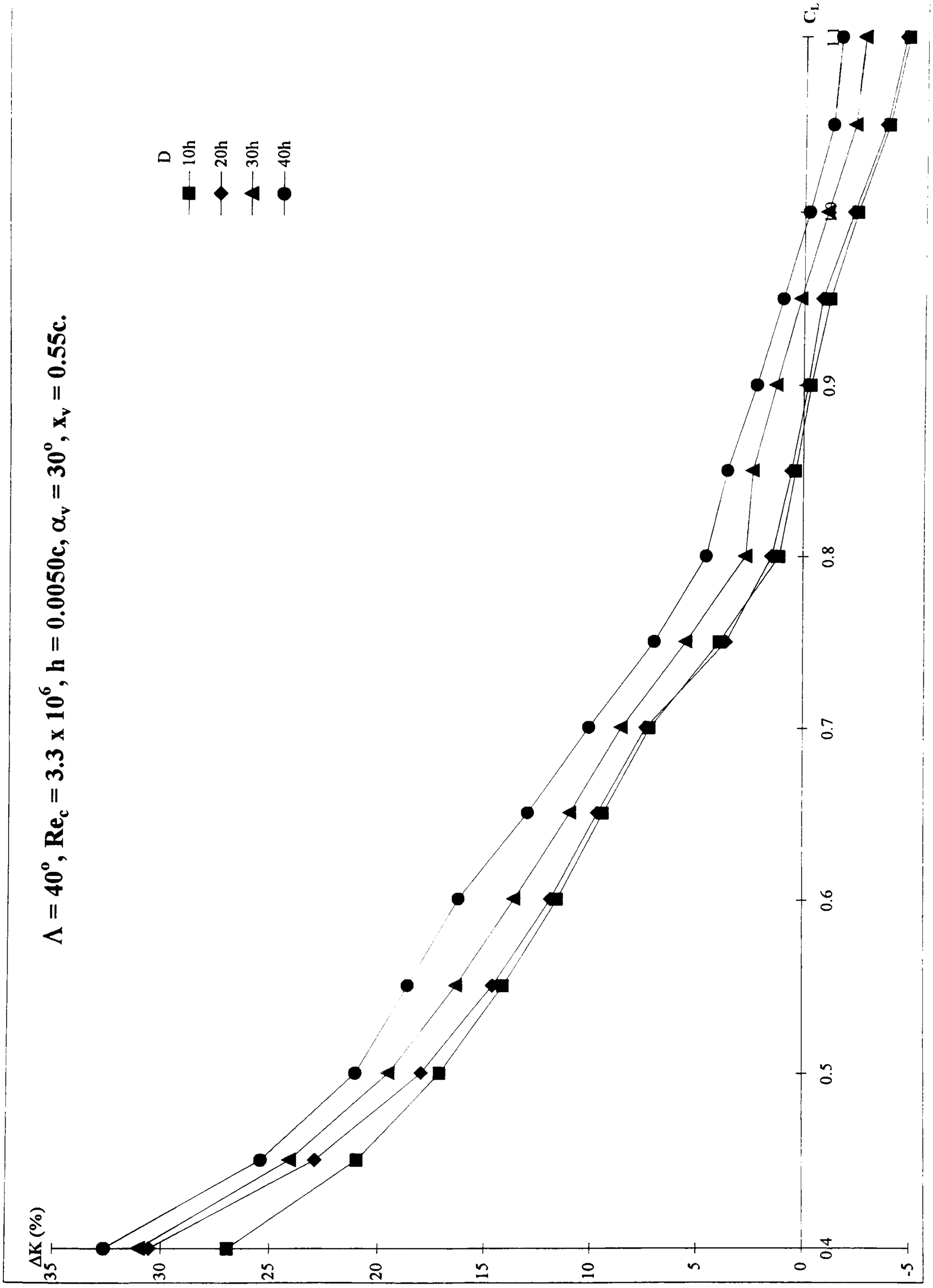

Figure 5-42f: Percentage change in lift dependent drag factor to that of the wing with separation versus lift coefficient for the DERA swept wing with cropped delta vane vortex generators at various spacings.

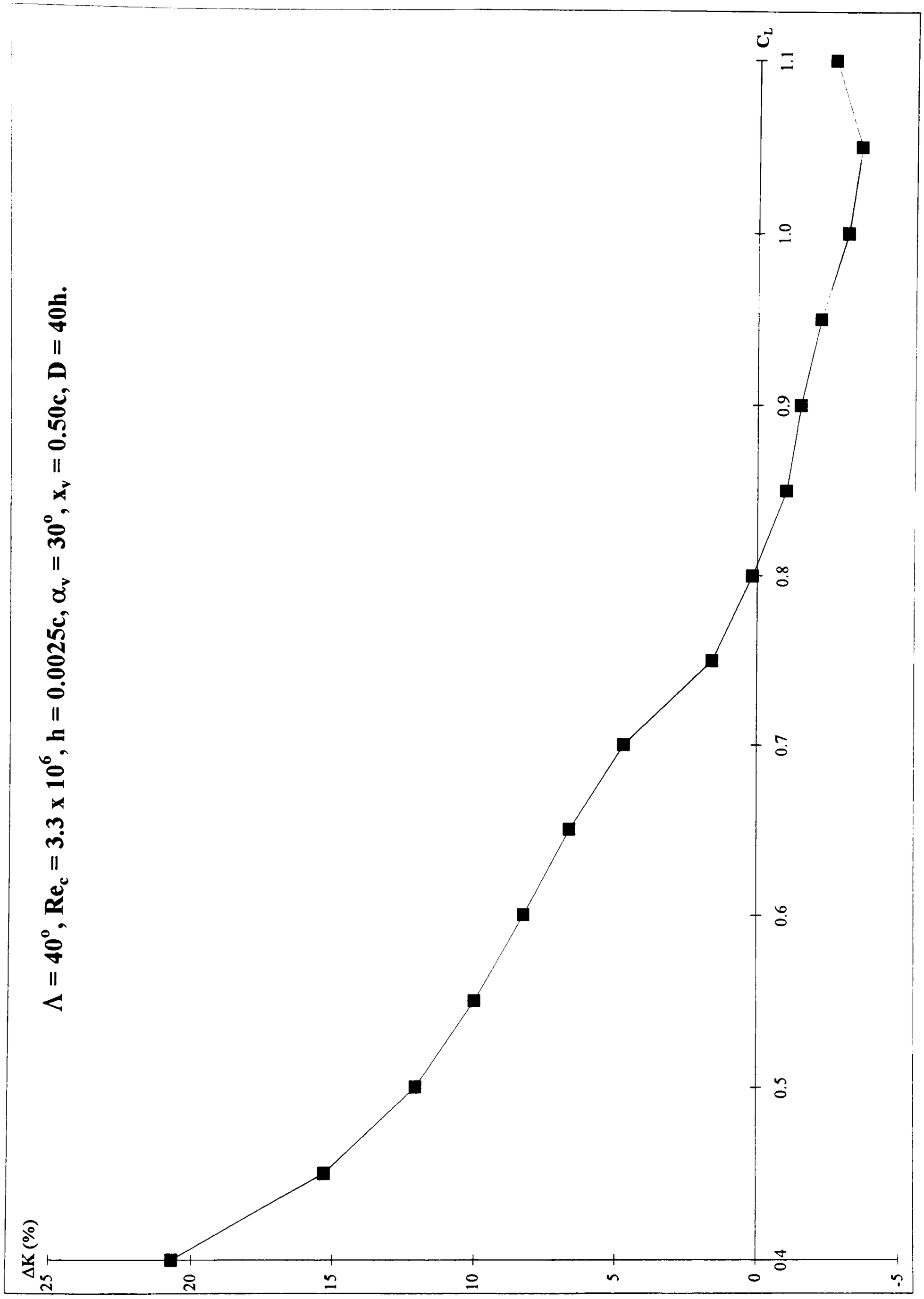

Figure 5-42g: Percentage change in lift dependent drag factor to that of the wing with separation versus lift coefficient for the DERA swept wing with cropped delta vane vortex generators.

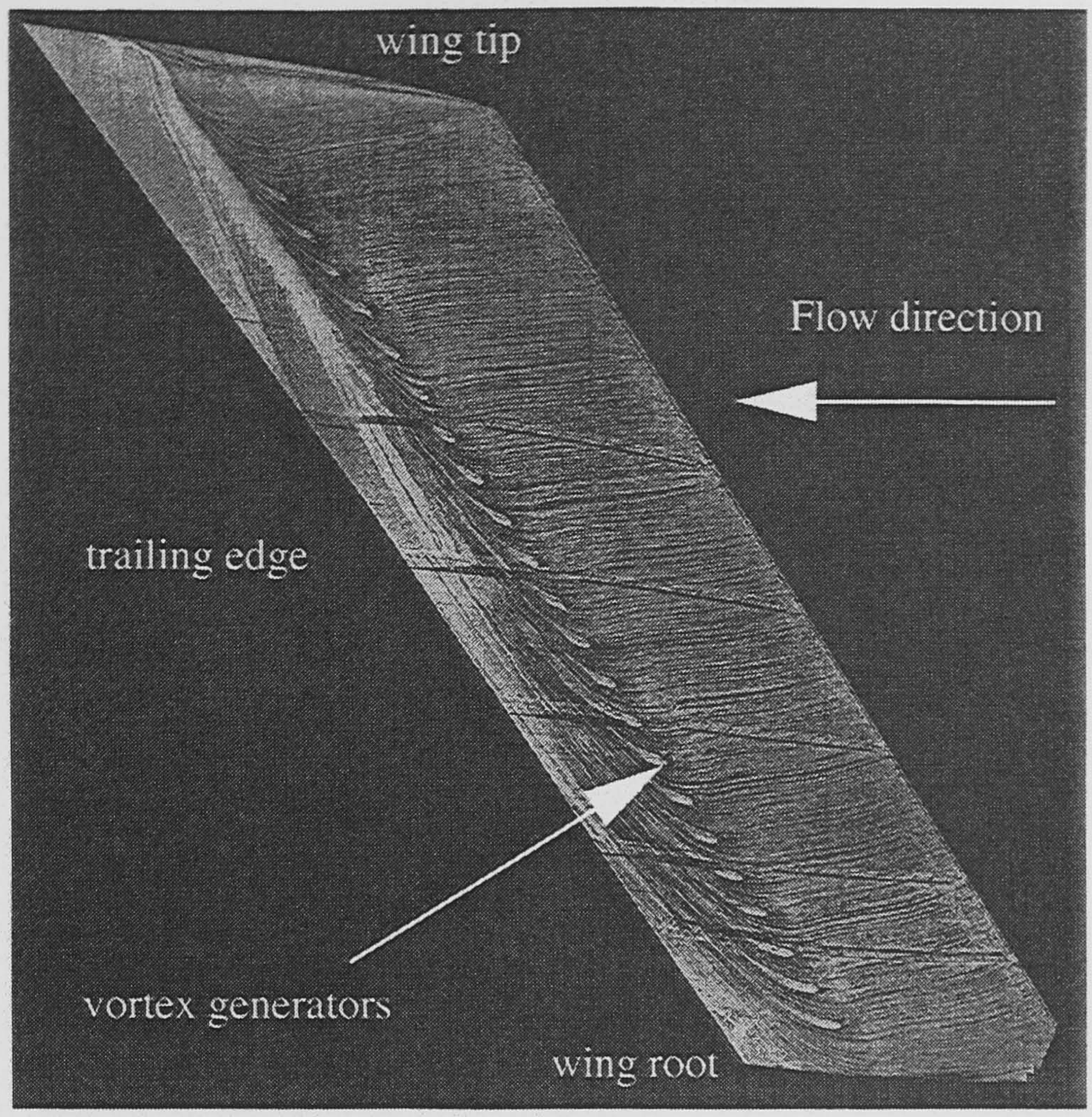

Figure 5-43: Surface oil flow visualisation results for the DERA swept wing with a co-rotating array of concave slat vortex generators.
$\Lambda = 40°$, $\alpha = 8°$, $Re_c = 3.3 \times 10^6$, $h = 0.0126c$, $\alpha_v = 25°$, $x_v = 0.65c$, $D = 8h$.

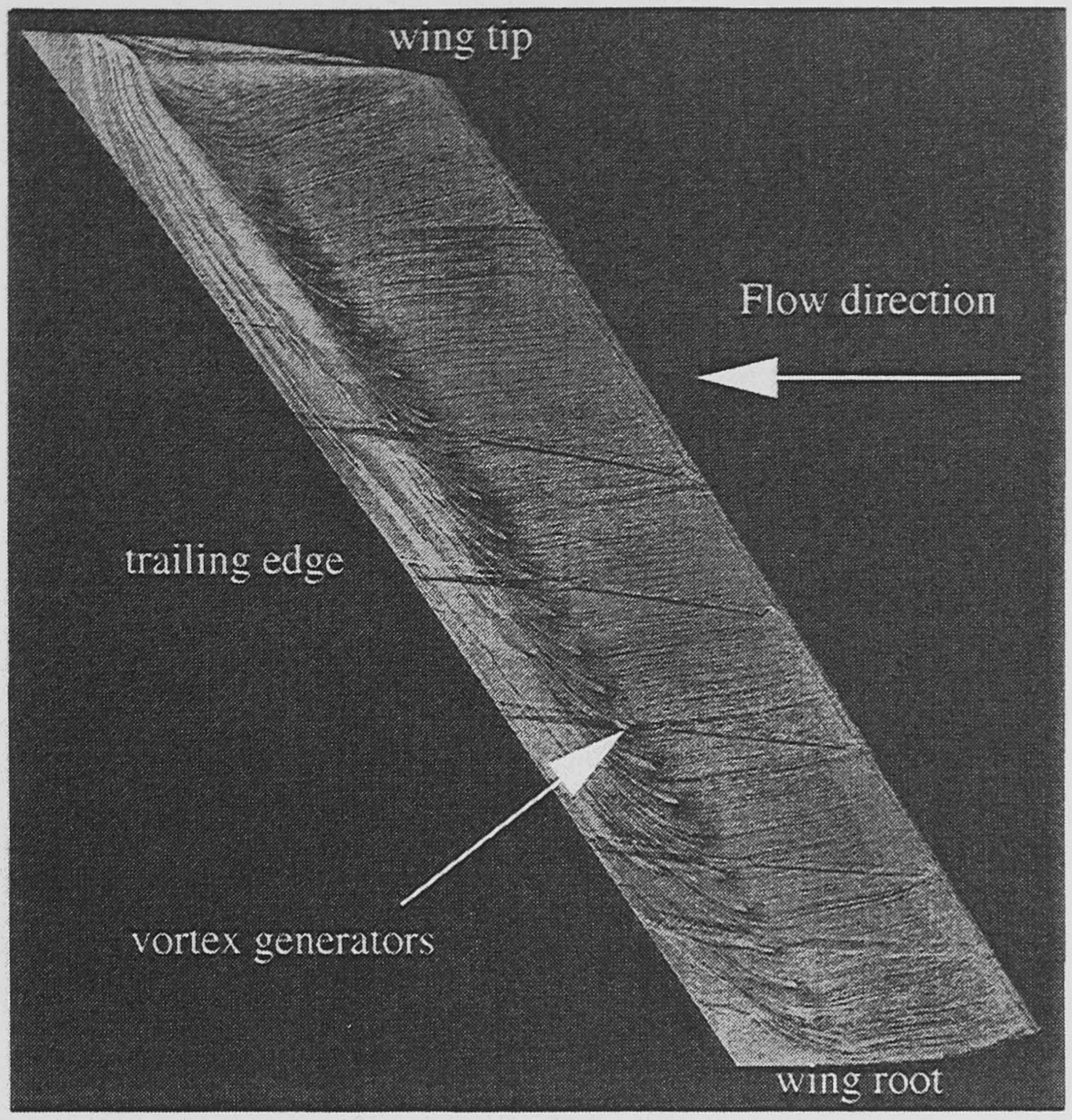

Figure 5-44: Surface oil flow visualisation results for the DERA swept wing with a co-rotating array of canted cropped delta vane vortex generators.
$\Lambda = 40°$, $\alpha = 8°$, $Re_c = 3.3 \times 10^6$, $h = 0.0126c$, $\alpha_v = 25°$, $x_v = 0.65c$, $D = 8h$.

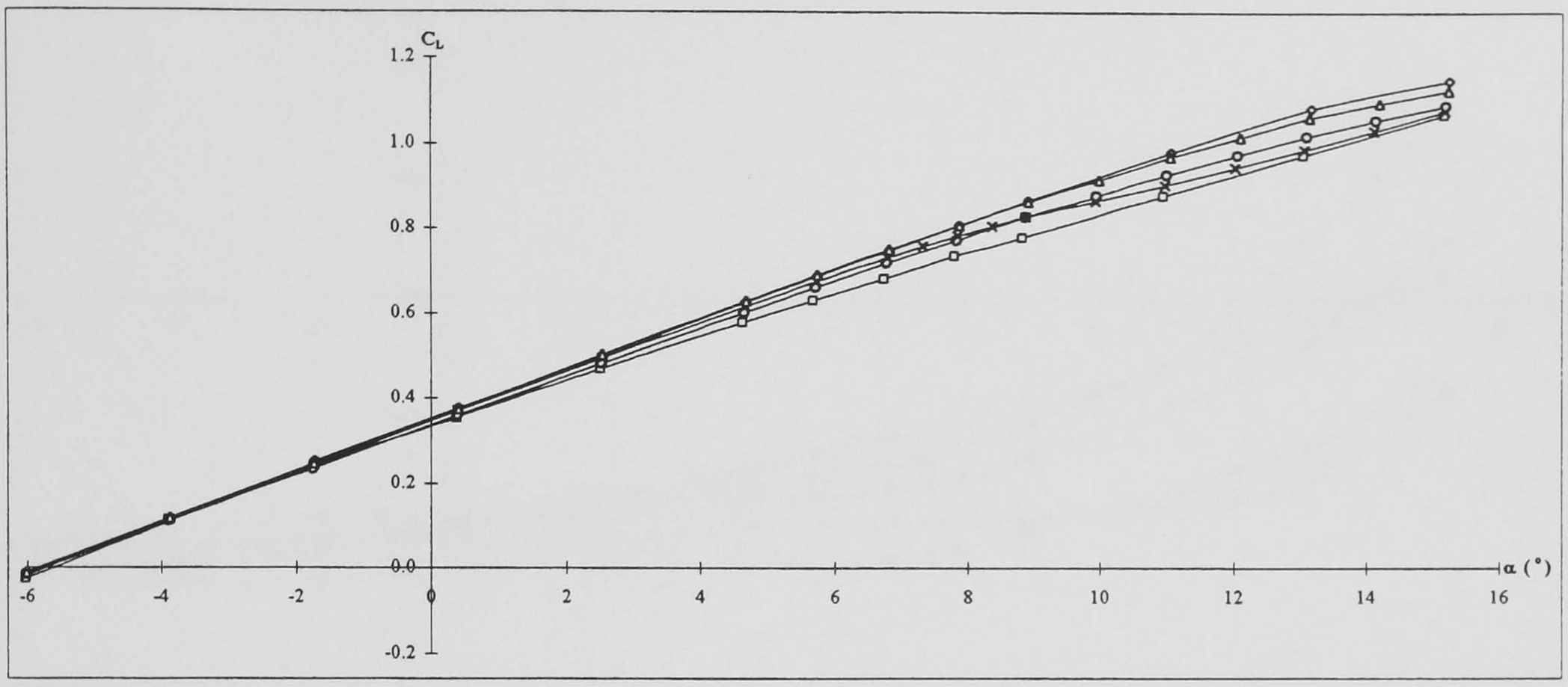

Lift

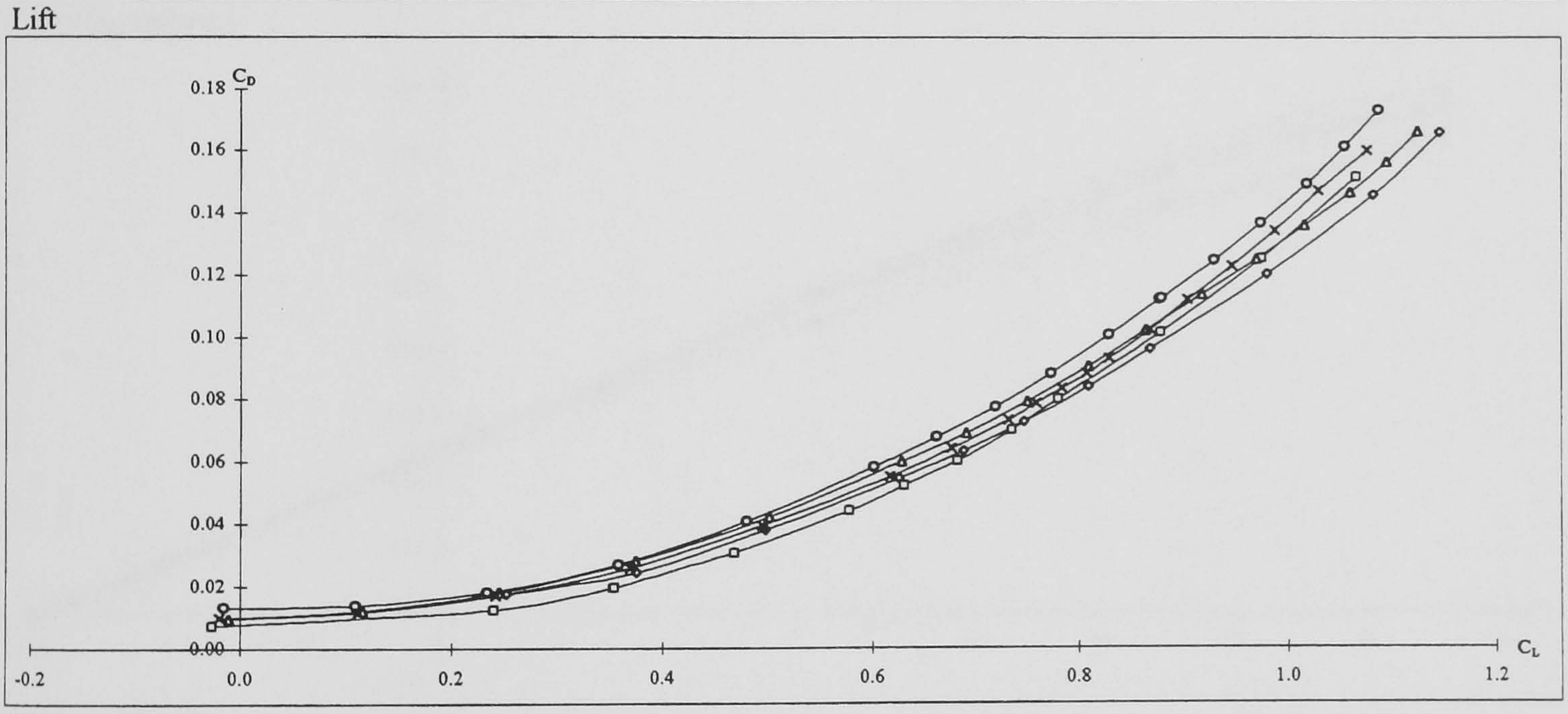

Drag polar

Key

—□—	no vortex generators
—◇—	cropped delta vanes
—△—	canted cropped delta vanes
—○—	concave slats
—×—	bent wires

vortex generator type

Figure 5-45: DERA swept wing aerodynamic forces and moments with and without vortex generators of various types.
$\Lambda = 40°$, $Re_c = 3.3 \times 10^6$, $h = 0.0126c$, $x_v = 0.65c$, $\alpha_v = 25°$, $D = 8h$.

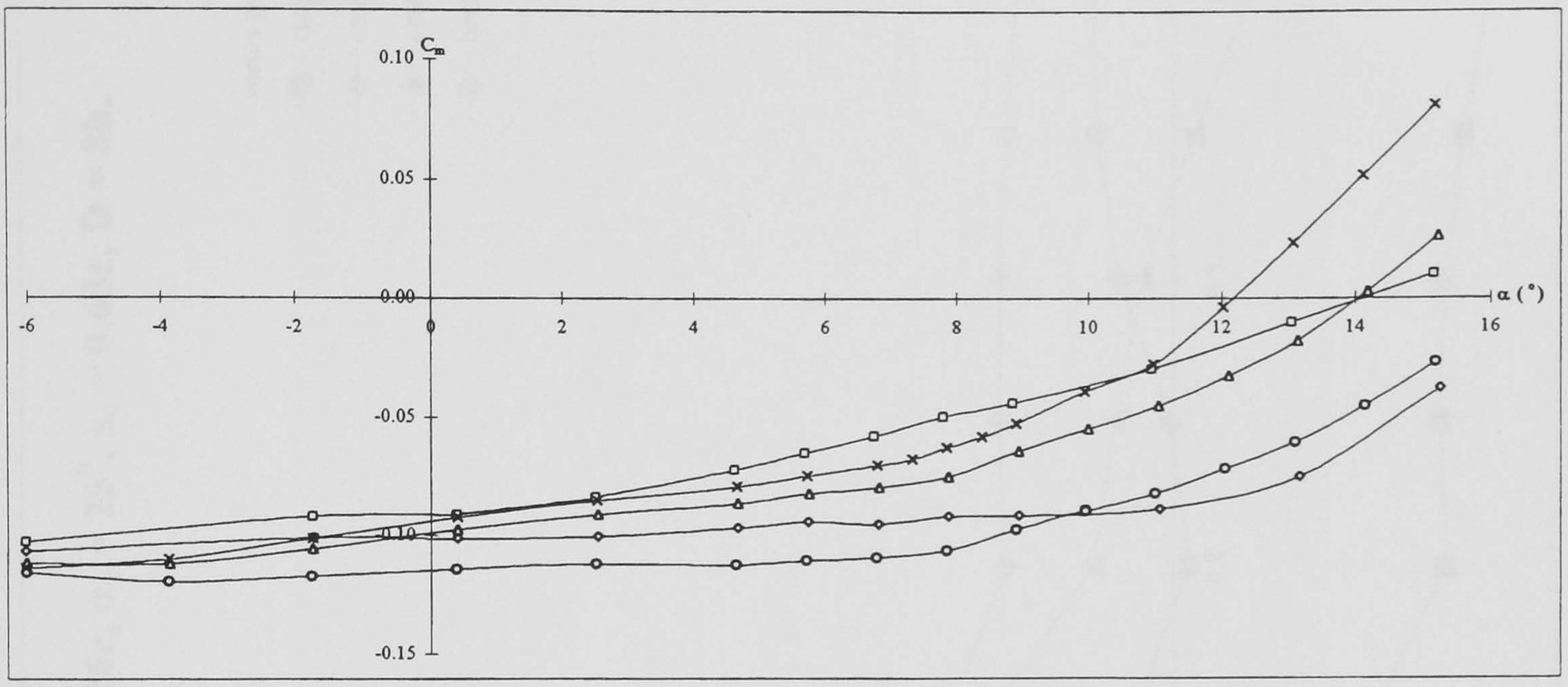

Pitching moment

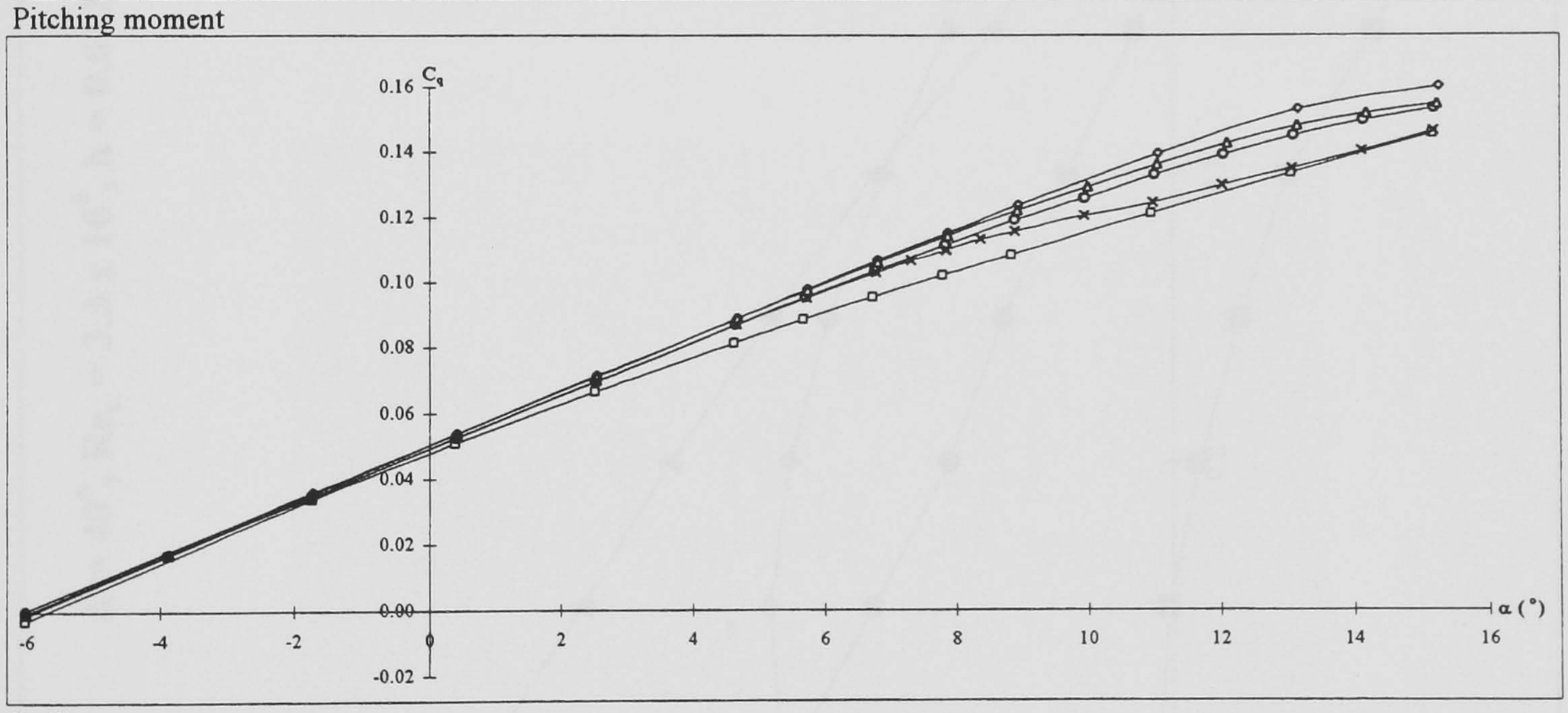

Rolling moment

Key

- vortex generator type
- no vortex generators
- cropped delta vanes
- canted cropped delta vanes
- concave slats
- bent wires

Figure 5-45 cont.: DERA swept wing aerodynamic forces and moments with and without vortex generators of various types.
$\Lambda = 40°$, $Re_c = 3.3 \times 10^6$, $h = 0.0126c$, $x_v = 0.65c$, $\alpha_v = 25°$, $D = 8h$.

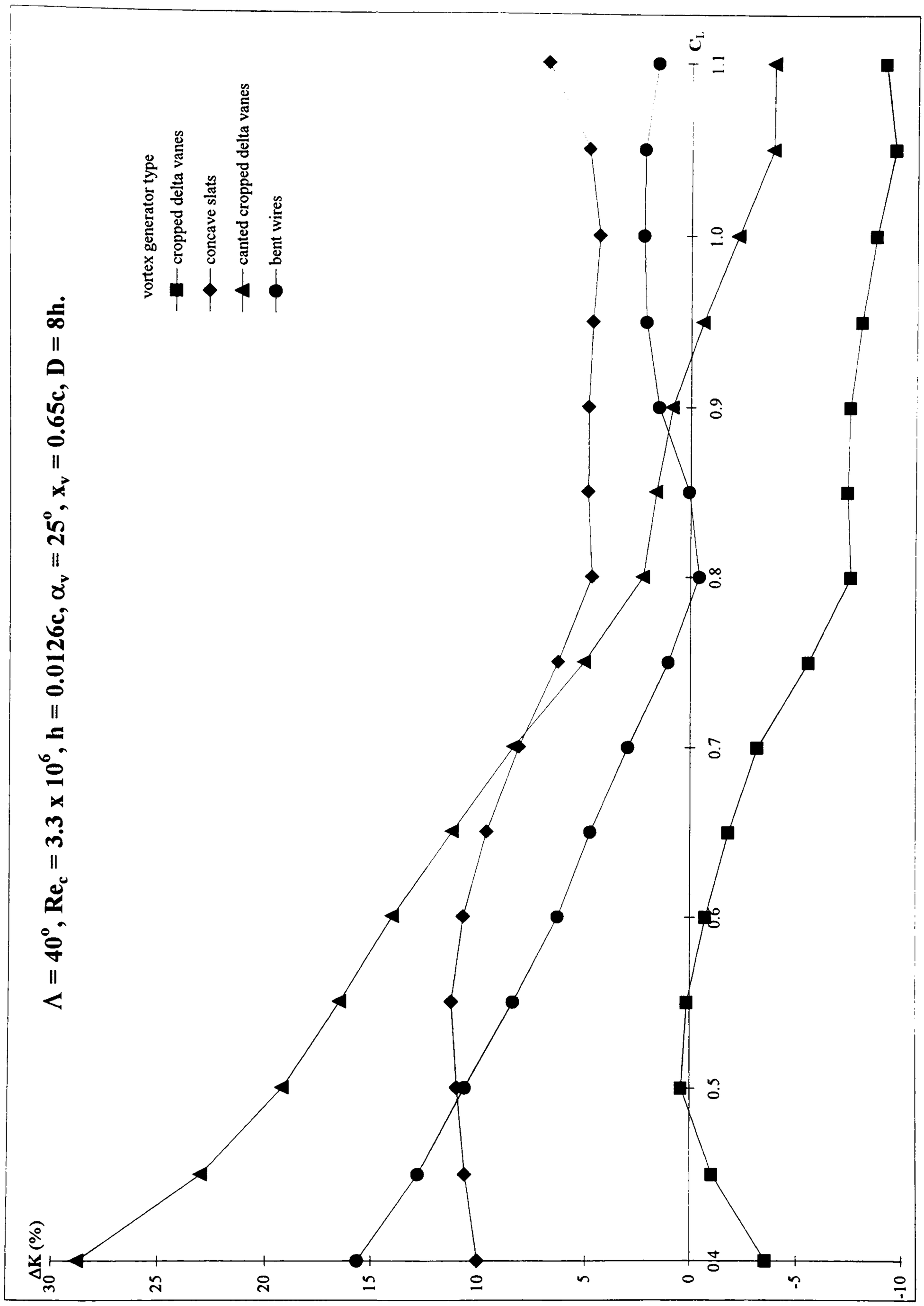

Figure 5-46: Percentage change in lift dependent drag factor to that of the wing with separation versus lift coefficient for the DERA swept wing with various type vortex generators.

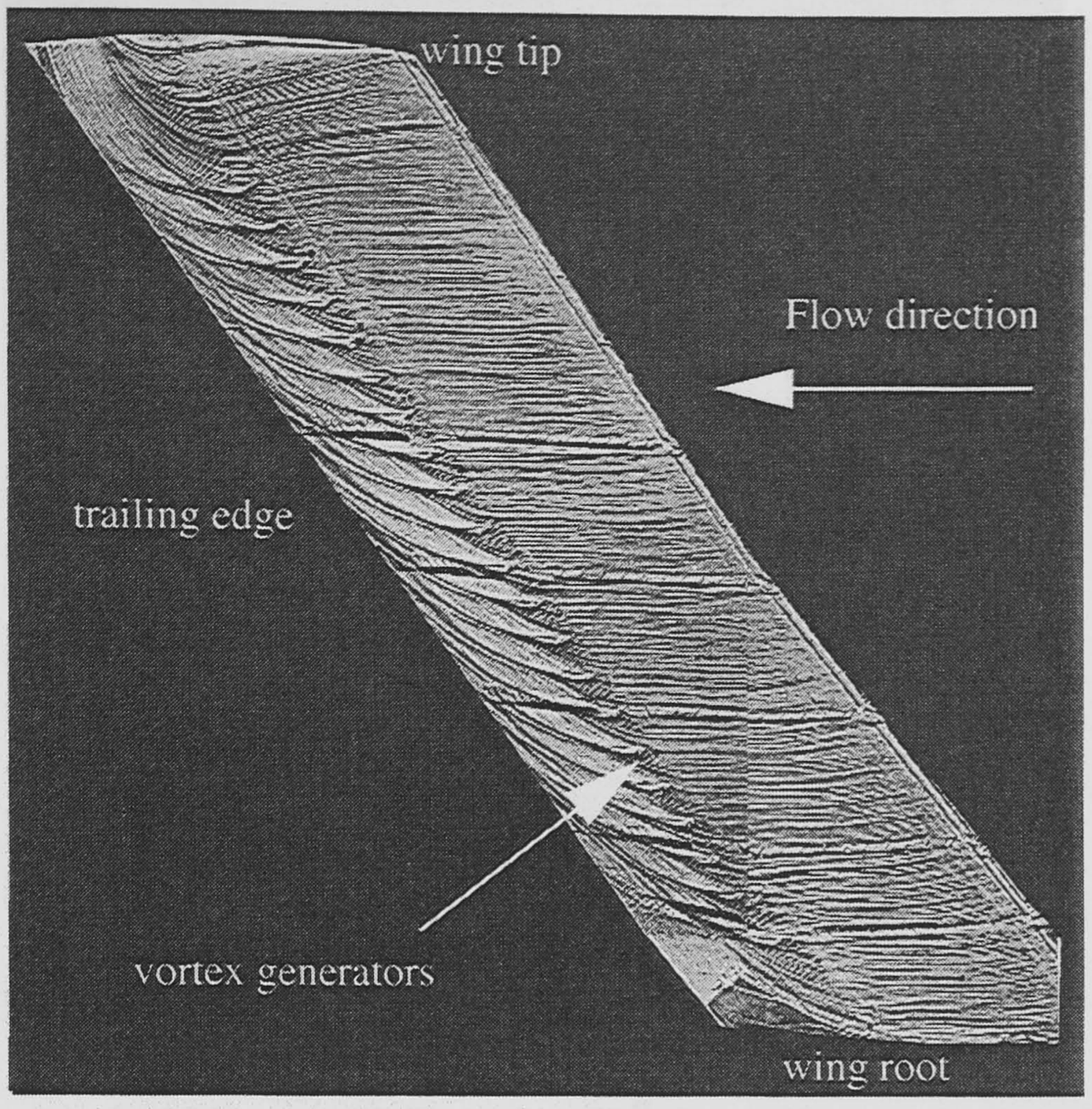

h = 0.0105c, x_v = 0.65c, $\alpha_v = 25^o$, D = 8h

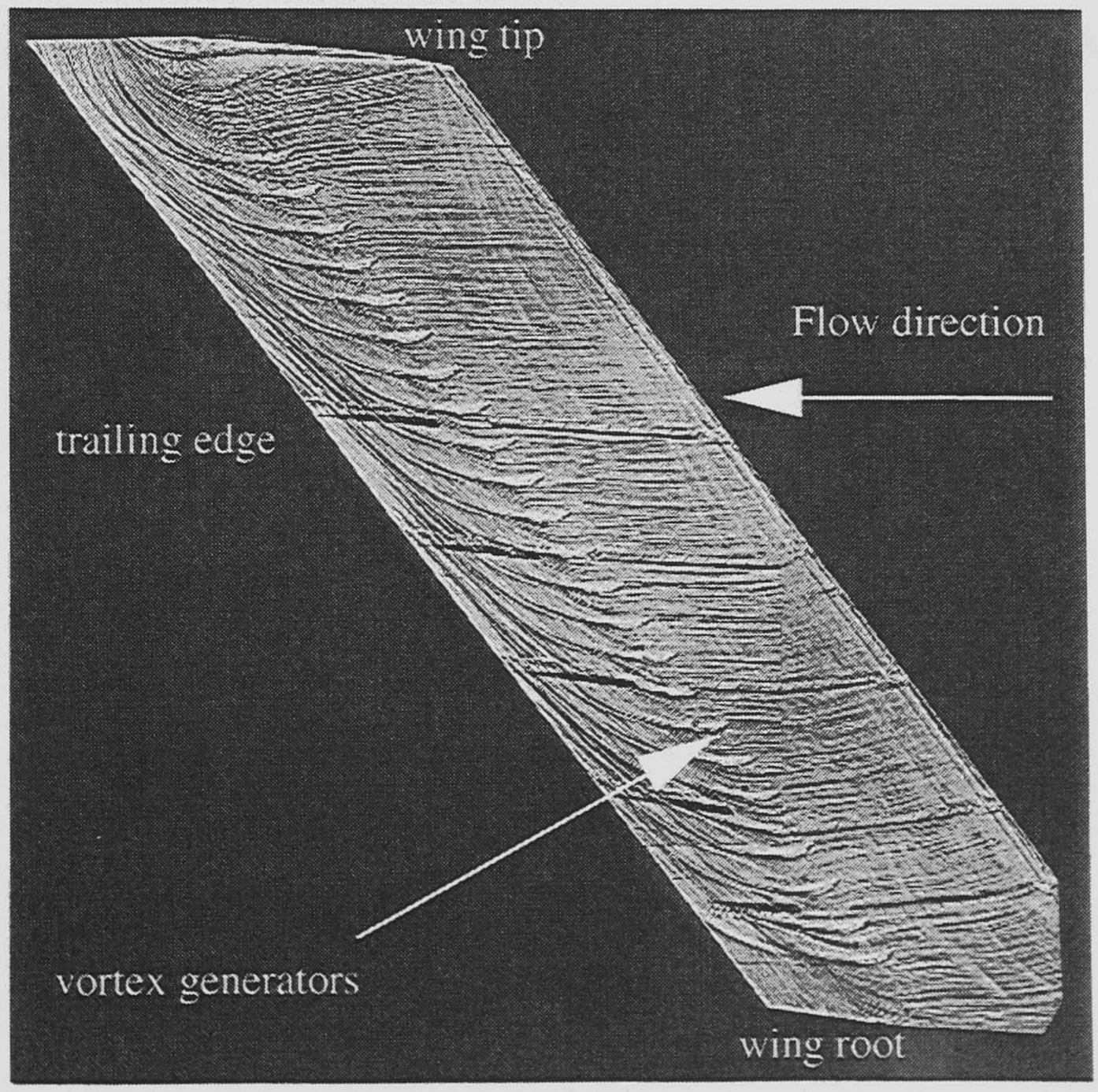

h = 0.0040c, x_v = 0.55c, $\alpha_v = 30^o$, D = 20h

Figure 5-47: Surface oil flow visualisation results for the DERA swept wing with a co-rotating array of cropped delta vane vortex generators.
$\Lambda = 50°$, $\alpha = 10°$, $Re_c = 3.9 \times 10^6$.

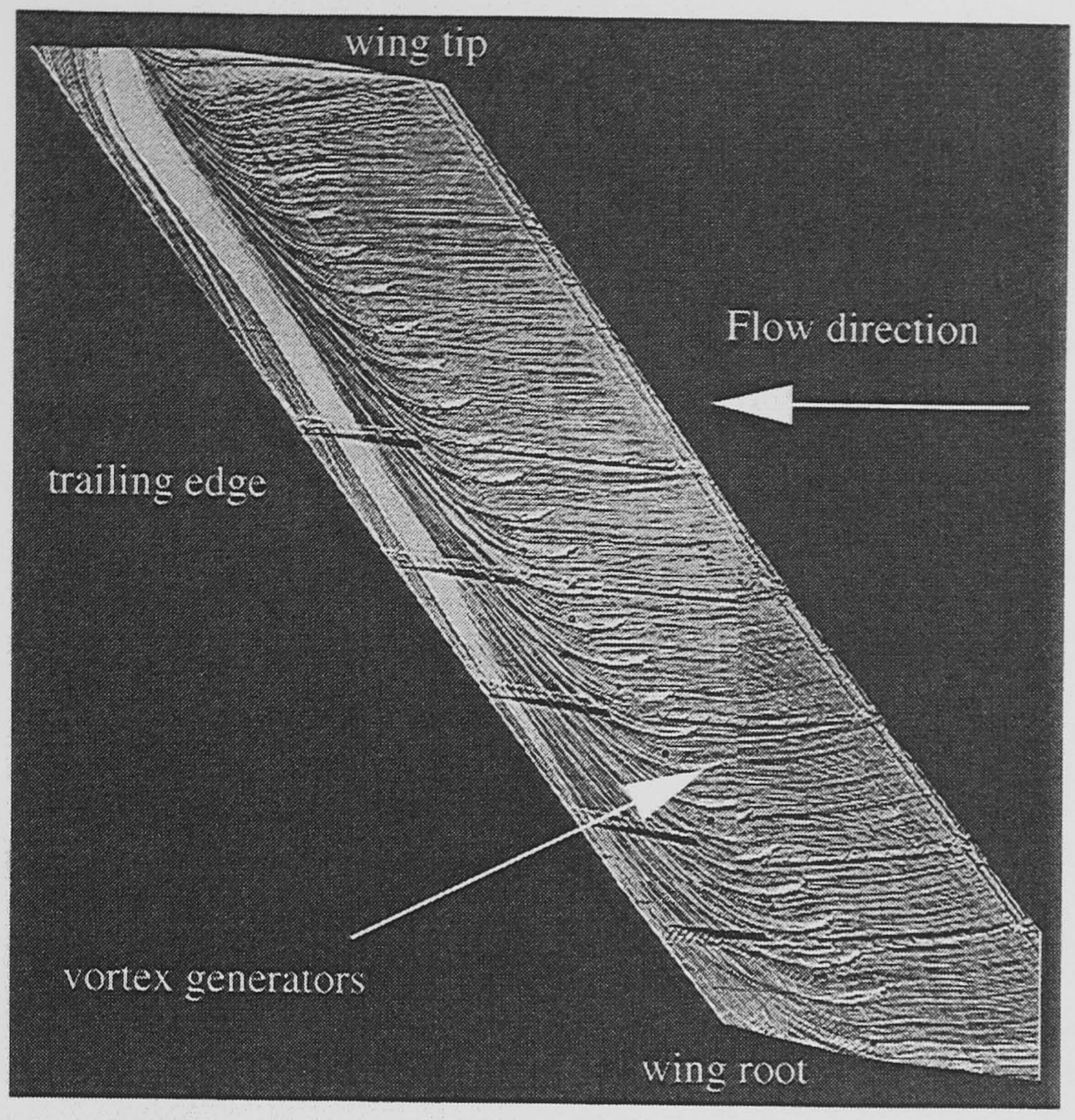

h = 0.0020c, x_v = 0.50c, $\alpha_v = 30^o$, D = 40h

Figure 5-47 cont.: Surface oil flow visualisation results for the DERA swept wing with a co-rotating array of cropped delta vane vortex generators.
$\Lambda = 50°$, $\alpha = 10°$, $Re_c = 3.9 \times 10^6$.

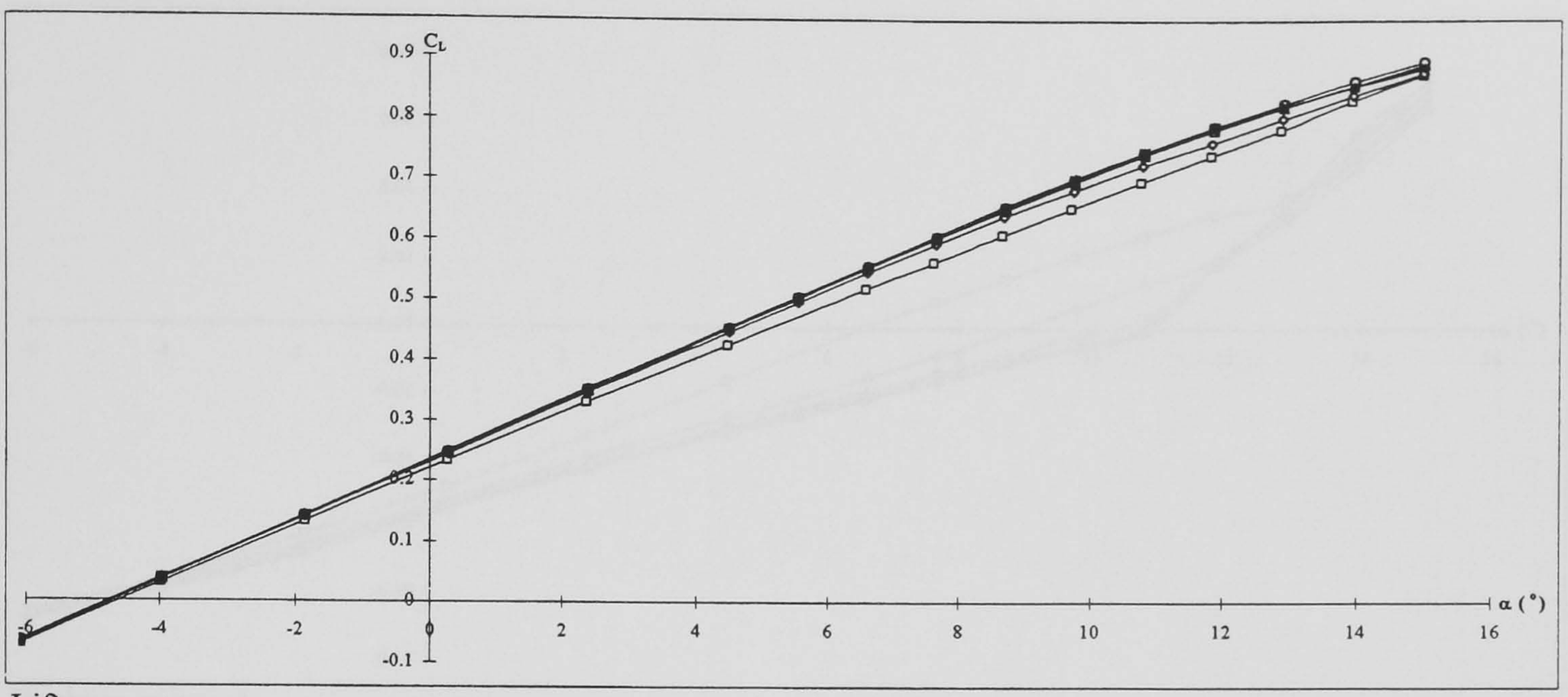

Lift

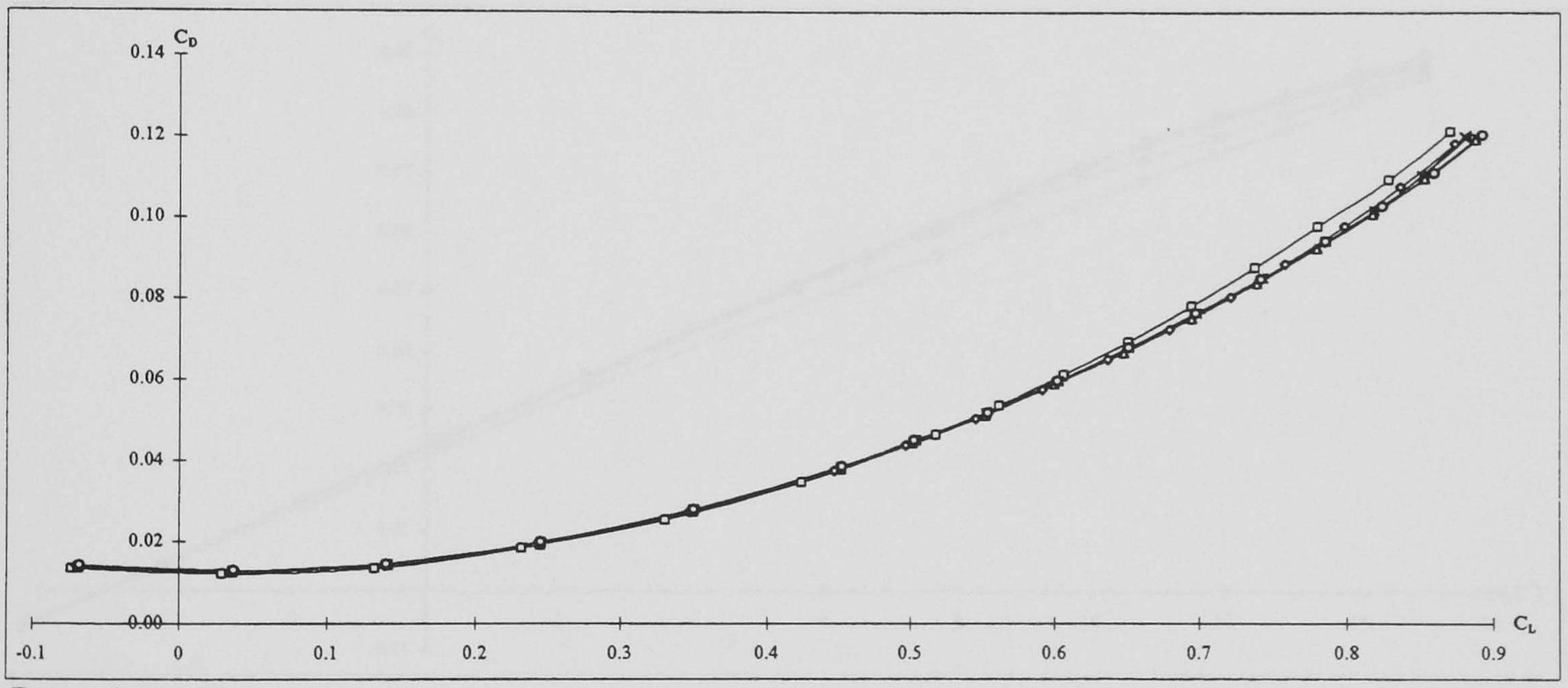

Drag polar

Key

	configuration
—□—	without vortex generators
—◇—	$h = 0.0020c$, $x_v = 0.50c$, $\alpha_v = 30°$, $D = 40h$
—△—	$h = 0.0040c$, $x_v = 0.55c$, $\alpha_v = 30°$, $D = 20h$
—○—	$h = 0.0040c$, $x_v = 0.55c$, $\alpha_v = 40°$, $D = 20h$
—×—	$h = 0.0105c$, $x_v = 0.65c$, $\alpha_v = 25°$, $D = 8h$
—+—	$h = 0.0105c$, $x_v = 0.65c$, $\alpha_v = 30°$, $D = 8h$

Figure 5-48: DERA swept wing aerodynamic forces and moments with and without cropped delta vane vortex generators.
$\Lambda = 50°$, $Re_c = 3.9 \times 10^6$.

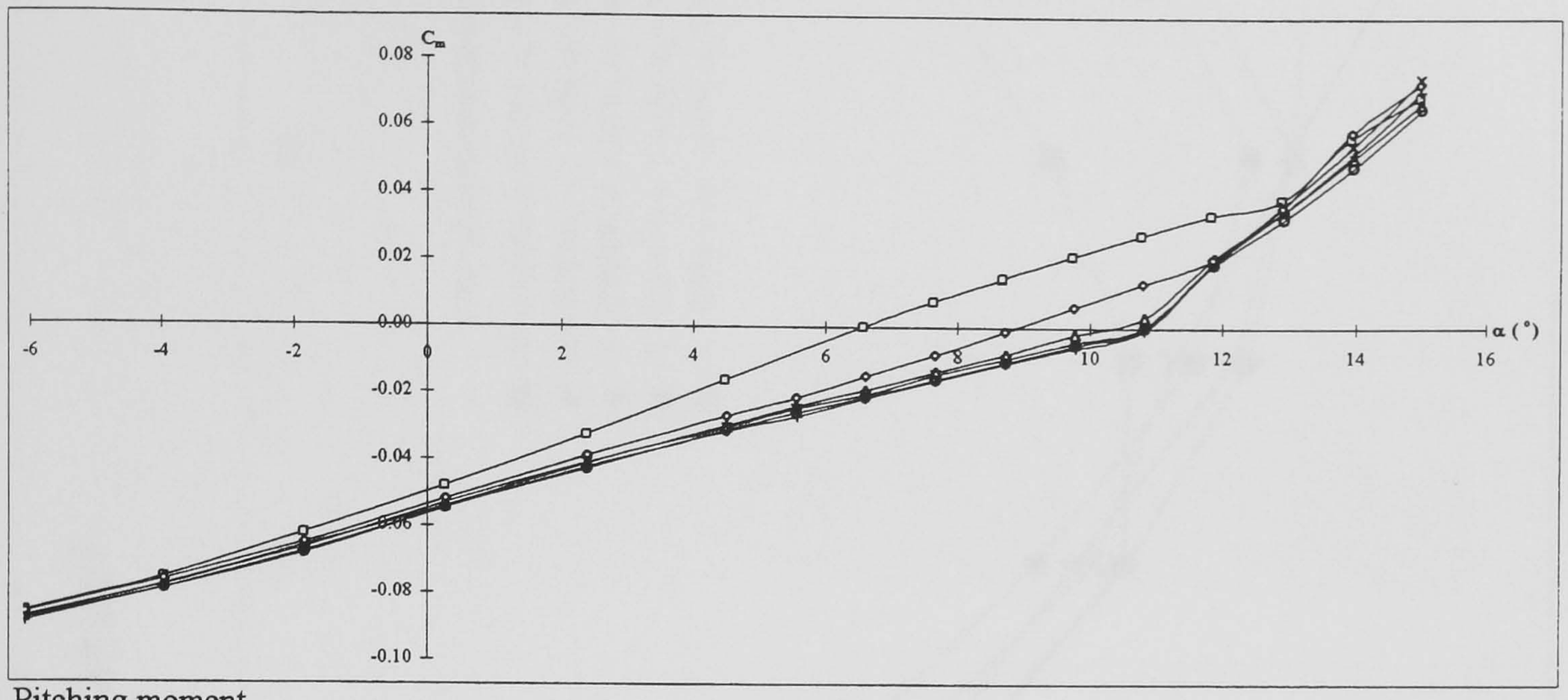

Pitching moment

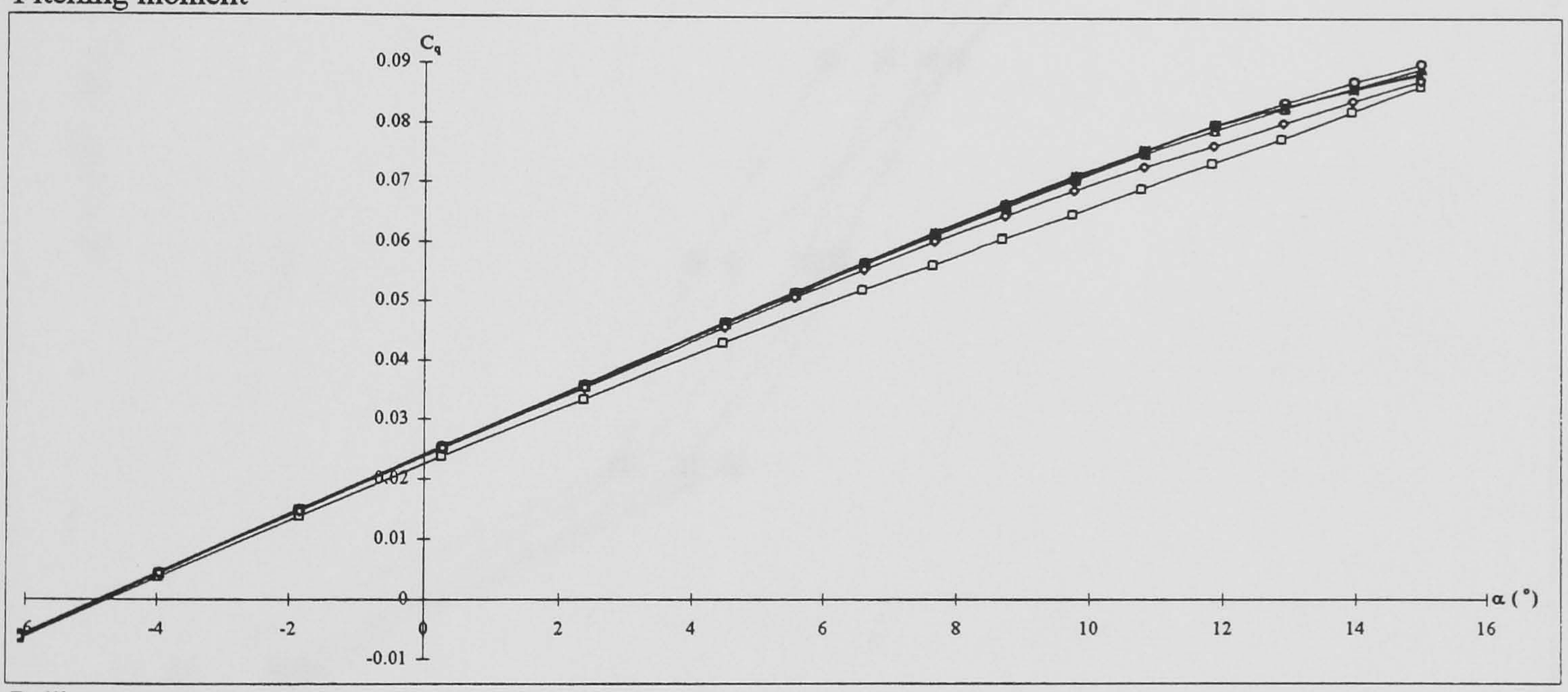

Rolling moment

Key

	configuration
—□—	without vortex generators
—◇—	h = 0.0020c, x_v = 0.50c, α_v = 30°, D = 40h
—△—	h = 0.0040c, x_v = 0.55c, α_v = 30°, D = 20h
—○—	h = 0.0040c, x_v = 0.55c, α_v = 40°, D = 20h
—×—	h = 0.0105c, x_v = 0.65c, α_v = 25°, D = 8h
—+—	h = 0.0105c, x_v = 0.65c, α_v = 30°, D = 8h

Figure 5-48 cont.: DERA swept wing aerodynamic forces and moments with and without cropped delta vane vortex generators.
$\Lambda = 50°$, $Re_c = 3.9 \times 10^6$.

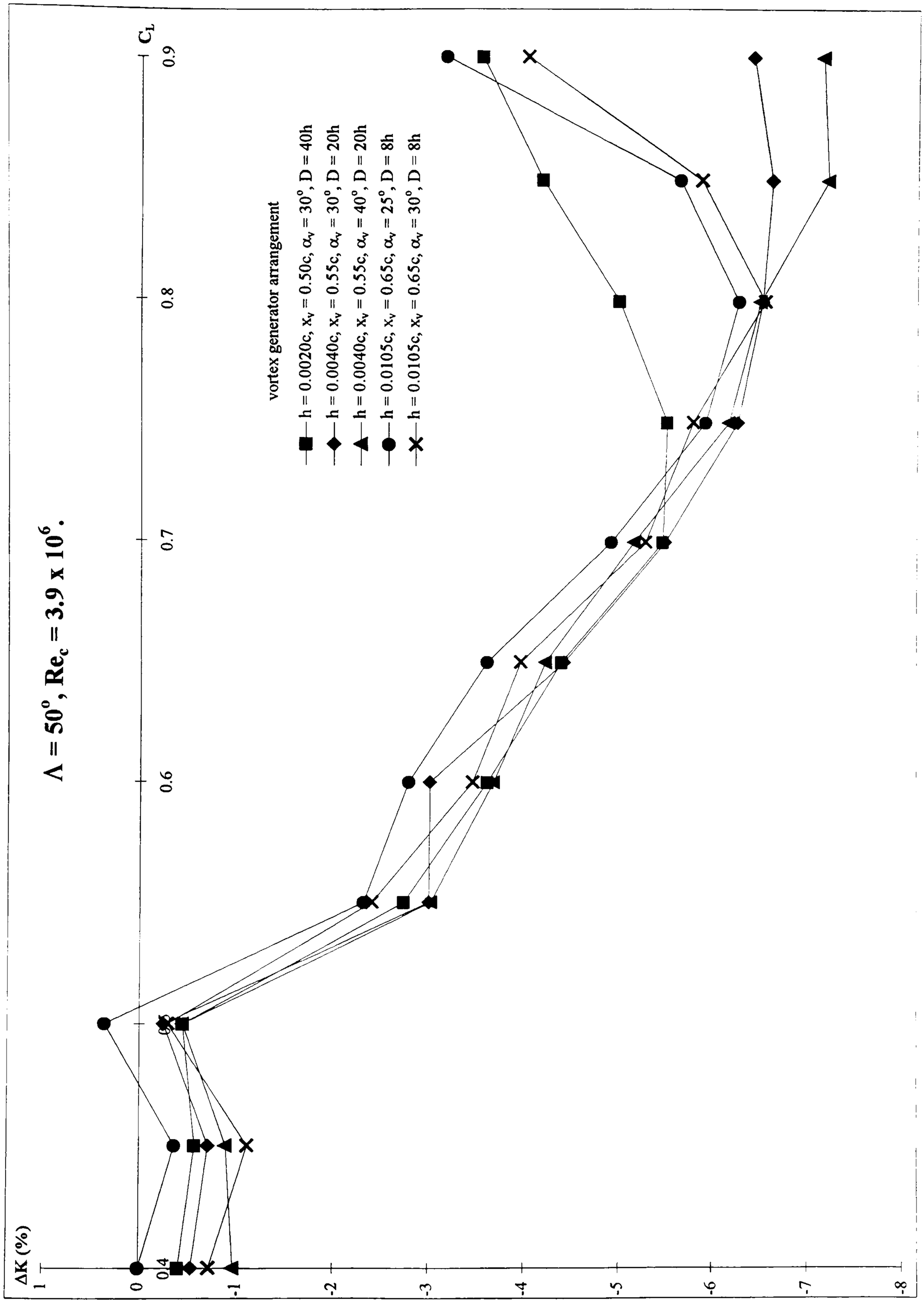

Figure 5-49: Percentage change in lift dependent drag factor to that of the wing with separation versus lift coefficient for the DERA swept wing with cropped delta vane vortex generators.

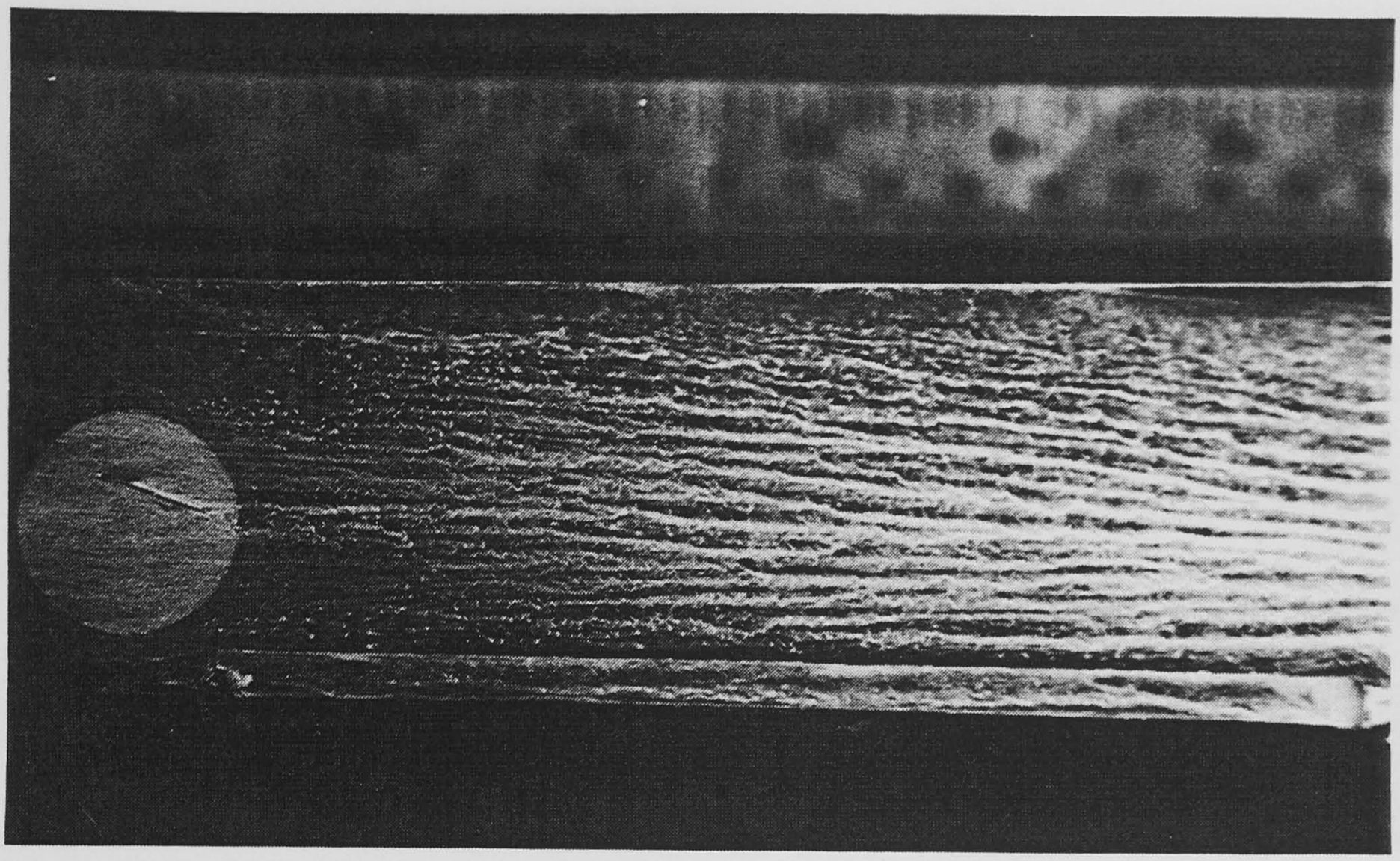

Without a vortex

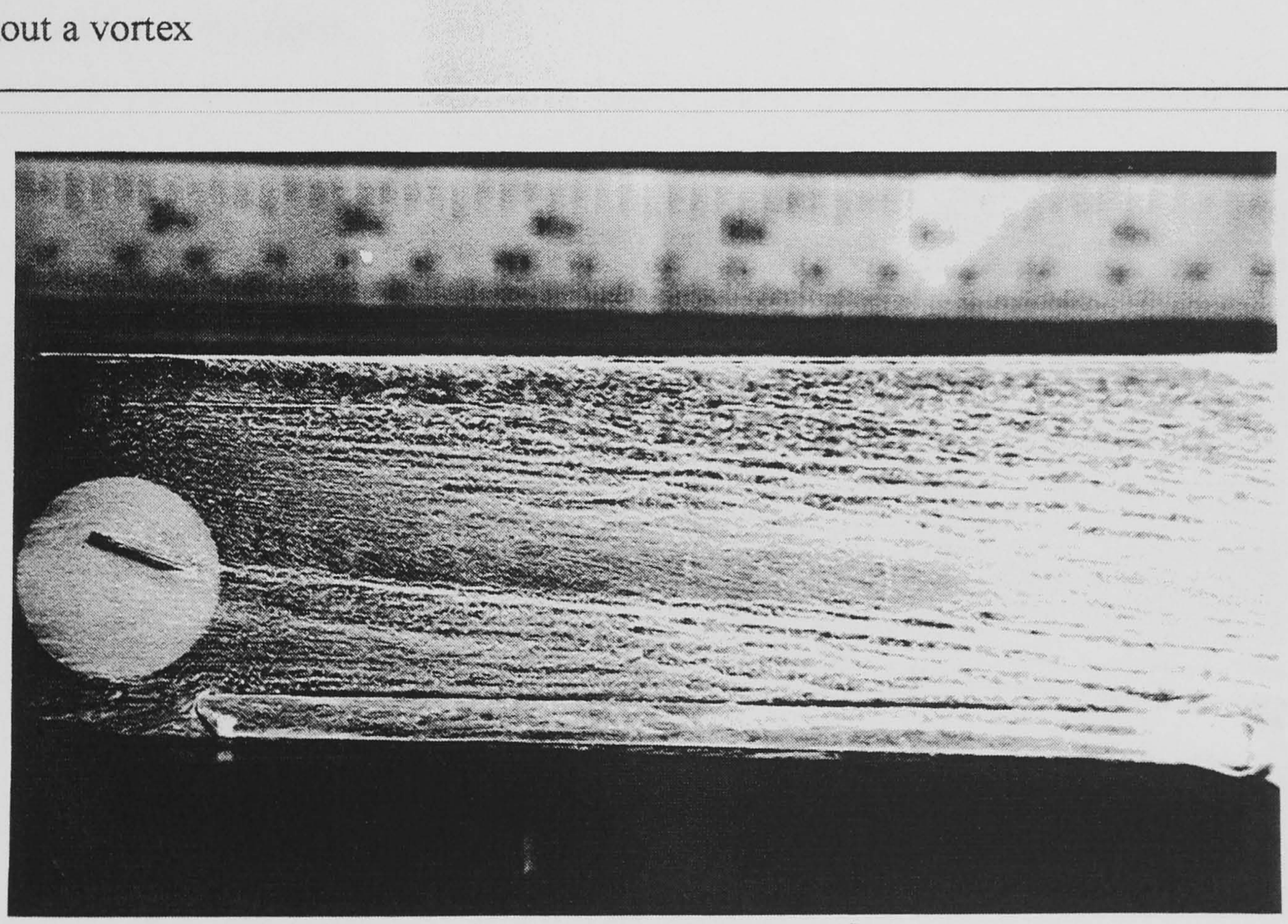

With a vortex. $h = 0.333\delta$.

Figure 5-50: Surface oil flow visualisation results of the flow along the 2.5" x 2.5" Transonic wind tunnel wall with and without a vortex and a sketch of the surface flow with a vortex present. V = 67 m/s.

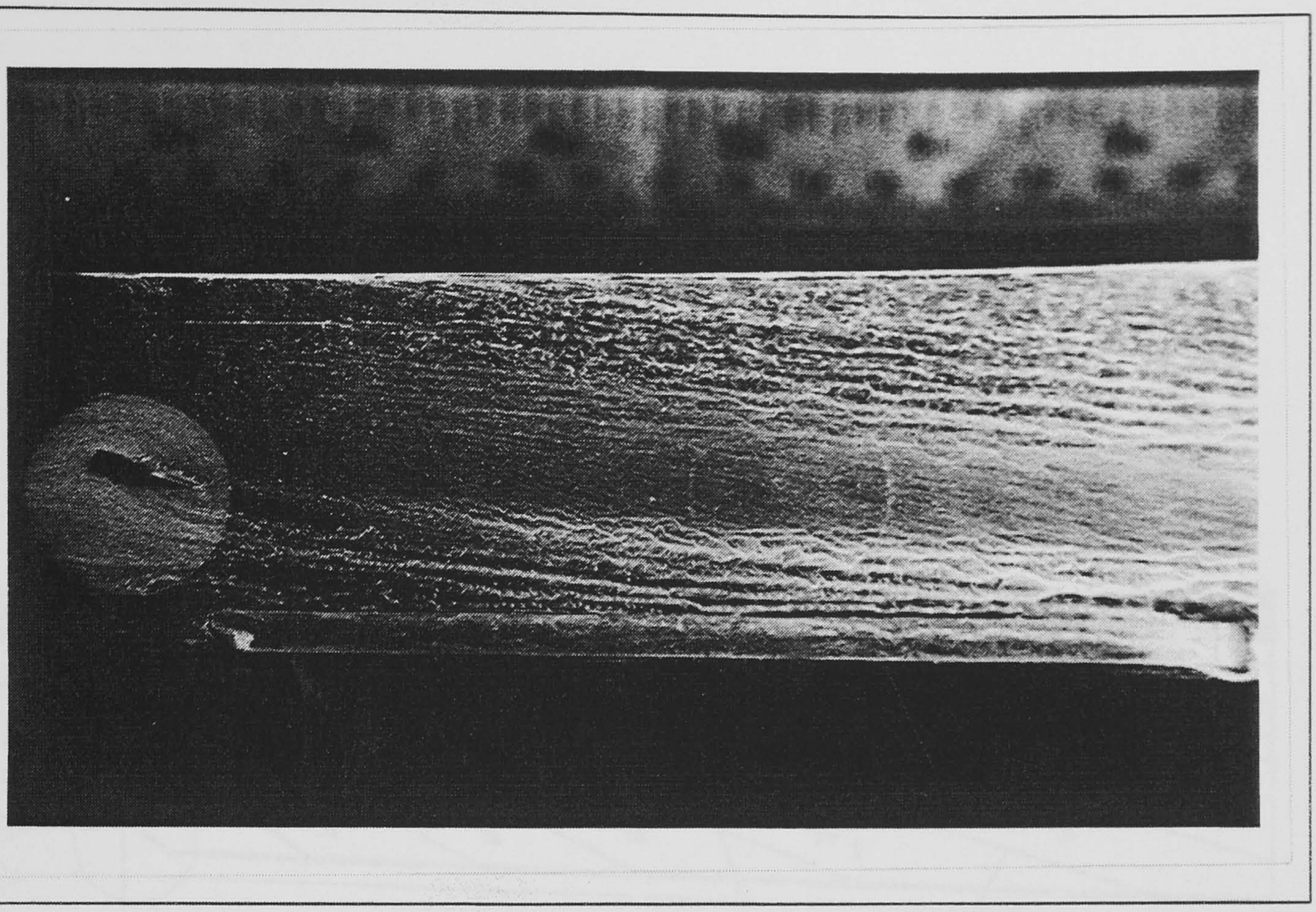

With a vortex. $h = 0.666\delta$.

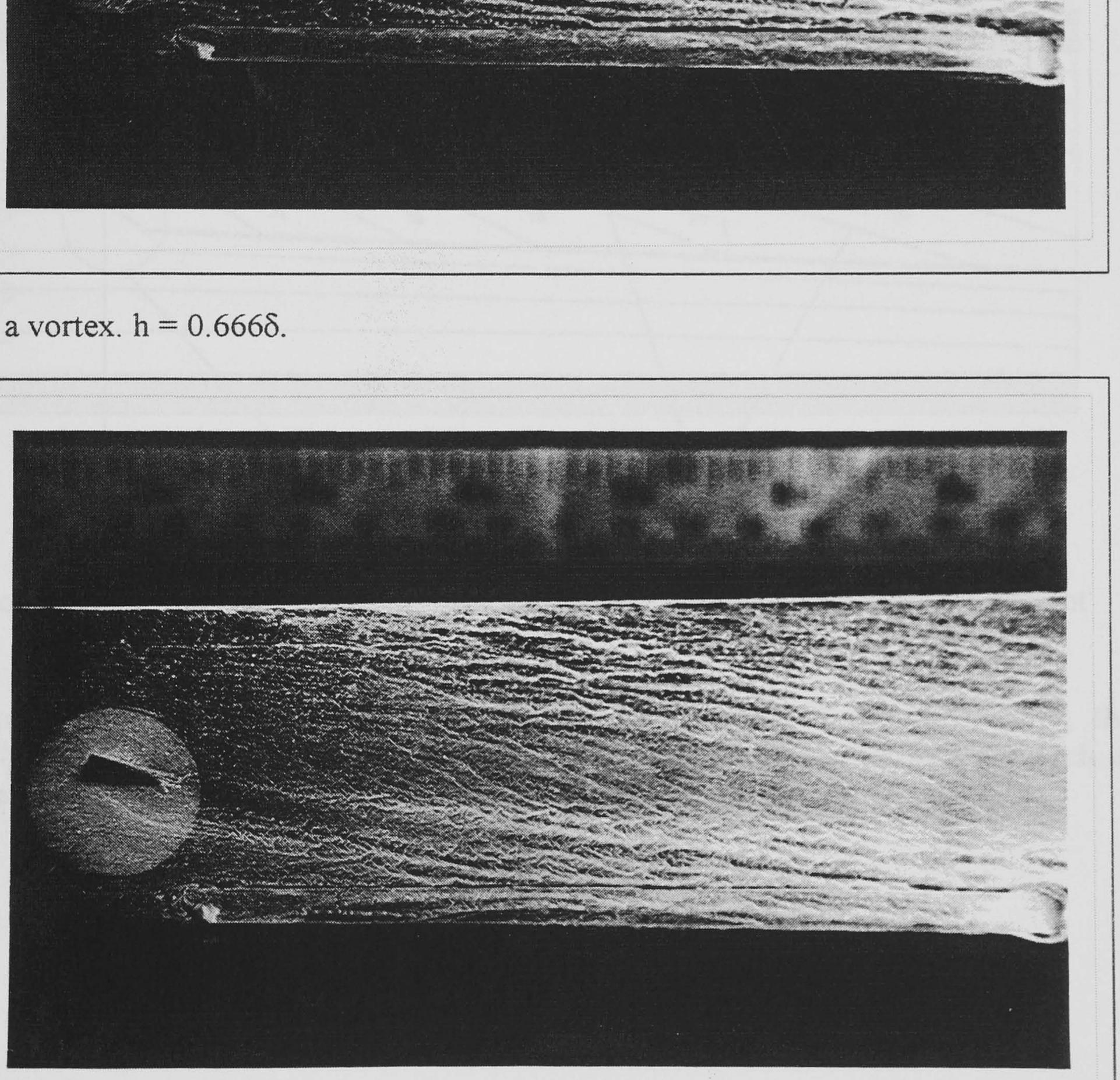

With a vortex. $h = \delta$.

Figure 5-50 cont.: Surface oil flow visualisation results of the flow along the 2.5" x 2.5" Transonic wind tunnel wall with and without a vortex and a sketch of the surface flow with a vortex present. V = 67 m/s.

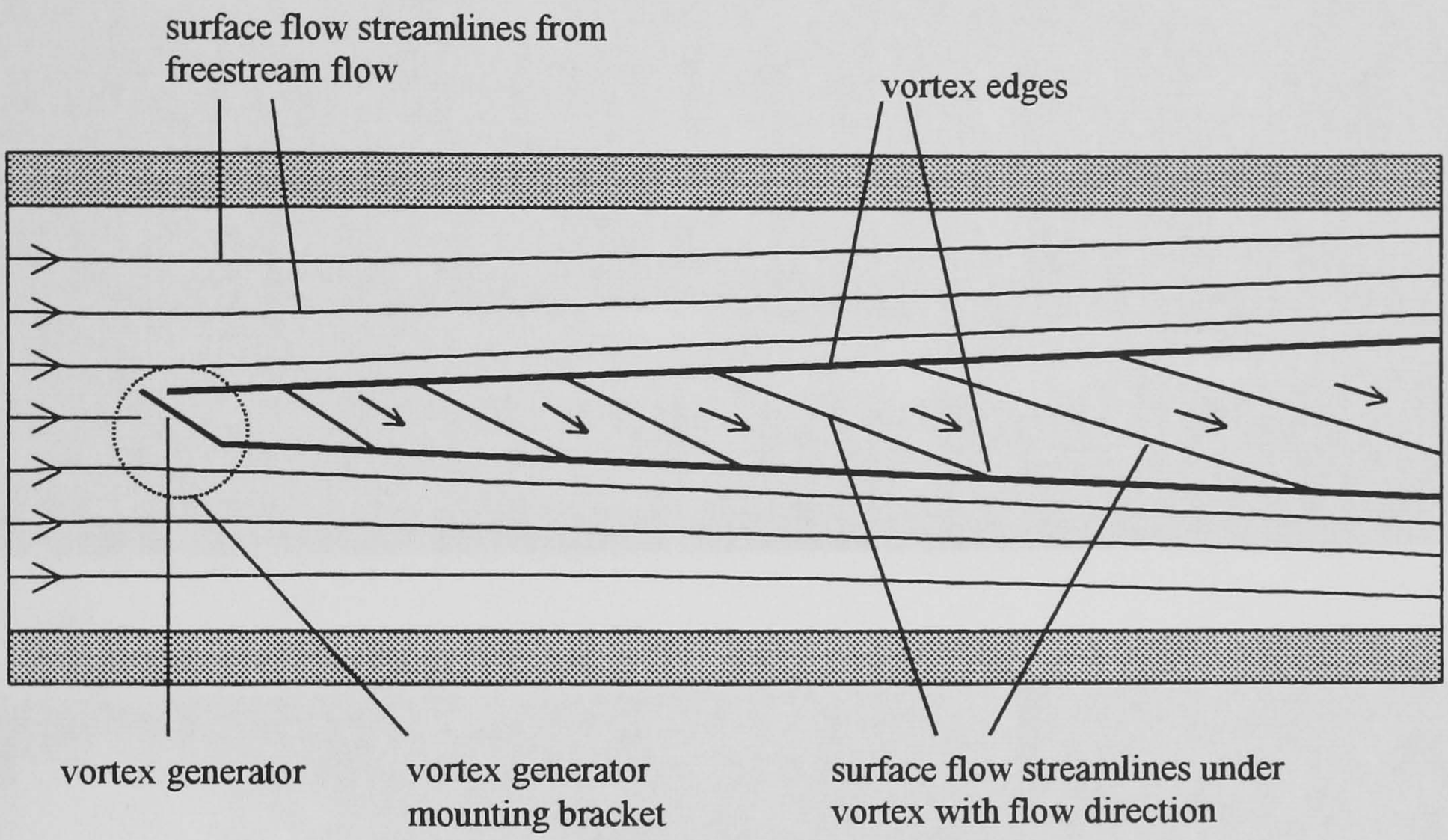

Sketch representing the surface oil flow visualisation results when a vortex is present

Figure 5-50 cont.: Surface oil flow visualisation results of the flow along the 2.5" x 2.5" Transonic wind tunnel wall with and without a vortex and a sketch of the surface flow with a vortex present. V = 67 m/s.

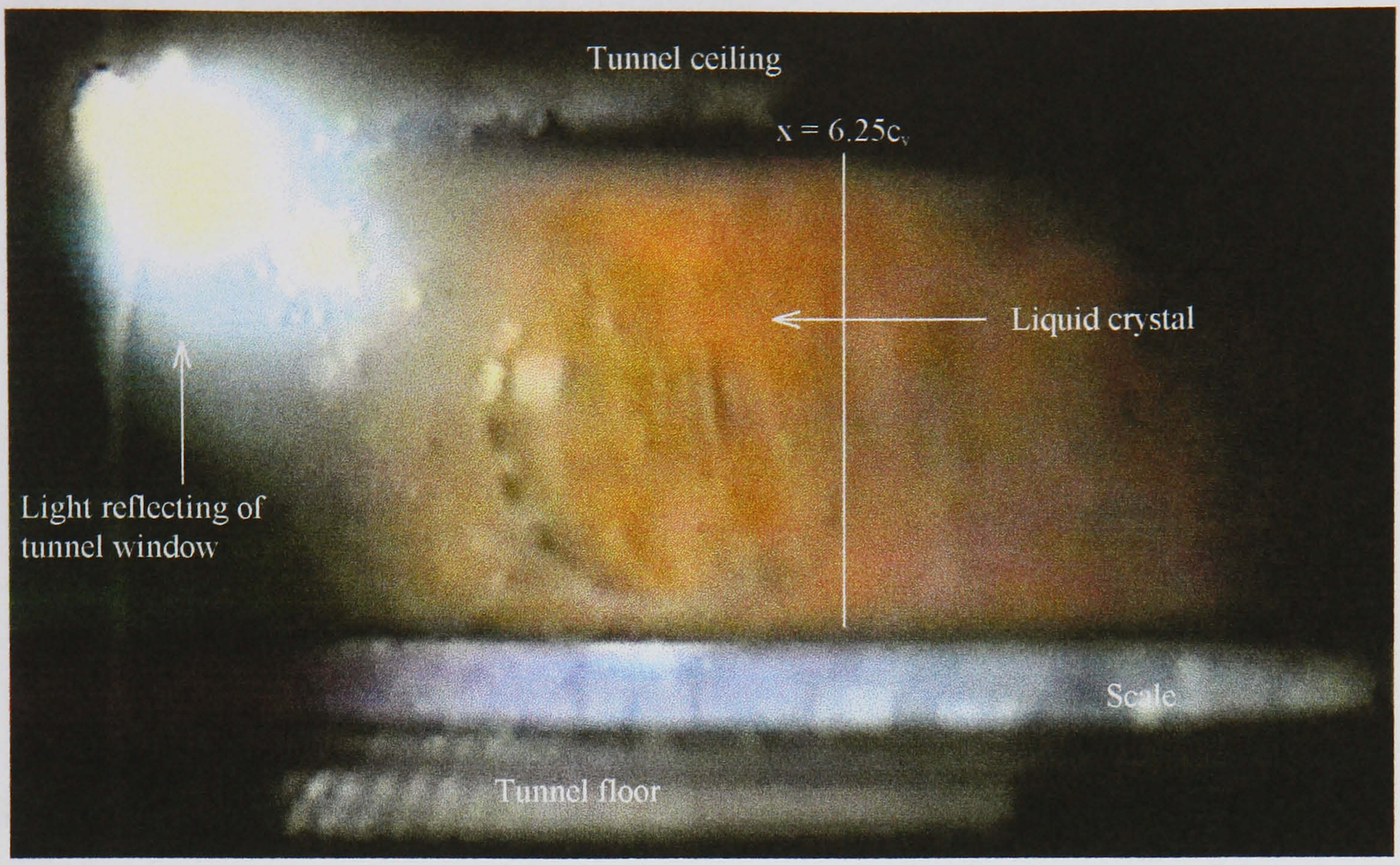

Wind off.

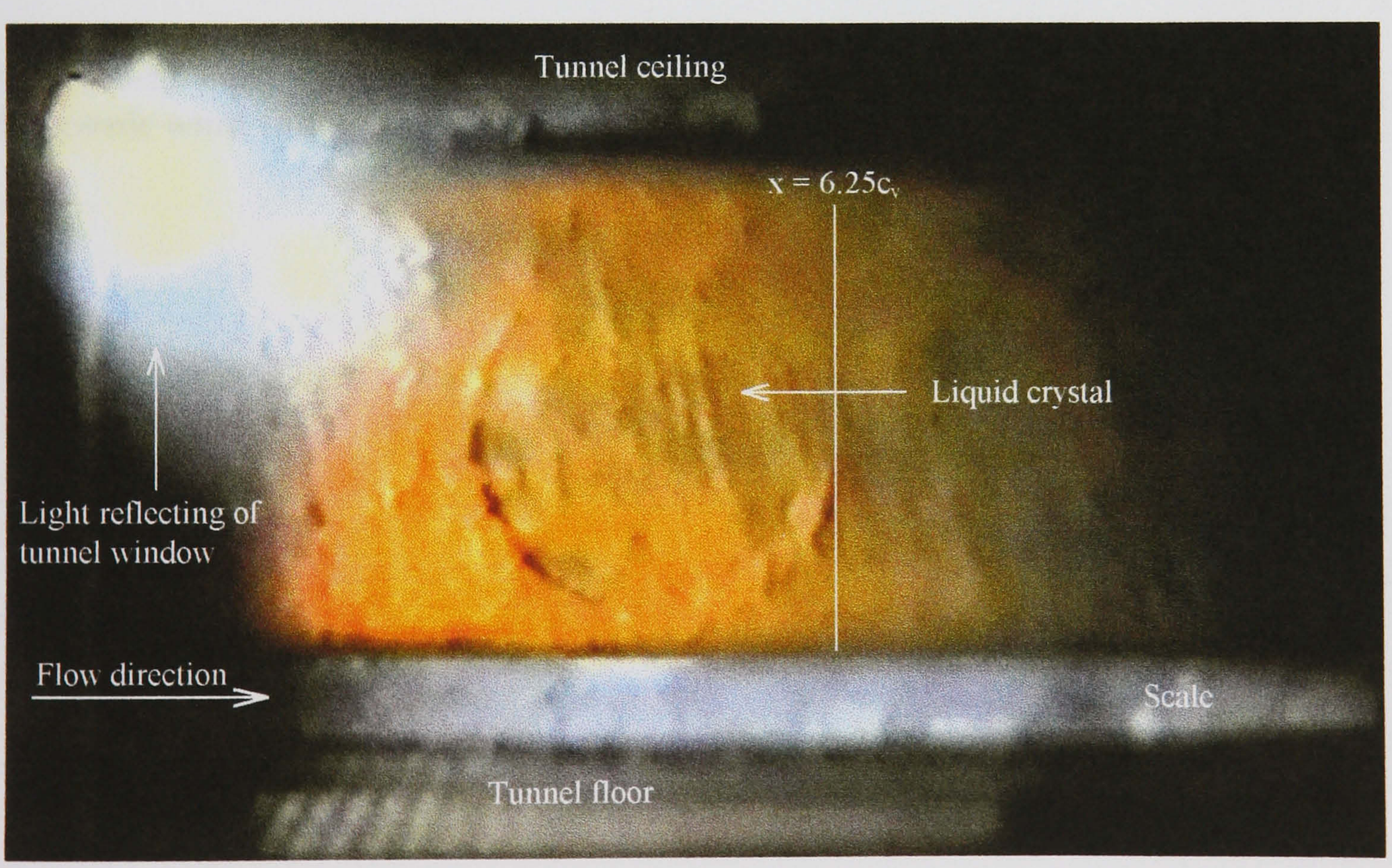

Wind on without a vortex. V = 67 m/s.

Figure 5-51: Shear stress sensitive liquid crystal images in the 2.5" x 2.5" Transonic wind tunnel at x = 6.25c_v with and without wind and with a vortex.

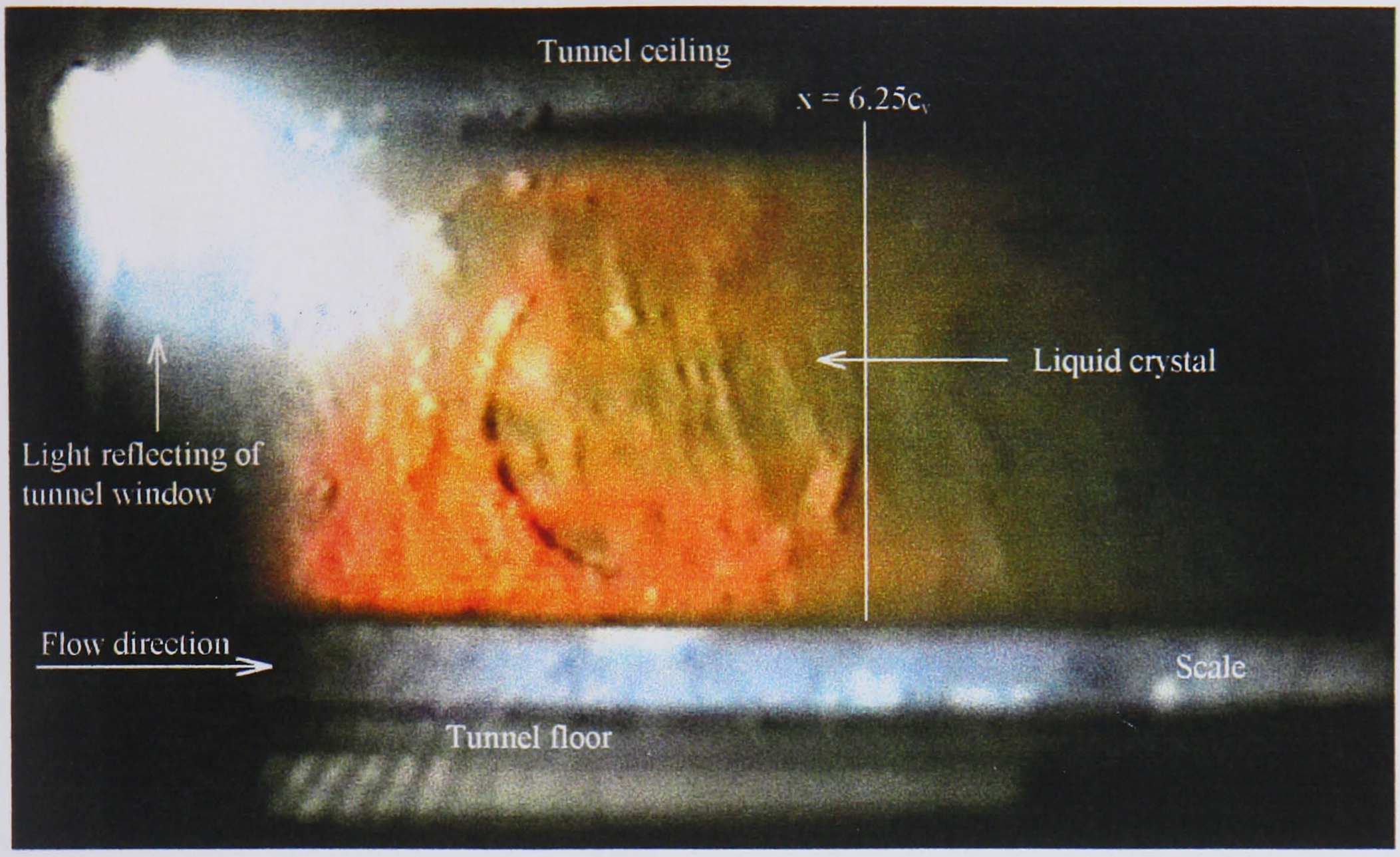

Wind on with a vortex. V = 67 m/s.

Figure 5-51 cont.: Shear stress sensitive liquid crystal images in the 2.5" x 2.5" Transonic wind tunnel at $x = 6.25c_v$ with and without wind and with a vortex.

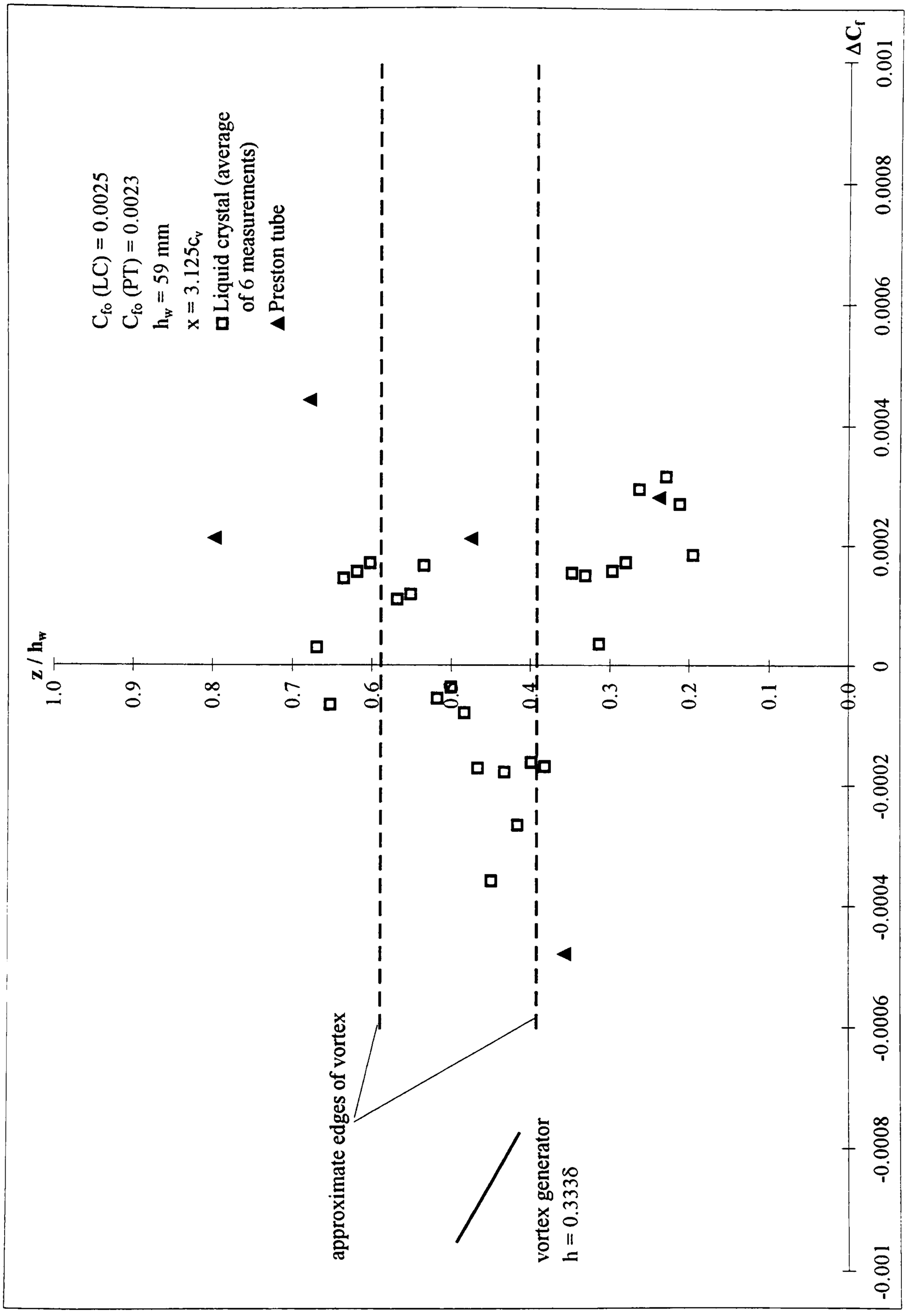

Figure 5-52: The change in skin friction coefficient across the wind tunnel working section, when a vortex is present, measured using shear stress sensitive liquid crystal and Preston tubes. V = 67 m/s.

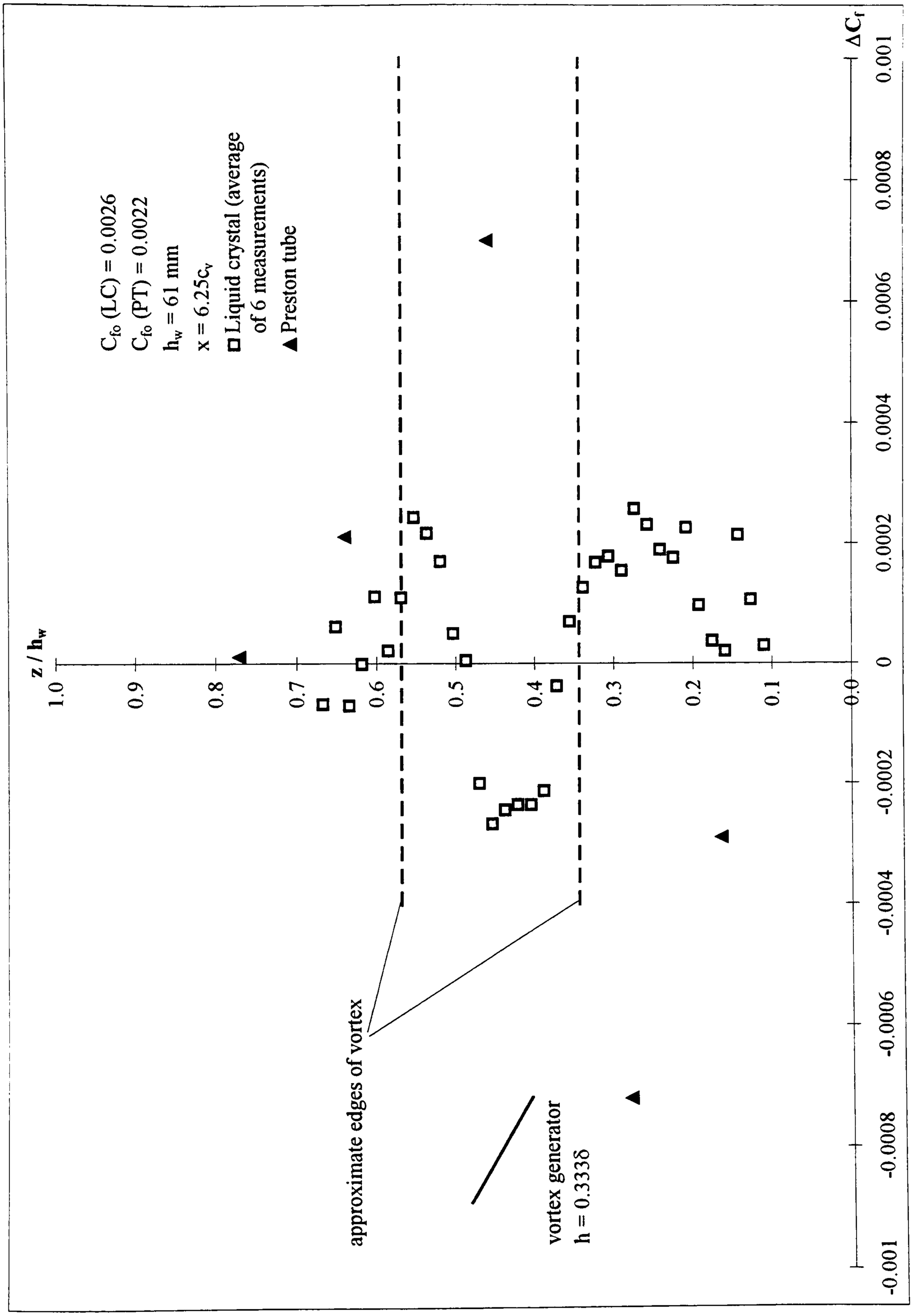

Figure 5-52 cont.: The change in skin friction coefficient across the wind tunnel working section, when a vortex is present, measured using shear stress sensitive liquid crystal and Preston tubes. V = 67 m/s.

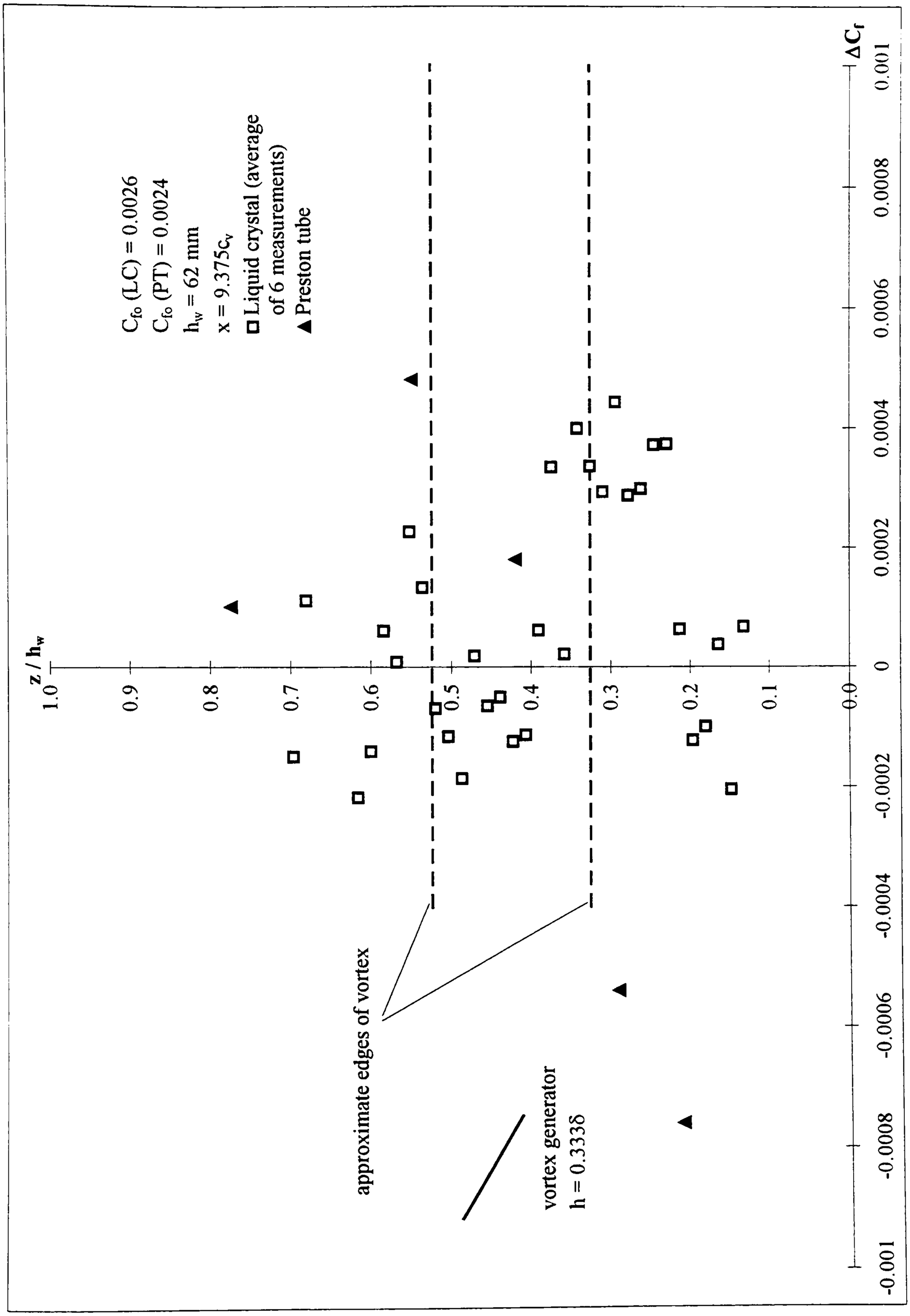

Figure 5-52 cont.: The change in skin friction coefficient across the wind tunnel working section, when a vortex is present, measured using shear stress sensitive liquid crystal and Preston tubes. V = 67 m/s.

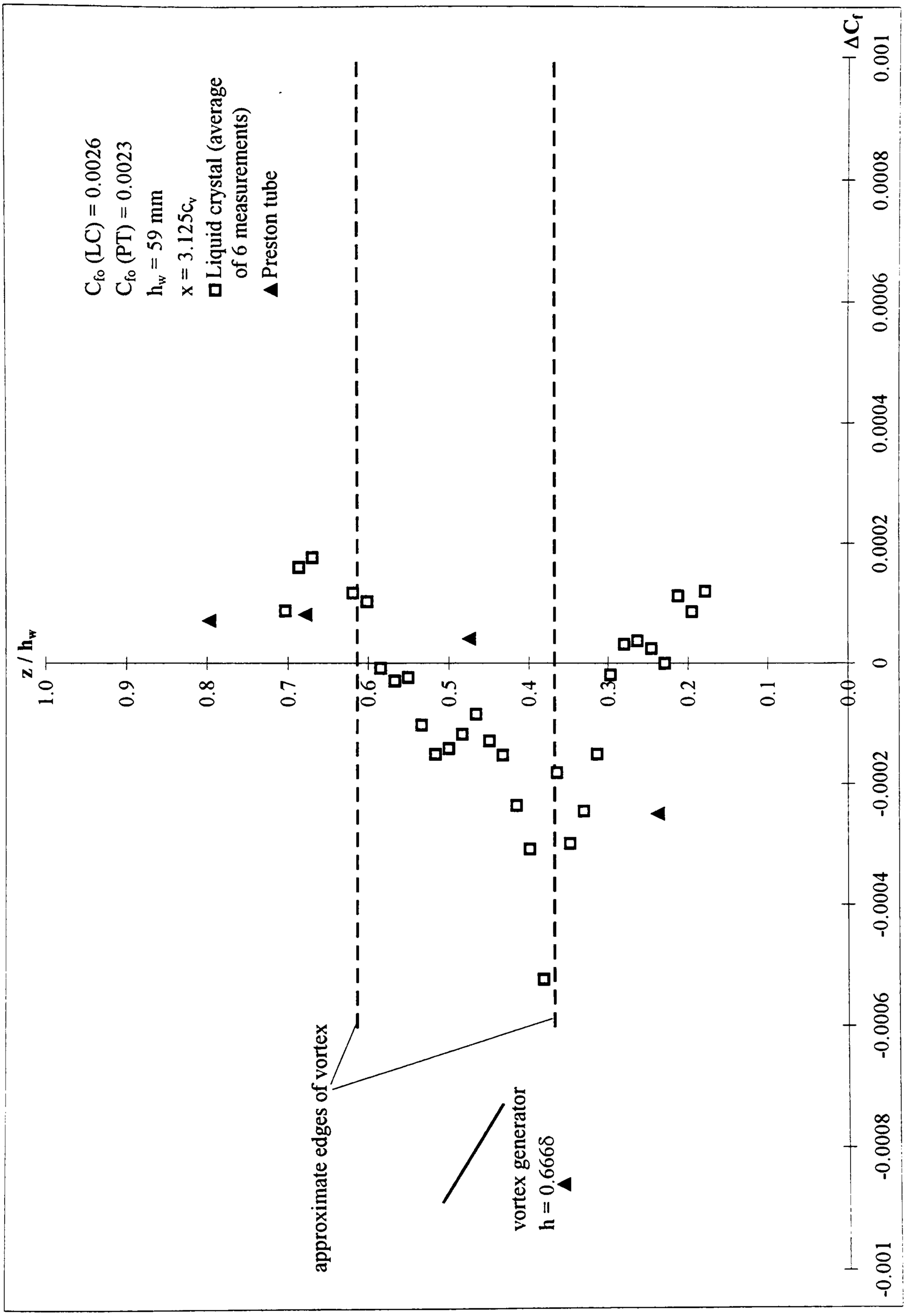

Figure 5-53: The change in skin friction coefficient across the wind tunnel working section, when a vortex is present, measured using shear stress sensitive liquid crystal and Preston tubes. V = 67 m/s.

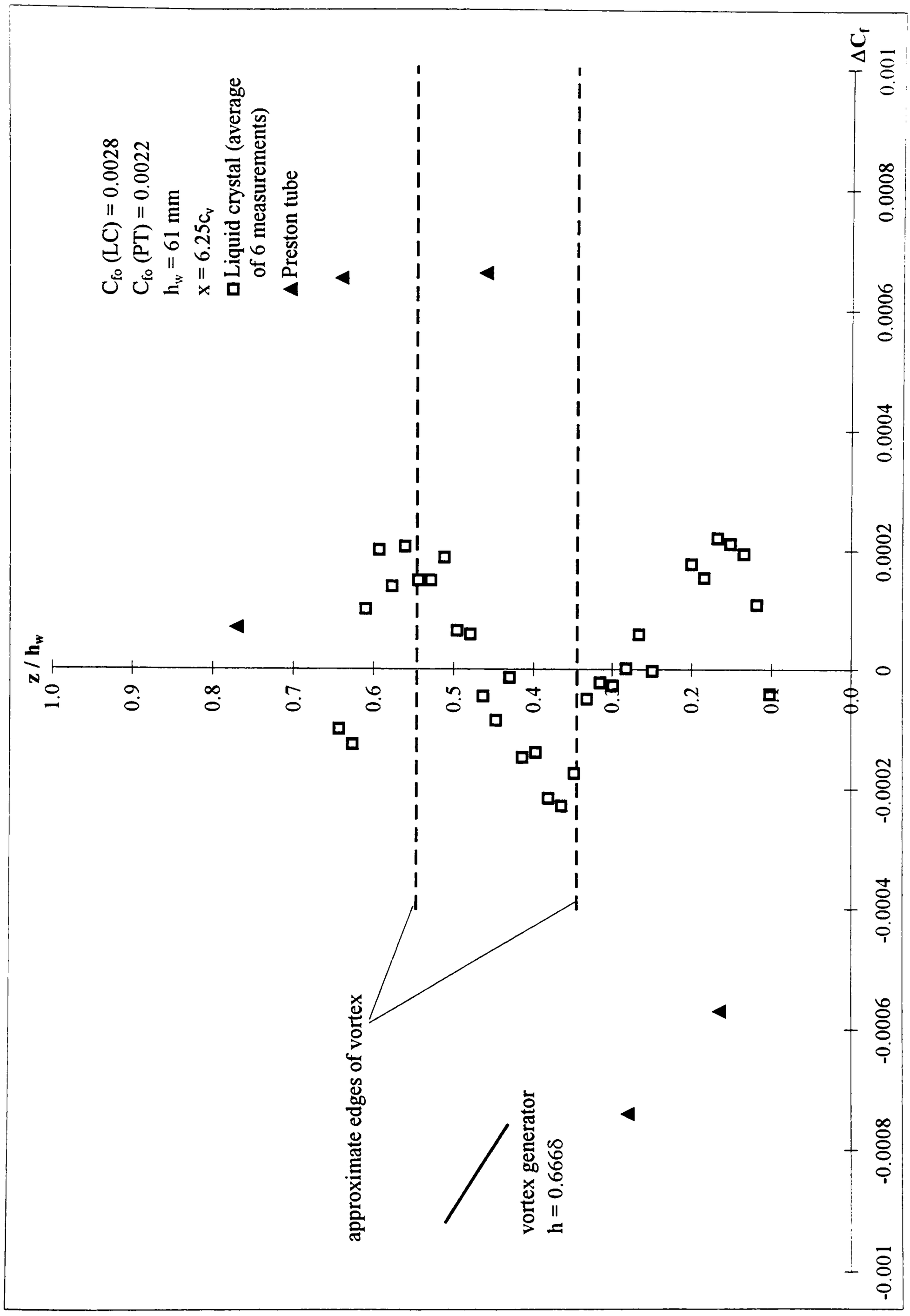

Figure 5-53 cont.: The change in skin friction coefficient across the wind tunnel working section, when a vortex is present, measured using shear stress sensitive liquid crystal and Preston tubes. V = 67 m/s.

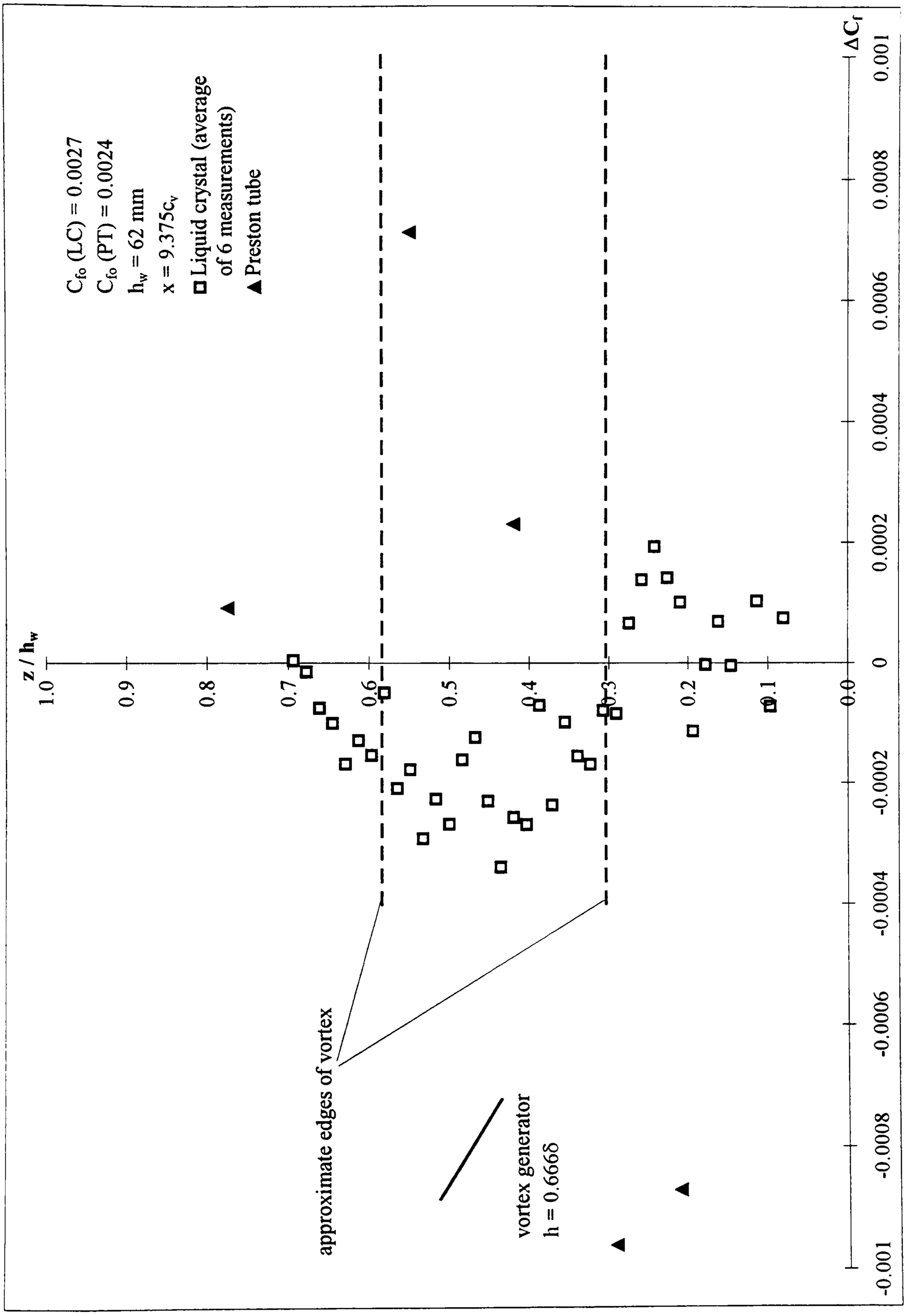

Figure 5-53 cont.: The change in skin friction coefficient across the wind tunnel working section, when a vortex is present, measured using shear stress sensitive liquid crystal and Preston tubes. V = 67 m/s.

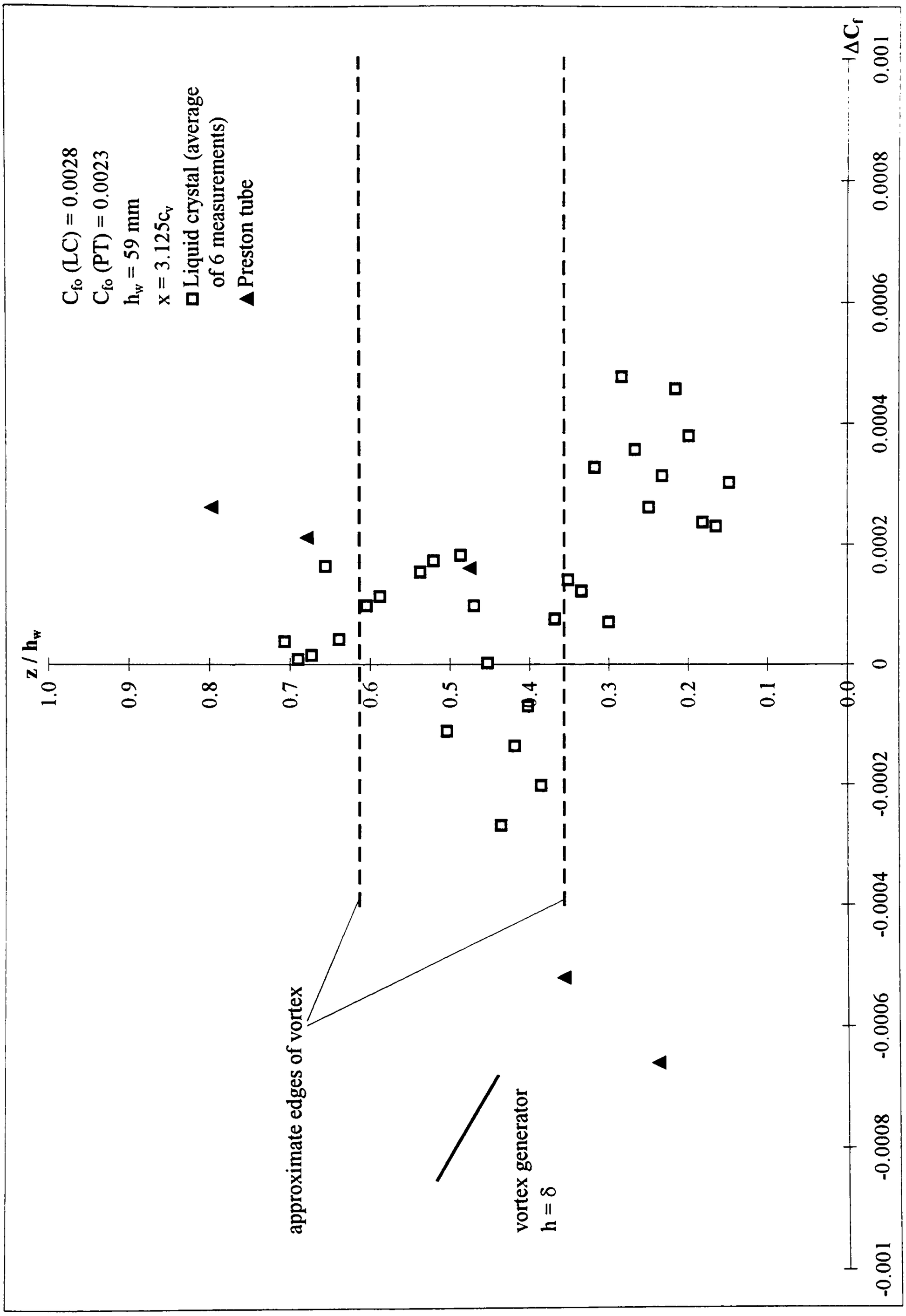

Figure 5-54: The change in skin friction coefficient across the wind tunnel working section, when a vortex is present, measured using shear stress sensitive liquid crystal and Preston tubes. V = 67 m/s.

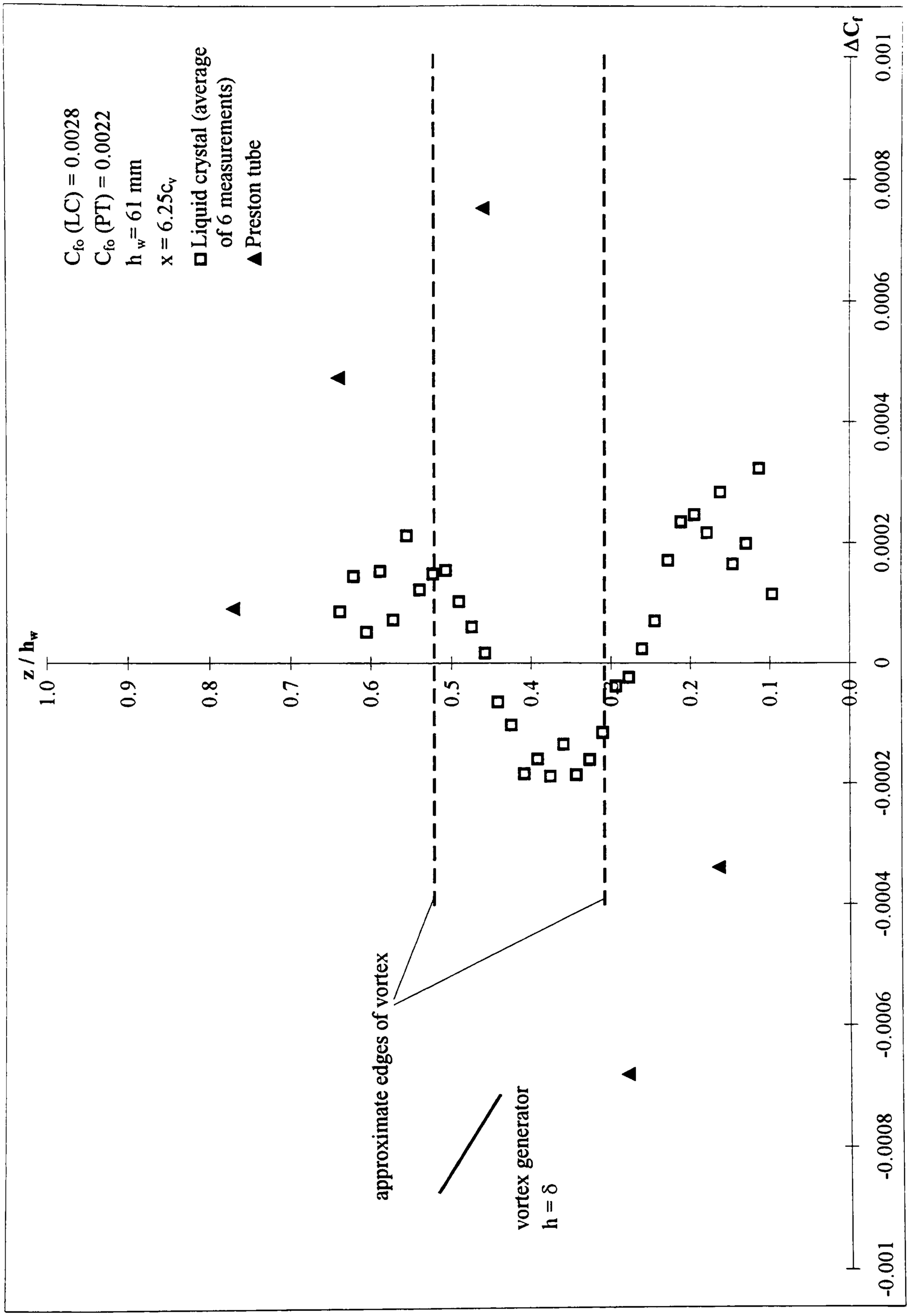

Figure 5-54 cont.: The change in skin friction coefficient across the wind tunnel working section, when a vortex is present, measured using shear stress sensitive liquid crystal and Preston tubes. V = 67 m/s.

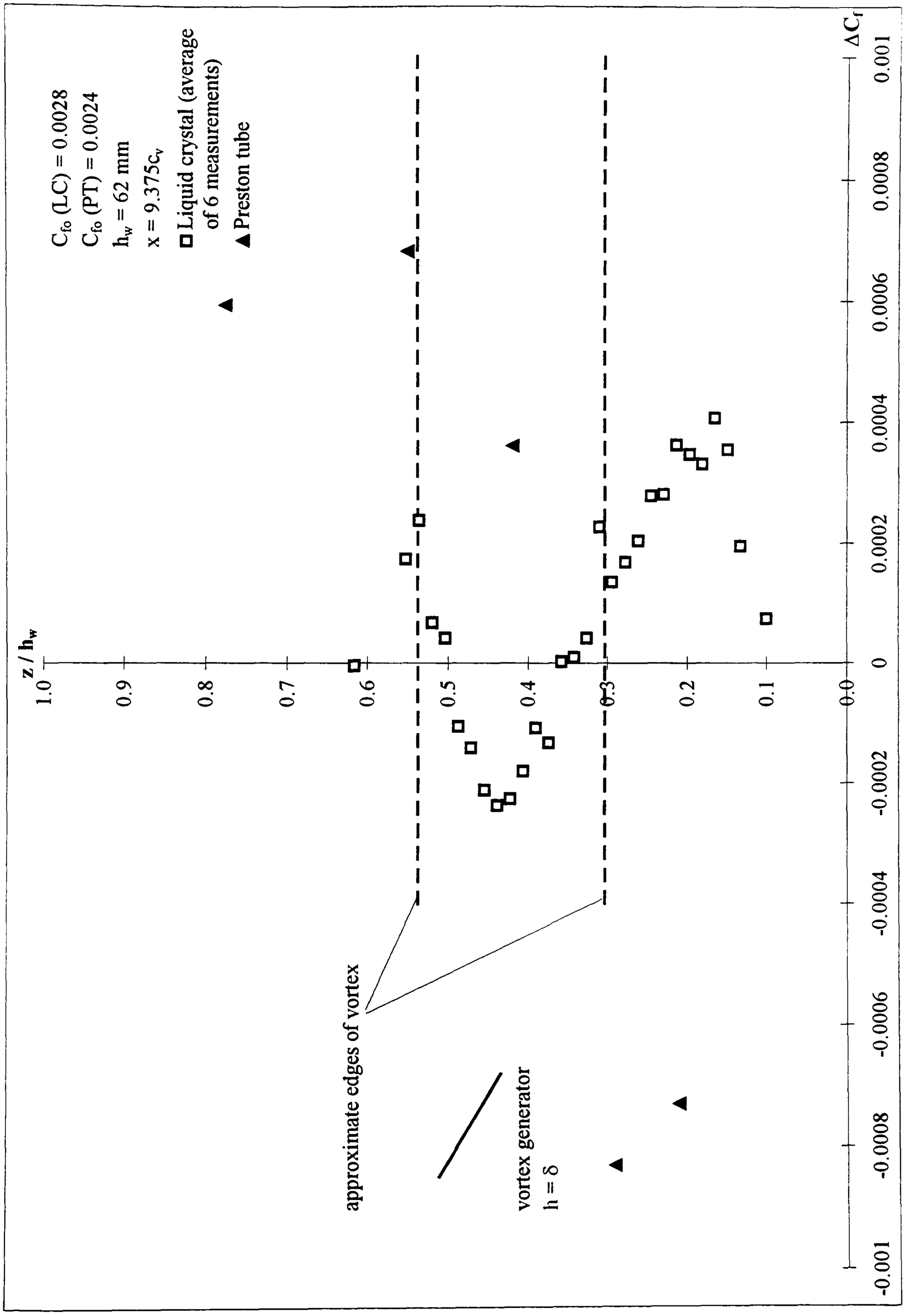

Figure 5-54 cont.: The change in skin friction coefficient across the wind tunnel working section, when a vortex is present, measured using shear stress sensitive liquid crystal and Preston tubes. V = 67 m/s.

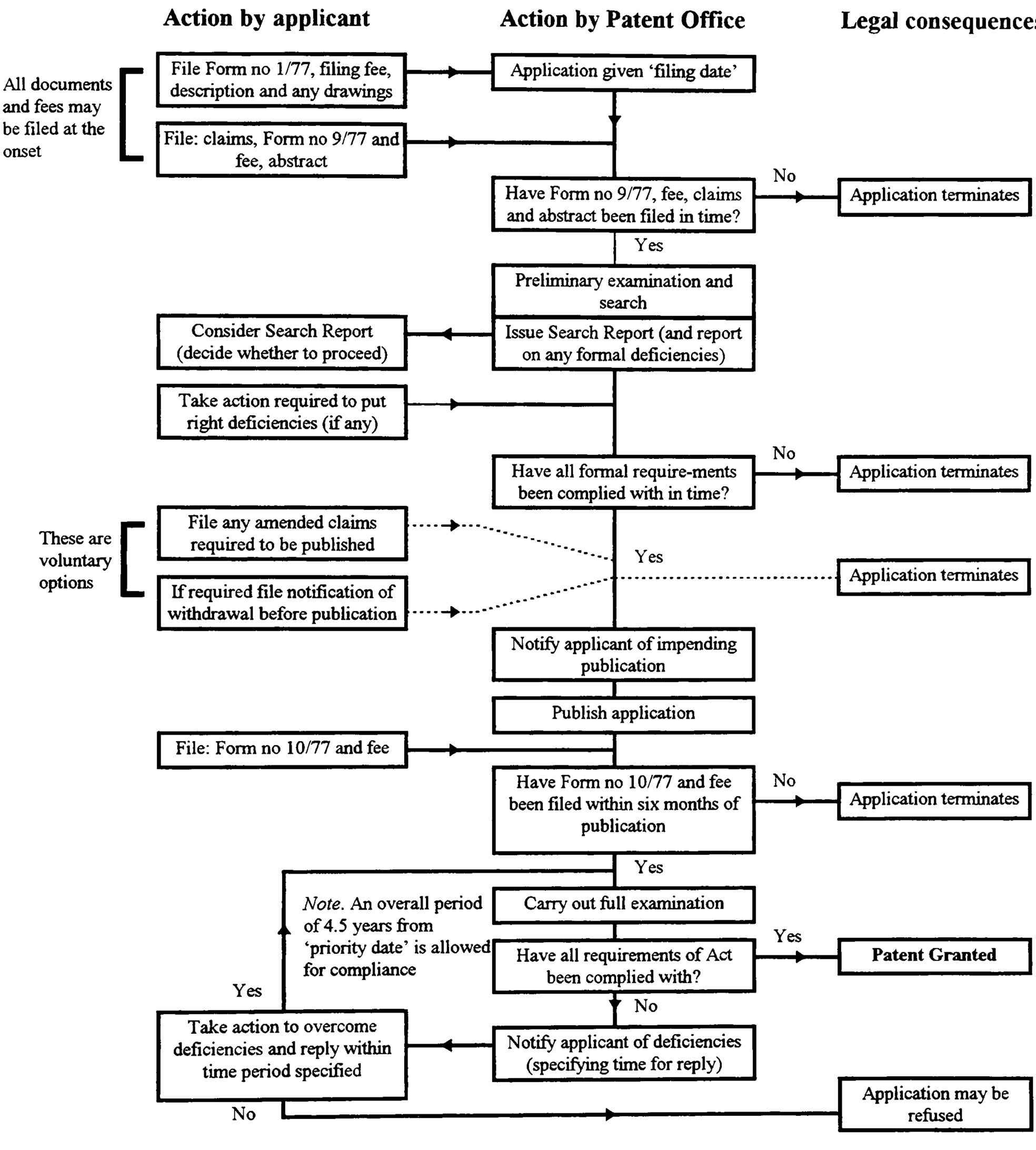

Figure 7-1: Flow chart of a UK patent application.

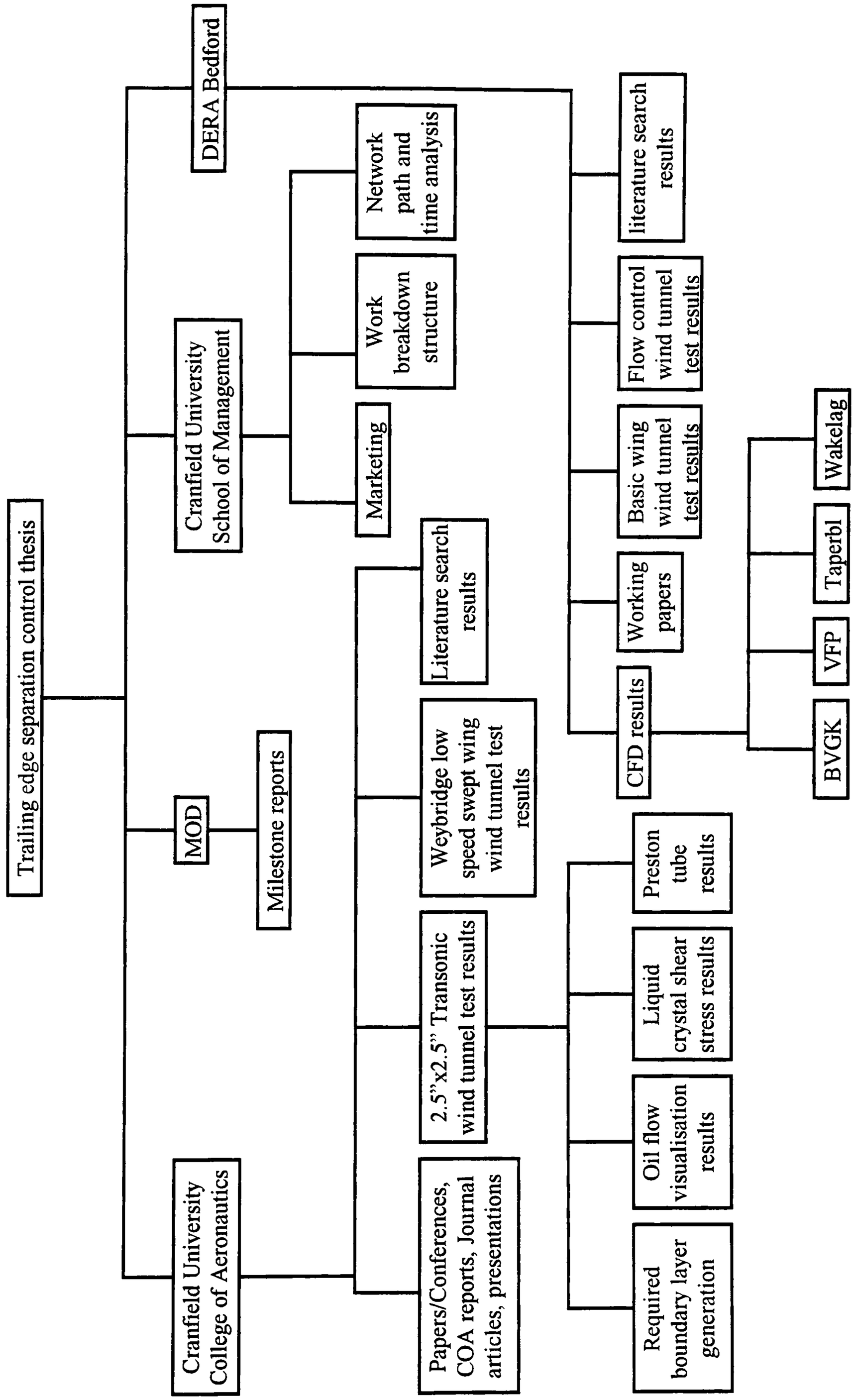

Figure 7-2: Work breakdown structure.

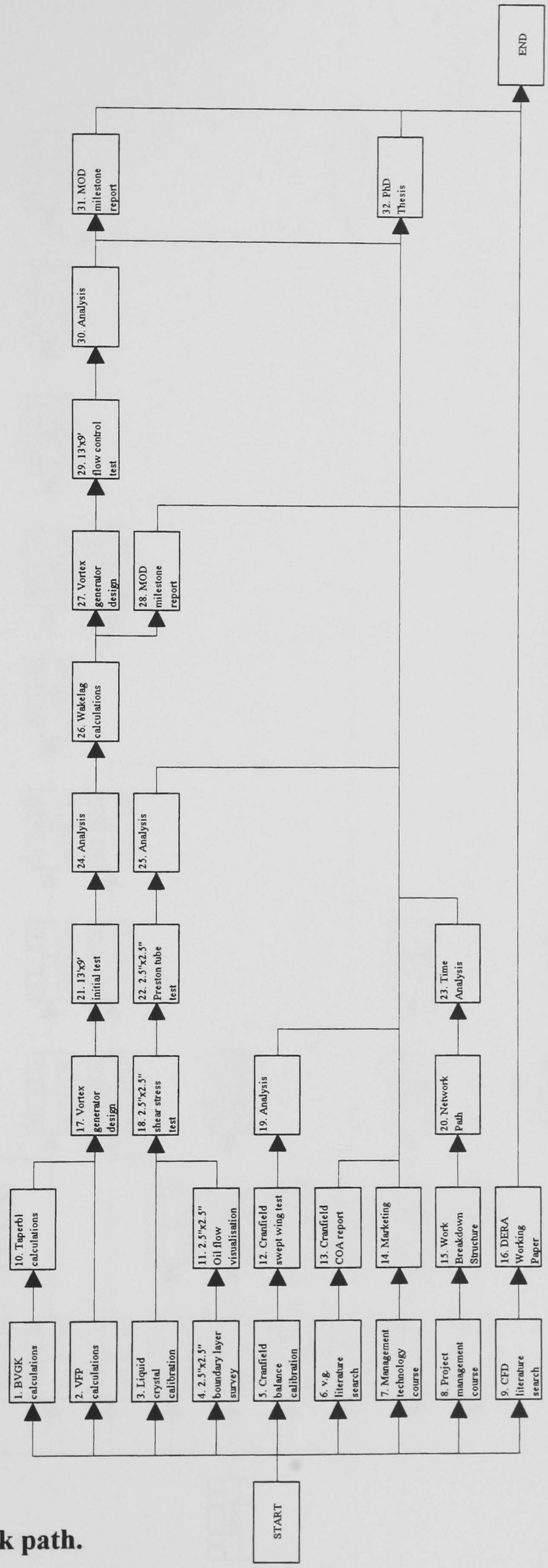

Figure 7-3: Network path.

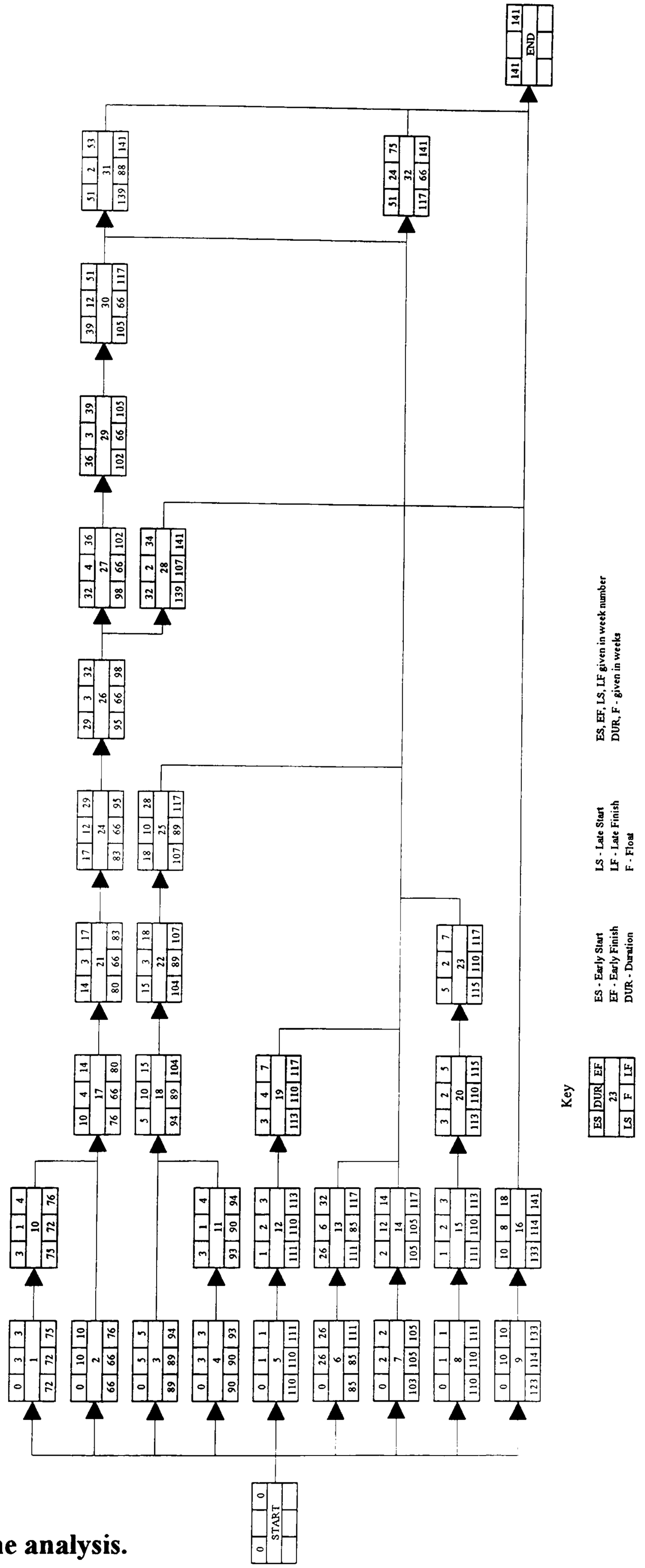

Figure 7-4: Time analysis.

Figure 7-5: Gantt chart.

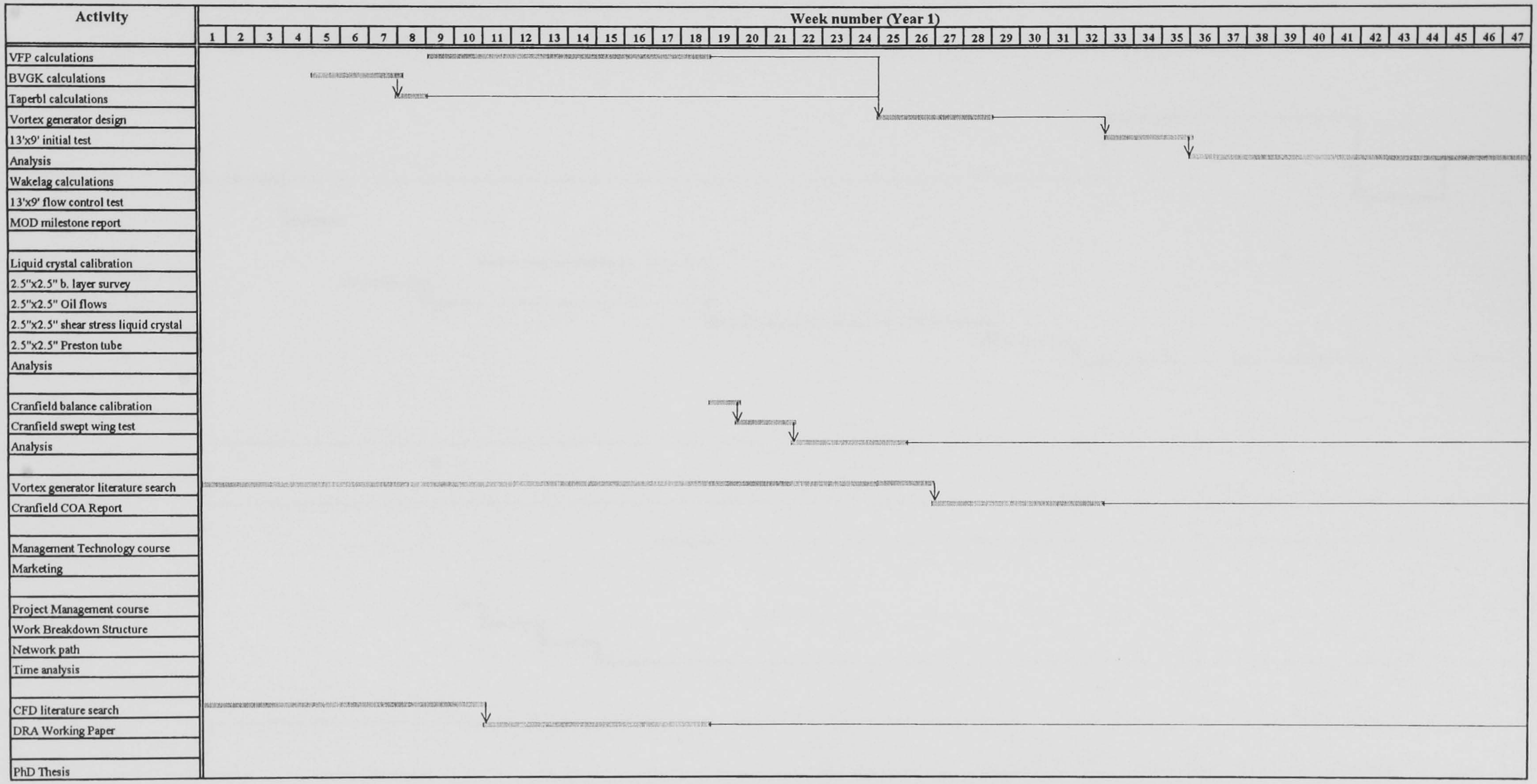

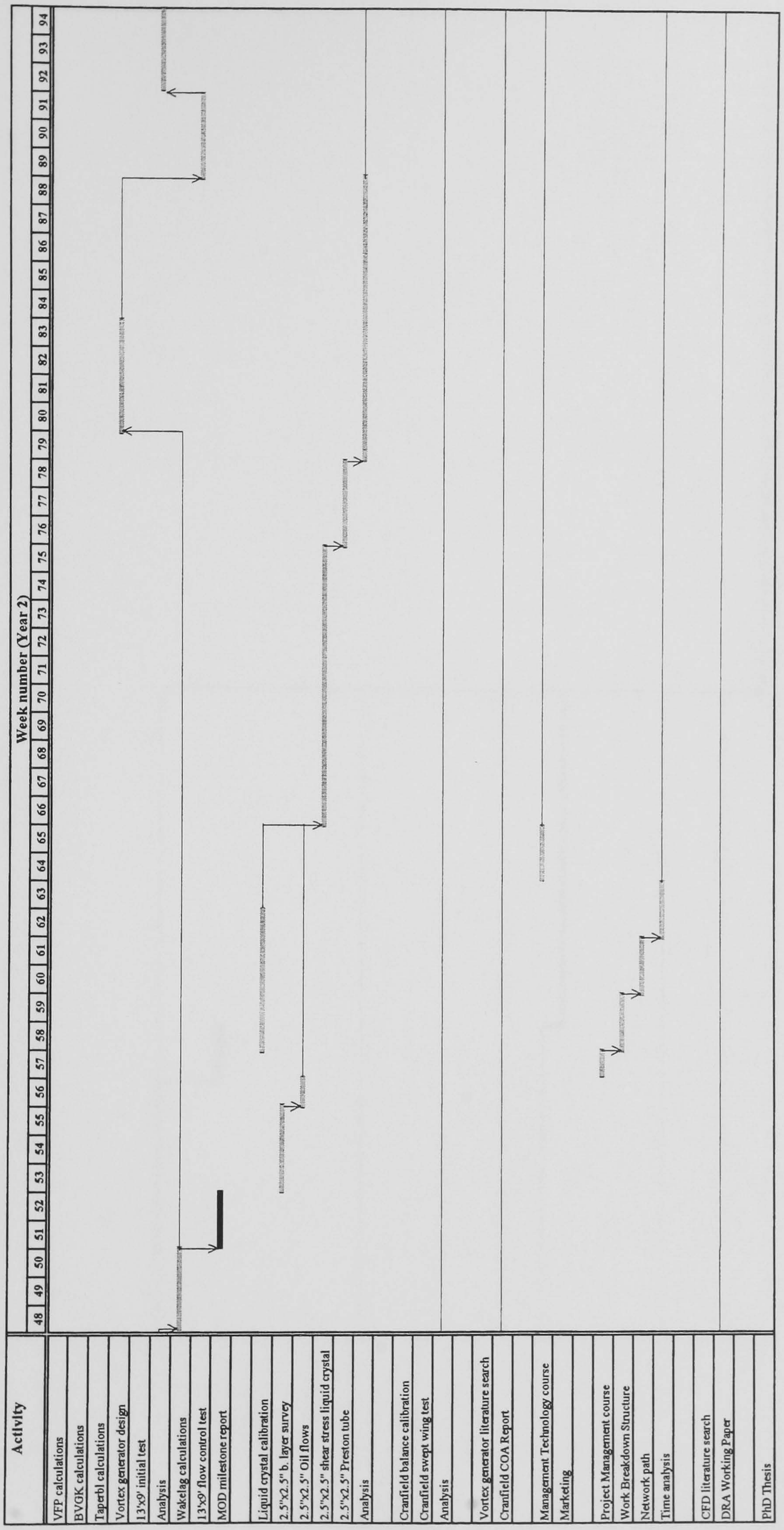

Figure 7-5 cont.: Gantt chart.

Figure 7-5 cont.: Gantt chart.

Appendices

Appendix I

Weybridge wind tunnel calibration

The working section wind speed is determined from a calibration of the working section dynamic pressure, q, against the difference in pressure, Δp, between the two static pressure rings in the nozzle and settling chamber over a range of wind speeds[112] (Figure A-1). The working section dynamic pressure is measured via a pitot static tube in the working section at the centre of where the model is going to be positioned, which usually is on the centreline of the tunnel and in the middle of the working section. The calibration factor, k, is found to be 0.851. i.e. $\Delta p = kq$.

With the model in the working section the difference in pressure between the static pressure rings is translated into a working section dynamic pressure by using the calibration constant for the wind tunnel and the tunnel wind speed determined from knowing the atmospheric pressure and temperature.

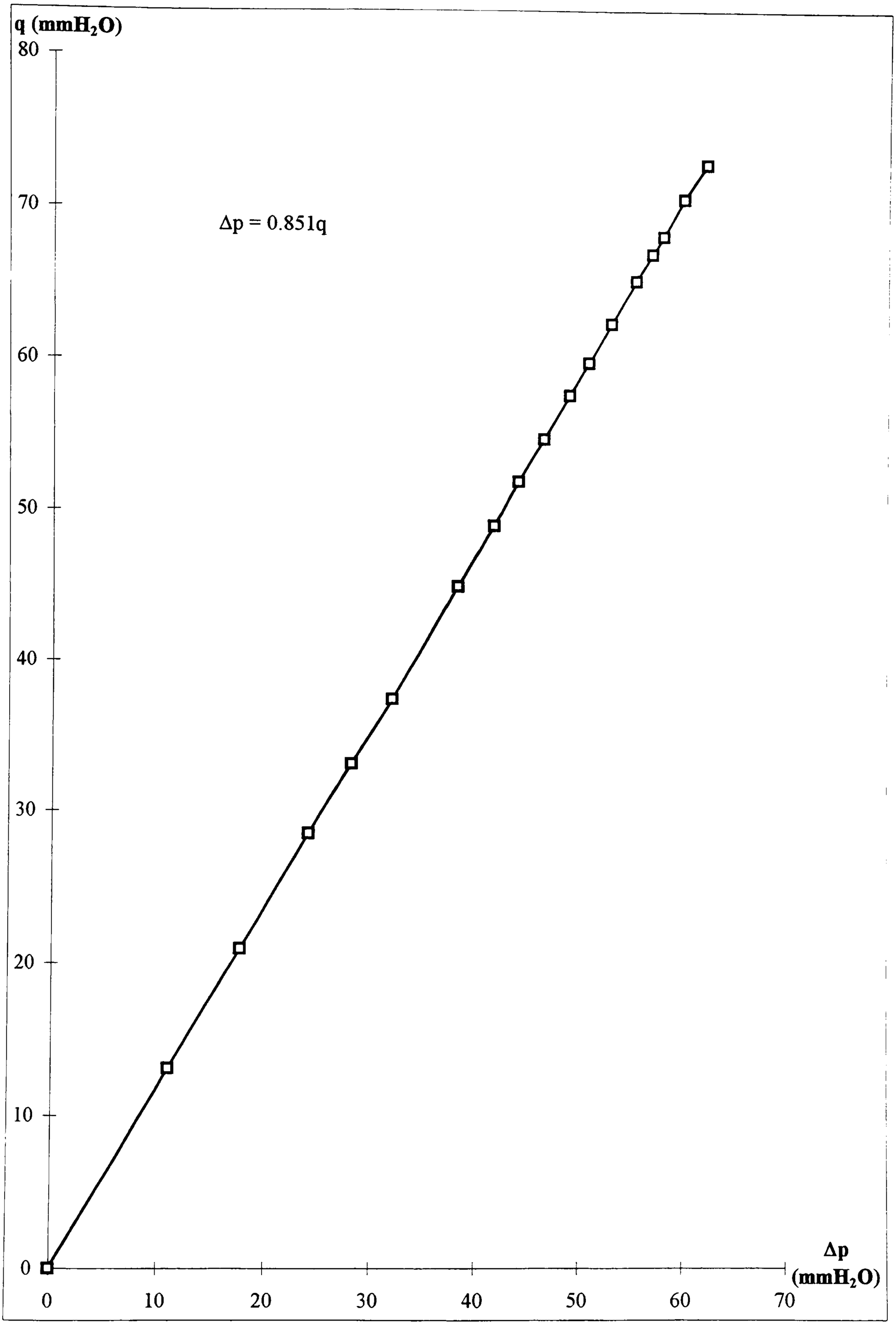

Figure A-1: Weybridge wind tunnel calibration.

Appendix II

Weybridge balance calibration

The 5 component root balance was mounted in the 'Ocean Ranger' balance calibration rig, a rigid framework with a series of pulleys to enable forces and pure moments to be applied to the balance, and, through the application of known forces and moments, each balance output channel was calibrated separately for applied lift and drag forces and for pure applied pitching, rolling and yawing moments (Figure A-2). The calibration gradients for each of these channels was then written in a matrix format, the load matrix, such that for any applied forces and moments the balance output could be calculated, M1. This matrix is then inverted to enable unknown loads to be calculated from the balance outputs, M2. This matrix is the balance calibration matrix.

Load matrix
Balance output (Volts) = load (known) x calibration gradient for each channel (Volts/N or Volts/Nm)

$$(\mathrm{Ch1}\quad \mathrm{Ch2}\quad \mathrm{Ch3}\quad \mathrm{Ch4}\quad \mathrm{Ch5}) = (\mathrm{L}\quad \mathrm{D}\quad \mathrm{PM}\quad \mathrm{RM}\quad \mathrm{YM}) \times (\mathrm{M})$$

$$(\mathrm{M}) = \begin{pmatrix} -0.01549 & -0.00024 & 0.04029 & 0.00098 & 0.00025 \\ 0.00122 & -0.00034 & -0.00041 & 0.03685 & 0.01168 \\ -0.00163 & 0.05219 & 0.00204 & 0.00047 & -0.00052 \\ -0.06558 & 0.00159 & 0.05050 & 0.00394 & 0.00266 \\ 0.00534 & 0.00073 & -0.00354 & 0.04623 & 0.04542 \end{pmatrix} \qquad \text{M1}$$

Calibration matrix
load (unknown) = balance output (Volts) x inverse of calibration matrix (N/Volts or Nm/Volts)

$$(\mathrm{L}\quad \mathrm{D}\quad \mathrm{PM}\quad \mathrm{RM}\quad \mathrm{YM}) = (\mathrm{Ch1}\quad \mathrm{Ch2}\quad \mathrm{Ch3}\quad \mathrm{Ch4}\quad \mathrm{Ch5}) \times (\mathrm{M})^{-1}$$

$$(\mathrm{M})^{-1} = \begin{pmatrix} 27.10893 & 0.23898 & 0.76877 & -21.57959 & 1.06561 \\ -0.52387 & -0.73471 & 19.15872 & -0.33102 & 0.43052 \\ 35.25448 & -0.63769 & 0.40469 & -8.31118 & 0.46435 \\ -0.54709 & 40.06650 & 0.40201 & 0.02378 & -10.29603 \\ 0.12582 & -40.84698 & -0.77636 & 1.87042 & 32.39987 \end{pmatrix} \qquad \text{M2}$$

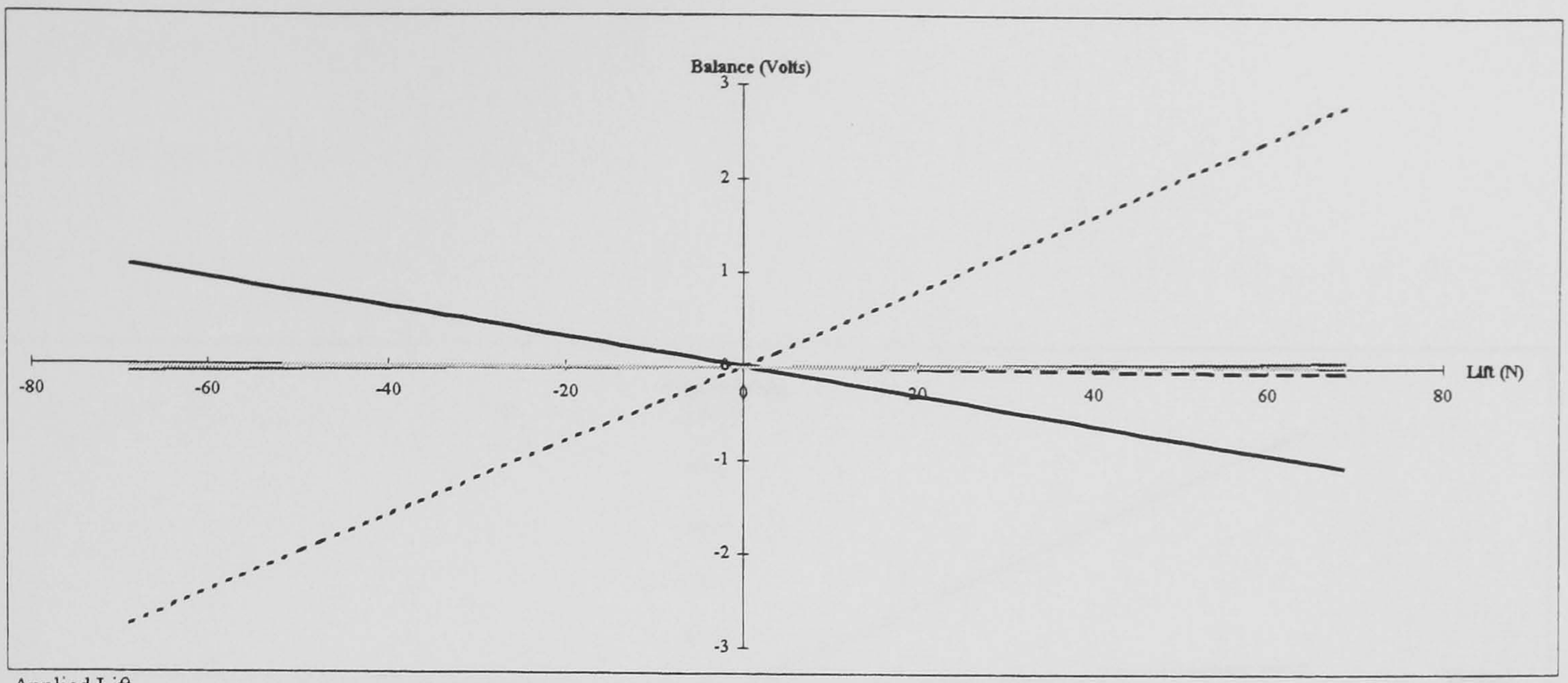

Applied Lift

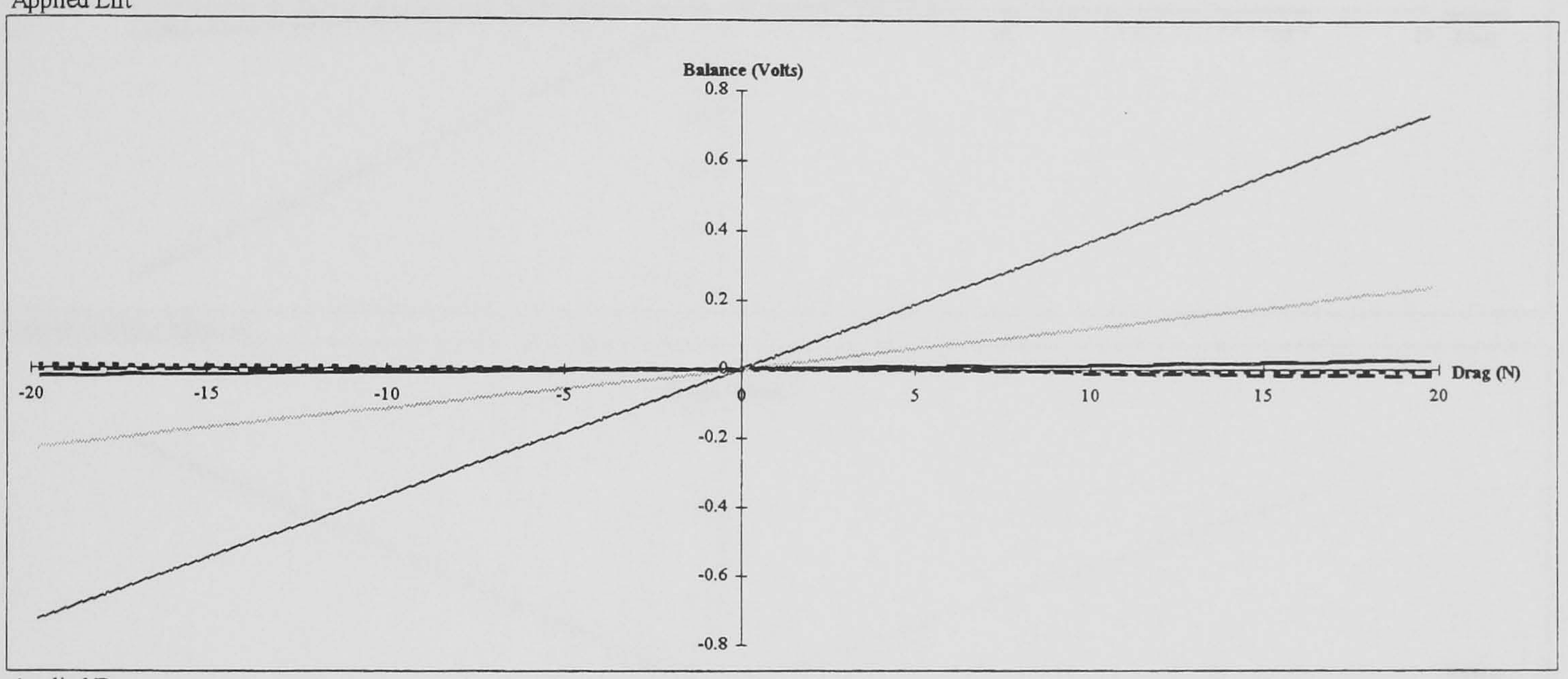

Applied Drag

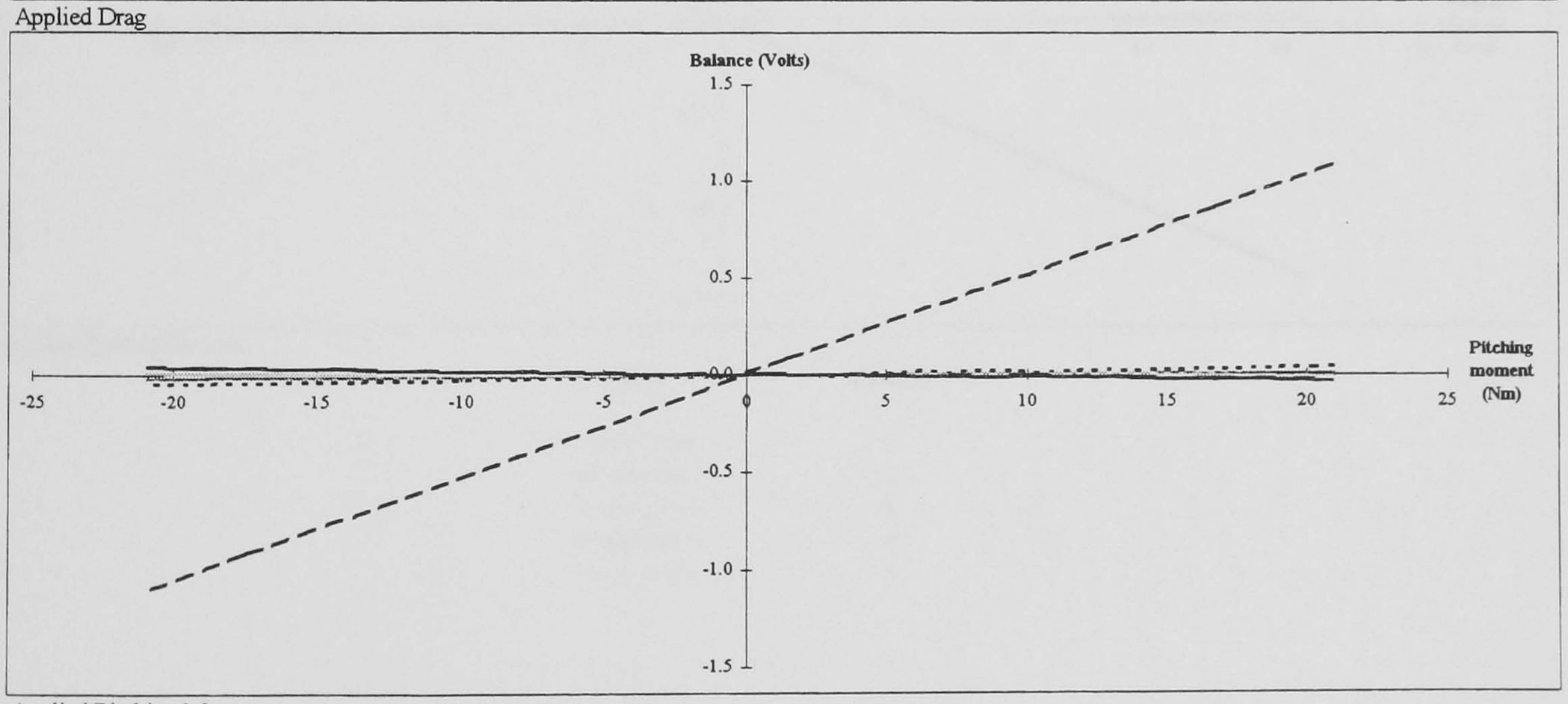

Applied Pitching Moment

Key	Channel
———	1
– – – – ·	2
· · · · · · · ·	3
———	4
———	5

Figure A-2: Weybridge balance calibration data.

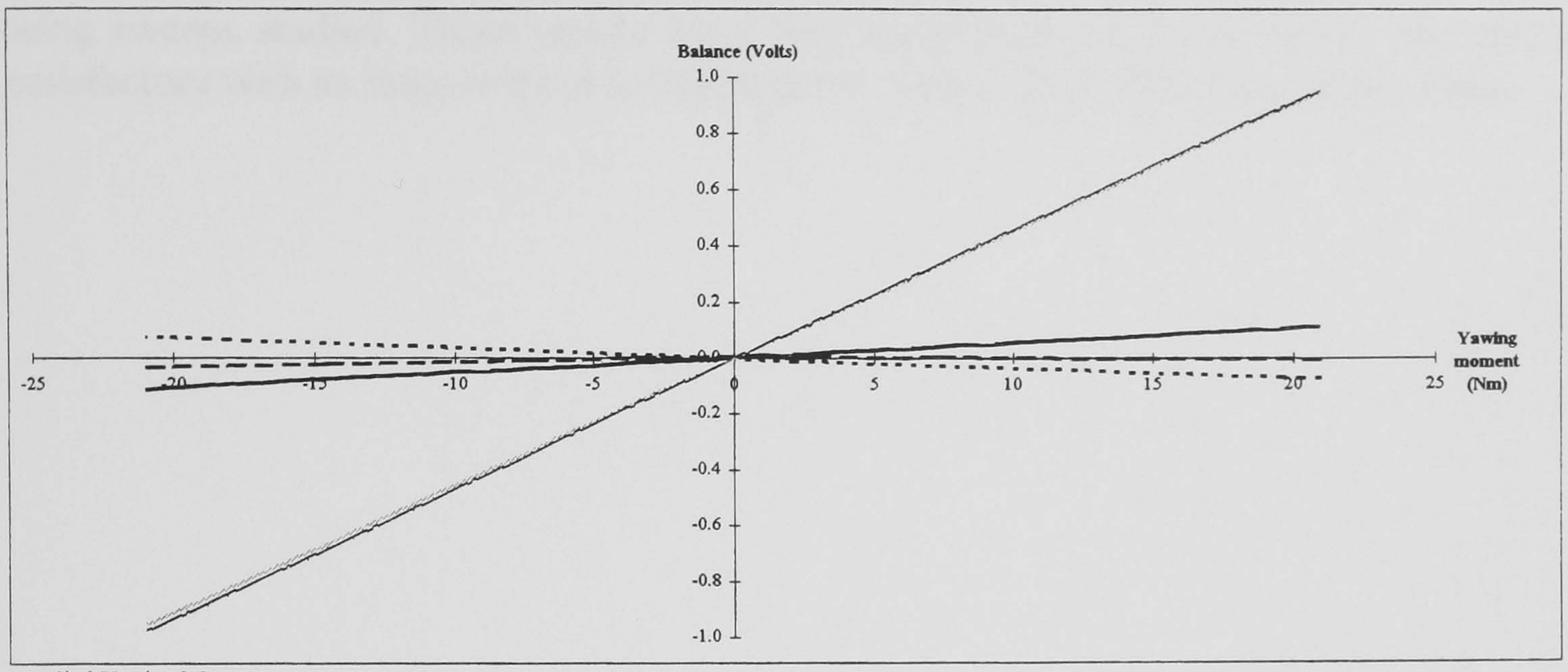

Figure A-2 cont.: Weybridge balance calibration data.

Appendix III

Weybridge balance repeatability

The repeatability from one run to the next of the aerodynamic forces and moments measured on the balance in the Weybridge wind tunnel are shown in Figure A-3 for all wing sweeps studied. These results show that repeatability from one run to the next is satisfactory with an improvement in repeatability with an increased wing sweep angle.

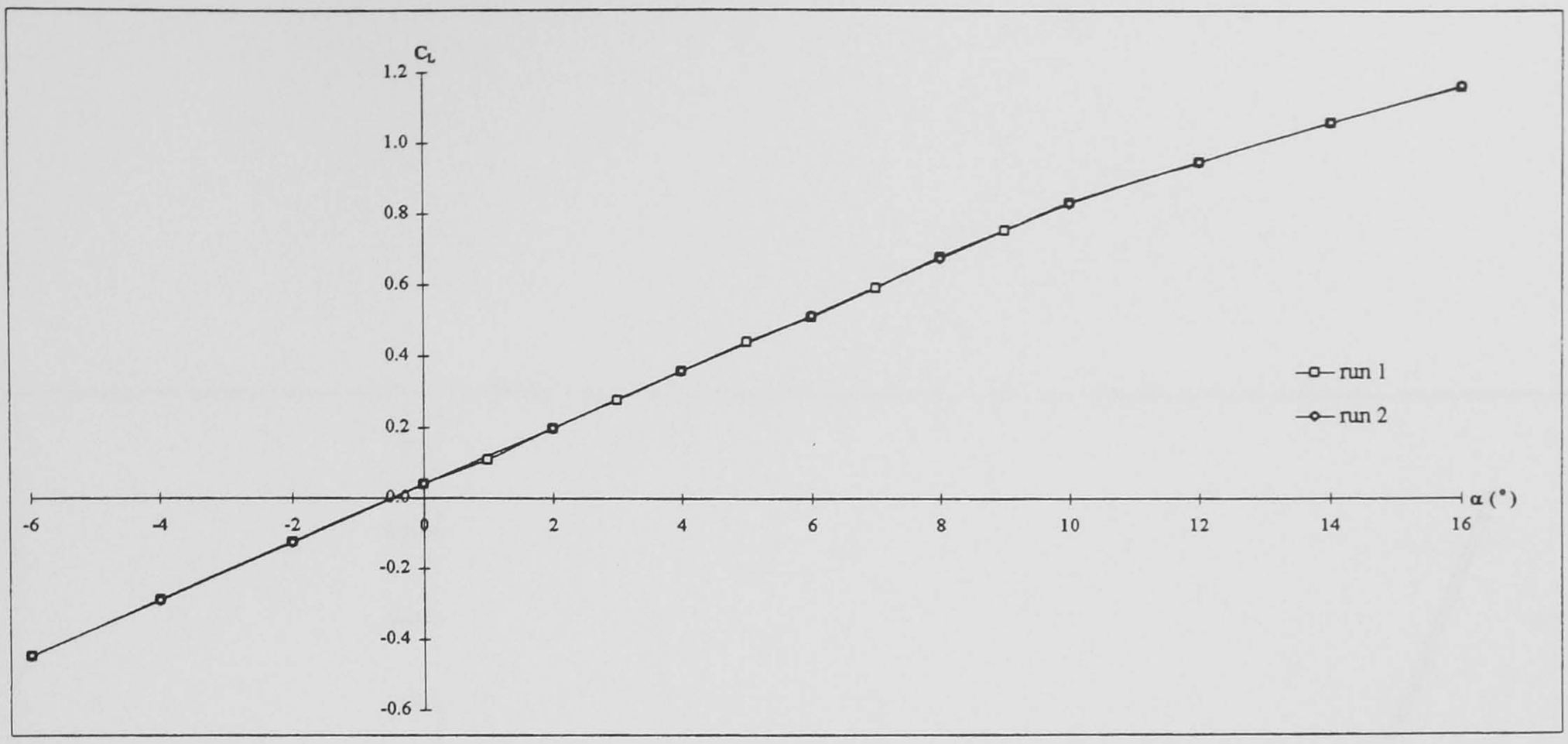

Lift

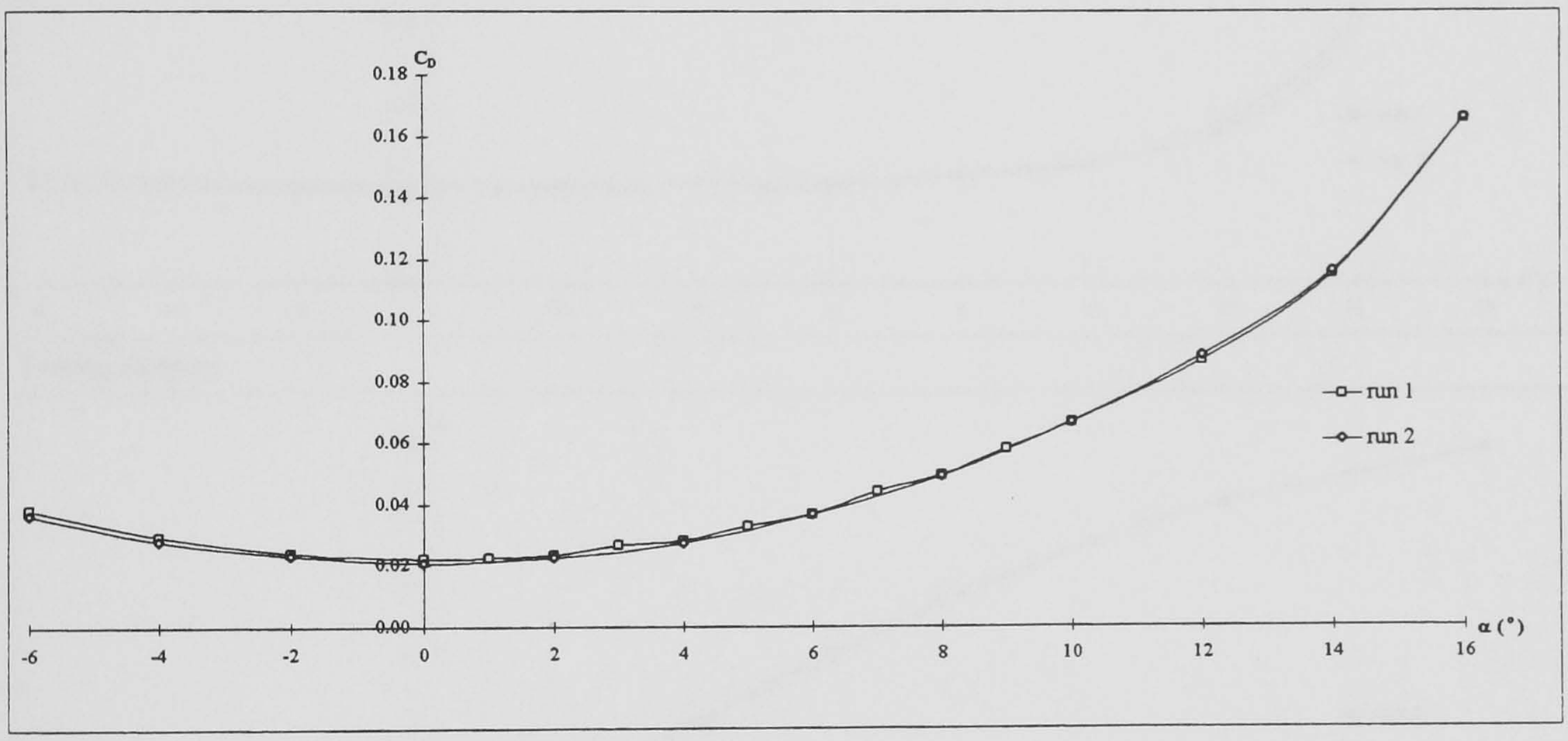

Drag

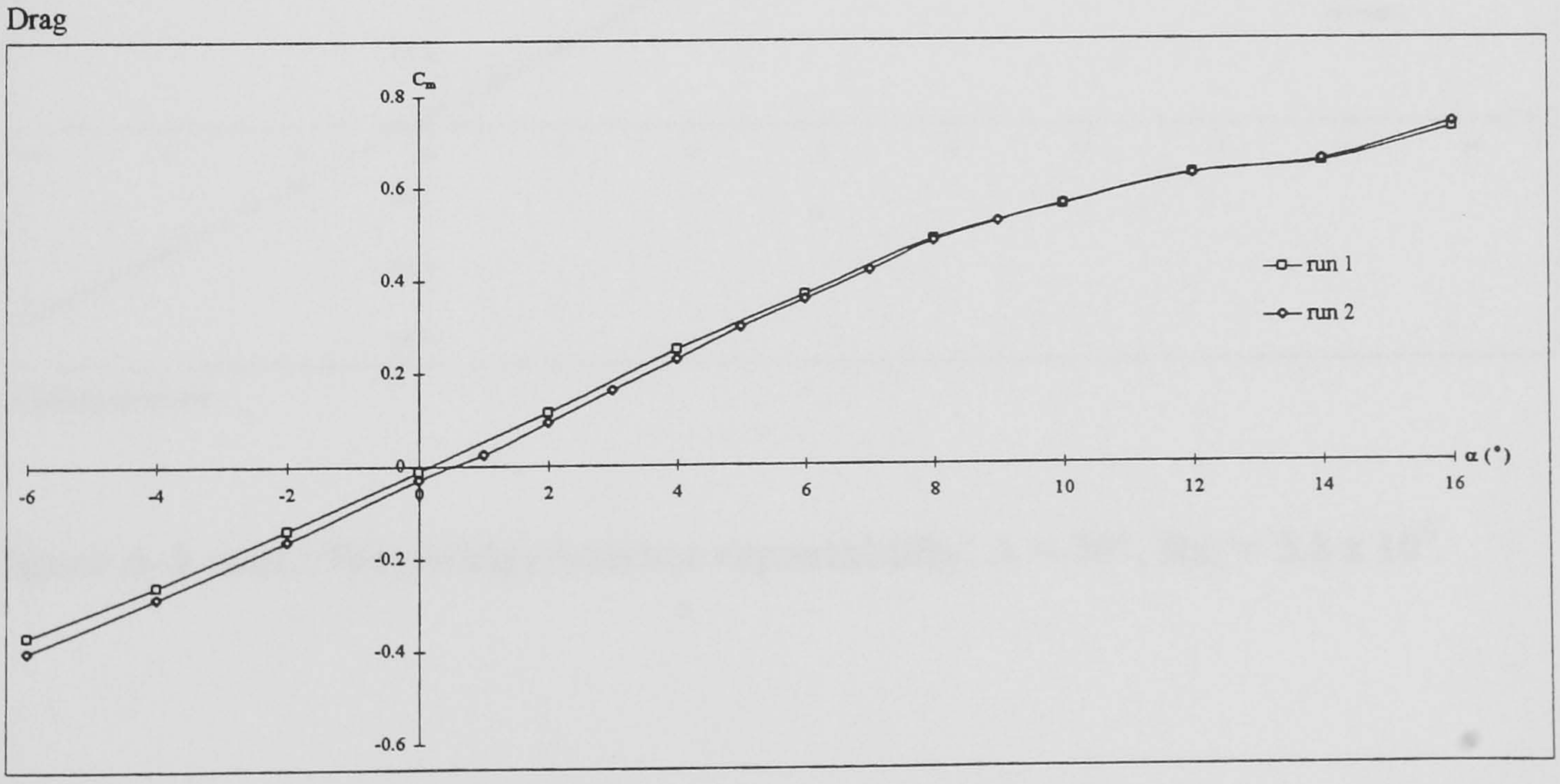

Pitching moment

Figure A-3: Weybridge balance repeatability. $\Lambda = 30°$, $Re_c = 3.8 \times 10^5$.

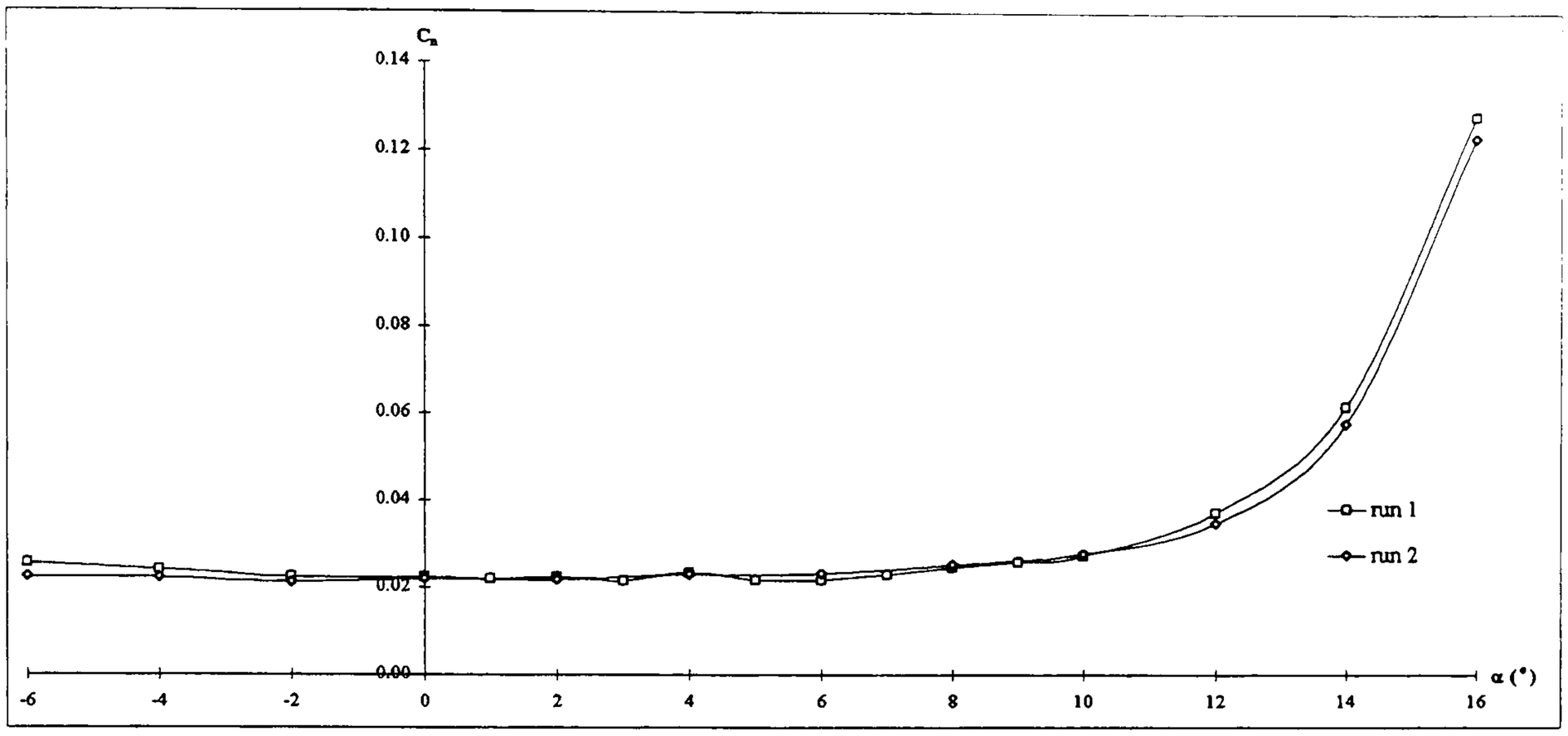

Yawing moment

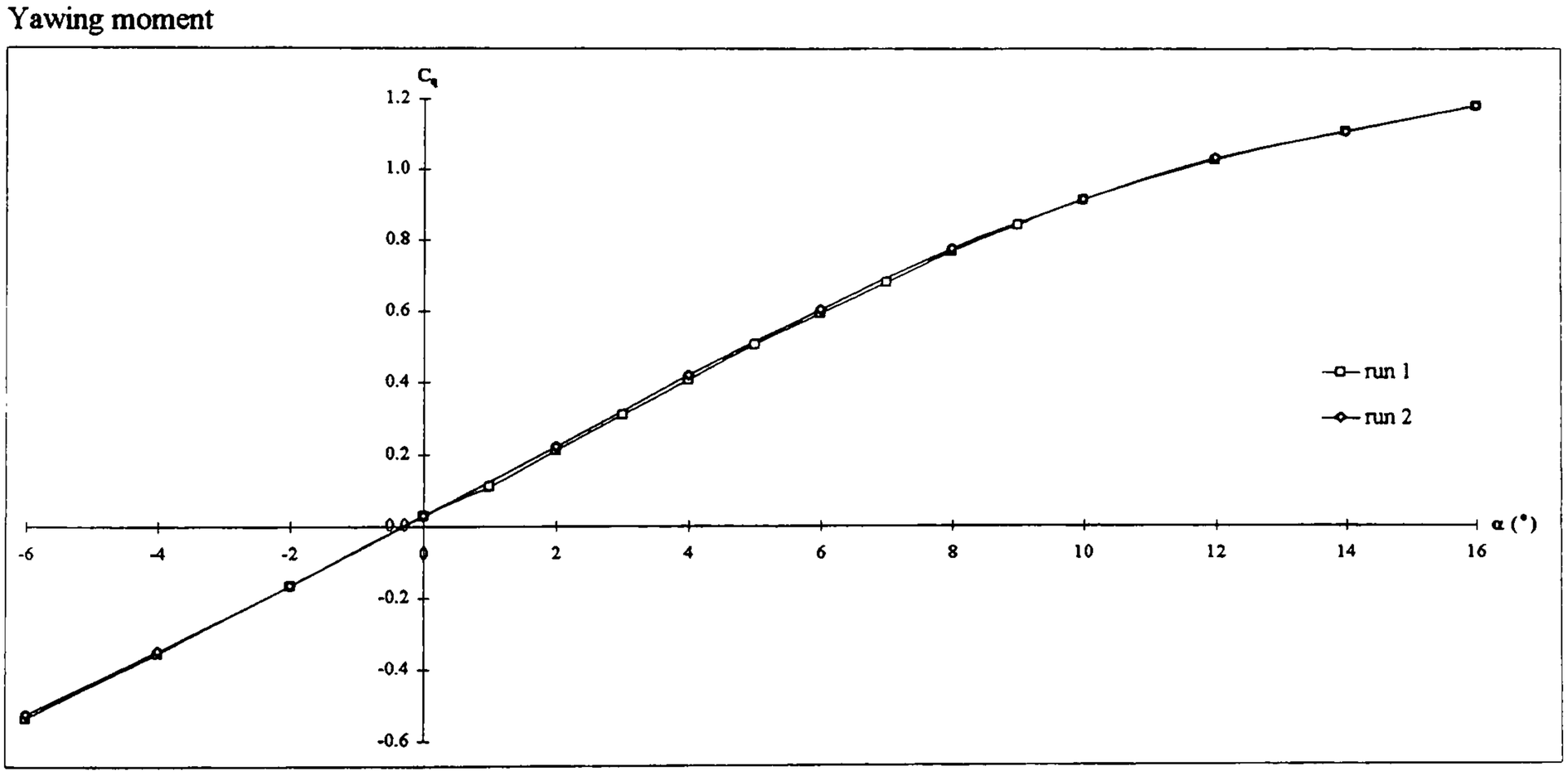

Rolling moment

Figure A-3 cont.: Weybridge balance repeatability. $\Lambda = 30°$, $Re_c = 3.8 \times 10^5$.

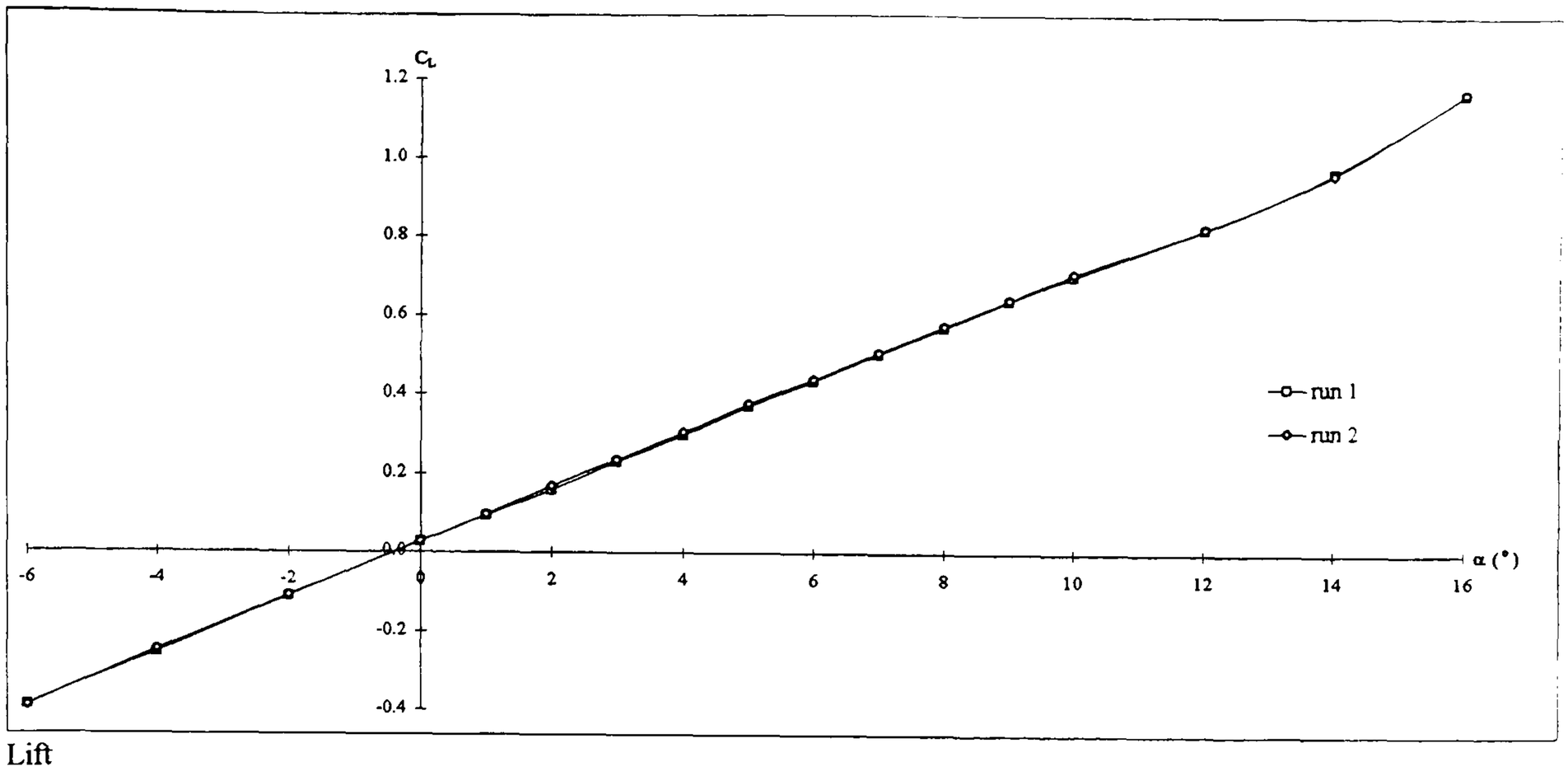

Lift

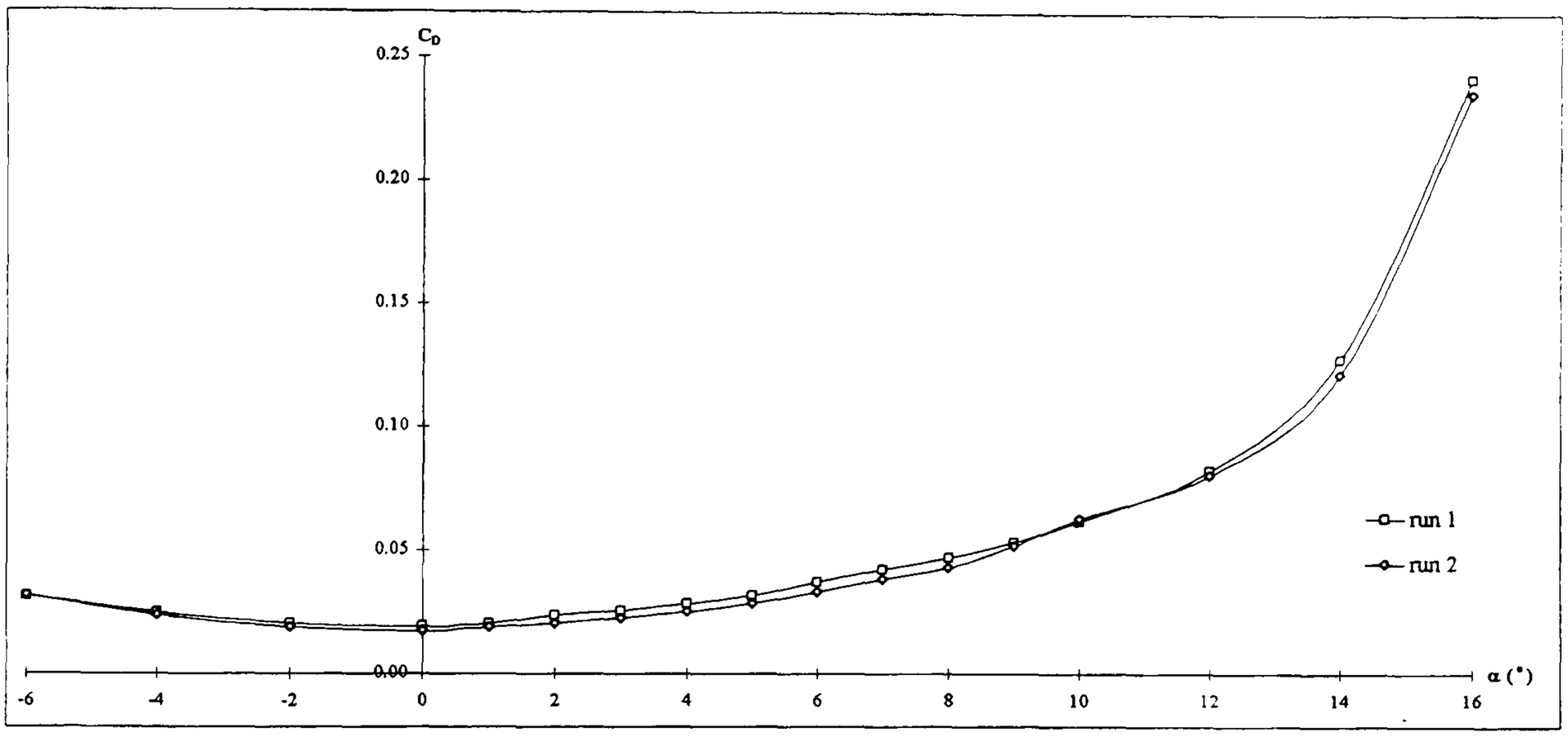

Drag

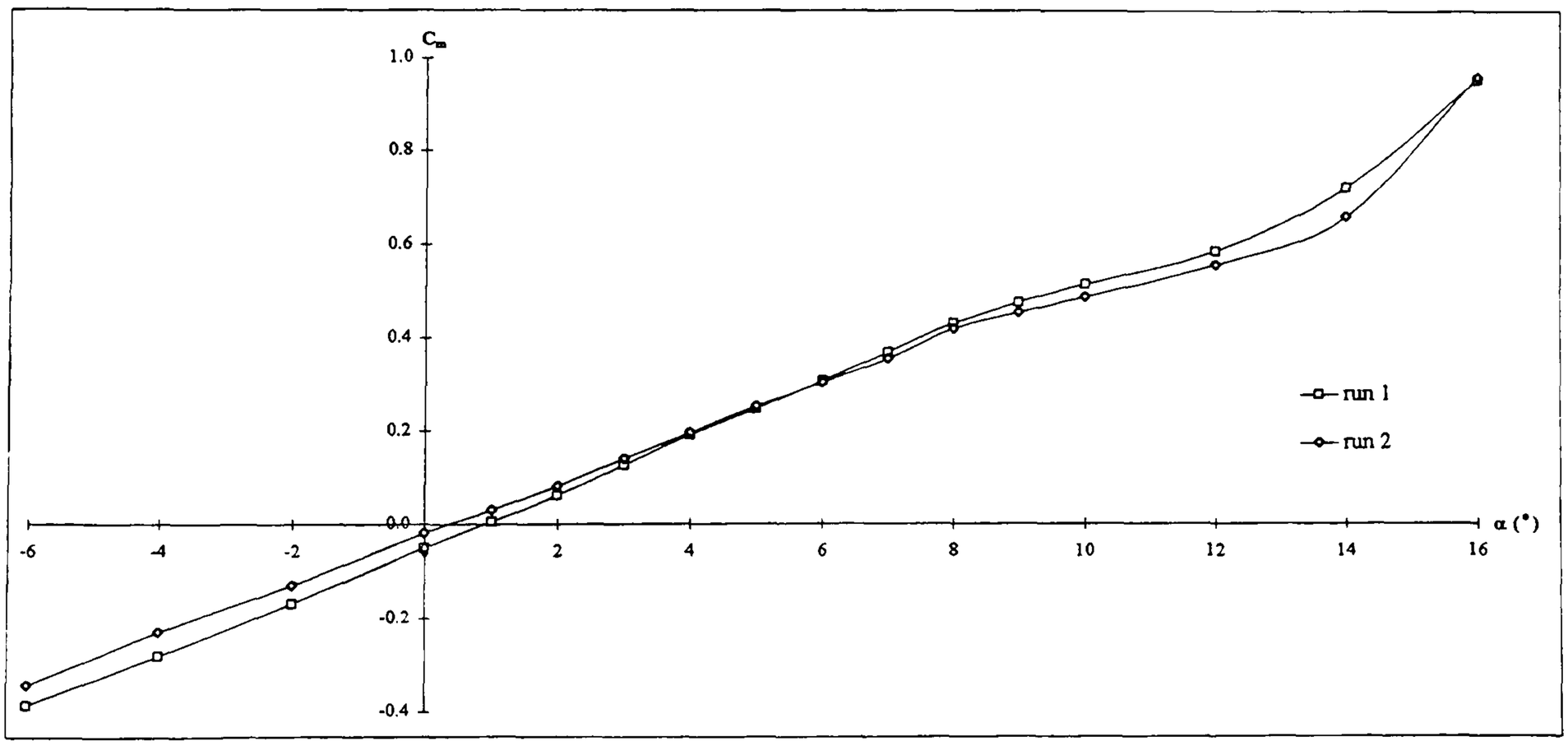

Pitching moment

Figure A-3 cont.: Weybridge balance repeatability. $\Lambda = 40°$, $Re_c = 4.3 \times 10^5$.

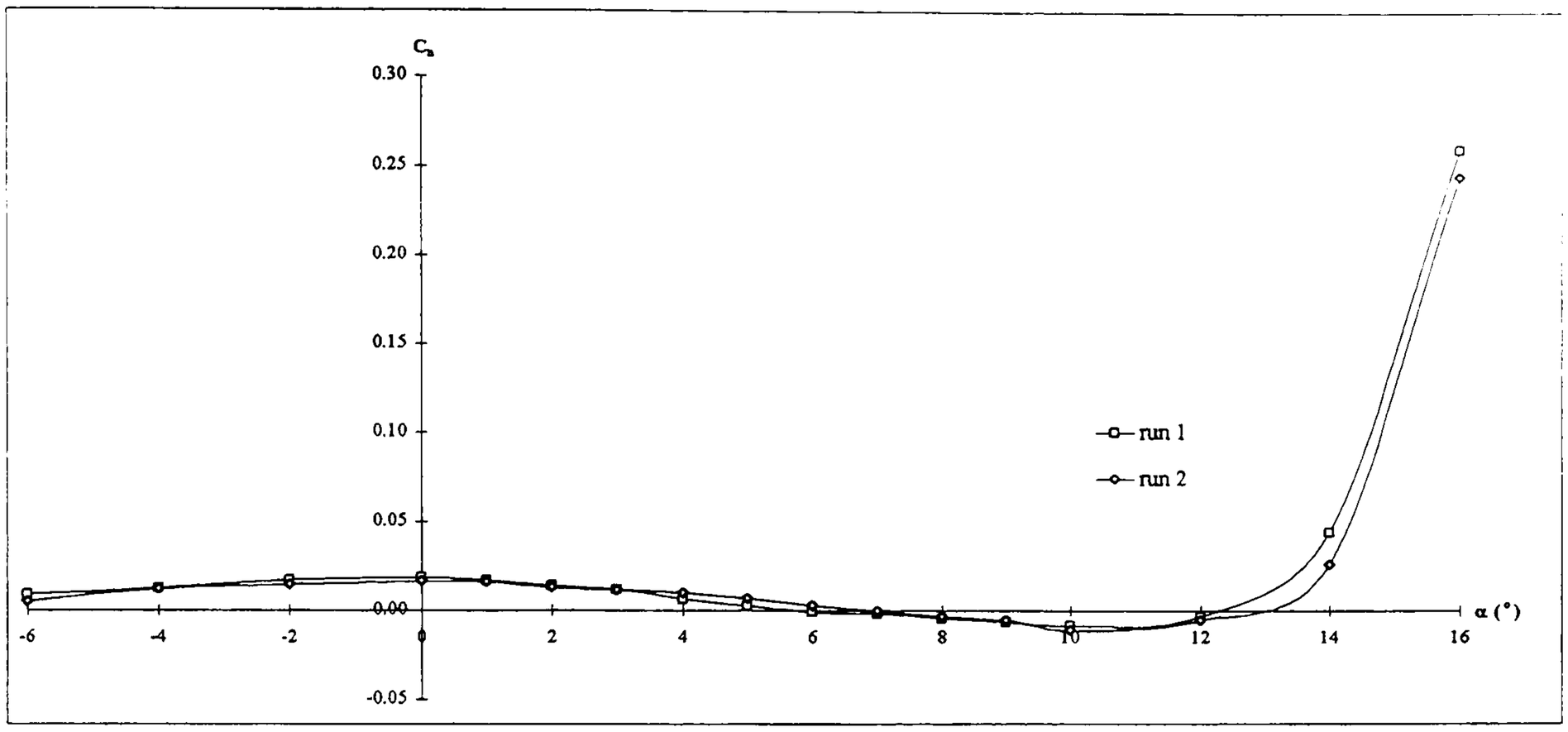

Yawing moment

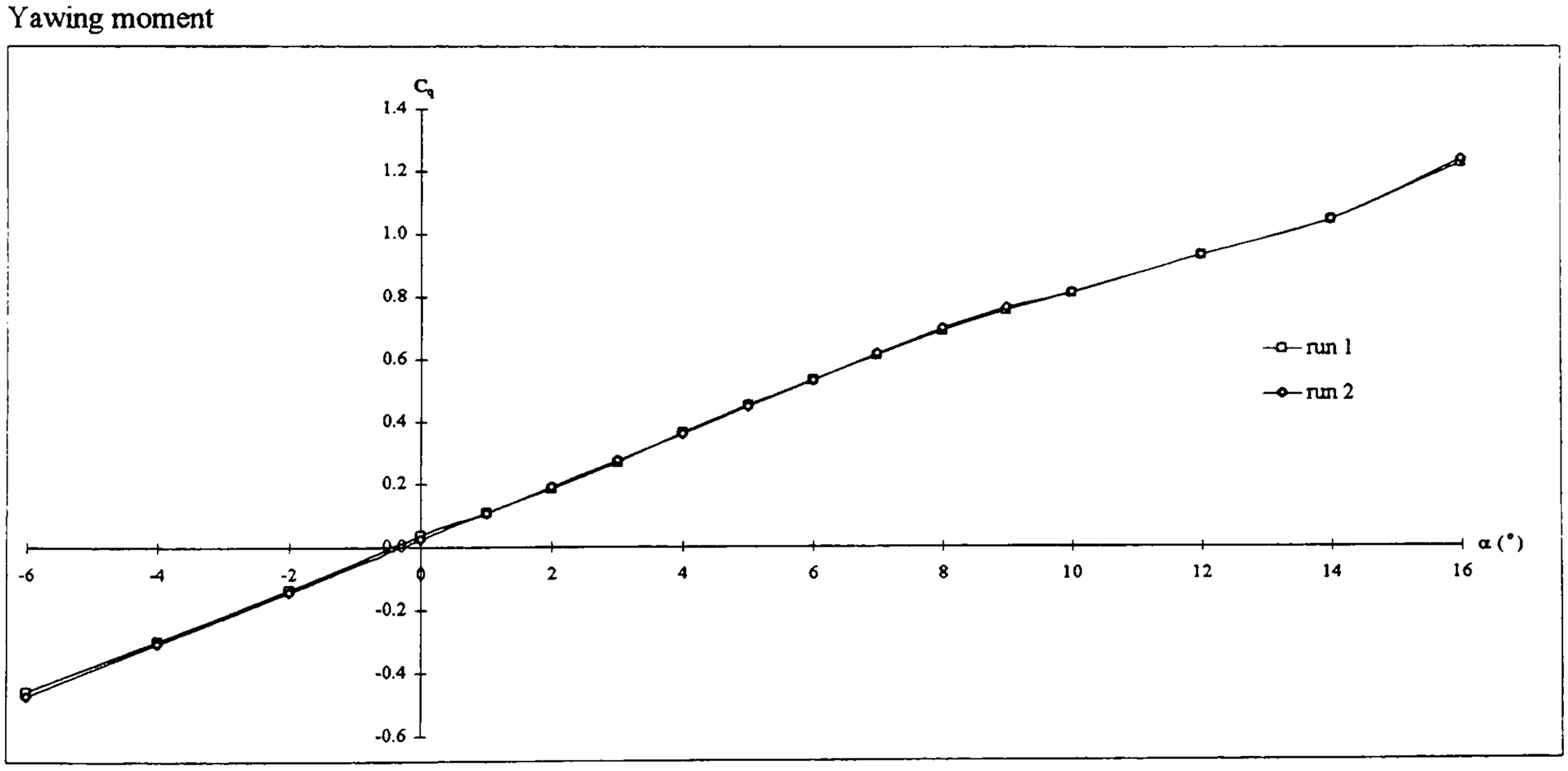

Rolling moment

Figure A-3 cont.: Weybridge balance repeatability. $\Lambda = 40°$, $Re_c = 4.3 \times 10^5$.

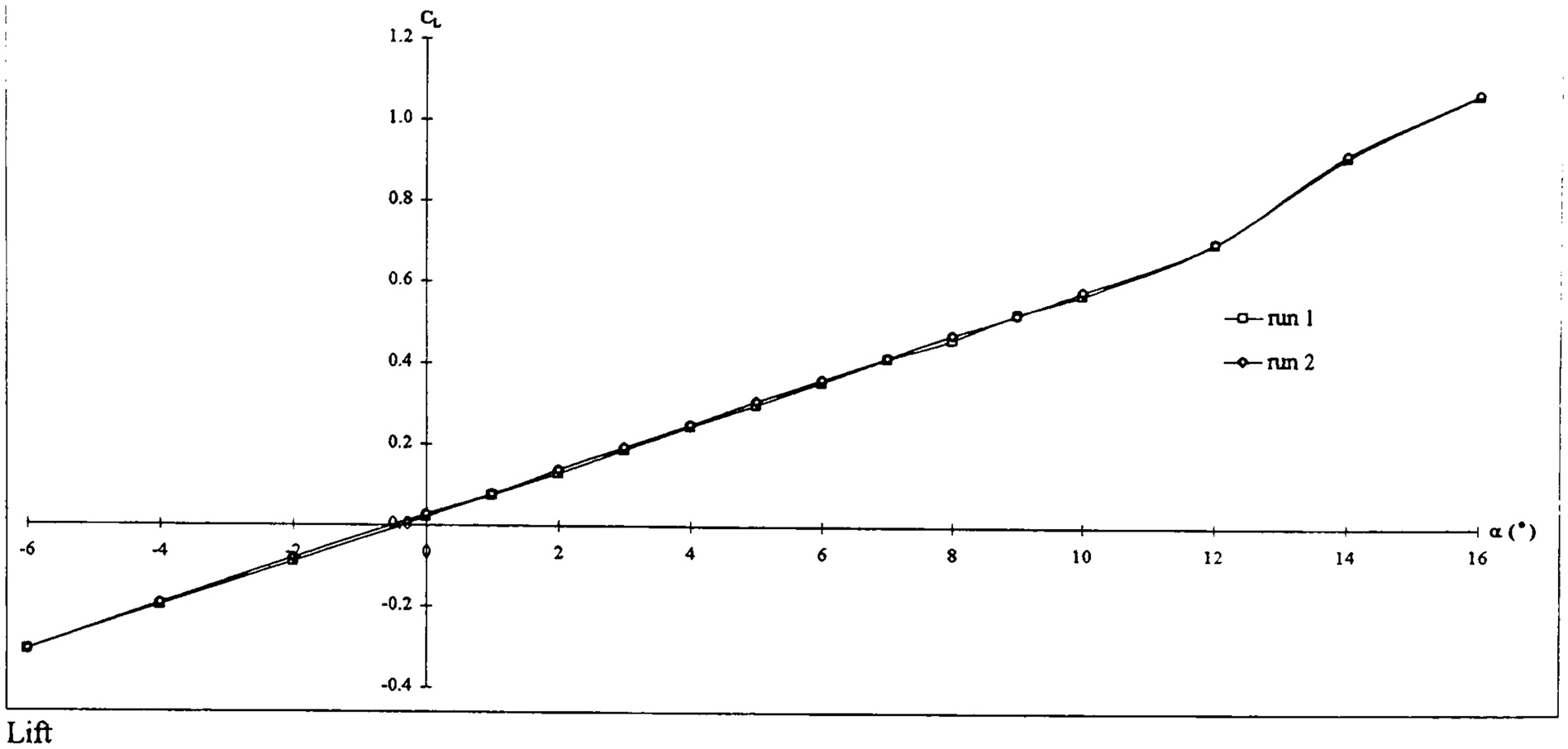

Lift

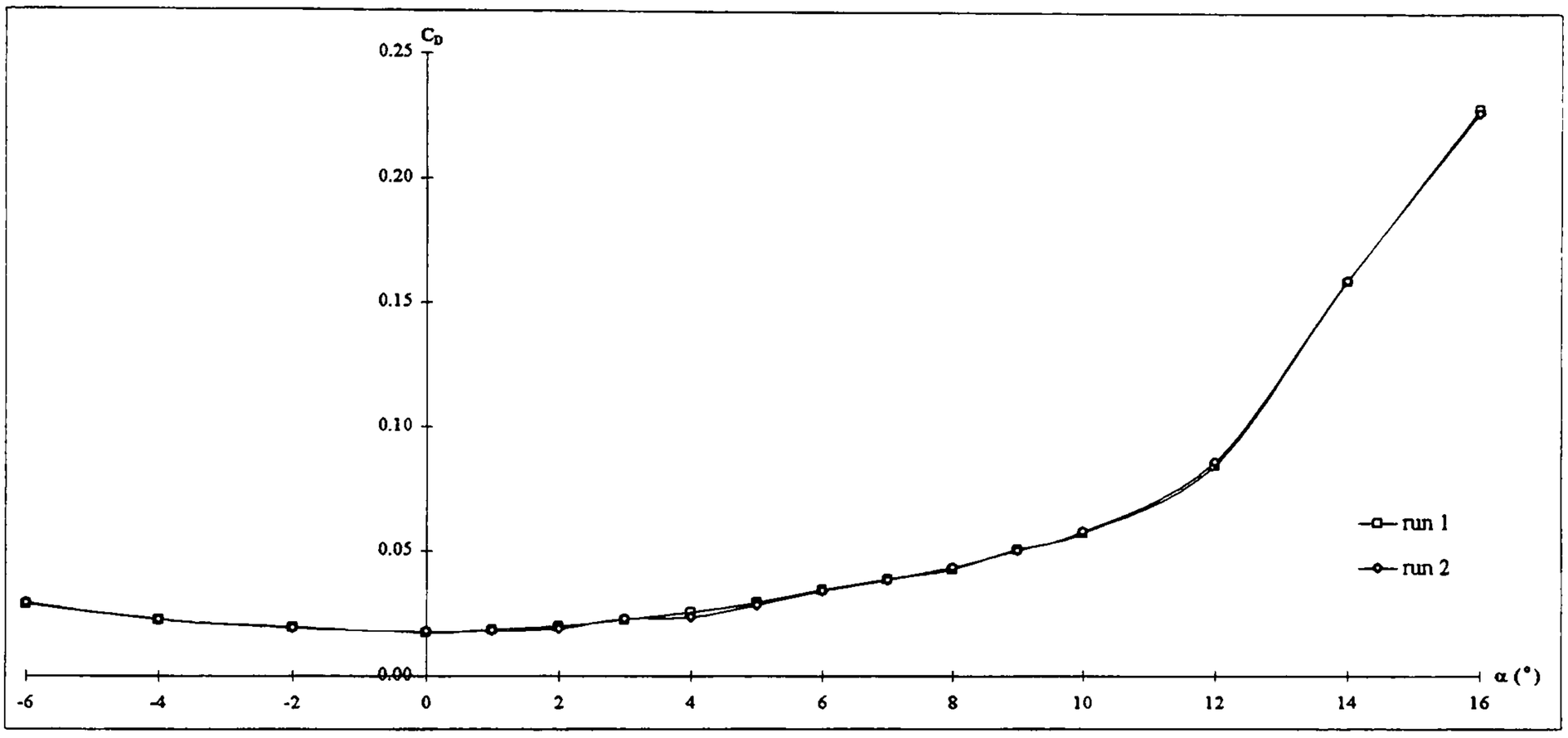

Drag

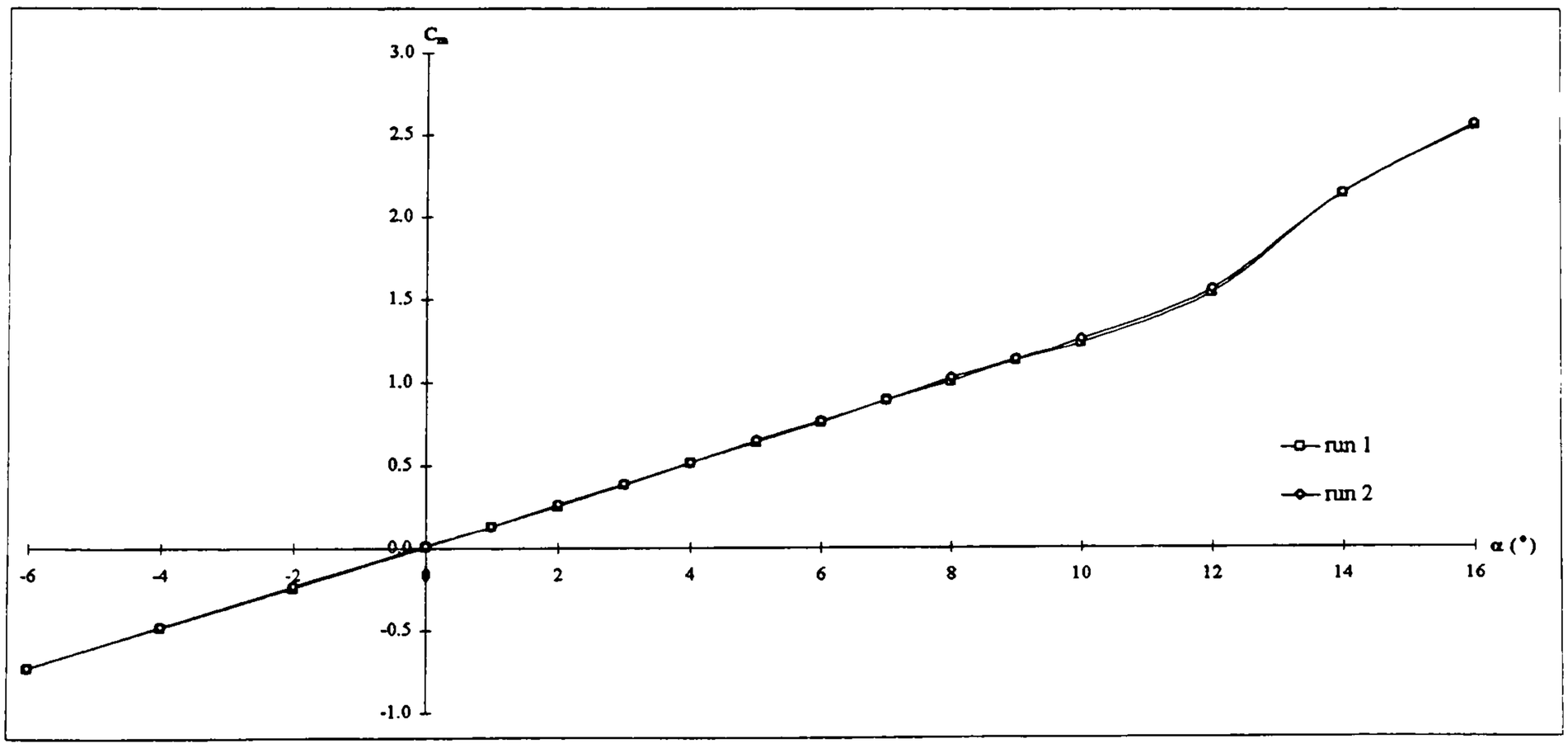

Pitching moment

Figure A-3 cont.: Weybridge balance repeatability. $\Lambda = 50°$, $Re_c = 5.1 \times 10^5$.

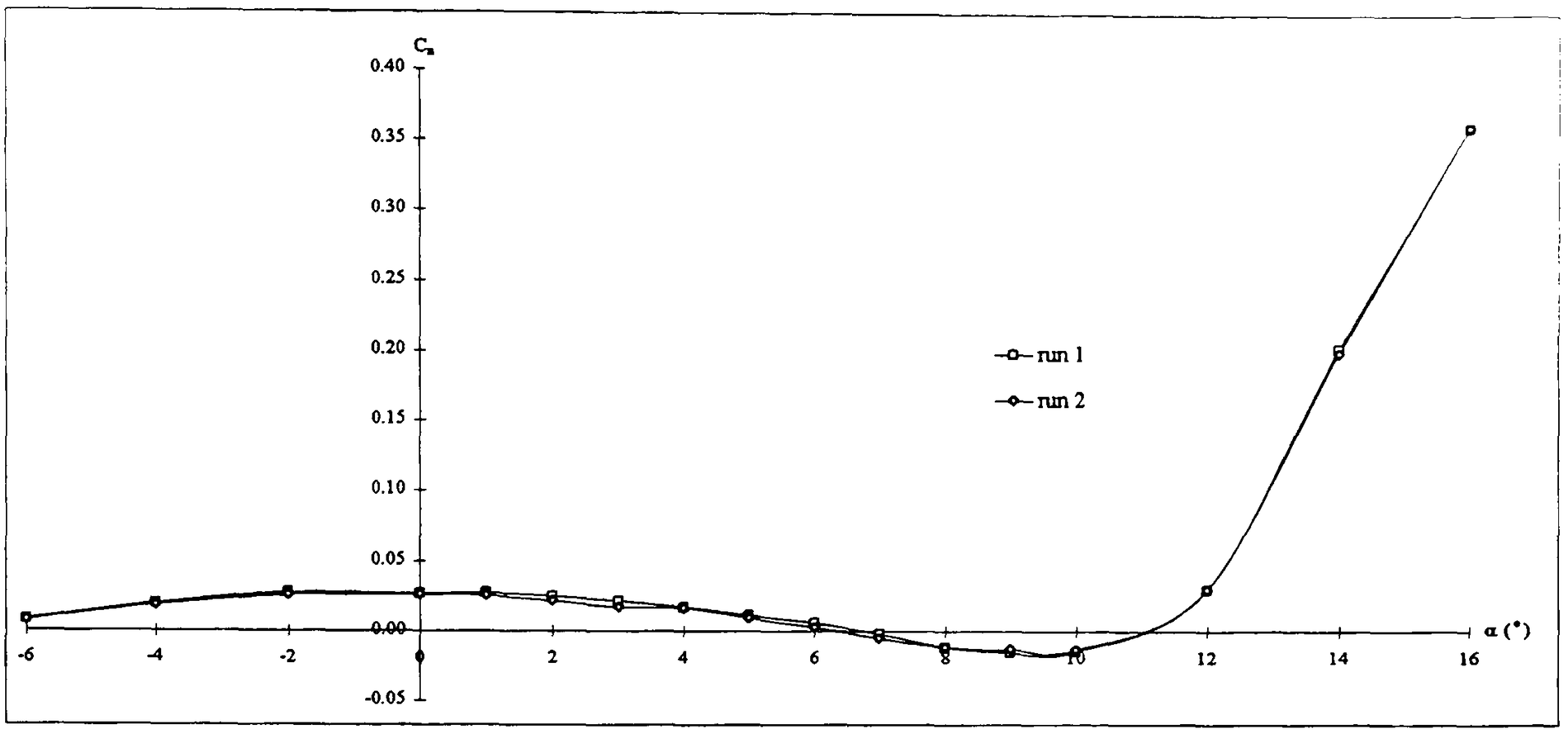

Yawing moment

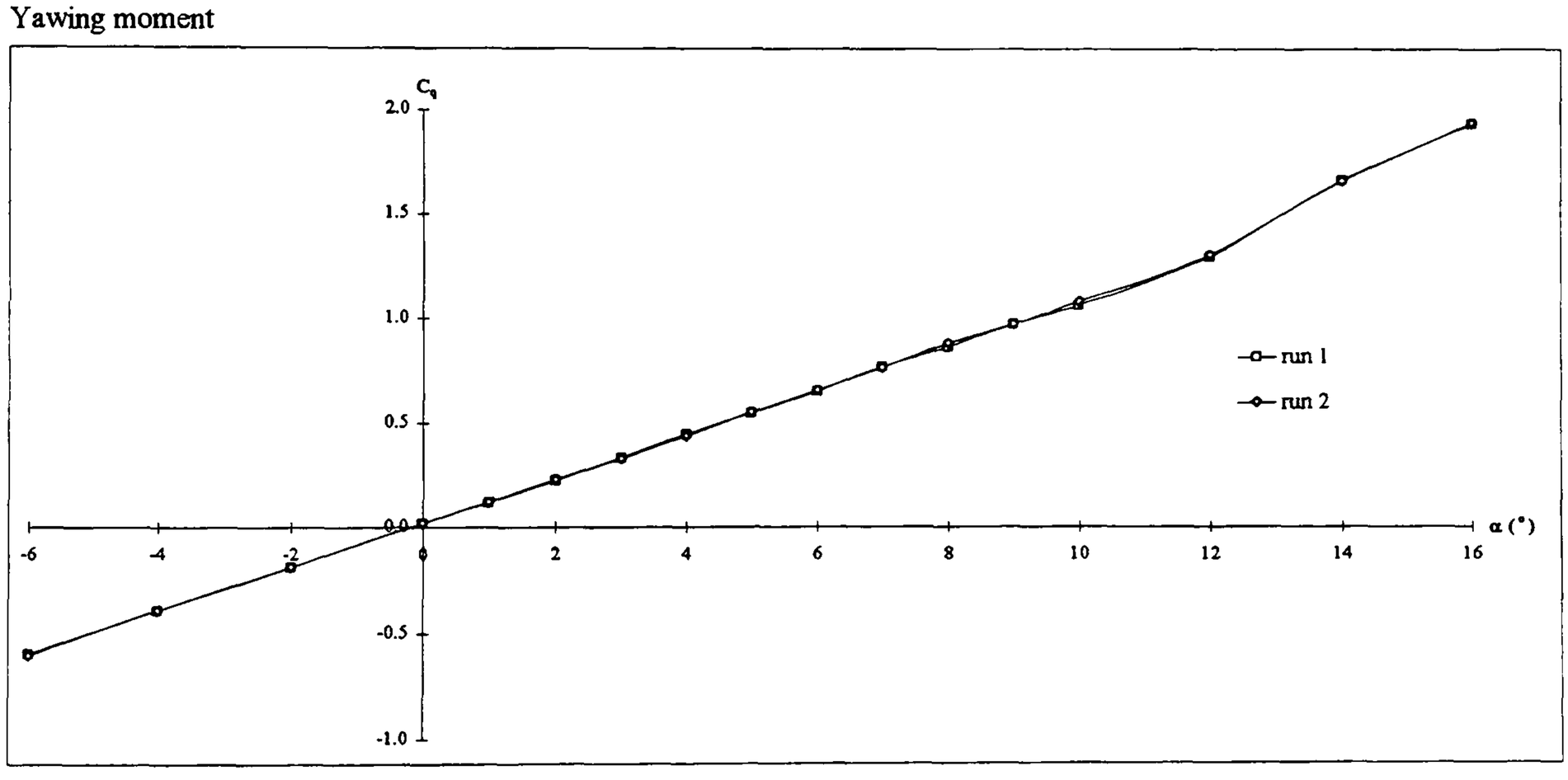

Rolling moment

Figure A-3 cont.: Weybridge balance repeatability. $\Lambda = 50°$, $Re_c = 5.1 \times 10^5$.

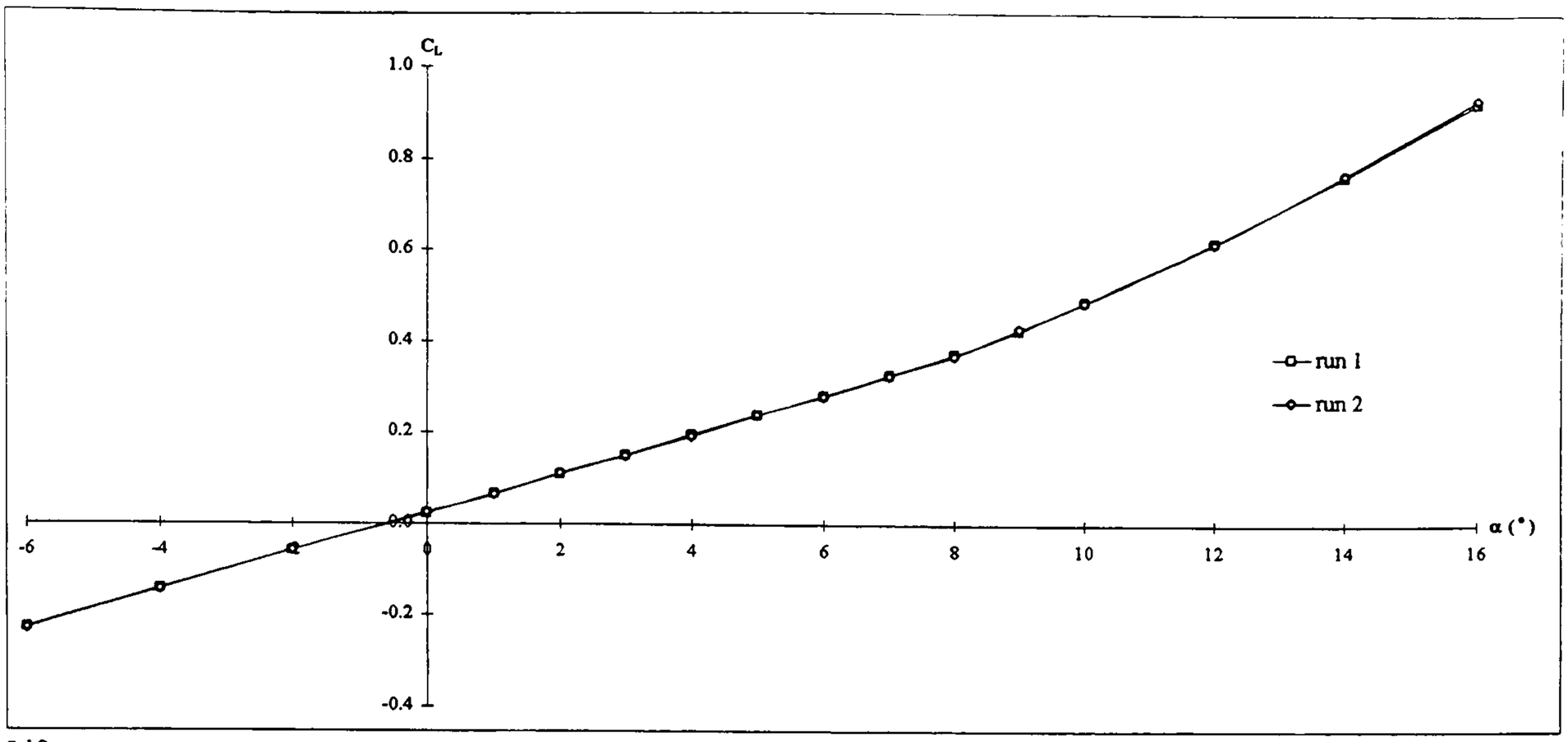

Lift

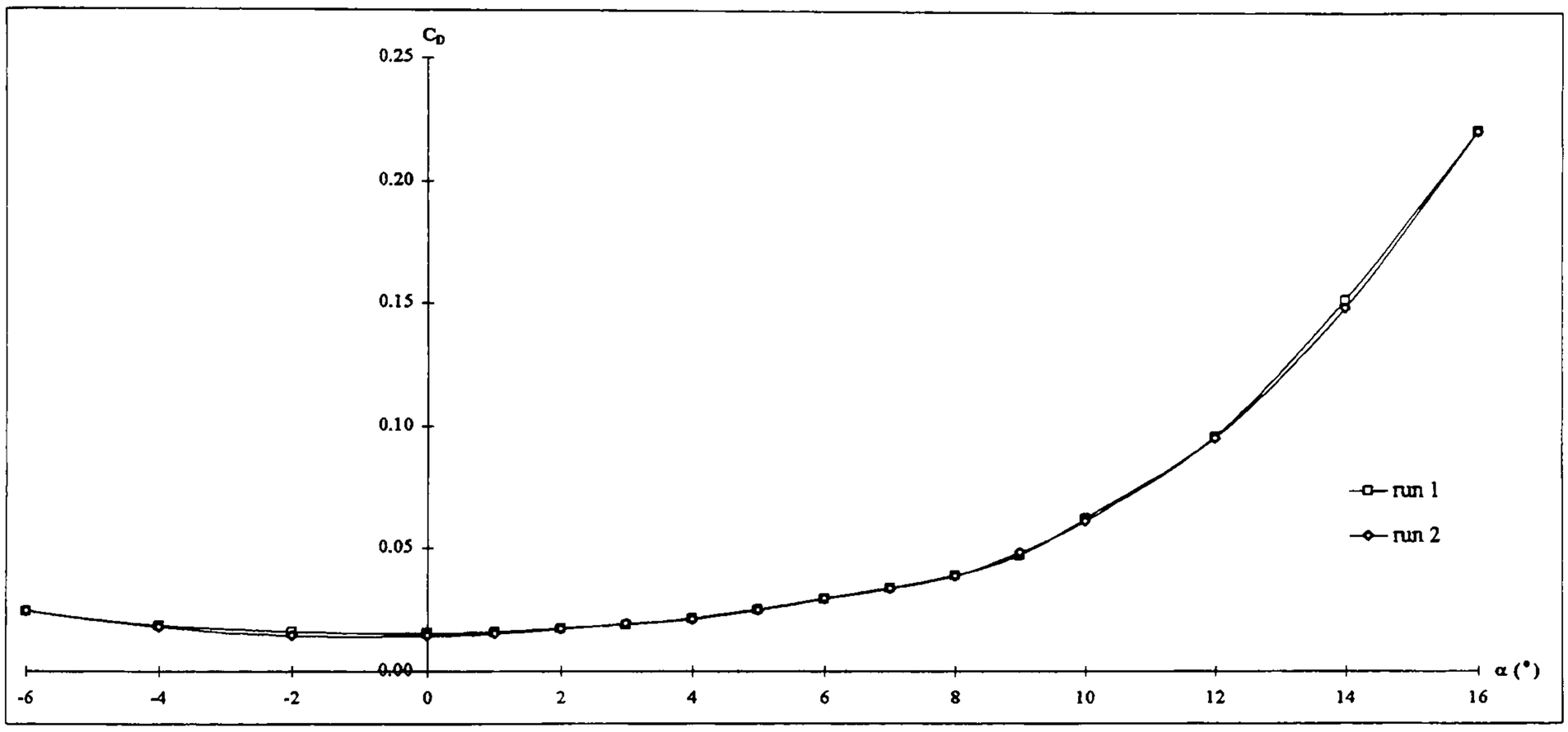

Drag

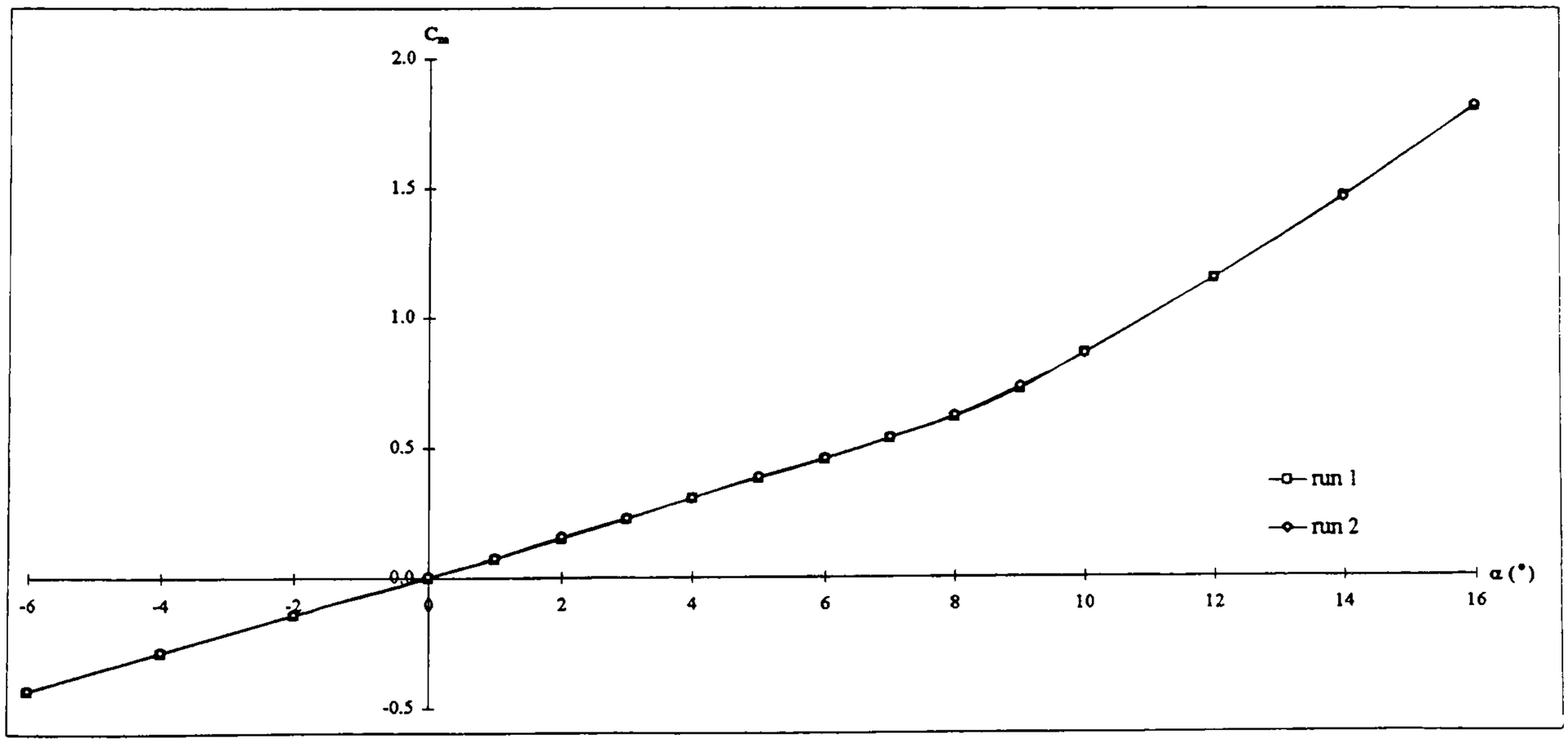

Pitching moment

Figure A-3 cont.: Weybridge balance repeatability. $\Lambda = 60°$, $Re_c = 6.5 \times 10^5$.

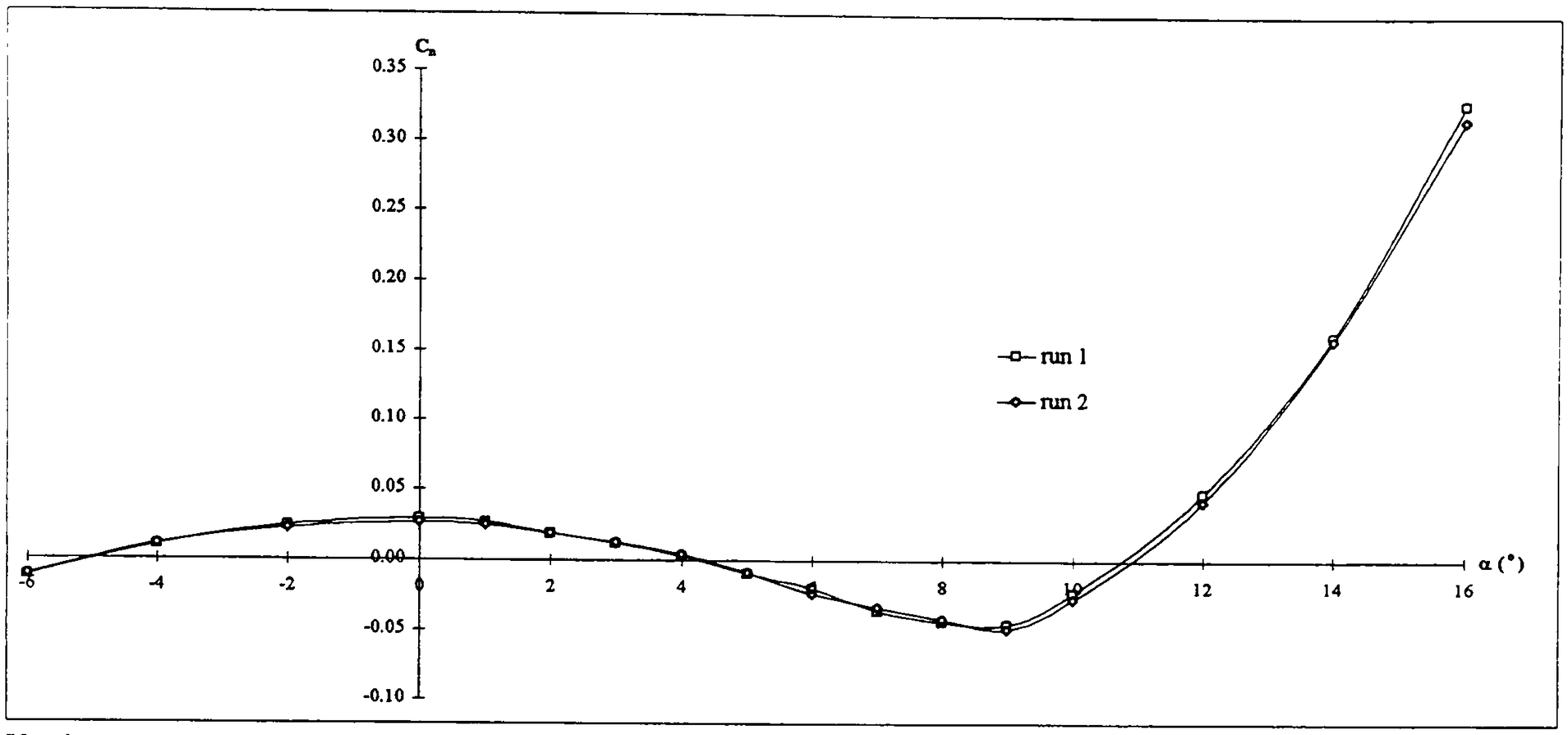

Yawing moment

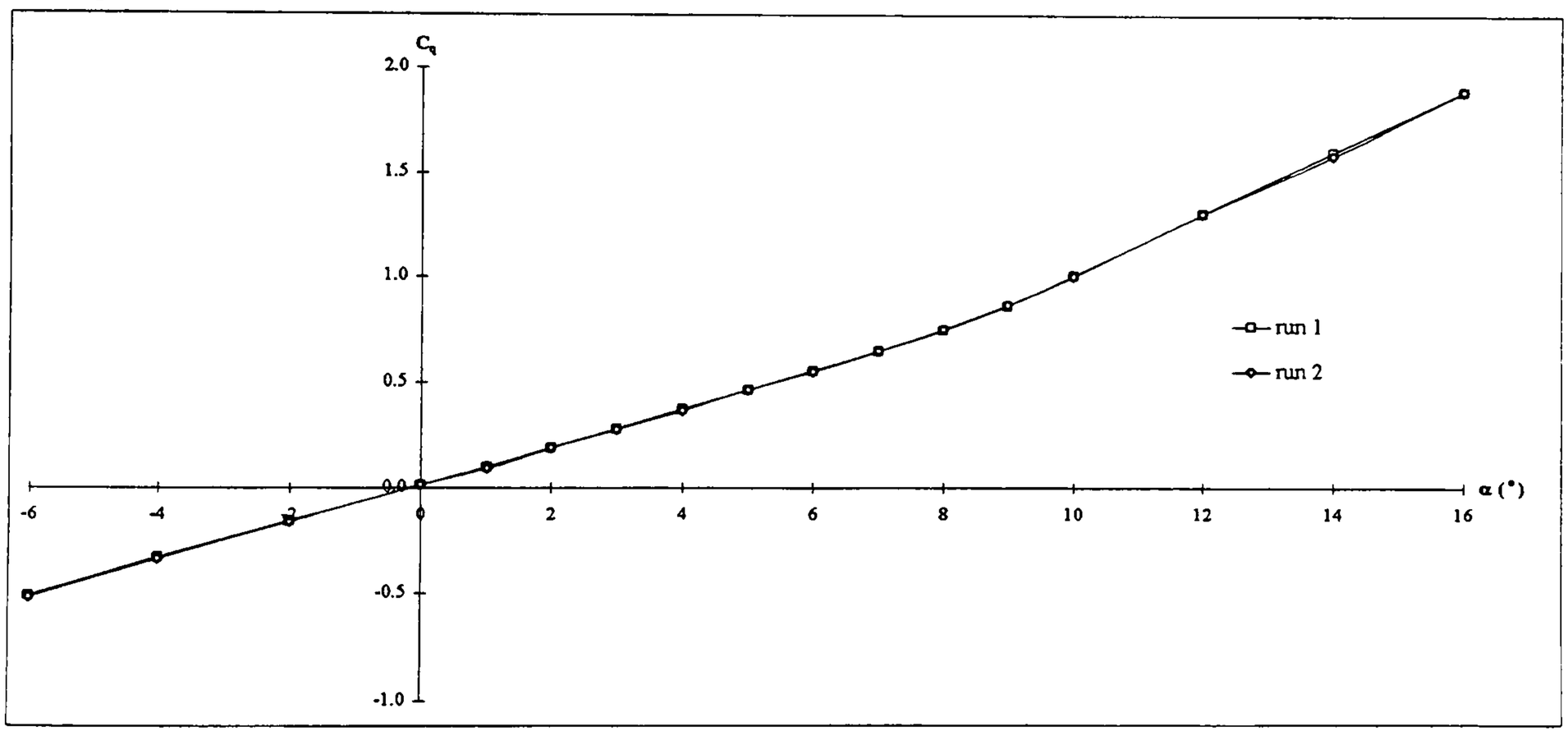

Rolling moment

Figure A-3 cont.: Weybridge balance repeatability. $\Lambda = 60°$, $Re_c = 6.5 \times 10^5$.

Appendix IV

DERA wing pressure tapping positions.

The pressure tapping positions on the DERA wing are at 5 spanwise locations:-

$\eta = 0.06b$, $\eta = 0.16b$, $\eta = 0.30b$, $\eta = 0.45b$ & $\eta = 0.59b$.

At each location there are 36 pressure tappings on the upper surface and 16 on the lower surface. These are in the same chordwise positions at each spanwise location. These chordwise positions are therefore given in Table A-1 in non-dimensional form based on the normal chord (0.610m).

Upper surface		Lower surface	
x / c	z / c	x / c	z / c
0	-0.0422	0.001	-0.0460
0.0005	-0.0370	0.005	-0.0518
0.0010	-0.0352	0.01	-0.0556
0.0020	-0.0328	0.05	-0.0666
0.0050	-0.0281	0.10	-0.0716
0.0075	-0.0251	0.20	-0.0754
0.01	-0.0226	0.30	-0.0758
0.03	-0.0084	0.40	-0.0733
0.05	0.0018	0.50	-0.0633
0.08	0.0144	0.58	-0.0496
0.10	0.0215	0.70	-0.0416
0.15	0.0364	0.80	-0.0418
0.20	0.0478	0.84	-0.0439
0.25	0.0561	0.88	-0.0475
0.30	0.0616	0.92	-0.0526
0.35	0.0645	0.96	-0.0595
0.40	0.0662		
0.45	0.0669		
0.50	0.0667		
0.55	0.0657		
0.58	0.0635		
0.62	0.0574		
0.65	0.0501		
0.70	0.0349		
0.75	0.0184		
0.80	0.0016		
0.82	-0.0053		
0.84	-0.0121		
0.86	-0.0190		
0.88	-0.0258		
0.90	-0.0327		
0.92	-0.0395		
0.94	-0.0463		
0.96	-0.0529		
0.98	-0.0595		
1	-0.0658		

Table A-1: Chordwise pressure tapping positions on the DERA wing.

Appendix V

The DERA Bedford method for determining the size of particle for fixing transition

$$R_K = A(R_{xK})^{1/4} (1+0.2M^2)$$

where

R_K	-	Reynolds number based on the particle size for fixing transition
K	-	particle size for fixing transition
A	-	42.6
xK	-	streamwise position of the transition trip
M	-	local Mach number
R_{xK}	-	Reynolds number based on xK

Appendix VI

Wind tunnel corrections used in the DERA 13' x 9' low speed wind tunnel

Two corrections are applied to the wind tunnel balance and pressure results. The first is a blockage correction[113,114] and the second is a correction for the induced upwash on the wing due to the interference caused by the tunnel walls[115-117]. In calculating the blockage, the "solid blockage" effect produced by the presence of the model itself and the "wake blockage" effect which arises from the constriction caused by the reduced velocity in the wake of the body are considered separately and summed to give the total blockage.

The solid blockage correction is given by :-

$$\varepsilon_s = 0.000456(1+1.2t/c)\omega/\beta^3$$

which is based on the principle that the effect of the tunnel walls can be represented by an array of images of the body in the tunnel walls. The velocity induced at the middle of the tunnel from these images is calculated from potential theory, with the assumption that the velocity is uniform over the span and length of the model and the images are small enough to be replaced by equivalent doublets, to give the solid blockage correction. The factor (1+1.2t/c) is included to account for the aerofoils finite thickness and β to correct for compressibility effects.

The wake blockage correction is given by:-

$$\varepsilon_w = C_D S/4A_T\beta^2$$

which is again calculated from images with the wake represented by an equivalent source. β is again included to correct for compressibility effects.

These two blockage correction factors are then applied to the Mach number using:-

$$\Delta M/M = (1+0.2M^2)\varepsilon$$

obtained from differentiation of the adiabatic isentropic flow equations using the fact that the total head is constant.

Corrections are then applied to the force, moment and pressure coefficients calculated from uncorrected freestream velocity and density. These are obtained from assuming the

flow is isentropic and adiabatic and, for typical non-dimensional coefficients, using the correction to the stream dynamic pressure to give:-

$$\Delta C_A/C_A = -(2-M^2)\varepsilon$$

The pressure coefficient correction includes an additional correction for changes in the static pressure and is given by:-

$$\Delta C_p = \{2-(2-M^2)C_p\}\varepsilon$$

The wind tunnel interference is the change in the transverse flow normal to the direction of motion behind a wing moving in an unlimited fluid due to a boundary. These boundaries, tunnel walls, are represented by a set of images whose induced velocities are used to calculate the tunnel interference.

In a closed tunnel a wing experiences an upwash and thus at a given value of the lift coefficient the angle of incidence and the drag in a closed tunnel will be lower than in free flow. Due to this upward induced velocity the line of action of the lift force on the wing is inclined forwards and therefore corrections are applied to the observed values of the incidence and the drag coefficient given by:-

$$\Delta\alpha = \delta S C_L$$

and

$$\Delta C_D = (\pi/180)\delta S C_L^{\,2}$$

where δ represents the magnitude of the tunnel constraint[116], which for the DERA wing are 0.067200, 0.067896 and 0.068736 for wing sweeps of 30°, 40° and 50° respectively.

Appendix VII

Creating the required boundary layer profile in the 2.5" x 2.5" transonic wind tunnel

The total pressure at several distances from the wind tunnel surface and at four streamwise positions, Figure A-4, was measured using a small swanneck Preston tube, Figure A-5, attached to a micrometer and aligned to the flow. The Preston tube and micrometer are mounted in a purposely built brass plug with the Preston tube electrically insulated such that when the end of the tube touches the tunnel wall an audible signal is heard enabling the zero height of the probe to be set. The Preston tube pressure transducer results were then translated into absolute pressures and the dynamic pressure at each point calculated after measuring the surface static pressure at each streamwise position from a brass plug with a static pressure tapping machined into the surface. The streamwise velocity at each point were then calculated and a small correction applied when the Preston tube was close to the wall, Figure A-6. The edge of the boundary layer was then estimated from plotting the distance from the tunnel surface to the effective centre of the Preston tube against the ratio of the local measured velocity to the freestream velocity since the edge of the boundary layer can be taken to be where this velocity ratio is 0.99. The boundary layer profile was then obtained at each streamwise position from plotting this velocity ratio against the non-dimensional distance from the tunnel surface using the estimated boundary layer thickness. The development of the boundary layer with distance along the tunnel surface was also obtained from plotting streamwise position against the estimated boundary layer thickness. This procedure was repeated with strips of sandpaper (of various grades) inserted at various positions on the tunnel surface to generate a boundary layer of approximately 12 mm thickness at a downstream distance 203 mm from the leading edge of the tunnel surface since this is where the vortex generators will be positioned. This boundary layer thickness was achieved with a 26 mm wide strip of <P50 sandpaper spanning the test section 52 mm from the leading edge of the tunnel surface at a wind speed of 67 m/s. The wind speed was chosen after preliminary tests with liquid crystal showed this to be the greatest wind speed at which the liquid crystals did not get blown off the tunnel wall. Figure A-7 shows the results for the chosen boundary layer together with a theoretical boundary layer profile (a 1/5 or 1/6 power law) which shows the boundary layer to be turbulent.

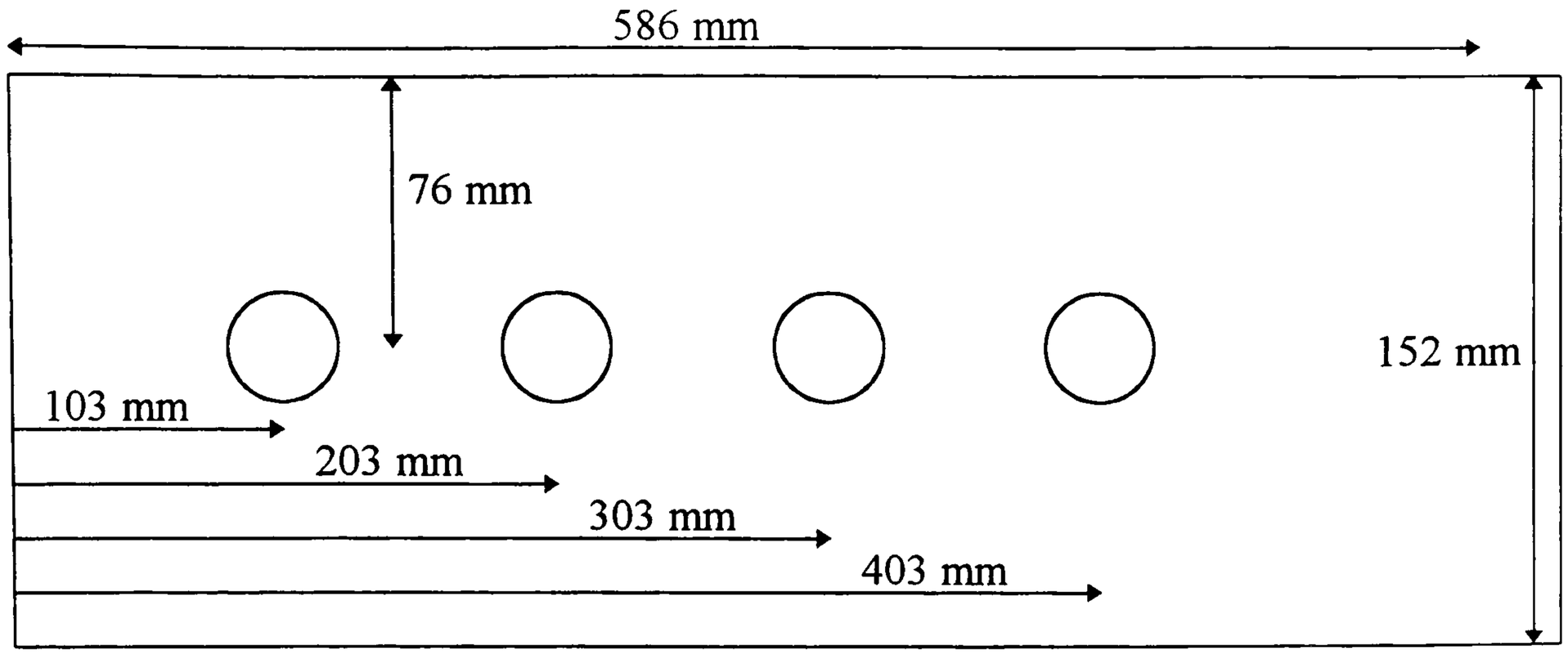

Figure A-4: Wind tunnel surface showing plug positions.

Side view with brass plug (micrometer mechanism not shown)

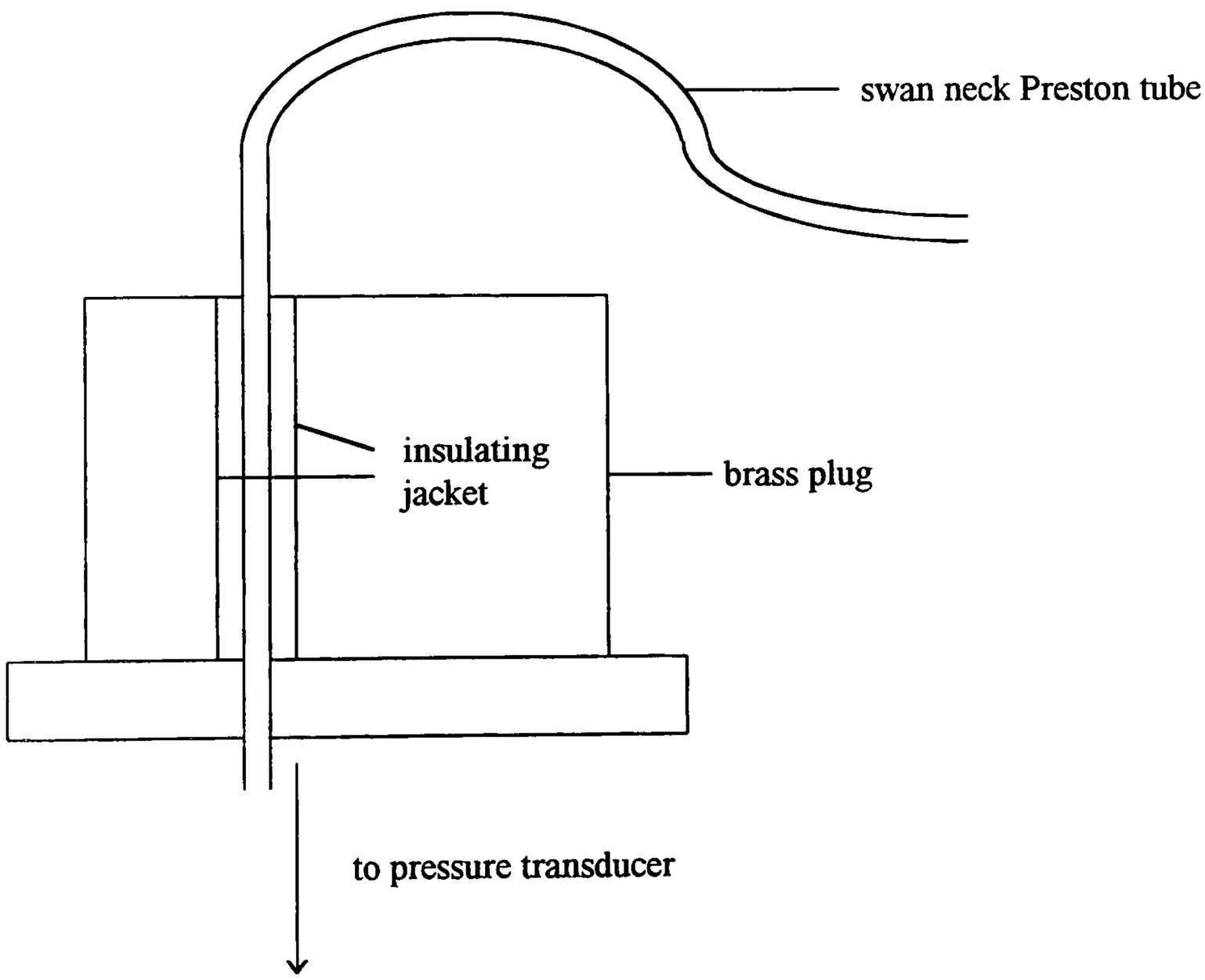

End view

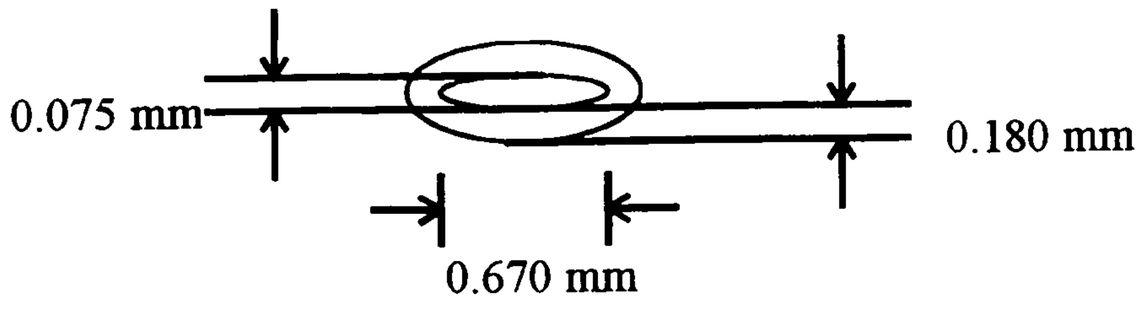

Figure A-5: The swan-neck Preston tube.

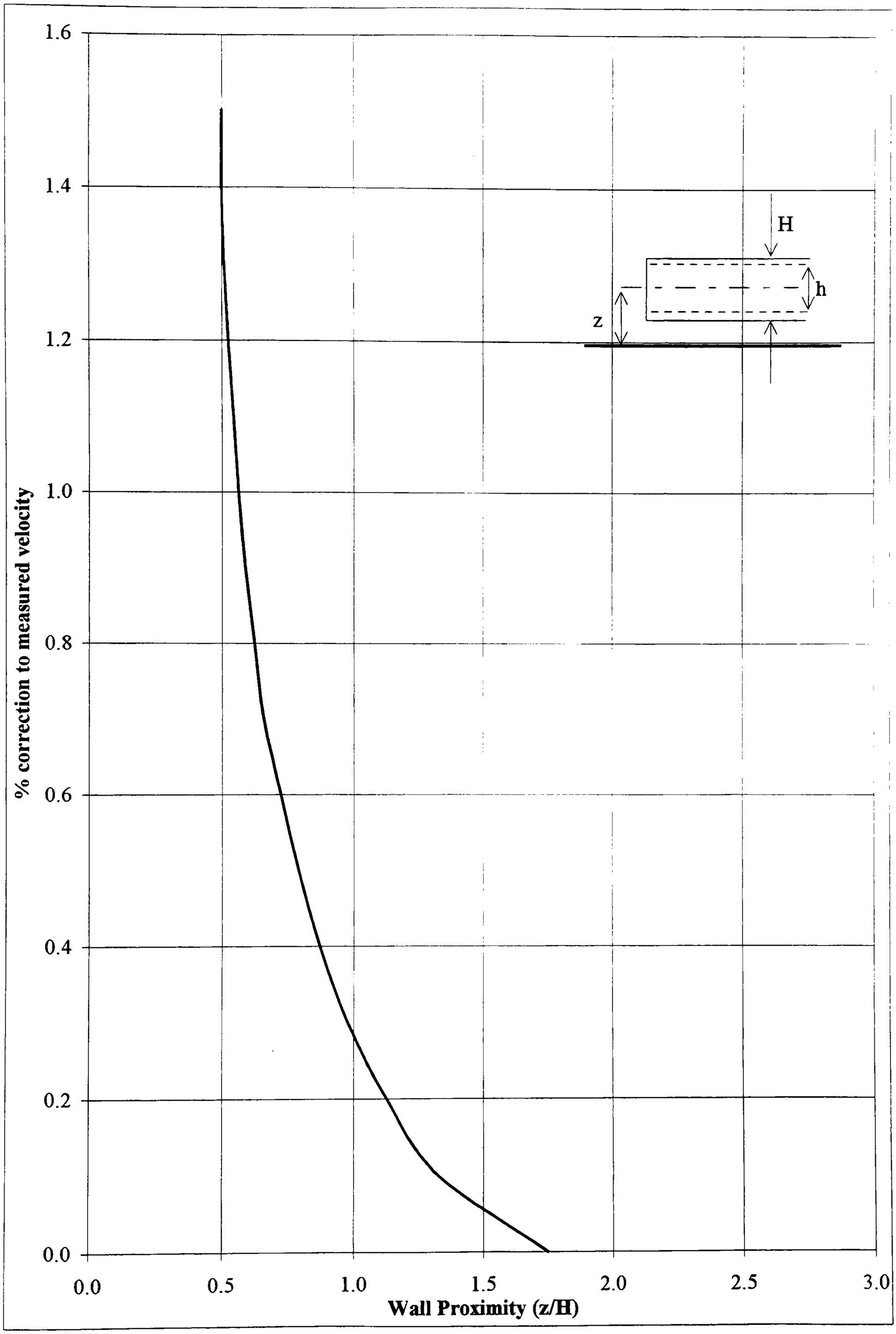

Figure A-6: Correction to measured velocity close to the surface.

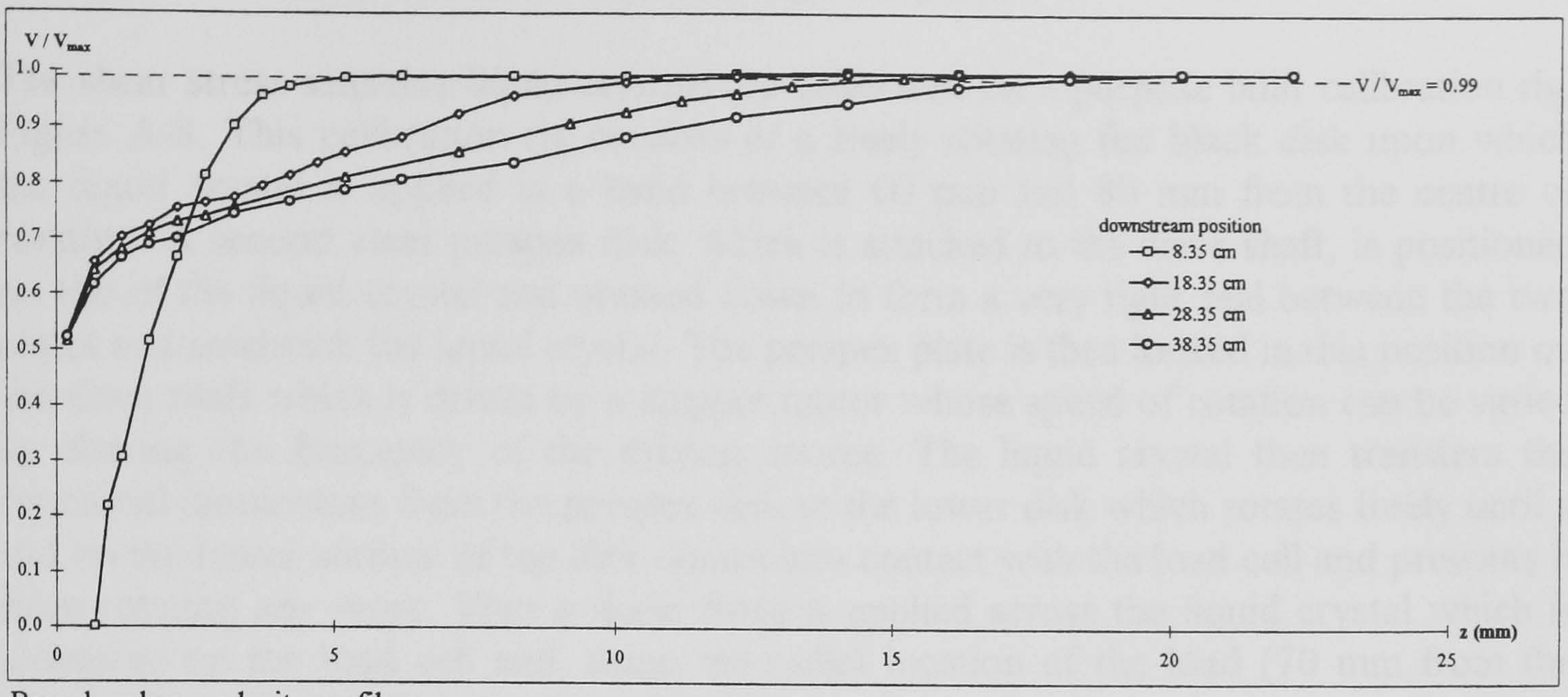

Boundary layer velocity profiles

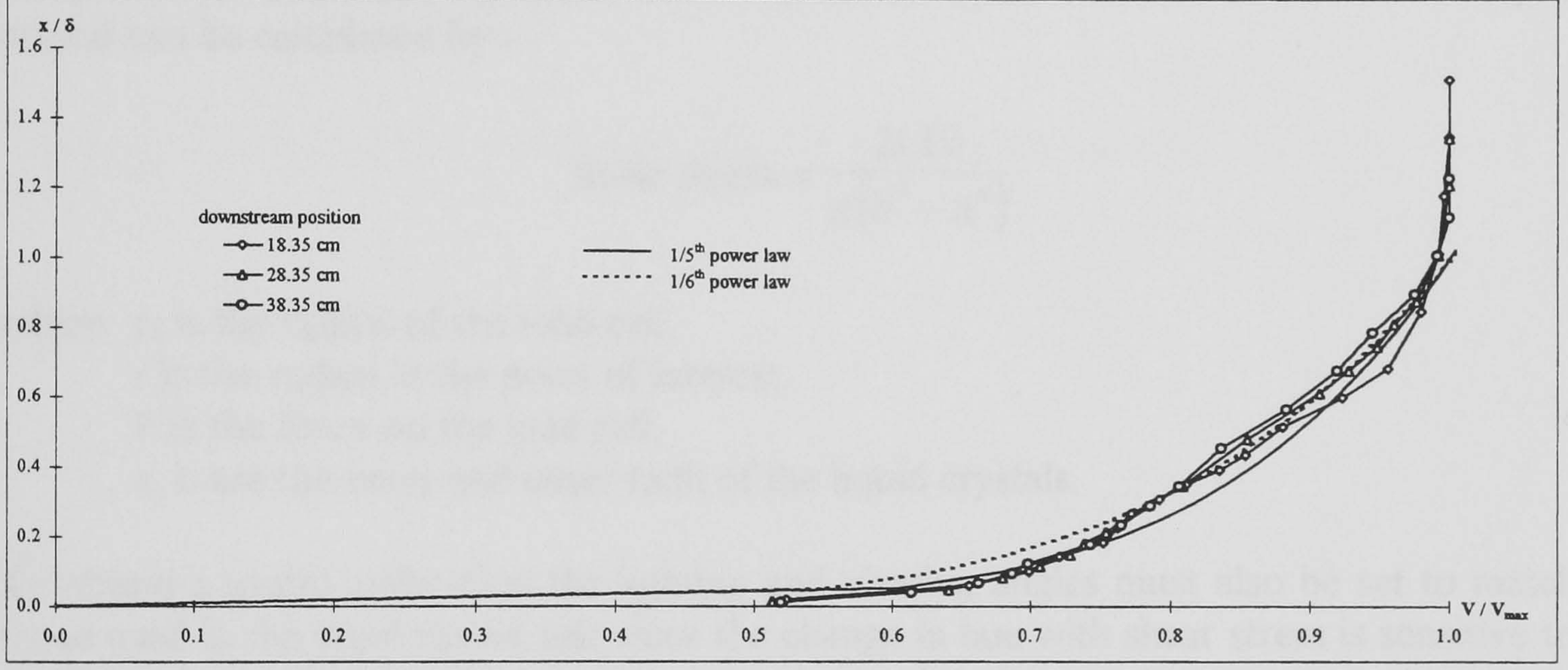

Boundary layer profiles

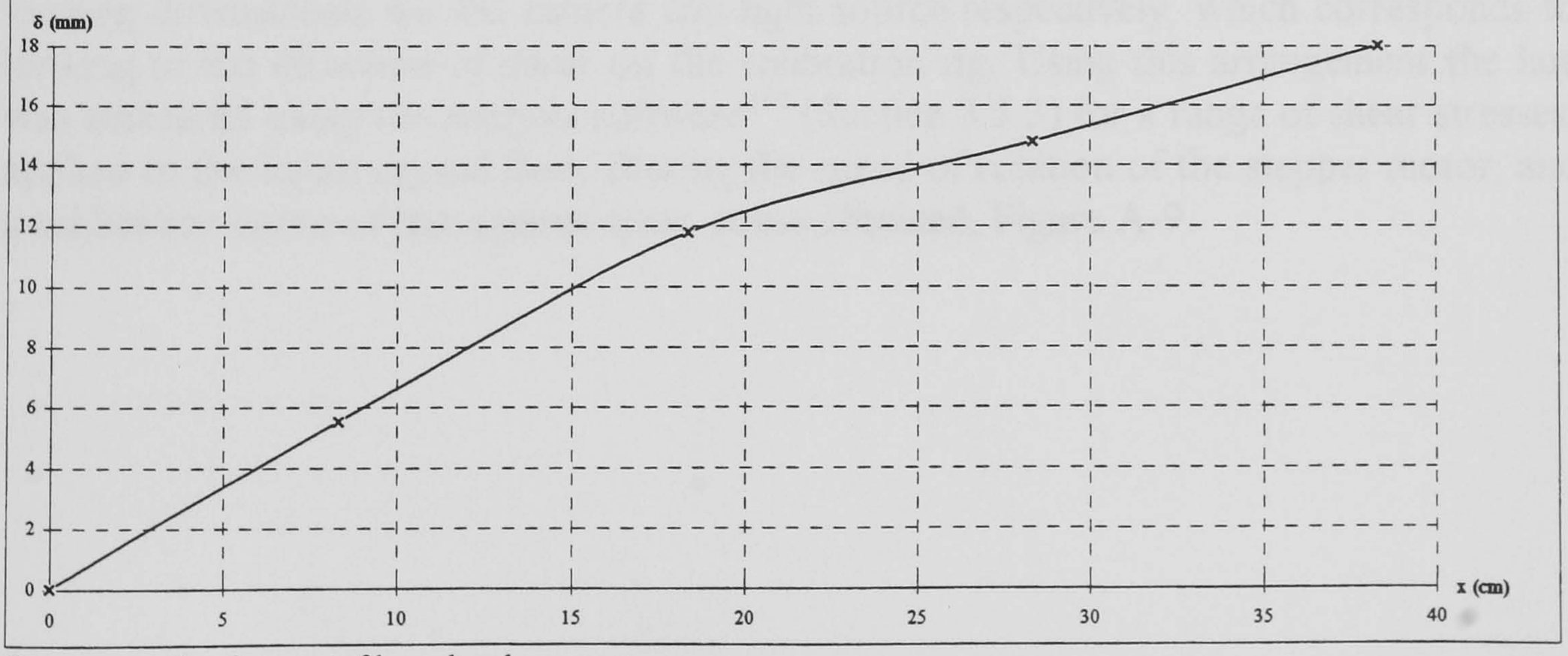

Downstream development of boundary layer

Figure A-7: The chosen boundary layer.

Appendix VIII

Calibration of the shear stress sensitive liquid crystal

The shear stress sensitive liquid crystals are calibrated on a purpose built calibration rig, Figure A-8. This calibration rig consists of a freely rotating flat black disk upon which the liquid crystal is applied in a band between 60 mm and 80 mm from the centre of rotation. A second clear perspex disk, which is attached to the drive shaft, is positioned on top of the liquid crystal and pressed down to form a very tight seal between the two plates and sandwich the liquid crystal. The perspex plate is then locked in this position on the drive shaft which is driven by a stepper motor whose speed of rotation can be varied by altering the frequency of the driving source. The liquid crystal then transfers the rotational momentum from the perspex disk to the lower disk which rotates freely until a rod on the lower surface of the disk comes into contact with the load cell and prevents it from rotating any more. Thus a shear force is applied across the liquid crystal which is measured on the load cell and, using the radial location of the load (70 mm from the centre of rotation) and properties of Newtonian fluids, the shear stress across the liquid crystal can be calculated by:-

$$\text{shear stress} = \frac{2r_1 Fr}{\pi\left(b^4 - a^4\right)}$$

where r_1 is the radius of the load cell,
r is the radius at the point of interest,
F is the force on the load cell,
a, b are the inner and outer radii of the liquid crystals.

To obtain a useful calibration the lighting and viewing angles must also be set to match those used in the wind tunnel test since the change in hue with shear stress is sensitive to both viewing and illumination angles. In this case they are 75° and 65° from the normal looking downstream for the camera and light source respectively, which corresponds to looking in the direction of shear on the calibration rig. Using this arrangement the hue was measured using the analysis software[102] (Section 3.3.3) for a range of shear stresses, applied to the liquid crystal from altering the speed of rotation of the stepper motor, and a calibration curve of hue against shear stress obtained, Figure A-9.

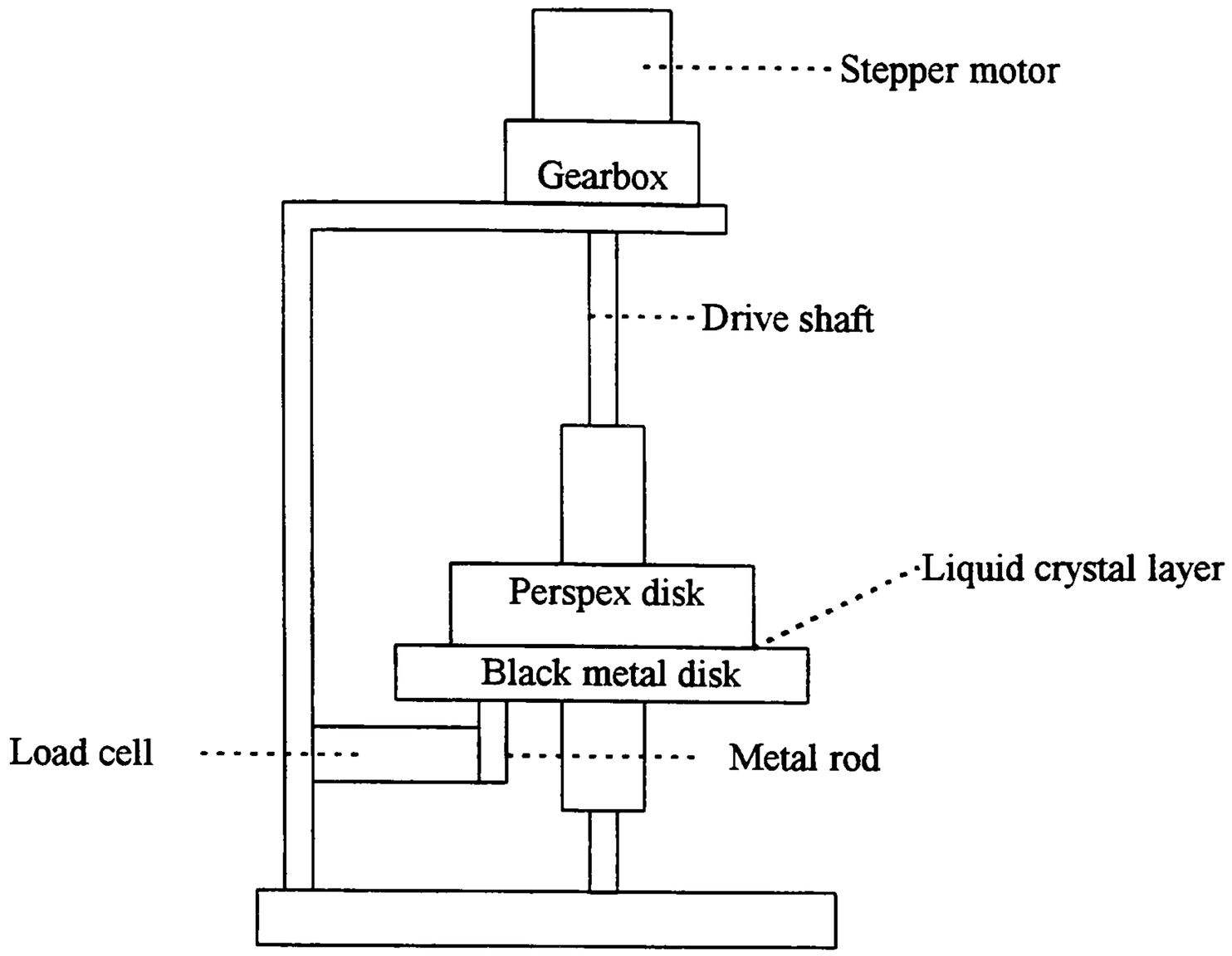

Figure A-8: Shear stress sensitive liquid crystal calibration rig.

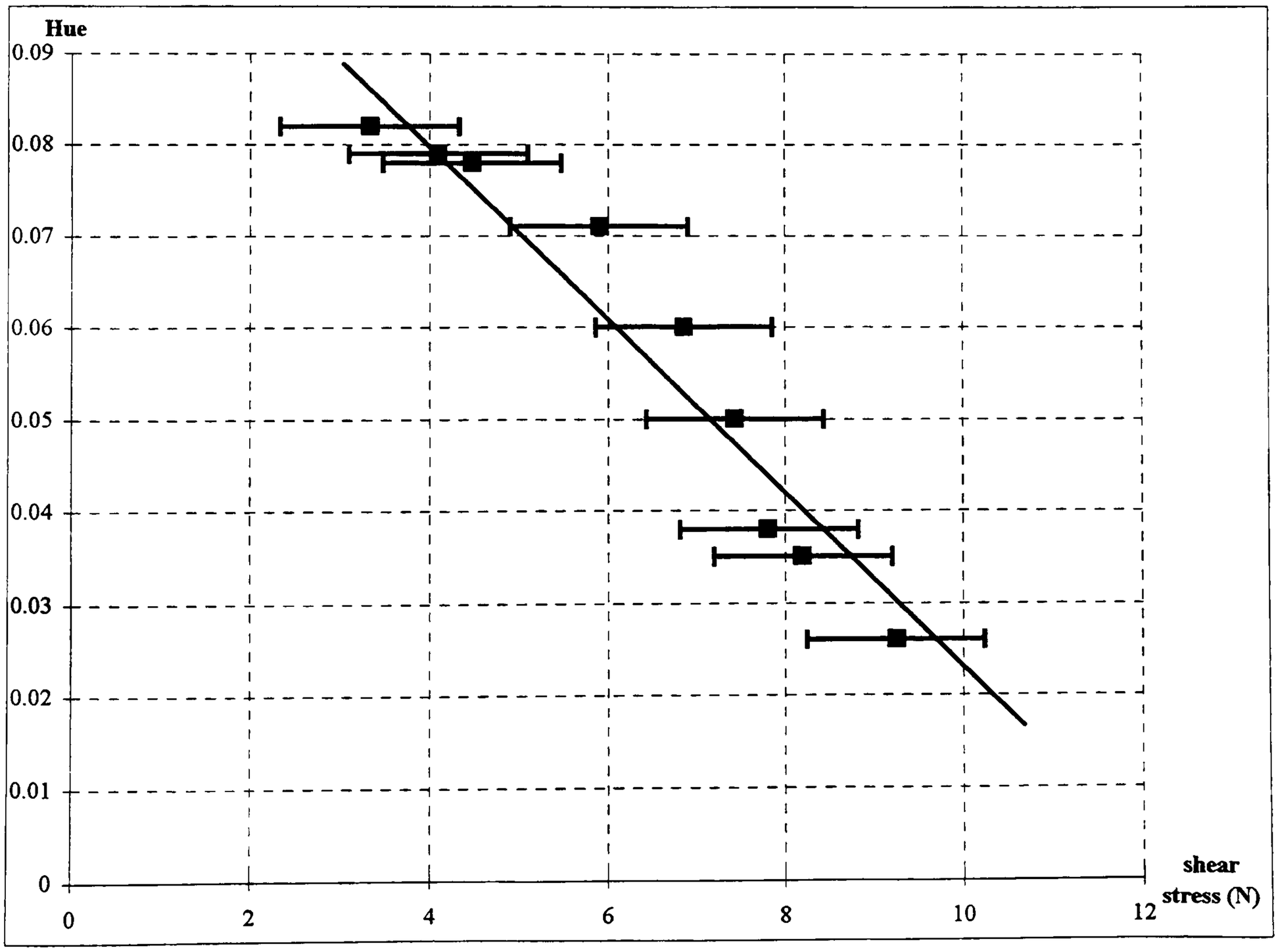

Figure A-9: Shear stress sensitive liquid crystal calibration.

Appendix IX

Shear stress sensitive liquid crystal decay on tunnel surface

It was observed during preliminary tests that when the vortex generator was present in the test section the liquid crystal behind the vane was blown away before the test conditions were reached. This increase in decay of the liquid crystal on the tunnel surface is clearly illustrated in Figure A-10 which compares the rate at which the average hue across the working section changes with time for the tunnel empty and with each of the vortex generators present (as the liquid crystal becomes depleted the hue of the surface rises since it is painted matt black and therefore 1-Hue_{av} decreases). As well as showing a more rapid depletion in the liquid crystal when a vane is present which increases with vane size the figure also shows that during the first second after the vane has been inserted the liquid crystal remains relatively unaffected and attached to the surface and this is the period in which measurements are made.

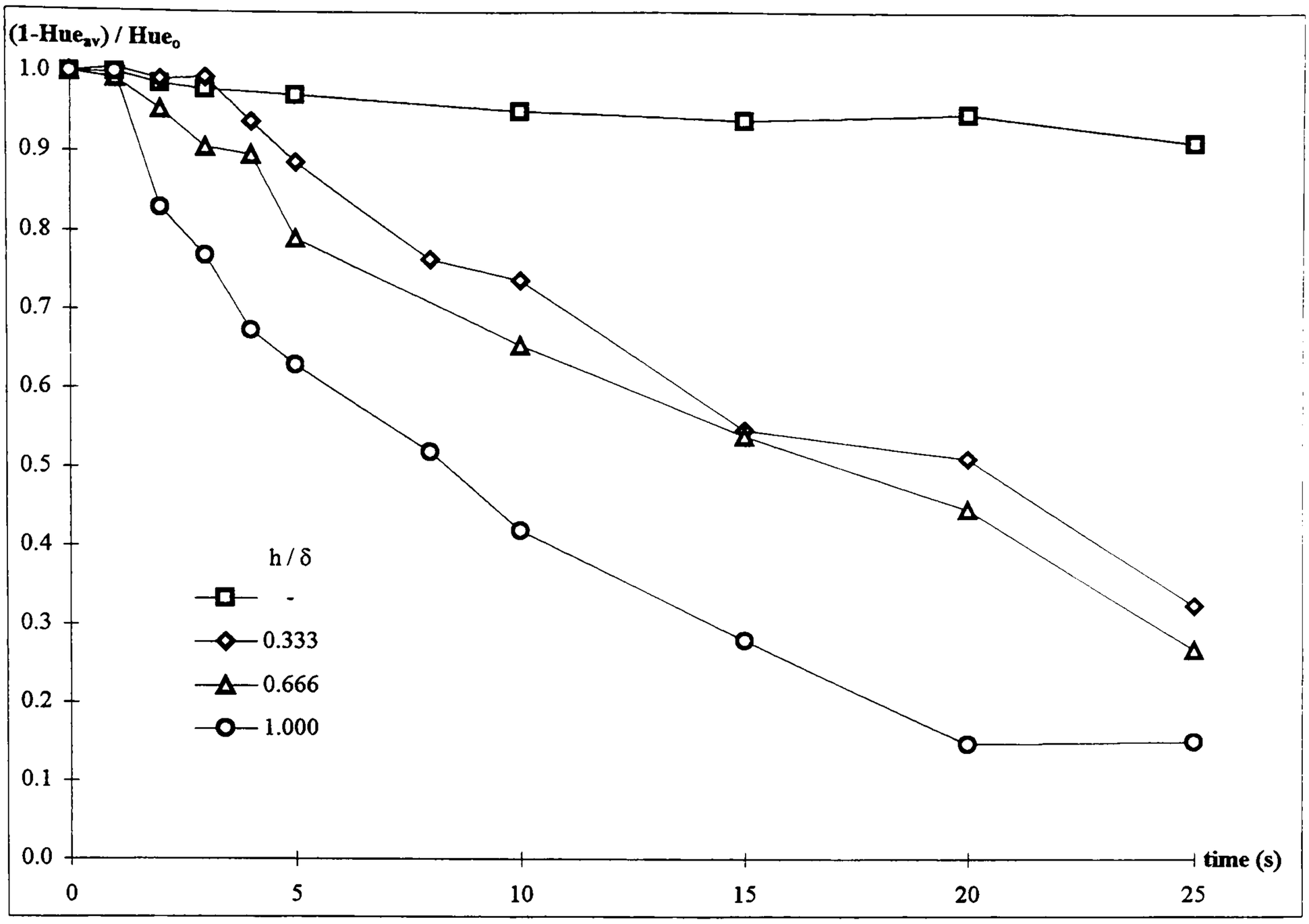

Figure A-10: Shear stress sensitive liquid crystal dissipation from the wind tunnel wall with and without a vortex. V = 67 m/s.

Appendix X

Liquid crystal repeatability results for shear stress measurements

The spanwise hue values obtained from the liquid crystal measurements in the 2.5" x 2.5" transonic wind tunnel are shown in Figure A-11 from several tests at a position $6.25c_v$ downstream for the empty tunnel and with a 0.333δ tall vortex generator. These results clearly show a change in hue between the empty tunnel and the tunnel with a vortex present even though there is a spread in the data. However the majority of the hue measurements will be within $\pm$ 0.01 of the average hue in both cases which corresponds to an error in skin friction of ± 0.0003.

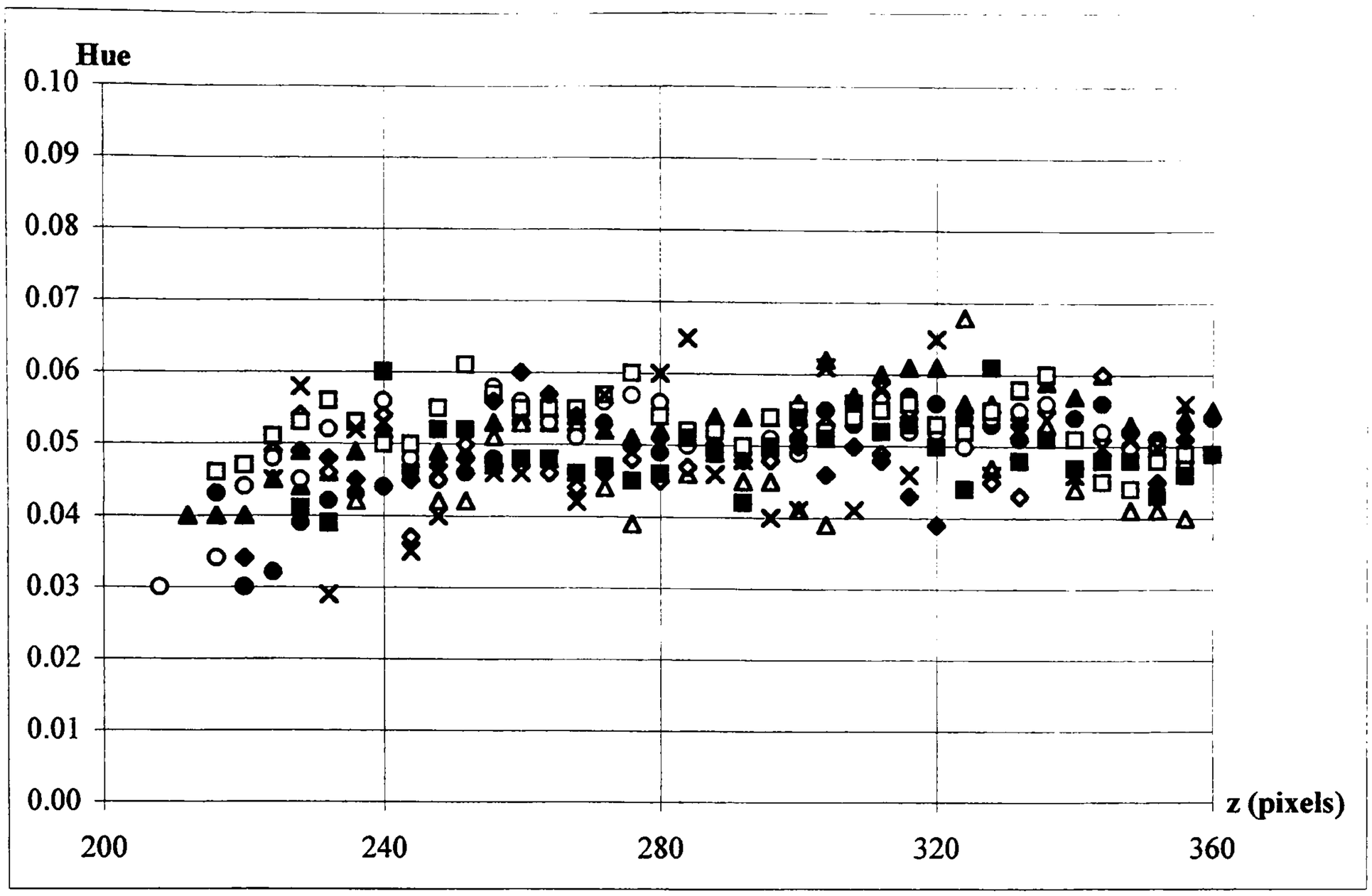

Smooth wall

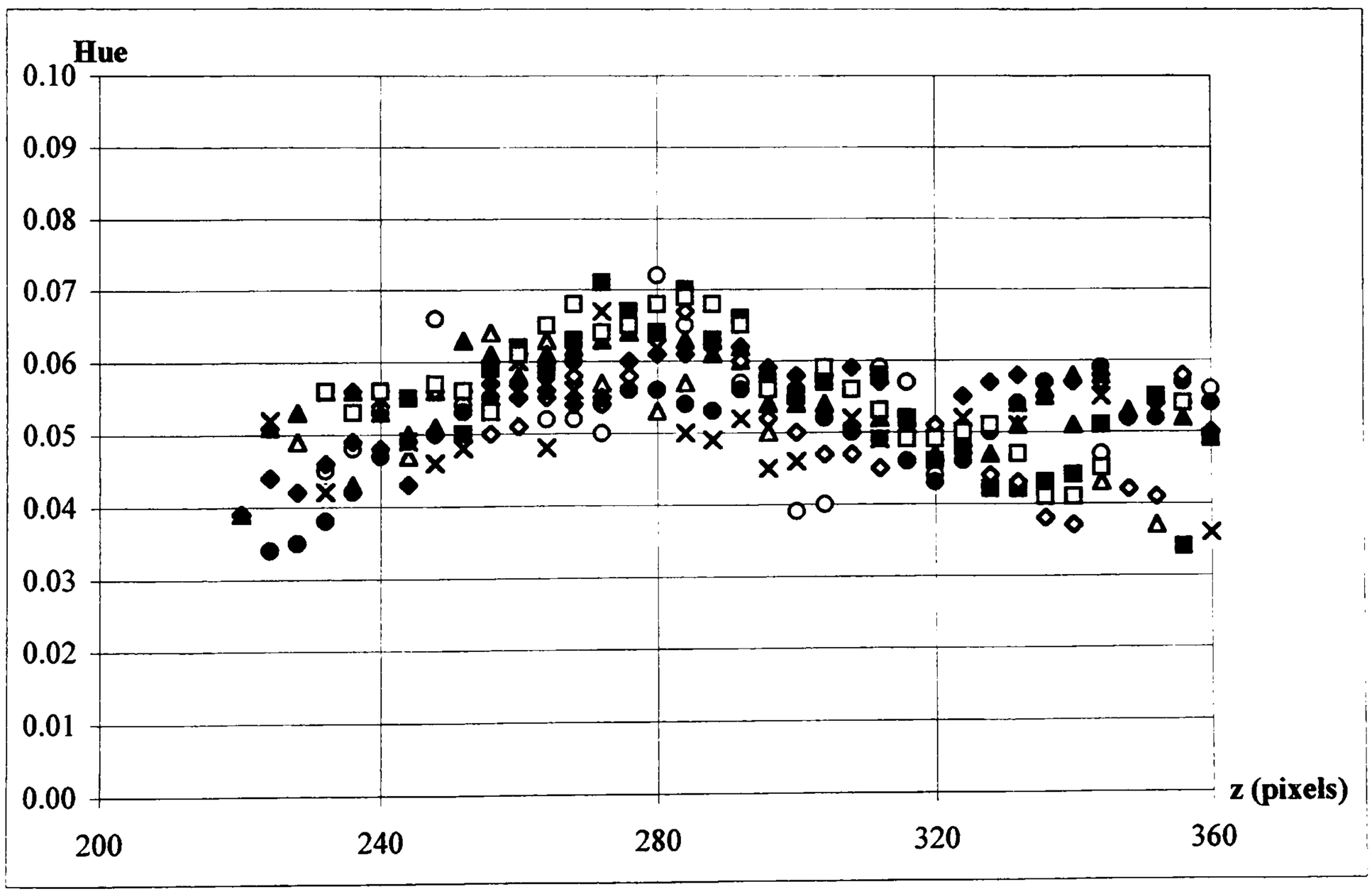

Vortex present

Figure A-11: Liquid crystal repeatability for the smooth wall and with a vortex present.

Appendix XI

Preston tube repeatability results for shear stress measurements

The streamwise skin friction coefficients obtained from the Preston tube measurements in the 2.5" x 2.5" transonic wind tunnel are shown in Table A-2 from two separate tests at a position $6.25c_v$ downstream for the empty tunnel and with a 0.333δ tall vortex generator. These results show that the repeatability of the measurements is to within $C_f \pm 0.0001$. Similarly the streamwise skin friction coefficients are shown in Table A-3 for each Preston tube positioned at $0.34h_w$ and $0.64h_w$ at a position $6.25c_v$ downstream for the empty tunnel. These results show that each Preston tube is able to measure the skin friction to within $C_f \pm 0.0001$ of the other Preston tubes and so the results are not dependent on a particular Preston tube being used in a particular position.

z/h_w	C_f (1) (empty tunnel)	C_f (2) (empty tunnel)	C_f (1) ($h = 0.333\delta$)	C_f (2) ($h = 0.333\delta$)
0.77	0.0023	0.0023	0.0023	0.0023
0.64	0.0021	0.0021	0.0023	0.0024
0.46	0.0019	0.0018	0.0026	0.0025
0.28	0.0025	0.0025	0.0018	0.0017
0.16	0.0023	0.0024	0.0020	0.0019

Table A-2: Shear stress Preston tube measurements with and without a vortex generator. $x = 6.25c_v$, $h = 0.333\delta$.

Preston tube	z/h_w	C_f	z/h_w	C_f
1	0.34	0.0025	0.64	0.0022
2	0.34	0.0026	0.64	0.0023
3	0.34	0.0025	0.64	0.0022
4	0.34	0.0026	0.64	0.0021
5	0.34	0.0025	0.64	0.0021

Table A-3: Shear stress Preston tube measurements for each Preston tube at two locations on the tunnel surface without a vortex generator present. $x = 6.25c_v$.

Appendix XII

Theoretical local skin friction coefficient on a flat plate

Theoretical method (from Blasius and Prandtl study of pipe flows extended to flat plates[118]) for calculating the local skin friction coefficient on a flat plate with a turbulent boundary layer in a zero pressure gradient based on the boundary layer thickness.

$$C_f = \frac{0.0456}{Re_\delta^{1/4}}$$

where

Re_δ - Reynolds number based on boundary layer thickness

Appendix XIII

WAKELAG results for the DERA wing swept 40° and 50°

η	0.06b			0.16b			0.30b			0.45b			0.59b		
x/c	α_c (°)	β_c (°)	δ^*/c	α_c (°)	β_c (°)	δ^*/c	α_c (°)	β_c (°)	δ^*/c	α_c (°)	β_c (°)	δ^*/c	α_c (°)	β_c (°)	δ^*/c
0.0556	52.58	-2.82	1.82E-04	52.23	-2.60	1.84E-04	52.41	-2.88	1.81E-04				51.39	-2.70	1.80E-04
0.0631	50.72	-5.25	1.88E-04	50.61	-4.76	1.94E-04	50.46	-5.43	1.84E-04				49.67	-5.05	1.85E-04
0.0710	49.08	-6.26	1.96E-04	49.12	-5.73	2.03E-04	48.71	-6.58	1.90E-04				48.15	-6.14	1.91E-04
0.0794	47.70	-6.57	2.10E-04	47.65	-6.31	2.12E-04	47.21	-7.03	2.00E-04				46.79	-6.57	2.02E-04
0.0882	46.56	-6.57	2.29E-04	46.09	-6.88	2.20E-04	45.93	-7.16	2.14E-04				45.55	-6.58	2.22E-04
0.0974	45.53	-6.51	2.48E-04	44.67	-7.25	2.31E-04	44.80	-7.18	2.30E-04				44.44	-6.46	2.44E-04
0.1070	44.54	-6.57	2.62E-04	43.63	-7.26	2.48E-04	43.82	-7.08	2.47E-04				43.42	-6.50	2.59E-04
0.1170	43.59	-6.68	2.74E-04	42.77	-7.15	2.65E-04	42.95	-6.92	2.65E-04				42.46	-6.60	2.71E-04
0.1274	42.69	-6.76	2.86E-04	42.04	-6.96	2.84E-04	42.17	-6.75	2.83E-04				41.58	-6.67	2.83E-04
0.1381	41.87	-6.79	3.00E-04	41.39	-6.75	3.03E-04	41.45	-6.59	3.01E-04				40.80	-6.66	2.98E-04
0.1493	41.15	-6.74	3.16E-04	40.77	-6.55	3.21E-04	40.77	-6.46	3.18E-04				40.14	-6.56	3.16E-04
0.1607	40.53	-6.61	3.35E-04	40.17	-6.38	3.39E-04	40.10	-6.36	3.34E-04				39.60	-6.36	3.37E-04
0.1726	39.96	-6.46	3.54E-04	39.62	-6.22	3.57E-04	39.48	-6.27	3.51E-04				39.12	-6.14	3.59E-04
0.1847	39.44	-6.31	3.73E-04	39.10	-6.07	3.75E-04	38.89	-6.19	3.67E-04				38.67	-5.93	3.80E-04
0.1972	38.94	-6.16	3.91E-04	38.59	-5.96	3.92E-04	38.35	-6.09	3.85E-04				38.23	-5.76	4.00E-04
0.2100	38.45	-6.05	4.09E-04	38.05	-5.92	4.06E-04	37.84	-6.00	4.02E-04				37.77	-5.65	4.17E-04
0.2230	37.96	-5.96	4.25E-04	37.47	-5.94	4.17E-04	37.33	-5.94	4.18E-04				37.30	-5.59	4.32E-04
0.2364	37.52	-5.85	4.43E-04	36.96	-5.92	4.32E-04	36.89	-5.84	4.37E-04				36.87	-5.51	4.49E-04
0.2500	37.17	-5.69	4.65E-04	36.62	-5.75	4.56E-04	36.58	-5.63	4.62E-04				36.53	-5.37	4.71E-04
0.2639	36.89	-5.49	4.91E-04	36.43	-5.47	4.88E-04	36.39	-5.33	4.94E-04				36.27	-5.18	4.97E-04
0.2780	36.64	-5.27	5.17E-04	36.29	-5.16	5.22E-04	36.24	-5.02	5.27E-04				36.05	-4.98	5.24E-04
0.2923	36.44	-5.05	5.45E-04	36.16	-4.85	5.55E-04	36.12	-4.72	5.59E-04				35.87	-4.76	5.52E-04
0.3068	36.29	-4.80	5.75E-04	36.04	-4.57	5.86E-04	35.99	-4.45	5.90E-04				35.75	-4.51	5.85E-04
0.3216	36.18	-4.53	6.08E-04	35.93	-4.31	6.17E-04	35.88	-4.20	6.21E-04				35.69	-4.21	6.21E-04
0.3365	36.09	-4.27	6.41E-04	35.82	-4.08	6.48E-04	35.78	-3.98	6.51E-04				35.65	-3.92	6.57E-04
0.3515	35.97	-4.07	6.71E-04	35.71	-3.89	6.76E-04	35.67	-3.79	6.80E-04				35.58	-3.70	6.90E-04
0.3668	35.83	-3.93	6.96E-04	35.59	-3.73	7.03E-04	35.55	-3.63	7.07E-04				35.46	-3.55	7.17E-04
0.3821	35.66	-3.83	7.19E-04	35.46	-3.60	7.29E-04	35.43	-3.51	7.34E-04				35.33	-3.44	7.41E-04
0.3976	35.48	-3.77	7.39E-04	35.32	-3.51	7.53E-04	35.29	-3.43	7.57E-04				35.18	-3.37	7.63E-04
0.4132	35.27	-3.74	7.56E-04	35.15	-3.46	7.73E-04	35.11	-3.40	7.76E-04				35.04	-3.31	7.85E-04
0.4288	35.04	-3.76	7.71E-04	34.97	-3.45	7.91E-04	34.91	-3.41	7.92E-04				34.88	-3.28	8.05E-04
0.4446	34.80	-3.79	7.84E-04	34.77	-3.46	8.07E-04	34.70	-3.44	8.06E-04				34.71	-3.28	8.23E-04
0.4604	34.57	-3.82	7.97E-04	34.55	-3.50	8.21E-04	34.50	-3.46	8.22E-04				34.51	-3.31	8.38E-04
0.4762	34.35	-3.86	8.11E-04	34.32	-3.55	8.32E-04	34.31	-3.48	8.38E-04				34.30	-3.36	8.50E-04
0.4921	34.10	-3.92	8.22E-04	34.06	-3.64	8.40E-04	34.10	-3.53	8.51E-04				34.06	-3.44	8.58E-04
0.5079	33.78	-4.05	8.23E-04	33.75	-3.79	8.40E-04	33.80	-3.66	8.54E-04				33.74	-3.60	8.58E-04
0.5238	33.33	-4.29	8.10E-04	33.32	-4.03	8.28E-04	33.35	-3.93	8.37E-04				33.29	-3.87	8.41E-04
0.5396	32.83	-4.55	7.92E-04	32.84	-4.30	8.10E-04	32.83	-4.25	8.13E-04				32.79	-4.18	8.19E-04
0.5554	32.33	-4.80	7.77E-04	32.33	-4.56	7.93E-04	32.30	-4.54	7.92E-04				32.28	-4.45	8.00E-04
0.5712	31.79	-5.06	7.59E-04	31.73	-4.88	7.67E-04	31.69	-4.87	7.64E-04				31.72	-4.75	7.78E-04
0.5868	31.50	-5.13	7.71E-04	31.51	-4.91	7.86E-04	31.50	-4.88	7.85E-04				31.53	-4.77	7.99E-04
0.6024	31.33	-5.12	7.97E-04	31.45	-4.83	8.24E-04	31.47	-4.78	8.25E-04				31.49	-4.68	8.36E-04
0.6179	31.23	-5.05	8.30E-04	31.43	-4.70	8.67E-04	31.49	-4.63	8.70E-04				31.49	-4.55	8.79E-04
0.6332	31.67	-4.52	9.37E-04	31.86	-4.17	9.74E-04	31.91	-4.12	9.72E-04				31.93	-4.00	9.88E-04
0.6485	32.63	-3.33	1.14E-03	32.74	-3.04	1.17E-03	32.75	-3.06	1.15E-03				32.82	-2.86	1.18E-03
0.6635	33.22	-2.39	1.29E-03	33.34	-2.09	1.32E-03	33.36	-2.12	1.31E-03				33.43	-1.90	1.34E-03
0.6784	33.76	-1.44	1.44E-03	33.89	-1.12	1.48E-03	33.93	-1.11	1.47E-03				33.98	-0.93	1.50E-03
0.6932	34.24	-0.53	1.59E-03	34.40	-0.17	1.63E-03	34.46	-0.12	1.63E-03				34.49	0.04	1.66E-03
0.7077	34.69	0.35	1.73E-03	34.85	0.73	1.78E-03	34.91	0.78	1.78E-03				34.96	0.97	1.81E-03
0.7220	35.10	1.20	1.87E-03	35.26	1.57	1.92E-03	35.33	1.61	1.92E-03				35.40	1.86	1.97E-03
0.7361	35.49	1.99	2.01E-03	35.65	2.37	2.07E-03	35.71	2.38	2.06E-03				35.81	2.70	2.12E-03
0.7500	35.86	2.73	2.14E-03	36.02	3.11	2.21E-03	36.07	3.10	2.19E-03				36.19	3.47	2.27E-03
0.7636	36.19	3.39	2.27E-03	36.37	3.81	2.35E-03	36.41	3.75	2.33E-03				36.53	4.15	2.41E-03
0.7770	36.50	3.99	2.40E-03	36.70	4.46	2.48E-03	36.72	4.34	2.46E-03				36.85	4.76	2.54E-03
0.7900	36.81	4.56	2.53E-03	37.01	5.05	2.62E-03	37.03	4.91	2.59E-03				37.15	5.34	2.68E-03
0.8028	37.11	5.14	2.66E-03	37.29	5.56	2.74E-03	37.34	5.48	2.73E-03				37.46	5.92	2.82E-03
0.8153	37.43	5.73	2.80E-03	37.55	5.98	2.86E-03	37.66	6.09	2.88E-03				37.77	6.49	2.96E-03
0.8274	37.68	6.14	2.92E-03	37.81	6.42	2.98E-03	37.91	6.49	2.99E-03				38.05	7.00	3.10E-03
0.8393	37.90	6.46	3.02E-03	38.07	6.86	3.11E-03	38.12	6.77	3.09E-03				38.31	7.45	3.24E-03
0.8507	38.18	6.99	3.17E-03	38.29	7.20	3.22E-03	38.35	7.15	3.21E-03				38.56	7.87	3.37E-03
0.8619	38.46	7.49	3.31E-03	38.52	7.54	3.34E-03	38.58	7.51	3.33E-03				38.79	8.23	3.49E-03
0.8726	38.66	7.79	3.42E-03	38.76	7.96	3.47E-03	38.78	7.78	3.43E-03				38.98	8.48	3.60E-03
0.8830	38.86	8.08	3.53E-03	38.99	8.37	3.61E-03	38.98	8.09	3.55E-03				39.18	8.76	3.71E-03
0.8930	39.06	8.41	3.64E-03	39.21	8.73	3.73E-03	39.22	8.50	3.69E-03				39.40	9.13	3.84E-03
0.9026	39.27	8.76	3.76E-03	39.42	9.09	3.86E-03	39.41	8.80	3.80E-03				39.61	9.51	3.98E-03
0.9118	39.47	9.11	3.89E-03	39.62	9.45	3.99E-03	39.54	8.90	3.87E-03				39.82	9.89	4.11E-03
0.9206	39.66	9.46	4.01E-03	39.82	9.78	4.12E-03	39.68	9.07	3.95E-03				40.02	10.24	4.25E-03
0.9290	39.85	9.82	4.14E-03	39.99	10.06	4.23E-03	39.89	9.47	4.09E-03				40.20	10.55	4.37E-03
0.9369	40.04	10.15	4.27E-03	40.14	10.31	4.34E-03	40.13	9.98	4.26E-03				40.36	10.81	4.48E-03
0.9444	40.18	10.38	4.36E-03	40.29	10.53	4.43E-03	40.35	10.50	4.43E-03				40.50	11.01	4.58E-03
0.9515	40.30	10.51	4.44E-03	40.42	10.72	4.53E-03	40.58	11.07	4.62E-03				40.61	11.14	4.66E-03
0.9581	40.41	10.66	4.52E-03	40.54	10.89	4.61E-03	40.78	11.54	4.78E-03				40.73	11.31	4.75E-03
0.9642	40.54	10.90	4.61E-03	40.65	11.05	4.69E-03	40.93	11.85	4.90E-03				40.87	11.57	4.85E-03
0.9699	40.68	11.19	4.73E-03	40.76	11.21	4.77E-03	41.06	12.12	5.01E-03				41.02	11.90	4.98E-03
0.9750	40.83	11.51	4.84E-03	40.85	11.36	4.84E-03	41.15	12.26	5.08E-03				41.17	12.27	5.11E-03
0.9798	40.96	11.82	4.95E-03	40.94	11.49	4.91E-03	41.20	12.24	5.11E-03				41.31	12.63	5.24E-03
0.9840	41.08	12.11	5.06E-03	41.02	11.62	4.97E-03	41.14	11.80	5.02E-03				41.44	12.97	5.37E-03
0.9877	41.19	12.38	5.16E-03	41.09	11.73	5.03E-03	40.95	10.92	4.82E-03				41.56	13.28	5.48E-03
0.9910	41.28	12.62	5.25E-03	41.15	11.83	5.08E-03	40.70	9.96	4.58E-03				41.66	13.56	5.59E-03
0.9937	41.36	12.82	5.32E-03	41.20	11.91	5.12E-03	40.45	9.10	4.36E-03				41.74	13.81	5.68E-03
0.9960	41.43	12.99	5.39E-03	41.25	11.98	5.15E-03	40.23	8.40	4.19E-03				41.82	14.01	5.75E-03
0.9977	41.48	13.13	5.44E-03	41.28	12.04	5.18E-03	40.06	7.87	4.05E-03				41.87	14.18	5.81E-03
0.9990	41.52	13.23	5.47E-03	41.31	12.08	5.20E-03	39.93	7.51	3.96E-03				41.91	14.29	5.85E-03
0.9998	41.54	13.29	5.49E-03	41.32	12.10	5.21E-03	39.85	7.30	3.91E-03				41.94	14.37	5.88E-03
1.0000	41.55	13.31	5.50E-03	41.32	12.11	5.22E-03	39.83	7.23	3.89E-03				41.94	14.39	5.89E-03

The local freestream flow direction, twist in the boundary layer and boundary layer displacement thickness from WAKELAG over the upper surface of the DERA wing. $\Lambda = 40°$, $\alpha = -6.0°$, $Re_c = 3.3 \times 10^6$.

η	0.06b			0.16b			0.30b			0.45b			0.59b		
x/c	α_c (°)	β_c (°)	δ^*/c	α_c (°)	β_c (°)	δ^*/c	α_c (°)	β_c (°)	δ^*/c	α_c (°)	β_c (°)	δ^*/c	α_c (°)	β_c (°)	δ^*/c
0.0556	42.13	-1.45	1.71E-04	41.46	-1.19	1.71E-04	41.00	-1.23	1.70E-04	40.33	-1.12	1.69E-04	40.12	-1.15	1.67E-04
0.0631	41.19	-2.87	1.89E-04	40.74	-2.30	1.94E-04	40.19	-2.48	1.90E-04	39.63	-2.22	1.91E-04	39.39	-2.32	1.86E-04
0.0710	40.35	-3.52	2.04E-04	40.05	-2.88	2.10E-04	39.43	-3.14	2.04E-04	38.97	-2.76	2.08E-04	38.72	-2.93	2.00E-04
0.0794	39.65	-3.73	2.22E-04	39.31	-3.33	2.25E-04	38.72	-3.51	2.18E-04	38.35	-3.06	2.25E-04	38.12	-3.19	2.17E-04
0.0882	39.08	-3.73	2.45E-04	38.41	-3.89	2.36E-04	38.05	-3.77	2.34E-04	37.75	-3.27	2.45E-04	37.59	-3.21	2.41E-04
0.0974	38.57	-3.72	2.67E-04	37.56	-4.31	2.50E-04	37.43	-3.94	2.51E-04	37.20	-3.43	2.64E-04	37.10	-3.20	2.67E-04
0.1070	38.04	-3.81	2.85E-04	37.03	-4.34	2.71E-04	36.93	-3.97	2.71E-04	36.72	-3.53	2.84E-04	36.61	-3.32	2.86E-04
0.1170	37.51	-3.95	3.01E-04	36.60	-4.27	2.92E-04	36.51	-3.92	2.92E-04	36.29	-3.60	3.02E-04	36.10	-3.51	3.01E-04
0.1274	36.99	-4.09	3.15E-04	36.24	-4.16	3.14E-04	36.13	-3.85	3.14E-04	35.89	-3.64	3.21E-04	35.61	-3.68	3.16E-04
0.1381	36.52	-4.18	3.31E-04	35.92	-4.02	3.36E-04	35.77	-3.78	3.36E-04	35.53	-3.65	3.40E-04	35.18	-3.78	3.33E-04
0.1493	36.10	-4.20	3.50E-04	35.60	-3.92	3.57E-04	35.43	-3.73	3.56E-04	35.18	-3.65	3.59E-04	34.84	-3.77	3.53E-04
0.1607	35.75	-4.15	3.70E-04	35.29	-3.83	3.77E-04	35.07	-3.72	3.75E-04	34.85	-3.65	3.78E-04	34.58	-3.66	3.78E-04
0.1726	35.42	-4.09	3.92E-04	35.00	-3.75	3.98E-04	34.73	-3.71	3.94E-04	34.53	-3.65	3.97E-04	34.36	-3.52	4.03E-04
0.1847	35.12	-4.02	4.13E-04	34.72	-3.68	4.19E-04	34.41	-3.70	4.13E-04	34.23	-3.63	4.17E-04	34.16	-3.39	4.28E-04
0.1972	34.83	-3.97	4.33E-04	34.44	-3.65	4.39E-04	34.11	-3.68	4.33E-04	33.96	-3.60	4.38E-04	33.96	-3.30	4.51E-04
0.2100	34.52	-3.94	4.52E-04	34.11	-3.68	4.55E-04	33.82	-3.67	4.53E-04	33.70	-3.56	4.59E-04	33.72	-3.26	4.71E-04
0.2230	34.21	-3.93	4.70E-04	33.74	-3.77	4.68E-04	33.51	-3.69	4.71E-04	33.45	-3.53	4.79E-04	33.45	-3.28	4.89E-04
0.2364	33.93	-3.90	4.89E-04	33.42	-3.81	4.84E-04	33.26	-3.66	4.92E-04	33.23	-3.48	5.01E-04	33.21	-3.27	5.08E-04
0.2500	33.73	-3.80	5.13E-04	33.24	-3.70	5.11E-04	33.11	-3.52	5.20E-04	33.08	-3.35	5.28E-04	33.04	-3.18	5.34E-04
0.2639	33.59	-3.64	5.42E-04	33.19	-3.46	5.47E-04	33.06	-3.28	5.55E-04	33.01	-3.15	5.60E-04	32.95	-3.03	5.64E-04
0.2780	33.49	-3.47	5.72E-04	33.18	-3.19	5.85E-04	33.06	-3.00	5.94E-04	32.98	-2.94	5.95E-04	32.89	-2.86	5.96E-04
0.2923	33.41	-3.28	6.04E-04	33.19	-2.92	6.23E-04	33.07	-2.74	6.32E-04	32.96	-2.72	6.30E-04	32.86	-2.67	6.30E-04
0.3068	33.36	-3.07	6.37E-04	33.18	-2.68	6.59E-04	33.08	-2.50	6.68E-04	32.94	-2.51	6.65E-04	32.86	-2.45	6.67E-04
0.3216	33.36	-2.84	6.74E-04	33.18	-2.47	6.94E-04	33.08	-2.29	7.04E-04	32.95	-2.30	7.01E-04	32.93	-2.17	7.11E-04
0.3365	33.37	-2.61	7.12E-04	33.18	-2.28	7.29E-04	33.09	-2.09	7.40E-04	32.96	-2.10	7.38E-04	33.02	-1.88	7.56E-04
0.3515	33.34	-2.44	7.45E-04	33.16	-2.12	7.62E-04	33.09	-1.94	7.73E-04	32.97	-1.93	7.73E-04	33.06	-1.67	7.95E-04
0.3668	33.28	-2.33	7.73E-04	33.12	-2.01	7.92E-04	33.07	-1.81	8.05E-04	32.98	-1.77	8.08E-04	33.06	-1.55	8.27E-04
0.3821	33.20	-2.27	7.98E-04	33.07	-1.93	8.20E-04	33.05	-1.71	8.36E-04	32.99	-1.63	8.43E-04	33.03	-1.49	8.56E-04
0.3976	33.10	-2.24	8.21E-04	33.01	-1.88	8.46E-04	33.00	-1.66	8.63E-04	32.98	-1.54	8.74E-04	32.98	-1.45	8.82E-04
0.4132	32.99	-2.24	8.41E-04	32.93	-1.86	8.70E-04	32.92	-1.65	8.86E-04	32.92	-1.51	9.00E-04	32.92	-1.43	9.07E-04
0.4288	32.85	-2.27	8.59E-04	32.84	-1.86	8.92E-04	32.81	-1.69	9.05E-04	32.84	-1.53	9.21E-04	32.85	-1.43	9.30E-04
0.4446	32.70	-2.31	8.75E-04	32.73	-1.88	9.12E-04	32.69	-1.74	9.22E-04	32.73	-1.58	9.39E-04	32.76	-1.46	9.51E-04
0.4604	32.55	-2.36	8.92E-04	32.60	-1.93	9.28E-04	32.57	-1.79	9.40E-04	32.60	-1.65	9.54E-04	32.65	-1.52	9.68E-04
0.4762	32.41	-2.41	9.08E-04	32.45	-2.01	9.42E-04	32.46	-1.83	9.59E-04	32.45	-1.75	9.66E-04	32.52	-1.60	9.82E-04
0.4921	32.24	-2.48	9.20E-04	32.27	-2.12	9.51E-04	32.32	-1.90	9.74E-04	32.27	-1.87	9.74E-04	32.36	-1.72	9.92E-04
0.5079	32.00	-2.62	9.24E-04	32.04	-2.29	9.52E-04	32.12	-2.05	9.78E-04	32.03	-2.05	9.74E-04	32.13	-1.90	9.93E-04
0.5238	31.64	-2.88	9.10E-04	31.69	-2.56	9.37E-04	31.76	-2.36	9.59E-04	31.60	-2.43	9.45E-04	31.77	-2.22	9.72E-04
0.5396	31.22	-3.18	8.90E-04	31.28	-2.87	9.17E-04	31.33	-2.71	9.33E-04	31.09	-2.84	9.09E-04	31.35	-2.57	9.47E-04
0.5554	30.81	-3.44	8.74E-04	30.86	-3.17	8.97E-04	30.89	-3.03	9.09E-04	30.64	-3.16	8.86E-04	30.94	-2.87	9.26E-04
0.5712	30.36	-3.72	8.54E-04	30.36	-3.50	8.69E-04	30.37	-3.39	8.77E-04	30.36	-3.31	8.88E-04	30.49	-3.18	9.02E-04
0.5868	30.17	-3.78	8.70E-04	30.22	-3.52	8.92E-04	30.25	-3.40	9.01E-04	30.33	-3.25	9.25E-04	30.37	-3.20	9.26E-04
0.6024	30.09	-3.73	9.03E-04	30.23	-3.41	9.37E-04	30.31	-3.26	9.50E-04	30.38	-3.12	9.71E-04	30.41	-3.08	9.72E-04
0.6179	30.06	-3.66	9.41E-04	30.29	-3.27	9.87E-04	30.42	-3.08	1.01E-03	30.46	-2.95	1.02E-03	30.50	-2.92	1.02E-03
0.6332	30.53	-3.09	1.06E-03	30.76	-2.68	1.11E-03	30.88	-2.51	1.12E-03	30.94	-2.36	1.15E-03	30.98	-2.32	1.15E-03
0.6485	31.51	-1.80	1.29E-03	31.67	-1.46	1.33E-03	31.74	-1.35	1.33E-03	31.82	-1.13	1.37E-03	31.89	-1.07	1.38E-03
0.6635	32.15	-0.78	1.47E-03	32.29	-0.44	1.51E-03	32.39	-0.30	1.52E-03	32.46	-0.07	1.56E-03	32.53	-0.02	1.57E-03
0.6784	32.72	0.26	1.65E-03	32.87	0.60	1.69E-03	33.01	0.83	1.72E-03	33.05	1.02	1.75E-03	33.13	1.07	1.76E-03
0.6932	33.24	1.28	1.82E-03	33.40	1.64	1.88E-03	33.58	1.97	1.91E-03	33.60	2.12	1.95E-03	33.68	2.16	1.96E-03
0.7077	33.72	2.27	2.00E-03	33.89	2.65	2.06E-03	34.08	3.01	2.10E-03	34.10	3.17	2.14E-03	34.19	3.23	2.16E-03
0.7220	34.17	3.23	2.17E-03	34.35	3.65	2.25E-03	34.53	3.99	2.29E-03	34.57	4.20	2.33E-03	34.67	4.30	2.36E-03
0.7361	34.59	4.15	2.35E-03	34.79	4.62	2.44E-03	34.96	4.92	2.48E-03	35.02	5.18	2.53E-03	35.13	5.33	2.57E-03
0.7500	34.99	5.02	2.52E-03	35.19	5.54	2.62E-03	35.36	5.80	2.66E-03	35.43	6.12	2.73E-03	35.54	6.28	2.77E-03
0.7636	35.36	5.82	2.69E-03	35.58	6.41	2.81E-03	35.73	6.61	2.84E-03	35.83	7.04	2.93E-03	35.92	7.12	2.96E-03
0.7770	35.70	6.56	2.86E-03	35.95	7.24	3.00E-03	36.08	7.36	3.02E-03	36.21	7.95	3.14E-03	36.26	7.89	3.14E-03
0.7900	36.04	7.28	3.03E-03	36.29	8.00	3.18E-03	36.42	8.07	3.20E-03	36.56	8.76	3.33E-03	36.60	8.64	3.33E-03
0.8028	36.38	8.04	3.22E-03	36.60	8.65	3.35E-03	36.75	8.76	3.38E-03	36.87	9.39	3.51E-03	36.94	9.43	3.53E-03
0.8153	36.74	8.84	3.42E-03	36.88	9.19	3.51E-03	37.06	9.43	3.57E-03	37.13	9.84	3.66E-03	37.30	10.27	3.76E-03
0.8274	37.03	9.43	3.59E-03	37.18	9.78	3.69E-03	37.34	9.96	3.73E-03	37.42	10.42	3.83E-03	37.61	10.98	3.96E-03
0.8393	37.29	9.89	3.74E-03	37.48	10.43	3.88E-03	37.59	10.40	3.89E-03	37.72	11.09	4.04E-03	37.90	11.58	4.16E-03
0.8507	37.58	10.52	3.93E-03	37.76	11.00	4.06E-03	37.87	10.96	4.07E-03	38.00	11.66	4.23E-03	38.16	12.09	4.34E-03
0.8619	37.86	11.11	4.12E-03	38.02	11.56	4.24E-03	38.13	11.47	4.25E-03	38.26	12.20	4.41E-03	38.40	12.57	4.51E-03
0.8726	38.09	11.53	4.27E-03	38.28	12.11	4.43E-03	38.34	11.80	4.39E-03	38.52	12.75	4.61E-03	38.64	13.03	4.69E-03
0.8830	38.32	11.97	4.44E-03	38.52	12.60	4.61E-03	38.55	12.17	4.54E-03	38.76	13.24	4.79E-03	38.87	13.49	4.87E-03
0.8930	38.56	12.50	4.62E-03	38.74	12.99	4.77E-03	38.79	12.64	4.72E-03	38.97	13.65	4.96E-03	39.09	13.93	5.05E-03
0.9026	38.80	13.06	4.81E-03	38.95	13.40	4.94E-03	39.00	13.08	4.89E-03	39.18	14.07	5.14E-03	39.31	14.38	5.23E-03
0.9118	39.03	13.61	5.01E-03	39.16	13.86	5.12E-03	39.20	13.44	5.05E-03	39.40	14.52	5.32E-03	39.52	14.85	5.43E-03
0.9206	39.24	14.10	5.19E-03	39.36	14.28	5.29E-03	39.40	13.85	5.22E-03	39.59	14.91	5.50E-03	39.72	15.26	5.60E-03
0.9290	39.44	14.55	5.37E-03	39.53	14.60	5.44E-03	39.62	14.44	5.43E-03	39.75	15.21	5.64E-03	39.88	15.57	5.76E-03
0.9369	39.62	14.95	5.53E-03	39.69	14.87	5.58E-03	39.84	15.03	5.65E-03	39.91	15.47	5.78E-03	40.03	15.81	5.89E-03
0.9444	39.77	15.22	5.67E-03	39.83	15.13	5.71E-03	40.01	15.42	5.82E-03	40.07	15.80	5.94E-03	40.16	15.96	6.01E-03
0.9515	39.89	15.39	5.78E-03	39.97	15.38	5.84E-03	40.16	15.70	5.95E-03	40.24	16.25	6.12E-03	40.26	16.03	6.09E-03
0.9581	40.01	15.57	5.88E-03	40.10	15.62	5.96E-03	40.28	15.89	6.07E-03	40.34	16.35	6.22E-03	40.36	16.12	6.18E-03
0.9642	40.14	15.83	6.01E-03	40.22	15.85	6.08E-03	40.39	16.09	6.18E-03	40.32	15.80	6.12E-03	40.47	16.28	6.28E-03
0.9699	40.27	16.12	6.14E-03	40.34	16.06	6.19E-03	40.51	16.33	6.30E-03	40.20	14.84	5.91E-03	40.58	16.50	6.40E-03
0.9750	40.39	16.43	6.27E-03	40.44	16.27	6.30E-03	40.59	16.42	6.38E-03	40.04	13.81	5.67E-03	40.69	16.73	6.52E-03
0.9798	40.50	16.73	6.40E-03	40.54	16.47	6.40E-03	40.62	16.26	6.38E-03	39.87	12.88	5.45E-03	40.79	16.95	6.63E-03
0.9840	40.61	17.01	6.52E-03	40.62	16.65	6.50E-03	40.59	15.85	6.30E-03	39.72	12.11	5.26E-03	40.88	17.17	6.74E-03
0.9877	40.70	17.26	6.64E-03	40.70	16.81	6.58E-03	40.53	15.31	6.19E-03	39.59	11.48	5.11E-03	40.96	17.36	6.83E-03
0.9910	40.78	17.49	6.73E-03	40.77	16.96	6.66E-03	40.46	14.77	6.06E-03	39.48	10.97	4.99E-03	41.04	17.53	6.92E-03
0.9937	40.85	17.69	6.82E-03	40.82	17.09	6.72E-03	40.39	14.29	5.94E-03	39.39	10.56	4.89E-03	41.10	17.68	6.99E-03
0.9960	40.90	17.86	6.89E-03	40.87	17.19	6.78E-03	40.32	13.88	5.85E-03	39.31	10.24	4.81E-03	41.15	17.81	7.06E-03
0.9977	40.95	17.99	6.95E-03	40.91	17.28	6.82E-03	40.27	13.57	5.77E-03	39.25	10.00	4.76E-03	41.18	17.91	7.11E-03
0.9990	40.98	18.08	6.99E-03	40.93	17.34	6.85E-03	40.23	13.35	5.72E-03	39.21	9.83	4.72E-03	41.21	17.98	7.14E-03
0.9998	41.00	18.14	7.02E-03	40.95	17.38	6.87E-03	40.21	13.22	5.69E-03	39.18	9.73	4.69E-03	41.23	18.02	7.16E-03
1.0000	41.00	18.16	7.03E-03	40.95	17.39	6.88E-03	40.20	13.18	5.68E-03	39.17	9.70	4.68E-03	41.23	18.04	7.17E-03

The local freestream flow direction, twist in the boundary layer and boundary layer displacement thickness from WAKELAG over the upper surface of the DERA wing. $\Lambda = 40°$, $\alpha = -1.7°$, $Re_c = 3.3 \times 10^6$.

η	0.06b			0.16b			0.30b			0.45b			0.59b		
x/c	α_c (°)	β_c (°)	δ^-/c	α_c (°)	β_c (°)	δ^-/c	α_c (°)	β_c (°)	δ^-/c	α_c (°)	β_c (°)	δ^-/c	α_c (°)	β_c (°)	δ^-/c
0.0556	38.16	-0.91	1.64E-04	37.34	-0.67	1.64E-04	36.75	-0.71	1.62E-04	36.19	-0.57	1.61E-04	35.92	-0.61	1.59E-04
0.0631	37.57	-1.85	1.87E-04	36.93	-1.34	1.90E-04	36.27	-1.48	1.86E-04	35.82	-1.18	1.88E-04	35.52	-1.30	1.83E-04
0.0710	37.03	-2.30	2.05E-04	36.51	-1.73	2.10E-04	35.80	-1.93	2.04E-04	35.44	-1.54	2.08E-04	35.12	-1.70	2.00E-04
0.0794	36.56	-2.48	2.26E-04	36.03	-2.08	2.28E-04	35.36	-2.20	2.21E-04	35.06	-1.78	2.28E-04	34.75	-1.90	2.19E-04
0.0882	36.17	-2.53	2.49E-04	35.38	-2.61	2.42E-04	34.93	-2.41	2.40E-04	34.66	-2.01	2.49E-04	34.43	-1.95	2.45E-04
0.0974	35.81	-2.57	2.73E-04	34.74	-3.05	2.56E-04	34.53	-2.56	2.60E-04	34.28	-2.20	2.71E-04	34.12	-1.98	2.73E-04
0.1070	35.43	-2.68	2.93E-04	34.38	-3.07	2.80E-04	34.21	-2.60	2.82E-04	33.97	-2.30	2.92E-04	33.80	-2.11	2.95E-04
0.1170	35.06	-2.82	3.10E-04	34.11	-3.01	3.04E-04	33.93	-2.60	3.04E-04	33.70	-2.36	3.13E-04	33.47	-2.28	3.12E-04
0.1274	34.69	-2.95	3.27E-04	33.88	-2.91	3.27E-04	33.68	-2.58	3.27E-04	33.46	-2.39	3.35E-04	33.14	-2.43	3.30E-04
0.1381	34.34	-3.04	3.45E-04	33.68	-2.81	3.51E-04	33.44	-2.55	3.50E-04	33.23	-2.39	3.57E-04	32.85	-2.53	3.49E-04
0.1493	34.04	-3.08	3.65E-04	33.48	-2.73	3.74E-04	33.21	-2.54	3.73E-04	33.02	-2.40	3.78E-04	32.64	-2.52	3.72E-04
0.1607	33.79	-3.06	3.87E-04	33.27	-2.68	3.96E-04	32.98	-2.55	3.94E-04	32.81	-2.40	4.00E-04	32.50	-2.42	3.99E-04
0.1726	33.56	-3.03	4.10E-04	33.07	-2.63	4.18E-04	32.75	-2.56	4.15E-04	32.61	-2.41	4.22E-04	32.39	-2.30	4.26E-04
0.1847	33.34	-2.99	4.32E-04	32.88	-2.60	4.41E-04	32.54	-2.56	4.37E-04	32.43	-2.40	4.44E-04	32.29	-2.18	4.54E-04
0.1972	33.13	-2.96	4.54E-04	32.68	-2.59	4.62E-04	32.34	-2.56	4.59E-04	32.25	-2.39	4.67E-04	32.18	-2.11	4.80E-04
0.2100	32.90	-2.95	4.75E-04	32.44	-2.65	4.79E-04	32.14	-2.56	4.81E-04	32.08	-2.39	4.89E-04	32.03	-2.09	5.02E-04
0.2230	32.67	-2.97	4.94E-04	32.15	-2.77	4.93E-04	31.95	-2.57	5.02E-04	31.90	-2.40	5.10E-04	31.85	-2.14	5.22E-04
0.2364	32.46	-2.96	5.15E-04	31.89	-2.84	5.10E-04	31.78	-2.56	5.25E-04	31.75	-2.38	5.33E-04	31.68	-2.16	5.42E-04
0.2500	32.32	-2.89	5.40E-04	31.76	-2.77	5.37E-04	31.69	-2.45	5.54E-04	31.66	-2.30	5.62E-04	31.58	-2.10	5.69E-04
0.2639	32.24	-2.75	5.70E-04	31.76	-2.55	5.75E-04	31.69	-2.25	5.91E-04	31.64	-2.13	5.96E-04	31.56	-1.96	6.02E-04
0.2780	32.18	-2.60	6.02E-04	31.80	-2.30	6.15E-04	31.73	-2.01	6.30E-04	31.66	-1.93	6.33E-04	31.56	-1.80	6.38E-04
0.2923	32.15	-2.43	6.35E-04	31.86	-2.03	6.57E-04	31.78	-1.77	6.71E-04	31.69	-1.73	6.71E-04	31.59	-1.61	6.76E-04
0.3068	32.14	-2.25	6.70E-04	31.91	-1.80	6.96E-04	31.83	-1.56	7.10E-04	31.73	-1.54	7.09E-04	31.65	-1.40	7.16E-04
0.3216	32.18	-2.03	7.10E-04	31.96	-1.58	7.36E-04	31.88	-1.35	7.49E-04	31.79	-1.34	7.49E-04	31.77	-1.13	7.63E-04
0.3365	32.23	-1.81	7.50E-04	32.01	-1.38	7.75E-04	31.94	-1.17	7.88E-04	31.85	-1.14	7.89E-04	31.90	-0.85	8.12E-04
0.3515	32.24	-1.65	7.86E-04	32.05	-1.23	8.11E-04	31.98	-1.02	8.26E-04	31.90	-0.98	8.28E-04	31.99	-0.65	8.55E-04
0.3668	32.22	-1.55	8.16E-04	32.05	-1.13	8.44E-04	32.01	-0.90	8.61E-04	31.96	-0.83	8.67E-04	32.03	-0.54	8.92E-04
0.3821	32.18	-1.50	8.44E-04	32.04	-1.06	8.74E-04	32.03	-0.81	8.95E-04	32.01	-0.70	9.05E-04	32.05	-0.47	9.25E-04
0.3976	32.12	-1.48	8.69E-04	32.02	-1.02	9.02E-04	32.03	-0.76	9.25E-04	32.03	-0.62	9.39E-04	32.05	-0.44	9.55E-04
0.4132	32.05	-1.48	8.91E-04	31.98	-1.01	9.28E-04	31.99	-0.76	9.51E-04	32.02	-0.59	9.68E-04	32.03	-0.44	9.81E-04
0.4288	31.95	-1.51	9.11E-04	31.92	-1.03	9.51E-04	31.92	-0.80	9.72E-04	31.98	-0.61	9.92E-04	31.98	-0.48	1.00E-03
0.4446	31.84	-1.56	9.29E-04	31.84	-1.07	9.72E-04	31.84	-0.87	9.91E-04	31.92	-0.66	1.01E-03	31.92	-0.54	1.03E-03
0.4604	31.73	-1.62	9.46E-04	31.75	-1.13	9.90E-04	31.77	-0.92	1.01E-03	31.83	-0.74	1.03E-03	31.85	-0.61	1.04E-03
0.4762	31.61	-1.68	9.63E-04	31.64	-1.22	1.01E-03	31.69	-0.97	1.03E-03	31.71	-0.87	1.04E-03	31.77	-0.68	1.06E-03
0.4921	31.47	-1.77	9.76E-04	31.50	-1.33	1.02E-03	31.59	-1.05	1.05E-03	31.55	-1.02	1.05E-03	31.66	-0.79	1.08E-03
0.5079	31.27	-1.92	9.80E-04	31.30	-1.50	1.02E-03	31.43	-1.20	1.05E-03	31.35	-1.21	1.05E-03	31.48	-0.97	1.08E-03
0.5238	30.94	-2.20	9.65E-04	31.00	-1.79	1.00E-03	31.11	-1.53	1.03E-03	30.97	-1.61	1.02E-03	31.17	-1.31	1.06E-03
0.5396	30.56	-2.51	9.44E-04	30.64	-2.10	9.84E-04	30.72	-1.89	1.01E-03	30.51	-2.03	9.82E-04	30.79	-1.68	1.03E-03
0.5554	30.19	-2.77	9.28E-04	30.27	-2.40	9.64E-04	30.34	-2.22	9.82E-04	30.11	-2.36	9.58E-04	30.42	-2.00	1.01E-03
0.5712	29.80	-3.04	9.11E-04	29.82	-2.74	9.36E-04	29.88	-2.58	9.51E-04	29.87	-2.51	9.61E-04	30.01	-2.34	9.81E-04
0.5868	29.65	-3.09	9.30E-04	29.71	-2.77	9.60E-04	29.79	-2.60	9.75E-04	29.87	-2.45	9.99E-04	29.92	-2.36	1.01E-03
0.6024	29.61	-3.04	9.65E-04	29.75	-2.65	1.01E-03	29.88	-2.45	1.03E-03	29.95	-2.31	1.05E-03	30.00	-2.22	1.06E-03
0.6179	29.61	-2.96	1.01E-03	29.83	-2.50	1.06E-03	30.03	-2.23	1.09E-03	30.06	-2.12	1.11E-03	30.13	-2.03	1.12E-03
0.6332	30.09	-2.37	1.13E-03	30.33	-1.88	1.19E-03	30.53	-1.60	1.22E-03	30.57	-1.47	1.25E-03	30.65	-1.37	1.26E-03
0.6485	31.07	-1.04	1.37E-03	31.27	-0.56	1.44E-03	31.42	-0.34	1.46E-03	31.50	-0.13	1.49E-03	31.59	-0.01	1.51E-03
0.6635	31.72	0.04	1.57E-03	31.92	0.54	1.64E-03	32.09	0.79	1.66E-03	32.17	1.02	1.70E-03	32.26	1.13	1.72E-03
0.6784	32.31	1.13	1.76E-03	32.52	1.68	1.85E-03	32.72	1.99	1.88E-03	32.79	2.23	1.93E-03	32.88	2.32	1.95E-03
0.6932	32.86	2.23	1.96E-03	33.08	2.81	2.05E-03	33.30	3.20	2.10E-03	33.37	3.46	2.15E-03	33.46	3.53	2.17E-03
0.7077	33.36	3.30	2.16E-03	33.59	3.92	2.26E-03	33.82	4.35	2.32E-03	33.89	4.62	2.38E-03	33.98	4.70	2.40E-03
0.7220	33.83	4.37	2.36E-03	34.06	5.02	2.48E-03	34.31	5.47	2.54E-03	34.37	5.75	2.60E-03	34.48	5.88	2.64E-03
0.7361	34.28	5.41	2.57E-03	34.51	6.09	2.69E-03	34.76	6.56	2.77E-03	34.83	6.84	2.83E-03	34.95	7.02	2.88E-03
0.7500	34.69	6.39	2.77E-03	34.94	7.11	2.91E-03	35.19	7.58	2.99E-03	35.26	7.91	3.06E-03	35.38	8.10	3.11E-03
0.7636	35.08	7.30	2.97E-03	35.33	8.08	3.13E-03	35.58	8.54	3.21E-03	35.68	8.98	3.31E-03	35.78	9.11	3.35E-03
0.7770	35.44	8.15	3.16E-03	35.71	9.02	3.35E-03	35.96	9.46	3.44E-03	36.08	10.05	3.56E-03	36.16	10.07	3.58E-03
0.7900	35.79	8.98	3.37E-03	36.06	9.89	3.56E-03	36.32	10.32	3.66E-03	36.45	11.03	3.81E-03	36.51	10.98	3.82E-03
0.8028	36.14	9.83	3.58E-03	36.39	10.67	3.77E-03	36.66	11.13	3.88E-03	36.77	11.79	4.02E-03	36.86	11.87	4.06E-03
0.8153	36.50	10.71	3.81E-03	36.70	11.34	3.97E-03	36.99	11.91	4.11E-03	37.05	12.33	4.21E-03	37.19	12.71	4.31E-03
0.8274	36.81	11.42	4.02E-03	37.01	12.07	4.19E-03	37.28	12.53	4.31E-03	37.35	13.03	4.43E-03	37.53	13.59	4.57E-03
0.8393	37.09	12.02	4.21E-03	37.32	12.83	4.42E-03	37.54	13.06	4.50E-03	37.66	13.84	4.68E-03	37.84	14.40	4.83E-03
0.8507	37.40	12.79	4.45E-03	37.60	13.49	4.64E-03	37.81	13.65	4.71E-03	37.94	14.50	4.91E-03	38.07	14.81	5.01E-03
0.8619	37.69	13.50	4.68E-03	37.87	14.08	4.85E-03	38.06	14.20	4.92E-03	38.20	15.08	5.13E-03	38.28	15.17	5.18E-03
0.8726	37.93	14.00	4.87E-03	38.11	14.58	5.05E-03	38.28	14.59	5.09E-03	38.43	15.57	5.33E-03	38.52	15.71	5.39E-03
0.8830	38.17	14.49	5.06E-03	38.34	15.09	5.25E-03	38.50	15.01	5.27E-03	38.65	16.00	5.52E-03	38.75	16.20	5.60E-03
0.8930	38.40	15.05	5.26E-03	38.57	15.63	5.46E-03	38.73	15.52	5.48E-03	38.86	16.38	5.71E-03	38.96	16.60	5.79E-03
0.9026	38.63	15.62	5.48E-03	38.78	16.10	5.66E-03	38.94	15.98	5.68E-03	39.05	16.75	5.89E-03	39.15	16.96	5.97E-03
0.9118	38.84	16.17	5.69E-03	38.97	16.46	5.84E-03	39.13	16.34	5.86E-03	39.24	17.14	6.08E-03	39.32	17.25	6.14E-03
0.9206	39.04	16.66	5.89E-03	39.14	16.78	6.00E-03	39.32	16.78	6.06E-03	39.41	17.46	6.25E-03	39.49	17.55	6.31E-03
0.9290	39.23	17.12	6.09E-03	39.31	17.08	6.16E-03	39.57	17.60	6.35E-03	39.56	17.69	6.40E-03	39.67	17.96	6.51E-03
0.9369	39.40	17.52	6.27E-03	39.46	17.35	6.31E-03	39.79	18.37	6.64E-03	39.69	17.84	6.52E-03	39.83	18.32	6.69E-03
0.9444	39.54	17.73	6.40E-03	39.60	17.59	6.45E-03	39.92	18.50	6.76E-03	39.82	18.02	6.65E-03	39.94	18.40	6.79E-03
0.9515	39.65	17.80	6.49E-03	39.72	17.80	6.58E-03	39.98	18.31	6.79E-03	39.96	18.27	6.80E-03	40.02	18.29	6.84E-03
0.9581	39.75	17.90	6.59E-03	39.84	17.99	6.71E-03	40.04	18.13	6.81E-03	40.03	18.20	6.85E-03	40.09	18.21	6.89E-03
0.9642	39.87	18.15	6.73E-03	39.95	18.18	6.83E-03	40.12	18.12	6.87E-03	40.01	17.57	6.74E-03	40.18	18.27	6.98E-03
0.9699	40.00	18.49	6.88E-03	40.06	18.36	6.94E-03	40.21	18.24	6.97E-03	39.91	16.59	6.52E-03	40.28	18.39	7.08E-03
0.9750	40.13	18.88	7.05E-03	40.15	18.53	7.05E-03	40.29	18.30	7.05E-03	39.77	15.57	6.28E-03	40.37	18.55	7.18E-03
0.9798	40.25	19.27	7.22E-03	40.24	18.69	7.15E-03	40.33	18.19	7.07E-03	39.63	14.64	6.05E-03	40.45	18.71	7.29E-03
0.9840	40.36	19.64	7.38E-03	40.32	18.84	7.24E-03	40.34	17.94	7.04E-03	39.51	13.87	5.86E-03	40.53	18.87	7.38E-03
0.9877	40.46	19.98	7.52E-03	40.38	18.98	7.33E-03	40.34	17.66	7.00E-03	39.40	13.24	5.71E-03	40.60	19.01	7.47E-03
0.9910	40.54	20.29	7.65E-03	40.45	19.10	7.40E-03	40.33	17.38	6.95E-03	39.30	12.73	5.58E-03	40.66	19.14	7.55E-03
0.9937	40.62	20.56	7.77E-03	40.50	19.21	7.47E-03	40.32	17.12	6.90E-03	39.22	12.31	5.48E-03	40.72	19.25	7.62E-03
0.9960	40.68	20.78	7.86E-03	40.54	19.30	7.52E-03	40.31	16.91	6.86E-03	39.16	11.99	5.40E-03	40.76	19.34	7.67E-03
0.9977	40.72	20.96	7.94E-03	40.57	19.37	7.57E-03	40.30	16.74	6.83E-03	39.11	11.75	5.34E-03	40.79	19.41	7.72E-03
0.9990	40.76	21.09	8.00E-03	40.60	19.42	7.60E-03	40.29	16.63	6.81E-03	39.07	11.58	5.30E-03	40.82	19.47	7.75E-03
0.9998	40.78	21.17	8.03E-03	40.61	19.45	7.62E-03	40.29	16.55	6.79E-03	39.05	11.48	5.28E-03	40.83	19.50	7.77E-03
1.0000	40.79	21.20	8.04E-03	40.62	19.46	7.62E-03	40.29	16.53	6.79E-03	39.04	11.44	5.27E-03	40.84	19.51	7.77E-03

The local freestream flow direction, twist in the boundary layer and boundary layer displacement thickness from WAKELAG over the upper surface of the DERA wing. $\Lambda = 40°$, $\alpha = 0.4°$, $Re_c = 3.3 \times 10^6$.

η	0.06b			0.16b			0.30b			0.45b			0.59b		
x/c	α_c (°)	β_c (°)	δ^*/c	α_c (°)	β_c (°)	δ^*/c	α_c (°)	β_c (°)	δ^*/c	α_c (°)	β_c (°)	δ^*/c	α_c (°)	β_c (°)	δ^*/c
0.0556	34.91	-0.54	1.57E-04	33.97	-0.27	1.56E-04	33.28	-0.26	1.55E-04	32.69	-0.15	1.53E-04	32.57	-0.13	1.52E-04
0.0631	34.55	-1.14	1.83E-04	33.78	-0.59	1.86E-04	33.06	-0.65	1.82E-04	32.57	-0.37	1.83E-04	32.42	-0.43	1.79E-04
0.0710	34.20	-1.44	2.04E-04	33.57	-0.83	2.08E-04	32.80	-0.94	2.02E-04	32.41	-0.56	2.06E-04	32.23	-0.69	1.99E-04
0.0794	33.91	-1.56	2.26E-04	33.30	-1.07	2.30E-04	32.56	-1.14	2.23E-04	32.24	-0.72	2.30E-04	32.03	-0.86	2.20E-04
0.0882	33.70	-1.56	2.53E-04	32.85	-1.57	2.46E-04	32.33	-1.28	2.45E-04	32.02	-0.92	2.53E-04	31.86	-0.94	2.47E-04
0.0974	33.49	-1.56	2.79E-04	32.34	-2.04	2.61E-04	32.10	-1.39	2.67E-04	31.78	-1.12	2.76E-04	31.68	-1.01	2.77E-04
0.1070	33.26	-1.65	3.01E-04	32.11	-2.05	2.86E-04	31.92	-1.45	2.91E-04	31.61	-1.21	3.00E-04	31.49	-1.13	3.01E-04
0.1170	33.00	-1.79	3.21E-04	31.95	-2.00	3.12E-04	31.75	-1.47	3.15E-04	31.47	-1.25	3.24E-04	31.29	-1.28	3.22E-04
0.1274	32.74	-1.94	3.39E-04	31.82	-1.91	3.38E-04	31.60	-1.48	3.40E-04	31.35	-1.26	3.49E-04	31.08	-1.42	3.41E-04
0.1381	32.48	-2.06	3.58E-04	31.71	-1.83	3.63E-04	31.47	-1.48	3.64E-04	31.24	-1.27	3.73E-04	30.90	-1.50	3.63E-04
0.1493	32.26	-2.13	3.79E-04	31.59	-1.77	3.88E-04	31.33	-1.50	3.88E-04	31.12	-1.28	3.97E-04	30.78	-1.49	3.88E-04
0.1607	32.08	-2.14	4.02E-04	31.47	-1.73	4.12E-04	31.18	-1.52	4.12E-04	31.00	-1.31	4.20E-04	30.73	-1.39	4.17E-04
0.1726	31.92	-2.13	4.26E-04	31.36	-1.69	4.36E-04	31.04	-1.55	4.35E-04	30.88	-1.34	4.44E-04	30.71	-1.27	4.48E-04
0.1847	31.77	-2.11	4.49E-04	31.25	-1.66	4.61E-04	30.91	-1.57	4.59E-04	30.77	-1.36	4.67E-04	30.69	-1.15	4.78E-04
0.1972	31.62	-2.10	4.73E-04	31.12	-1.66	4.84E-04	30.79	-1.58	4.83E-04	30.67	-1.37	4.92E-04	30.66	-1.07	5.07E-04
0.2100	31.46	-2.11	4.95E-04	30.96	-1.71	5.04E-04	30.66	-1.60	5.07E-04	30.57	-1.37	5.17E-04	30.59	-1.07	5.32E-04
0.2230	31.29	-2.14	5.16E-04	30.76	-1.83	5.21E-04	30.53	-1.63	5.29E-04	30.47	-1.38	5.41E-04	30.49	-1.12	5.54E-04
0.2364	31.14	-2.14	5.38E-04	30.58	-1.91	5.40E-04	30.42	-1.63	5.54E-04	30.40	-1.37	5.67E-04	30.38	-1.16	5.77E-04
0.2500	31.05	-2.08	5.66E-04	30.49	-1.87	5.67E-04	30.38	-1.56	5.84E-04	30.36	-1.30	5.97E-04	30.33	-1.13	6.05E-04
0.2639	31.02	-1.95	5.98E-04	30.52	-1.68	6.05E-04	30.42	-1.37	6.22E-04	30.39	-1.15	6.34E-04	30.35	-1.02	6.39E-04
0.2780	31.02	-1.80	6.32E-04	30.61	-1.43	6.49E-04	30.51	-1.12	6.67E-04	30.46	-0.96	6.74E-04	30.40	-0.86	6.78E-04
0.2923	31.03	-1.63	6.68E-04	30.71	-1.16	6.94E-04	30.63	-0.86	7.13E-04	30.55	-0.74	7.17E-04	30.48	-0.67	7.20E-04
0.3068	31.07	-1.46	7.06E-04	30.80	-0.94	7.36E-04	30.73	-0.64	7.56E-04	30.64	-0.56	7.59E-04	30.58	-0.47	7.63E-04
0.3216	31.15	-1.24	7.48E-04	30.89	-0.74	7.79E-04	30.83	-0.44	7.99E-04	30.74	-0.37	8.02E-04	30.74	-0.20	8.15E-04
0.3365	31.23	-1.02	7.91E-04	30.97	-0.55	8.20E-04	30.93	-0.26	8.41E-04	30.84	-0.18	8.46E-04	30.91	0.09	8.68E-04
0.3515	31.28	-0.87	8.29E-04	31.04	-0.41	8.60E-04	31.01	-0.11	8.82E-04	30.94	-0.01	8.89E-04	31.04	0.28	9.16E-04
0.3668	31.29	-0.80	8.61E-04	31.09	-0.30	8.96E-04	31.08	0.01	9.21E-04	31.04	0.15	9.33E-04	31.11	0.39	9.55E-04
0.3821	31.27	-0.77	8.89E-04	31.13	-0.22	9.31E-04	31.14	0.10	9.59E-04	31.14	0.30	9.78E-04	31.17	0.45	9.92E-04
0.3976	31.23	-0.77	9.15E-04	31.15	-0.18	9.63E-04	31.17	0.14	9.93E-04	31.21	0.39	1.02E-03	31.21	0.48	1.03E-03
0.4132	31.19	-0.78	9.39E-04	31.14	-0.17	9.92E-04	31.17	0.13	1.02E-03	31.23	0.39	1.05E-03	31.23	0.48	1.06E-03
0.4288	31.12	-0.83	9.60E-04	31.12	-0.19	1.02E-03	31.13	0.07	1.04E-03	31.22	0.35	1.07E-03	31.23	0.45	1.08E-03
0.4446	31.04	-0.88	9.80E-04	31.08	-0.24	1.04E-03	31.09	0.00	1.06E-03	31.19	0.28	1.10E-03	31.21	0.40	1.11E-03
0.4604	30.96	-0.94	9.99E-04	31.02	-0.31	1.06E-03	31.04	-0.06	1.09E-03	31.14	0.19	1.11E-03	31.18	0.33	1.13E-03
0.4762	30.87	-1.01	1.02E-03	30.94	-0.41	1.08E-03	31.00	-0.12	1.11E-03	31.06	0.07	1.13E-03	31.13	0.24	1.15E-03
0.4921	30.77	-1.09	1.03E-03	30.82	-0.54	1.09E-03	30.94	-0.20	1.13E-03	30.97	-0.06	1.14E-03	31.06	0.13	1.17E-03
0.5079	30.60	-1.25	1.04E-03	30.67	-0.72	1.09E-03	30.81	-0.37	1.13E-03	30.82	-0.26	1.15E-03	30.93	-0.06	1.17E-03
0.5238	30.31	-1.53	1.02E-03	30.40	-1.01	1.08E-03	30.53	-0.70	1.12E-03	30.48	-0.67	1.12E-03	30.65	-0.42	1.15E-03
0.5396	29.97	-1.85	1.00E-03	30.08	-1.34	1.06E-03	30.18	-1.08	1.09E-03	30.07	-1.13	1.08E-03	30.31	-0.81	1.12E-03
0.5554	29.64	-2.12	9.88E-04	29.75	-1.64	1.04E-03	29.84	-1.42	1.06E-03	29.70	-1.48	1.05E-03	29.99	-1.14	1.10E-03
0.5712	29.29	-2.39	9.70E-04	29.37	-1.98	1.01E-03	29.44	-1.79	1.03E-03	29.49	-1.65	1.05E-03	29.64	-1.48	1.07E-03
0.5868	29.17	-2.43	9.91E-04	29.28	-2.01	1.04E-03	29.36	-1.82	1.05E-03	29.52	-1.58	1.09E-03	29.57	-1.51	1.10E-03
0.6024	29.17	-2.36	1.03E-03	29.37	-1.87	1.09E-03	29.49	-1.64	1.11E-03	29.64	-1.41	1.15E-03	29.69	-1.34	1.16E-03
0.6179	29.21	-2.26	1.08E-03	29.50	-1.67	1.15E-03	29.69	-1.37	1.19E-03	29.81	-1.17	1.22E-03	29.89	-1.08	1.23E-03
0.6332	29.70	-1.65	1.21E-03	30.03	-1.00	1.30E-03	30.23	-0.68	1.33E-03	30.36	-0.45	1.37E-03	30.45	-0.35	1.39E-03
0.6485	30.69	-0.24	1.47E-03	30.97	0.40	1.56E-03	31.13	0.68	1.59E-03	31.29	0.98	1.64E-03	31.41	1.13	1.67E-03
0.6635	31.36	0.90	1.68E-03	31.63	1.57	1.78E-03	31.82	1.91	1.82E-03	31.99	2.26	1.89E-03	32.12	2.42	1.92E-03
0.6784	31.98	2.09	1.90E-03	32.26	2.79	2.01E-03	32.49	3.24	2.07E-03	32.66	3.64	2.15E-03	32.79	3.81	2.18E-03
0.6932	32.55	3.28	2.12E-03	32.83	4.03	2.25E-03	33.10	4.61	2.33E-03	33.28	5.05	2.42E-03	33.41	5.24	2.46E-03
0.7077	33.07	4.46	2.35E-03	33.36	5.26	2.49E-03	33.65	5.93	2.59E-03	33.83	6.39	2.69E-03	33.98	6.65	2.74E-03
0.7220	33.56	5.65	2.58E-03	33.87	6.52	2.74E-03	34.17	7.27	2.87E-03	34.34	7.72	2.96E-03	34.52	8.10	3.04E-03
0.7361	34.03	6.82	2.82E-03	34.35	7.77	3.00E-03	34.66	8.59	3.14E-03	34.82	9.02	3.25E-03	35.03	9.54	3.35E-03
0.7500	34.47	7.95	3.06E-03	34.79	8.98	3.27E-03	35.11	9.82	3.42E-03	35.28	10.29	3.53E-03	35.50	10.91	3.66E-03
0.7636	34.87	9.02	3.29E-03	35.21	10.15	3.53E-03	35.52	10.92	3.69E-03	35.71	11.60	3.84E-03	35.92	12.22	3.98E-03
0.7770	35.26	10.04	3.54E-03	35.61	11.29	3.81E-03	35.89	11.92	3.95E-03	36.14	12.92	4.16E-03	36.33	13.49	4.30E-03
0.7900	35.63	11.04	3.78E-03	35.99	12.37	4.08E-03	36.26	12.91	4.21E-03	36.52	14.13	4.48E-03	36.71	14.69	4.62E-03
0.8028	36.00	12.04	4.04E-03	36.33	13.30	4.34E-03	36.62	13.96	4.51E-03	36.85	15.06	4.75E-03	37.05	15.77	4.93E-03
0.8153	36.36	13.05	4.31E-03	36.64	14.09	4.58E-03	37.00	15.14	4.84E-03	37.13	15.71	4.99E-03	37.38	16.73	5.23E-03
0.8274	36.67	13.87	4.56E-03	36.94	14.88	4.84E-03	37.28	15.82	5.08E-03	37.41	16.42	5.24E-03	37.67	17.56	5.52E-03
0.8393	36.96	14.57	4.80E-03	37.24	15.65	5.10E-03	37.50	16.20	5.26E-03	37.69	17.14	5.51E-03	37.94	18.22	5.78E-03
0.8507	37.27	15.42	5.07E-03	37.49	16.25	5.33E-03	37.73	16.61	5.46E-03	37.93	17.64	5.73E-03	38.15	18.58	5.98E-03
0.8619	37.56	16.23	5.34E-03	37.74	16.81	5.55E-03	37.94	16.96	5.64E-03	38.14	18.00	5.92E-03	38.34	18.81	6.15E-03
0.8726	37.81	16.89	5.58E-03	37.99	17.42	5.79E-03	38.13	17.16	5.79E-03	38.33	18.28	6.10E-03	38.53	19.02	6.32E-03
0.8830	38.05	17.51	5.83E-03	38.20	17.91	6.01E-03	38.32	17.50	5.98E-03	38.50	18.43	6.25E-03	38.69	19.13	6.46E-03
0.8930	38.28	18.12	6.07E-03	38.39	18.24	6.20E-03	38.56	18.14	6.24E-03	38.64	18.44	6.35E-03	38.83	19.15	6.58E-03
0.9026	38.49	18.69	6.30E-03	38.57	18.50	6.36E-03	38.75	18.49	6.43E-03	38.78	18.47	6.47E-03	38.96	19.08	6.67E-03
0.9118	38.69	19.22	6.53E-03	38.73	18.73	6.52E-03	38.86	18.44	6.52E-03	38.92	18.57	6.60E-03	39.06	18.91	6.73E-03
0.9206	38.88	19.70	6.75E-03	38.87	18.89	6.66E-03	38.98	18.38	6.60E-03	39.04	18.59	6.70E-03	39.16	18.77	6.79E-03
0.9290	39.06	20.16	6.97E-03	39.00	18.96	6.77E-03	39.10	18.48	6.72E-03	39.13	18.42	6.75E-03	39.27	18.76	6.88E-03
0.9369	39.22	20.54	7.17E-03	39.11	18.99	6.87E-03	39.23	18.59	6.84E-03	39.20	18.22	6.78E-03	39.37	18.70	6.96E-03
0.9444	39.35	20.71	7.31E-03	39.22	19.09	6.99E-03	39.33	18.60	6.93E-03	39.28	18.11	6.83E-03	39.42	18.42	6.96E-03
0.9515	39.45	20.74	7.40E-03	39.34	19.21	7.10E-03	39.41	18.55	6.99E-03	39.38	18.12	6.91E-03	39.44	17.99	6.92E-03
0.9581	39.54	20.76	7.49E-03	39.45	19.35	7.22E-03	39.49	18.49	7.05E-03	39.43	17.90	6.92E-03	39.47	17.63	6.89E-03
0.9642	39.64	20.88	7.61E-03	39.55	19.50	7.34E-03	39.55	18.39	7.09E-03	39.39	17.25	6.80E-03	39.51	17.47	6.91E-03
0.9699	39.74	21.05	7.73E-03	39.64	19.64	7.45E-03	39.60	18.25	7.12E-03	39.27	16.25	6.56E-03	39.57	17.41	6.95E-03
0.9750	39.83	21.22	7.85E-03	39.73	19.77	7.55E-03	39.65	18.17	7.15E-03	39.12	15.20	6.30E-03	39.64	17.40	7.01E-03
0.9798	39.92	21.40	7.96E-03	39.81	19.90	7.65E-03	39.72	18.21	7.22E-03	38.96	14.25	6.06E-03	39.70	17.42	7.06E-03
0.9840	40.00	21.57	8.07E-03	39.88	20.02	7.74E-03	39.81	18.44	7.33E-03	38.82	13.47	5.85E-03	39.76	17.45	7.12E-03
0.9877	40.07	21.72	8.17E-03	39.95	20.13	7.82E-03	39.92	18.82	7.50E-03	38.69	12.82	5.69E-03	39.81	17.47	7.17E-03
0.9910	40.13	21.86	8.25E-03	40.00	20.23	7.89E-03	40.03	19.28	7.68E-03	38.59	12.30	5.56E-03	39.85	17.49	7.21E-03
0.9937	40.18	21.98	8.33E-03	40.05	20.32	7.95E-03	40.14	19.75	7.86E-03	38.50	11.88	5.45E-03	39.89	17.51	7.25E-03
0.9960	40.22	22.08	8.39E-03	40.09	20.39	8.00E-03	40.23	20.18	8.02E-03	38.42	11.56	5.36E-03	39.92	17.53	7.28E-03
0.9977	40.26	22.16	8.44E-03	40.12	20.45	8.04E-03	40.31	20.54	8.16E-03	38.37	11.31	5.30E-03	39.94	17.54	7.30E-03
0.9990	40.28	22.22	8.48E-03	40.14	20.49	8.07E-03	40.36	20.80	8.26E-03	38.33	11.14	5.26E-03	39.96	17.55	7.32E-03
0.9998	40.29	22.26	8.50E-03	40.16	20.52	8.09E-03	40.39	20.97	8.33E-03	38.30	11.03	5.23E-03	39.97	17.56	7.33E-03
1.0000	40.30	22.27	8.51E-03	40.16	20.52	8.10E-03	40.40	21.03	8.35E-03	38.29	11.00	5.22E-03	39.97	17.56	7.33E-03

The local freestream flow direction, twist in the boundary layer and boundary layer displacement thickness from WAKELAG over the upper surface of the DERA wing. $\Lambda = 40°$, $\alpha = 2.5°$, $Re_c = 3.3 \times 10^6$.

η	0.06b			0.16b			0.30b			0.45b			0.59b		
x/c	α_e (°)	β_e (°)	δ^*/c	α_e (°)	β_e (°)	δ^*/c	α_e (°)	β_e (°)	δ^*/c	α_e (°)	β_e (°)	δ^*/c	α_e (°)	β_e (°)	δ^*/c
0.0556	32.16	-0.22	1.51E-04	31.15	0.01	1.49E-04	30.37	0.01	1.47E-04	29.86	0.11	1.45E-04	29.70	0.07	1.44E-04
0.0631	31.98	-0.54	1.79E-04	31.12	-0.06	1.80E-04	30.34	-0.07	1.77E-04	29.92	0.19	1.78E-04	29.73	0.11	1.74E-04
0.0710	31.79	-0.74	2.01E-04	31.06	-0.17	2.05E-04	30.27	-0.18	2.00E-04	29.95	0.20	2.04E-04	29.74	0.11	1.97E-04
0.0794	31.64	-0.81	2.26E-04	30.97	-0.27	2.30E-04	30.19	-0.28	2.23E-04	29.96	0.15	2.31E-04	29.74	0.07	2.22E-04
0.0882	31.54	-0.78	2.54E-04	30.71	-0.66	2.50E-04	30.09	-0.40	2.47E-04	29.88	-0.03	2.57E-04	29.70	-0.02	2.51E-04
0.0974	31.46	-0.76	2.82E-04	30.35	-1.12	2.67E-04	29.97	-0.53	2.71E-04	29.74	-0.26	2.81E-04	29.64	-0.12	2.82E-04
0.1070	31.34	-0.82	3.07E-04	30.23	-1.13	2.94E-04	29.89	-0.57	2.97E-04	29.66	-0.35	3.07E-04	29.57	-0.22	3.09E-04
0.1170	31.18	-0.95	3.29E-04	30.16	-1.07	3.21E-04	29.83	-0.57	3.24E-04	29.61	-0.37	3.33E-04	29.47	-0.34	3.32E-04
0.1274	31.00	-1.10	3.49E-04	30.11	-0.99	3.49E-04	29.79	-0.55	3.51E-04	29.58	-0.37	3.60E-04	29.37	-0.47	3.55E-04
0.1381	30.82	-1.22	3.69E-04	30.08	-0.91	3.76E-04	29.76	-0.53	3.79E-04	29.56	-0.37	3.87E-04	29.27	-0.55	3.78E-04
0.1493	30.68	-1.29	3.91E-04	30.03	-0.87	4.03E-04	29.71	-0.53	4.06E-04	29.52	-0.37	4.13E-04	29.22	-0.56	4.05E-04
0.1607	30.57	-1.30	4.16E-04	29.98	-0.84	4.29E-04	29.65	-0.56	4.31E-04	29.48	-0.40	4.39E-04	29.23	-0.48	4.36E-04
0.1726	30.48	-1.30	4.42E-04	29.93	-0.81	4.55E-04	29.57	-0.61	4.56E-04	29.43	-0.43	4.65E-04	29.28	-0.36	4.69E-04
0.1847	30.39	-1.28	4.68E-04	29.88	-0.80	4.81E-04	29.50	-0.66	4.81E-04	29.38	-0.46	4.91E-04	29.33	-0.23	5.03E-04
0.1972	30.31	-1.28	4.93E-04	29.82	-0.81	5.07E-04	29.44	-0.68	5.07E-04	29.34	-0.47	5.17E-04	29.37	-0.14	5.36E-04
0.2100	30.21	-1.29	5.18E-04	29.72	-0.87	5.29E-04	29.38	-0.70	5.34E-04	29.31	-0.48	5.44E-04	29.37	-0.14	5.64E-04
0.2230	30.10	-1.32	5.41E-04	29.58	-0.99	5.48E-04	29.33	-0.72	5.60E-04	29.27	-0.49	5.72E-04	29.33	-0.18	5.89E-04
0.2364	30.01	-1.34	5.65E-04	29.46	-1.08	5.68E-04	29.29	-0.71	5.88E-04	29.25	-0.48	6.00E-04	29.29	-0.23	6.14E-04
0.2500	29.96	-1.29	5.93E-04	29.40	-1.07	5.96E-04	29.28	-0.66	6.20E-04	29.26	-0.43	6.32E-04	29.28	-0.22	6.44E-04
0.2639	29.97	-1.18	6.27E-04	29.46	-0.90	6.35E-04	29.35	-0.50	6.59E-04	29.32	-0.29	6.70E-04	29.34	-0.11	6.81E-04
0.2780	30.00	-1.03	6.64E-04	29.59	-0.64	6.83E-04	29.49	-0.25	7.06E-04	29.44	-0.09	7.15E-04	29.45	0.07	7.25E-04
0.2923	30.06	-0.87	7.03E-04	29.75	-0.35	7.34E-04	29.65	0.02	7.57E-04	29.58	0.14	7.62E-04	29.60	0.29	7.72E-04
0.3068	30.13	-0.70	7.43E-04	29.88	-0.12	7.80E-04	29.79	0.24	8.04E-04	29.71	0.34	8.09E-04	29.75	0.51	8.22E-04
0.3216	30.24	-0.49	7.87E-04	30.02	0.10	8.27E-04	29.93	0.45	8.52E-04	29.85	0.53	8.56E-04	29.94	0.80	8.78E-04
0.3365	30.35	-0.28	8.33E-04	30.14	0.30	8.74E-04	30.06	0.64	8.99E-04	29.99	0.73	9.05E-04	30.15	1.09	9.37E-04
0.3515	30.43	-0.14	8.73E-04	30.24	0.44	9.16E-04	30.18	0.79	9.44E-04	30.13	0.90	9.53E-04	30.31	1.29	9.90E-04
0.3668	30.47	-0.07	9.08E-04	30.32	0.53	9.55E-04	30.29	0.90	9.87E-04	30.27	1.07	1.00E-03	30.43	1.41	1.04E-03
0.3821	30.49	-0.03	9.40E-04	30.38	0.58	9.91E-04	30.38	0.99	1.03E-03	30.40	1.23	1.05E-03	30.54	1.48	1.08E-03
0.3976	30.49	-0.03	9.69E-04	30.42	0.61	1.02E-03	30.44	1.03	1.07E-03	30.51	1.32	1.10E-03	30.62	1.52	1.12E-03
0.4132	30.48	-0.04	9.96E-04	30.44	0.60	1.06E-03	30.47	1.01	1.10E-03	30.56	1.32	1.13E-03	30.67	1.52	1.15E-03
0.4288	30.45	-0.09	1.02E-03	30.45	0.58	1.08E-03	30.48	0.96	1.12E-03	30.59	1.29	1.16E-03	30.72	1.49	1.18E-03
0.4446	30.40	-0.14	1.04E-03	30.43	0.53	1.11E-03	30.48	0.90	1.15E-03	30.60	1.22	1.19E-03	30.74	1.44	1.21E-03
0.4604	30.35	-0.21	1.06E-03	30.41	0.45	1.13E-03	30.47	0.83	1.17E-03	30.58	1.13	1.21E-03	30.75	1.37	1.24E-03
0.4762	30.30	-0.27	1.08E-03	30.36	0.36	1.15E-03	30.45	0.77	1.20E-03	30.55	1.01	1.23E-03	30.74	1.28	1.26E-03
0.4921	30.22	-0.36	1.10E-03	30.29	0.24	1.17E-03	30.42	0.67	1.22E-03	30.49	0.87	1.24E-03	30.70	1.16	1.28E-03
0.5079	30.08	-0.52	1.11E-03	30.17	0.06	1.17E-03	30.32	0.50	1.23E-03	30.38	0.68	1.25E-03	30.60	0.96	1.29E-03
0.5238	29.82	-0.83	1.09E-03	29.93	-0.25	1.16E-03	30.08	0.15	1.21E-03	30.11	0.27	1.22E-03	30.38	0.59	1.27E-03
0.5396	29.51	-1.16	1.07E-03	29.65	-0.59	1.14E-03	29.79	-0.23	1.18E-03	29.76	-0.19	1.18E-03	30.10	0.20	1.24E-03
0.5554	29.22	-1.44	1.06E-03	29.36	-0.91	1.12E-03	29.50	-0.57	1.16E-03	29.45	-0.55	1.16E-03	29.84	-0.13	1.22E-03
0.5712	28.91	-1.72	1.04E-03	29.01	-1.25	1.09E-03	29.16	-0.93	1.13E-03	29.27	-0.73	1.16E-03	29.56	-0.46	1.20E-03
0.5868	28.82	-1.76	1.06E-03	28.95	-1.28	1.11E-03	29.10	-0.97	1.15E-03	29.32	-0.66	1.20E-03	29.50	-0.51	1.22E-03
0.6024	28.85	-1.67	1.10E-03	29.11	-1.07	1.18E-03	29.27	-0.75	1.22E-03	29.50	-0.42	1.27E-03	29.69	-0.28	1.29E-03
0.6179	28.92	-1.54	1.16E-03	29.36	-0.74	1.27E-03	29.54	-0.40	1.31E-03	29.77	-0.08	1.36E-03	29.97	0.09	1.39E-03
0.6332	29.45	-0.88	1.30E-03	29.91	0.00	1.43E-03	30.12	0.39	1.48E-03	30.37	0.77	1.54E-03	30.61	0.99	1.58E-03
0.6485	30.45	0.61	1.58E-03	30.79	1.39	1.70E-03	31.05	1.91	1.77E-03	31.33	2.40	1.86E-03	31.64	2.75	1.92E-03
0.6635	31.14	1.84	1.82E-03	31.48	2.66	1.95E-03	31.79	3.31	2.04E-03	32.09	3.91	2.15E-03	32.42	4.36	2.24E-03
0.6784	31.77	3.11	2.06E-03	32.15	4.06	2.22E-03	32.49	4.87	2.34E-03	32.82	5.60	2.48E-03	33.17	6.13	2.58E-03
0.6932	32.35	4.41	2.31E-03	32.77	5.52	2.50E-03	33.15	6.50	2.66E-03	33.50	7.37	2.83E-03	33.86	7.99	2.96E-03
0.7077	32.89	5.71	2.56E-03	33.33	6.94	2.79E-03	33.73	8.08	2.98E-03	34.09	9.06	3.18E-03	34.47	9.82	3.34E-03
0.7220	33.41	7.03	2.83E-03	33.86	8.40	3.09E-03	34.30	9.74	3.33E-03	34.66	10.83	3.56E-03	35.07	11.80	3.76E-03
0.7361	33.89	8.35	3.10E-03	34.36	9.86	3.41E-03	34.82	11.38	3.69E-03	35.19	12.58	3.95E-03	35.62	13.78	4.21E-03
0.7500	34.34	9.63	3.38E-03	34.81	11.26	3.72E-03	35.28	12.86	4.04E-03	35.64	14.15	4.32E-03	36.07	15.39	4.60E-03
0.7636	34.76	10.85	3.66E-03	35.24	12.62	4.05E-03	35.69	14.16	4.37E-03	36.06	15.61	4.70E-03	36.43	16.62	4.94E-03
0.7770	35.16	12.03	3.95E-03	35.65	13.97	4.38E-03	36.06	15.34	4.69E-03	36.45	17.04	5.08E-03	36.76	17.69	5.26E-03
0.7900	35.54	13.19	4.24E-03	36.03	15.21	4.71E-03	36.41	16.40	5.01E-03	36.78	18.17	5.42E-03	37.04	18.48	5.54E-03
0.8028	35.91	14.34	4.55E-03	36.35	16.21	5.01E-03	36.72	17.30	5.30E-03	37.03	18.70	5.65E-03	37.28	18.93	5.76E-03
0.8153	36.27	15.50	4.87E-03	36.64	16.98	5.28E-03	37.01	18.11	5.59E-03	37.22	18.77	5.79E-03	37.48	19.09	5.92E-03
0.8274	36.57	16.35	5.15E-03	36.91	17.67	5.53E-03	37.22	18.40	5.77E-03	37.40	18.84	5.93E-03	37.64	18.99	6.03E-03
0.8393	36.84	17.02	5.40E-03	37.17	18.28	5.78E-03	37.39	18.37	5.88E-03	37.57	18.84	6.05E-03	37.77	18.73	6.09E-03
0.8507	37.14	17.94	5.71E-03	37.41	18.87	6.03E-03	37.55	18.36	6.00E-03	37.69	18.58	6.11E-03	37.89	18.42	6.14E-03
0.8619	37.42	18.79	6.01E-03	37.63	19.32	6.25E-03	37.70	18.32	6.11E-03	37.80	18.26	6.15E-03	37.98	18.04	6.16E-03
0.8726	37.65	19.35	6.25E-03	37.82	19.54	6.43E-03	37.84	18.25	6.20E-03	37.91	17.97	6.19E-03	38.06	17.59	6.16E-03
0.8830	37.86	19.83	6.48E-03	37.98	19.68	6.58E-03	37.96	18.13	6.28E-03	38.00	17.65	6.22E-03	38.12	17.16	6.16E-03
0.8930	38.06	20.30	6.71E-03	38.13	19.77	6.71E-03	38.07	17.97	6.35E-03	38.07	17.28	6.23E-03	38.19	16.78	6.16E-03
0.9026	38.24	20.71	6.92E-03	38.27	19.80	6.83E-03	38.17	17.81	6.41E-03	38.14	16.95	6.24E-03	38.25	16.45	6.17E-03
0.9118	38.41	21.06	7.12E-03	38.40	19.79	6.94E-03	38.27	17.67	6.47E-03	38.21	16.67	6.26E-03	38.33	16.23	6.19E-03
0.9206	38.56	21.31	7.29E-03	38.51	19.71	7.02E-03	38.36	17.49	6.51E-03	38.27	16.39	6.27E-03	38.38	15.93	6.20E-03
0.9290	38.70	21.49	7.45E-03	38.59	19.52	7.07E-03	38.42	17.23	6.53E-03	38.31	16.08	6.26E-03	38.39	15.48	6.15E-03
0.9369	38.82	21.60	7.58E-03	38.67	19.31	7.11E-03	38.47	16.97	6.54E-03	38.35	15.77	6.25E-03	38.39	15.02	6.09E-03
0.9444	38.93	21.60	7.68E-03	38.75	19.19	7.16E-03	38.54	16.81	6.57E-03	38.38	15.49	6.24E-03	38.40	14.67	6.06E-03
0.9515	39.02	21.52	7.75E-03	38.83	19.13	7.23E-03	38.61	16.71	6.61E-03	38.41	15.26	6.24E-03	38.41	14.38	6.03E-03
0.9581	39.10	21.45	7.82E-03	38.91	19.11	7.30E-03	38.66	16.59	6.65E-03	38.42	14.94	6.21E-03	38.43	14.14	6.02E-03
0.9642	39.18	21.44	7.90E-03	38.99	19.09	7.37E-03	38.70	16.39	6.65E-03	38.38	14.46	6.12E-03	38.45	13.95	6.01E-03
0.9699	39.26	21.46	7.98E-03	39.06	19.08	7.43E-03	38.71	16.13	6.63E-03	38.30	13.85	5.98E-03	38.48	13.81	6.02E-03
0.9750	39.33	21.50	8.06E-03	39.12	19.08	7.49E-03	38.73	15.91	6.61E-03	38.20	13.24	5.84E-03	38.50	13.70	6.03E-03
0.9798	39.40	21.54	8.14E-03	39.18	19.09	7.55E-03	38.76	15.79	6.62E-03	38.10	12.68	5.70E-03	38.53	13.60	6.04E-03
0.9840	39.46	21.59	8.21E-03	39.24	19.09	7.60E-03	38.89	16.20	6.79E-03	38.01	12.20	5.59E-03	38.55	13.52	6.05E-03
0.9877	39.52	21.63	8.28E-03	39.28	19.10	7.65E-03	39.17	17.42	7.22E-03	37.93	11.80	5.49E-03	38.57	13.45	6.06E-03
0.9910	39.56	21.67	8.34E-03	39.33	19.11	7.69E-03	39.52	19.22	7.83E-03	37.86	11.47	5.41E-03	38.59	13.39	6.06E-03
0.9937	39.61	21.71	8.39E-03	39.36	19.12	7.73E-03	39.88	21.40	8.58E-03	37.81	11.20	5.34E-03	38.61	13.34	6.07E-03
0.9960	39.64	21.74	8.43E-03	39.39	19.13	7.76E-03	40.21	23.82	9.41E-03	37.76	10.98	5.29E-03	38.62	13.30	6.08E-03
0.9977	39.66	21.77	8.46E-03	39.41	19.13	7.78E-03	40.48	26.26	1.03E-02	37.72	10.82	5.25E-03	38.63	13.27	6.08E-03
0.9990	39.68	21.79	8.48E-03	39.43	19.14	7.80E-03	40.68	28.47	1.11E-02	37.70	10.70	5.22E-03	38.64	13.25	6.09E-03
0.9998	39.69	21.80	8.50E-03	39.44	19.14	7.81E-03	40.81	30.06	1.17E-02	37.68	10.64	5.20E-03	38.64	13.24	6.09E-03
1.0000	39.70	21.80	8.50E-03	39.44	19.14	7.81E-03	40.85	30.65	1.19E-02	37.67	10.61	5.20E-03	38.64	13.23	6.09E-03

The local freestream flow direction, twist in the boundary layer and boundary layer displacement thickness from WAKELAG over the upper surface of the DERA wing. $\Lambda = 40°$, $\alpha = 4.6°$, $Re_c = 3.3 \times 10^6$.

η	0.06b			0.16b			0.30b			0.45b			0.59b		
x/c	α_c (°)	β_c (°)	δ^*/c	α_c (°)	β_c (°)	δ^*/c	α_c (°)	β_c (°)	δ^*/c	α_c (°)	β_c (°)	δ^*/c	α_c (°)	β_c (°)	δ^*/c
0.0556	29.79	0.02	1.44E-04	28.73	0.21	1.42E-04	28.04	0.48	1.73E-04						
0.0631	29.77	-0.02	1.75E-04	28.86	0.43	1.76E-04	28.17	0.58	2.00E-04						
0.0710	29.74	-0.07	2.00E-04	28.97	0.51	2.04E-04	28.23	0.53	2.26E-04						
0.0794	29.71	-0.11	2.26E-04	29.02	0.47	2.31E-04	28.21	0.38	2.50E-04						
0.0882	29.70	-0.11	2.55E-04	28.84	0.02	2.51E-04	28.19	0.26	2.76E-04						
0.0974	29.68	-0.11	2.85E-04	28.53	-0.50	2.68E-04	28.19	0.21	3.03E-04						
0.1070	29.64	-0.16	3.11E-04	28.49	-0.49	2.97E-04	28.21	0.21	3.32E-04						
0.1170	29.57	-0.26	3.35E-04	28.50	-0.40	3.27E-04	28.24	0.24	3.62E-04						
0.1274	29.47	-0.39	3.57E-04	28.54	-0.27	3.58E-04	28.28	0.27	3.92E-04						
0.1381	29.37	-0.50	3.80E-04	28.59	-0.16	3.88E-04	28.30	0.27	4.22E-04						
0.1493	29.29	-0.56	4.04E-04	28.62	-0.08	4.18E-04	28.30	0.24	4.49E-04						
0.1607	29.24	-0.57	4.30E-04	28.63	-0.05	4.46E-04	28.29	0.18	4.76E-04						
0.1726	29.20	-0.57	4.58E-04	28.64	-0.03	4.74E-04	28.27	0.13	5.03E-04						
0.1847	29.17	-0.57	4.85E-04	28.64	-0.03	5.02E-04	28.25	0.09	5.31E-04						
0.1972	29.13	-0.56	5.12E-04	28.63	-0.04	5.29E-04	28.25	0.08	5.60E-04						
0.2100	29.08	-0.58	5.39E-04	28.59	-0.10	5.54E-04	28.25	0.07	5.89E-04						
0.2230	29.03	-0.61	5.64E-04	28.52	-0.19	5.77E-04	28.26	0.08	6.20E-04						
0.2364	28.98	-0.62	5.90E-04	28.45	-0.28	6.00E-04	28.29	0.12	6.53E-04						
0.2500	28.97	-0.59	6.20E-04	28.43	-0.29	6.28E-04	28.39	0.27	6.95E-04						
0.2639	29.00	-0.50	6.55E-04	28.51	-0.15	6.68E-04	28.57	0.54	7.47E-04						
0.2780	29.07	-0.36	6.94E-04	28.67	0.11	7.18E-04	28.77	0.83	8.02E-04						
0.2923	29.16	-0.19	7.35E-04	28.86	0.41	7.73E-04	28.95	1.06	8.54E-04						
0.3068	29.25	-0.03	7.77E-04	29.02	0.64	8.23E-04	29.12	1.28	9.07E-04						
0.3216	29.38	0.18	8.25E-04	29.18	0.86	8.74E-04	29.29	1.48	9.59E-04						
0.3365	29.52	0.39	8.74E-04	29.34	1.06	9.24E-04	29.44	1.64	1.01E-03						
0.3515	29.63	0.53	9.17E-04	29.47	1.20	9.70E-04	29.58	1.77	1.06E-03						
0.3668	29.70	0.60	9.55E-04	29.57	1.30	1.01E-03	29.71	1.87	1.10E-03						
0.3821	29.75	0.64	9.90E-04	29.67	1.36	1.05E-03	29.81	1.92	1.15E-03						
0.3976	29.78	0.65	1.02E-03	29.74	1.39	1.09E-03	29.87	1.91	1.18E-03						
0.4132	29.80	0.64	1.05E-03	29.80	1.40	1.13E-03	29.92	1.86	1.21E-03						
0.4288	29.79	0.59	1.08E-03	29.84	1.38	1.16E-03	29.94	1.79	1.24E-03						
0.4446	29.78	0.53	1.10E-03	29.86	1.34	1.19E-03	29.97	1.73	1.27E-03						
0.4604	29.75	0.47	1.13E-03	29.86	1.26	1.21E-03	29.99	1.67	1.30E-03						
0.4762	29.72	0.39	1.15E-03	29.84	1.16	1.24E-03	29.98	1.58	1.32E-03						
0.4921	29.66	0.29	1.17E-03	29.79	1.03	1.25E-03	29.92	1.40	1.33E-03						
0.5079	29.56	0.13	1.17E-03	29.70	0.84	1.26E-03	29.72	1.05	1.32E-03						
0.5238	29.33	-0.17	1.16E-03	29.51	0.53	1.25E-03	29.48	0.66	1.29E-03						
0.5396	29.06	-0.51	1.14E-03	29.26	0.18	1.23E-03	29.24	0.33	1.27E-03						
0.5554	28.80	-0.79	1.12E-03	29.02	-0.13	1.21E-03	28.99	0.00	1.25E-03						
0.5712	28.52	-1.07	1.11E-03	28.73	-0.47	1.18E-03	28.93	-0.07	1.27E-03						
0.5868	28.46	-1.11	1.13E-03	28.67	-0.52	1.21E-03	29.17	0.22	1.35E-03						
0.6024	28.53	-1.00	1.18E-03	28.84	-0.30	1.28E-03	29.53	0.70	1.47E-03						
0.6179	28.65	-0.83	1.24E-03	29.11	0.04	1.37E-03	30.18	1.68	1.68E-03						
0.6332	29.20	-0.11	1.40E-03	29.70	0.87	1.55E-03	31.18	3.49	2.03E-03						
0.6485	30.20	1.47	1.71E-03	30.67	2.50	1.87E-03	31.98	5.24	2.37E-03						
0.6635	30.91	2.79	1.96E-03	31.40	3.97	2.16E-03	32.77	7.25	2.76E-03						
0.6784	31.57	4.20	2.24E-03	32.11	5.58	2.48E-03	33.47	9.35	3.18E-03						
0.6932	32.18	5.65	2.52E-03	32.76	7.26	2.82E-03	34.07	11.27	3.59E-03						
0.7077	32.74	7.11	2.81E-03	33.33	8.91	3.16E-03	34.64	13.30	4.04E-03						
0.7220	33.28	8.64	3.13E-03	33.89	10.65	3.53E-03	35.15	15.26	4.49E-03						
0.7361	33.79	10.20	3.46E-03	34.40	12.40	3.92E-03	35.56	16.73	4.88E-03						
0.7500	34.26	11.68	3.79E-03	34.86	13.99	4.30E-03	35.89	17.72	5.18E-03						
0.7636	34.68	13.07	4.12E-03	35.26	15.44	4.66E-03	36.18	18.50	5.46E-03						
0.7770	35.07	14.40	4.46E-03	35.64	16.83	5.03E-03	36.42	18.97	5.69E-03						
0.7900	35.45	15.69	4.80E-03	35.98	18.01	5.38E-03	36.62	19.08	5.84E-03						
0.8028	35.81	16.96	5.15E-03	36.26	18.81	5.66E-03	36.78	18.95	5.94E-03						
0.8153	36.16	18.24	5.53E-03	36.50	19.29	5.89E-03	36.89	18.54	5.97E-03						
0.8274	36.46	19.21	5.85E-03	36.72	19.68	6.10E-03	36.97	17.99	5.96E-03						
0.8393	36.73	19.96	6.14E-03	36.92	19.95	6.29E-03	37.04	17.49	5.96E-03						
0.8507	36.98	20.64	6.42E-03	37.09	19.98	6.43E-03	37.11	17.02	5.95E-03						
0.8619	37.20	21.14	6.67E-03	37.23	19.86	6.52E-03	37.18	16.60	5.95E-03						
0.8726	37.38	21.39	6.86E-03	37.35	19.64	6.59E-03	37.23	16.13	5.93E-03						
0.8830	37.55	21.57	7.03E-03	37.45	19.34	6.63E-03	37.25	15.58	5.87E-03						
0.8930	37.71	21.75	7.20E-03	37.53	18.98	6.65E-03	37.28	15.18	5.86E-03						
0.9026	37.85	21.87	7.35E-03	37.61	18.62	6.67E-03	37.36	15.04	5.90E-03						
0.9118	37.99	21.95	7.48E-03	37.67	18.28	6.68E-03	37.42	14.82	5.92E-03						
0.9206	38.11	21.96	7.60E-03	37.74	17.96	6.68E-03	37.42	14.39	5.87E-03						
0.9290	38.22	21.93	7.70E-03	37.79	17.63	6.68E-03	37.41	13.96	5.81E-03						
0.9369	38.32	21.85	7.79E-03	37.83	17.33	6.68E-03	37.43	13.70	5.80E-03						
0.9444	38.41	21.74	7.86E-03	37.88	17.09	6.69E-03	37.47	13.57	5.82E-03						
0.9515	38.49	21.60	7.91E-03	37.93	16.88	6.70E-03	37.50	13.42	5.83E-03						
0.9581	38.56	21.46	7.96E-03	37.98	16.70	6.71E-03	37.50	13.17	5.80E-03						
0.9642	38.62	21.35	8.01E-03	38.02	16.55	6.73E-03	37.49	12.88	5.75E-03						
0.9699	38.69	21.25	8.05E-03	38.06	16.41	6.75E-03	37.46	12.61	5.71E-03						
0.9750	38.74	21.17	8.10E-03	38.09	16.29	6.76E-03	37.45	12.41	5.68E-03						
0.9798	38.79	21.10	8.14E-03	38.13	16.19	6.78E-03	37.65	12.97	5.90E-03						
0.9840	38.84	21.04	8.18E-03	38.16	16.10	6.79E-03	38.17	14.88	6.54E-03						
0.9877	38.88	20.99	8.21E-03	38.18	16.02	6.80E-03	38.84	18.01	7.59E-03						
0.9910	38.92	20.94	8.24E-03	38.21	15.96	6.82E-03	39.56	22.56	9.15E-03						
0.9937	38.95	20.91	8.27E-03	38.23	15.91	6.83E-03	40.25	29.28	1.16E-02						
0.9960	38.97	20.89	8.29E-03	38.24	15.86	6.83E-03	40.83	45.62	1.85E-02						
0.9977	38.99	20.87	8.31E-03	38.26	15.83	6.84E-03	41.28	39.32	1.73E-02						
0.9990	39.00	20.85	8.32E-03	38.26	15.81	6.85E-03	41.55								
0.9998	39.01	20.84	8.33E-03	38.27	15.79	6.85E-03	41.64								
1.0000	39.02	20.84	8.33E-03	38.27	15.79	6.85E-03									

The local freestream flow direction, twist in the boundary layer and boundary layer displacement thickness from WAKELAG over the upper surface of the DERA wing. $\Lambda = 40°$, $\alpha = 6.8°$, $Re_c = 3.3 \times 10^6$.

η	0.06b			0.16b			0.30b			0.45b			0.59b		
x/c	α_c (°)	β_c (°)	δ^*/c	α_c (°)	β_c (°)	δ^*/c	α_c (°)	β_c (°)	δ^*/c	α_c (°)	β_c (°)	δ^*/c	α_c (°)	β_c (°)	δ^*/c
0.0556	28.70	0.10	1.41E-04				26.78	0.36	1.37E-04	26.42	0.41	1.36E-04	26.50	0.27	1.34E-04
0.0631	28.75	0.17	1.73E-04				27.01	0.77	1.71E-04	26.68	0.85	1.71E-04	26.66	0.54	1.65E-04
0.0710	28.79	0.19	1.99E-04				27.22	0.95	2.00E-04	26.91	1.04	2.01E-04	26.80	0.67	1.91E-04
0.0794	28.83	0.20	2.27E-04				27.33	0.90	2.27E-04	27.05	1.00	2.30E-04	26.92	0.70	2.18E-04
0.0882	28.86	0.21	2.57E-04				27.35	0.72	2.52E-04	27.09	0.83	2.58E-04	27.00	0.68	2.49E-04
0.0974	28.88	0.21	2.87E-04				27.36	0.59	2.78E-04	27.13	0.72	2.87E-04	27.08	0.65	2.84E-04
0.1070	28.88	0.16	3.14E-04				27.39	0.54	3.06E-04	27.18	0.68	3.16E-04	27.13	0.62	3.14E-04
0.1170	28.84	0.07	3.39E-04				27.44	0.54	3.36E-04	27.25	0.70	3.46E-04	27.16	0.57	3.42E-04
0.1274	28.77	-0.05	3.62E-04				27.51	0.57	3.67E-04	27.33	0.74	3.77E-04	27.18	0.52	3.69E-04
0.1381	28.71	-0.16	3.85E-04				27.57	0.61	3.98E-04	27.41	0.78	4.08E-04	27.20	0.48	3.96E-04
0.1493	28.65	-0.22	4.10E-04				27.63	0.62	4.29E-04	27.47	0.80	4.38E-04	27.24	0.48	4.25E-04
0.1607	28.63	-0.24	4.37E-04				27.66	0.59	4.58E-04	27.52	0.78	4.68E-04	27.32	0.57	4.59E-04
0.1726	28.61	-0.24	4.65E-04				27.67	0.55	4.87E-04	27.56	0.76	4.97E-04	27.45	0.72	4.97E-04
0.1847	28.59	-0.24	4.94E-04				27.69	0.52	5.15E-04	27.59	0.73	5.26E-04	27.59	0.89	5.36E-04
0.1972	28.58	-0.24	5.22E-04				27.71	0.49	5.45E-04	27.63	0.72	5.57E-04	27.71	1.01	5.74E-04
0.2100	28.56	-0.25	5.49E-04				27.73	0.48	5.75E-04	27.68	0.73	5.88E-04	27.78	1.03	6.07E-04
0.2230	28.52	-0.28	5.76E-04				27.75	0.47	6.06E-04	27.73	0.74	6.21E-04	27.83	1.01	6.37E-04
0.2364	28.50	-0.29	6.03E-04				27.78	0.47	6.37E-04	27.79	0.77	6.55E-04	27.88	0.99	6.68E-04
0.2500	28.50	-0.26	6.34E-04				27.83	0.51	6.72E-04	27.86	0.83	6.91E-04	27.95	1.02	7.03E-04
0.2639	28.55	-0.17	6.69E-04				27.95	0.66	7.15E-04	27.99	0.97	7.34E-04	28.07	1.14	7.46E-04
0.2780	28.64	-0.02	7.10E-04				28.14	0.92	7.68E-04	28.16	1.19	7.85E-04	28.24	1.34	7.96E-04
0.2923	28.75	0.15	7.54E-04				28.35	1.21	8.25E-04	28.36	1.43	8.39E-04	28.44	1.58	8.51E-04
0.3068	28.86	0.32	7.98E-04				28.54	1.45	8.80E-04	28.54	1.65	8.93E-04	28.65	1.83	9.09E-04
0.3216	29.01	0.53	8.47E-04				28.74	1.69	9.35E-04	28.74	1.89	9.50E-04	28.91	2.17	9.76E-04
0.3365	29.16	0.74	8.97E-04				28.93	1.91	9.92E-04	28.95	2.12	1.01E-03	29.18	2.52	1.05E-03
0.3515	29.28	0.88	9.42E-04				29.10	2.08	1.05E-03	29.14	2.33	1.07E-03	29.40	2.76	1.11E-03
0.3668	29.36	0.96	9.82E-04				29.25	2.21	1.10E-03	29.33	2.52	1.13E-03	29.58	2.90	1.17E-03
0.3821	29.43	1.01	1.02E-03				29.39	2.31	1.15E-03	29.52	2.69	1.18E-03	29.73	3.00	1.22E-03
0.3976	29.48	1.02	1.05E-03				29.51	2.37	1.19E-03	29.67	2.79	1.24E-03	29.87	3.06	1.27E-03
0.4132	29.51	1.00	1.08E-03				29.59	2.36	1.23E-03	29.78	2.81	1.28E-03	29.99	3.09	1.31E-03
0.4288	29.51	0.95	1.11E-03				29.65	2.32	1.26E-03	29.86	2.79	1.32E-03	30.10	3.10	1.36E-03
0.4446	29.50	0.88	1.14E-03				29.70	2.26	1.29E-03	29.93	2.74	1.35E-03	30.20	3.09	1.40E-03
0.4604	29.49	0.81	1.16E-03				29.75	2.21	1.33E-03	29.97	2.66	1.38E-03	30.27	3.05	1.44E-03
0.4762	29.47	0.74	1.18E-03				29.79	2.17	1.36E-03	30.00	2.57	1.41E-03	30.34	3.01	1.47E-03
0.4921	29.43	0.64	1.20E-03				29.81	2.09	1.39E-03	30.01	2.44	1.43E-03	30.38	2.92	1.50E-03
0.5079	29.33	0.47	1.21E-03				29.76	1.91	1.40E-03	29.97	2.25	1.45E-03	30.36	2.72	1.52E-03
0.5238	29.12	0.16	1.20E-03				29.58	1.54	1.38E-03	29.83	1.92	1.44E-03	30.24	2.39	1.51E-03
0.5396	28.86	-0.18	1.18E-03				29.36	1.14	1.36E-03	29.63	1.54	1.41E-03	30.09	2.05	1.49E-03
0.5554	28.62	-0.46	1.16E-03				29.16	0.83	1.34E-03	29.45	1.22	1.40E-03	29.98	1.79	1.49E-03
0.5712	28.37	-0.74	1.15E-03				28.96	0.53	1.32E-03	29.35	1.03	1.40E-03	29.88	1.58	1.49E-03
0.5868	28.31	-0.78	1.17E-03				28.91	0.46	1.34E-03	29.40	1.06	1.44E-03	29.89	1.53	1.52E-03
0.6024	28.41	-0.64	1.23E-03				29.18	0.80	1.44E-03	29.72	1.49	1.55E-03	30.28	2.08	1.66E-03
0.6179	28.56	-0.45	1.29E-03				29.60	1.37	1.57E-03	30.19	2.17	1.71E-03	30.88	3.01	1.86E-03
0.6332	29.12	0.32	1.46E-03				30.30	2.47	1.81E-03	30.98	3.53	2.00E-03	31.78	4.72	2.21E-03
0.6485	30.14	1.98	1.78E-03				31.33	4.48	2.20E-03	32.10	5.95	2.47E-03	32.98	7.64	2.78E-03
0.6635	30.87	3.38	2.06E-03				32.16	6.44	2.59E-03	32.99	8.32	2.94E-03	33.85	10.24	3.31E-03
0.6784	31.54	4.87	2.35E-03				32.97	8.74	3.04E-03	33.86	11.19	3.52E-03	34.68	13.29	3.94E-03
0.6932	32.16	6.42	2.66E-03				33.69	11.09	3.52E-03	34.57	13.90	4.09E-03	35.32	15.89	4.52E-03
0.7077	32.73	7.97	2.98E-03				34.26	13.07	3.96E-03	35.00	15.40	4.46E-03	35.65	16.81	4.80E-03
0.7220	33.28	9.59	3.32E-03				34.79	15.12	4.43E-03	35.37	16.57	4.79E-03	35.90	17.22	5.00E-03
0.7361	33.79	11.24	3.67E-03				35.26	16.99	4.89E-03	35.69	17.41	5.08E-03	36.10	17.33	5.15E-03
0.7500	34.25	12.81	4.03E-03				35.60	18.09	5.22E-03	35.91	17.69	5.25E-03	36.25	17.08	5.22E-03
0.7636	34.68	14.31	4.39E-03				35.83	18.44	5.41E-03	36.06	17.52	5.33E-03	36.33	16.53	5.21E-03
0.7770	35.08	15.77	4.76E-03				36.03	18.51	5.55E-03	36.17	17.16	5.37E-03	36.37	15.84	5.17E-03
0.7900	35.45	17.14	5.13E-03				36.19	18.36	5.65E-03	36.25	16.64	5.37E-03	36.40	15.15	5.11E-03
0.8028	35.78	18.31	5.48E-03				36.31	18.04	5.70E-03	36.30	15.99	5.33E-03	36.43	14.53	5.07E-03
0.8153	36.08	19.29	5.81E-03				36.42	17.63	5.73E-03	36.32	15.21	5.26E-03	36.47	13.98	5.04E-03
0.8274	36.36	20.08	6.10E-03				36.49	17.02	5.70E-03	36.36	14.67	5.23E-03	36.47	13.37	4.98E-03
0.8393	36.60	20.70	6.37E-03				36.53	16.35	5.65E-03	36.41	14.23	5.22E-03	36.46	12.76	4.92E-03
0.8507	36.82	21.21	6.62E-03				36.58	15.86	5.63E-03	36.42	13.65	5.16E-03	36.47	12.34	4.89E-03
0.8619	37.02	21.54	6.83E-03				36.63	15.38	5.62E-03	36.41	13.08	5.10E-03	36.48	11.93	4.86E-03
0.8726	37.19	21.63	6.99E-03				36.66	14.90	5.58E-03	36.40	12.59	5.05E-03	36.45	11.44	4.80E-03
0.8830	37.33	21.63	7.12E-03				36.67	14.36	5.53E-03	36.39	12.10	4.99E-03	36.43	11.02	4.76E-03
0.8930	37.47	21.59	7.23E-03				36.65	13.74	5.45E-03	36.35	11.59	4.92E-03	36.43	10.70	4.73E-03
0.9026	37.58	21.50	7.32E-03				36.65	13.29	5.40E-03	36.32	11.17	4.87E-03	36.41	10.38	4.70E-03
0.9118	37.69	21.38	7.40E-03				36.70	13.09	5.42E-03	36.32	10.87	4.85E-03	36.39	10.06	4.66E-03
0.9206	37.79	21.22	7.47E-03				36.73	12.84	5.41E-03	36.31	10.57	4.82E-03	36.35	9.73	4.62E-03
0.9290	37.88	21.04	7.53E-03				36.69	12.38	5.34E-03	36.27	10.25	4.77E-03	36.30	9.39	4.57E-03
0.9369	37.96	20.85	7.57E-03				36.65	11.94	5.27E-03	36.23	9.91	4.72E-03	36.25	9.07	4.51E-03
0.9444	38.04	20.67	7.62E-03				36.65	11.69	5.25E-03	36.17	9.56	4.66E-03	36.19	8.78	4.46E-03
0.9515	38.11	20.51	7.66E-03				36.69	11.58	5.27E-03	36.08	9.16	4.58E-03	36.13	8.49	4.41E-03
0.9581	38.17	20.38	7.71E-03				36.72	11.48	5.28E-03	36.03	8.88	4.53E-03	36.09	8.28	4.38E-03
0.9642	38.24	20.30	7.76E-03				36.72	11.30	5.27E-03	36.03	8.77	4.53E-03	36.08	8.15	4.37E-03
0.9699	38.31	20.26	7.82E-03				36.71	11.10	5.24E-03	36.08	8.77	4.56E-03	36.09	8.07	4.37E-03
0.9750	38.37	20.24	7.88E-03				36.70	10.91	5.22E-03	36.14	8.83	4.60E-03	36.10	8.03	4.38E-03
0.9798	38.43	20.23	7.94E-03				36.69	10.76	5.21E-03	36.20	8.90	4.65E-03	36.12	7.99	4.40E-03
0.9840	38.48	20.23	7.99E-03				36.92	11.38	5.43E-03	36.26	8.97	4.70E-03	36.14	7.97	4.41E-03
0.9877	38.53	20.23	8.04E-03				37.53	13.38	6.10E-03	36.31	9.03	4.74E-03	36.16	7.95	4.42E-03
0.9910	38.57	20.23	8.08E-03				38.33	16.74	7.23E-03	36.36	9.08	4.77E-03	36.17	7.93	4.43E-03
0.9937	38.60	20.24	8.12E-03				39.20	21.84	8.98E-03	36.40	9.13	4.80E-03	36.18	7.91	4.44E-03
0.9960	38.63	20.24	8.15E-03				40.03	30.01	1.19E-02	36.43	9.17	4.83E-03	36.19	7.90	4.45E-03
0.9977	38.66	20.25	8.18E-03				40.75	28.96	1.29E-02	36.45	9.20	4.85E-03	36.20	7.89	4.45E-03
0.9990	38.67	20.25	8.19E-03				41.30	42.29	1.90E-02	36.47	9.22	4.86E-03	36.20	7.88	4.46E-03
0.9998	38.68	20.25	8.20E-03				41.64	87.94	1.00E+00	36.48	9.24	4.87E-03	36.21	7.88	4.46E-03
1.0000	38.68	20.25	8.21E-03				41.76	88.04	2.32E+00	36.48	9.24	4.87E-03	36.21	7.88	4.46E-03

The local freestream flow direction, twist in the boundary layer and boundary layer displacement thickness from WAKELAG over the upper surface of the DERA wing. $\Lambda = 40°$, $\alpha = 7.8°$, $Re_c = 3.3 \times 10^6$.

η	0.06b			0.16b			0.30b			0.45b			0.59b		
x/c	α_c (°)	β_c (°)	δ^*/c	α_c (°)	β_c (°)	δ^*/c	α_c (°)	β_c (°)	δ^*/c	α_c (°)	β_c (°)	δ^*/c	α_c (°)	β_c (°)	δ^*/c
0.0556				26.12	0.24	1.33E-04	25.25	0.28	1.31E-04	24.86	0.36	1.30E-04	24.81	0.35	1.29E-04
0.0631				26.27	0.49	1.66E-04	25.41	0.53	1.62E-04	25.07	0.70	1.63E-04	25.01	0.68	1.60E-04
0.0710				26.40	0.59	1.93E-04	25.55	0.66	1.89E-04	25.27	0.85	1.91E-04	25.19	0.85	1.86E-04
0.0794				26.46	0.52	2.20E-04	25.68	0.72	2.17E-04	25.43	0.92	2.21E-04	25.37	0.94	2.14E-04
0.0882				26.41	0.30	2.45E-04	25.79	0.75	2.46E-04	25.56	0.94	2.53E-04	25.53	1.00	2.48E-04
0.0974				26.33	0.11	2.70E-04	25.89	0.78	2.75E-04	25.69	0.97	2.86E-04	25.69	1.05	2.85E-04
0.1070				26.33	0.07	2.98E-04	26.00	0.84	3.06E-04	25.82	1.03	3.18E-04	25.81	1.07	3.18E-04
0.1170				26.40	0.19	3.29E-04	26.13	0.93	3.39E-04	25.95	1.10	3.50E-04	25.91	1.08	3.49E-04
0.1274				26.53	0.40	3.64E-04	26.25	1.01	3.72E-04	26.07	1.17	3.82E-04	26.00	1.08	3.78E-04
0.1381				26.68	0.61	3.99E-04	26.37	1.08	4.06E-04	26.20	1.24	4.15E-04	26.09	1.09	4.09E-04
0.1493				26.80	0.75	4.33E-04	26.47	1.11	4.38E-04	26.31	1.28	4.47E-04	26.20	1.15	4.42E-04
0.1607				26.88	0.79	4.64E-04	26.55	1.10	4.69E-04	26.41	1.30	4.79E-04	26.34	1.26	4.79E-04
0.1726				26.96	0.83	4.95E-04	26.61	1.08	5.00E-04	26.50	1.31	5.12E-04	26.51	1.42	5.19E-04
0.1847				27.03	0.85	5.27E-04	26.67	1.06	5.31E-04	26.59	1.32	5.45E-04	26.69	1.58	5.61E-04
0.1972				27.08	0.85	5.57E-04	26.73	1.05	5.63E-04	26.68	1.34	5.79E-04	26.84	1.70	6.01E-04
0.2100				27.10	0.80	5.85E-04	26.80	1.06	5.96E-04	26.77	1.38	6.14E-04	26.95	1.72	6.36E-04
0.2230				27.10	0.72	6.11E-04	26.86	1.07	6.30E-04	26.87	1.41	6.50E-04	27.04	1.71	6.70E-04
0.2364				27.10	0.66	6.38E-04	26.94	1.10	6.65E-04	26.97	1.45	6.87E-04	27.13	1.71	7.05E-04
0.2500				27.13	0.64	6.69E-04	27.03	1.16	7.03E-04	27.09	1.54	7.28E-04	27.25	1.76	7.44E-04
0.2639				27.24	0.77	7.11E-04	27.18	1.32	7.50E-04	27.26	1.70	7.76E-04	27.41	1.91	7.92E-04
0.2780				27.46	1.06	7.68E-04	27.40	1.59	8.06E-04	27.47	1.95	8.32E-04	27.63	2.16	8.49E-04
0.2923				27.70	1.40	8.30E-04	27.63	1.89	8.67E-04	27.70	2.23	8.93E-04	27.88	2.45	9.13E-04
0.3068				27.90	1.66	8.87E-04	27.85	2.14	9.26E-04	27.93	2.48	9.53E-04	28.14	2.76	9.79E-04
0.3216				28.10	1.89	9.43E-04	28.07	2.39	9.86E-04	28.16	2.74	1.02E-03	28.44	3.14	1.06E-03
0.3365				28.30	2.10	1.00E-03	28.28	2.62	1.05E-03	28.39	2.99	1.08E-03	28.74	3.53	1.14E-03
0.3515				28.46	2.26	1.05E-03	28.48	2.81	1.11E-03	28.62	3.21	1.14E-03	29.00	3.81	1.21E-03
0.3668				28.61	2.37	1.10E-03	28.66	2.96	1.16E-03	28.83	3.42	1.21E-03	29.22	3.99	1.27E-03
0.3821				28.75	2.46	1.15E-03	28.84	3.09	1.22E-03	29.04	3.61	1.27E-03	29.42	4.13	1.33E-03
0.3976				28.86	2.51	1.19E-03	28.99	3.17	1.27E-03	29.23	3.75	1.33E-03	29.60	4.23	1.39E-03
0.4132				28.96	2.52	1.24E-03	29.10	3.19	1.32E-03	29.40	3.83	1.39E-03	29.78	4.31	1.45E-03
0.4288				29.04	2.51	1.28E-03	29.20	3.18	1.36E-03	29.55	3.89	1.44E-03	29.94	4.37	1.51E-03
0.4446				29.11	2.48	1.31E-03	29.29	3.15	1.40E-03	29.67	3.90	1.49E-03	30.09	4.42	1.56E-03
0.4604				29.15	2.41	1.34E-03	29.38	3.13	1.44E-03	29.78	3.88	1.54E-03	30.24	4.46	1.62E-03
0.4762				29.18	2.33	1.37E-03	29.46	3.12	1.48E-03	29.87	3.83	1.58E-03	30.39	4.51	1.68E-03
0.4921				29.18	2.21	1.39E-03	29.52	3.05	1.51E-03	29.93	3.75	1.61E-03	30.51	4.50	1.73E-03
0.5079				29.14	2.03	1.41E-03	29.50	2.87	1.53E-03	29.97	3.62	1.64E-03	30.55	4.35	1.75E-03
0.5238				29.00	1.72	1.40E-03	29.40	2.55	1.52E-03	29.94	3.40	1.65E-03	30.53	4.08	1.76E-03
0.5396				28.83	1.39	1.38E-03	29.26	2.21	1.51E-03	29.89	3.15	1.66E-03	30.50	3.84	1.77E-03
0.5554				28.67	1.10	1.37E-03	29.15	1.94	1.50E-03	29.85	2.93	1.66E-03	30.54	3.73	1.80E-03
0.5712				28.49	0.82	1.36E-03	29.04	1.72	1.50E-03	29.84	2.80	1.68E-03	30.64	3.77	1.85E-03
0.5868				28.45	0.74	1.38E-03	29.04	1.66	1.53E-03	29.94	2.86	1.73E-03	30.84	3.98	1.94E-03
0.6024				28.71	1.06	1.47E-03	29.43	2.18	1.66E-03	30.45	3.66	1.92E-03	31.47	5.09	2.18E-03
0.6179				29.10	1.60	1.61E-03	30.00	3.09	1.86E-03	31.18	5.01	2.21E-03	32.32	6.92	2.57E-03
0.6332				29.78	2.68	1.84E-03	30.84	4.66	2.19E-03	32.21	7.38	2.69E-03	33.40	9.85	3.17E-03
0.6485				30.78	4.64	2.24E-03	31.93	7.29	2.70E-03	33.37	10.89	3.39E-03	34.46	13.56	3.94E-03
0.6635				31.58	6.52	2.62E-03	32.78	9.75	3.20E-03	34.02	13.02	3.87E-03	34.89	14.83	4.28E-03
0.6784				32.36	8.69	3.06E-03	33.59	12.65	3.80E-03	34.59	15.13	4.36E-03	35.25	15.80	4.58E-03
0.6932				33.05	10.89	3.52E-03	34.23	15.17	4.35E-03	35.01	16.52	4.74E-03	35.51	16.22	4.78E-03
0.7077				33.58	12.69	3.93E-03	34.58	16.21	4.65E-03	35.20	16.56	4.86E-03	35.64	15.93	4.84E-03
0.7220				34.07	14.51	4.35E-03	34.85	16.82	4.89E-03	35.32	16.16	4.90E-03	35.71	15.31	4.82E-03
0.7361				34.51	16.17	4.77E-03	35.08	17.13	5.06E-03	35.40	15.62	4.90E-03	35.74	14.61	4.78E-03
0.7500				34.84	17.24	5.08E-03	35.24	16.99	5.15E-03	35.46	15.03	4.88E-03	35.77	13.96	4.74E-03
0.7636				35.08	17.74	5.29E-03	35.33	16.48	5.16E-03	35.50	14.45	4.86E-03	35.79	13.39	4.70E-03
0.7770				35.28	18.02	5.46E-03	35.39	15.81	5.13E-03	35.53	13.86	4.82E-03	35.80	12.84	4.66E-03
0.7900				35.45	18.04	5.59E-03	35.43	15.14	5.09E-03	35.53	13.24	4.76E-03	35.80	12.31	4.62E-03
0.8028				35.59	17.81	5.65E-03	35.47	14.58	5.06E-03	35.51	12.58	4.69E-03	35.79	11.81	4.58E-03
0.8153				35.68	17.39	5.67E-03	35.53	14.13	5.05E-03	35.46	11.88	4.60E-03	35.78	11.31	4.53E-03
0.8274				35.77	16.96	5.69E-03	35.51	13.43	4.97E-03	35.44	11.35	4.55E-03	35.78	10.91	4.51E-03
0.8393				35.85	16.52	5.69E-03	35.46	12.65	4.87E-03	35.43	10.91	4.51E-03	35.78	10.57	4.49E-03
0.8507				35.91	16.03	5.68E-03	35.45	12.14	4.81E-03	35.39	10.43	4.45E-03	35.77	10.19	4.45E-03
0.8619				35.95	15.55	5.65E-03	35.44	11.69	4.77E-03	35.34	9.96	4.39E-03	35.74	9.82	4.42E-03
0.8726				35.99	15.09	5.63E-03	35.43	11.24	4.73E-03	35.29	9.54	4.34E-03	35.71	9.49	4.38E-03
0.8830				36.02	14.63	5.60E-03	35.38	10.74	4.66E-03	35.22	9.12	4.28E-03	35.67	9.15	4.34E-03
0.8930				36.04	14.19	5.56E-03	35.27	10.12	4.54E-03	35.14	8.69	4.21E-03	35.62	8.82	4.30E-03
0.9026				36.04	13.75	5.52E-03	35.18	9.60	4.45E-03	35.06	8.30	4.14E-03	35.57	8.51	4.25E-03
0.9118				36.03	13.28	5.46E-03	35.13	9.22	4.40E-03	34.99	7.96	4.09E-03	35.52	8.24	4.22E-03
0.9206				36.02	12.88	5.42E-03	35.06	8.86	4.34E-03	34.92	7.65	4.04E-03	35.48	7.99	4.19E-03
0.9290				36.03	12.57	5.39E-03	34.97	8.44	4.26E-03	34.84	7.34	3.98E-03	35.43	7.76	4.15E-03
0.9369				36.04	12.31	5.38E-03	34.87	8.07	4.18E-03	34.76	7.07	3.93E-03	35.39	7.54	4.12E-03
0.9444				36.05	12.07	5.36E-03	34.83	7.84	4.15E-03	34.70	6.85	3.90E-03	35.35	7.35	4.09E-03
0.9515				36.05	11.84	5.34E-03	34.81	7.68	4.14E-03	34.66	6.67	3.87E-03	35.31	7.17	4.07E-03
0.9581				36.05	11.63	5.32E-03	34.82	7.58	4.14E-03	34.64	6.55	3.86E-03	35.28	7.04	4.06E-03
0.9642				36.05	11.45	5.31E-03	34.84	7.54	4.16E-03	34.67	6.54	3.88E-03	35.29	6.98	4.06E-03
0.9699				36.05	11.28	5.29E-03	34.89	7.56	4.19E-03	34.75	6.64	3.94E-03	35.32	6.97	4.08E-03
0.9750				36.06	11.14	5.28E-03	34.94	7.60	4.23E-03	34.86	6.80	4.01E-03	35.35	6.98	4.11E-03
0.9798				36.06	11.01	5.27E-03	34.99	7.64	4.26E-03	34.97	6.97	4.09E-03	35.39	7.00	4.14E-03
0.9840				36.06	10.90	5.27E-03	35.32	8.35	4.51E-03	35.07	7.14	4.16E-03	35.42	7.03	4.16E-03
0.9877				36.06	10.80	5.26E-03	36.12	10.45	5.21E-03	35.16	7.29	4.23E-03	35.45	7.04	4.19E-03
0.9910				36.06	10.72	5.25E-03	37.19	14.08	6.43E-03	35.24	7.42	4.29E-03	35.48	7.06	4.21E-03
0.9937				36.06	10.65	5.25E-03	38.38	20.02	8.43E-03	35.31	7.53	4.34E-03	35.50	7.08	4.22E-03
0.9960				36.06	10.59	5.25E-03	39.54	31.12	1.24E-02	35.37	7.63	4.38E-03	35.52	7.09	4.24E-03
0.9977				36.06	10.55	5.24E-03	40.56	49.18	2.36E-02	35.41	7.70	4.41E-03	35.53	7.10	4.25E-03
0.9990				36.06	10.52	5.24E-03	41.37	36.76	1.94E-02	35.44	7.76	4.44E-03	35.54	7.10	4.25E-03
0.9998				36.06	10.50	5.24E-03	41.87			35.46	7.79	4.45E-03	35.55	7.11	4.26E-03
1.0000				36.06	10.50	5.24E-03	42.05			35.47	7.80	4.45E-03	35.55	7.11	4.26E-03

The local freestream flow direction, twist in the boundary layer and boundary layer displacement thickness from WAKELAG over the upper surface of the DERA wing. $\Lambda = 40°$, $\alpha = 10.0°$, $Re_c = 3.3 \times 10^6$.

η	0.06b			0.16b			0.30b			0.45b			0.59b		
x/c	α_c (°)	β_c (°)	δ^*/c	α_c (°)	β_c (°)	δ^*/c	α_c (°)	β_c (°)	δ^*/c	α_c (°)	β_c (°)	δ^*/c	α_c (°)	β_c (°)	δ^*/c
0.0556	25.47	0.24	1.31E-04	24.31	0.47	1.29E-04	23.60	0.43	1.26E-04	23.28	0.48	1.25E-04	23.28	0.49	1.25E-04
0.0631	25.60	0.44	1.62E-04	24.61	0.96	1.63E-04	23.85	0.83	1.59E-04	23.55	0.92	1.58E-04	23.55	0.95	1.56E-04
0.0710	25.72	0.54	1.90E-04	24.87	1.16	1.93E-04	24.08	1.03	1.87E-04	23.81	1.13	1.88E-04	23.82	1.20	1.84E-04
0.0794	25.86	0.64	2.19E-04	25.01	1.10	2.22E-04	24.28	1.13	2.17E-04	24.04	1.24	2.20E-04	24.06	1.33	2.14E-04
0.0882	26.02	0.78	2.53E-04	25.04	0.87	2.48E-04	24.46	1.19	2.47E-04	24.24	1.30	2.54E-04	24.28	1.39	2.49E-04
0.0974	26.17	0.90	2.87E-04	25.07	0.74	2.77E-04	24.62	1.26	2.79E-04	24.42	1.37	2.88E-04	24.49	1.44	2.88E-04
0.1070	26.26	0.90	3.17E-04	25.13	0.71	3.06E-04	24.79	1.33	3.12E-04	24.61	1.47	3.23E-04	24.66	1.49	3.23E-04
0.1170	26.33	0.87	3.45E-04	25.25	0.83	3.39E-04	24.96	1.43	3.46E-04	24.79	1.58	3.57E-04	24.82	1.53	3.56E-04
0.1274	26.38	0.83	3.73E-04	25.43	1.03	3.75E-04	25.12	1.52	3.81E-04	24.97	1.69	3.92E-04	24.96	1.57	3.88E-04
0.1381	26.43	0.80	4.01E-04	25.61	1.23	4.13E-04	25.28	1.60	4.16E-04	25.14	1.78	4.27E-04	25.10	1.62	4.21E-04
0.1493	26.48	0.79	4.30E-04	25.77	1.36	4.48E-04	25.42	1.63	4.51E-04	25.30	1.85	4.62E-04	25.26	1.71	4.57E-04
0.1607	26.54	0.80	4.61E-04	25.89	1.40	4.81E-04	25.54	1.64	4.84E-04	25.44	1.89	4.97E-04	25.45	1.85	4.98E-04
0.1726	26.61	0.82	4.92E-04	26.00	1.44	5.15E-04	25.64	1.64	5.18E-04	25.58	1.91	5.33E-04	25.65	2.03	5.41E-04
0.1847	26.67	0.84	5.24E-04	26.10	1.46	5.48E-04	25.75	1.64	5.52E-04	25.71	1.94	5.69E-04	25.87	2.21	5.86E-04
0.1972	26.73	0.86	5.56E-04	26.19	1.46	5.81E-04	25.85	1.65	5.87E-04	25.84	1.99	6.06E-04	26.06	2.35	6.29E-04
0.2100	26.78	0.86	5.87E-04	26.26	1.42	6.12E-04	25.96	1.68	6.24E-04	25.98	2.04	6.45E-04	26.22	2.40	6.69E-04
0.2230	26.82	0.84	6.18E-04	26.30	1.36	6.41E-04	26.07	1.71	6.61E-04	26.12	2.09	6.85E-04	26.36	2.43	7.08E-04
0.2364	26.86	0.83	6.49E-04	26.34	1.31	6.71E-04	26.18	1.76	7.00E-04	26.26	2.16	7.26E-04	26.50	2.46	7.48E-04
0.2500	26.92	0.86	6.84E-04	26.41	1.31	7.05E-04	26.32	1.85	7.43E-04	26.42	2.28	7.72E-04	26.66	2.55	7.94E-04
0.2639	27.02	0.96	7.24E-04	26.55	1.45	7.51E-04	26.51	2.03	7.94E-04	26.63	2.48	8.26E-04	26.88	2.74	8.48E-04
0.2780	27.17	1.13	7.70E-04	26.78	1.74	8.10E-04	26.74	2.31	8.54E-04	26.88	2.76	8.88E-04	27.14	3.02	9.12E-04
0.2923	27.33	1.32	8.20E-04	27.04	2.08	8.75E-04	27.00	2.61	9.18E-04	27.15	3.07	9.55E-04	27.42	3.36	9.83E-04
0.3068	27.50	1.51	8.71E-04	27.27	2.33	9.36E-04	27.24	2.88	9.82E-04	27.41	3.36	1.02E-03	27.72	3.71	1.06E-03
0.3216	27.69	1.73	9.26E-04	27.48	2.57	9.96E-04	27.49	3.15	1.05E-03	27.68	3.65	1.09E-03	28.05	4.14	1.14E-03
0.3365	27.88	1.94	9.83E-04	27.70	2.79	1.06E-03	27.74	3.42	1.12E-03	27.95	3.96	1.17E-03	28.39	4.60	1.24E-03
0.3515	28.03	2.09	1.03E-03	27.89	2.96	1.12E-03	27.97	3.64	1.18E-03	28.21	4.23	1.24E-03	28.70	4.95	1.32E-03
0.3668	28.16	2.16	1.08E-03	28.06	3.09	1.17E-03	28.18	3.83	1.25E-03	28.47	4.49	1.32E-03	28.96	5.19	1.40E-03
0.3821	28.27	2.21	1.12E-03	28.22	3.19	1.22E-03	28.39	4.00	1.31E-03	28.73	4.74	1.40E-03	29.21	5.39	1.48E-03
0.3976	28.36	2.23	1.16E-03	28.36	3.26	1.27E-03	28.57	4.11	1.37E-03	28.96	4.93	1.47E-03	29.44	5.56	1.55E-03
0.4132	28.43	2.21	1.20E-03	28.48	3.28	1.32E-03	28.73	4.15	1.43E-03	29.17	5.06	1.54E-03	29.68	5.73	1.63E-03
0.4288	28.49	2.18	1.23E-03	28.59	3.28	1.36E-03	28.86	4.16	1.48E-03	29.36	5.16	1.60E-03	29.90	5.88	1.70E-03
0.4446	28.53	2.13	1.27E-03	28.68	3.25	1.40E-03	28.99	4.16	1.52E-03	29.53	5.23	1.67E-03	30.12	6.01	1.78E-03
0.4604	28.56	2.07	1.30E-03	28.75	3.20	1.44E-03	29.11	4.18	1.58E-03	29.70	5.28	1.73E-03	30.33	6.14	1.86E-03
0.4762	28.59	2.00	1.33E-03	28.81	3.14	1.48E-03	29.25	4.22	1.63E-03	29.85	5.31	1.79E-03	30.53	6.26	1.93E-03
0.4921	28.59	1.90	1.35E-03	28.85	3.03	1.50E-03	29.35	4.20	1.68E-03	30.00	5.33	1.85E-03	30.72	6.35	2.01E-03
0.5079	28.54	1.73	1.36E-03	28.83	2.84	1.52E-03	29.38	4.03	1.70E-03	30.14	5.34	1.90E-03	30.88	6.37	2.07E-03
0.5238	28.40	1.43	1.35E-03	28.74	2.55	1.51E-03	29.33	3.73	1.70E-03	30.25	5.30	1.95E-03	30.99	6.29	2.12E-03
0.5396	28.23	1.12	1.34E-03	28.62	2.24	1.51E-03	29.28	3.46	1.70E-03	30.35	5.25	2.00E-03	31.12	6.26	2.17E-03
0.5554	28.08	0.87	1.33E-03	28.51	1.99	1.50E-03	29.27	3.30	1.72E-03	30.46	5.24	2.05E-03	31.32	6.41	2.26E-03
0.5712	27.93	0.64	1.33E-03	28.41	1.76	1.50E-03	29.31	3.23	1.75E-03	30.61	5.32	2.12E-03	31.64	6.87	2.40E-03
0.5868	27.90	0.58	1.35E-03	28.40	1.69	1.53E-03	29.43	3.31	1.81E-03	30.88	5.69	2.24E-03	32.08	7.68	2.61E-03
0.6024	28.08	0.80	1.43E-03	28.74	2.13	1.65E-03	29.95	4.17	2.01E-03	31.63	7.26	2.58E-03	32.90	9.72	3.05E-03
0.6179	28.35	1.16	1.53E-03	29.24	2.89	1.83E-03	30.70	5.62	2.32E-03	32.56	9.70	3.09E-03	33.76	12.36	3.63E-03
0.6332	28.99	2.12	1.74E-03	30.00	4.25	2.12E-03	31.69	8.01	2.81E-03	33.50	12.73	3.74E-03	34.47	14.72	4.18E-03
0.6485	30.01	4.04	2.13E-03	31.02	6.54	2.59E-03	32.76	11.40	3.49E-03	34.30	15.77	4.42E-03	35.01	16.52	4.67E-03
0.6635	30.76	5.73	2.47E-03	31.81	8.65	3.03E-03	33.36	13.46	3.96E-03	34.59	16.32	4.65E-03	35.19	16.44	4.78E-03
0.6784	31.48	7.58	2.85E-03	32.57	11.06	3.54E-03	33.90	15.43	4.43E-03	34.81	16.52	4.81E-03	35.30	15.99	4.81E-03
0.6932	32.12	9.45	3.24E-03	33.19	13.26	4.03E-03	34.30	16.70	4.79E-03	34.97	16.34	4.90E-03	35.37	15.41	4.80E-03
0.7077	32.65	11.15	3.61E-03	33.59	14.58	4.37E-03	34.48	16.73	4.91E-03	35.05	15.77	4.90E-03	35.43	14.82	4.79E-03
0.7220	33.16	12.91	4.01E-03	33.94	15.69	4.68E-03	34.60	16.36	4.95E-03	35.07	14.97	4.84E-03	35.47	14.18	4.76E-03
0.7361	33.62	14.58	4.41E-03	34.24	16.51	4.95E-03	34.68	15.83	4.96E-03	35.06	14.14	4.76E-03	35.48	13.55	4.71E-03
0.7500	33.98	15.82	4.75E-03	34.45	16.80	5.12E-03	34.74	15.24	4.94E-03	35.05	13.41	4.69E-03	35.49	12.97	4.67E-03
0.7636	34.27	16.61	5.01E-03	34.59	16.65	5.20E-03	34.78	14.58	4.90E-03	35.05	12.83	4.64E-03	35.48	12.42	4.63E-03
0.7770	34.52	17.20	5.23E-03	34.69	16.33	5.24E-03	34.79	13.89	4.84E-03	35.05	12.30	4.60E-03	35.47	11.89	4.58E-03
0.7900	34.74	17.59	5.42E-03	34.77	15.87	5.24E-03	34.79	13.24	4.78E-03	35.04	11.76	4.55E-03	35.45	11.41	4.54E-03
0.8028	34.93	17.79	5.58E-03	34.82	15.30	5.21E-03	34.79	12.69	4.74E-03	34.99	11.17	4.48E-03	35.45	11.01	4.51E-03
0.8153	35.10	17.85	5.71E-03	34.84	14.64	5.16E-03	34.81	12.23	4.71E-03	34.90	10.52	4.38E-03	35.45	10.67	4.49E-03
0.8274	35.23	17.62	5.77E-03	34.86	14.08	5.12E-03	34.74	11.51	4.61E-03	34.84	10.02	4.32E-03	35.46	10.36	4.48E-03
0.8393	35.32	17.26	5.80E-03	34.88	13.57	5.08E-03	34.60	10.66	4.46E-03	34.81	9.62	4.28E-03	35.45	10.06	4.46E-03
0.8507	35.43	17.00	5.85E-03	34.86	12.93	5.00E-03	34.53	10.10	4.38E-03	34.75	9.22	4.23E-03	35.42	9.70	4.43E-03
0.8619	35.52	16.69	5.88E-03	34.81	12.28	4.91E-03	34.45	9.58	4.30E-03	34.69	8.81	4.17E-03	35.38	9.36	4.39E-03
0.8726	35.58	16.28	5.87E-03	34.76	11.68	4.83E-03	34.34	9.02	4.20E-03	34.58	8.34	4.09E-03	35.36	9.11	4.37E-03
0.8830	35.63	15.90	5.87E-03	34.71	11.13	4.75E-03	34.19	8.42	4.08E-03	34.47	7.90	4.01E-03	35.33	8.82	4.34E-03
0.8930	35.68	15.56	5.87E-03	34.65	10.62	4.67E-03	33.97	7.69	3.92E-03	34.35	7.48	3.93E-03	35.25	8.47	4.28E-03
0.9026	35.73	15.26	5.87E-03	34.59	10.16	4.60E-03	33.78	7.13	3.80E-03	34.26	7.17	3.87E-03	35.19	8.18	4.24E-03
0.9118	35.78	15.00	5.87E-03	34.54	9.77	4.54E-03	33.66	6.74	3.72E-03	34.22	6.96	3.85E-03	35.16	7.96	4.21E-03
0.9206	35.83	14.80	5.89E-03	34.50	9.42	4.49E-03	33.55	6.41	3.66E-03	34.18	6.78	3.83E-03	35.13	7.77	4.19E-03
0.9290	35.89	14.66	5.92E-03	34.45	9.09	4.44E-03	33.42	6.05	3.58E-03	34.13	6.58	3.80E-03	35.09	7.59	4.17E-03
0.9369	35.96	14.54	5.96E-03	34.40	8.79	4.39E-03	33.32	5.79	3.53E-03	34.09	6.42	3.78E-03	35.06	7.43	4.16E-03
0.9444	36.00	14.40	5.98E-03	34.36	8.53	4.35E-03	33.31	5.69	3.53E-03	34.08	6.33	3.78E-03	35.05	7.31	4.15E-03
0.9515	36.04	14.23	5.99E-03	34.32	8.30	4.32E-03	33.34	5.68	3.55E-03	34.10	6.28	3.80E-03	35.04	7.21	4.15E-03
0.9581	36.08	14.13	6.01E-03	34.28	8.10	4.29E-03	33.40	5.72	3.59E-03	34.13	6.28	3.82E-03	35.05	7.15	4.15E-03
0.9642	36.16	14.16	6.08E-03	34.25	7.92	4.26E-03	33.49	5.83	3.65E-03	34.20	6.34	3.87E-03	35.06	7.12	4.17E-03
0.9699	36.25	14.33	6.18E-03	34.22	7.76	4.24E-03	33.67	6.11	3.77E-03	34.31	6.52	3.95E-03	35.09	7.11	4.19E-03
0.9750	36.36	14.56	6.29E-03	34.19	7.61	4.22E-03	33.88	6.47	3.90E-03	34.46	6.75	4.05E-03	35.13	7.12	4.22E-03
0.9798	36.47	14.81	6.41E-03	34.17	7.49	4.20E-03	34.07	6.81	4.04E-03	34.61	7.00	4.15E-03	35.16	7.14	4.24E-03
0.9840	36.56	15.05	6.52E-03	34.14	7.38	4.18E-03	34.53	7.75	4.37E-03	34.74	7.23	4.25E-03	35.19	7.16	4.27E-03
0.9877	36.65	15.26	6.62E-03	34.13	7.28	4.17E-03	35.46	10.08	5.15E-03	34.86	7.45	4.34E-03	35.21	7.17	4.29E-03
0.9910	36.72	15.45	6.71E-03	34.11	7.20	4.16E-03	36.67	14.15	6.52E-03	34.97	7.64	4.42E-03	35.24	7.18	4.31E-03
0.9937	36.79	15.62	6.79E-03	34.09	7.13	4.15E-03	38.00	21.17	8.92E-03	35.06	7.81	4.49E-03	35.26	7.20	4.32E-03
0.9960	36.84	15.76	6.86E-03	34.08	7.08	4.14E-03	39.32	37.64	1.51E-02	35.14	7.95	4.55E-03	35.27	7.21	4.34E-03
0.9977	36.88	15.87	6.91E-03	34.07	7.03	4.13E-03	40.49			35.20	8.06	4.60E-03	35.29	7.21	4.35E-03
0.9990	36.91	15.95	6.95E-03	34.07	7.00	4.13E-03	41.42			35.24	8.15	4.63E-03	35.30	7.22	4.35E-03
0.9998	36.93	15.99	6.97E-03	34.06	6.99	4.13E-03	42.01			35.27	8.19	4.65E-03	35.30	7.22	4.36E-03
1.0000	36.93	16.01	6.98E-03	34.06	6.98	4.13E-03	42.21			35.27	8.21	4.66E-03	35.30	7.22	4.36E-03

The local freestream flow direction, twist in the boundary layer and boundary layer displacement thickness from WAKELAG over the upper surface of the DERA wing. $\Lambda = 40°$, $\alpha = 12.0°$, $Re_c = 3.3 \times 10^6$.

η	0.06b			0.16b			0.30b			0.45b			0.59b		
x/c	α_c (°)	β_c (°)	δ^*/c	α_c (°)	β_c (°)	δ^*/c	α_c (°)	β_c (°)	δ^*/c	α_c (°)	β_c (°)	δ^*/c	α_c (°)	β_c (°)	δ^*/c
0.0556	64.43	-2.73	1.53E-04	64.45	-2.54	1.55E-04	65.04	-2.87	1.52E-04	65.41	-3.08	1.46E-04	63.05	-2.46	1.54E-04
0.0631	62.64	-4.48	1.61E-04	62.83	-4.13	1.66E-04	63.02	-4.86	1.56E-04	63.23	-5.29	1.46E-04	61.64	-3.95	1.66E-04
0.0710	61.05	-5.16	1.74E-04	61.30	-4.86	1.79E-04	61.15	-5.76	1.64E-04	61.26	-6.21	1.53E-04	60.40	-4.53	1.79E-04
0.0794	59.67	-5.50	1.91E-04	59.75	-5.52	1.90E-04	59.52	-6.26	1.76E-04	59.58	-6.62	1.66E-04	59.18	-4.96	1.93E-04
0.0882	58.49	-5.63	2.11E-04	58.02	-6.29	1.97E-04	58.10	-6.52	1.91E-04	58.12	-6.79	1.81E-04	57.90	-5.30	2.11E-04
0.0974	57.41	-5.72	2.30E-04	56.39	-6.84	2.06E-04	56.84	-6.66	2.06E-04	56.79	-6.89	1.97E-04	56.69	-5.52	2.31E-04
0.1070	56.34	-5.94	2.43E-04	55.26	-6.92	2.23E-04	55.75	-6.67	2.23E-04	55.68	-6.85	2.13E-04	55.61	-5.74	2.46E-04
0.1170	55.28	-6.22	2.53E-04	54.35	-6.84	2.41E-04	54.78	-6.61	2.41E-04	54.70	-6.77	2.31E-04	54.63	-5.95	2.59E-04
0.1274	54.26	-6.46	2.63E-04	53.58	-6.69	2.60E-04	53.91	-6.53	2.58E-04	53.84	-6.65	2.48E-04	53.72	-6.12	2.72E-04
0.1381	53.33	-6.61	2.75E-04	52.89	-6.51	2.80E-04	53.11	-6.45	2.76E-04	53.04	-6.54	2.66E-04	52.88	-6.24	2.85E-04
0.1493	52.52	-6.64	2.90E-04	52.21	-6.38	2.98E-04	52.35	-6.39	2.93E-04	52.28	-6.46	2.83E-04	52.11	-6.31	2.98E-04
0.1607	51.85	-6.57	3.08E-04	51.55	-6.29	3.14E-04	51.62	-6.36	3.09E-04	51.55	-6.40	2.99E-04	51.40	-6.34	3.13E-04
0.1726	51.24	-6.46	3.27E-04	50.93	-6.20	3.31E-04	50.93	-6.33	3.25E-04	50.85	-6.36	3.14E-04	50.73	-6.34	3.28E-04
0.1847	50.67	-6.34	3.46E-04	50.34	-6.13	3.48E-04	50.27	-6.29	3.41E-04	50.20	-6.31	3.31E-04	50.10	-6.32	3.44E-04
0.1972	50.13	-6.24	3.65E-04	49.77	-6.08	3.64E-04	49.66	-6.26	3.56E-04	49.60	-6.25	3.47E-04	49.50	-6.30	3.60E-04
0.2100	49.59	-6.16	3.81E-04	49.18	-6.08	3.78E-04	49.04	-6.25	3.71E-04	49.03	-6.19	3.64E-04	48.92	-6.27	3.75E-04
0.2230	49.07	-6.11	3.97E-04	48.57	-6.12	3.90E-04	48.42	-6.28	3.84E-04	48.48	-6.14	3.81E-04	48.35	-6.26	3.90E-04
0.2364	48.58	-6.04	4.14E-04	48.02	-6.13	4.05E-04	47.87	-6.26	4.00E-04	47.98	-6.06	3.98E-04	47.83	-6.21	4.06E-04
0.2500	48.16	-5.93	4.34E-04	47.61	-6.01	4.26E-04	47.49	-6.10	4.22E-04	47.58	-5.92	4.20E-04	47.42	-6.08	4.27E-04
0.2639	47.80	-5.79	4.55E-04	47.34	-5.79	4.53E-04	47.25	-5.82	4.52E-04	47.27	-5.72	4.44E-04	47.09	-5.90	4.51E-04
0.2780	47.48	-5.64	4.78E-04	47.13	-5.53	4.82E-04	47.09	-5.50	4.85E-04	47.00	-5.51	4.70E-04	46.81	-5.70	4.76E-04
0.2923	47.21	-5.47	5.02E-04	46.94	-5.27	5.12E-04	46.95	-5.19	5.17E-04	46.77	-5.29	4.97E-04	46.59	-5.48	5.03E-04
0.3068	46.99	-5.27	5.29E-04	46.76	-5.04	5.40E-04	46.79	-4.93	5.46E-04	46.58	-5.06	5.25E-04	46.43	-5.21	5.34E-04
0.3216	46.83	-5.03	5.59E-04	46.60	-4.82	5.68E-04	46.63	-4.71	5.74E-04	46.43	-4.81	5.55E-04	46.35	-4.89	5.68E-04
0.3365	46.70	-4.80	5.90E-04	46.45	-4.61	5.96E-04	46.47	-4.51	6.01E-04	46.30	-4.58	5.85E-04	46.30	-4.57	6.04E-04
0.3515	46.54	-4.63	6.16E-04	46.29	-4.45	6.22E-04	46.31	-4.35	6.26E-04	46.17	-4.37	6.14E-04	46.20	-4.33	6.35E-04
0.3668	46.34	-4.51	6.39E-04	46.12	-4.31	6.47E-04	46.15	-4.21	6.51E-04	46.05	-4.18	6.43E-04	46.05	-4.19	6.59E-04
0.3821	46.12	-4.44	6.59E-04	45.95	-4.21	6.70E-04	45.99	-4.10	6.75E-04	45.94	-4.00	6.72E-04	45.86	-4.10	6.80E-04
0.3976	45.89	-4.40	6.77E-04	45.76	-4.14	6.91E-04	45.81	-4.02	6.97E-04	45.80	-3.88	6.97E-04	45.66	-4.04	6.99E-04
0.4132	45.62	-4.41	6.91E-04	45.55	-4.10	7.09E-04	45.60	-4.00	7.15E-04	45.62	-3.83	7.17E-04	45.45	-4.01	7.17E-04
0.4288	45.32	-4.46	7.02E-04	45.32	-4.10	7.25E-04	45.37	-4.01	7.30E-04	45.40	-3.83	7.33E-04	45.23	-4.00	7.33E-04
0.4446	45.02	-4.51	7.13E-04	45.07	-4.13	7.39E-04	45.12	-4.04	7.44E-04	45.16	-3.86	7.47E-04	45.00	-4.02	7.48E-04
0.4604	44.76	-4.53	7.27E-04	44.81	-4.17	7.50E-04	44.88	-4.07	7.58E-04	44.91	-3.90	7.60E-04	44.78	-4.03	7.63E-04
0.4762	44.54	-4.52	7.44E-04	44.53	-4.24	7.60E-04	44.65	-4.10	7.72E-04	44.67	-3.95	7.73E-04	44.57	-4.04	7.79E-04
0.4921	44.29	-4.55	7.57E-04	44.22	-4.34	7.67E-04	44.38	-4.17	7.81E-04	44.38	-4.04	7.81E-04	44.32	-4.10	7.90E-04
0.5079	43.92	-4.69	7.59E-04	43.84	-4.51	7.66E-04	44.02	-4.33	7.81E-04	44.01	-4.21	7.80E-04	43.97	-4.26	7.90E-04
0.5238	43.39	-4.98	7.43E-04	43.25	-4.87	7.44E-04	43.51	-4.63	7.66E-04	43.50	-4.51	7.66E-04	43.45	-4.57	7.73E-04
0.5396	42.79	-5.30	7.24E-04	42.57	-5.25	7.17E-04	42.93	-4.96	7.46E-04	42.93	-4.84	7.49E-04	42.86	-4.91	7.51E-04
0.5554	42.24	-5.56	7.12E-04	41.96	-5.56	7.00E-04	42.34	-5.27	7.27E-04	42.38	-5.11	7.37E-04	42.29	-5.21	7.33E-04
0.5712	41.70	-5.79	7.02E-04	41.53	-5.72	7.00E-04	41.66	-5.64	7.02E-04	41.80	-5.39	7.25E-04	41.66	-5.54	7.13E-04
0.5868	41.35	-5.88	7.10E-04	41.35	-5.69	7.23E-04	41.40	-5.67	7.18E-04	41.49	-5.45	7.39E-04	41.41	-5.57	7.29E-04
0.6024	41.11	-5.89	7.28E-04	41.23	-5.62	7.51E-04	41.35	-5.55	7.53E-04	41.52	-5.27	7.83E-04	41.35	-5.46	7.62E-04
0.6179	40.98	-5.81	7.58E-04	41.20	-5.48	7.86E-04	41.40	-5.36	7.96E-04	41.78	-4.88	8.50E-04	41.38	-5.28	8.03E-04
0.6332	41.50	-5.18	8.57E-04	41.67	-4.89	8.80E-04	41.86	-4.78	8.87E-04	42.23	-4.29	9.42E-04	41.87	-4.68	8.99E-04
0.6485	42.54	-3.92	1.03E-03	42.57	-3.76	1.04E-03	42.71	-3.72	1.04E-03	42.80	-3.51	1.06E-03	42.79	-3.54	1.06E-03
0.6635	43.13	-3.02	1.16E-03	43.20	-2.82	1.18E-03	43.35	-2.79	1.17E-03	43.43	-2.59	1.19E-03	43.42	-2.61	1.20E-03
0.6784	43.64	-2.20	1.28E-03	43.78	-1.89	1.31E-03	43.95	-1.83	1.31E-03	44.06	-1.60	1.33E-03	43.99	-1.69	1.33E-03
0.6932	44.09	-1.41	1.40E-03	44.30	-0.99	1.44E-03	44.50	-0.90	1.45E-03	44.60	-0.68	1.47E-03	44.51	-0.80	1.47E-03
0.7077	44.53	-0.63	1.52E-03	44.76	-0.17	1.57E-03	44.96	-0.07	1.58E-03	45.01	0.06	1.59E-03	44.98	0.05	1.60E-03
0.7220	44.95	0.12	1.64E-03	45.17	0.58	1.69E-03	45.38	0.68	1.70E-03	45.40	0.75	1.71E-03	45.42	0.84	1.73E-03
0.7361	45.34	0.83	1.75E-03	45.55	1.28	1.81E-03	45.75	1.37	1.82E-03	45.78	1.44	1.83E-03	45.82	1.58	1.86E-03
0.7500	45.71	1.50	1.87E-03	45.92	1.93	1.93E-03	46.11	2.00	1.94E-03	46.15	2.11	1.95E-03	46.20	2.26	1.98E-03
0.7636	46.05	2.11	1.99E-03	46.28	2.57	2.05E-03	46.43	2.56	2.05E-03	46.52	2.78	2.08E-03	46.54	2.87	2.10E-03
0.7770	46.37	2.67	2.10E-03	46.62	3.19	2.18E-03	46.73	3.06	2.16E-03	46.89	3.46	2.21E-03	46.86	3.41	2.22E-03
0.7900	46.67	3.20	2.21E-03	46.93	3.73	2.30E-03	47.02	3.54	2.27E-03	47.23	4.06	2.34E-03	47.16	3.92	2.34E-03
0.8028	46.96	3.70	2.32E-03	47.20	4.16	2.40E-03	47.33	4.06	2.39E-03	47.49	4.47	2.45E-03	47.46	4.43	2.46E-03
0.8153	47.25	4.18	2.44E-03	47.42	4.47	2.49E-03	47.66	4.63	2.53E-03	47.68	4.70	2.52E-03	47.76	4.92	2.58E-03
0.8274	47.51	4.58	2.54E-03	47.68	4.90	2.60E-03	47.89	4.99	2.63E-03	47.93	5.10	2.63E-03	48.06	5.42	2.72E-03
0.8393	47.74	4.93	2.64E-03	47.98	5.39	2.73E-03	48.08	5.22	2.71E-03	48.24	5.62	2.77E-03	48.35	5.92	2.85E-03
0.8507	48.01	5.38	2.76E-03	48.22	5.75	2.84E-03	48.32	5.59	2.82E-03	48.49	6.00	2.89E-03	48.60	6.32	2.97E-03
0.8619	48.27	5.81	2.89E-03	48.43	6.05	2.94E-03	48.56	5.94	2.93E-03	48.71	6.34	2.99E-03	48.82	6.64	3.08E-03
0.8726	48.49	6.13	2.99E-03	48.60	6.25	3.02E-03	48.74	6.18	3.02E-03	48.93	6.66	3.10E-03	49.01	6.85	3.17E-03
0.8830	48.70	6.44	3.09E-03	48.85	6.65	3.15E-03	48.93	6.43	3.11E-03	49.15	6.97	3.21E-03	49.20	7.11	3.27E-03
0.8930	48.91	6.77	3.20E-03	49.31	7.67	3.41E-03	49.13	6.70	3.21E-03	49.36	7.30	3.33E-03	49.42	7.47	3.39E-03
0.9026	49.12	7.09	3.31E-03	49.56	8.13	3.56E-03	49.34	7.03	3.33E-03	49.56	7.62	3.44E-03	49.64	7.83	3.52E-03
0.9118	49.31	7.41	3.42E-03	49.58	7.92	3.56E-03	49.58	7.47	3.47E-03	49.77	7.96	3.56E-03	49.86	8.18	3.65E-03
0.9206	49.50	7.71	3.53E-03	49.61	7.77	3.56E-03	49.81	7.87	3.60E-03	49.97	8.30	3.69E-03	50.05	8.51	3.77E-03
0.9290	49.69	8.02	3.65E-03	49.74	7.91	3.64E-03	49.98	8.13	3.71E-03	50.16	8.61	3.80E-03	50.24	8.81	3.89E-03
0.9369	49.86	8.29	3.75E-03	49.90	8.15	3.73E-03	50.14	8.37	3.80E-03	50.33	8.90	3.91E-03	50.40	9.07	4.00E-03
0.9444	49.97	8.41	3.82E-03	50.05	8.36	3.83E-03	50.32	8.70	3.93E-03	50.48	9.13	4.01E-03	50.54	9.25	4.09E-03
0.9515	50.04	8.41	3.85E-03	50.20	8.59	3.92E-03	50.53	9.12	4.07E-03	50.62	9.35	4.11E-03	50.65	9.37	4.16E-03
0.9581	50.12	8.45	3.90E-03	50.32	8.76	4.00E-03	50.71	9.46	4.20E-03	50.74	9.52	4.19E-03	50.76	9.50	4.23E-03
0.9642	50.24	8.63	3.97E-03	50.29	8.52	3.97E-03	50.82	9.63	4.28E-03	50.17	7.71	3.75E-03	50.88	9.69	4.32E-03
0.9699	50.39	8.92	4.08E-03	49.88	7.26	3.67E-03	50.91	9.72	4.34E-03	47.85	2.90	2.55E-03	51.01	9.92	4.41E-03
0.9750	50.55	9.26	4.20E-03	49.23	5.66	3.27E-03	50.97	9.76	4.38E-03	45.13	-0.52	1.74E-03	51.13	10.14	4.51E-03
0.9798	50.71	9.60	4.32E-03	48.48	4.13	2.89E-03	51.02	9.77	4.41E-03	42.75	-2.49	1.28E-03	51.23	10.30	4.58E-03
0.9840	50.85	9.92	4.43E-03	47.72	2.83	2.57E-03	50.66	8.57	4.10E-03	40.87	-3.61	1.02E-03	50.62	8.36	4.06E-03
0.9877	50.98	10.22	4.54E-03	47.01	1.78	2.32E-03	49.73	6.17	3.46E-03	39.41	-4.28	8.57E-04	49.08	4.79	3.11E-03
0.9910	51.09	10.48	4.63E-03	46.38	0.96	2.13E-03	48.63	3.96	2.89E-03	38.26	-4.71	7.52E-04	47.33	1.96	2.38E-03
0.9937	51.19	10.71	4.72E-03	45.85	0.34	1.98E-03	47.59	2.29	2.47E-03	37.35	-4.99	6.81E-04	45.74	0.05	1.90E-03
0.9960	51.27	10.91	4.79E-03	45.42	-0.13	1.87E-03	46.71	1.12	2.18E-03	36.66	-5.18	6.32E-04	44.44	-1.18	1.60E-03
0.9977	51.33	11.06	4.84E-03	45.09	-0.46	1.79E-03	46.03	0.32	1.98E-03	36.15	-5.30	5.98E-04	43.46	-1.96	1.41E-03
0.9990	51.37	11.17	4.88E-03	44.85	-0.69	1.73E-03	45.55	-0.18	1.86E-03	35.79	-5.38	5.76E-04	42.79	-2.43	1.30E-03
0.9998	51.40	11.24	4.91E-03	44.72	-0.82	1.70E-03	45.27	-0.46	1.79E-03	35.59	-5.43	5.64E-04	42.40	-2.68	1.24E-03
1.0000	51.41	11.26	4.92E-03	44.67	-0.86	1.69E-03	45.18	-0.55	1.77E-03	35.52	-5.44	5.60E-04	42.27	-2.76	1.22E-03

The local freestream flow direction, twist in the boundary layer and boundary layer displacement thickness from WAKELAG over the upper surface of the DERA wing. $\Lambda = 50°$, $\alpha = -6.1°$, $Re_c = 3.9 \times 10^6$.

η	0.06b			0.16b			0.30b			0.45b			0.59b		
x/c	α_c (°)	β_c (°)	δ^*/c	α_c (°)	β_c (°)	δ^*/c	α_c (°)	β_c (°)	δ^*/c	α_c (°)	β_c (°)	δ^*/c	α_c (°)	β_c (°)	δ^*/c
0.0556	48.42	-0.99	1.43E-04	47.78	-0.76	1.44E-04	47.20	-0.79	1.43E-04	46.36	-0.62	1.40E-04	45.87	-0.59	1.41E-04
0.0631	47.80	-1.90	1.65E-04	47.33	-1.41	1.68E-04	46.65	-1.63	1.64E-04	45.98	-1.23	1.63E-04	45.54	-1.09	1.64E-04
0.0710	47.22	-2.29	1.83E-04	46.88	-1.77	1.88E-04	46.09	-2.11	1.81E-04	45.59	-1.58	1.80E-04	45.24	-1.34	1.83E-04
0.0794	46.73	-2.47	2.04E-04	46.35	-2.15	2.06E-04	45.57	-2.42	1.98E-04	45.18	-1.86	1.98E-04	44.92	-1.54	2.03E-04
0.0882	46.33	-2.51	2.27E-04	45.61	-2.79	2.19E-04	45.07	-2.65	2.16E-04	44.73	-2.16	2.15E-04	44.55	-1.74	2.26E-04
0.0974	45.95	-2.55	2.51E-04	44.84	-3.33	2.32E-04	44.62	-2.81	2.35E-04	44.30	-2.40	2.34E-04	44.17	-1.91	2.52E-04
0.1070	45.54	-2.70	2.70E-04	44.42	-3.37	2.54E-04	44.25	-2.86	2.56E-04	43.95	-2.50	2.54E-04	43.85	-2.05	2.74E-04
0.1170	45.10	-2.92	2.85E-04	44.10	-3.32	2.76E-04	43.93	-2.85	2.78E-04	43.66	-2.54	2.74E-04	43.55	-2.17	2.95E-04
0.1274	44.65	-3.13	3.00E-04	43.84	-3.21	2.98E-04	43.66	-2.81	3.00E-04	43.40	-2.54	2.96E-04	43.27	-2.26	3.14E-04
0.1381	44.24	-3.29	3.16E-04	43.61	-3.09	3.21E-04	43.40	-2.77	3.22E-04	43.15	-2.53	3.17E-04	43.02	-2.33	3.34E-04
0.1493	43.89	-3.35	3.34E-04	43.38	-3.01	3.42E-04	43.14	-2.76	3.43E-04	42.91	-2.54	3.38E-04	42.79	-2.37	3.54E-04
0.1607	43.62	-3.31	3.56E-04	43.14	-2.96	3.63E-04	42.87	-2.79	3.62E-04	42.66	-2.58	3.57E-04	42.57	-2.40	3.75E-04
0.1726	43.38	-3.26	3.78E-04	42.92	-2.91	3.84E-04	42.60	-2.82	3.82E-04	42.40	-2.61	3.77E-04	42.37	-2.41	3.96E-04
0.1847	43.16	-3.19	4.01E-04	42.70	-2.88	4.05E-04	42.34	-2.85	4.02E-04	42.17	-2.64	3.97E-04	42.18	-2.42	4.17E-04
0.1972	42.95	-3.14	4.22E-04	42.48	-2.87	4.26E-04	42.10	-2.86	4.22E-04	41.96	-2.65	4.18E-04	41.98	-2.43	4.38E-04
0.2100	42.72	-3.13	4.42E-04	42.22	-2.91	4.43E-04	41.87	-2.88	4.41E-04	41.77	-2.63	4.39E-04	41.79	-2.46	4.58E-04
0.2230	42.47	-3.14	4.61E-04	41.93	-3.01	4.59E-04	41.63	-2.92	4.60E-04	41.59	-2.61	4.61E-04	41.58	-2.49	4.78E-04
0.2364	42.25	-3.13	4.81E-04	41.67	-3.07	4.76E-04	41.42	-2.92	4.81E-04	41.43	-2.57	4.85E-04	41.40	-2.50	5.00E-04
0.2500	42.09	-3.07	5.04E-04	41.51	-3.00	5.00E-04	41.30	-2.82	5.07E-04	41.33	-2.48	5.11E-04	41.29	-2.44	5.25E-04
0.2639	41.98	-2.95	5.31E-04	41.48	-2.81	5.32E-04	41.28	-2.61	5.40E-04	41.29	-2.32	5.41E-04	41.24	-2.31	5.55E-04
0.2780	41.90	-2.80	5.60E-04	41.50	-2.56	5.68E-04	41.33	-2.34	5.78E-04	41.28	-2.14	5.74E-04	41.22	-2.14	5.87E-04
0.2923	41.86	-2.64	5.90E-04	41.54	-2.30	6.05E-04	41.39	-2.06	6.16E-04	41.29	-1.94	6.08E-04	41.25	-1.94	6.22E-04
0.3068	41.83	-2.46	6.22E-04	41.56	-2.08	6.40E-04	41.44	-1.84	6.52E-04	41.33	-1.74	6.43E-04	41.30	-1.72	6.59E-04
0.3216	41.86	-2.25	6.57E-04	41.59	-1.88	6.75E-04	41.49	-1.63	6.88E-04	41.39	-1.52	6.80E-04	41.42	-1.42	7.02E-04
0.3365	41.89	-2.04	6.93E-04	41.62	-1.70	7.09E-04	41.53	-1.43	7.24E-04	41.46	-1.30	7.19E-04	41.56	-1.12	7.48E-04
0.3515	41.89	-1.90	7.25E-04	41.64	-1.55	7.42E-04	41.57	-1.28	7.58E-04	41.53	-1.11	7.57E-04	41.65	-0.91	7.88E-04
0.3668	41.85	-1.82	7.53E-04	41.65	-1.42	7.74E-04	41.60	-1.14	7.92E-04	41.59	-0.94	7.93E-04	41.68	-0.80	8.20E-04
0.3821	41.78	-1.78	7.77E-04	41.65	-1.33	8.05E-04	41.62	-1.03	8.25E-04	41.64	-0.80	8.29E-04	41.68	-0.74	8.49E-04
0.3976	41.69	-1.78	7.99E-04	41.63	-1.27	8.32E-04	41.62	-0.97	8.54E-04	41.66	-0.71	8.62E-04	41.66	-0.71	8.76E-04
0.4132	41.57	-1.83	8.16E-04	41.57	-1.26	8.56E-04	41.57	-0.97	8.78E-04	41.64	-0.70	8.88E-04	41.64	-0.70	9.02E-04
0.4288	41.41	-1.92	8.30E-04	41.49	-1.29	8.77E-04	41.49	-1.02	8.97E-04	41.59	-0.73	9.10E-04	41.61	-0.70	9.27E-04
0.4446	41.25	-2.01	8.43E-04	41.39	-1.35	8.95E-04	41.40	-1.09	9.15E-04	41.51	-0.80	9.29E-04	41.55	-0.74	9.49E-04
0.4604	41.12	-2.06	8.61E-04	41.27	-1.43	9.11E-04	41.31	-1.14	9.34E-04	41.42	-0.87	9.48E-04	41.48	-0.80	9.69E-04
0.4762	41.02	-2.07	8.81E-04	41.14	-1.52	9.25E-04	41.24	-1.18	9.55E-04	41.32	-0.95	9.64E-04	41.39	-0.87	9.86E-04
0.4921	40.89	-2.13	8.98E-04	40.98	-1.64	9.35E-04	41.13	-1.26	9.71E-04	41.18	-1.08	9.76E-04	41.26	-1.00	9.98E-04
0.5079	40.67	-2.28	9.03E-04	40.75	-1.84	9.36E-04	40.93	-1.44	9.75E-04	40.97	-1.29	9.78E-04	41.05	-1.21	9.99E-04
0.5238	40.30	-2.60	8.89E-04	40.32	-2.24	9.13E-04	40.58	-1.79	9.58E-04	40.63	-1.64	9.63E-04	40.69	-1.58	9.80E-04
0.5396	39.86	-2.95	8.70E-04	39.82	-2.68	8.83E-04	40.16	-2.18	9.34E-04	40.23	-2.02	9.44E-04	40.28	-1.98	9.56E-04
0.5554	39.47	-3.23	8.57E-04	39.36	-3.03	8.63E-04	39.74	-2.54	9.14E-04	39.85	-2.34	9.30E-04	39.89	-2.33	9.36E-04
0.5712	39.06	-3.50	8.45E-04	39.08	-3.21	8.64E-04	39.25	-2.93	8.87E-04	39.46	-2.64	9.19E-04	39.45	-2.69	9.14E-04
0.5868	38.86	-3.58	8.59E-04	39.04	-3.15	8.95E-04	39.12	-2.97	9.06E-04	39.23	-2.78	9.28E-04	39.33	-2.73	9.33E-04
0.6024	38.79	-3.54	8.87E-04	39.09	-3.01	9.35E-04	39.22	-2.80	9.53E-04	39.31	-2.61	9.75E-04	39.41	-2.57	9.79E-04
0.6179	38.78	-3.44	9.23E-04	39.19	-2.82	9.84E-04	39.39	-2.53	1.01E-03	39.66	-2.17	1.06E-03	39.58	-2.32	1.04E-03
0.6332	39.36	-2.73	1.04E-03	39.74	-2.12	1.10E-03	39.94	-1.84	1.13E-03	40.22	-1.45	1.18E-03	40.17	-1.57	1.16E-03
0.6485	40.48	-1.23	1.27E-03	40.71	-0.78	1.31E-03	40.87	-0.55	1.33E-03	40.91	-0.47	1.34E-03	41.19	-0.14	1.39E-03
0.6635	41.12	-0.21	1.42E-03	41.40	0.32	1.48E-03	41.59	0.58	1.51E-03	41.68	0.74	1.53E-03	41.93	1.06	1.58E-03
0.6784	41.67	0.72	1.57E-03	42.04	1.43	1.66E-03	42.27	1.77	1.70E-03	42.44	2.09	1.75E-03	42.61	2.27	1.78E-03
0.6932	42.17	1.61	1.72E-03	42.63	2.53	1.84E-03	42.89	2.95	1.90E-03	43.10	3.37	1.96E-03	43.23	3.47	1.98E-03
0.7077	42.67	2.54	1.88E-03	43.17	3.58	2.03E-03	43.44	4.01	2.09E-03	43.60	4.38	2.14E-03	43.78	4.59	2.19E-03
0.7220	43.16	3.48	2.05E-03	43.68	4.60	2.21E-03	43.93	5.00	2.28E-03	44.07	5.35	2.33E-03	44.30	5.66	2.39E-03
0.7361	43.62	4.41	2.22E-03	44.15	5.57	2.40E-03	44.38	5.93	2.46E-03	44.54	6.33	2.53E-03	44.77	6.68	2.60E-03
0.7500	44.06	5.31	2.40E-03	44.59	6.48	2.59E-03	44.81	6.80	2.65E-03	44.98	7.30	2.73E-03	45.22	7.64	2.81E-03
0.7636	44.48	6.17	2.57E-03	45.00	7.33	2.78E-03	45.19	7.58	2.83E-03	45.42	8.29	2.95E-03	45.64	8.53	3.02E-03
0.7770	44.88	7.00	2.75E-03	45.38	8.13	2.97E-03	45.55	8.29	3.01E-03	45.85	9.30	3.18E-03	46.02	9.37	3.23E-03
0.7900	45.25	7.79	2.94E-03	45.74	8.87	3.15E-03	45.90	8.99	3.19E-03	46.25	10.21	3.41E-03	46.39	10.15	3.44E-03
0.8028	45.62	8.54	3.12E-03	46.08	9.57	3.34E-03	46.27	9.76	3.40E-03	46.58	10.90	3.60E-03	46.74	10.90	3.65E-03
0.8153	45.97	9.26	3.31E-03	46.40	10.22	3.53E-03	46.66	10.66	3.64E-03	46.85	11.35	3.76E-03	47.08	11.61	3.87E-03
0.8274	46.28	9.86	3.49E-03	46.71	10.81	3.71E-03	46.95	11.20	3.82E-03	47.16	12.01	3.97E-03	47.41	12.35	4.10E-03
0.8393	46.56	10.39	3.66E-03	46.99	11.36	3.89E-03	47.19	11.55	3.96E-03	47.50	12.80	4.22E-03	47.73	13.07	4.34E-03
0.8507	46.88	11.08	3.86E-03	47.27	11.87	4.07E-03	47.48	12.16	4.17E-03	47.77	13.31	4.41E-03	48.00	13.60	4.54E-03
0.8619	47.18	11.73	4.07E-03	47.53	12.39	4.26E-03	47.77	12.79	4.38E-03	48.01	13.72	4.59E-03	48.24	14.04	4.73E-03
0.8726	47.43	12.20	4.24E-03	47.78	12.86	4.44E-03	48.03	13.32	4.58E-03	48.23	14.09	4.76E-03	48.46	14.43	4.90E-03
0.8830	47.68	12.68	4.42E-03	48.12	13.74	4.72E-03	48.26	13.72	4.76E-03	48.45	14.46	4.93E-03	48.68	14.80	5.08E-03
0.8930	47.93	13.23	4.62E-03	48.69	15.98	5.35E-03	48.44	13.96	4.90E-03	48.67	14.87	5.12E-03	48.89	15.19	5.27E-03
0.9026	48.17	13.81	4.82E-03	48.95	16.72	5.63E-03	48.63	14.27	5.05E-03	48.87	15.26	5.30E-03	49.09	15.57	5.46E-03
0.9118	48.40	14.35	5.03E-03	48.91	15.78	5.48E-03	48.85	14.74	5.25E-03	49.06	15.64	5.48E-03	49.29	15.94	5.64E-03
0.9206	48.61	14.83	5.22E-03	48.90	15.12	5.38E-03	49.05	15.17	5.44E-03	49.24	15.98	5.65E-03	49.46	16.23	5.81E-03
0.9290	48.81	15.25	5.40E-03	49.02	15.17	5.47E-03	49.23	15.50	5.61E-03	49.40	16.27	5.81E-03	49.60	16.41	5.94E-03
0.9369	48.98	15.61	5.57E-03	49.18	15.48	5.63E-03	49.38	15.79	5.76E-03	49.54	16.48	5.95E-03	49.72	16.51	6.05E-03
0.9444	49.13	15.86	5.71E-03	49.34	15.77	5.78E-03	49.53	16.08	5.92E-03	49.66	16.61	6.06E-03	49.82	16.54	6.14E-03
0.9515	49.25	16.02	5.82E-03	49.50	16.12	5.95E-03	49.68	16.36	6.07E-03	49.77	16.69	6.15E-03	49.91	16.49	6.20E-03
0.9581	49.36	16.18	5.93E-03	49.63	16.36	6.09E-03	49.80	16.57	6.20E-03	49.85	16.70	6.23E-03	49.98	16.45	6.25E-03
0.9642	49.48	16.40	6.05E-03	49.63	16.00	6.04E-03	49.90	16.70	6.30E-03	49.41	14.17	5.53E-03	50.06	16.45	6.32E-03
0.9699	49.60	16.65	6.18E-03	49.38	14.45	5.63E-03	49.99	16.79	6.39E-03	47.56	8.13	3.84E-03	50.14	16.48	6.39E-03
0.9750	49.71	16.91	6.31E-03	48.96	12.52	5.11E-03	50.06	16.80	6.45E-03	45.34	3.83	2.70E-03	50.21	16.50	6.45E-03
0.9798	49.82	17.16	6.44E-03	48.46	10.67	4.60E-03	50.10	16.72	6.47E-03	43.33	1.24	2.03E-03	50.26	16.46	6.48E-03
0.9840	49.91	17.39	6.55E-03	47.94	9.09	4.17E-03	49.91	15.47	6.12E-03	41.71	-0.30	1.64E-03	49.85	14.34	5.85E-03
0.9877	50.00	17.61	6.66E-03	47.45	7.79	3.83E-03	49.39	13.07	5.42E-03	40.42	-1.28	1.39E-03	48.83	10.58	4.71E-03
0.9910	50.07	17.80	6.76E-03	47.01	6.77	3.55E-03	48.75	10.79	4.75E-03	39.39	-1.93	1.23E-03	47.62	7.45	3.80E-03
0.9937	50.13	17.97	6.84E-03	46.64	5.97	3.34E-03	48.13	8.98	4.23E-03	38.58	-2.38	1.12E-03	46.48	5.22	3.17E-03
0.9960	50.18	18.11	6.91E-03	46.33	5.37	3.18E-03	47.59	7.65	3.85E-03	37.95	-2.69	1.04E-03	45.53	3.71	2.75E-03
0.9977	50.22	18.23	6.97E-03	46.09	4.93	3.07E-03	47.17	6.71	3.58E-03	37.48	-2.90	9.82E-04	44.80	2.71	2.47E-03
0.9990	50.25	18.31	7.01E-03	45.92	4.63	2.99E-03	46.87	6.10	3.41E-03	37.16	-3.04	9.46E-04	44.29	2.08	2.30E-03
0.9998	50.27	18.36	7.03E-03	45.82	4.46	2.94E-03	46.69	5.75	3.32E-03	36.97	-3.12	9.26E-04	43.99	1.74	2.21E-03
1.0000	50.28	18.37	7.04E-03	45.78	4.41	2.93E-03	46.63	5.64	3.29E-03	36.91	-3.14	9.19E-04	43.89	1.63	2.18E-03

The local freestream flow direction, twist in the boundary layer and boundary layer displacement thickness from WAKELAG over the upper surface of the DERA wing. $\Lambda = 50°$, $\alpha = 0.3°$, $Re_c = 3.9 \times 10^6$.

η	0.06b			0.16b			0.30b			0.45b			0.59b		
x/c	α_c (°)	β_c (°)	δ*/c	α_c (°)	β_c (°)	δ*/c	α_c (°)	β_c (°)	δ*/c	α_c (°)	β_c (°)	δ*/c	α_c (°)	β_c (°)	δ*/c
0.0556	44.56	-0.57	1.38E-04	43.65	-0.32	1.38E-04	42.90	-0.28	1.37E-04	42.08	-0.12	1.34E-04	41.66	-0.15	1.34E-04
0.0631	44.19	-1.13	1.63E-04	43.45	-0.64	1.65E-04	42.67	-0.68	1.62E-04	42.00	-0.26	1.61E-04	41.60	-0.24	1.61E-04
0.0710	43.84	-1.40	1.83E-04	43.21	-0.87	1.86E-04	42.39	-0.99	1.81E-04	41.90	-0.38	1.81E-04	41.54	-0.28	1.83E-04
0.0794	43.54	-1.53	2.05E-04	42.92	-1.13	2.07E-04	42.11	-1.22	2.01E-04	41.74	-0.57	2.01E-04	41.44	-0.38	2.05E-04
0.0882	43.30	-1.56	2.30E-04	42.43	-1.67	2.23E-04	41.81	-1.44	2.21E-04	41.49	-0.88	2.20E-04	41.25	-0.62	2.29E-04
0.0974	43.08	-1.59	2.55E-04	41.87	-2.18	2.38E-04	41.52	-1.62	2.41E-04	41.20	-1.18	2.39E-04	41.00	-0.88	2.54E-04
0.1070	42.82	-1.70	2.76E-04	41.61	-2.21	2.61E-04	41.31	-1.66	2.63E-04	41.00	-1.29	2.61E-04	40.81	-1.02	2.78E-04
0.1170	42.53	-1.88	2.94E-04	41.43	-2.15	2.85E-04	41.15	-1.64	2.87E-04	40.85	-1.32	2.83E-04	40.65	-1.11	3.01E-04
0.1274	42.23	-2.06	3.11E-04	41.29	-2.05	3.09E-04	41.01	-1.60	3.12E-04	40.73	-1.31	3.07E-04	40.52	-1.16	3.24E-04
0.1381	41.94	-2.21	3.28E-04	41.18	-1.94	3.34E-04	40.89	-1.55	3.36E-04	40.62	-1.30	3.31E-04	40.41	-1.18	3.47E-04
0.1493	41.70	-2.28	3.48E-04	41.05	-1.87	3.57E-04	40.76	-1.54	3.59E-04	40.50	-1.31	3.54E-04	40.31	-1.18	3.70E-04
0.1607	41.51	-2.28	3.70E-04	40.92	-1.83	3.80E-04	40.61	-1.57	3.81E-04	40.36	-1.35	3.76E-04	40.23	-1.17	3.94E-04
0.1726	41.35	-2.25	3.93E-04	40.80	-1.80	4.03E-04	40.46	-1.60	4.03E-04	40.23	-1.39	3.97E-04	40.15	-1.15	4.19E-04
0.1847	41.20	-2.22	4.16E-04	40.68	-1.77	4.26E-04	40.32	-1.63	4.25E-04	40.09	-1.43	4.19E-04	40.07	-1.14	4.43E-04
0.1972	41.06	-2.19	4.39E-04	40.55	-1.77	4.48E-04	40.17	-1.66	4.47E-04	39.98	-1.45	4.42E-04	39.98	-1.16	4.66E-04
0.2100	40.90	-2.18	4.61E-04	40.38	-1.82	4.68E-04	40.03	-1.70	4.69E-04	39.88	-1.45	4.66E-04	39.87	-1.20	4.88E-04
0.2230	40.75	-2.19	4.82E-04	40.18	-1.92	4.85E-04	39.87	-1.76	4.89E-04	39.78	-1.44	4.90E-04	39.75	-1.26	5.10E-04
0.2364	40.60	-2.18	5.04E-04	40.00	-2.00	5.04E-04	39.73	-1.79	5.11E-04	39.71	-1.41	5.15E-04	39.65	-1.29	5.33E-04
0.2500	40.50	-2.13	5.29E-04	39.90	-1.96	5.28E-04	39.67	-1.72	5.38E-04	39.68	-1.33	5.44E-04	39.60	-1.25	5.59E-04
0.2639	40.45	-2.02	5.57E-04	39.90	-1.79	5.61E-04	39.72	-1.51	5.74E-04	39.70	-1.18	5.76E-04	39.61	-1.13	5.92E-04
0.2780	40.43	-1.89	5.88E-04	39.97	-1.56	5.99E-04	39.85	-1.21	6.17E-04	39.77	-0.98	6.13E-04	39.68	-0.95	6.28E-04
0.2923	40.43	-1.73	6.20E-04	40.06	-1.31	6.38E-04	40.00	-0.90	6.61E-04	39.86	-0.77	6.52E-04	39.77	-0.74	6.67E-04
0.3068	40.46	-1.57	6.54E-04	40.14	-1.10	6.76E-04	40.11	-0.66	7.02E-04	39.96	-0.56	6.90E-04	39.89	-0.50	7.09E-04
0.3216	40.53	-1.35	6.92E-04	40.24	-0.87	7.16E-04	40.22	-0.45	7.41E-04	40.08	-0.34	7.32E-04	40.09	-0.17	7.59E-04
0.3365	40.61	-1.14	7.30E-04	40.34	-0.66	7.56E-04	40.31	-0.26	7.80E-04	40.21	-0.12	7.74E-04	40.31	0.18	8.12E-04
0.3515	40.65	-1.00	7.65E-04	40.42	-0.50	7.93E-04	40.40	-0.12	8.17E-04	40.34	0.09	8.17E-04	40.46	0.42	8.58E-04
0.3668	40.65	-0.93	7.94E-04	40.46	-0.40	8.26E-04	40.46	-0.01	8.52E-04	40.49	0.31	8.63E-04	40.54	0.51	8.94E-04
0.3821	40.62	-0.91	8.20E-04	40.49	-0.33	8.57E-04	40.52	0.07	8.86E-04	40.64	0.52	9.09E-04	40.58	0.54	9.25E-04
0.3976	40.57	-0.92	8.43E-04	40.49	-0.30	8.86E-04	40.55	0.11	9.17E-04	40.73	0.64	9.48E-04	40.61	0.55	9.54E-04
0.4132	40.48	-0.98	8.63E-04	40.48	-0.30	9.12E-04	40.55	0.11	9.44E-04	40.74	0.61	9.75E-04	40.64	0.56	9.84E-04
0.4288	40.37	-1.07	8.79E-04	40.45	-0.33	9.36E-04	40.52	0.07	9.68E-04	40.69	0.50	9.94E-04	40.66	0.55	1.01E-03
0.4446	40.26	-1.16	8.94E-04	40.39	-0.38	9.57E-04	40.49	0.01	9.90E-04	40.62	0.37	1.01E-03	40.65	0.51	1.04E-03
0.4604	40.16	-1.22	9.13E-04	40.32	-0.46	9.76E-04	40.45	-0.04	1.01E-03	40.56	0.26	1.03E-03	40.63	0.45	1.06E-03
0.4762	40.09	-1.25	9.34E-04	40.23	-0.56	9.92E-04	40.42	-0.09	1.04E-03	40.50	0.15	1.05E-03	40.60	0.37	1.08E-03
0.4921	39.99	-1.31	9.52E-04	40.11	-0.69	1.00E-03	40.35	-0.17	1.05E-03	40.40	0.01	1.06E-03	40.52	0.25	1.10E-03
0.5079	39.81	-1.48	9.58E-04	39.93	-0.89	1.01E-03	40.20	-0.37	1.06E-03	40.23	-0.22	1.06E-03	40.36	0.02	1.10E-03
0.5238	39.48	-1.80	9.44E-04	39.55	-1.31	9.83E-04	39.89	-0.75	1.04E-03	39.93	-0.59	1.05E-03	40.06	-0.38	1.08E-03
0.5396	39.10	-2.15	9.26E-04	39.09	-1.78	9.51E-04	39.52	-1.17	1.02E-03	39.58	-0.99	1.03E-03	39.70	-0.81	1.06E-03
0.5554	38.75	-2.44	9.14E-04	38.68	-2.15	9.30E-04	39.15	-1.54	9.95E-04	39.26	-1.31	1.01E-03	39.35	-1.18	1.03E-03
0.5712	38.40	-2.70	9.04E-04	38.43	-2.33	9.31E-04	38.73	-1.93	9.70E-04	38.95	-1.60	1.01E-03	38.96	-1.57	1.01E-03
0.5868	38.25	-2.77	9.20E-04	38.42	-2.27	9.63E-04	38.63	-1.98	9.89E-04	38.76	-1.75	1.02E-03	38.87	-1.62	1.03E-03
0.6024	38.22	-2.71	9.51E-04	38.51	-2.12	1.01E-03	38.77	-1.77	1.04E-03	38.88	-1.58	1.07E-03	39.01	-1.41	1.08E-03
0.6179	38.25	-2.60	9.91E-04	38.65	-1.90	1.06E-03	39.01	-1.45	1.11E-03	39.26	-1.09	1.16E-03	39.26	-1.09	1.16E-03
0.6332	38.85	-1.85	1.12E-03	39.22	-1.16	1.19E-03	39.60	-0.68	1.24E-03	39.86	-0.30	1.30E-03	39.90	-0.25	1.30E-03
0.6485	39.98	-0.27	1.36E-03	40.21	0.26	1.41E-03	40.55	0.70	1.47E-03	40.59	0.80	1.48E-03	40.95	1.33	1.55E-03
0.6635	40.65	0.82	1.53E-03	40.94	1.47	1.61E-03	41.29	1.95	1.67E-03	41.41	2.17	1.70E-03	41.73	2.69	1.78E-03
0.6784	41.22	1.82	1.70E-03	41.63	2.72	1.82E-03	42.01	3.28	1.89E-03	42.23	3.73	1.96E-03	42.46	4.11	2.02E-03
0.6932	41.75	2.79	1.87E-03	42.26	3.96	2.03E-03	42.67	4.61	2.13E-03	42.94	5.25	2.23E-03	43.13	5.53	2.28E-03
0.7077	42.27	3.81	2.05E-03	42.82	5.13	2.24E-03	43.24	5.83	2.35E-03	43.49	6.47	2.46E-03	43.74	6.90	2.54E-03
0.7220	42.77	4.84	2.24E-03	43.34	6.24	2.46E-03	43.77	6.99	2.58E-03	44.03	7.71	2.70E-03	44.32	8.27	2.82E-03
0.7361	43.25	5.86	2.43E-03	43.82	7.31	2.67E-03	44.26	8.11	2.82E-03	44.54	8.98	2.96E-03	44.85	9.61	3.10E-03
0.7500	43.71	6.86	2.63E-03	44.28	8.34	2.90E-03	44.72	9.16	3.05E-03	45.02	10.19	3.23E-03	45.33	10.85	3.38E-03
0.7636	44.14	7.80	2.84E-03	44.72	9.36	3.13E-03	45.14	10.16	3.29E-03	45.47	11.36	3.50E-03	45.75	11.90	3.65E-03
0.7770	44.54	8.70	3.04E-03	45.13	10.35	3.36E-03	45.54	11.10	3.53E-03	45.89	12.50	3.79E-03	46.13	12.81	3.90E-03
0.7900	44.93	9.60	3.26E-03	45.52	11.28	3.60E-03	45.92	11.99	3.77E-03	46.28	13.53	4.07E-03	46.51	13.76	4.18E-03
0.8028	45.33	10.52	3.49E-03	45.87	12.09	3.83E-03	46.29	12.86	4.03E-03	46.61	14.33	4.31E-03	46.92	15.00	4.53E-03
0.8153	45.72	11.47	3.74E-03	46.18	12.77	4.04E-03	46.64	13.71	4.29E-03	46.89	14.90	4.53E-03	47.41	16.75	5.01E-03
0.8274	46.06	12.27	3.97E-03	46.50	13.50	4.27E-03	46.94	14.38	4.52E-03	47.19	15.58	4.77E-03	47.65	17.18	5.21E-03
0.8393	46.38	13.01	4.19E-03	46.81	14.22	4.51E-03	47.20	14.91	4.73E-03	47.48	16.29	5.03E-03	47.79	16.97	5.28E-03
0.8507	46.81	14.32	4.55E-03	47.05	14.62	4.69E-03	47.48	15.53	4.96E-03	47.72	16.69	5.23E-03	47.99	17.18	5.44E-03
0.8619	47.16	15.34	4.87E-03	47.28	15.02	4.87E-03	47.73	16.07	5.19E-03	47.93	16.98	5.40E-03	48.19	17.46	5.62E-03
0.8726	47.33	15.47	4.99E-03	47.53	15.55	5.09E-03	47.95	16.46	5.38E-03	48.12	17.21	5.57E-03	48.38	17.70	5.79E-03
0.8830	47.50	15.64	5.11E-03	47.86	16.57	5.43E-03	48.15	16.79	5.56E-03	48.31	17.49	5.74E-03	48.55	17.85	5.94E-03
0.8930	47.72	16.08	5.31E-03	48.41	19.19	6.20E-03	48.34	17.09	5.74E-03	48.52	17.88	5.95E-03	48.70	17.91	6.06E-03
0.9026	47.95	16.66	5.54E-03	48.65	19.96	6.51E-03	48.52	17.33	5.90E-03	48.69	18.16	6.13E-03	48.84	17.95	6.18E-03
0.9118	48.17	17.27	5.78E-03	48.59	18.60	6.25E-03	48.67	17.50	6.04E-03	48.83	18.25	6.25E-03	48.98	17.99	6.29E-03
0.9206	48.38	17.79	6.00E-03	48.56	17.67	6.09E-03	48.81	17.61	6.17E-03	48.94	18.23	6.34E-03	49.10	17.99	6.39E-03
0.9290	48.57	18.27	6.22E-03	48.69	17.73	6.20E-03	48.92	17.61	6.26E-03	49.04	18.17	6.41E-03	49.20	17.94	6.47E-03
0.9369	48.74	18.68	6.42E-03	48.85	18.09	6.39E-03	49.03	17.61	6.34E-03	49.13	18.10	6.48E-03	49.29	17.84	6.53E-03
0.9444	48.88	18.92	6.58E-03	48.98	18.26	6.52E-03	49.15	17.78	6.48E-03	49.23	18.06	6.55E-03	49.35	17.61	6.55E-03
0.9515	48.99	19.01	6.69E-03	49.10	18.39	6.64E-03	49.30	18.10	6.65E-03	49.32	18.03	6.62E-03	49.38	17.30	6.53E-03
0.9581	49.09	19.11	6.79E-03	49.18	18.36	6.71E-03	49.43	18.35	6.80E-03	49.39	17.95	6.67E-03	49.42	17.05	6.52E-03
0.9642	49.20	19.30	6.92E-03	49.17	17.83	6.61E-03	49.51	18.39	6.89E-03	49.00	15.53	5.99E-03	49.49	16.99	6.57E-03
0.9699	49.31	19.55	7.07E-03	48.97	16.36	6.22E-03	49.58	18.37	6.95E-03	47.41	9.77	4.31E-03	49.57	17.07	6.66E-03
0.9750	49.42	19.80	7.21E-03	48.65	14.59	5.73E-03	49.63	18.25	6.97E-03	45.45	5.48	3.12E-03	49.65	17.15	6.74E-03
0.9798	49.51	20.06	7.35E-03	48.27	12.88	5.26E-03	49.64	18.00	6.94E-03	43.66	2.80	2.40E-03	49.71	17.14	6.79E-03
0.9840	49.60	20.31	7.48E-03	47.88	11.41	4.85E-03	49.51	16.97	6.66E-03	42.19	1.14	1.96E-03	49.41	15.44	6.28E-03
0.9877	49.68	20.53	7.60E-03	47.51	10.18	4.51E-03	49.17	15.14	6.11E-03	41.02	0.07	1.69E-03	48.61	12.26	5.27E-03
0.9910	49.75	20.74	7.71E-03	47.17	9.19	4.23E-03	48.76	13.34	5.56E-03	40.07	-0.66	1.50E-03	47.66	9.44	4.41E-03
0.9937	49.81	20.91	7.81E-03	46.88	8.41	4.02E-03	48.36	11.84	5.11E-03	39.32	-1.17	1.36E-03	46.75	7.33	3.78E-03
0.9960	49.86	21.06	7.89E-03	46.64	7.82	3.86E-03	48.00	10.69	4.77E-03	38.73	-1.53	1.27E-03	45.98	5.84	3.34E-03
0.9977	49.90	21.18	7.95E-03	46.45	7.38	3.74E-03	47.72	9.86	4.52E-03	38.29	-1.78	1.21E-03	45.38	4.84	3.05E-03
0.9990	49.92	21.27	8.00E-03	46.32	7.08	3.66E-03	47.52	9.31	4.36E-03	37.99	-1.94	1.16E-03	44.96	4.20	2.87E-03
0.9998	49.94	21.32	8.03E-03	46.24	6.91	3.61E-03	47.40	8.99	4.27E-03	37.81	-2.03	1.14E-03	44.71	3.84	2.77E-03
1.0000	49.94	21.34	8.04E-03	46.21	6.85	3.59E-03	47.36	8.89	4.24E-03	37.75	-2.06	1.13E-03	44.63	3.72	2.73E-03

The local freestream flow direction, twist in the boundary layer and boundary layer displacement thickness from WAKELAG over the upper surface of the DERA wing. $\Lambda = 50°$, $\alpha = 2.4°$, $Re_c = 3.9 \times 10^6$.

η	0.06b			0.16b			0.30b			0.45b			0.59b		
x/c	α_c (°)	β_c (°)	δ^*/c	α_c (°)	β_c (°)	δ^*/c	α_c (°)	β_c (°)	δ^*/c	α_c (°)	β_c (°)	δ^*/c	α_c (°)	β_c (°)	δ^*/c
0.0556	41.17	-0.19	1.33E-04	40.13	0.06	1.33E-04	39.21	0.07	1.31E-04	38.39	0.31	1.28E-04	38.11	0.24	1.29E-04
0.0631	41.02	-0.44	1.60E-04	40.13	0.03	1.61E-04	39.22	0.07	1.59E-04	38.58	0.64	1.58E-04	38.26	0.50	1.57E-04
0.0710	40.87	-0.59	1.82E-04	40.10	-0.05	1.85E-04	39.20	0.00	1.81E-04	38.71	0.72	1.82E-04	38.39	0.61	1.81E-04
0.0794	40.74	-0.66	2.06E-04	40.03	-0.16	2.09E-04	39.15	-0.09	2.04E-04	38.75	0.59	2.04E-04	38.45	0.56	2.05E-04
0.0882	40.65	-0.65	2.32E-04	39.72	-0.65	2.27E-04	39.04	-0.27	2.26E-04	38.66	0.27	2.24E-04	38.42	0.35	2.31E-04
0.0974	40.57	-0.64	2.59E-04	39.28	-1.23	2.42E-04	38.88	-0.48	2.47E-04	38.53	-0.01	2.45E-04	38.35	0.15	2.59E-04
0.1070	40.46	-0.72	2.83E-04	39.14	-1.24	2.67E-04	38.79	-0.54	2.71E-04	38.46	-0.13	2.68E-04	38.31	0.04	2.86E-04
0.1170	40.29	-0.88	3.03E-04	39.08	-1.16	2.93E-04	38.75	-0.54	2.96E-04	38.43	-0.17	2.93E-04	38.28	-0.02	3.11E-04
0.1274	40.09	-1.06	3.21E-04	39.05	-1.04	3.19E-04	38.72	-0.50	3.23E-04	38.42	-0.15	3.19E-04	38.26	-0.05	3.36E-04
0.1381	39.90	-1.21	3.40E-04	39.04	-0.91	3.46E-04	38.70	-0.46	3.49E-04	38.42	-0.14	3.45E-04	38.24	-0.07	3.61E-04
0.1493	39.75	-1.29	3.61E-04	39.01	-0.83	3.71E-04	38.67	-0.45	3.75E-04	38.40	-0.14	3.70E-04	38.24	-0.07	3.87E-04
0.1607	39.65	-1.29	3.85E-04	38.97	-0.79	3.96E-04	38.61	-0.48	3.99E-04	38.36	-0.19	3.94E-04	38.24	-0.06	4.13E-04
0.1726	39.58	-1.25	4.11E-04	38.94	-0.75	4.21E-04	38.55	-0.53	4.22E-04	38.31	-0.25	4.18E-04	38.24	-0.05	4.39E-04
0.1847	39.52	-1.21	4.36E-04	38.90	-0.73	4.46E-04	38.48	-0.57	4.46E-04	38.25	-0.31	4.41E-04	38.24	-0.04	4.65E-04
0.1972	39.45	-1.19	4.61E-04	38.85	-0.73	4.71E-04	38.41	-0.61	4.70E-04	38.21	-0.34	4.66E-04	38.24	-0.04	4.92E-04
0.2100	39.35	-1.21	4.84E-04	38.76	-0.79	4.92E-04	38.35	-0.65	4.94E-04	38.19	-0.34	4.92E-04	38.22	-0.07	5.17E-04
0.2230	39.24	-1.26	5.05E-04	38.63	-0.90	5.12E-04	38.27	-0.70	5.17E-04	38.17	-0.33	5.19E-04	38.19	-0.10	5.43E-04
0.2364	39.14	-1.29	5.27E-04	38.52	-0.98	5.32E-04	38.22	-0.72	5.42E-04	38.18	-0.30	5.47E-04	38.18	-0.11	5.69E-04
0.2500	39.08	-1.26	5.53E-04	38.47	-0.97	5.58E-04	38.21	-0.67	5.71E-04	38.21	-0.22	5.78E-04	38.20	-0.07	5.99E-04
0.2639	39.08	-1.16	5.83E-04	38.52	-0.81	5.92E-04	38.30	-0.48	6.08E-04	38.29	-0.07	6.14E-04	38.27	0.05	6.34E-04
0.2780	39.11	-1.02	6.16E-04	38.65	-0.56	6.34E-04	38.48	-0.17	6.54E-04	38.43	0.14	6.55E-04	38.40	0.23	6.74E-04
0.2923	39.17	-0.86	6.51E-04	38.81	-0.29	6.78E-04	38.68	0.16	7.03E-04	38.58	0.37	6.98E-04	38.55	0.46	7.18E-04
0.3068	39.24	-0.69	6.88E-04	38.94	-0.06	7.20E-04	38.85	0.42	7.48E-04	38.74	0.59	7.41E-04	38.73	0.70	7.64E-04
0.3216	39.35	-0.48	7.28E-04	39.07	0.15	7.62E-04	39.01	0.65	7.92E-04	38.91	0.83	7.87E-04	38.96	1.04	8.18E-04
0.3365	39.47	-0.26	7.70E-04	39.21	0.35	8.04E-04	39.17	0.85	8.37E-04	39.09	1.07	8.35E-04	39.21	1.38	8.75E-04
0.3515	39.55	-0.12	8.07E-04	39.32	0.50	8.44E-04	39.30	1.01	8.79E-04	39.26	1.27	8.81E-04	39.41	1.61	9.25E-04
0.3668	39.59	-0.06	8.39E-04	39.40	0.60	8.81E-04	39.42	1.12	9.18E-04	39.42	1.44	9.27E-04	39.54	1.72	9.67E-04
0.3821	39.59	-0.04	8.67E-04	39.47	0.67	9.15E-04	39.51	1.20	9.56E-04	39.57	1.59	9.72E-04	39.64	1.78	1.01E-03
0.3976	39.58	-0.06	8.92E-04	39.52	0.70	9.47E-04	39.59	1.24	9.90E-04	39.69	1.68	1.01E-03	39.73	1.81	1.04E-03
0.4132	39.54	-0.11	9.15E-04	39.55	0.70	9.76E-04	39.63	1.23	1.02E-03	39.76	1.69	1.05E-03	39.81	1.83	1.08E-03
0.4288	39.48	-0.20	9.33E-04	39.55	0.66	1.00E-03	39.65	1.18	1.05E-03	39.80	1.65	1.08E-03	39.88	1.83	1.11E-03
0.4446	39.41	-0.28	9.52E-04	39.53	0.59	1.03E-03	39.65	1.12	1.07E-03	39.82	1.58	1.10E-03	39.93	1.80	1.14E-03
0.4604	39.35	-0.34	9.73E-04	39.49	0.50	1.05E-03	39.65	1.06	1.10E-03	39.82	1.49	1.13E-03	39.96	1.75	1.17E-03
0.4762	39.32	-0.38	9.96E-04	39.44	0.40	1.06E-03	39.66	1.01	1.12E-03	39.80	1.38	1.15E-03	39.98	1.69	1.20E-03
0.4921	39.25	-0.45	1.02E-03	39.35	0.26	1.08E-03	39.62	0.91	1.14E-03	39.75	1.22	1.16E-03	39.96	1.56	1.22E-03
0.5079	39.10	-0.62	1.02E-03	39.20	0.04	1.08E-03	39.50	0.69	1.15E-03	39.62	0.98	1.17E-03	39.85	1.32	1.22E-03
0.5238	38.80	-0.97	1.01E-03	38.88	-0.38	1.06E-03	39.25	0.31	1.13E-03	39.38	0.59	1.15E-03	39.59	0.88	1.20E-03
0.5396	38.45	-1.34	9.88E-04	38.48	-0.85	1.03E-03	38.93	-0.12	1.11E-03	39.09	0.18	1.13E-03	39.27	0.42	1.17E-03
0.5554	38.14	-1.64	9.76E-04	38.13	-1.22	1.01E-03	38.62	-0.50	1.09E-03	38.84	-0.15	1.12E-03	38.98	0.04	1.15E-03
0.5712	37.83	-1.92	9.65E-04	37.93	-1.41	1.01E-03	38.26	-0.89	1.06E-03	38.60	-0.43	1.12E-03	38.69	-0.33	1.13E-03
0.5868	37.72	-1.98	9.83E-04	37.95	-1.34	1.05E-03	38.18	-0.95	1.08E-03	38.45	-0.58	1.13E-03	38.62	-0.39	1.15E-03
0.6024	37.74	-1.89	1.02E-03	38.09	-1.13	1.10E-03	38.39	-0.69	1.15E-03	38.61	-0.37	1.19E-03	38.85	-0.11	1.22E-03
0.6179	37.82	-1.74	1.07E-03	38.31	-0.84	1.17E-03	38.71	-0.27	1.23E-03	39.05	0.20	1.30E-03	39.20	0.35	1.31E-03
0.6332	38.43	-0.97	1.20E-03	38.94	0.00	1.31E-03	39.38	0.64	1.39E-03	39.70	1.12	1.46E-03	39.92	1.38	1.49E-03
0.6485	39.53	0.65	1.46E-03	39.97	1.59	1.57E-03	40.40	2.27	1.66E-03	40.51	2.41	1.68E-03	41.04	3.25	1.80E-03
0.6635	40.23	1.81	1.65E-03	40.72	2.91	1.79E-03	41.19	3.71	1.90E-03	41.40	4.05	1.96E-03	41.88	4.89	2.09E-03
0.6784	40.83	2.91	1.83E-03	41.41	4.26	2.02E-03	41.93	5.24	2.17E-03	42.28	5.94	2.28E-03	42.67	6.64	2.40E-03
0.6932	41.39	3.99	2.03E-03	42.05	5.62	2.27E-03	42.62	6.77	2.45E-03	43.05	7.83	2.63E-03	43.39	8.41	2.74E-03
0.7077	41.94	5.13	2.23E-03	42.64	6.94	2.52E-03	43.23	8.23	2.73E-03	43.64	9.34	2.93E-03	44.04	10.14	3.09E-03
0.7220	42.48	6.32	2.46E-03	43.20	8.27	2.78E-03	43.80	9.69	3.03E-03	44.22	10.95	3.26E-03	44.66	11.95	3.47E-03
0.7361	43.00	7.51	2.69E-03	43.72	9.57	3.05E-03	44.33	11.11	3.34E-03	44.77	12.62	3.62E-03	45.22	13.74	3.88E-03
0.7500	43.48	8.67	2.93E-03	44.21	10.82	3.33E-03	44.80	12.39	3.65E-03	45.26	14.14	3.98E-03	45.69	15.23	4.25E-03
0.7636	43.92	9.75	3.17E-03	44.66	12.04	3.62E-03	45.22	13.53	3.94E-03	45.69	15.52	4.33E-03	46.08	16.38	4.58E-03
0.7770	44.34	10.78	3.41E-03	45.08	13.24	3.92E-03	45.60	14.55	4.23E-03	46.09	16.84	4.69E-03	46.42	17.31	4.88E-03
0.7900	44.74	11.82	3.67E-03	45.48	14.35	4.22E-03	45.96	15.49	4.51E-03	46.44	17.93	5.03E-03	46.73	18.04	5.16E-03
0.8028	45.15	12.92	3.95E-03	45.83	15.29	4.49E-03	46.30	16.38	4.80E-03	46.72	18.59	5.28E-03	46.99	18.57	5.40E-03
0.8153	45.56	14.13	4.27E-03	46.13	16.03	4.75E-03	46.62	17.27	5.10E-03	46.94	18.84	5.46E-03	47.23	18.95	5.61E-03
0.8274	45.91	15.06	4.55E-03	46.44	16.81	5.02E-03	46.86	17.69	5.31E-03	47.17	19.17	5.67E-03	47.41	18.97	5.75E-03
0.8393	46.21	15.82	4.81E-03	46.74	17.61	5.31E-03	47.06	17.84	5.46E-03	47.38	19.46	5.86E-03	47.55	18.75	5.82E-03
0.8507	46.54	16.75	5.11E-03	47.00	18.21	5.56E-03	47.29	18.30	5.69E-03	47.54	19.37	5.97E-03	47.66	18.41	5.86E-03
0.8619	46.83	17.61	5.41E-03	47.24	18.72	5.80E-03	47.51	18.67	5.90E-03	47.66	19.11	6.03E-03	47.77	18.12	5.90E-03
0.8726	47.09	18.26	5.67E-03	47.44	19.05	6.00E-03	47.67	18.71	6.02E-03	47.77	18.78	6.06E-03	47.91	18.05	6.00E-03
0.8830	47.33	18.87	5.93E-03	47.71	19.91	6.33E-03	47.81	18.68	6.13E-03	47.87	18.48	6.10E-03	48.02	17.86	6.06E-03
0.8930	47.55	19.50	6.19E-03	48.17	22.59	7.18E-03	47.94	18.63	6.23E-03	47.97	18.24	6.14E-03	48.09	17.49	6.06E-03
0.9026	47.77	20.10	6.45E-03	48.38	23.31	7.51E-03	48.07	18.59	6.33E-03	48.07	18.02	6.19E-03	48.16	17.14	6.07E-03
0.9118	47.96	20.64	6.70E-03	48.33	21.63	7.16E-03	48.19	18.60	6.43E-03	48.16	17.85	6.24E-03	48.23	16.86	6.08E-03
0.9206	48.14	21.08	6.93E-03	48.31	20.43	6.93E-03	48.31	18.59	6.53E-03	48.24	17.70	6.29E-03	48.29	16.59	6.09E-03
0.9290	48.30	21.44	7.14E-03	48.39	20.22	6.98E-03	48.41	18.50	6.60E-03	48.32	17.54	6.33E-03	48.34	16.31	6.09E-03
0.9369	48.44	21.70	7.32E-03	48.51	20.29	7.10E-03	48.50	18.40	6.66E-03	48.38	17.34	6.35E-03	48.38	16.03	6.09E-03
0.9444	48.55	21.74	7.43E-03	48.60	20.21	7.17E-03	48.58	18.32	6.72E-03	48.44	17.12	6.36E-03	48.40	15.71	6.06E-03
0.9515	48.63	21.60	7.49E-03	48.69	20.14	7.24E-03	48.66	18.27	6.79E-03	48.48	16.90	6.37E-03	48.40	15.36	6.02E-03
0.9581	48.71	21.53	7.55E-03	48.74	19.90	7.25E-03	48.73	18.17	6.83E-03	48.52	16.64	6.36E-03	48.41	15.07	5.99E-03
0.9642	48.81	21.65	7.68E-03	48.72	19.25	7.12E-03	48.78	18.01	6.85E-03	48.21	14.94	5.89E-03	48.44	14.88	5.99E-03
0.9699	48.92	21.90	7.83E-03	48.59	18.03	6.80E-03	48.82	17.86	6.87E-03	47.03	10.71	4.63E-03	48.48	14.78	6.01E-03
0.9750	49.02	22.20	8.01E-03	48.39	16.63	6.41E-03	48.84	17.62	6.85E-03	45.55	7.13	3.59E-03	48.52	14.68	6.02E-03
0.9798	49.12	22.53	8.18E-03	48.15	15.27	6.03E-03	48.83	17.24	6.78E-03	44.15	4.66	2.90E-03	48.53	14.53	6.02E-03
0.9840	49.21	22.84	8.34E-03	47.90	14.06	5.68E-03	48.76	16.66	6.63E-03	42.98	3.04	2.45E-03	48.33	13.62	5.75E-03
0.9877	49.29	23.13	8.50E-03	47.67	13.03	5.39E-03	48.66	15.96	6.43E-03	42.02	1.93	2.15E-03	47.85	11.89	5.21E-03
0.9910	49.36	23.39	8.64E-03	47.45	12.18	5.15E-03	48.54	15.26	6.24E-03	41.24	1.15	1.94E-03	47.27	10.16	4.68E-03
0.9937	49.42	23.63	8.76E-03	47.26	11.50	4.96E-03	48.42	14.65	6.06E-03	40.61	0.58	1.79E-03	46.71	8.73	4.24E-03
0.9960	49.47	23.83	8.86E-03	47.11	10.97	4.81E-03	48.32	14.15	5.92E-03	40.11	0.18	1.68E-03	46.21	7.64	3.90E-03
0.9977	49.51	23.99	8.95E-03	46.98	10.58	4.70E-03	48.23	13.77	5.81E-03	39.74	-0.11	1.61E-03	45.83	6.86	3.67E-03
0.9990	49.54	24.10	9.01E-03	46.90	10.31	4.63E-03	48.17	13.50	5.73E-03	39.48	-0.30	1.56E-03	45.55	6.35	3.52E-03
0.9998	49.55	24.18	9.05E-03	46.85	10.15	4.58E-03	48.14	13.35	5.68E-03	39.32	-0.41	1.53E-03	45.39	6.05	3.43E-03
1.0000	49.56	24.20	9.06E-03	46.83	10.10	4.57E-03	48.13	13.30	5.67E-03	39.27	-0.45	1.52E-03	45.33	5.96	3.40E-03

The local freestream flow direction, twist in the boundary layer and boundary layer displacement thickness from WAKELAG over the upper surface of the DERA wing. $\Lambda = 50°$, $\alpha = 4.5°$, $Re_c = 3.9 \times 10^6$.

η	0.06b			0.16b			0.30b			0.45b			0.59b		
x/c	α_c (°)	β_c (°)	δ"/c	α_c (°)	β_c (°)	δ"/c	α_c (°)	β_c (°)	δ"/c	α_c (°)	β_c (°)	δ"/c	α_c (°)	β_c (°)	δ"/c
0.0556	38.26	0.11	1.28E-04	37.06	0.34	1.27E-04				35.43	0.60	1.23E-04	35.19	0.49	1.23E-04
0.0631	38.31	0.17	1.57E-04	37.28	0.72	1.59E-04				35.76	1.18	1.54E-04	35.50	1.03	1.53E-04
0.0710	38.33	0.17	1.81E-04	37.47	0.86	1.85E-04				36.02	1.34	1.79E-04	35.77	1.28	1.79E-04
0.0794	38.35	0.15	2.07E-04	37.54	0.75	2.11E-04				36.14	1.21	2.02E-04	35.94	1.26	2.04E-04
0.0882	38.35	0.12	2.34E-04	37.34	0.20	2.29E-04				36.17	0.96	2.24E-04	36.02	1.05	2.31E-04
0.0974	38.34	0.07	2.61E-04	37.02	-0.38	2.45E-04				36.18	0.79	2.48E-04	36.08	0.90	2.61E-04
0.1070	38.31	0.00	2.85E-04	36.96	-0.42	2.71E-04				36.22	0.72	2.73E-04	36.14	0.84	2.90E-04
0.1170	38.24	-0.12	3.08E-04	36.97	-0.33	2.98E-04				36.29	0.72	3.00E-04	36.21	0.83	3.18E-04
0.1274	38.15	-0.25	3.29E-04	37.04	-0.18	3.27E-04				36.38	0.77	3.28E-04	36.29	0.84	3.46E-04
0.1381	38.06	-0.37	3.50E-04	37.12	-0.01	3.56E-04				36.47	0.82	3.57E-04	36.36	0.86	3.74E-04
0.1493	37.99	-0.43	3.73E-04	37.18	0.09	3.85E-04				36.55	0.84	3.84E-04	36.44	0.89	4.02E-04
0.1607	37.95	-0.43	3.98E-04	37.22	0.14	4.12E-04				36.59	0.81	4.11E-04	36.52	0.91	4.30E-04
0.1726	37.94	-0.41	4.25E-04	37.26	0.19	4.39E-04				36.63	0.77	4.37E-04	36.59	0.93	4.59E-04
0.1847	37.93	-0.37	4.51E-04	37.28	0.21	4.66E-04				36.65	0.73	4.64E-04	36.66	0.95	4.88E-04
0.1972	37.92	-0.35	4.78E-04	37.30	0.21	4.92E-04				36.69	0.71	4.91E-04	36.73	0.96	5.17E-04
0.2100	37.89	-0.36	5.03E-04	37.28	0.16	5.16E-04				36.73	0.71	5.20E-04	36.78	0.95	5.46E-04
0.2230	37.85	-0.39	5.28E-04	37.22	0.05	5.38E-04				36.78	0.71	5.49E-04	36.82	0.93	5.74E-04
0.2364	37.82	-0.41	5.53E-04	37.16	-0.04	5.60E-04				36.84	0.74	5.80E-04	36.86	0.91	6.03E-04
0.2500	37.82	-0.38	5.80E-04	37.15	-0.05	5.87E-04				36.92	0.82	6.13E-04	36.94	0.95	6.36E-04
0.2639	37.86	-0.28	6.12E-04	37.24	0.09	6.23E-04				37.06	0.97	6.52E-04	37.07	1.09	6.75E-04
0.2780	37.93	-0.15	6.47E-04	37.42	0.35	6.67E-04				37.24	1.20	6.97E-04	37.25	1.31	7.20E-04
0.2923	38.03	0.01	6.85E-04	37.62	0.65	7.16E-04				37.45	1.45	7.45E-04	37.47	1.58	7.70E-04
0.3068	38.14	0.18	7.23E-04	37.80	0.89	7.61E-04				37.66	1.69	7.93E-04	37.70	1.86	8.22E-04
0.3216	38.28	0.39	7.67E-04	37.98	1.13	8.09E-04				37.88	1.94	8.44E-04	37.98	2.22	8.82E-04
0.3365	38.43	0.60	8.11E-04	38.16	1.35	8.56E-04				38.10	2.19	8.97E-04	38.28	2.59	9.46E-04
0.3515	38.54	0.73	8.50E-04	38.32	1.51	9.00E-04				38.31	2.41	9.49E-04	38.52	2.85	1.00E-03
0.3668	38.61	0.79	8.85E-04	38.44	1.61	9.40E-04				38.52	2.62	1.00E-03	38.71	2.99	1.05E-03
0.3821	38.66	0.81	9.16E-04	38.54	1.67	9.78E-04				38.73	2.80	1.05E-03	38.87	3.08	1.10E-03
0.3976	38.68	0.79	9.44E-04	38.63	1.70	1.01E-03				38.89	2.91	1.10E-03	39.01	3.14	1.14E-03
0.4132	38.67	0.73	9.67E-04	38.70	1.71	1.05E-03				38.99	2.90	1.14E-03	39.14	3.18	1.18E-03
0.4288	38.63	0.62	9.86E-04	38.76	1.70	1.08E-03				39.06	2.84	1.17E-03	39.26	3.19	1.22E-03
0.4446	38.58	0.52	1.01E-03	38.79	1.65	1.11E-03				39.11	2.75	1.20E-03	39.36	3.17	1.26E-03
0.4604	38.56	0.46	1.03E-03	38.79	1.56	1.13E-03				39.16	2.67	1.23E-03	39.43	3.13	1.30E-03
0.4762	38.56	0.43	1.06E-03	38.76	1.44	1.15E-03				39.19	2.59	1.26E-03	39.50	3.08	1.33E-03
0.4921	38.53	0.37	1.08E-03	38.71	1.28	1.17E-03				39.20	2.45	1.28E-03	39.53	2.96	1.35E-03
0.5079	38.41	0.20	1.09E-03	38.60	1.06	1.17E-03				39.12	2.21	1.29E-03	39.47	2.71	1.36E-03
0.5238	38.16	-0.15	1.07E-03	38.32	0.63	1.15E-03				38.93	1.81	1.27E-03	39.29	2.29	1.35E-03
0.5396	37.85	-0.53	1.06E-03	37.98	0.15	1.12E-03				38.70	1.40	1.26E-03	39.07	1.86	1.32E-03
0.5554	37.59	-0.83	1.04E-03	37.67	-0.24	1.10E-03				38.53	1.09	1.25E-03	38.89	1.52	1.31E-03
0.5712	37.32	-1.10	1.04E-03	37.50	-0.43	1.10E-03				38.37	0.84	1.25E-03	38.71	1.23	1.31E-03
0.5868	37.24	-1.16	1.06E-03	37.54	-0.37	1.14E-03				38.29	0.70	1.27E-03	38.70	1.17	1.33E-03
0.6024	37.30	-1.06	1.10E-03	37.72	-0.14	1.20E-03				38.53	0.99	1.34E-03	39.04	1.61	1.43E-03
0.6179	37.42	-0.88	1.15E-03	37.98	0.20	1.27E-03				39.06	1.73	1.48E-03	39.56	2.34	1.57E-03
0.6332	37.98	-0.15	1.28E-03	38.64	1.12	1.44E-03				39.81	2.90	1.69E-03	40.44	3.78	1.82E-03
0.6485	38.99	1.38	1.53E-03	39.70	2.85	1.72E-03				40.73	4.56	1.98E-03	41.67	6.31	2.26E-03
0.6635	39.75	2.67	1.75E-03	40.49	4.35	1.98E-03				41.71	6.70	2.35E-03	42.62	8.60	2.68E-03
0.6784	40.45	4.03	1.98E-03	41.24	5.93	2.26E-03				42.67	9.19	2.80E-03	43.51	11.17	3.16E-03
0.6932	41.11	5.41	2.23E-03	41.92	7.53	2.56E-03				43.47	11.60	3.27E-03	44.26	13.67	3.68E-03
0.7077	41.71	6.76	2.47E-03	42.53	9.05	2.86E-03				44.03	13.33	3.64E-03	44.83	15.61	4.12E-03
0.7220	42.27	8.11	2.74E-03	43.10	10.56	3.17E-03				44.56	15.13	4.05E-03	45.34	17.45	4.58E-03
0.7361	42.80	9.46	3.01E-03	43.63	12.04	3.50E-03				45.05	16.91	4.48E-03	45.77	19.02	5.01E-03
0.7500	43.29	10.78	3.29E-03	44.10	13.44	3.83E-03				45.45	18.25	4.85E-03	46.08	19.85	5.31E-03
0.7636	43.75	12.05	3.58E-03	44.54	14.78	4.16E-03				45.76	19.12	5.15E-03	46.28	19.85	5.45E-03
0.7770	44.18	13.29	3.88E-03	44.95	16.08	4.51E-03				46.02	19.74	5.40E-03	46.42	19.45	5.50E-03
0.7900	44.59	14.52	4.20E-03	45.32	17.27	4.85E-03				46.24	19.95	5.58E-03	46.53	18.92	5.51E-03
0.8028	44.99	15.77	4.53E-03	45.66	18.30	5.18E-03				46.38	19.63	5.64E-03	46.65	18.46	5.54E-03
0.8153	45.38	17.05	4.89E-03	45.97	19.16	5.48E-03				46.45	18.90	5.60E-03	46.76	18.07	5.57E-03
0.8274	45.71	18.09	5.22E-03	46.22	19.72	5.74E-03				46.56	18.46	5.62E-03	46.82	17.42	5.53E-03
0.8393	46.01	18.95	5.53E-03	46.44	20.07	5.94E-03				46.68	18.17	5.67E-03	46.84	16.68	5.46E-03
0.8507	46.30	19.88	5.86E-03	46.66	20.52	6.18E-03				46.75	17.62	5.65E-03	46.89	16.14	5.42E-03
0.8619	46.57	20.65	6.17E-03	46.87	20.89	6.41E-03				46.80	17.07	5.61E-03	46.93	15.64	5.39E-03
0.8726	46.78	21.09	6.40E-03	47.04	20.94	6.55E-03				46.86	16.62	5.60E-03	46.95	15.12	5.35E-03
0.8830	46.98	21.51	6.63E-03	47.28	21.70	6.89E-03				46.91	16.18	5.58E-03	46.96	14.62	5.30E-03
0.8930	47.18	22.04	6.89E-03	47.79	25.31	8.04E-03				46.95	15.74	5.56E-03	46.96	14.13	5.25E-03
0.9026	47.37	22.59	7.16E-03	47.98	25.99	8.39E-03				46.98	15.34	5.53E-03	46.96	13.72	5.21E-03
0.9118	47.55	23.07	7.42E-03	47.82	22.93	7.62E-03				47.01	14.99	5.51E-03	46.98	13.40	5.19E-03
0.9206	47.71	23.42	7.64E-03	47.71	21.02	7.17E-03				47.03	14.66	5.49E-03	46.98	13.05	5.15E-03
0.9290	47.85	23.61	7.82E-03	47.76	20.55	7.14E-03				47.04	14.32	5.46E-03	46.94	12.62	5.09E-03
0.9369	47.97	23.74	7.97E-03	47.86	20.48	7.22E-03				47.03	13.95	5.42E-03	46.89	12.18	5.01E-03
0.9444	48.09	23.88	8.13E-03	47.95	20.40	7.30E-03				47.01	13.56	5.36E-03	46.83	11.77	4.94E-03
0.9515	48.20	24.00	8.27E-03	48.05	20.43	7.40E-03				46.97	13.17	5.29E-03	46.77	11.37	4.86E-03
0.9581	48.30	24.13	8.42E-03	48.12	20.33	7.45E-03				46.92	12.75	5.22E-03	46.72	11.05	4.81E-03
0.9642	48.40	24.31	8.57E-03	48.15	19.98	7.42E-03				46.72	11.91	5.00E-03	46.71	10.86	4.79E-03
0.9699	48.50	24.50	8.72E-03	48.14	19.48	7.32E-03				46.16	10.15	4.50E-03	46.72	10.76	4.79E-03
0.9750	48.59	24.71	8.88E-03	48.11	18.93	7.21E-03				45.44	8.34	3.97E-03	46.74	10.67	4.80E-03
0.9798	48.67	24.91	9.02E-03	48.08	18.39	7.08E-03				44.74	6.85	3.55E-03	46.73	10.53	4.78E-03
0.9840	48.74	25.11	9.16E-03	48.03	17.88	6.96E-03				44.13	5.72	3.23E-03	46.69	10.34	4.74E-03
0.9877	48.81	25.29	9.28E-03	47.99	17.42	6.85E-03				43.60	4.86	2.99E-03	46.64	10.12	4.70E-03
0.9910	48.86	25.46	9.40E-03	47.95	17.02	6.75E-03				43.16	4.21	2.81E-03	46.58	9.92	4.65E-03
0.9937	48.91	25.61	9.50E-03	47.91	16.69	6.67E-03				42.80	3.71	2.67E-03	46.53	9.73	4.60E-03
0.9960	48.95	25.73	9.58E-03	47.88	16.43	6.60E-03				42.51	3.33	2.57E-03	46.49	9.58	4.57E-03
0.9977	48.98	25.83	9.65E-03	47.85	16.22	6.55E-03				42.29	3.05	2.49E-03	46.45	9.46	4.54E-03
0.9990	49.01	25.91	9.70E-03	47.84	16.08	6.51E-03				42.14	2.86	2.44E-03	46.43	9.38	4.52E-03
0.9998	49.02	25.95	9.73E-03	47.82	16.00	6.49E-03				42.04	2.75	2.41E-03	46.41	9.33	4.51E-03
1.0000	49.02	25.97	9.74E-03	47.82	15.97	6.49E-03				42.01	2.71	2.40E-03	46.41	9.31	4.50E-03

The local freestream flow direction, twist in the boundary layer and boundary layer displacement thickness from WAKELAG over the upper surface of the DERA wing. $\Lambda = 50°$, $\alpha = 6.6°$, $Re_c = 3.9 \times 10^6$.

η	0.06b			0.16b			0.30b			0.45b			0.59b		
x/c	α_c (°)	β_c (°)	δ^-/c	α_c (°)	β_c (°)	δ^-/c	α_c (°)	β_c (°)	δ^-/c	α_c (°)	β_c (°)	δ^-/c	α_c (°)	β_c (°)	δ^-/c
0.0556				35.68	0.50	1.25E-04	35.17	0.15	1.21E-04	33.94	0.82	1.21E-04	33.89	0.57	1.20E-04
0.0631				36.02	1.09	1.58E-04	35.24	0.25	1.48E-04	34.39	1.61	1.53E-04	34.23	1.17	1.51E-04
0.0710				36.32	1.33	1.86E-04	35.31	0.30	1.72E-04	34.75	1.89	1.80E-04	34.54	1.45	1.76E-04
0.0794				36.42	1.14	2.11E-04	35.37	0.33	1.96E-04	34.97	1.78	2.04E-04	34.76	1.48	2.02E-04
0.0882				36.25	0.54	2.29E-04	35.43	0.36	2.21E-04	35.06	1.52	2.27E-04	34.90	1.33	2.31E-04
0.0974				36.03	0.04	2.48E-04	35.48	0.38	2.47E-04	35.15	1.36	2.52E-04	35.02	1.23	2.62E-04
0.1070				35.98	-0.04	2.73E-04	35.56	0.44	2.74E-04	35.25	1.30	2.79E-04	35.15	1.23	2.93E-04
0.1170				36.03	0.05	3.01E-04	35.65	0.54	3.02E-04	35.36	1.29	3.06E-04	35.28	1.26	3.23E-04
0.1274				36.14	0.23	3.31E-04	35.76	0.65	3.32E-04	35.47	1.30	3.34E-04	35.40	1.30	3.52E-04
0.1381				36.27	0.43	3.62E-04	35.87	0.74	3.61E-04	35.58	1.31	3.63E-04	35.53	1.35	3.81E-04
0.1493				36.38	0.55	3.92E-04	35.96	0.79	3.90E-04	35.68	1.31	3.92E-04	35.65	1.39	4.11E-04
0.1607				36.45	0.60	4.20E-04	36.01	0.78	4.18E-04	35.76	1.29	4.19E-04	35.76	1.43	4.41E-04
0.1726				36.51	0.64	4.48E-04	36.05	0.76	4.45E-04	35.83	1.25	4.47E-04	35.87	1.46	4.71E-04
0.1847				36.57	0.66	4.76E-04	36.08	0.72	4.71E-04	35.89	1.21	4.75E-04	35.98	1.48	5.01E-04
0.1972				36.61	0.66	5.03E-04	36.12	0.70	4.99E-04	35.95	1.20	5.04E-04	36.07	1.49	5.32E-04
0.2100				36.62	0.60	5.28E-04	36.16	0.69	5.27E-04	36.03	1.21	5.34E-04	36.15	1.48	5.62E-04
0.2230				36.59	0.51	5.51E-04	36.18	0.67	5.55E-04	36.11	1.23	5.65E-04	36.21	1.44	5.91E-04
0.2364				36.57	0.42	5.75E-04	36.22	0.67	5.84E-04	36.20	1.27	5.98E-04	36.28	1.42	6.21E-04
0.2500				36.58	0.41	6.03E-04	36.29	0.73	6.16E-04	36.32	1.35	6.33E-04	36.38	1.46	6.55E-04
0.2639				36.69	0.55	6.40E-04	36.45	0.92	6.57E-04	36.48	1.51	6.74E-04	36.54	1.61	6.96E-04
0.2780				36.89	0.82	6.86E-04	36.69	1.24	7.08E-04	36.69	1.75	7.21E-04	36.76	1.86	7.45E-04
0.2923				37.11	1.11	7.36E-04	36.95	1.59	7.63E-04	36.92	2.01	7.71E-04	37.01	2.15	7.98E-04
0.3068				37.30	1.35	7.83E-04	37.18	1.87	8.14E-04	37.15	2.26	8.22E-04	37.27	2.46	8.55E-04
0.3216				37.50	1.59	8.32E-04	37.41	2.13	8.66E-04	37.40	2.54	8.77E-04	37.57	2.84	9.19E-04
0.3365				37.69	1.81	8.81E-04	37.63	2.37	9.18E-04	37.66	2.81	9.34E-04	37.89	3.24	9.87E-04
0.3515				37.87	1.98	9.27E-04	37.82	2.55	9.67E-04	37.89	3.04	9.89E-04	38.16	3.53	1.05E-03
0.3668				38.01	2.10	9.70E-04	38.00	2.68	1.01E-03	38.11	3.24	1.04E-03	38.39	3.71	1.10E-03
0.3821				38.15	2.18	1.01E-03	38.15	2.78	1.06E-03	38.32	3.40	1.10E-03	38.59	3.84	1.16E-03
0.3976				38.26	2.23	1.05E-03	38.29	2.83	1.10E-03	38.49	3.50	1.15E-03	38.76	3.93	1.21E-03
0.4132				38.34	2.23	1.09E-03	38.39	2.83	1.14E-03	38.63	3.52	1.19E-03	38.92	3.97	1.25E-03
0.4288				38.41	2.21	1.12E-03	38.47	2.80	1.17E-03	38.73	3.50	1.23E-03	39.06	3.99	1.30E-03
0.4446				38.45	2.15	1.15E-03	38.54	2.75	1.20E-03	38.82	3.44	1.26E-03	39.18	3.98	1.34E-03
0.4604				38.47	2.06	1.17E-03	38.60	2.71	1.24E-03	38.90	3.38	1.29E-03	39.29	3.95	1.38E-03
0.4762				38.47	1.95	1.20E-03	38.67	2.68	1.27E-03	38.97	3.31	1.33E-03	39.39	3.92	1.42E-03
0.4921				38.44	1.80	1.21E-03	38.70	2.59	1.30E-03	39.00	3.19	1.35E-03	39.45	3.82	1.45E-03
0.5079				38.35	1.58	1.22E-03	38.65	2.38	1.31E-03	38.95	2.95	1.36E-03	39.43	3.58	1.46E-03
0.5238				38.11	1.15	1.20E-03	38.49	2.01	1.30E-03	38.81	2.57	1.36E-03	39.31	3.19	1.45E-03
0.5396				37.80	0.68	1.17E-03	38.28	1.61	1.28E-03	38.64	2.19	1.34E-03	39.15	2.80	1.44E-03
0.5554				37.52	0.29	1.15E-03	38.08	1.26	1.27E-03	38.51	1.90	1.34E-03	39.05	2.52	1.44E-03
0.5712				37.37	0.09	1.15E-03	37.85	0.91	1.25E-03	38.40	1.66	1.35E-03	38.97	2.30	1.44E-03
0.5868				37.42	0.15	1.19E-03	37.81	0.83	1.27E-03	38.36	1.53	1.37E-03	39.01	2.28	1.47E-03
0.6024				37.62	0.41	1.26E-03	38.12	1.22	1.36E-03	38.64	1.89	1.46E-03	39.45	2.88	1.60E-03
0.6179				37.93	0.81	1.34E-03	38.59	1.87	1.49E-03	39.22	2.74	1.62E-03	40.09	3.89	1.79E-03
0.6332				38.60	1.78	1.52E-03	39.35	3.06	1.70E-03	40.04	4.10	1.86E-03	41.08	5.74	2.12E-03
0.6485				39.64	3.56	1.82E-03	40.42	5.06	2.04E-03	41.01	6.03	2.20E-03	42.36	8.79	2.66E-03
0.6635				40.46	5.17	2.10E-03	41.28	6.95	2.37E-03	42.04	8.51	2.65E-03	43.27	11.36	3.16E-03
0.6784				41.25	6.92	2.41E-03	42.12	9.05	2.76E-03	43.01	11.36	3.18E-03	44.11	14.21	3.74E-03
0.6932				41.96	8.69	2.75E-03	42.85	11.14	3.17E-03	43.77	13.98	3.71E-03	44.76	16.68	4.29E-03
0.7077				42.58	10.34	3.08E-03	43.44	12.90	3.55E-03	44.25	15.51	4.07E-03	45.15	17.86	4.63E-03
0.7220				43.15	11.99	3.43E-03	43.98	14.62	3.94E-03	44.68	16.94	4.44E-03	45.45	18.50	4.88E-03
0.7361				43.68	13.59	3.79E-03	44.46	16.18	4.33E-03	45.07	18.22	4.80E-03	45.69	18.74	5.06E-03
0.7500				44.14	15.04	4.15E-03	44.84	17.33	4.67E-03	45.36	18.93	5.06E-03	45.87	18.61	5.16E-03
0.7636				44.55	16.34	4.49E-03	45.14	18.04	4.93E-03	45.56	19.02	5.20E-03	45.99	18.16	5.19E-03
0.7770				44.93	17.54	4.83E-03	45.40	18.48	5.14E-03	45.71	18.81	5.28E-03	46.07	17.51	5.17E-03
0.7900				45.26	18.58	5.16E-03	45.62	18.70	5.31E-03	45.82	18.39	5.31E-03	46.12	16.79	5.12E-03
0.8028				45.55	19.39	5.45E-03	45.81	18.76	5.45E-03	45.91	17.82	5.29E-03	46.15	16.08	5.06E-03
0.8153				45.81	19.96	5.71E-03	45.99	18.73	5.57E-03	45.96	17.13	5.25E-03	46.16	15.36	4.99E-03
0.8274				46.04	20.37	5.93E-03	46.08	18.27	5.58E-03	46.01	16.52	5.21E-03	46.18	14.77	4.95E-03
0.8393				46.25	20.63	6.13E-03	46.14	17.63	5.54E-03	46.06	15.96	5.18E-03	46.21	14.26	4.91E-03
0.8507				46.43	20.75	6.29E-03	46.24	17.32	5.57E-03	46.09	15.40	5.14E-03	46.22	13.77	4.87E-03
0.8619				46.60	20.82	6.44E-03	46.34	17.04	5.61E-03	46.11	14.87	5.10E-03	46.23	13.31	4.84E-03
0.8726				46.74	20.75	6.55E-03	46.42	16.72	5.63E-03	46.13	14.40	5.06E-03	46.23	12.90	4.80E-03
0.8830				46.97	21.34	6.84E-03	46.47	16.29	5.61E-03	46.13	13.92	5.02E-03	46.21	12.44	4.75E-03
0.8930				47.43	24.27	7.80E-03	46.48	15.74	5.55E-03	46.12	13.42	4.96E-03	46.15	11.90	4.67E-03
0.9026				47.60	24.65	8.06E-03	46.51	15.33	5.53E-03	46.09	12.95	4.90E-03	46.08	11.39	4.59E-03
0.9118				47.43	21.89	7.37E-03	46.57	15.13	5.55E-03	46.07	12.53	4.85E-03	46.02	10.95	4.52E-03
0.9206				47.31	20.10	6.95E-03	46.63	14.94	5.58E-03	46.04	12.15	4.80E-03	45.94	10.50	4.44E-03
0.9290				47.35	19.60	6.91E-03	46.67	14.69	5.57E-03	46.01	11.77	4.75E-03	45.82	9.98	4.33E-03
0.9369				47.43	19.45	6.96E-03	46.71	14.47	5.58E-03	45.96	11.40	4.69E-03	45.70	9.50	4.24E-03
0.9444				47.49	19.24	6.98E-03	46.78	14.41	5.62E-03	45.91	11.04	4.63E-03	45.62	9.15	4.17E-03
0.9515				47.55	19.05	7.01E-03	46.88	14.50	5.71E-03	45.86	10.70	4.57E-03	45.56	8.89	4.13E-03
0.9581				47.62	18.96	7.05E-03	46.96	14.53	5.77E-03	45.79	10.35	4.51E-03	45.53	8.70	4.11E-03
0.9642				47.70	18.99	7.14E-03	46.98	14.37	5.77E-03	45.69	9.95	4.42E-03	45.53	8.59	4.10E-03
0.9699				47.80	19.14	7.25E-03	46.97	14.10	5.74E-03	45.57	9.53	4.32E-03	45.54	8.53	4.11E-03
0.9750				47.90	19.37	7.39E-03	46.96	13.85	5.70E-03	45.44	9.11	4.23E-03	45.58	8.52	4.13E-03
0.9798				48.00	19.65	7.54E-03	46.97	13.70	5.69E-03	45.32	8.74	4.14E-03	45.62	8.54	4.17E-03
0.9840				48.10	19.96	7.70E-03	47.14	14.18	5.88E-03	45.20	8.42	4.06E-03	45.75	8.75	4.25E-03
0.9877				48.19	20.27	7.85E-03	47.55	15.65	6.40E-03	45.11	8.15	3.99E-03	45.98	9.23	4.43E-03
0.9910				48.28	20.57	7.99E-03	48.07	17.93	7.21E-03	45.02	7.92	3.94E-03	46.27	9.86	4.65E-03
0.9937				48.35	20.84	8.12E-03	48.61	21.01	8.33E-03	44.95	7.73	3.89E-03	46.56	10.55	4.89E-03
0.9960				48.41	21.07	8.24E-03	49.12	25.12	9.88E-03	44.89	7.59	3.86E-03	46.82	11.21	5.12E-03
0.9977				48.46	21.26	8.33E-03	49.54	31.79	1.25E-02	44.85	7.47	3.83E-03	47.04	11.80	5.33E-03
0.9990				48.49	21.40	8.39E-03	49.85			44.82	7.39	3.81E-03	47.20	12.25	5.49E-03
0.9998				48.51	21.48	8.43E-03	50.04			44.80	7.34	3.80E-03	47.29	12.53	5.59E-03
1.0000				48.52	21.51	8.45E-03	50.11			44.79	7.33	3.80E-03	47.33	12.62	5.63E-03

The local freestream flow direction, twist in the boundary layer and boundary layer displacement thickness from WAKELAG over the upper surface of the DERA wing. $\Lambda = 50°$, $\alpha = 7.7°$, $Re_c = 3.9 \times 10^6$.

η	0.06b			0.16b			0.30b			0.45b			0.59b		
x/c	α_c (°)	β_c (°)	δ^-/c	α_c (°)	β_c (°)	δ^-/c	α_c (°)	β_c (°)	δ^-/c	α_c (°)	β_c (°)	δ^-/c	α_c (°)	β_c (°)	δ^-/c
0.0556	33.58	0.40	1.19E-04	32.36	0.57	1.17E-04	31.42	0.48	1.14E-04				30.43	0.78	1.13E-04
0.0631	33.81	0.76	1.49E-04	32.72	1.17	1.49E-04	31.69	0.91	1.43E-04				30.90	1.61	1.44E-04
0.0710	34.02	0.94	1.75E-04	33.04	1.42	1.76E-04	31.94	1.12	1.69E-04				31.34	2.04	1.72E-04
0.0794	34.22	1.06	2.03E-04	33.21	1.34	2.02E-04	32.18	1.26	1.95E-04				31.70	2.18	2.00E-04
0.0882	34.43	1.18	2.33E-04	33.24	1.05	2.26E-04	32.40	1.38	2.23E-04				31.97	2.10	2.31E-04
0.0974	34.61	1.27	2.64E-04	33.26	0.87	2.51E-04	32.60	1.49	2.52E-04				32.23	2.07	2.65E-04
0.1070	34.73	1.25	2.92E-04	33.33	0.83	2.77E-04	32.81	1.60	2.83E-04				32.47	2.13	2.99E-04
0.1170	34.82	1.20	3.18E-04	33.48	0.97	3.07E-04	33.02	1.72	3.14E-04				32.71	2.24	3.32E-04
0.1274	34.88	1.13	3.43E-04	33.68	1.20	3.40E-04	33.23	1.84	3.46E-04				32.94	2.36	3.65E-04
0.1381	34.93	1.08	3.68E-04	33.90	1.44	3.74E-04	33.42	1.93	3.78E-04				33.17	2.48	3.99E-04
0.1493	35.00	1.05	3.95E-04	34.09	1.60	4.07E-04	33.59	1.98	4.10E-04				33.39	2.58	4.33E-04
0.1607	35.08	1.07	4.24E-04	34.24	1.67	4.38E-04	33.74	2.00	4.41E-04				33.60	2.67	4.67E-04
0.1726	35.17	1.10	4.53E-04	34.38	1.73	4.69E-04	33.88	2.01	4.72E-04				33.81	2.75	5.02E-04
0.1847	35.26	1.13	4.83E-04	34.52	1.77	5.00E-04	34.01	2.02	5.04E-04				34.01	2.83	5.38E-04
0.1972	35.34	1.16	5.13E-04	34.63	1.78	5.31E-04	34.14	2.04	5.36E-04				34.20	2.89	5.75E-04
0.2100	35.41	1.16	5.42E-04	34.71	1.74	5.60E-04	34.27	2.06	5.69E-04				34.38	2.95	6.12E-04
0.2230	35.46	1.14	5.71E-04	34.77	1.67	5.87E-04	34.38	2.06	6.02E-04				34.55	2.98	6.48E-04
0.2364	35.52	1.13	6.00E-04	34.83	1.62	6.15E-04	34.50	2.08	6.36E-04				34.73	3.02	6.87E-04
0.2500	35.60	1.16	6.32E-04	34.92	1.63	6.47E-04	34.65	2.17	6.74E-04				34.93	3.14	7.30E-04
0.2639	35.72	1.26	6.68E-04	35.08	1.78	6.88E-04	34.88	2.38	7.20E-04				35.18	3.35	7.80E-04
0.2780	35.88	1.42	7.09E-04	35.33	2.06	7.39E-04	35.16	2.72	7.77E-04				35.47	3.65	8.38E-04
0.2923	36.05	1.61	7.53E-04	35.60	2.38	7.94E-04	35.47	3.08	8.37E-04				35.79	4.00	9.02E-04
0.3068	36.23	1.79	7.98E-04	35.84	2.65	8.48E-04	35.76	3.39	8.96E-04				36.13	4.37	9.70E-04
0.3216	36.43	2.00	8.46E-04	36.09	2.92	9.03E-04	36.04	3.68	9.57E-04				36.50	4.83	1.05E-03
0.3365	36.63	2.21	8.96E-04	36.34	3.17	9.60E-04	36.32	3.96	1.02E-03				36.89	5.31	1.13E-03
0.3515	36.79	2.34	9.41E-04	36.56	3.36	1.01E-03	36.57	4.18	1.08E-03				37.23	5.68	1.21E-03
0.3668	36.92	2.42	9.82E-04	36.75	3.49	1.06E-03	36.81	4.36	1.13E-03				37.53	5.94	1.28E-03
0.3821	37.04	2.46	1.02E-03	36.93	3.58	1.11E-03	37.03	4.51	1.19E-03				37.82	6.16	1.35E-03
0.3976	37.12	2.45	1.05E-03	37.08	3.63	1.15E-03	37.22	4.61	1.24E-03				38.08	6.34	1.42E-03
0.4132	37.17	2.38	1.08E-03	37.21	3.65	1.20E-03	37.39	4.64	1.29E-03				38.33	6.47	1.49E-03
0.4288	37.19	2.26	1.11E-03	37.33	3.65	1.24E-03	37.53	4.63	1.33E-03				38.56	6.58	1.55E-03
0.4446	37.20	2.15	1.13E-03	37.42	3.60	1.27E-03	37.66	4.60	1.38E-03				38.78	6.67	1.62E-03
0.4604	37.23	2.09	1.16E-03	37.48	3.51	1.30E-03	37.79	4.59	1.42E-03				39.00	6.78	1.69E-03
0.4762	37.29	2.07	1.19E-03	37.52	3.39	1.33E-03	37.93	4.60	1.47E-03				39.23	6.91	1.76E-03
0.4921	37.31	2.01	1.22E-03	37.54	3.24	1.35E-03	38.02	4.55	1.50E-03				39.44	6.99	1.83E-03
0.5079	37.25	1.82	1.23E-03	37.50	3.03	1.36E-03	38.04	4.35	1.52E-03				39.58	6.94	1.88E-03
0.5238	37.07	1.47	1.22E-03	37.37	2.67	1.35E-03	37.98	4.02	1.52E-03				39.67	6.76	1.91E-03
0.5396	36.85	1.09	1.20E-03	37.20	2.28	1.34E-03	37.89	3.68	1.52E-03				39.75	6.61	1.94E-03
0.5554	36.67	0.81	1.20E-03	37.04	1.95	1.33E-03	37.83	3.43	1.53E-03				39.92	6.66	2.01E-03
0.5712	36.51	0.56	1.20E-03	36.96	1.78	1.34E-03	37.80	3.24	1.54E-03				40.19	6.96	2.11E-03
0.5868	36.48	0.51	1.22E-03	37.04	1.83	1.38E-03	37.87	3.24	1.58E-03				40.60	7.58	2.26E-03
0.6024	36.65	0.71	1.28E-03	37.35	2.22	1.47E-03	38.34	3.91	1.72E-03				41.42	9.36	2.61E-03
0.6179	36.89	1.03	1.36E-03	37.79	2.84	1.60E-03	39.00	5.03	1.93E-03				42.39	11.92	3.12E-03
0.6332	38.01	2.76	1.65E-03	38.54	4.08	1.83E-03	39.91	6.83	2.26E-03				43.33	15.02	3.76E-03
0.6485	39.71	6.31	2.21E-03	39.59	6.15	2.19E-03	41.00	9.51	2.75E-03				44.13	18.14	4.45E-03
0.6635	40.13	7.12	2.38E-03	40.41	8.03	2.54E-03	41.80	11.75	3.19E-03				44.45	18.78	4.71E-03
0.6784	40.43	7.64	2.52E-03	41.19	10.08	2.93E-03	42.54	14.15	3.69E-03				44.66	18.78	4.84E-03
0.6932	40.74	8.18	2.65E-03	41.87	12.06	3.33E-03	43.11	16.09	4.14E-03				44.80	18.40	4.89E-03
0.7077	41.15	9.04	2.85E-03	42.40	13.64	3.69E-03	43.44	16.87	4.39E-03				44.90	17.84	4.91E-03
0.7220	41.67	10.35	3.13E-03	42.88	15.10	4.05E-03	43.69	17.17	4.56E-03				44.96	17.11	4.87E-03
0.7361	42.23	11.90	3.47E-03	43.30	16.37	4.39E-03	43.88	17.19	4.68E-03				44.99	16.30	4.81E-03
0.7500	42.72	13.35	3.81E-03	43.64	17.29	4.67E-03	44.03	16.96	4.75E-03				44.99	15.51	4.74E-03
0.7636	43.13	14.54	4.11E-03	43.91	17.85	4.89E-03	44.13	16.54	4.77E-03				44.99	14.76	4.67E-03
0.7770	43.51	15.67	4.42E-03	44.14	18.18	5.07E-03	44.19	15.99	4.75E-03				44.96	14.03	4.59E-03
0.7900	43.87	16.72	4.73E-03	44.33	18.33	5.22E-03	44.24	15.41	4.73E-03				44.92	13.33	4.51E-03
0.8028	44.20	17.71	5.04E-03	44.51	18.35	5.34E-03	44.28	14.87	4.70E-03				44.87	12.68	4.43E-03
0.8153	44.52	18.65	5.36E-03	44.66	18.26	5.43E-03	44.32	14.39	4.68E-03				44.82	12.07	4.35E-03
0.8274	44.79	19.31	5.63E-03	44.78	17.97	5.48E-03	44.31	13.78	4.62E-03				44.76	11.52	4.29E-03
0.8393	45.02	19.78	5.86E-03	44.86	17.56	5.49E-03	44.26	13.08	4.53E-03				44.69	11.01	4.22E-03
0.8507	45.24	20.26	6.09E-03	44.95	17.22	5.52E-03	44.15	12.27	4.41E-03				44.60	10.47	4.14E-03
0.8619	45.46	20.73	6.33E-03	45.03	16.87	5.53E-03	44.07	11.61	4.31E-03				44.47	9.89	4.04E-03
0.8726	45.67	21.22	6.58E-03	45.07	16.37	5.50E-03	44.06	11.25	4.28E-03				44.30	9.25	3.91E-03
0.8830	45.87	21.64	6.82E-03	45.19	16.33	5.58E-03	44.00	10.79	4.22E-03				44.11	8.65	3.79E-03
0.8930	46.03	21.89	7.00E-03	45.56	17.56	6.01E-03	43.85	10.11	4.09E-03				43.92	8.10	3.68E-03
0.9026	46.18	22.05	7.16E-03	45.70	17.68	6.14E-03	43.76	9.64	4.02E-03				43.75	7.62	3.59E-03
0.9118	46.32	22.30	7.34E-03	45.54	16.33	5.84E-03	43.75	9.44	4.01E-03				43.58	7.18	3.50E-03
0.9206	46.49	22.74	7.58E-03	45.43	15.40	5.65E-03	43.74	9.24	4.00E-03				43.46	6.86	3.44E-03
0.9290	46.69	23.52	7.93E-03	45.49	15.24	5.68E-03	43.67	8.90	3.94E-03				43.40	6.66	3.41E-03
0.9369	46.88	24.36	8.30E-03	45.60	15.32	5.77E-03	43.61	8.62	3.90E-03				43.37	6.53	3.40E-03
0.9444	47.03	24.85	8.57E-03	45.69	15.37	5.85E-03	43.64	8.55	3.92E-03				43.38	6.48	3.42E-03
0.9515	47.14	25.06	8.74E-03	45.78	15.42	5.93E-03	43.74	8.67	3.98E-03				43.42	6.48	3.45E-03
0.9581	47.25	25.36	8.94E-03	45.88	15.54	6.02E-03	43.86	8.84	4.07E-03				43.49	6.54	3.49E-03
0.9642	47.38	25.98	9.25E-03	46.04	15.91	6.19E-03	43.98	8.99	4.14E-03				43.59	6.66	3.55E-03
0.9699	47.53	26.89	9.65E-03	46.33	16.99	6.59E-03	44.09	9.16	4.22E-03				43.75	6.89	3.64E-03
0.9750	47.67	27.99	1.01E-02	46.73	18.74	7.21E-03	44.20	9.35	4.30E-03				43.93	7.16	3.75E-03
0.9798	47.81	29.27	1.07E-02	47.18	21.24	8.11E-03	44.32	9.54	4.38E-03				44.10	7.43	3.85E-03
0.9840	47.94	30.70	1.13E-02	47.66	24.80	9.41E-03	44.72	10.48	4.70E-03				44.44	8.05	4.07E-03
0.9877	48.05	32.37	1.20E-02	48.13	30.84	1.17E-02	45.60	13.01	5.53E-03				45.06	9.34	4.51E-03
0.9910	48.15	34.56	1.29E-02	48.57			46.73	17.50	7.04E-03				45.82	11.19	5.14E-03
0.9937	48.23	36.16	1.37E-02	48.97			47.96	26.31	1.02E-02				46.60	13.53	5.96E-03
0.9960	48.30	34.68	1.32E-02	49.31			49.15						47.34	16.28	6.95E-03
0.9977	48.35	37.81	1.46E-02	49.59			50.18						47.96	19.30	8.07E-03
0.9990	48.39	36.97	1.43E-02	49.79			50.98						48.43	22.33	9.23E-03
0.9998	48.42	36.53	1.42E-02	49.91			51.48						48.72	24.82	1.02E-02
1.0000	48.42	37.26	1.45E-02	49.95			51.65						48.81	25.85	1.06E-02

The local freestream flow direction, twist in the boundary layer and boundary layer displacement thickness from WAKELAG over the upper surface of the DERA wing. $\Lambda = 50°$, $\alpha = 10.8°$, $Re_c = 3.9 \times 10^6$.

Appendix XIV

DERA balance repeatability

The repeatability from one run to the next of the aerodynamic forces and moments measured on the balance in the DERA 13' x 9' wind tunnel are shown in Figure A-12 for all wing sweeps studied. These results show that repeatability from one run to the next is satisfactory.

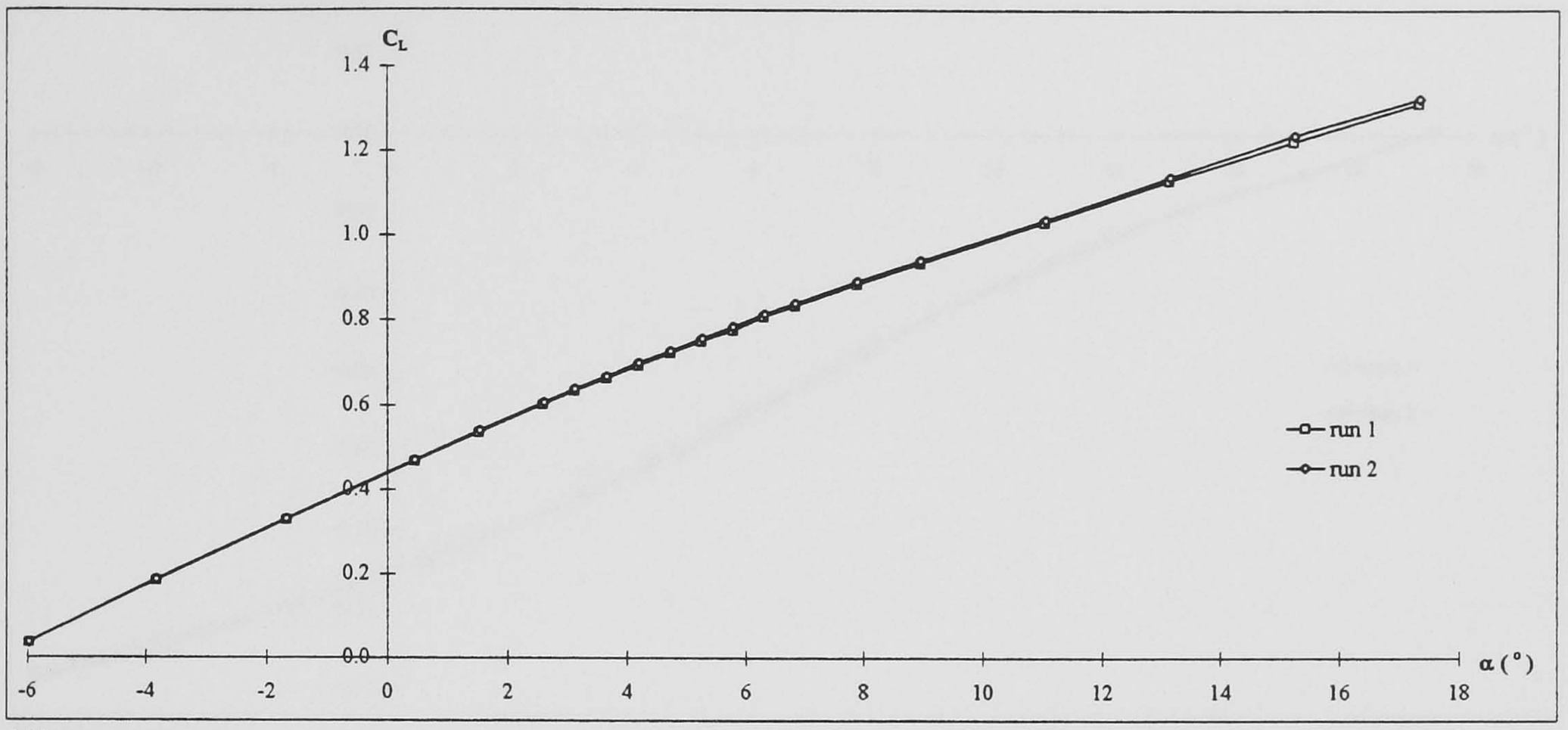

Lift

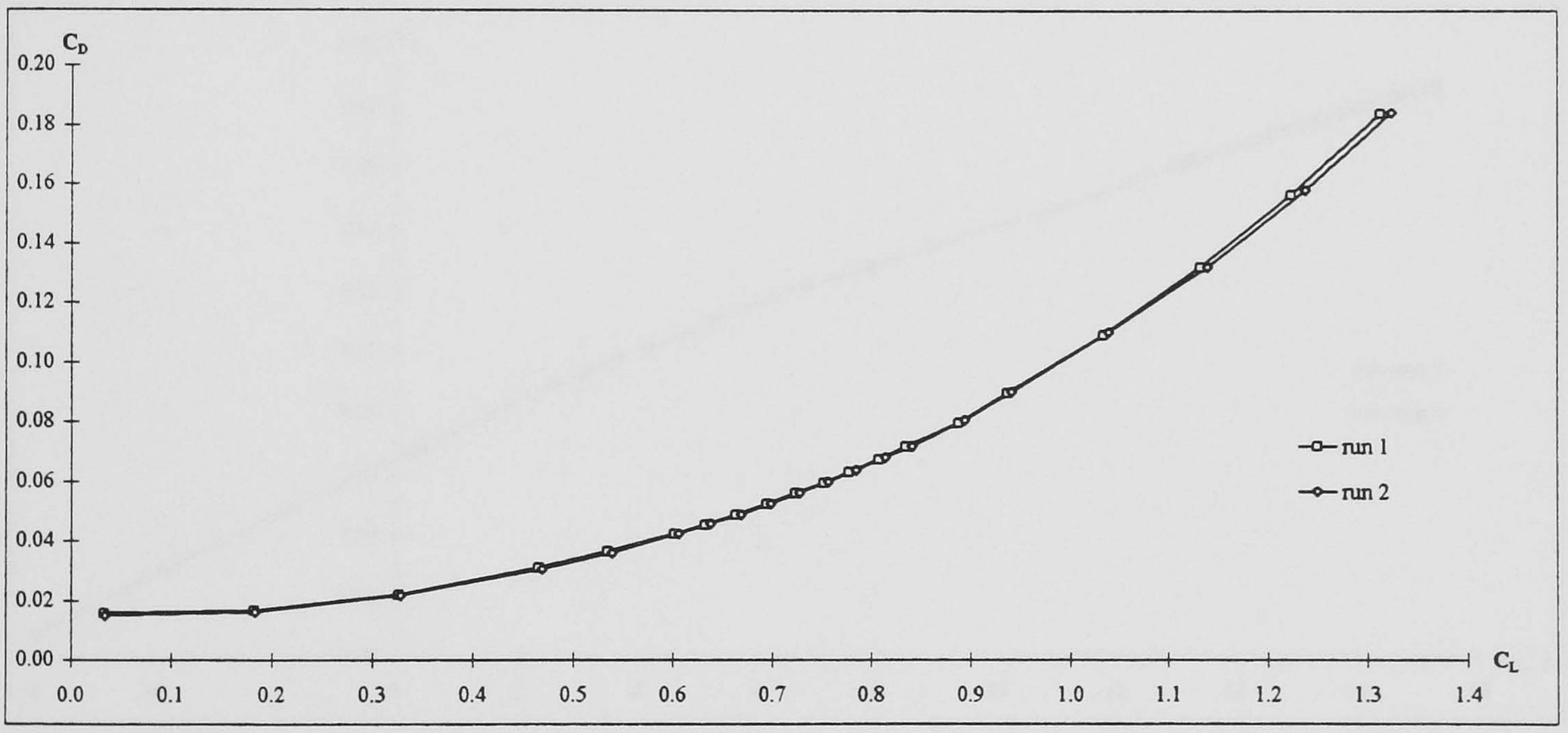

Drag polar

Figure A-12: DERA balance repeatability. $\Lambda = 30°$, $Re_c = 2.9 \times 10^6$.

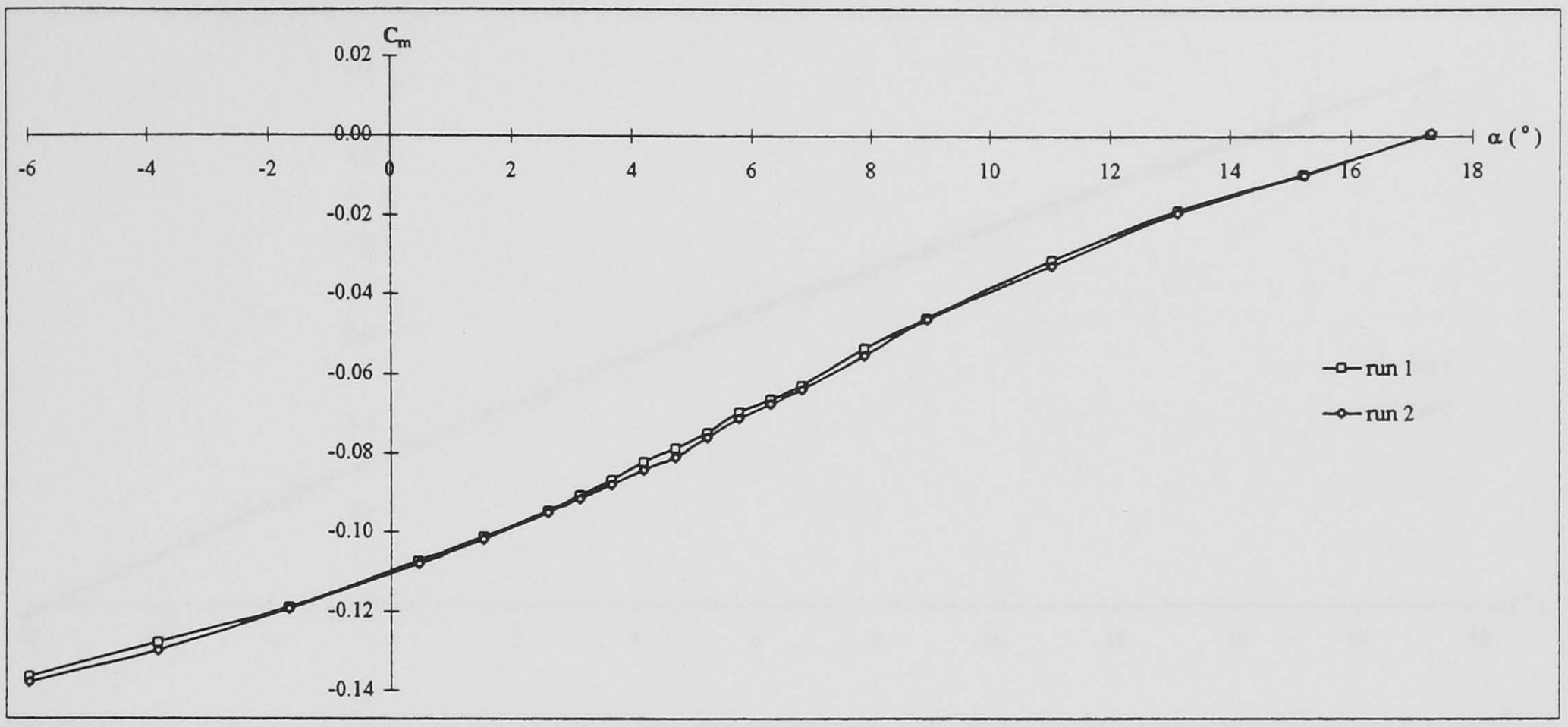

Pitching moment

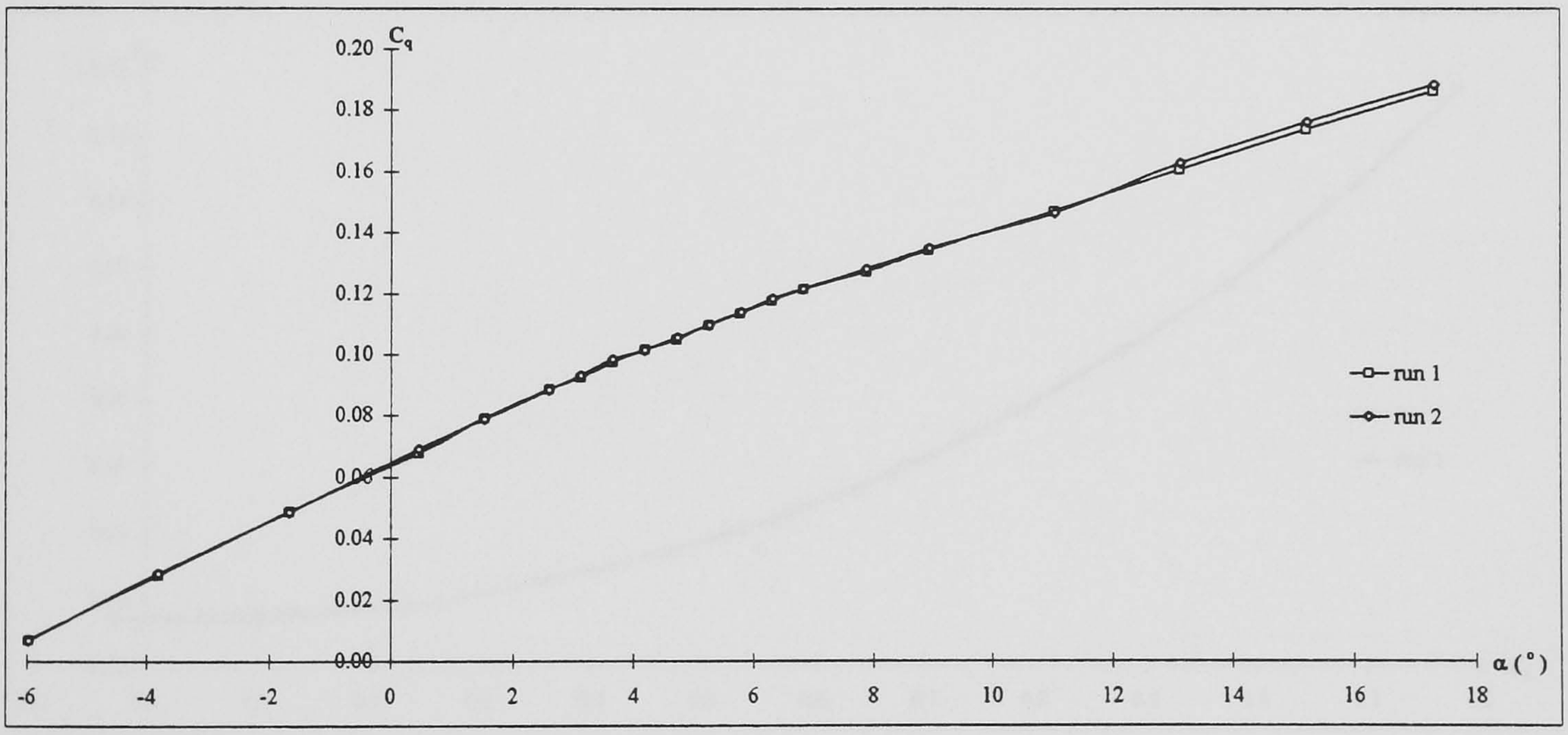

Rolling moment

Figure A-12 cont.: DERA balance repeatability. $\Lambda = 30°$, $Re_c = 2.9 \times 10^6$.

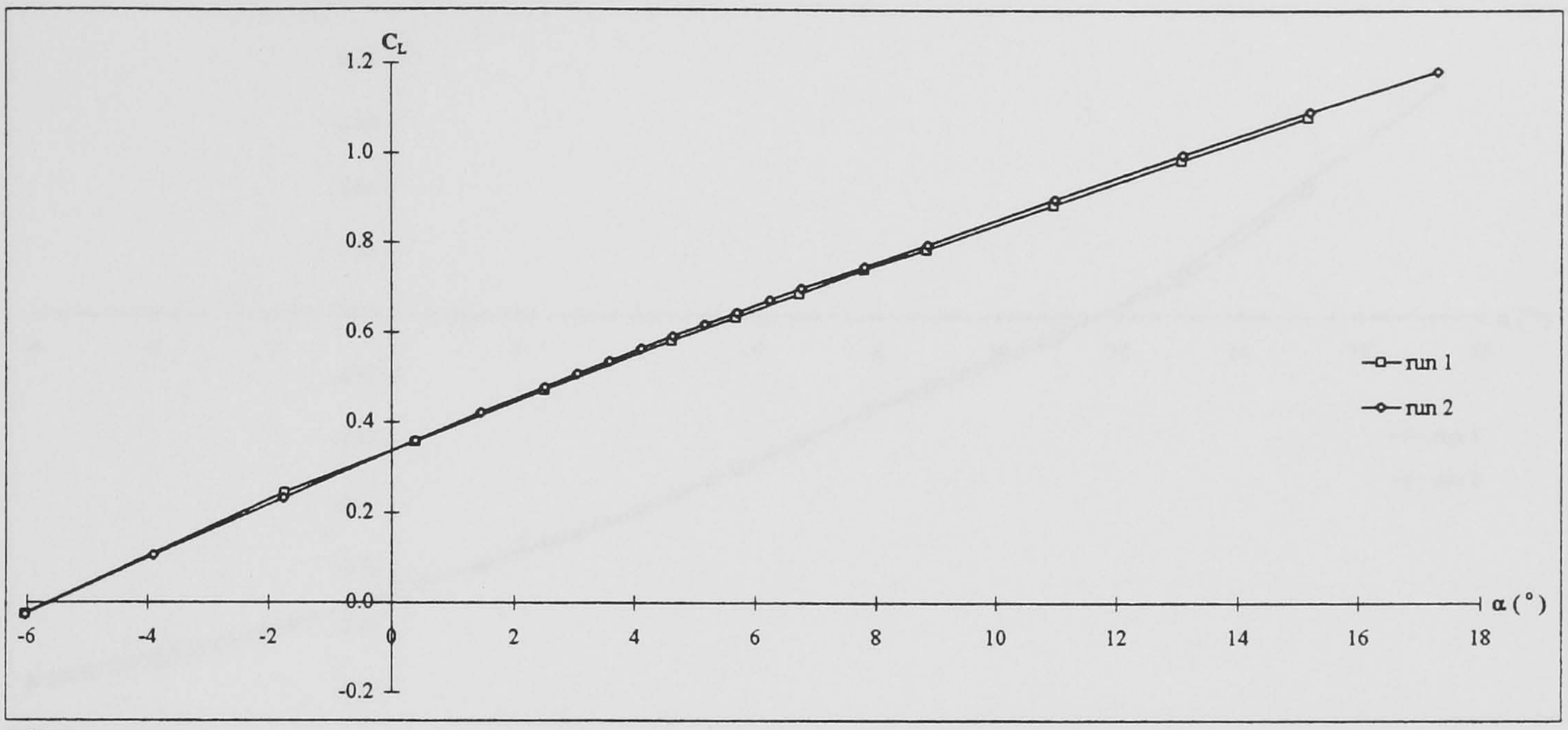

Lift

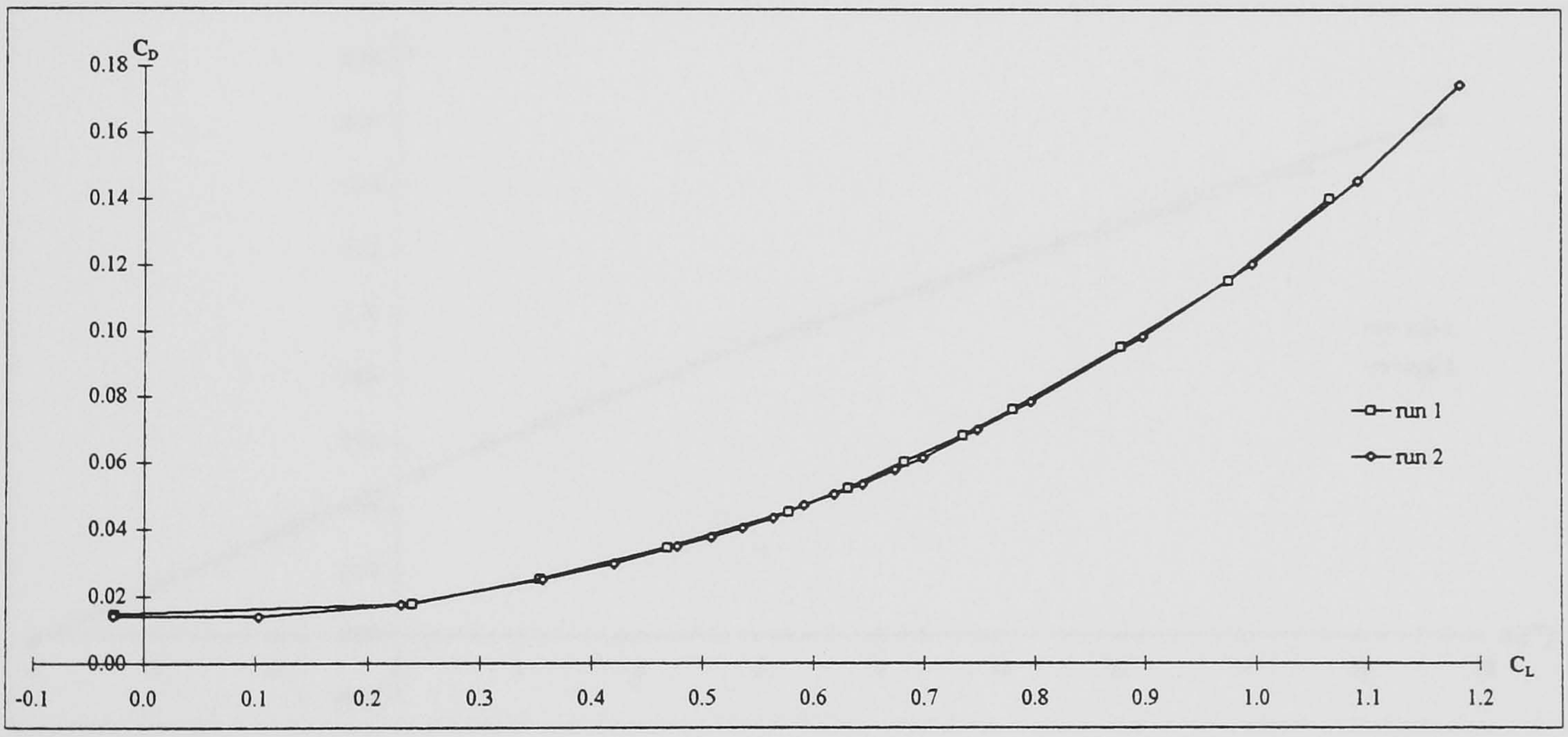

Drag polar

Figure A-12 cont.: DERA balance repeatability. $\Lambda = 40°$, $Re_c = 3.3 \times 10^6$.

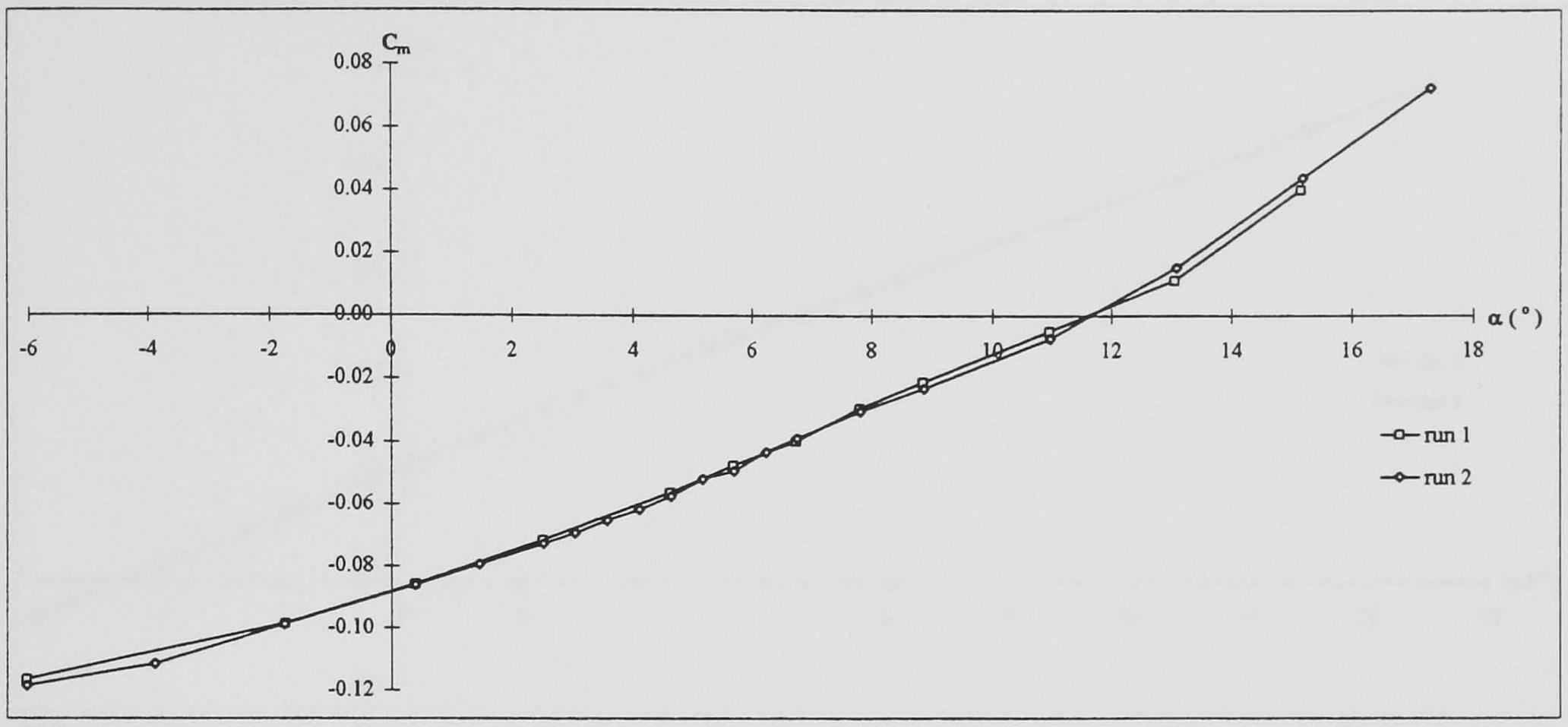

Pitching moment

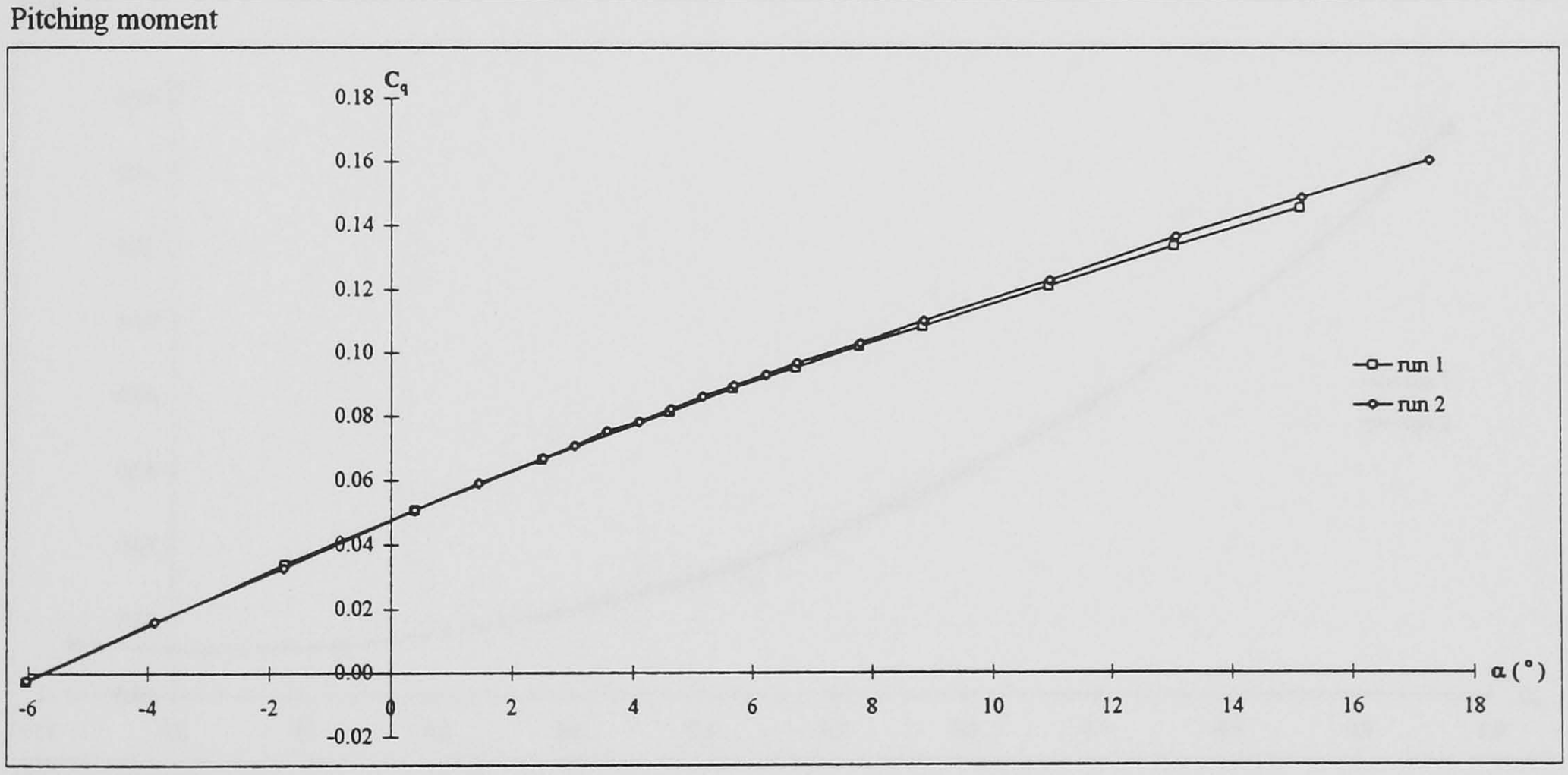

Rolling moment

Figure A-12 cont.: DERA balance repeatability. $\Lambda = 40°$, $Re_c = 3.3 \times 10^6$.

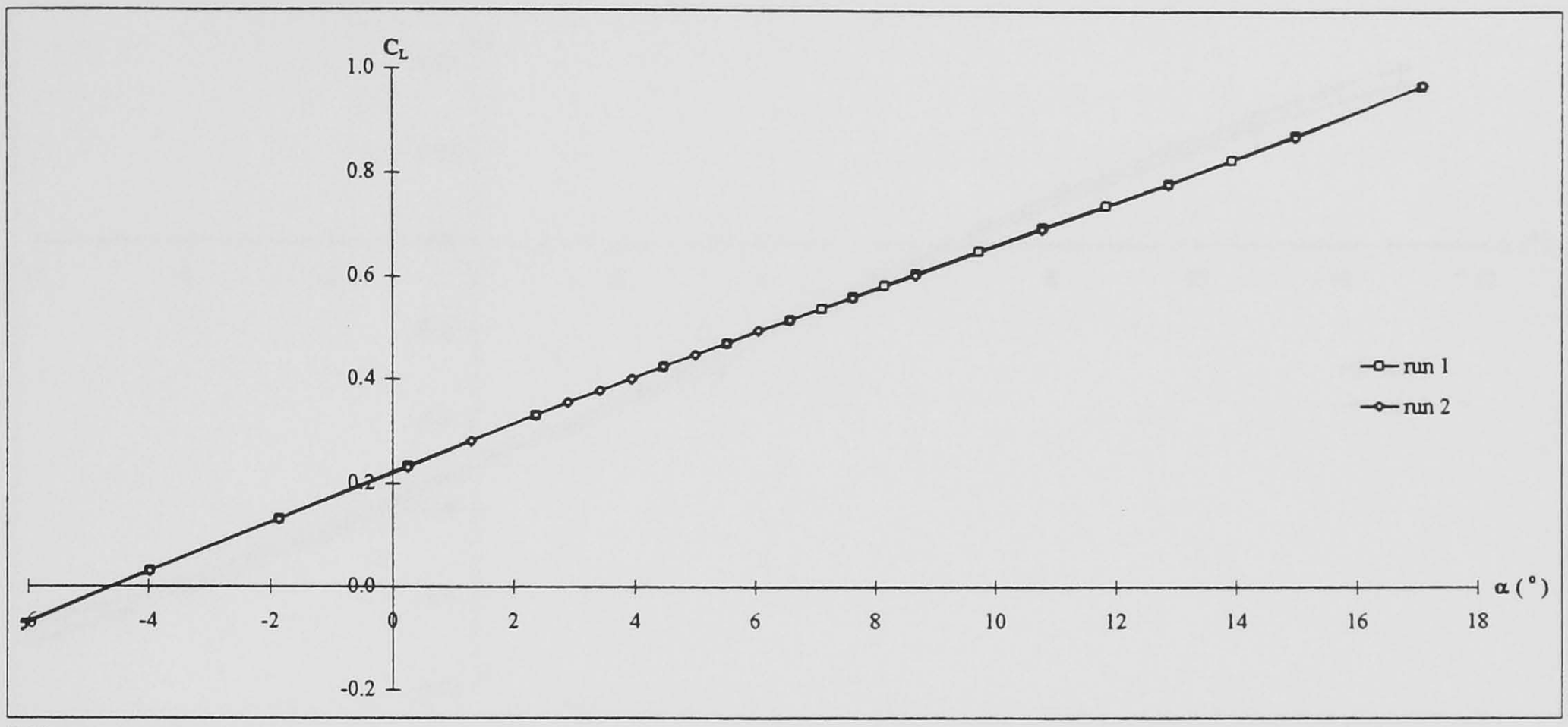

Lift

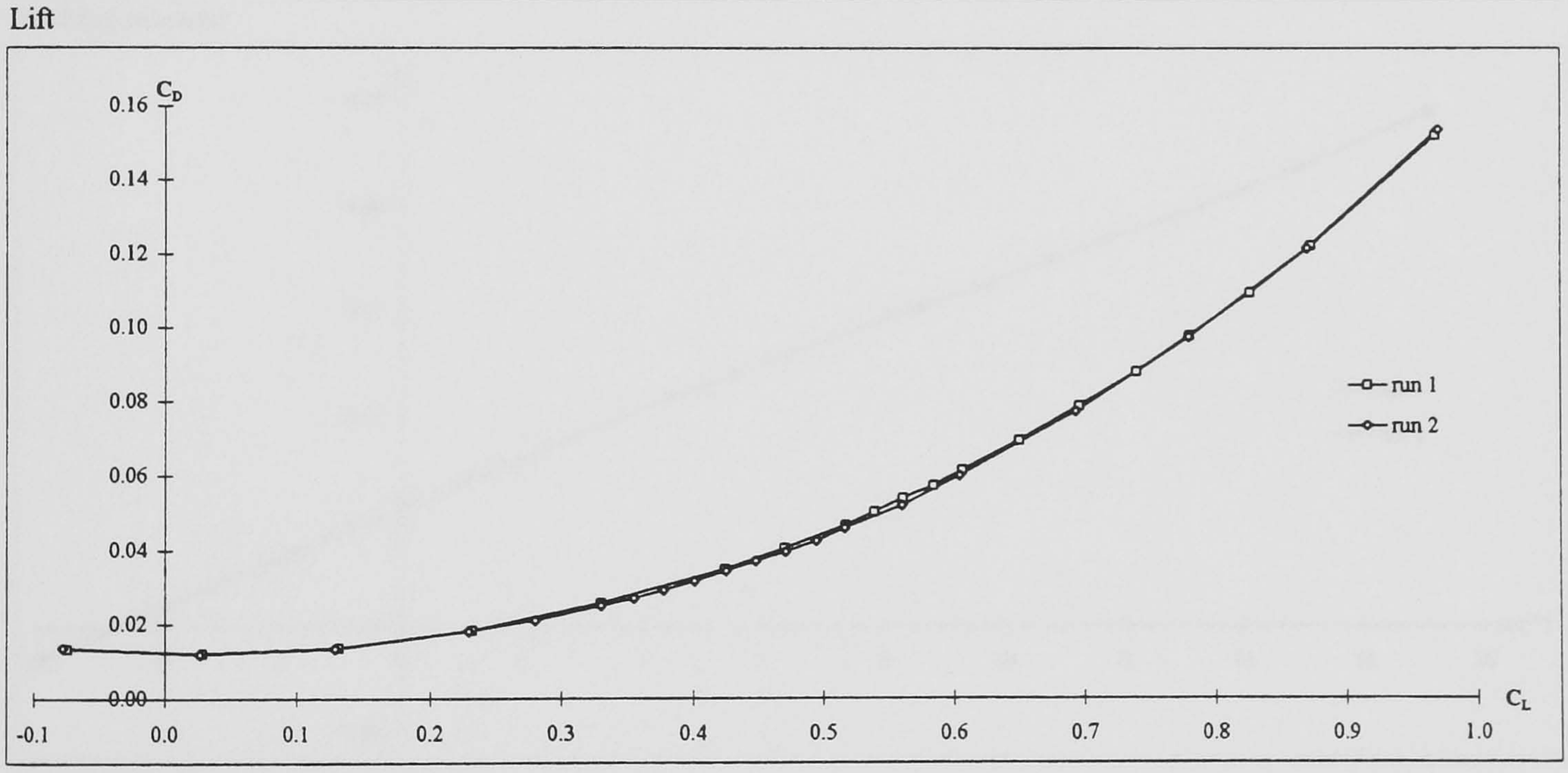

Drag polar

Figure A-12 cont.: DERA balance repeatability. $\Lambda = 50°$, $Re_c = 3.9 \times 10^6$.

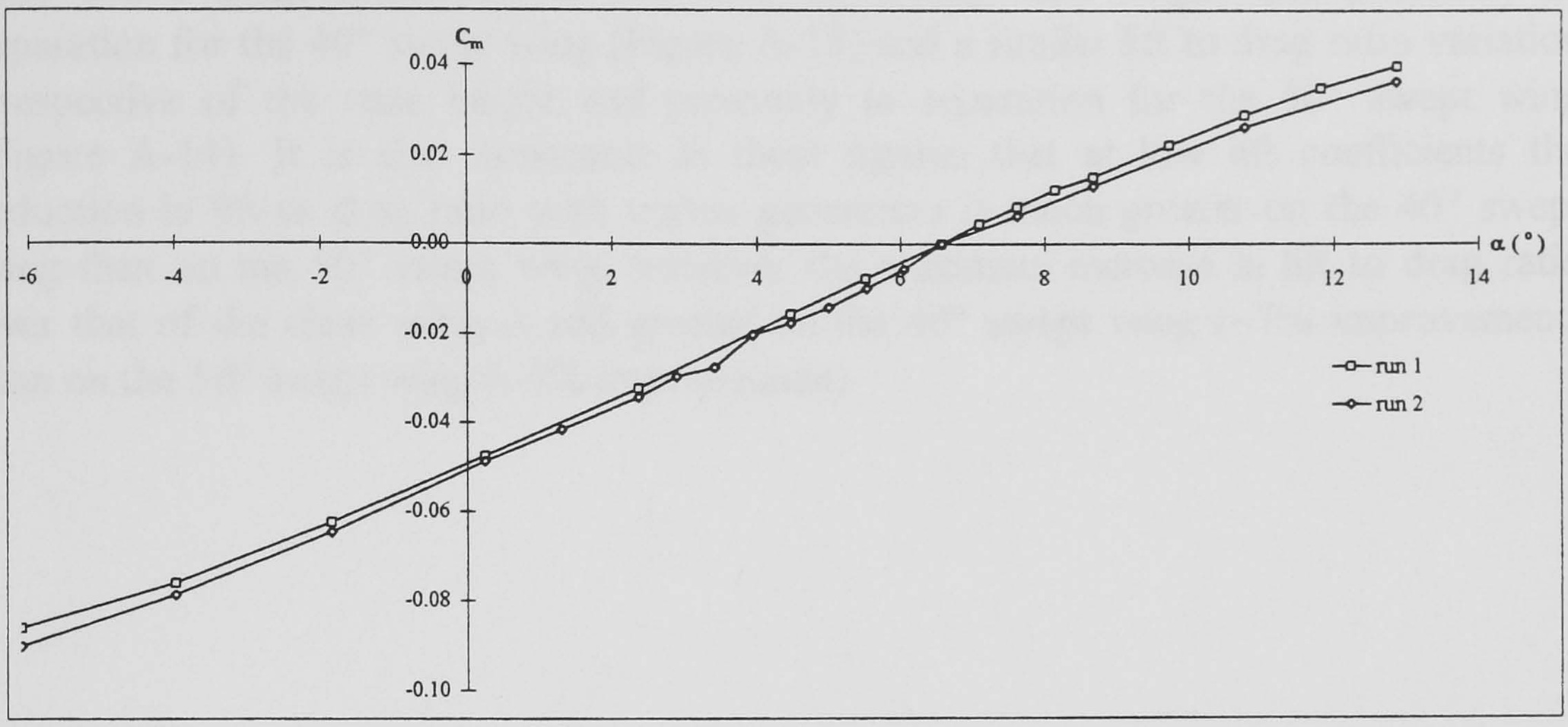

Pitching moment

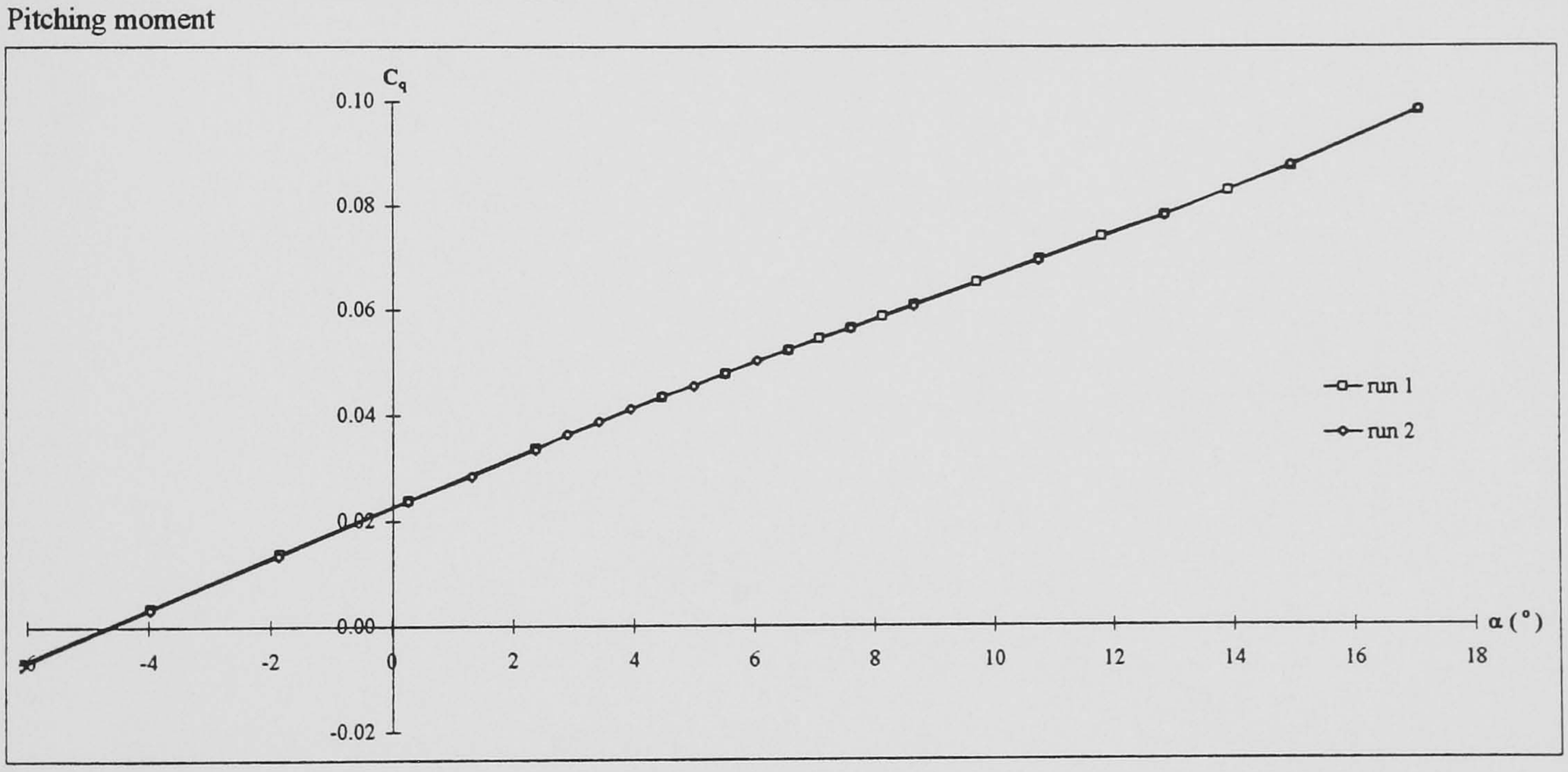

Rolling moment

Figure A-12 cont.: DERA balance repeatability. $\Lambda = 50°$, $Re_c = 3.9 \times 10^6$.

Appendix XV

Lift to drag ratio of the DERA wing with and without vortex generators

The lift to drag ratio variation with lift coefficient for the DERA wing swept at 40° and 50° with and without the more efficient vortex generator configurations are shown in Figures A-13 and A-14 respectively. These figures show an improvement in lift to drag ratio above a lift coefficient of 0.4 with increasing vane height and proximity to separation for the 40° swept wing (Figure A-13) and a similar lift to drag ratio variation irrespective of the vane height and proximity to separation for the 50° swept wing (Figure A-14). It is also noticeable in these figures that at low lift coefficients the reduction in lift to drag ratio with vortex generators is much greater on the 40° swept wing than on the 50° swept wing, however the maximum increase in lift to drag ratio over that of the clean wing is still greater on the 40° swept wing (~7% improvement) than on the 50° swept wing (~5% improvement).

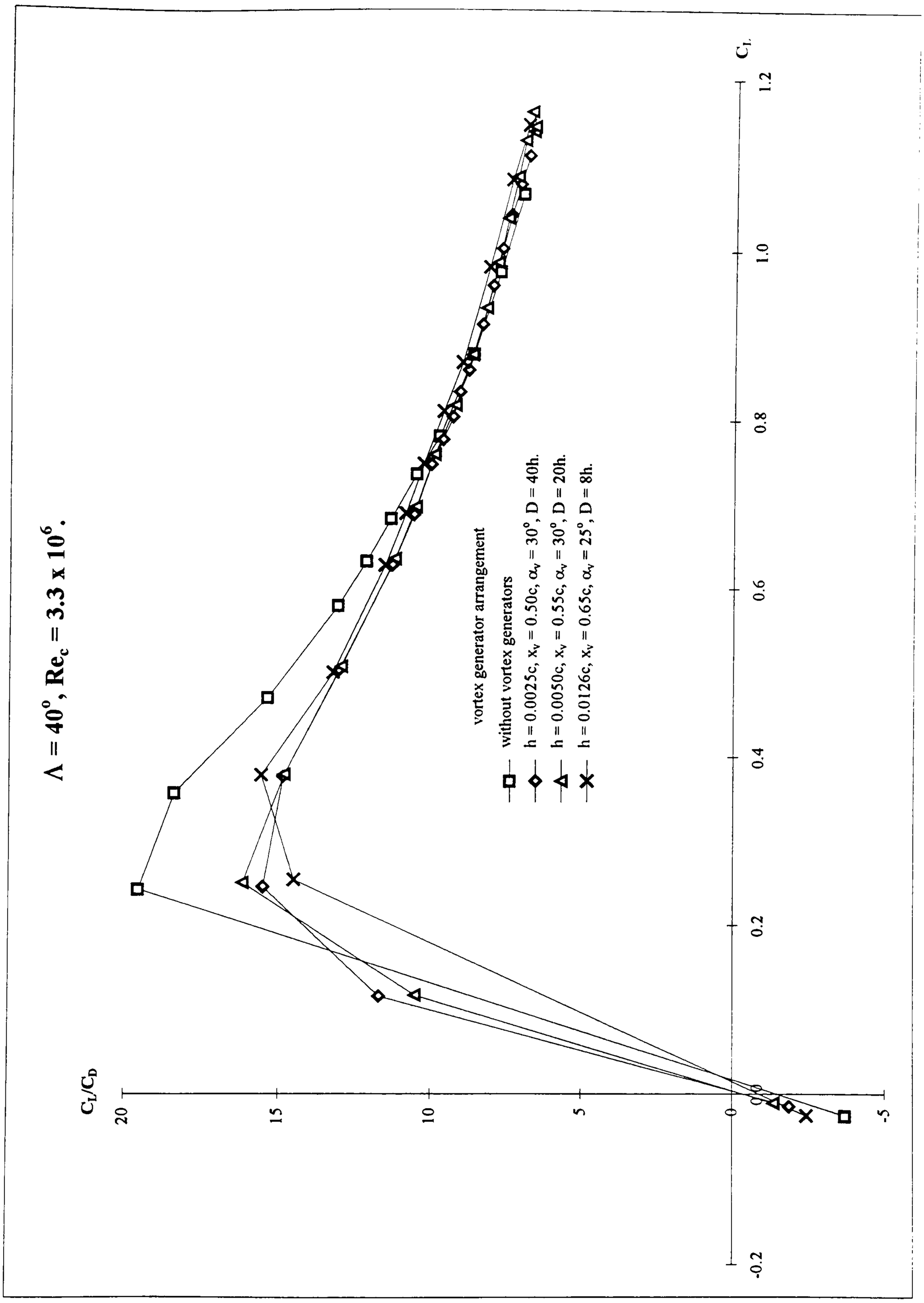

Figure A-13: Variation in lift to drag ratio with lift coefficient for the DERA swept wing with and without the more efficient configurations of cropped delta vane vortex generators.

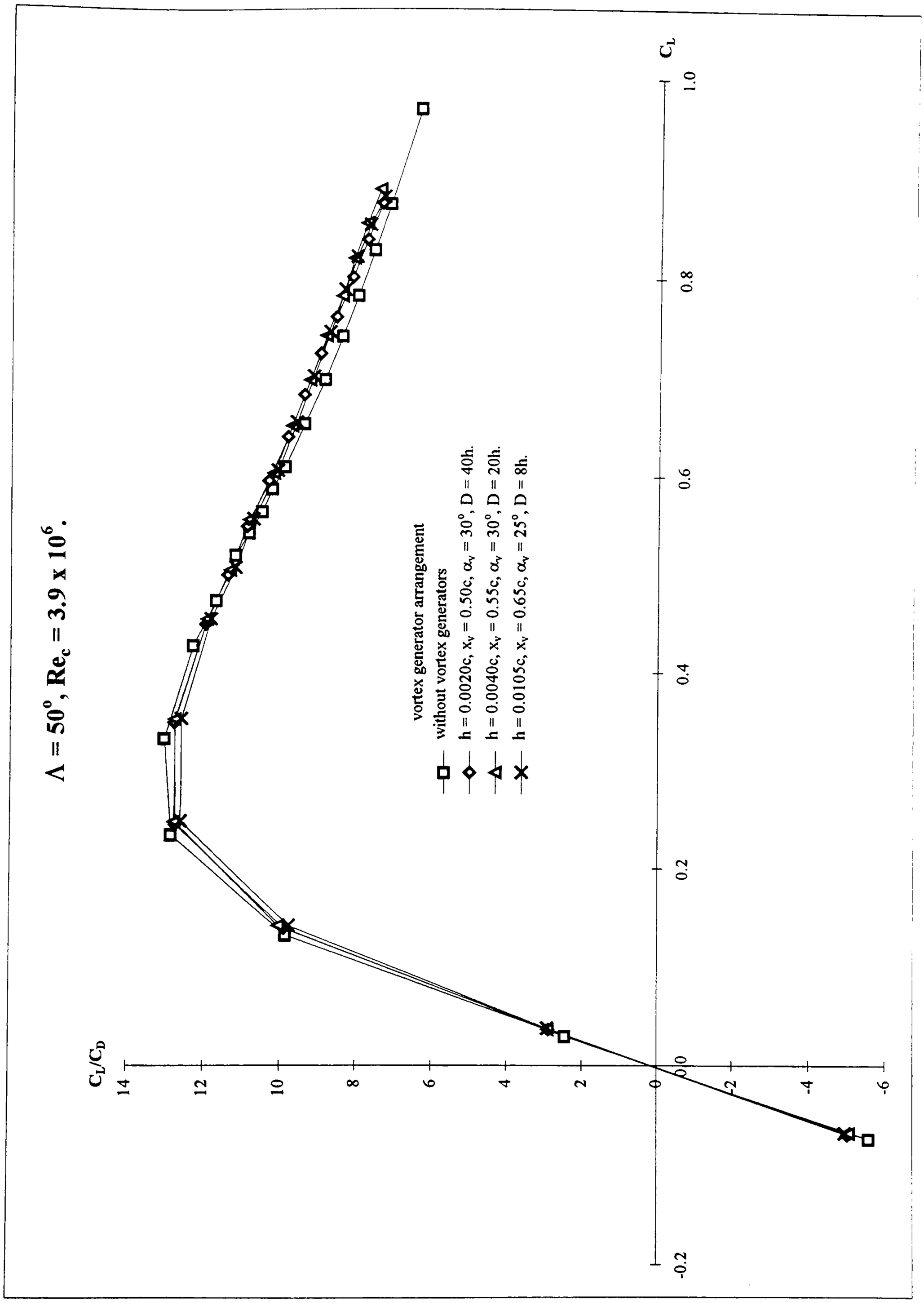

Figure A-14: Variation in lift to drag ratio with lift coefficient for the DERA swept wing with and without the more efficient configurations of cropped delta vane vortex generators.

Appendix XVI

Copy of AIAA-97-2319 'Effectiveness of Vortex Generator Position and Orientation on Highly Swept Wings' presented at 15th AIAA Applied Aerodynamics Conference, Atlanta, June 23rd - 25th 1997.

EFFECTIVENESS OF VORTEX GENERATOR POSITION AND ORIENTATION ON HIGHLY SWEPT WINGS

Ian Broadley, Kevin P. Garry
College of Aeronautics, Cranfield University,
Cranfield, Bedfordshire, MK43 0AL, England.

Abstract

The results from a low speed wind tunnel test on a 40° swept wing with a highly cambered aerofoil section are presented in order to examine the trailing edge flow separation mechanism. The tests involved oil flow visualisation, surface static pressure and force balance measurements at a chord Reynolds number of 4,000,000 and Mach number 0.17. A parametric study using cropped delta vane vortex generators in a co-rotating array was conducted to investigate the effect of vane chordwise position and orientation on the prevention of the trailing edge separation. The performance of these flow control devices is assessed in terms of changes in; surface oil flow visualisation photographs, lift curve slope and the lift-dependant drag factor. In addition comparisons are made between the clean wing and flow control wing measured pressure distributions. The results and analysis show that the performance of the vortex generators is improved when the height of the vortex generator is approximately equal to that of the local boundary layer thickness and when the vane angular deflection to the local upstream flow direction is between +18° and +23°. Similar performance improvements are observed with the wing swept to 50° using the positioning guidelines from this optimisation study.

Notation

A - Aspect ratio
C_D - drag coefficient
C_{Do} - zero lift drag coefficient
C_L - lift coefficient
C_p - pressure coefficient
c - wing chord
k - lift dependent drag factor ($=(C_D-C_{Do})\pi A/C_L^2$)
k_{cw} - clean wing lift dependent drag factor
M - Mach number
Re_c - Reynolds number based on chord
u - wind tunnel freestream velocity
x - aerofoil coordinate in freestream direction
x_{vg} - vortex generator chordwise location
z - aerofoil coordinate normal to freestream and spanwise directions
α - wing incidence
Δk - $k-k_{cw}$
Λ - wing sweep
ϕ - vortex generator orientation (+ toed out)

Introduction

For the foreseeable future weapons will be delivered on to surface targets from airborne platforms. The next generation of combat aircraft to perform these tasks will need to combine stealth with agility and long range, requiring the development and assessment of these technologies. Wing sweeps of 40° - 50° with highly swept trailing edges are favoured to combine stealth with agility. From an aerodynamic standpoint these configurations represent a high risk since the flows are more complex than those on wings with low sweep angles (less than 30° say), being susceptible to scale or Reynolds number effects and prone to three-dimensional boundary layer separation on the upper surface at low speeds or high angles of incidence. The likelihood of this type of separation increases if trailing edge flaps are deployed or the wing camber is increased. These separations increase drag significantly and degrade buffet characteristics of the aircraft. At present the full scale or flight characteristics of these wing flows cannot be predicted confidently by either CFD methods or from wind tunnel tests. Since wing efficiency governs the combat performance of aircraft, improvements in wing design will lead to significant reductions in aircraft drag and improved buffet performance. These improvements are only achieved by exploring experimentally the fundamental mechanisms of these complex wing flows.

The general aims for the programme are:

a) to investigate the fundamental flow characteristics on wings with highly swept leading and trailing edges,
b) to understand the nature of the associated flow separation,
and
c) to study the mechanisms by which this separation can be controlled and prevented through the use of vortex generators at low to high subsonic speeds.

This paper discusses experimental results from a low speed wind tunnel test on a highly swept wing, of the effectiveness of chordwise position and orientation of a toed out co-rotating array of cropped delta vane vortex generators on trailing edge separation control.

Experimental Details

Model Description

The wing section used in this study (Figure 1) has a 14% thickness/chord ratio and was designed deliberately, using established CFD methods, with significant rear camber to study viscous effects over aerofoils with severe adverse pressure gradients (Figure 2). In addition, to ensure that the flow remains attached at high incidence over the forward part of the aerofoil, the nose is drooped by 10° forward of 15% chord. The rear 25% of the section is drooped to give a pressure distribution representative of flows at high subsonic speeds or at manoeuvre conditions.

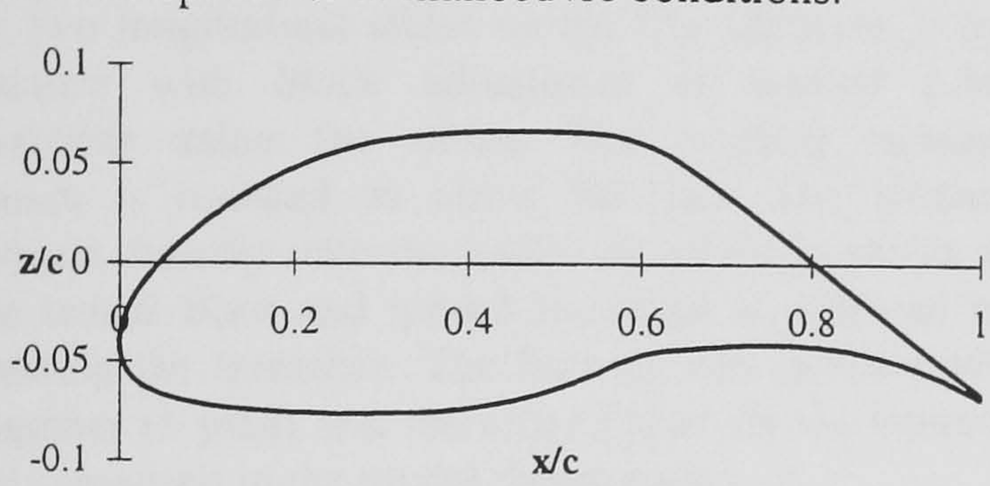

Figure 1 Aerofoil section

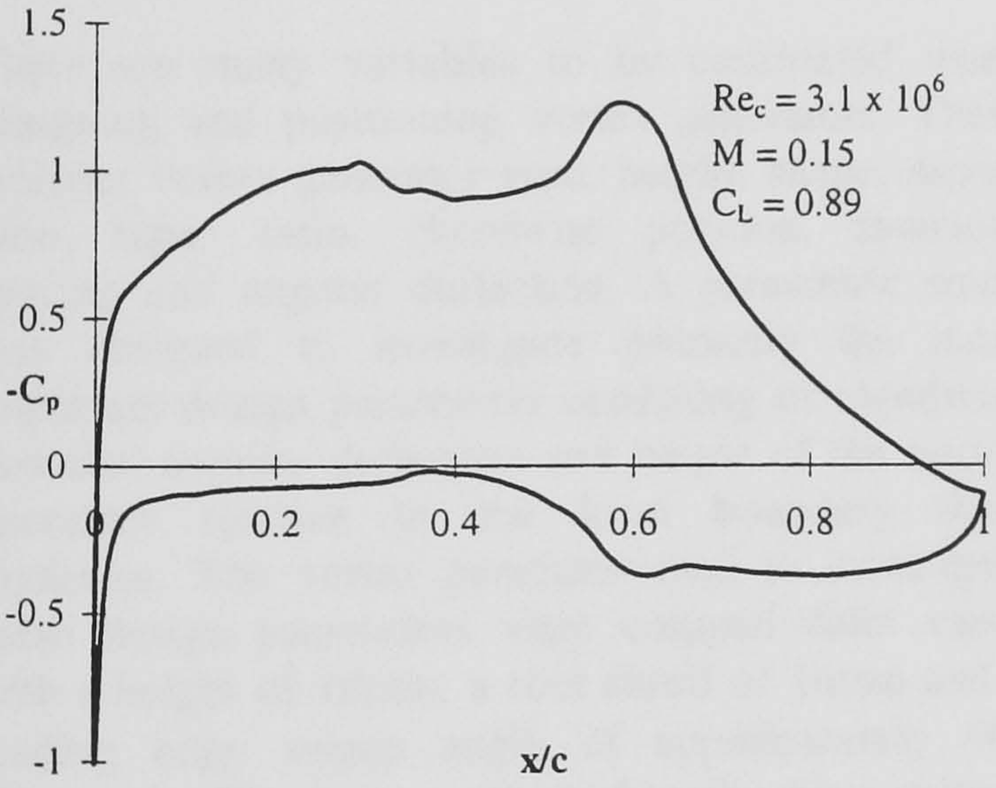

Figure 2 Typical pressure distribution at Λ = 0°

The wing (Photo 1) used for the test has a constant cross section with a chord of 0.61m and a semi-span of 1.83m at 0° sweep. The wing is capable of being swept aft from 0° to 60° in 5° intervals and has interchangeable tip sections to give streamwise tips at 30°, 45° and 60°. For this study the 45° tip was used giving a slightly inclined tip section to the freestream at 40°. A splitter plate, mounted horizontally 0.15m above the tunnel floor, prevents the tunnel floor boundary layer from interfering with the wing root flow. This splitter plate is not attached to the wing, the space between the wing and the splitter plate being sealed with soft foam rubber such that no loads are transferred to the balance.

The wing is pressure plotted at 5 spanwise stations, with 36 and 16 static pressure holes on the upper and lower surfaces respectively at each station. These pressure tappings are inclined at 45° to the leading edge such that at sweep angles of interest they are almost streamwise. The static-pressure holes are concentrated near the leading and trailing edges where pressure gradients are highest.

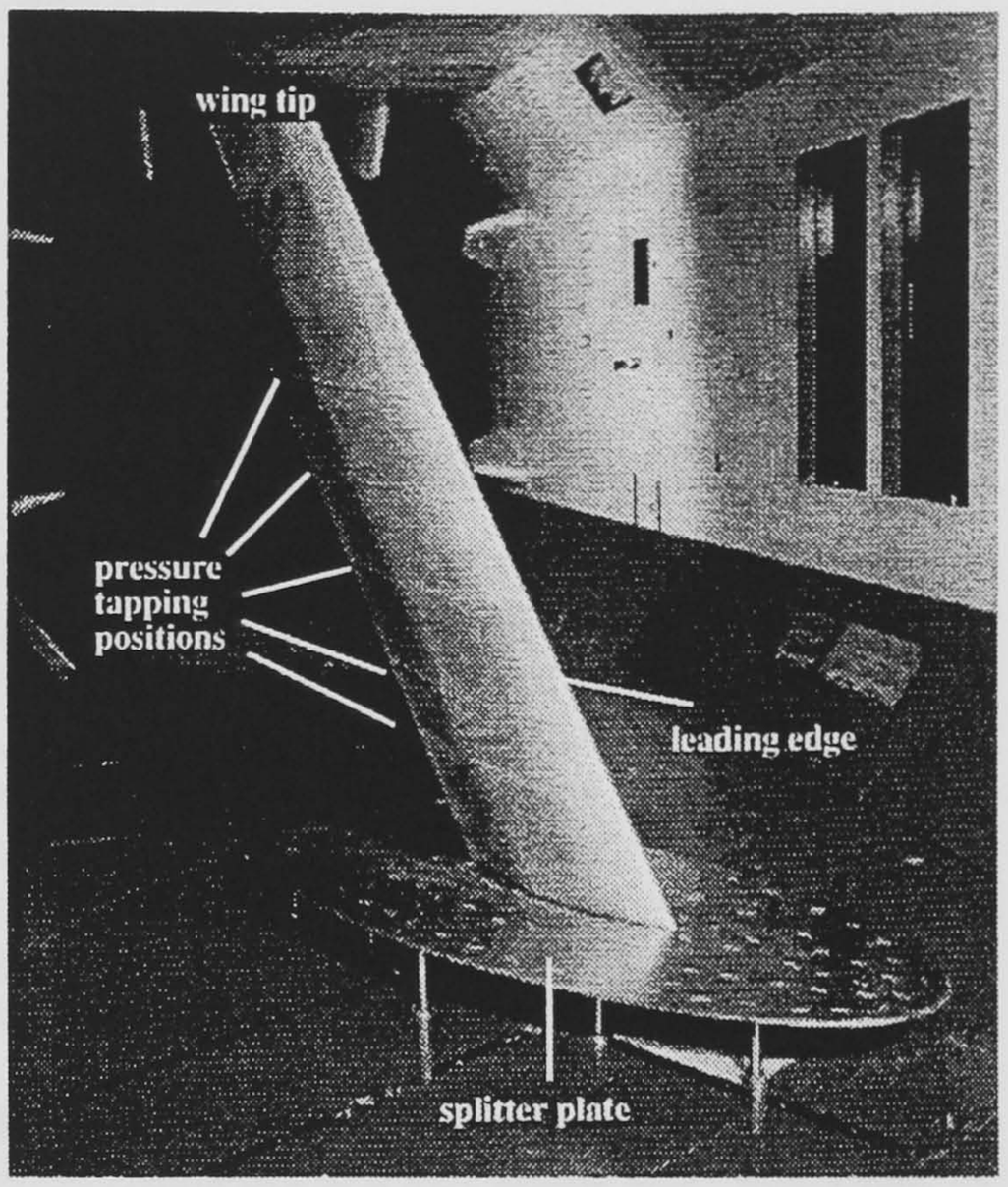

Photo 1 Model in wind tunnel

Transition is fixed on both the upper and lower surfaces at 5% chord using a 5mm band of grade 70 carborundum particles embedded in Araldite adhesive.

13' x 9' Low Speed Wind Tunnel Facility

The 13 ft x 9 ft low speed wind tunnel facility is a continuous closed circuit atmospheric tunnel with a minimum airspeed of 15m/s and a maximum airspeed of 91m/s. The settling chamber is octagonal in cross - section with a maximum breadth of 14m giving a contraction ratio of 16:1. The working section measures 13ft (3.96m) wide and 9ft (2.74m) high and has corner fillets tapering slightly over the length of the working section to ensure a negligible static pressure gradient along the working section. The tunnel working section centre is the point midway between the walls and roof and floor at the mid - streamwise station. Models are tested at or near to this centre. Turbulence levels (rms fluctuation) in the longitudinal direction are 0.02% of u at 15m/s rising to 0.04% of u at 61m/s. In the vertical and horizontal (transverse) directions turbulence levels are 0.02% of u rising to 0.1% of u for the same speed range.

The drive fan, of 9.35m diameter, is driven by a 1144kW ac synchronous motor with an 11kV ac feed. The speed control allows the tunnel operators to select the desired speed using the relationship between the pressure in the working section and the pressure in the settling chamber.

The Half Model Balance

The half model balance is a four component mechanical balance which measures normal force, axial force, pitching moment and root bending moment. Half model wings connect via a root block, directly onto the balance. The root block is mounted on two longitudinal slides on the live platform of the balance with block adjustment of around 1.8m available using the slides. The pitching moment datum is updated to allow for this. The balance mounts directly onto the underside of the turntable in the tunnel floor and model incidence is achieved by rotating the turntable. The balance and model rotate together in pitch and therefore forces on the balance are measured in the model datum axes.

Vortex Generators

There are many variables to be considered when designing and positioning vortex generators. These include: vortex generator type, height, shape, aspect ratio, taper ratio, chordwise position, spanwise spacing and angular deflection. A parametric study was designed to investigate primarily the more important design parameters consisting of chordwise position, angular deflection and height of the vortex generator relative to the local boundary layer thickness. The vortex generator used to investigate these design parameters were cropped delta vanes with a height of 10mm, a root chord of 16mm and a leading edge sweep angle of approximately 40° (Figure 3). These were attached to the wing surface by glue on the 2mm flange on the vane root.

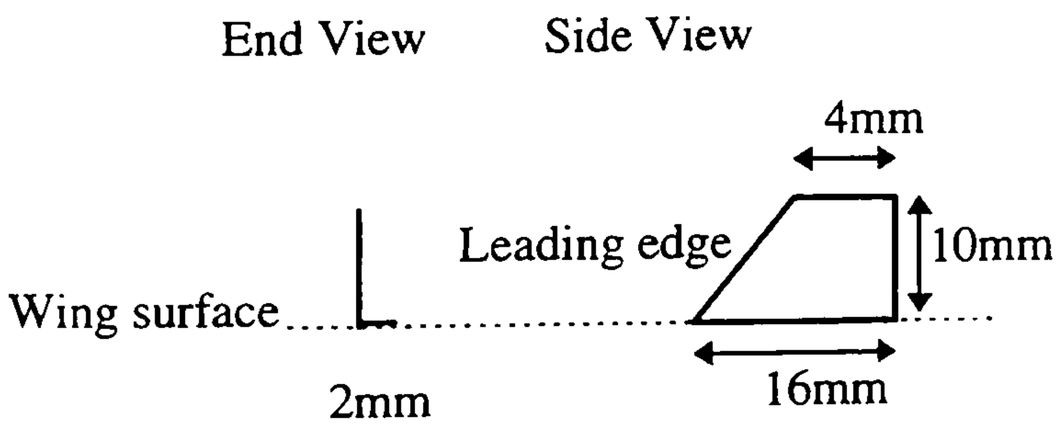

Figure 3 Cropped delta vane vortex generator

Test Procedure

Clean Wing

With the wing swept at 40°, force and moment results, together with the pressure distributions at the 5 spanwise stations, were taken for a wind tunnel speed of 60m/s, corresponding to a Reynolds number based on chord of 4×10^6 and a Mach number of 0.17, at wing incidences ranging from -6° to 16°; ie 2° intervals from -6° to 0° and 8° to 16°, 1° intervals from 0° to 2° and 6° to 8° and 0.5° intervals from 2° to 6°. Oil flow visualisation of the surface flow, using a diesel and fluorescent dye mix painted on the surface[1], were photographed at incidences of 2°, 4°, 6°, 8° and 12°.

Corrections are applied to the Mach number, pressure coefficient, lift coefficient and drag coefficient to account for solid and wake blockage[2]. An additional correction is also made to the wing incidence and drag coefficient for a wall-induced[3] lift constraint.

Vortex Generator Tests

The vortex generator tests were all performed at 60m/s with the wing swept at 40°. Force and moment results were taken for all the configurations tested together with oil flow visualisation photographs at similar wing incidences to those of the clean wing. Pressure distribution results were only taken for the vortex generator configurations which gave the greatest savings in drag compared to that of the clean wing.

Chordwise position was investigated first using the vortex generators in a co-rotating array consisting of 23 vanes with a spacing of 80mm. These were arranged on the wing upper surface at a chordwise position of 0.70c with an angular deflection to the freestream flow direction of +25°. This chordwise position was then varied in 0.05c intervals until the maximum drag saving was achieved. The performance of each configuration was determined by plotting lift dependent drag factor, k, against the vortex generator variable parameter. The chordwise position with the greatest reduction in k was then chosen and the angular deflection of the vane to the freestream flow direction varied in 5° intervals until again the maximum drag saving was achieved. It is important to recognise that values of k are calculated allowing for individual changes in C_{D_o} as a result of different vortex generator arrangements.

This optimum performance position was then tested on the wing swept at 50° and the results compared to those for the same configuration at a wing sweep of 40°.

Results

Clean Wing Flows

Figure 4 shows an oil flow result for the basic wing at an incidence of 8°. The oil flow pattern shows the chordwise separation position to be approximately at

0.70c and not to be highly dependent on spanwise position except near the tip where the flow is influenced by a tip vortex and near the wing root where the boundary layer on the wing is influenced by the boundary layer on the splitter plate. The spanwise velocity component in this region is reduced, moving the separation position further downstream.

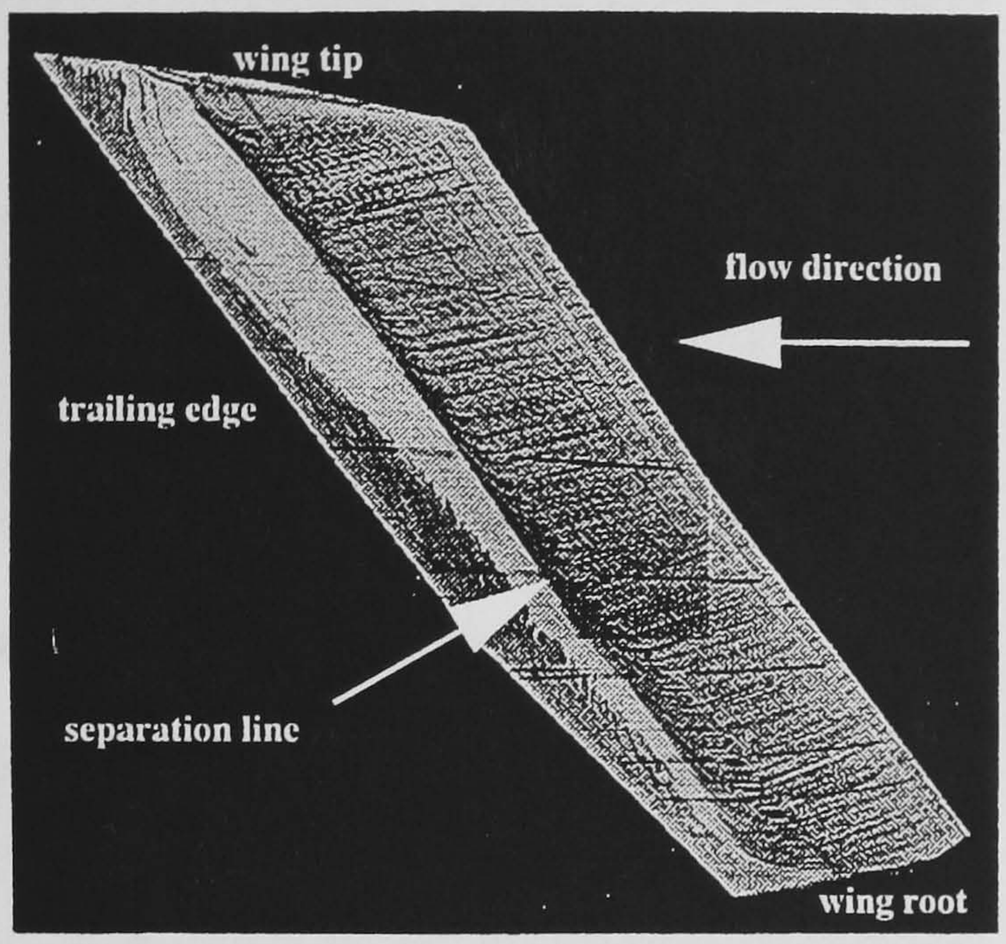

Figure 4 Clean wing oil flow. $\Lambda = 40°$, $\alpha = 8°$

Figure 5 shows a sketched interpretation of the flow pattern observed on the upper surface of the wing once separation has occurred. The surface flow direction is streamwise over the forward part of the wing and unsweeps over the rearward part until the flow direction is almost spanwise, downstream of which three dimensional flow separation occurs.

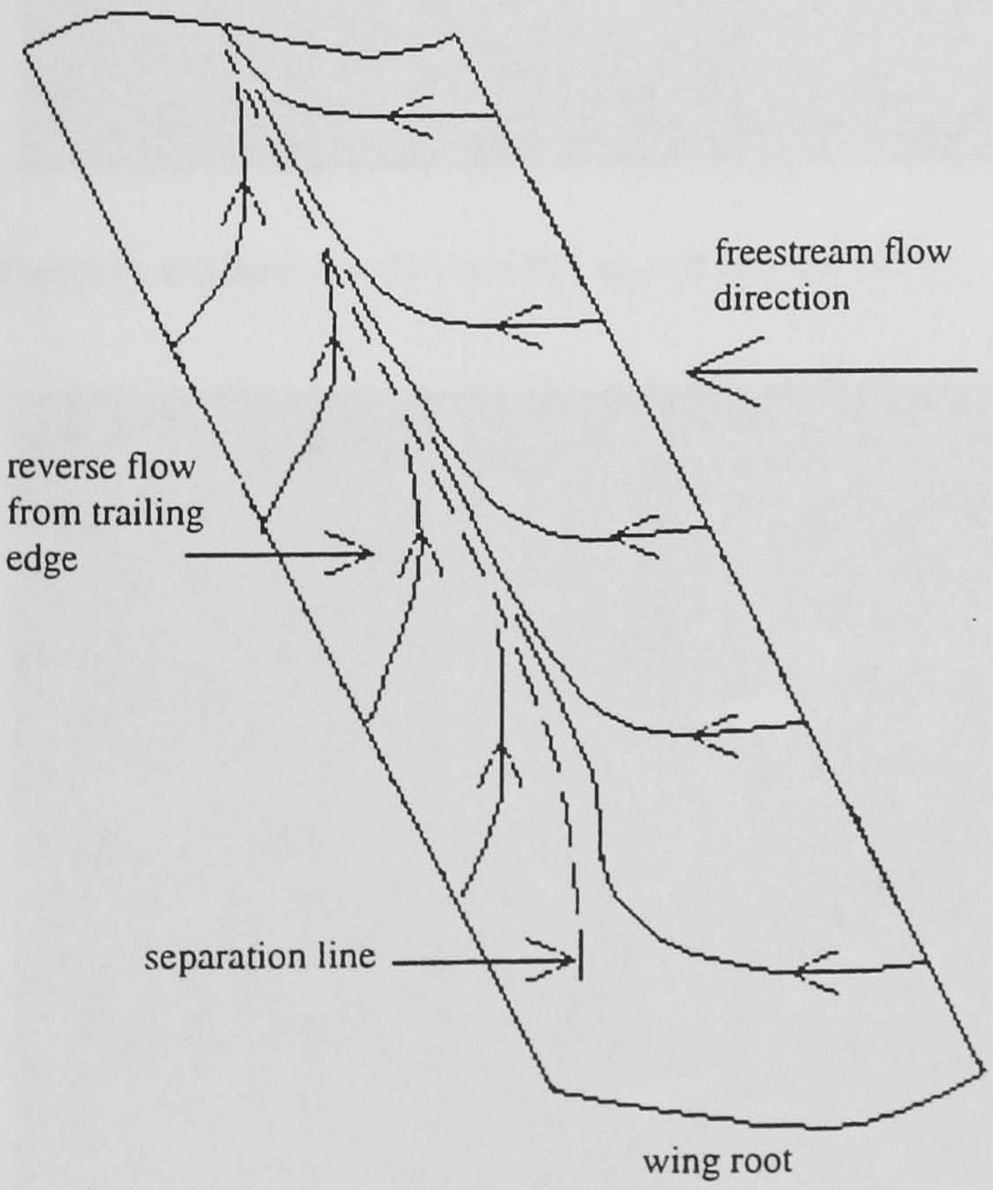

Figure 5 Flow interpretation

This separated flow rolls into a vortex (Figure 6) aligned in the spanwise direction and, due to the low pressure generated behind the vortex, draws air from the trailing edge region resulting in a reverse flow towards the separation line.

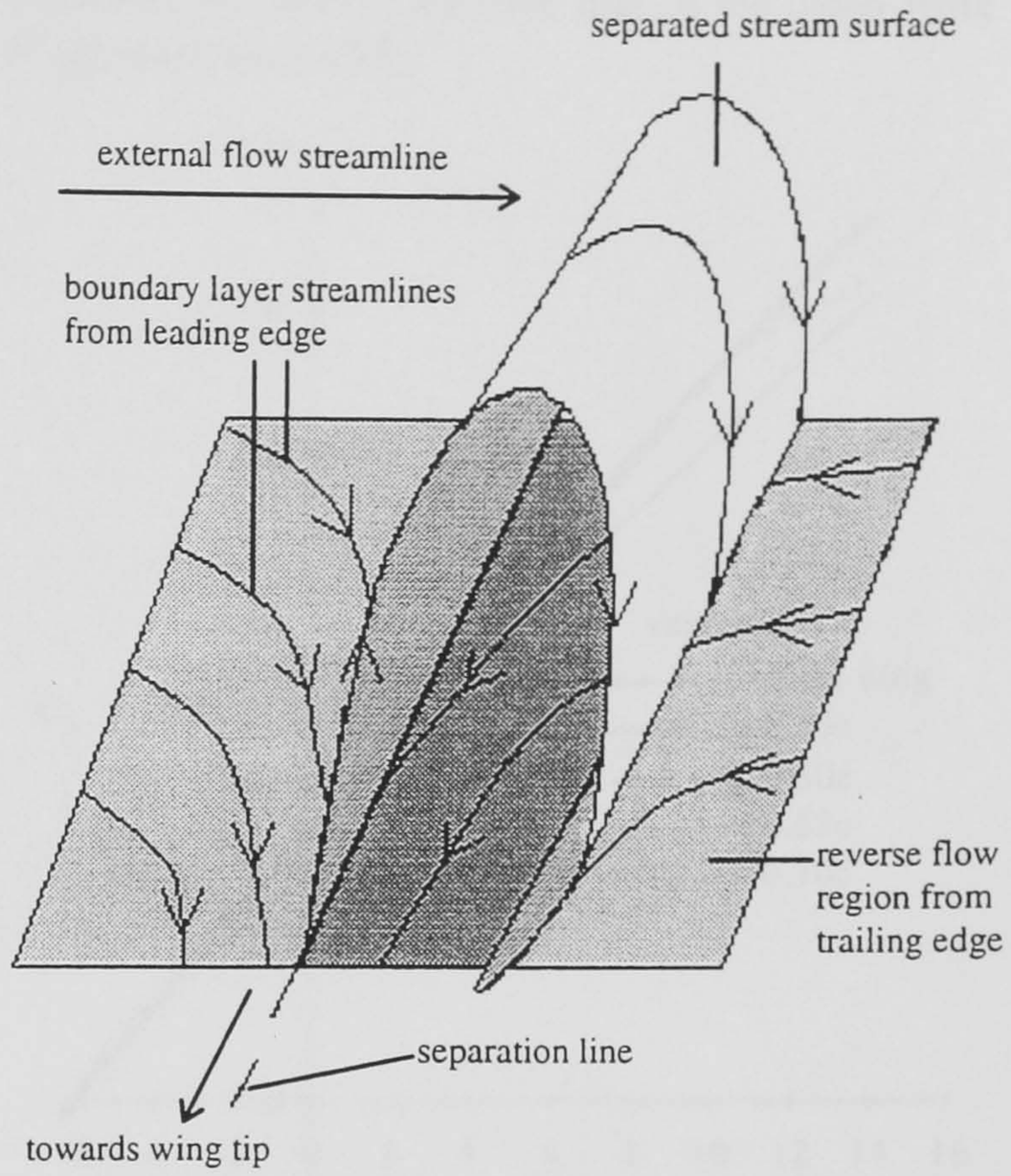

Figure 6 Mechanism for the separating flow

Vortex Generators

Position

The oil flow results (Figures 7a - 7d) show all the cropped delta vane vortex generator chordwise positions to be successful in controlling separation to some extent. However it is seen from these photographs that those positioned at 0.60c, 0.65c and 0.70c show stronger local vortices than those at 0.55c resulting in a reduced region of separation.

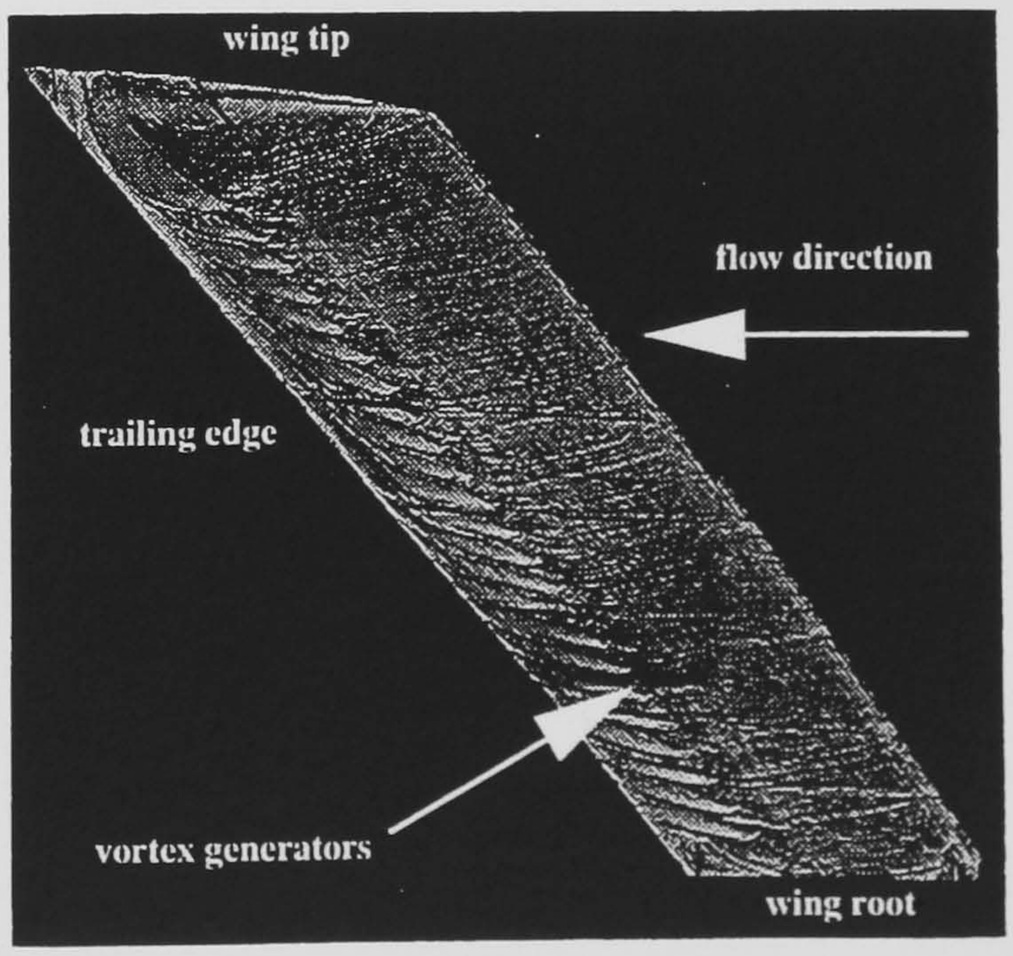

Figure 7a Oil flow $\Lambda = 40°$, $\alpha = 10°$, $x_{vg} = 0.70c$, $\phi = +25°$

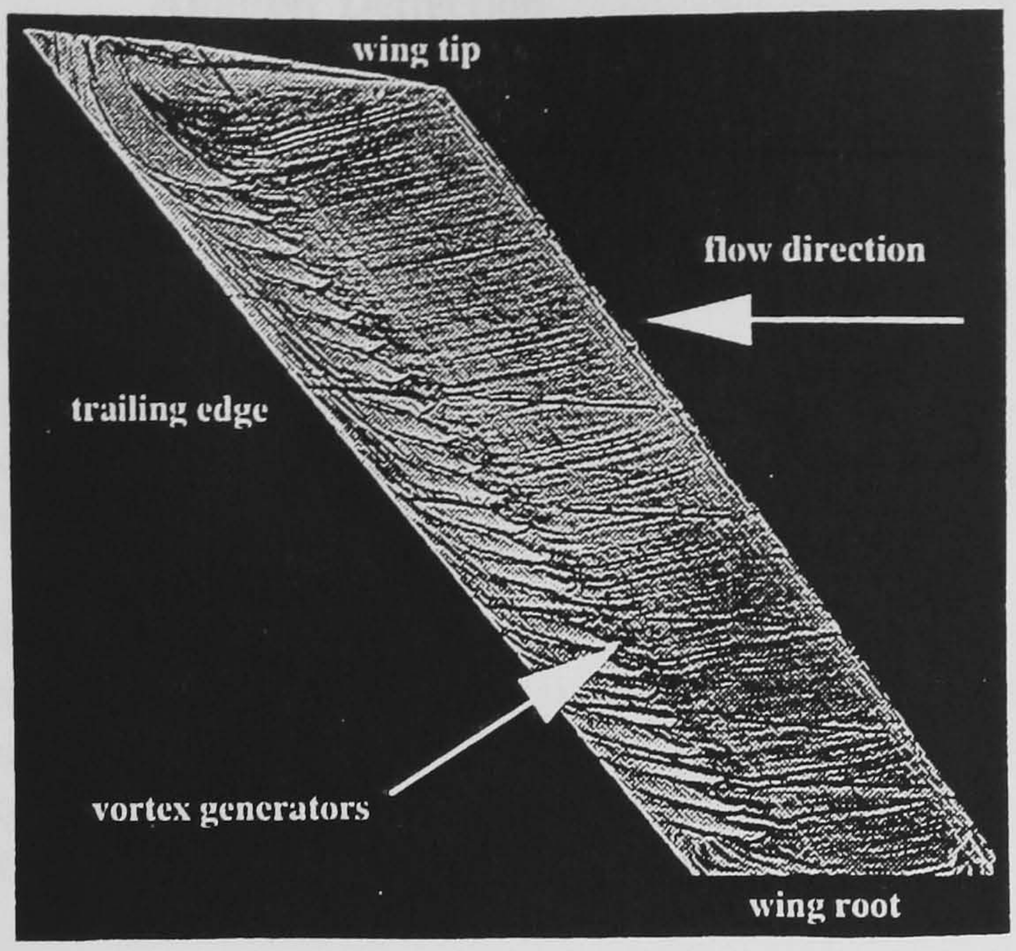

Figure 7b Oil flow $\Lambda = 40°$, $\alpha = 10°$, $x_{vg} = 0.65c$, $\phi = +25°$

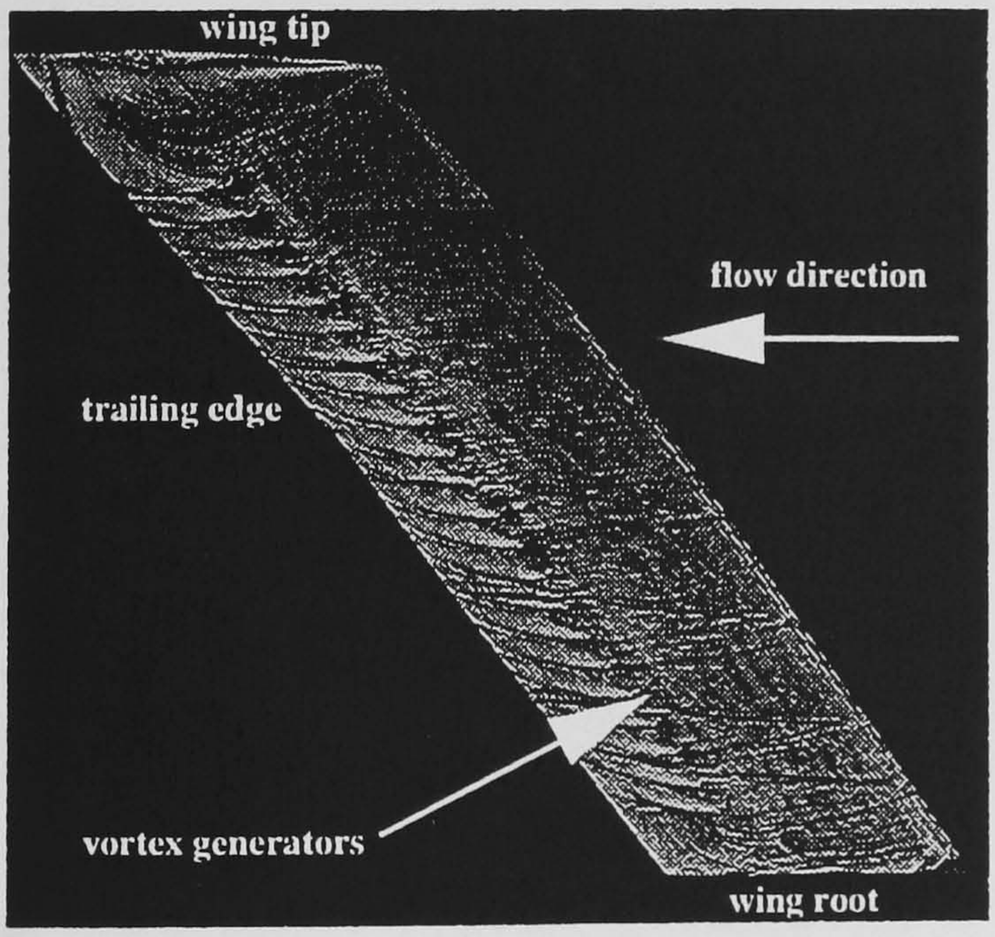

Figure 7c Oil flow $\Lambda = 40°$, $\alpha = 10°$, $x_{vg} = 0.60c$, $\phi = +25°$

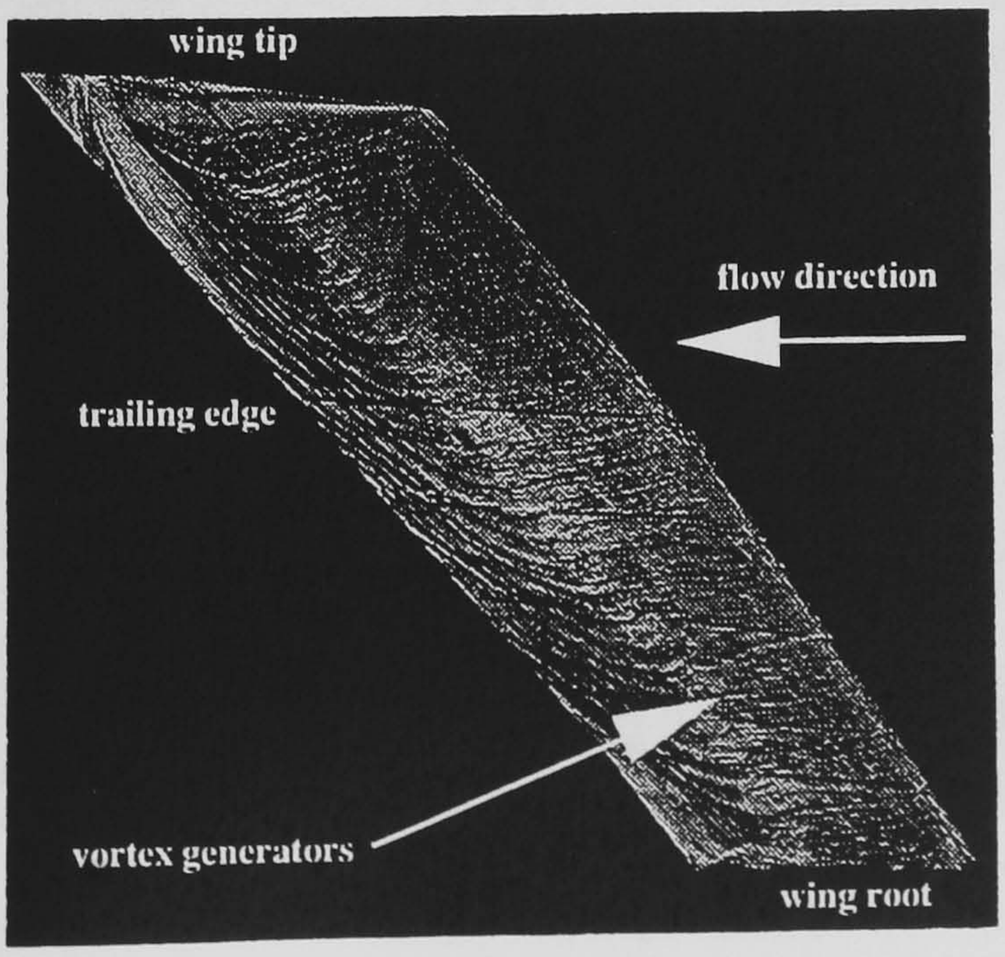

Figure 7d Oil flow $\Lambda = 40°$, $\alpha = 10°$, $x_{vg} = 0.55c$, $\phi = +25°$

The lift curves, Figure 8, reflect this in showing for all these configurations an increase in lift curve slope over that of the clean wing. Each configuration has a maximum increase in lift over that of the clean wing of approximately 10%.

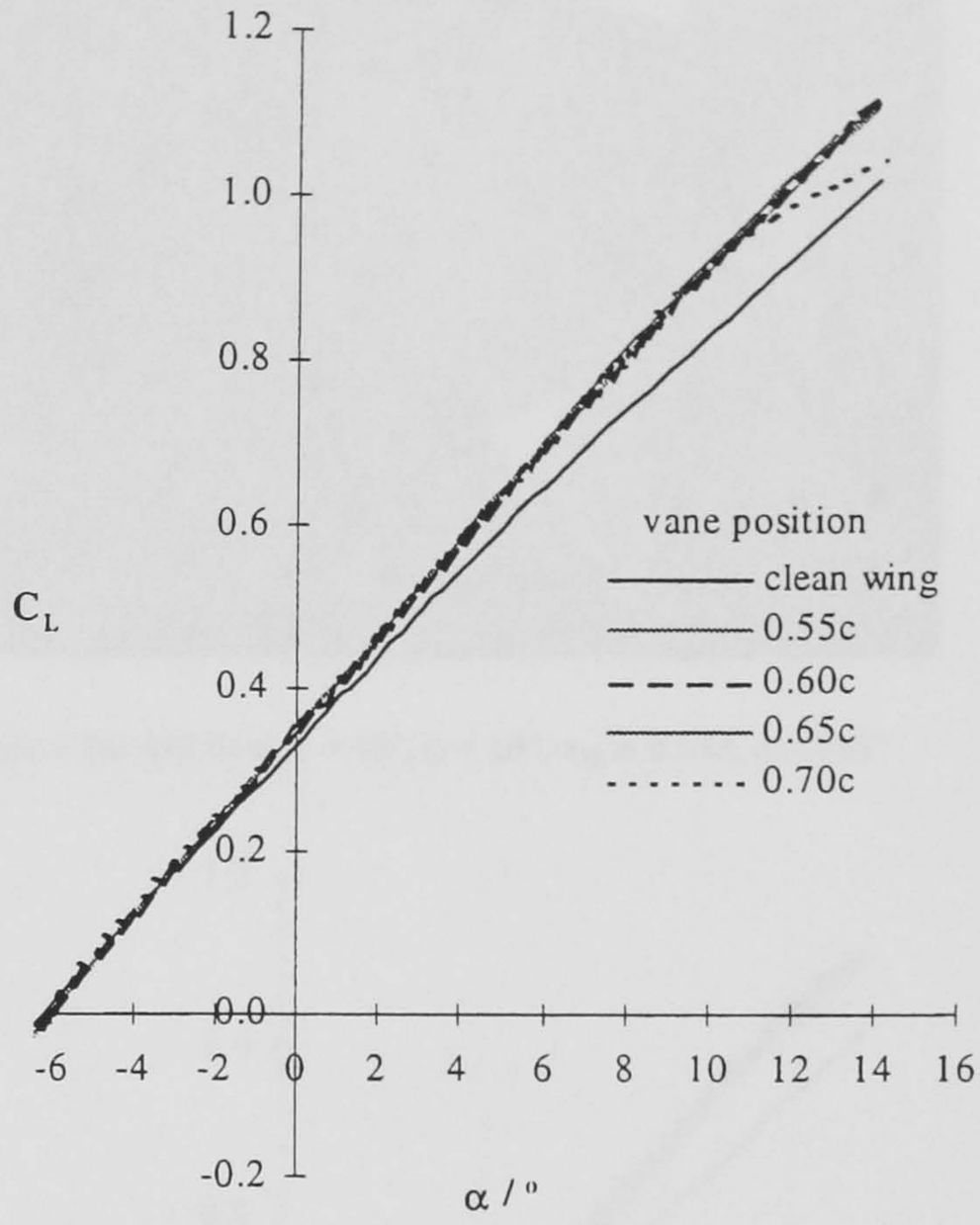

Figure 8 Lift curves for clean wing and for vortex generators at various chordwise positions

To determine the optimum chordwise position of the vortex generators the reduction in k relative to that of the clean wing is plotted against chordwise position at various lift coefficients, Figure 9. From this it is clearly seen that in terms of the percentage reduction in k a chordwise location of 0.65c is the optimum position with reductions in k of up to approximately 8% being achieved.

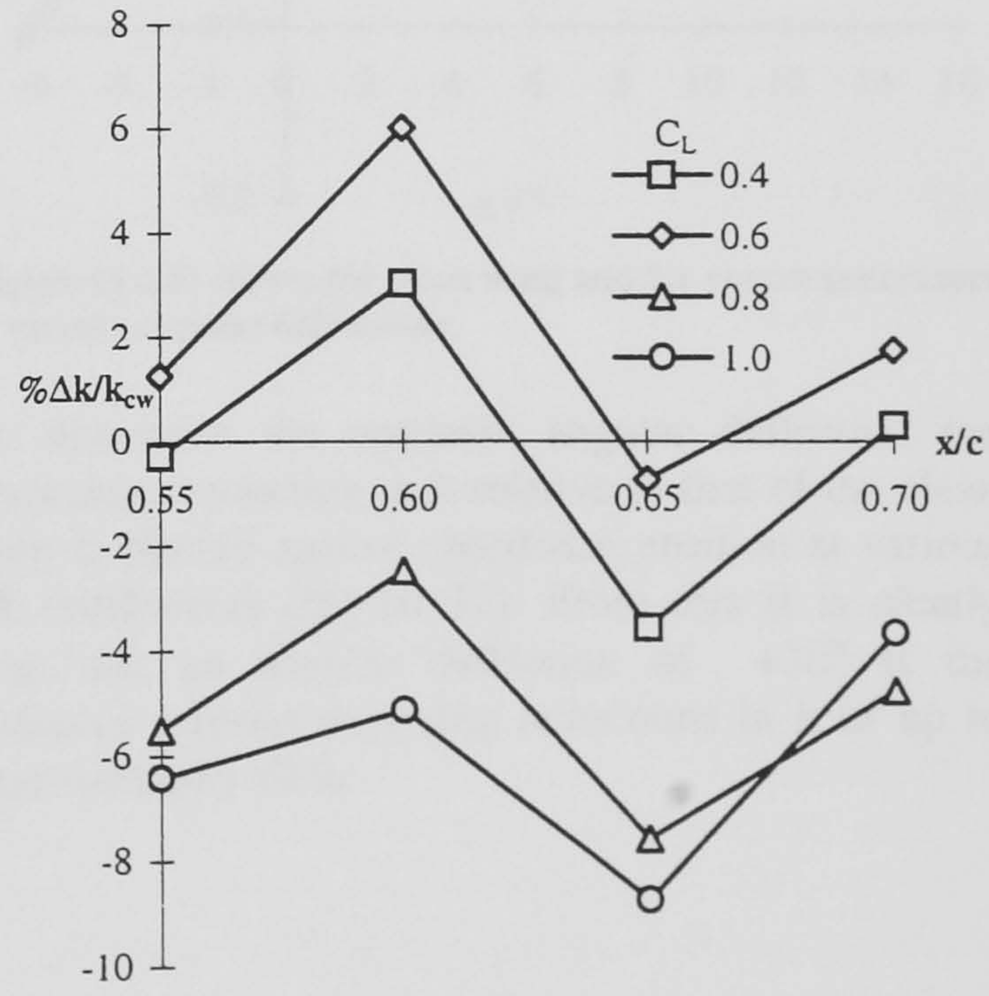

Figure 9 Lift dependent drag saving with vane chordwise position

Angular Deflection

The oil flow results (Figures 7b and 10a - 10c) show all the cropped delta vane vortex generator angular deflections to be successful in controlling separation to some extent. However it is seen from these photographs that those positioned at +25°, +30° and +35° show stronger local vortices than those positioned at +20° resulting in a reduced region of separation.

The lift curves, Figure 11, again reflect this in showing for all these configurations an increase in lift curve slope over that of the clean wing. Each configuration has a maximum increase in lift over that of the clean wing of approximately 10%.

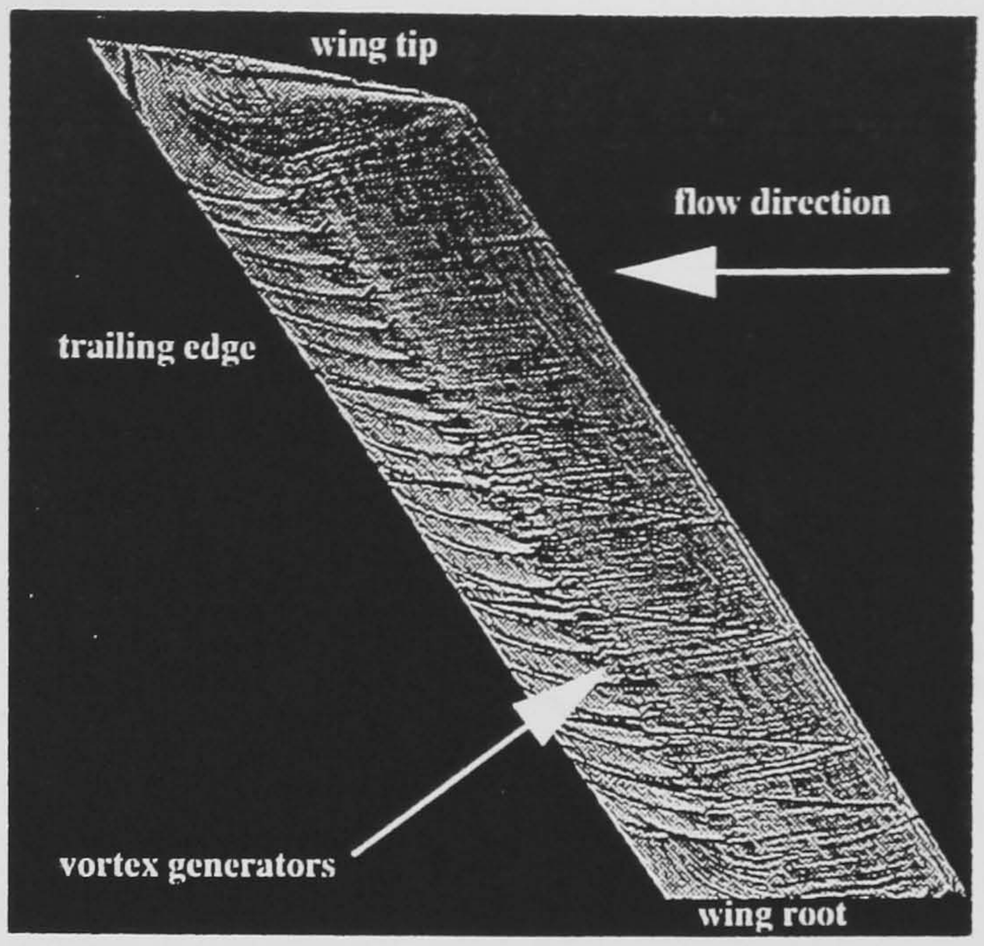

Figure 10c Oil flow $\Lambda = 40°$, $\alpha = 10°$, $x_{vg} = 0.65c$, $\phi = +35°$

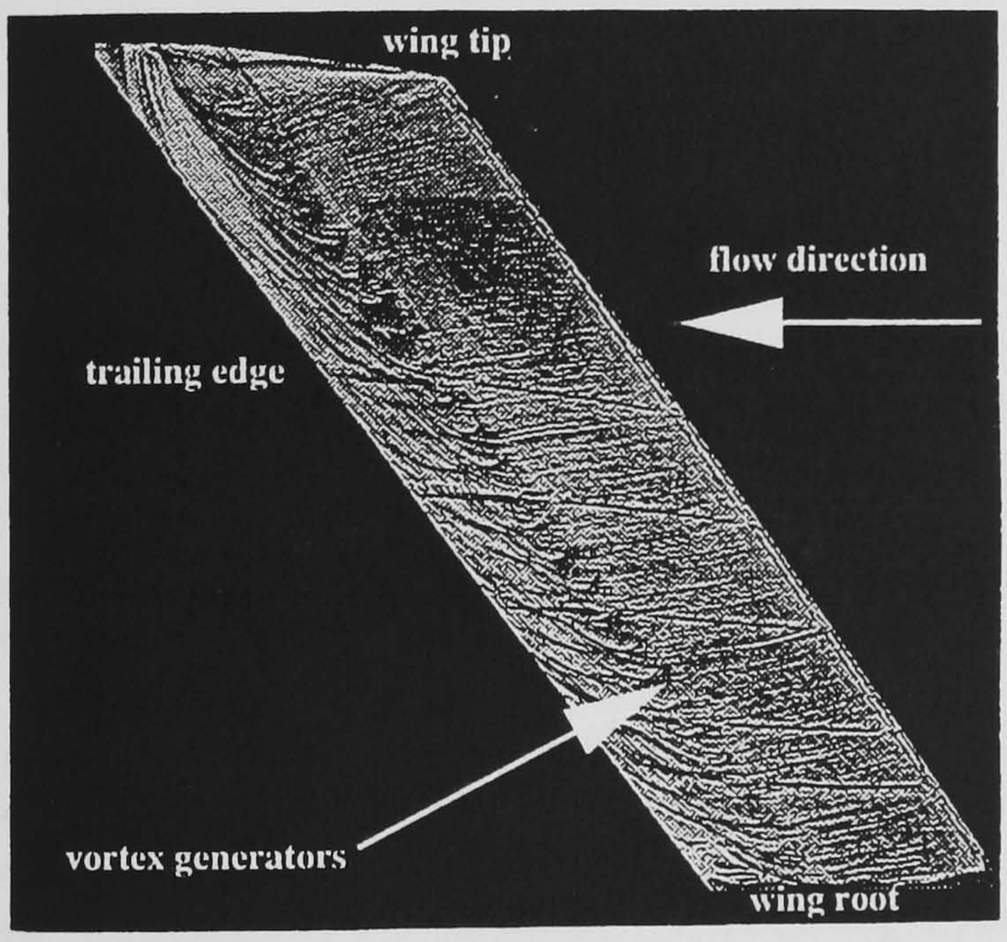

Figure 10a Oil flow $\Lambda = 40°$, $\alpha = 10°$, $x_{vg} = 0.65c$, $\phi = +20°$

Figure 10b Oil flow $\Lambda = 40°$, $\alpha = 10°$, $x_{vg} = 0.65c$, $\phi = +30°$

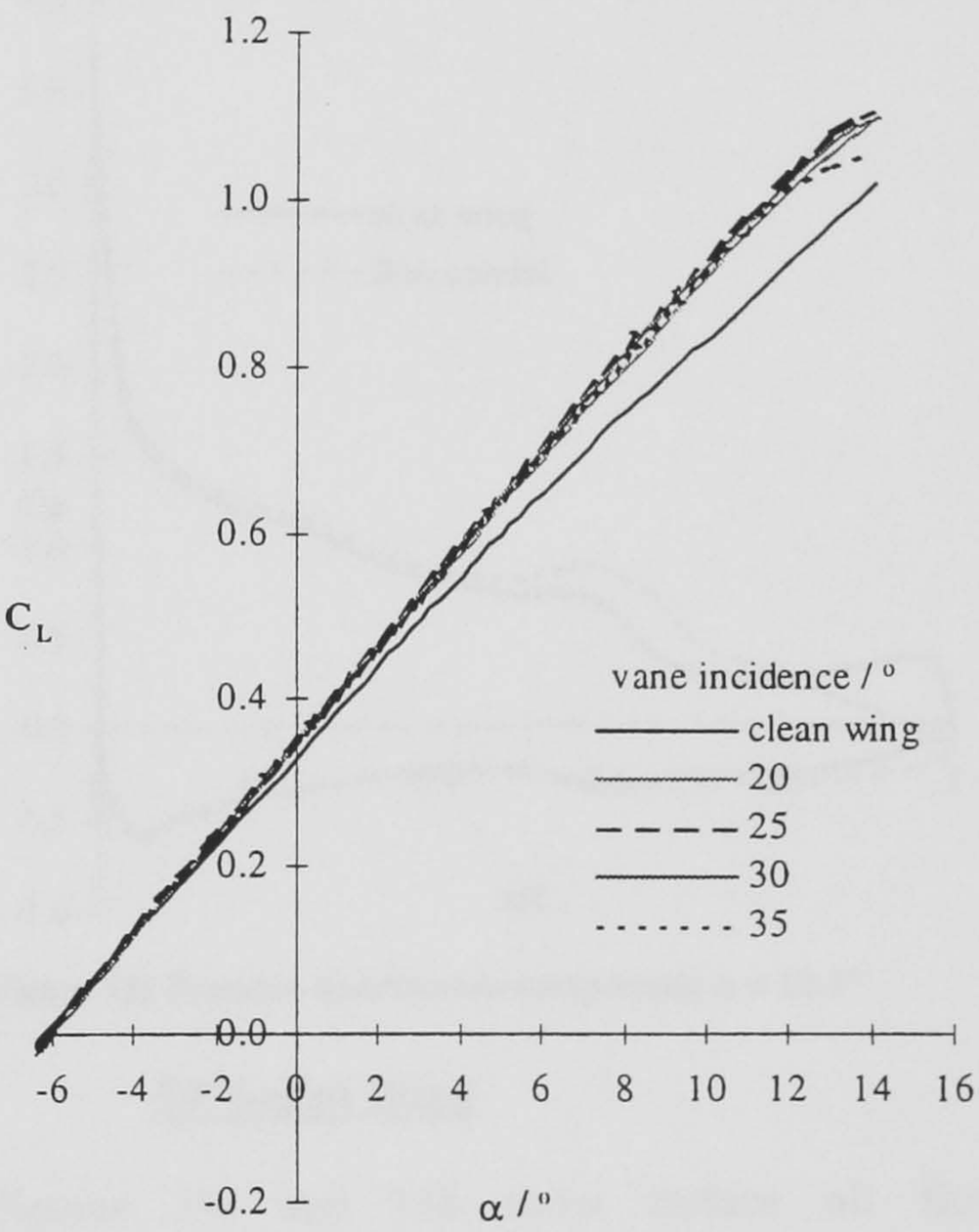

Figure 11 Lift curves for clean wing and for vortex generators at various angular deflections

To determine the optimum angular deflection the percentage reduction in k relative to that of the clean wing is plotted against chordwise position at various lift coefficients (Figure 12). From this it is clearly seen that an angular deflection of +30° is the optimum orientation giving reductions in k of up to approximately 10%.

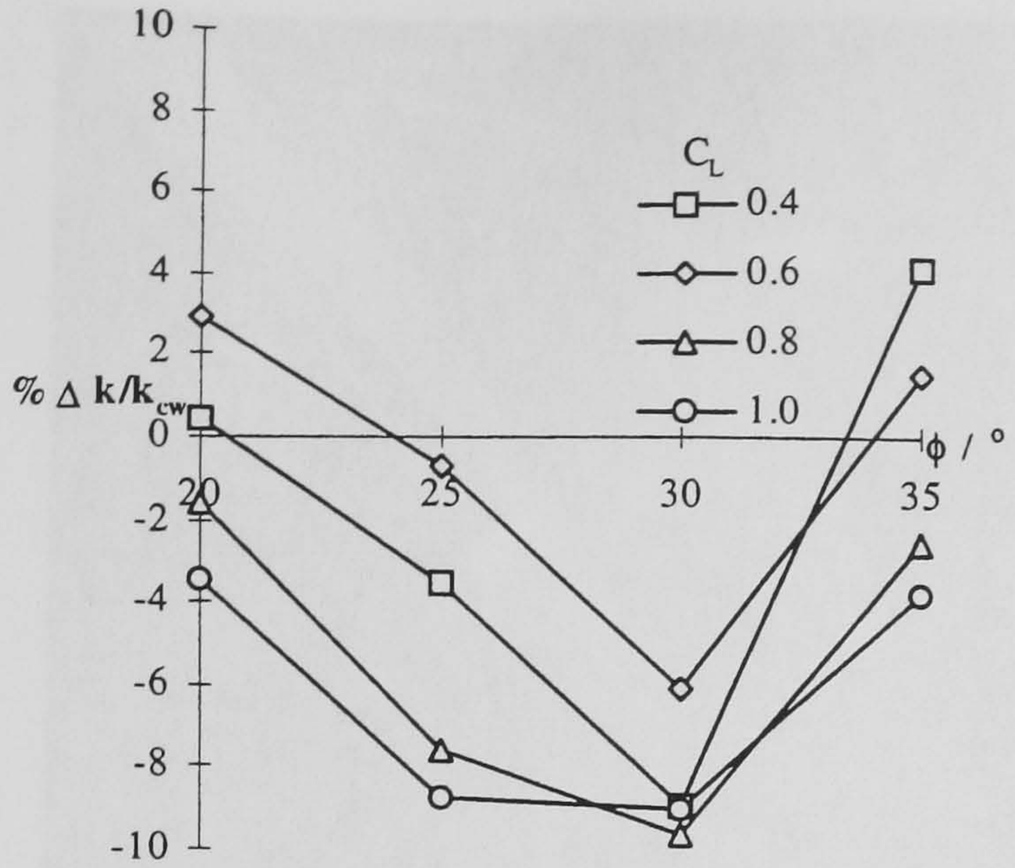

Figure 12 Lift dependent drag saving with vane angular deflection

Pressure Distributions

Figures 13a to 13c compare the measured pressure distributions of the wing without vortex generators and the wing with vortex generators positioned at 0.65c and toed out at an angular deflection of +25°. These figures show that at low wing incidences the two pressure distributions are similar except in the vicinity of the vortex generators.

However, as incidence is increased the clean wing develops a separated region just upstream of the trailing edge which spreads forwards as incidence is increased, until at 12° incidence it has reached 0.70c. With flow control the adverse pressure gradient over the rear of the section is increased and the trailing edge pressure is reduced giving a clear indication of the suppression of separation.

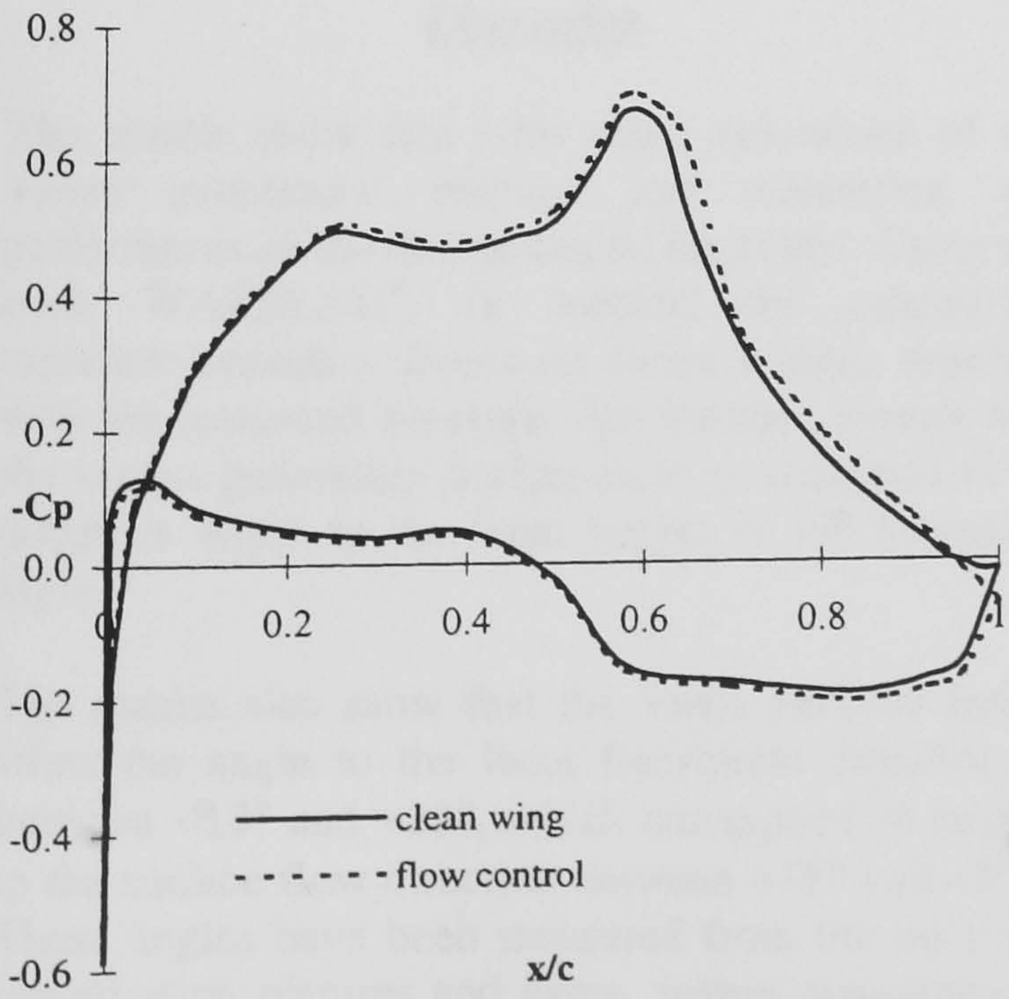

Figure 13a Pressure distribution comparison α = 0.4°

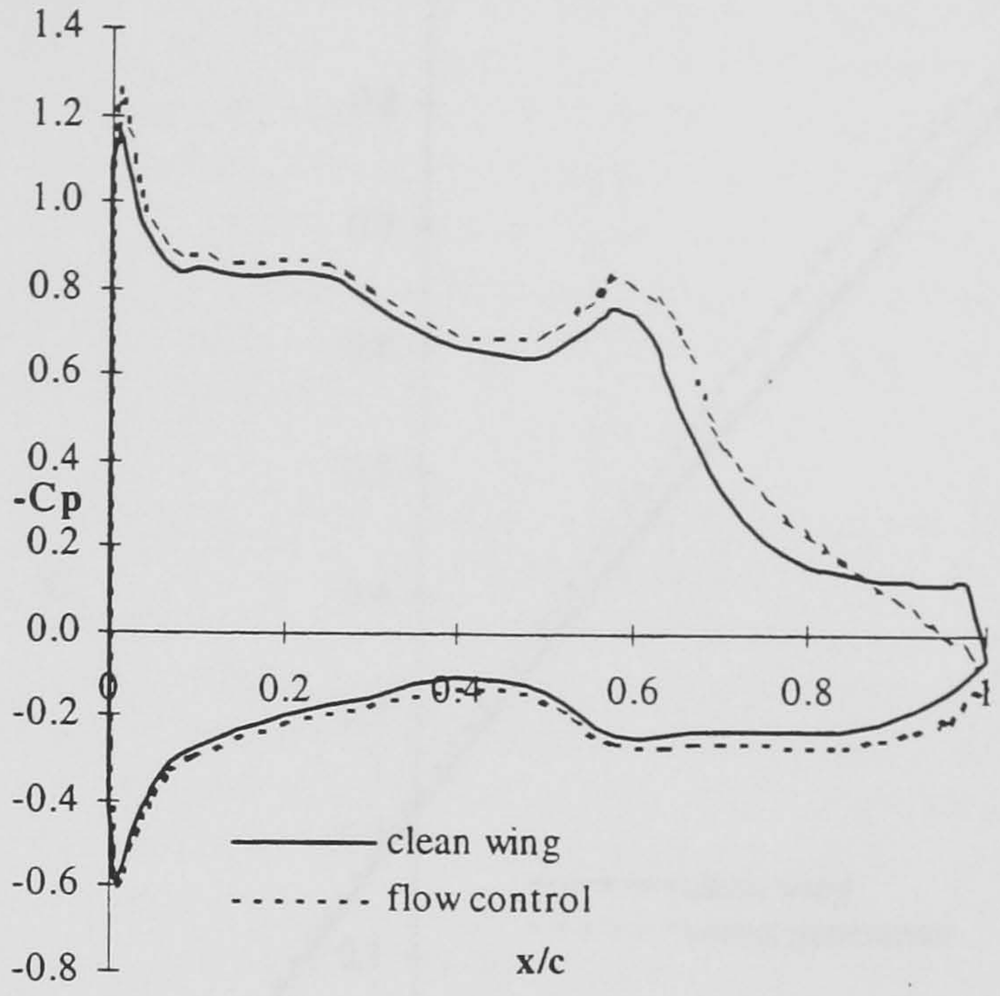

Figure 13b Pressure distribution comparison α = 6.8°

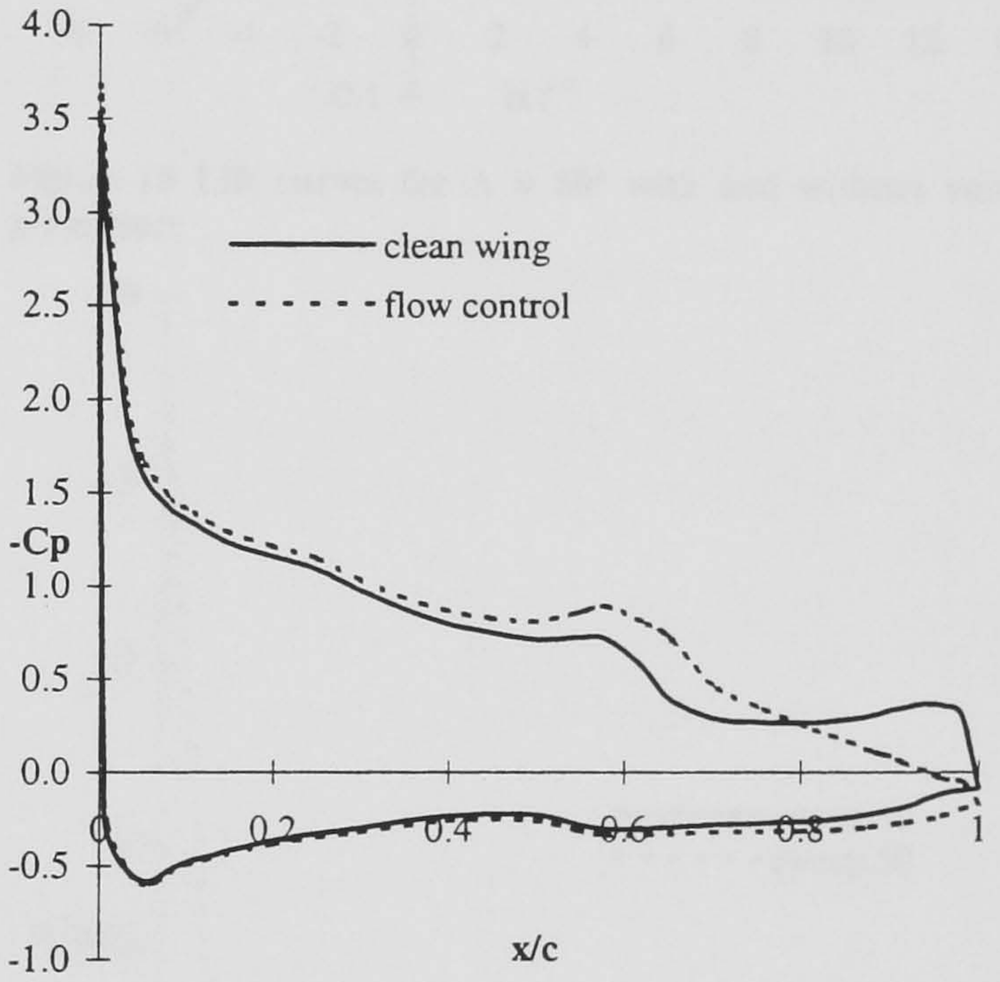

Figure 13c Pressure distribution comparison α = 12.1°

50° Swept Wing

Figures 14a and 14b show surface oil flow visualisation results for the wing swept to 50° with and without flow control. The vortex generators are positioned, from previous experience, at 0.65c and toed out to the freestream direction at +25°. From these photographs it is seen that the vortex generators effectively prevent separation as shown for the previous wing sweep with a similar flow control configuration (Figures 4 & 7b).

The lift curve, Figure 15, again shows a maximum increase in lift above that of the clean wing of approximately 8%. Figure 16 shows similar savings in k for both the 40° and 50° swept wings with a smaller saving on the 50° swept wing.

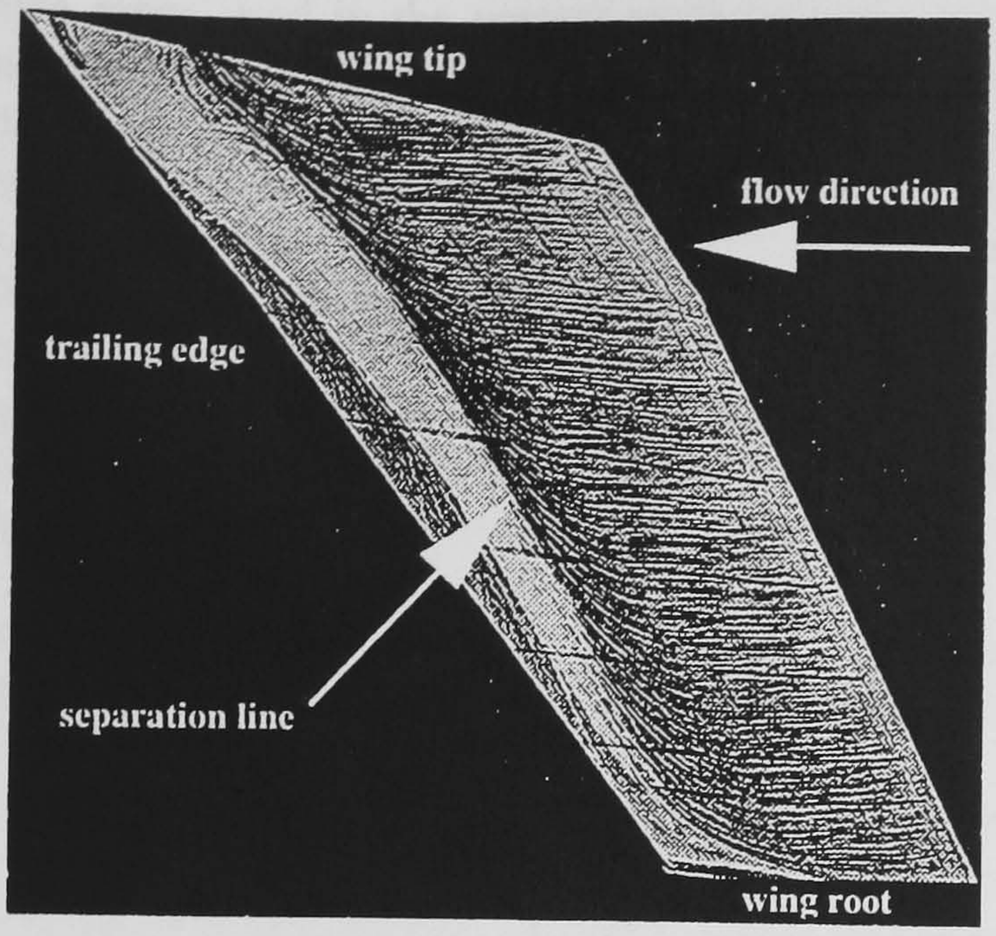

Figure 14a Clean wing oil flow. $\Lambda = 50°$, $\alpha = 6°$

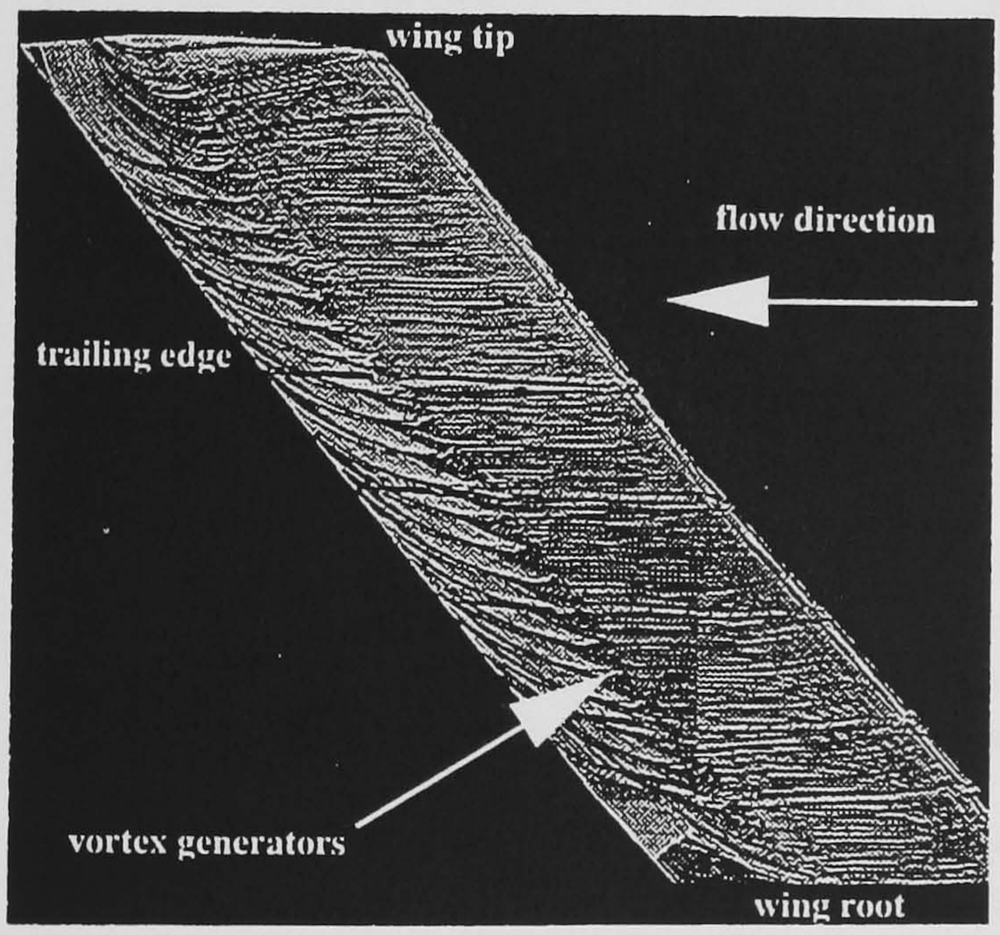

Figure 14b Oil flow $\Lambda = 50°$, $\alpha = 10°$, $x_{vg} = 0.65c$, $\phi = +25°$

Discussion

The results show that with small alterations of the vortex generators' position and orientation, the performance of the device can be improved. Using the code WAKELAG[4], (a method for calculating turbulent boundary layers on swept wings), together with the measured pressure distributions, reveals that the vortex generators performance is improved if its height is equal to the local height of the boundary layer.

The results also show that the vanes perform better when the angle to the local freestream direction is between +18° and +23°, which correspond to angles to the surface flow direction between +18° and +30°. These angles have been measured from the oil flow visualisation pictures and agree, within measurement

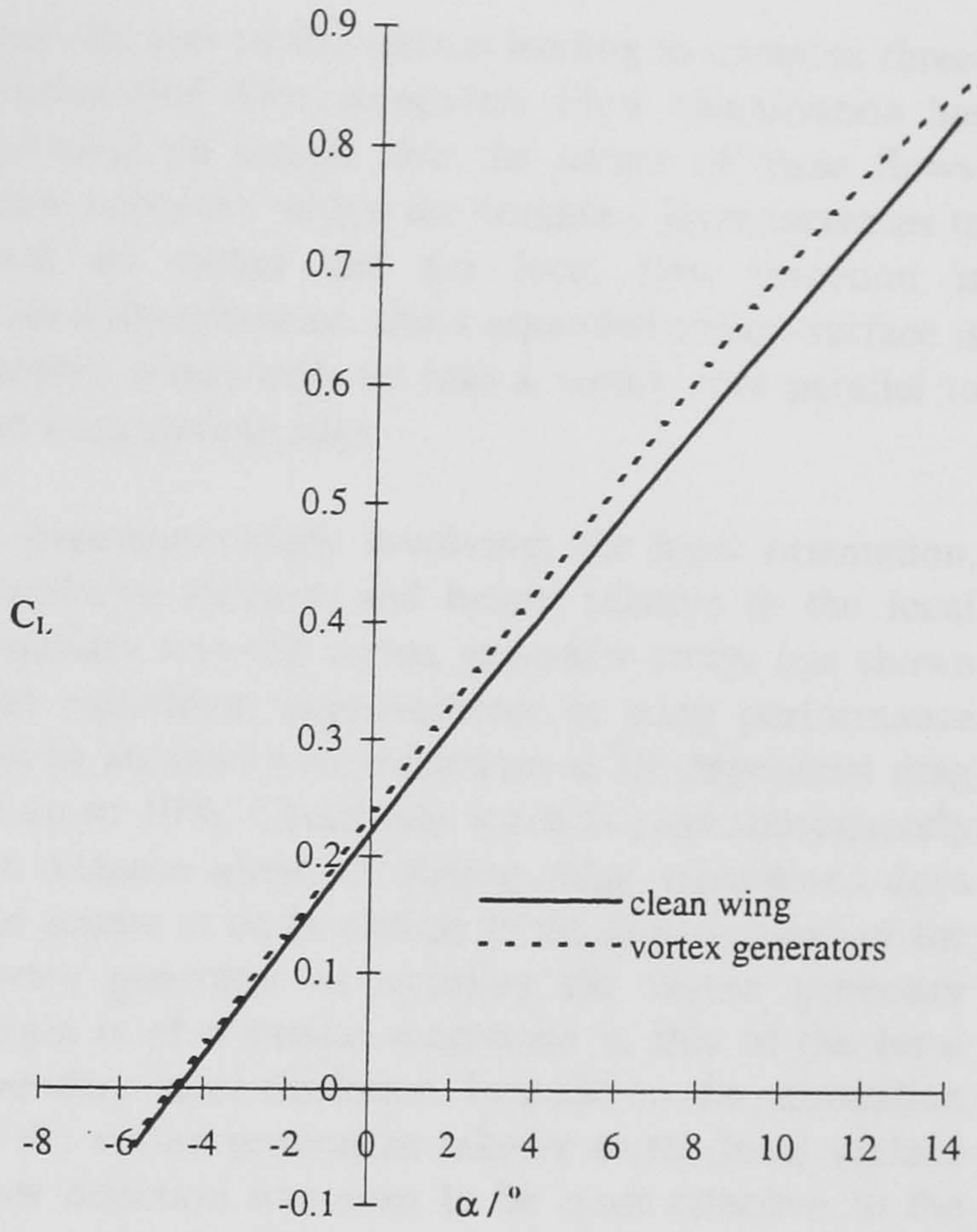

Figure 15 Lift curves for $\Lambda = 50°$ with and without vortex generators

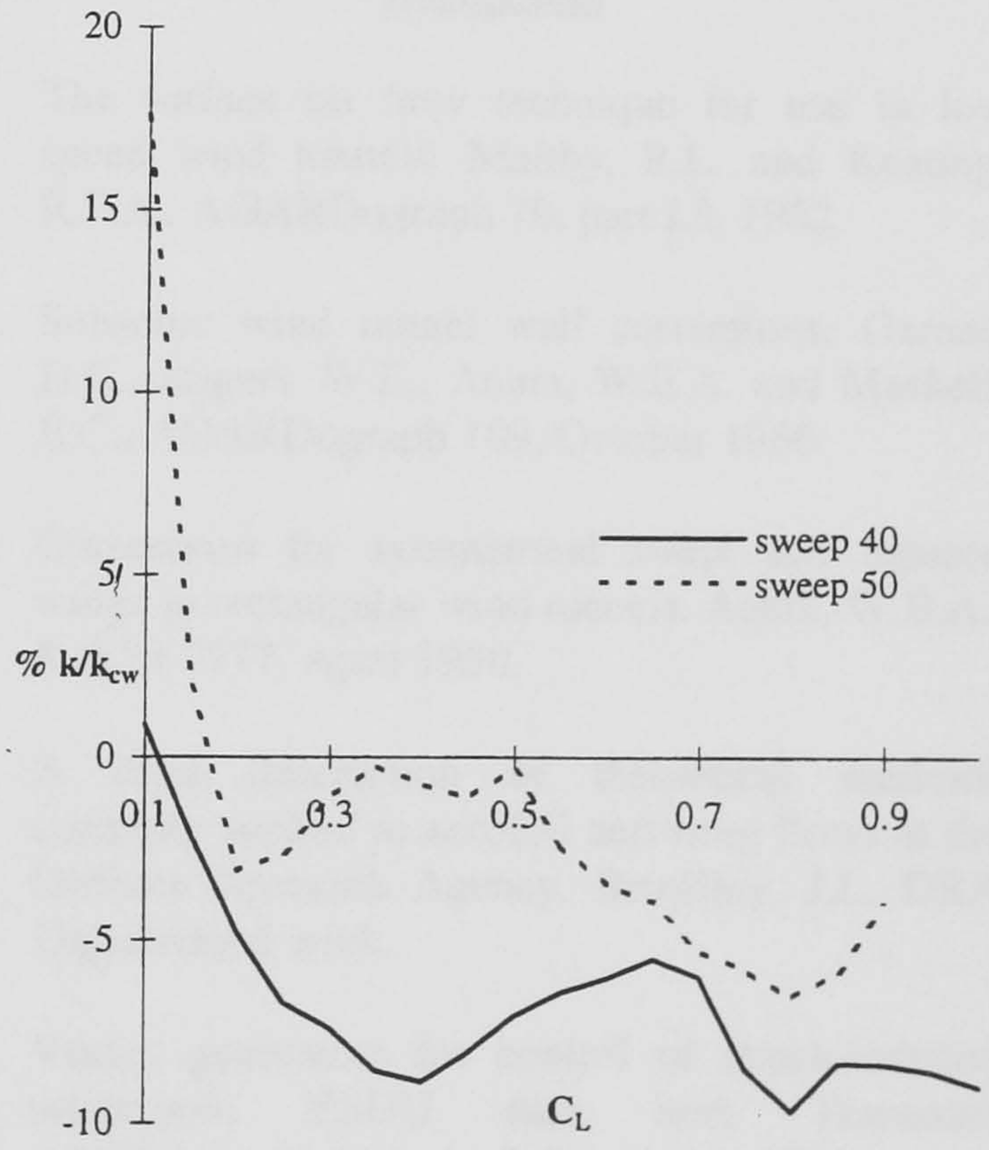

Figure 16 Comparison of lift dependent drag savings for 40° and 50° wing sweeps with vortex generators

error, with those calculated from the measured pressure distributions using WAKELAG[4]. The twist in the boundary layer between the surface flow direction and local freestream increases with incidence and chordwise position.

These results are similar to the guidelines given by ESDU[5] for positioning vortex generators, whereby the vane height should be approximately equal to that of the local boundary layer thickness and set to an angle

to the local flow direction of approximately 16°. The angle range used in the present study is larger than this due to the greater change in local flow direction with increasing incidence associated with swept wings. However the results show vortex generators work better closer to separation unlike those from the ESDU[5] guidelines, which recommend positioning the vortex generators further upstream from the separation position. The best chordwise position for the vortex generators in this study is only 0.05c upstream from the clean wing separation position.

These observations are believed to arise from five effects of the boundary layer.

1. The difference between the freestream flow direction and the flow close to the wing surface as separation approaches on swept wings produces strong shear layers through the boundary layer which can weaken the vortex and prevent its ability to control separation adequately if the distance between separation and the vortex generator is too great.
2. If the incidence of the vortex generator is too small then the strength of the vortex produced will not be sufficient to successfully overcome separation.
3. If the incidence of the vortex generator is too large the vortex it produces will breakdown reducing the separation control and increasing drag.
4. If the height of the vortex generator is greater than the local boundary layer thickness the vortex produced will be outside the boundary layer and not close enough to the wing surface to control the separation effectively.
5. If the height of the vortex generator is less than the local boundary layer thickness the vortex produced will be inside the boundary layer and weaker and will therefore not be able to control separation effectively.

The percentage improvement in drag and lift of the vortex generators on the 50° swept wing was not as great as that of the 40° swept wing because the positioning of the vortex generators was only optimised on the 40° swept wing. Time will need to be taken to optimise the positioning of the vortex generators on the 50° swept wing since there will be differences in boundary layer thickness and local flow directions compared to those of the 40° swept wing which will account for the drop in performance. However, the design guidelines from above appear to work at the higher wing sweep.

Conclusions

An experimental investigation using a highly swept wing planform with a constant cambered aerofoil is seen to generate strong adverse pressure gradients over the rear of the section leading to complex three-dimensional flow separation. Flow visualisation has provided an insight into the nature of these flows. Flow curvature within the boundary layer increases to such an extent that the local flow direction is eventually spanwise, and a separated stream-surface is created which rolls up into a vortex core parallel to the wing trailing edge.

A parametric study involving; the local orientation, chordwise location and height relative to the local boundary layer of vortex generator arrays has shown that significant improvements in wing performance can be attained with reductions in lift dependent drag of up to 10%. Chordwise location (and subsequently the distance ahead of trailing edge separation) does not appear to be as critical to the effectiveness of the vortex generator as ensuring the vortex generator height is of a similar magnitude to that of the local boundary layer thickness. In addition the orientation of the vortex generators relative to the local surface flow direction was seen to be most effective in the range +18° to +30° over a range of flow conditions.

References

1. The surface oil flow technique for use in low speed wind tunnels. Maltby, R.L. and Keating, R.F.A., AGARDograph 70, part I.3, 1962.

2. Subsonic wind tunnel wall corrections. Garner, H.C., Rogers, W.E., Acum, W.E.A. and Maskell, E.C., AGARDograph 109, October 1966.

3. Corrections for symmetrical swept and tapered wings in rectangular wind tunnels. Acum, W.E.A., R & M 2777, April 1950.

4. A brief description of theoretical methods currently applied to aerofoil and wing flows at the Defence Research Agency. Broadley, J.I., DRA Unpublished work.

5. Vortex generators for control of shock-induced separation. ESDU data item Transonic Aerodynamics, Volume 5, November 1996.

Acknowledgements

The authors would like to thank Dr Pat Ashill and Mr John Fulker of the DERA (Bedford) U.K. for their assistance with both the experimental programme and the preparation of this paper. Financial support for the first author was provided by the Engineering and Physical Sciences Research Council (EPSRC) and DERA (Bedford) under agreement 94316100 (1994).